A FINAL REPORT FROM THE

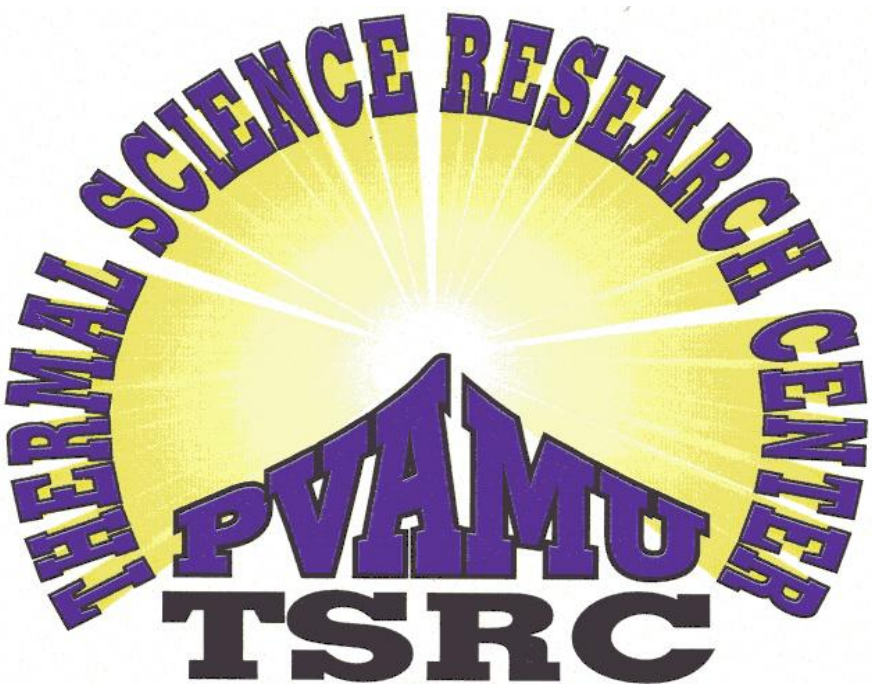

DIRECTOR: RONALD D. BOYD, Ph.D., PI
DISTINGUISHED PROFESSOR of MECHANICAL ENGINEERING, HONEYWELL ENDOWED PROFESSOR, DIRECTOR of the THERMAL SCIENCE RESEARCH CENTER (TSRC), and TEXAS A&M UNIVERSITY SYSTEM REGENTS PROFESSOR
ROY G. PERRY COLLEGE OF ENGINEERING
MS 2525/P.O. BOX 519
PRAIRIE VIEW A&M UNIVERSITY
PRAIRIE VIEW, TEXAS 77446-0519
PH: (936) 261-9962, 9971, or 9961
FAX: (936) 261-9974 or 5046
E-mail: rdboyd@pvamu.edu

INSTITUTE FOR HIGH HEAT FLUX REMOVAL (IHHFR): PHASES I, II, and III

FINAL REPORT

September 15, 1997 through August 31, 2014

Submitted to:

The U.S. Department of Energy (DOE)
Science Division
Office of Fusion Energy Sciences
Office of Science
SC-24/Germantown Building
1000 Independence Avenue, SW
Washington, D.C. 20585-1290

From the:
THERMAL SCIENCE RESEARCH CENTER (TSRC)

By:

Professor Ronald D. Boyd (PI), PhD
Distinguished Professor of Mechanical Engineering, Honeywell Endowed Professor of Engineering, Director of the Thermal Science Research Center (TSRC), and Texas A&M University System Regents Professor
Roy G. Perry College of Engineering
Prairie View A&M University
Mail Stop 2525
P.O. Box 519
Prairie View, TX 77446-0519
(936) 261-9962, 9971, or 9961
E-mail: rdboyd@pvamu.edu

Contracts #DE-FG02-97ER54452 and #DE-FG03-97ER54452

INSTITUTE FOR HIGH HEAT FLUX REMOVAL (IHHFR): PHASES I, II, and III

Ronald D. Boyd (P.I.), Distinguished Professor of Mechanical Engineering,
Honeywell Endowed Professor of Engineering, Director of the Thermal Science
Research Center (TSRC), and Texas A&M University System Regents Professor
Roy G. Perry College of Engineering
Prairie View A&M University
MS 2525/P.O. Box 519
Prairie View, TX 77446-0519
Phone: (936) 261-9962, 9971, or 9961
Fax: (936) 261-9974 or 5046

EXECUTIVE SUMMARY

Proir to the present funded work, the Thermal Science Research Center (TSRC) at Prairie View A&M University (PVAMU) has made significant contributions to high heat flux removal in plasma-facing components (PFC). In his 1994 Fusion Technology Paper (Reference [135]), R. D. Boyd predicted that the addition of a lower [than the monoblock] thermal conductivity (k) solid ring on the inside of a single-side heated flow channel would enhance the allowable incident heat flux. Later, international investigations such as Federici and Raffray (et al.) demonstrated [in References 153 and 154] that this enhancement could be higher than 30%. In the same paper, Boyd predicted that a void or material defect on the heated plane of symmetry near the inside of the flow channel could also enhance the high heat flux removal. In 2009, Escourbiac et al. [References 155] confirmed Boyd's prediction. Further, Boyd has made extensive fundamental critical heat flux measurements up to heat flux levels of 40.0 MW/m^2 and flow channel heated length to inside diameter ratio of 100.0. Boyd and his colleagues in the TSRC have extended his previous state-of-the-art contributions with additional contributions in the three phases of the Institute for High Heat Flux Removal.

As part of the present work, the TSRC at Prairie View A&M University has developed a new and unique high heat flux testing facility (Sections 2.0 through 11.0) for the study of high heat flux removal from simulation flow channels similar to those in plasma facing components (PFC) which are found in fusion reactors. This facility is part of the Institute for High Heat Flux Removal (IHHFR). In order to avoid the excess costs associated with using electron- or ion-beams to produce non-uniform high heat flux, this new facility was developed using DC electrical thermal power generation for the study of plasma-facing component (PFC) high heat flux removal using local three-dimensional conjugate heat transfer measurements and two-dimensional local subcooled flow boiling heat flux measurements. The facility is operational and

several speciality bus bars, test sections, and heater designs have been completed, constructed and tested. Although degassed and deionized water is the working fluid, the facility can be expanded to accommodate other working fluids. The facility consists of:

1. A 4.0 MPa closed water flow loop;
2. A 300.0 kW, 30.0 V D-C power supply for test section heating;
3. Utilities for the power supply;
4. A copper bus bar grid between the test sections and the power supply;
5. Monoblock and circular test sections (TS) and bus bar-TS interface;
6. An array of graphite heater elements;
7. Instrumentation and data acquisition; and,
8. A 250.0 kW, 30.0 V D-C power supply for the pre-heater.

The IHHFR focused on interdisciplinary applications as it relates to high heat flux engineering issues and problems which arise due to engineering systems being miniaturized, optimized, or requiring increased high heat flux performance.

The work in the IHHFR focused on water as a coolant and includes: (1) the development, design, and construction of the high heat flux flow loop and facility; (2) test section development, design, and fabrication; and, (3) single-side heat flux experiments to produce 2-D boiling curves and 3-D conjugate heat transfer measurements for single-side heated test sections. This work provides data for comparisons with previously developed and new single-side heated correlations and approaches that address the single-side heated effect on heat transfer. In addition, this work includes the addition of single-side heated circular TS and a monoblock test section with a helical wire insert. Finally, the present work includes: (1) data base expansion for the monoblock with a helical wire insert (only for the latter geometry), (2) prediction and verification using finite element, (3) monoblock model and methodology development analyses, and (4) an alternate model development for a hypervapotron and related conjugate heat transfer controlling parameters.

Conjugate heat transfer modeling has proved useful in forming baselines and identifying important parameters (Section 1.0) affecting peaking factors (PFs) and data reduction for the spectrum of high heat fluxes found in a wide variety of applications. For various applications requiring different fluids, the results show the following:

1. the coexistence of three flow boiling regimes inside single-side heated (SSH) flow channels (for water only),
2. the correlational dependence of the inside wall heat flux and temperature, and

3. inaccuracies that could arise in some data reduction procedures.

It is important to have the ability to verify conjugate heat transfer analyses used for predicting peaking factors (PFs) and local temperature gradients (and related thermal stresses) for SSH flow channels. The data produced in this work provide baselines for computational fluid dynamic codes.

The configurations studied consist of: (1) a SSH cylindrical-like test section with a circular coolant channel bored through the center, and (2) a SSH monoblock test section with a square cross-section and with a circular flow channel through the center line along its length. The theoretical or idealization of the cylindrical-like test section would be a circular cylinder with half of its outside boundary subjected to a uniform heat flux and the remaining half insulated. For the monoblock, a uniform heat flux was applied to one of the outside surfaces and the remaining surfaces were essentially insulated. The outside diameter of the cylindrical-like test section was 30.0 mm and its length was 200.0 mm. The monoblock square (cross-section) had 30.0 mm sides and the monoblock test section was 200.0 mm long. The inside diameter of the flow channel for both types of test sections was 10.0 mm. Water was the coolant. Thermocouples were placed at forty-eight locations inside the solid cylindrical-like or monoblock test section. For each of four axial stations, three thermocouples (at radial locations) were embedded at four (4) circumferential locations (0, 45, 135, and 180 degrees, where 0 degrees corresponds to that portion of the axis of symmetry close to the heated surface) in the wall of the test section. Finally, the mass velocity and exit pressure were varied in select cases.

The optimized design of one-side heated plasma-facing components (PFC) is dependent on knowing the local distribution of inside wall heat flux in the flow channels. The local inside wall heat flux can be obtain from selectively chosen local PFC wall temperatures close to the inside boundary of the flow channel. To this end, three-dimensional thermal measurements as noted above for all test sections were made (Sections 13.0 through 19.0) and show: (1) the three-dimensional variation of the flow channel wall temperature and (2) the resultant effects of thermally-developing laminar and turbulent flows on single-phase and local flow boiling on the 3-D wall temperature/outside heat flux relationship.

These results are very encouraging in that they:

1. are among the first full set of truly 3-D test section wall temperature measurements which contain the effect of conjugate heat transfer from thermally-developing laminar and turbulent, single-phase flow and flow boiling;
2. provide the basis, for the first time to obtain, 2-D boiling curves for single side heated

monoblock and circular test sections for the above noted flow conditions; and,

3. provide a unique two-phase, turbulent, flow boiling data base for SSH flow channels which can be used for comparisons with future computational fluid dynamic and heat transfer predictions.

After an extensive validation and verification finite element exercise (up to 50 MW/m^2 incident heat flux), a new high heat peaking factor simulation model (Section 20.0) was confirmed to produce accurate peaking factors for an incident heat flux up to at least 20 MW/m^2.

An alternate high heat flux removal study (Section 21.0) was made for a hypervapotron. The study identified: (1) a characteristic temperature and length, and (2) at least nine primary conjugate heat transfer high heat flux-side and wall controlling parameters.

The final comments in this summary deal with the evolution, structure, and other results of the "Institute for High Heat Flux Removal (IHHFR)." As in any endeavor, the most important aspects are the people involved. We have been fortunate in having over seventy (70) people contribute to the TSRC and over fifty (50) contribute to the IHHFR. See the Contributors' List on p. viii. These faculty, students, and staff worked together to develop, design, and build the IHHFR Laboratory which is presented in Appendix "A" in terms of a photo gallery [from the prospective of a newly hired undergraduate electrical engineering student]. The students and faculty were grouped into mentor-oriented conceptual design/development and testing teams. In some cases, selected students were allowed to register for an Internship Course as part of an IHHFR Need. Appendices "B" and"C" are examples of power-point presentations from these interships.

The IHHFR Laboratory has many new and noval devices and ideas--many of which could have been complied into patents. PVAMU and the Texas A&M University System provided support for one of our ideas to obtain a patent (US 6,824,305 B1). The patent (See Section 12.0) title is "Local Wall Heat Flux/Temperature Meter For Convective Flow and Method of Utilizing Same;" and the inventors were R. D. Boyd, A. Ekhlassi, and P. Cofie. Another example of a possible patent is the test section heater power distribution system (see Section 22.0 and Appendix B). This system was developed, designed, and built by one of the IHHFR Teams; and it measures the axial heater power distribution which was found to be approximately constant.

Section 22.0 presents results from the first phase of a correlation based on the above noted simulation. The correlation was compared with both the simulation model as well as finite element analysis predictions. The local predictions had very good comparative agreement for the

inside flow channel wall temperature, local heat flux, and peaking factor. Although proposed initially, the multi-material monoblock effect was not included in this work. However, an alternative analysis was completed for hypervapotron HHFR controlling parameters, 2-D temperature (and heat flux) distribution, and local peaking factor.

Section 24.0 contains a summary compilation of selected journal papers, conference/symposium presentations and publications, graduate theses, undergraduate projects and reports, project and poster presentations, graduate projects, student internships, and other reports. The extension of the above accomplishments may assist in the fulfillment of one ("Fusion Predictive Modelling") of four DOE *"Vision 2025"* Recommendations.

TSRC FUNDED CONTRIBUTORS*

Yasir Abbasi (G)
Mashlah Ali (U)
Emad Alzoebi (U)
Bernice Andrus (U)
Charles Balka (U)
Xavier Bennett (U)
Cordell Booker (G)
Brodny Carmichael (G)
Jermaine Chambers
Lisa Chenvert (U)
David Cheri, Jr. (U)
Kenneth Clark, Jr. (U)
Penrose Cofie (F)
Timothy Copeland (U)
Edward Cramer (U)
Abimbola Daramola (U)
Lori Davenport (G)
Corlisa Delesbore (U)
Ricardo Dunkley (U)
Kenneth Echols (U)
Ali Ekhlassi (F)
Richard Ellis (U)
Alicia Garrett (G)
Vivian Glover-Simmons (S)
Christian Guzman (U)
Reginald Harrison (U)
Shibee Hashem (U)
Shannon Halloway (U)
Randy Haynes (U)
Abdi Hussein (U)
Kenesha Hyatt (U)
Abdilqadir Jama (G)
Shawanna Jones (U)
Daniel Kalmus (U)
Kevin Lee (S)
Anthony Mack (U)
Francois Martin (U)
Richard Martin (U)
Haydn Maughan (G)
Aaron May (G)
Andrea McDade (S)
Ronhoward McNeil (U)
Xi Wei Meng (G)
Divine Mofa (U)
Cheryl Moore (S)
Dequan Nelson (U)
Gift Ngo (U)
Avione Northcutt (U)
Semaj Northcutt (U)
Charles Nyagami
David Ogbuaku (G)
Idara Okopide (U, G)
Quaid Peatiwala (G)
Jervale Phillips (U)
Nichole Pope (U)
Aris Poweranto (U)
Kenneth Rhoder (U)
Daniel Riley (U)
Mitchell Sands (U)
Levon Shade (U)
Alvin Smith (G)
Marcella Strahan (U)
Anthony Thomas (U)
Jerry Turknett (G)
Desmond Uzor (U)
Johnathan Walker (U)
David Wallace (U)
Arkesha Williams (U)
Donald Williams (U)
Eryka Williams (U)
Hongato Zhang (G)
Ronald D. Boyd (P.I., F)

*Faculty (F); Graduate Student (G); Staff (S); Undergraduate Student (U); and Principal Investigator (PI).

INSTITUTE FOR HIGH HEAT FLUX REMOVAL: PHASES I, II, and III

TABLE OF CONTENTS

NOMENCLATURE

A_H	outside heated surface area = 5.0tL (m^2)
a	related to the eigenvalues for Domain I_1
a_a	parameter for the thermal hydraulic diameter
A_b	total surface area of the top inner flow channel surface without the fins being added to that surface
A_c	cross section area of flow channel, m^2
A_T	total surface area of the top inner flow channel surface including the fins
AR	H_c/w_c, $(H_c-L_f/2)w_c$
Bi	Biot number, $h_m r_i/k$
Bi_m	$h_m \, r_i \diagup k$
$Bi_{w_{c_n}}$	See eq. (21-21c)
CHF	critical heat flux, (W/m^2)
D	coolant channel inside diameter, (m)
D_h	Hydraulic diameter, m
D_i	flow channel inside diameter, (m)
D_T	thermal-hydraulic diameter $D_T = a_a D_i$, m
E	related to the eigenvalues for Domain I_2
G	mass velocity (kg/m^2s)
Gz	Graetz number Re Pr $(L_H/D_i)^{-1}$
H	outside height of HV (see Fig. 224)
H_1	$H-2H_c-t$
H_c	one-half of the height from the base (or root) of the fin to the bottom inside surface of the HV flow channel (see Fig. 223)
$h(\varphi)$	Circumferentially varying flow channel inside wall convection heat transfer coefficient, W/m^2K
$h(\varphi)_1$	local circumferential heat transfer coefficient (HTC) for the inner circular flow channel boundaries
h	local heat transfer coefficient
h_{eq}	equivalent HTC for the upper hypervapotron (HV) inner flow channel surface (see eq. 21-1)
h_f	mean HTC of the HV finned surface
h_i	two-dimensional inside flow channel heat transfer coefficient distribution (W/m^2K)
h_m	mean circumferential heat transfer coefficient ($W/m^2 K$)
h_{m_1}	mean flow channel HTC
h_1	mean HTC of the HV finned side surfaces and bare surface between fins
h_2	mean HTC on the HV flow channel inner vertical
h_3	mean HTC on the HV flow channel inner bottom surface
i	specific enthalpy, kJ/kg
k	thermal conductivity of test section (TS), (W/mK)
k_1	mean flow channel wall thermal conductivity
k_{solid}	mean flow channel wall thermal conductivity
k_f	thermal conductivity of the fluid, (W/mK)
kVA	maximum operating voltage of the power supply system times its maximum current; kVA has been mistakenly considered to be synonymous with kilowatts. (kilovolt-amperes)

kW	This is the amount of power the system is capable of handling. It differs from kVA in an alternating current (AC) system. However, in a direct current (DC) system it has the same definition as kVA. (kilowatts)
kWh	This is the amount of energy dissipated when a power of one kW is sustained over a period of one hour.
k(T), k	Thermal conductivity of the flow channel, W/mK
L	heated length of the flow channel, m
L_f	length of the HV fin
L_H	heated length (m)
L_i	unheated inlet portion of the flow channel, m
L_o	unheated outlet portion of the flow channel, m
L^*	reference length
MCM	10^3 circular mils, which is the square of the diameter of a wire when the diameter is expressed in thousands of an inch
N_u	Nusselt number with temperature dependent properties evaluated at the local film temperature
Nu_o	Nusselt number with temperature dependent properties evaluated at the local bulk fluid temperature
Nu_{D_T}	local Nusselt number, h D_T/k_f
n	interger
P	exit pressure, MPA
PF	Peaking factor, $q''_{wi)_{\max}} / q''_{oo}$
PF_1	$\left[q'' \big\|_{inner\ wall} \right]_{\max} / q''_{\infty}$
P_{exit}	exit pressure of coolant (MPa)
P_{mean}	Mean flow pressure, MPa
P_R	electrical resistivity of the heater ($\Omega \cdot$ m)
Pr	Prandtl number
q	applied single-side heat flux (W/m^2)
q_i	two-dimensional inside flow channel wall heat flux distribution (W/m^2)
q_{i_1}	inside heat flux used in reference [16]
q_o	net rate of thermal energy transferred to the fluid in the TS, kW
q_{o_1}	single-side, incident, absorbed heat flux used in reference [16]
q''	heat flux, kW/m^2 or local radial monoblock wall heat flux, kW/m^2
q''_*	dimensionless local radial heat flux, $\frac{-q''(r,\varphi)}{R_0 q''_\infty}$
q''_1	local heat flux
q''_i	2-D (ϕ and Z) flow channel inside wall heat flux (also referred to as Inside HF), kW/m^2
q''_o	averaged, net incident (absorbed) heat flux (also referred to as incident HF), which is equal to the ratio of q_o to the outside heated surface area (Lw) of the TS, kW/m^2
q''_{oo}	incident heat flux, kW/m^2
q''_{∞_1}	`single-side, incident, absorbed heat flux
$q''_{wi)_{\max}}$	Peak value of q''_{wi}, W/m^2
R	r/r_i

R_1	radial coordinate used in references [3] and [16]
Re	Reynolds number, $G D_i/\mu$
R_o	aspect ratio, r_o/r_i
r	radial coordinate of the TS, m
r_i	inside radius of the flow channel, m
r_{i1}	inside flow channel radius used in references [3] and [16]
r_o	outside radius (and a function of ϕ) of the test section, m
r_{o1}	outside flow channel radius used in references [3] and [16]
R_o	Aspect ratio, r_o/r_i
r_1	radial location of embedded thermocouple closet to the inside radius of the flow channel, m
S	fin pitch
T	temperature, ^{0}C
T_1	local flow channel wall temperature
T_b	bulk temperature of the fluid, ^{0}C
T_{b1}	bulk temperature of coolant
TC	thermocouple
T_f	film temperature of the fluid, ^{0}C
T_{fdb}	onset of fully-developed boiling TS inside wall temperature, ^{0}C
T_{ONB}	onset of nucleate boiling TS inside wall temperature, ^{0}C
T_{ref}	Reference temperature, ^{0}C
T_{sat}	Saturation temperature, ^{0}C
T^*	dimensionless wall temperature difference (referred to as T STAR in plots) $[\theta/(q_o'' r_o/k)]$
T_{av}^* (R)	average circumferential value of T^* (referred to as AVERAGE T STAR in plots)
T_{inlet}	inlet bulk temperature (K)
T_i	two-dimensional inside flow channel wall temperature distribution (K)
T_{sat}	saturation temperature of the fluid at the exit pressure of the TS, ^{0}C
T_w	local wall temperature, ^{0}C
T_{wi}	inside TS flow channel boundary temperature, ^{0}C
$T_{wi)_{max}}$	Peak value of T_{wi}, ^{0}C
$T_w(r,\varphi)$	Local wall temperature, ^{0}C
T_{w1}	inside TS flow channel boundary temperature, ^{0}C
THW	special electrical cable with unique thermal and water resistance characteristics
TS	test section
T^*	reference temperature
t	heater thickness (m) or HV upper wall thickness from the surface with the single-side incident (absorbed) heat flux to the root or base of the fins (see Fig. 223)
$\left(\frac{\partial T}{\partial n_i}\right)_{max}$	inside flow channel maximum wall temperature gradient
V	heater voltage potential (V)
v	Fluid velocity, m/s
W	outside width of the HV (see Fig. 223)
w	heater width, m
w_c	HV inside flow channel half width
w_f	width of the HV flow channel slots on either side of the fins (see Figs. 222 and 223)

w_1	test section width, m
x	x-coordinate (e.g., see Fig. 223)
x_1	w/2-x (e.g., see Fig. 231)
y	y-coordinate (e.g., see Fig. 226)
y_2	H_c + t
y_3	H – t - Hc
Z	local axial coordinate with origin at the beginning of the TS heated section, m
Z_j	axial coordinate location for axial sections A-A ($Z = Z_4$), B-B ($Z = Z_3$), C-C ($Z = Z_2$), and D-D ($Z = Z_1$) where j = 1, 2, 3, or 4

Greek Symbols

η_o	overall fin surface efficiency
Θ	wall temperature excess above the bulk fluid temperature, ^{0}C
Θ^*	dimensionless wall temperature excess, $\frac{\Theta(r,\varphi)}{\left(\frac{q''_{oo}\, r_o}{k}\right)}$
θ	temperature and/or temperature difference (relative to T_b) used in each of the domains
$\theta\,(r,\phi)$	temperature excess above the bulk fluid temperature [$T\,(r,\phi) - T_b$]
ϕ	circumferential coordinate of TS ($\phi = 0$ on the heated side of the TS plane of symmetry), degrees
ϕ_1	circumferential coordinate with the origin at the heated side of the plane of symmetry of the coolant channel
ϕ_∞	half angle used in references [140 and 142] and shown in Figures 212 and 234
φ	circumferential coordinate with an origin shown in Fig. 2, degrees
λ	eigenvalue
δ	fin thickness
μ	dynamic viscosity, kg/ms

Subscripts

f	refers to a specific fin characteristic
n	integer index for the eigenvalues
I	index used for Domain I
I_1	index used for Domain I_1
I_2	index used for Domain I_2
II	index used for Domain II
III	index used for Domain III
IV	index used for Domain IV
V	index used for Domain V

1.0 SINGLE-SIDE CONJUGATE HEAT TRANSFER MODELING FOR HIGH HEAT FLUX COOLANT CHANNELS

1.1 INTRODUCTION

In the development of plasma-facing components (PFCs), many investigators have been investigating the effect of a single-side applied heat flux on the onset of local coolant boiling and the eventual critical heat flux (CHF). Although encouraging results have been obtained in characterizing peaking factors for local two-dimensional boiling curves and critical heat flux, additional experimental data and theoretical model development are needed to validate the applicability to PFCs. Both these and related issues will affect the flow boiling correlation and data reduction associated with the development of PFCs for fusion reactors and other physical problems that are dependent on conduction and conjugate heat transfer modeling in the heat flux spectrum of applications--which range from micro- to mega-heat flux levels. Both exact solutions and numerical conjugate analyses are presented for a one-side heated (OSH) circular flow channel with an outside circular boundary. Water is the channel coolant. The results show: (a) the coexistence of three flow regimes inside an OSH circular geometry, (b) the correlational dependence of the inside wall heat flux and temperature, and (c) inaccuracies that could arise in some data reduction procedures.

The conduction and conjugate heat flux spectrum ranges from very low absolute heat fluxes found in living systems to mid-range heat fluxes found in electronic systems to very high heat fluxes found in fusion reactor systems. Some commonalties in all such systems include the following two characteristics: (a) The applied heat flux is from one side or a portion of the entire surface, and results in multidimensional thermal conduction, and (b) other modes (convection, boiling, radiation, etc.) of heat transfer are also significant. This portion of the report deals with an example of such systems in the upper part of the conduction heat flux spectrum, namely, fusion reactor components.

One of the most critical technological needs to ensure the reliability of fusion reactor operation in the twenty-first century is the ability to accommodate the high heat fluxes generated near the PFCs. Accordingly, it is essential to have the ability to accurately predict the local heat transfer throughout the coolant channels of PFCs. The maximum value of the local heat flux,

which allows a safe channel wall temperature much below the wall melting temperature when water is the coolant, is below the CHF. An applied heat flux that is greater than the CHF may (will for uniformly heated channels; e.g. See Youchison [1], Celata and Cumo [2], Gaspari and Cattadori [3], Marshall [4], Schlosser et al. [5] and references [6-12]) cause local channel wall melting (burnout). It has been demonstrated that among the important parameters affecting the reliable correlation and prediction of the CHF are:

1. flow regime and flow parameters,
2. the applied heat flux profile, and
3. peaking factors for one-sided heated (OSH) PFC geometries relative to uniformly heated geometries (UHG).

Although the capability of consistently predicting the local flow boiling curve has been demonstrated for UHG, this capability must be extended to more complex PFC geometries (see Fig. 1). One possibility for this extension is discussed using a reference diameter for all heat transfer correlations that is based on an integral energy balance.

Sample conjugate heat transfer computations are presented specifically for water and are used to describe the circumferential variations in both the inside wall temperature and heat transfer coefficient. Next, a numerical study is presented and points to precautions for data reduction. This section of the report concludes with the presentation of conjugate heat transfer modeling results that are fluid independent. In this regard, other coolants in addition to water are being considered by other investigators for high-heat-flux PFCs.

Accurate peaking factor (PF) determination depends on the ability to both accurately predict the flow boiling curve for simple geometries and account for the complications in the prototype due to geometry and other effects. In this section of the report, the PF is defined [this definition will change later] as the ratio of the inside wall maximum heat flux for an OSH geometry to the inside wall maximum heat flux for an UHG, with the same flow conditions. Many papers have been published recently reporting either new flow boiling correlations (e.g., Boyd and Meng [6]), or assessments (Hall and Mudawar, [13,14], Celata et al., [15]; and Katto, [16]) and modifications of previously developed CHF correlations. Generally, there appears to be good confidence in predicting flow boiling for uniformly heated (UH) circular channels with or without twisted tapes. However, all PFCs involve OSH flow channels like that shown in Fig. 1. This poses the following questions:

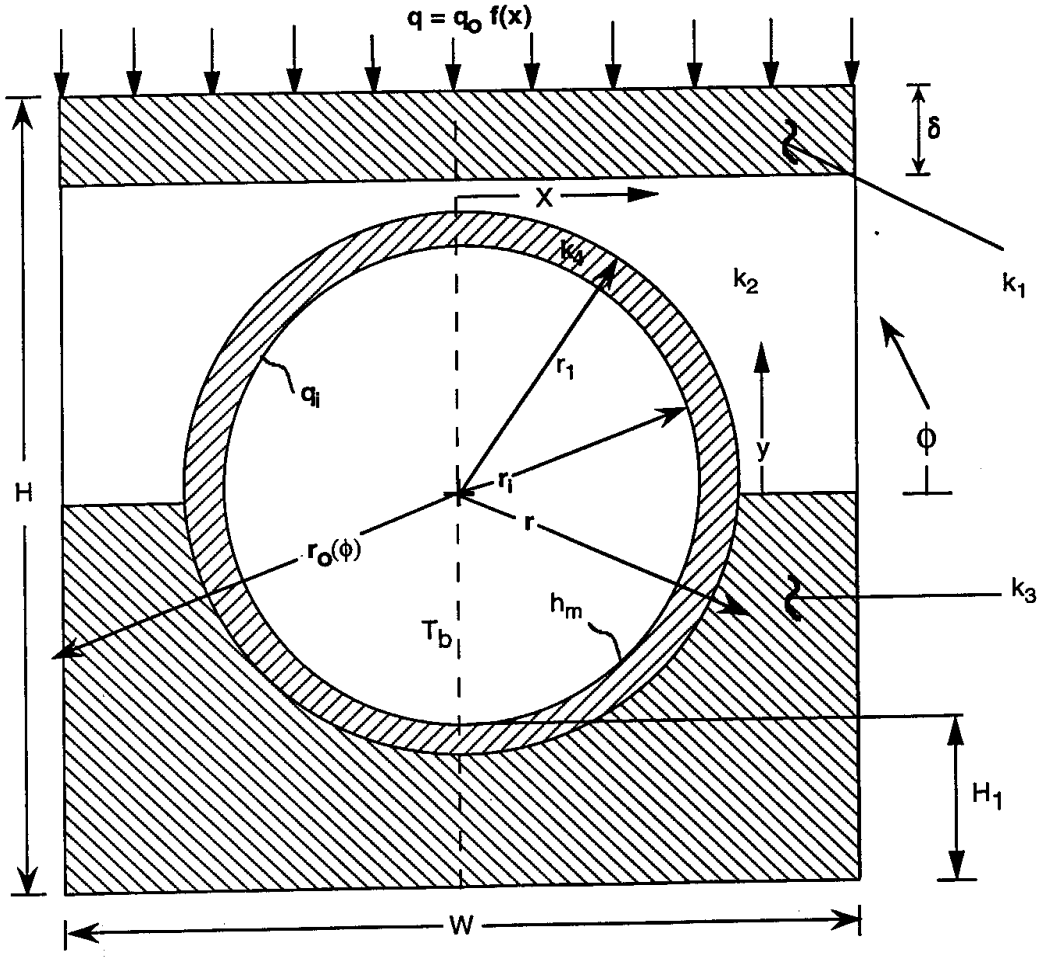

Figure 1: OSH Saddle Block Configuration That May be Found in a PFC (Note: In the prototype, f = f(x,z)).

How can the UH data be used for the OSH channels? The answer to this question lies in the existence of PFs. The intent of many ongoing investigations is to use the PFs along with the UH data to compute accurate conditions for CHF in OSH channels.

International efforts (e.g., Akiba et al., [17] Araki et al, [18,19] Baxi et al., [20] Boscary et al., [21,22] Boyd et al., [12,23] Boyd and Meng, [24] Escourbiac and Schlosser, [25] Falter and Thompson, [26] Marshall et al., [27] Inasaka and Nariari, [28] TORE SUPRA team, [29] and Youchison et al., [1]) are ongoing to produce enough OSH data to determine the appropriate

functional representations for the PFs. It has been demonstrated previously by Boyd [30] that the PF is dependent on: (a) the channel geometry, (b) incident heat flux profile, and (c) a characteristic Biot number. Although the PF has been defined and characterized for simple OSH geometries, few if any unified comparisons have been made with data. Several authors (e.g., Akiba et al., [17] and Inasaka and Nariari, [28]) have proposed empirical PF correlations, but these have not been proven to be consistently applicable for the full range of flow parameters and the wide range of PFC geometries.

1.2 SINGLE-SIDE HEAT TRANSFER

Currently, many investigators are using existing heat transfer correlations based on a uniform heat flux boundary condition to characterized the variation in h(ϕ) for systems that are subjected to a single-side heat flux. This has usually been accomplished using a finite element analysis with the convective boundary condition defined in terms of a heat transfer correlation for h. Because of the conjugate and nonlinear nature of this problem, the computations must be performed iteratively, where h should be computed at the local values of the circumferential heat flux and wall temperature.

The successful prediction of the local wall heat flux and temperature using heat transfer coefficient correlations depends, of course, on an appropriate definition for a reference diameter D_{ref}, which should be used in the heat transfer correlation that will result in the correct variation of h(ϕ) and inside wall temperature. This value of D_{ref} must satisfy the following equation for a single-side heated circular cylinder with inside and outside radii, r_i and r_o, respectively:

$$\int_{\pi/2}^{3\pi/2} h(\phi)\left[T_w(\phi) - T_b\right] r_i d\phi = \int_{\pi/2}^{3\pi/2} r_o q(\phi) d\phi, \tag{1-1}$$

where the applied external heat flux is q(ϕ), and T_w is the inside wall temperature. Although the definition of D_{ref} satisfies the conservation of global energy, it is not clear at this point whether a unique quantity will be capable of both satisfying a local conservation of energy at any ϕ and be completely sufficient in characterizing the conjugate problem. The following assumption is usually used: D_{ref} can be approximated to be the thermal-hydraulic diameter D_T, which is equal to four times the ratio of the flow cross-sectional area to the heated perimeter.

The feasibility of using D_T was examined using a closed form solution of the wall temperature distribution for the case of a circular channel heated externally from one side for the

circumferential coordinate ϕ ranging from -90.0 to +90.0 degrees. The remaining half of the channel was insulated. For this example, the flow was considered to be one with high velocity and highly subcooled water with an inlet temperature of 20.0 ^{o}C, a mass velocity of 30.0 Mg/m^{2}s, and subjected to an external single-side heat flux of 25.0 MW/m^2. The tube inside and outside diameters were 0.3 and 0.405 cm, respectively. The heated length was 28.97 cm and local heat transfer computations were performed at an axial location Z of 28.66 cm.

As was described earlier, an iterative computation was performed with convergence being assumed when Eq. (1) was satisfied. The mean heat transfer coefficient h_m was computed from each successive distribution $h(\phi)$. Finally, the updated distribution for $h(\phi)$ was obtained from the values of T_b at Z and the computation of inside wall heat flux $q_i(\phi)$ and temperature T_w from the exact solution using h_m as given by Boyd [30].

For these noted conditions, Fig. 2 shows that $h(\phi)$ varies significantly by a factor of 2.0 from the top of the heated portion to the bottom of the unheated portion of the channel. Also shown are the regions in which the flow structure vary in the circumferential direction from a single phase at the bottom of the channel to a subcooled partial nucleate boiling structure and finally to a fully developed boiling regime at the top of the channel. It is important to note that these computations predict *the coexistence of three very different flow regimes at one axial location*. The corresponding computations for T_w are shown in Fig. 3. The solid lines in Figs. 2 and 3 represent $h(\phi)$ and $T_w(\phi)$, respectively, computed using Eq. (1); D_T; $q_i(\phi)$; $T_b(Z)$; and the Boyd-Meng correlation [12]. The dotted curve results when h_m = constant = 163.57 kW/m^{2}K (from Fig. 2) is used rather than $h(\phi)$. As expected, the region where boiling occurs is essentially isothermal (see Fig. 3). As emphasized earlier, $h(\phi)$ was computed iteratively using an initial guess for h_m. Although present computations emphasize the large variation of $h(\phi)$, it should be emphasized that these computations are approximate and serve to emphasize the large circumferential variations of *both* $h(\phi)$ and flow regimes in OSH geometries.

As noted earlier, the subcooled flow boiling (SFB) [12] curve model predicts all three flow regimes (single phase, partial nucleate boiling, and fully developed boiling) to coexist around the perimeter of the OSH circular channel. *This coexistence was postulated by Boyd et al. [31] more than three decades ago*. However, quantitative comparisons must be made to determine how well the current approach compares with experimental data. Although the exact

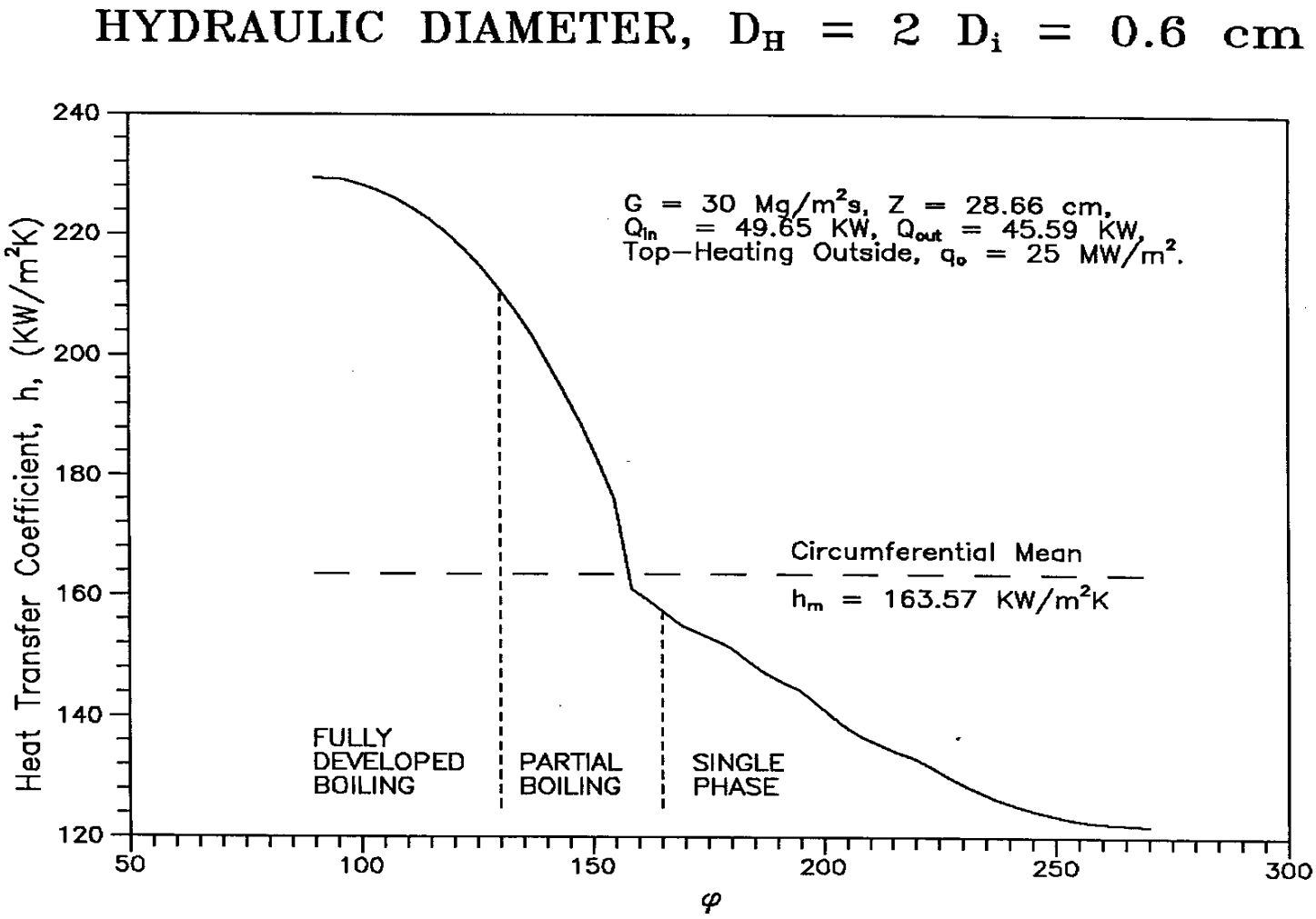

Figure 2: Computed Circumferential Heat Transfer Coefficient Distribution Due to Simultaneous Water Flow Boiling and Single-Phase Convection and using D_T and the Modified Boyd-Meng [12] Boiling Curve Model for Water (φ= 90 deg at the axis of symmetry on the heated surface).

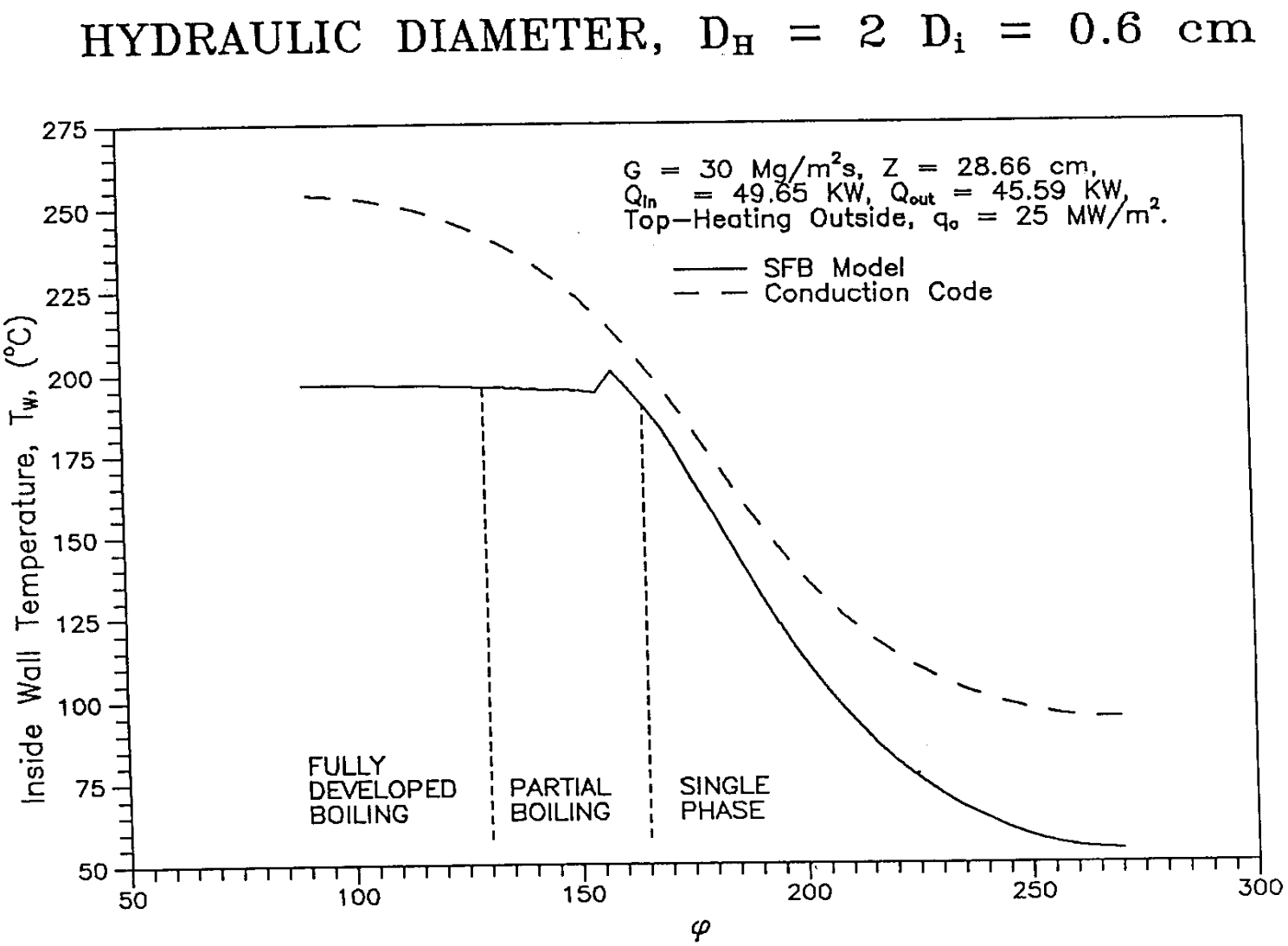

Figure 3: Prediction of a Local Circumferential ϕ Variation in the Wall Temperature Due to Simultaneous Water Flow Boiling and Single-Phase Convection and Using a Constant (dotted line) and Variable [12] (solid line) Circumferential Heat Transfer Coefficient (φ= 90 deg at the axis of symmetry on the heated surface).

form of the characteristic length for the SFB model in this approach is quite complex but is well defined by an energy balance [i.e., Eq. (1)], the characteristic length that resulted in acceptable results (~ 5.0% inaccuracy in some cases) was the thermal-hydraulic diameter D_T. To confirm that this thermal-hydraulic diameter approach does result in consistently good predictions of the local wall temperature and heat transfer coefficient for a wide variety of OSH channels, data must be generated for such comparisons. Currently, this is being done by a few international research and development groups (referenced previously). If comparisons prove to be discouraging, the exact form of the characteristic diameter should be used rather than the thermal-hydraulic diameter for final and accurate predictions. However if the comparisons are encouraging, D_T would be preferred because of its simplicity.

1.3 DATA REDUCTION

1.3.1 Numerical Example

To examine the direct applicability of UHG flow boiling correlations to two- and three-dimensional geometries, measured channel wall temperatures must be used to determine circumferential variations in the local heat transfer coefficient. Well-established inverse conduction techniques can be used to this end. However, because both the circumferential wall temperature and heat flux variations on the inside of a given coolant channel can be significant, many factors affect the reliability of the two- or three-dimensional numerical data reduction. An example of one such subtle factor will be considered. In this example, a bare copper tube (L = 286.6 mm; D = 6.0 mm; wall thickness = 1.05 mm) was subjected to an OSH flux of 25.0 MW/m^2 with T_b = 344.4 K. Four hundred circumferential nodes and nine radial nodes were used in the finite element analysis. In this example (Huque et al. [32]), the nodal radial centroidal distance between the innermost radial node and the inside channel surface was varied from 0.00025 to 0.0526 mm. This example required (idealization) the heat transfer coefficient on the inside wall to be constant (151.9 kW/m^2K). However, Fig. 4 shows that good or acceptable data reduction resulted only for the centroidal distances < 0.0025 mm. Later computations showed that the number of circumferential nodes had to be increased from 400 to 4000 for consistently accurate results.

1.3.2 Exact Solutions

Exact solutions for an OSH circular channel are very useful for the following purposes:

1. To serve as baseline cases for inverse analysis accuracy verification;

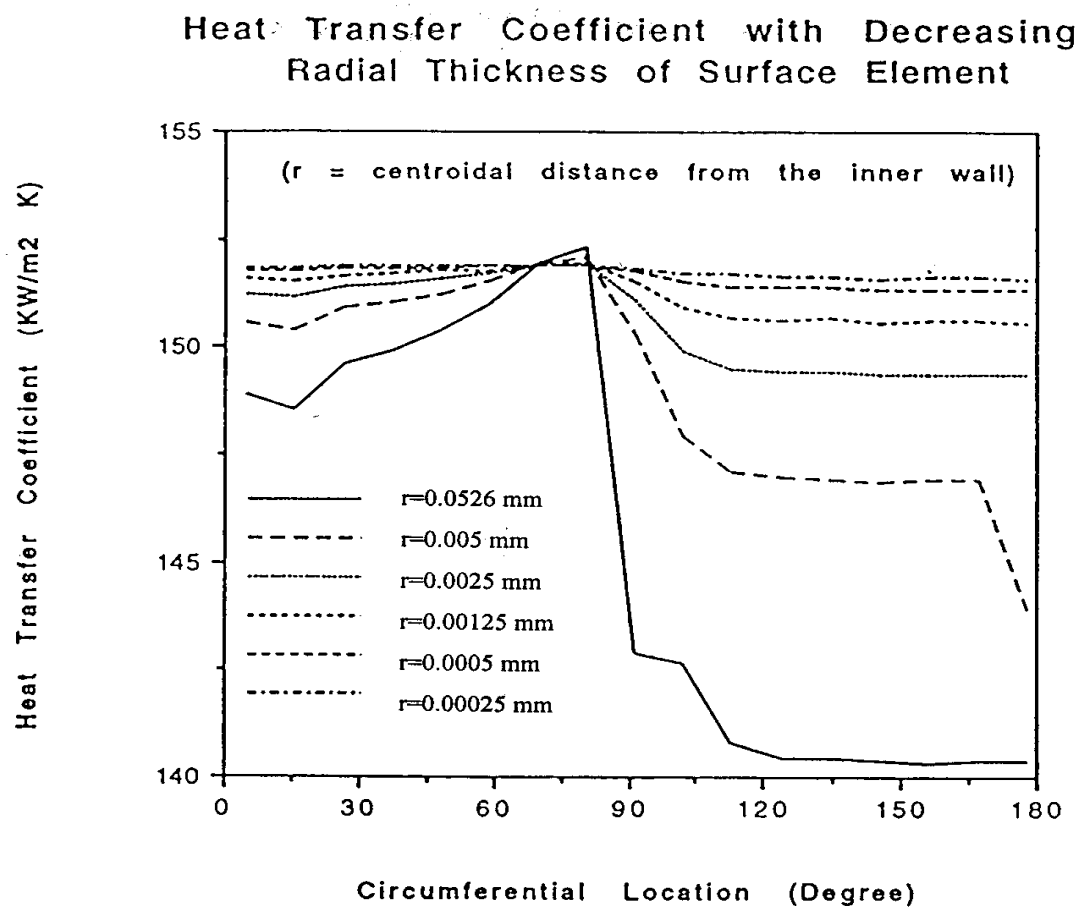

Figure 4: Circumferential Variation of Inside Heat Transfer Coefficient as a Function of the Centroidal Distance of the Innermost Elements from the Inside Wall Surface [32].

2. To provide a means of using temperature measurements to estimate the mean heat transfer coefficient;
3. To use external channel temperature measurements to infer the temperature variations on the inside of the flow channel; and
4. To identify some of the thermophysical parameters that influence PFs (Boyd [30]).

Consider a circular channel with inside and outside radii r_i and r_o, respectively, and constant thermal conductivity. For the case of a constant mean inside heat transfer coefficient h_m, Boyd [30] produced the exact solution for an outside uniform heat flux applied to one side of a circular channel, with the remaining side perfectly insulated. In experiments where the outside channel circumferentially averaged temperature T_{av} for this configuration is measured, the following expression relates T_{av} to the mean heat transfer coefficient

$$T_{av}^{*} = \frac{1}{2}\left(Bi^{-1} + \ln R_o \right)$$

$$= \frac{\theta_{av}}{\left(q_o'' r_o / k \right)}, \theta = T_{av} - T_b, \tag{1-2}$$

where the mean heat transfer coefficient h_m is obtained after the Biot number ($Bi = h_m r_i/k$) is computed from Eq. (1-2). The variation of T_{av}^{*} with respect to Bi and R_o is displayed in Fig. 5. This figure shows the circumferentially averaged channel temperature to be independent of the channel wall thickness for Bi < 0.1. Interestingly, Fig. 5 also shows that there is a Bi threshold beyond which the correlation sensitivity between T_{av}^{*} and Bi is poor. Therefore, T_{av}^{*} cannot be used to determine h_m above the corresponding threshold. This Bi threshold decreases as R_o increases and is approximately (see Fig. 5 for exact values) 20.0 and 300.0 for values of R_o of 3.0 and 1.04, respectively.

The previously noted exact solution can also be used to characterize the circumferential variation of the dimensionless inside channel wall temperature difference $[T^{*}(R=1,\phi)]$ with respect to the dimensionless outside wall temperature difference $[T^{*}(R_o,\phi)]$, which is characterized by the following relationship:

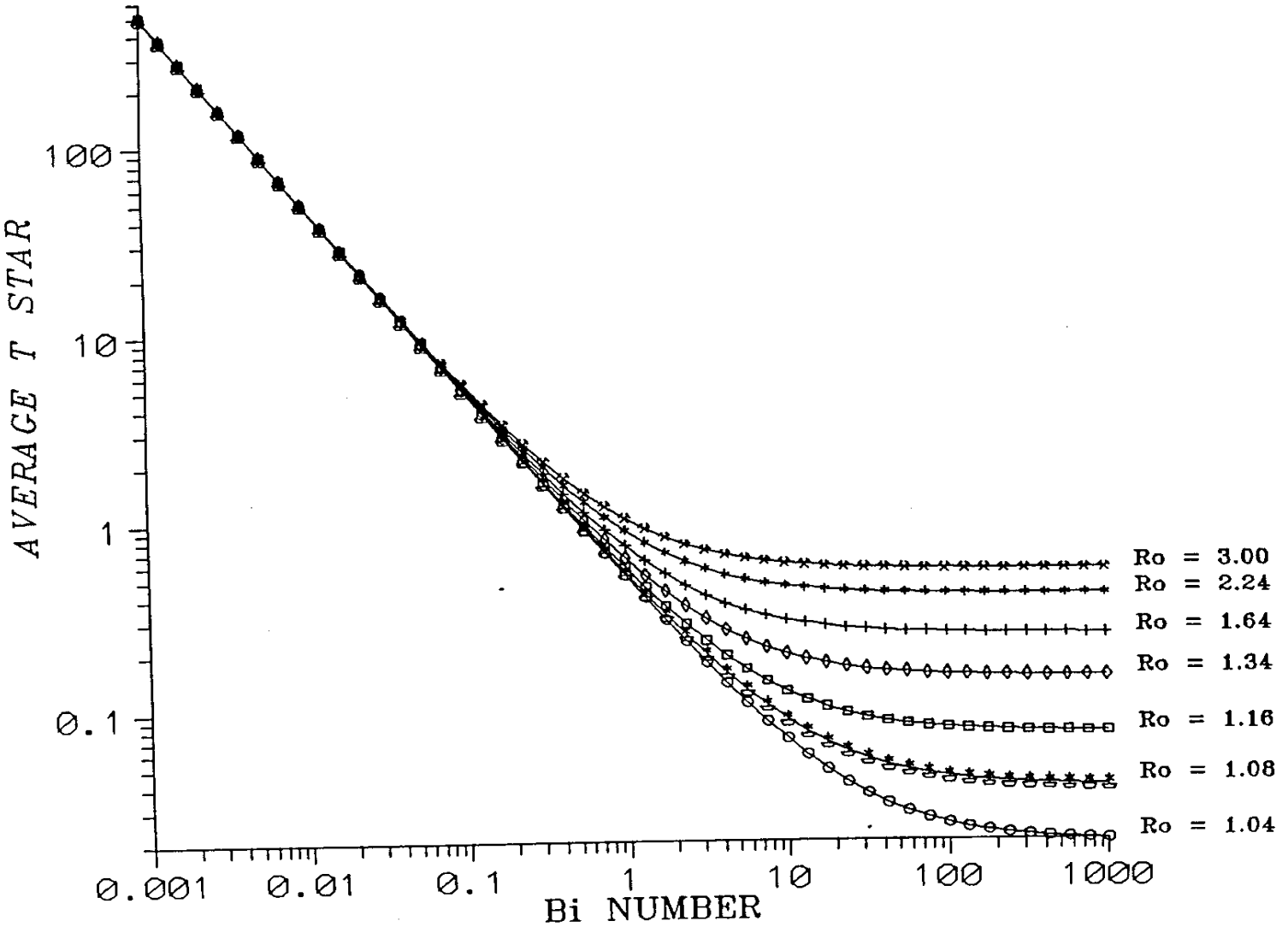

Figure 5: The Dimensionless Circumferentially Averaged Outside Wall Temperature Difference T^*_{ov} as a Function of the Biot Number (Bi) and the channel Radius Ration (R_o) for a Single-Side Uniformly Heated Circular Flow Channel (fluid independent).

$$\frac{T^*(1,\phi)}{T^*(R_o,\phi)} = \frac{\frac{1}{2B_i} + \sum_{n=1}^{\infty} \frac{4\sin n\left(\phi - \frac{\pi}{2}\right)}{\pi n R_o^n \left[\left(Bi+n\right) + \left(Bi-n\right)R_o^{-2n}\right]}}{\frac{1}{2}\left[\frac{1}{B_i} + \ln R_o\right] + \sum_{n=1}^{\infty} \frac{2\sin n\left(\phi - \frac{\pi}{2}\right)}{\pi n^2} \frac{\left[\left(Bi+n\right) - \left(Bi-n\right)R_o^{-2n}\right]}{\left[\left(Bi+n\right) + \left(Bi-n\right)R_o^{-2n}\right]}}, \qquad (1\text{-}3)$$

where the origin for the circumferential coordinate is on the axis of symmetry with $\phi = 0$ in the middle of the heated section. The circumferential variation of this ratio of temperature differences is plotted in Fig. 6 for $R_o = 3.0$ and the Biot number varying over six orders of magnitude. Figure 6 shows that for an OSH heat flux applied to a circular channel, there is no circumferential variation in this ratio for $Bi < 10^{-2}$ and $Bi > 10^{+2}$. However, for $10^{-2} < Bi < 10^{+2}$, there is a circumferential variation in the temperature difference ratio. For typical fusion divertor applications, Bi will be of the order of 0.5. For this Bi, the figures shows that this temperature difference ratio will be between 0.5 and 0.9. Other high heat (or low heat) flux applications will have a different characteristic Bi in Fig. 6. Regardless of the application, Fig. 6 (for $R_o = 3.0$) shows that between $0 < \phi < 90$ deg, this ratio has a nearly constant value; and for $90 < \phi < 180$ deg, the ratio has a different constant value. Because of the linear nature of this exact solution, the circumferential variation of this temperature difference ratio is independent of the actual level of the applied heat flux and the fluid flowing in the channel. Consequently, the exact solutions displayed in Fig. 6 and the preceding equations are dependent on only two dimensionless parameters (R_o and Bi) and apply to the entire high heat flux spectrum whenever the channel thermal conductivity does not vary appreciably with temperature.

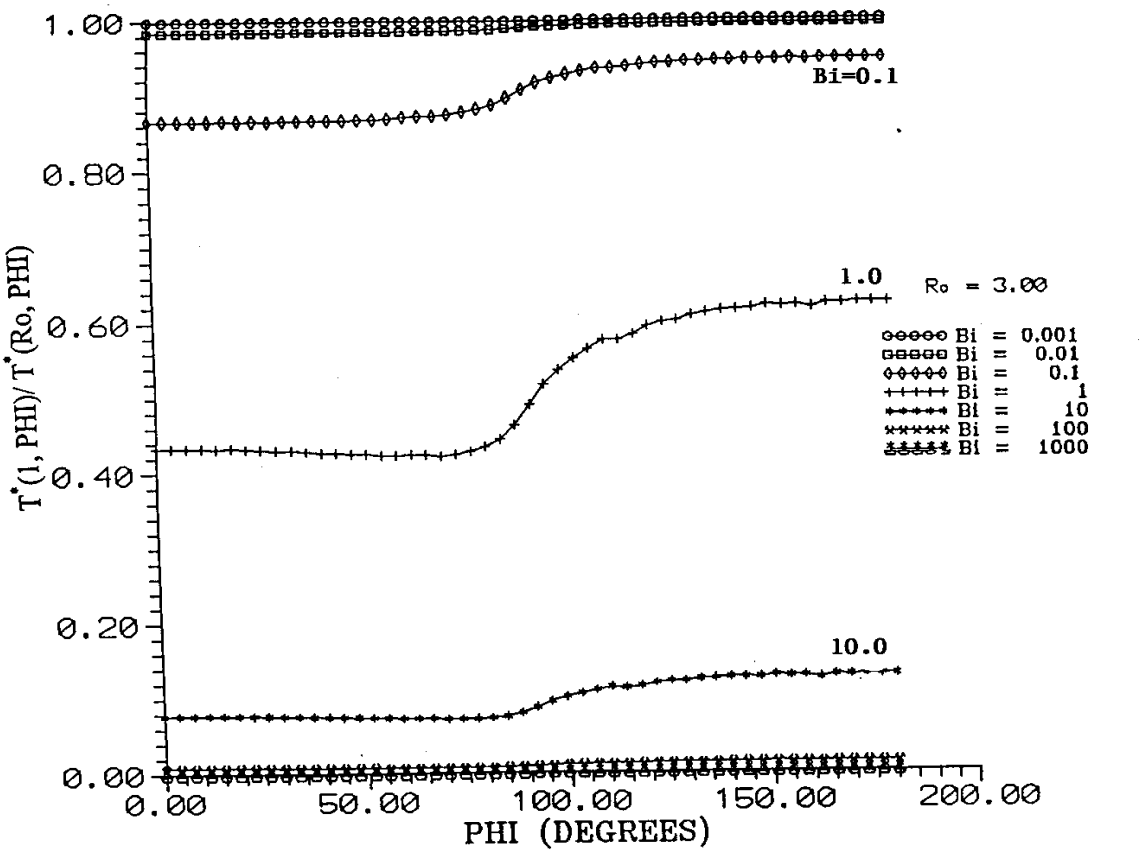

Figure 6: Circumferential Variation of the Ratio of the Inside Temperature Difference [T^* $(1,\phi)$] to the Outside Temperature Difference [T^* (R_o, ϕ)] as a Function of the Biot Number for a Circular Flow Channel; $R_o = 3.0$ (fluid independent).

2.0 DESIGN AND ADAPTATION OF A POWER SUPPLY

2.1 INTRODUCTION

This section describes the design of a power supply for a high heat flux experiment. The power supply is direct current (DC) with a regulation tolerance of less than 2%, and rated at a total of 300.0 kW, 30.0 V. To assure reliability, the system is connected directly from a main 750 kVA power substation via a 480/277 volt, 3-phase feeder. The power supply feeds heater elements in an experimental set-up through a copper bus duct/cabling (bus bar) system. This design will allow the expansion of the bus bar to other laboratories in the future. A personal computer (PC) which supports a data acquisition system controls and monitors in real time the power supply and its interaction with the rest of the equipment.

The adaptation of the power supply for high heat flux experiments is complete. This equipment is being used in experiments to determine local heat transfer and heat flux in one-sided resistively heated test sections (see Fig. 7).

One of the key components of the experimental apparatus is the power supply which feeds the heaters. This power supply is both manual and remote, (as shown in Figure 7) such that its power output remains within a specified regulation tolerance of not more than ±2%. Parameters which will be monitored and fed back to the PC to affect the power control are test section temperatures, supply voltage output, current flow through the heater elements and power dissipation.

The primary consideration of this section is to describe the design the adaptation of the power supply system including the adaptation of vendor supplied equipment to feed a set of resistive heaters in a high heat flux experiments.

2.2 DC POWER SUPPLY SYSTEM

2.2.1 Size and Specifications

In the experiments, a heat flux between 0 to 25 MW/m^2, was initially specified [33]. This heat flux was applied on a typical test piece of surface dimensions 5.0 cm by 20.0 cm. Thus the heater power capability of 300 kW (30.0 Vat 10^4 amperes) or 75 kWh (of energy supply if this

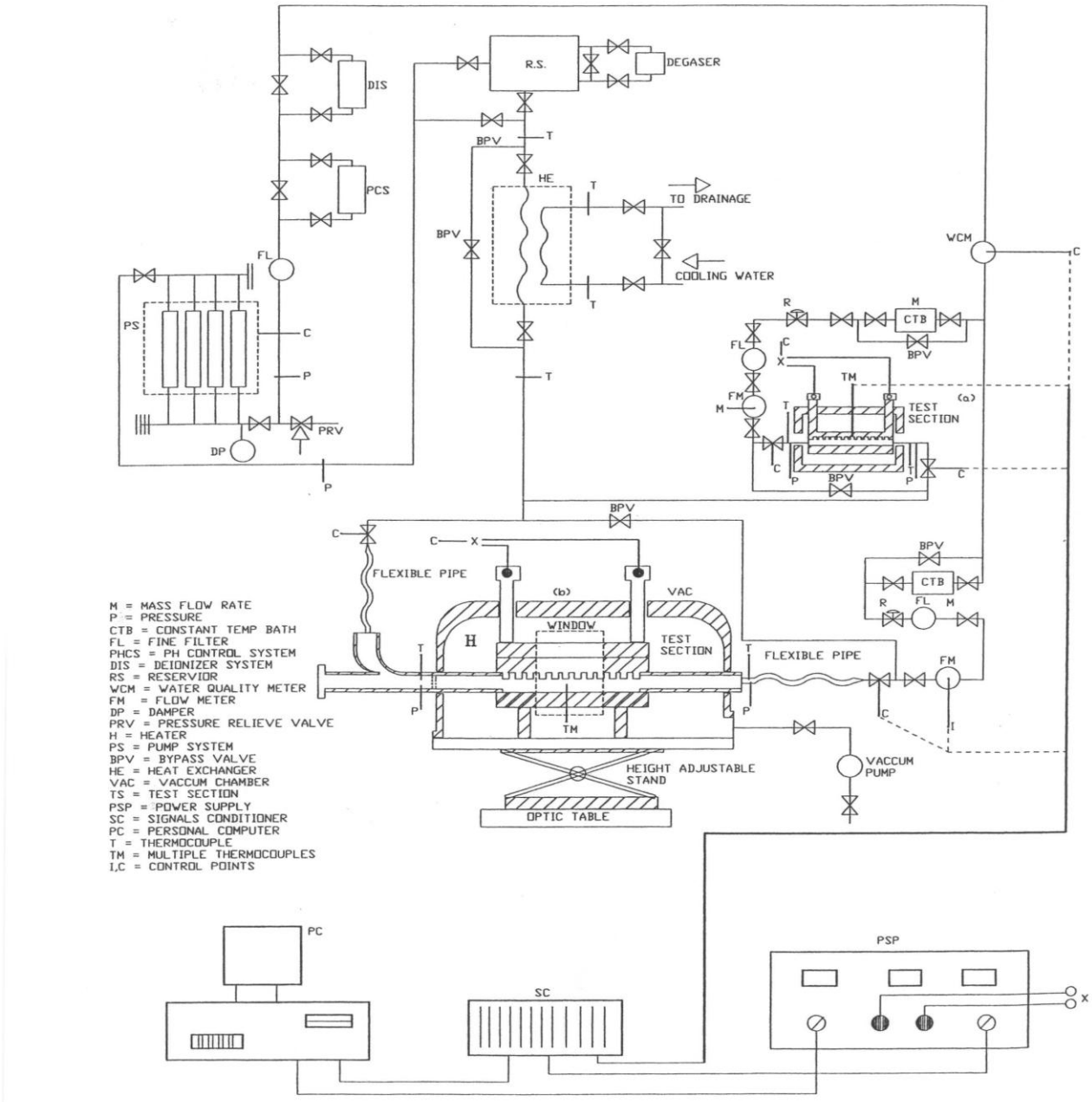

Figure 7: Schematic of the Flow Loop for the High Heat Flux (HHF): (a) HHF Test Section, and (b) Flow Visualization Test Section.

power is sustained for 15 minutes) is adequate for the present experiments. However, due to the stringent demand this power requirement will place on the main electrical substation feeding the laboratory area where the experiments will be performed, the heat flux constraint was relaxed resulting in a maximum power requirement of 250 kW for the experiments from the 300 kW source.

The DC power supply of 300 kW maximum capacity was however earmarked to feed the heaters. Expressing the power supply in total kilowatts (kW) alone does not specify a complete system. Decisions were necessary concerning the voltage range the system must provide for the required kilowatts of power. Due to the possible shock hazards and the large cable or bus duct sizes to implement the system, a voltage range from 0 to 30.0 Volts maximum was considered adequate.

A significant factor in the power output data is due the power regulation. A very high regulation tolerance is clearly undesirable. However, since a power regulation tolerance between 2% to 8% is typical for most high power DC supplies especially at 100% of maximum output voltage [34], use of a single power supply was considered inadequate in terms of meeting the 2% maximum power regulation tolerance specification for the experiments.

To overcome this tolerance problem it was decided to implement the supply system using three separate DC units rated at 2,500 amperes, 5,000 amperes, and 10,000 amperes. Together, these units can be controlled using their internal circuitry to achieve a tolerance of less than 2%. However, the superfluity of such an implementation is apparent. In fact, at any instant in time, two of the units could be idle; and, considering that each equipment cost ranges between $12,000 to $35,000, the system appears highly uneconomical.

Considerable improvement in regulation was possible if an external control circuit was used. The improved method utilized a personal computer controller with precision analog-to digital and digital-to-analog converters interfaced with appropriate software. Such a system provided the required regulation tolerance utilizing only one 10,000 ampere unit.

2.2.2 Type Selection

Based on the determined size and the achievable specification tolerance, a 300 kW, 30.0 Volt phase controlled silicon controlled rectifier (SCR) from Clinton Power Company was selected. The unit has heavy gage steel clad requiring three phase AC power input [35]. Aside from the rectifying circuitry, it incorporates a three phase heavy duty iron core air cooled

transformer. The natural air cooling is enhanced by a fan blower system mounted on the top of the unit. The overall dimension of the unit is 78.0 inches (2.0 m) high, 50.0 inches (1.27 m) wide and 38.0 inches (0.97 m) deep.

A much smaller remote control unit with start/stop buttons, voltage control pot and a current limit pot assists in controlling the rectifier. Automatic voltage control, automatic current control and automatic current limit control was possible with this unit.

Because of lack of room in the laboratory, it was initially planned to place the power supply equipment on a raised platform. However, unavailability of a suitable overhead crane to use in placing the equipment rendered this platform concept inconvenient and uneconomical. A better alternative was adopted and involved placing the power supply in an enclosed kiosk with bottom vents on one side and exhaust fan on top to assist in cooling. The enclosure (weather-proof enclosure) is located outside in the ambient but close to the laboratory area.

2.2.3 DC Power Controller

A personal computer (which forms part of the data acquisition, and instrumentation system of the experimental apparatus) was used to regulate the output of the DC power supply. A secondary remote control unit was installed and this unit made it possible to control the power supply near the test section for observation purposes. To accomplish the required computer control, as shown in Fig. 8, the computer monitors the supply's output voltage, output current, test piece temperature and power dissipation via a data acquisition board with appropriate input/output equipment and software.

2.3 AC POWER SOURCE

2.3.1 Direct Feeder System

Another important consideration in the design and adaptation of the power supply was the AC feeder system to be used. For the type of experiments being performed, it is important to avoid large transients and heavy electrical loading effects caused by other users connected from the same distribution panel. These transients and sudden heavy loading usually cause large local voltage swings which affects the regulation. In some solid state power equipment such as SCR DC power supplies, voltage transients may cause false firing which may result in saturation of

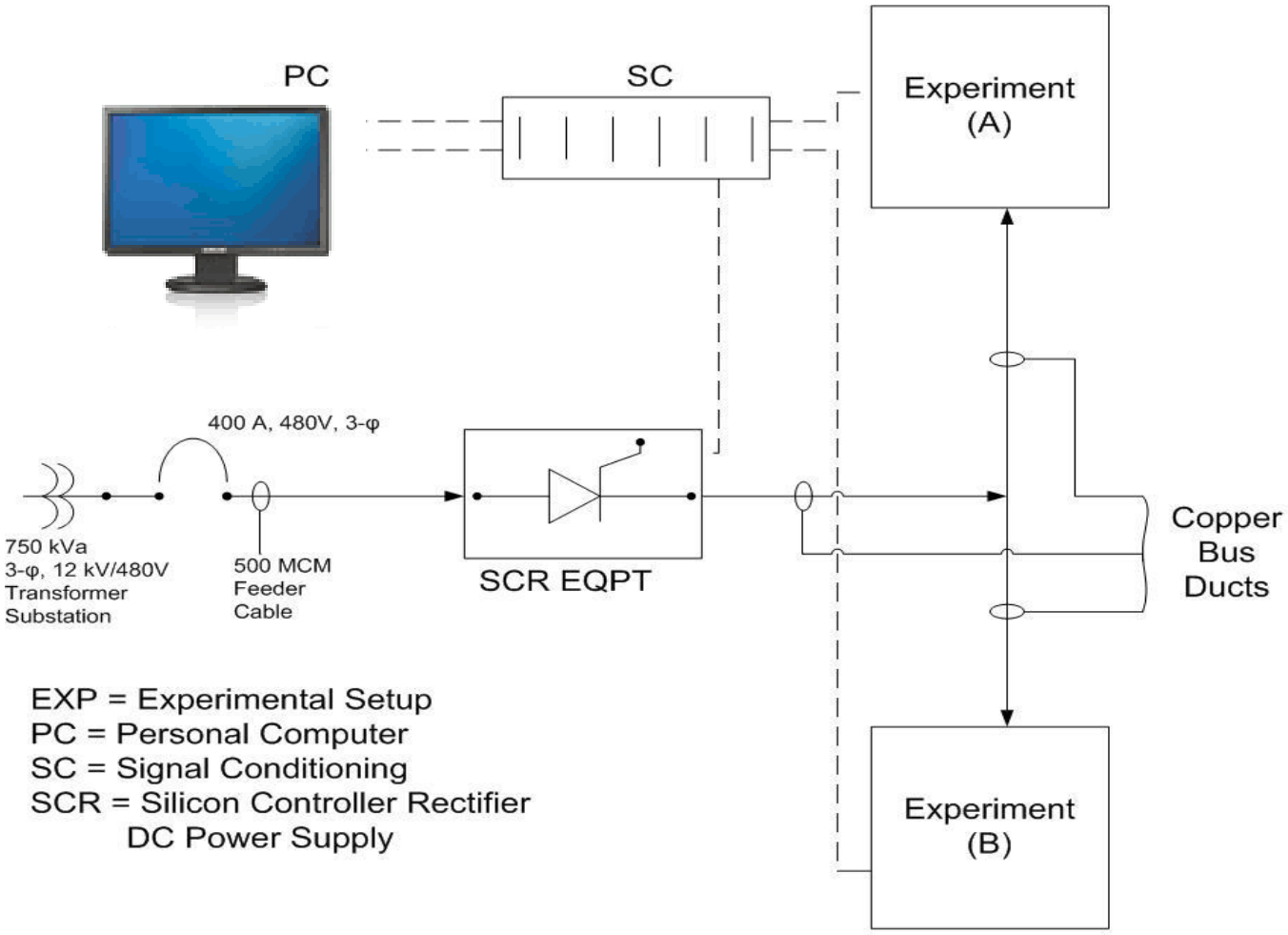

Figure 8: Power Supply for the High Heat Flux Experiments.

the transformer and damage to the control system.

To reduce the effects of transients, it was decided to route a direct 480 V/277 V, 3-phase AC feeder from a 750 kVA, 12 kV/480 V, 3-phase substation. Another alternative was to construct a separate 350 kVA, 12 kV/480 V, 3-phase substation to supply only the DC equipment. This latter alternative was not favored because of the high cost involved.

2.3.2 Single Line Diagram

A single line diagram of the designed supply system including the AC-DC system interface is shown in Fig. 8. A main 500 MCM THW cabling characterizes the 480 V, 3-phase feeder from the supplying substation. This feeder terminates in a 400 ampere fused disconnect. From this panel, cables connect on the AC input of the DC supply equipment. A split bus duct arrangement, as depicted in Figs. 7 and 8, supplies two separate experimental set-ups. The arrangement is such that the supply can feed two experiments simultaneously. Additional equipment and configurations will be needed to connect the present high heat flux electrical bus bar grid to a second experiment for simultaneous operation.

3.0 INSTRUMENTATION, CONTROL, AND DATA ACQUISITION SYSTEM

3.1 INTRODUCTION

Equipment design and adaptation for high heat flux experiments is complete. The experimental objectives, in part, include measuring the local heat transfer and heat flux in one-side resistively heated test sections as shown in Fig. 7. In the present experimental setups, forty-eight (48) Type-J micro-thermocouples embedded in the test section wall were used to make measurements of required temperatures. Also, the electrical power for the heat source was controlled so the power output remains within a specified power error tolerance. Other experimental parameters that require precise control and monitoring are: (1) fluid mass flow rates; (2) test section pressures; (3) the level of insulation of dielectric material utilized to prevent the test section from having direct contact with the electric heater; (4) power supply voltage and current; (5) water quality, which includes ph, resistivity and gas content; (6) regulating valves upstream and downstream of each test section; (7) the level of vacuum in the vacuum space; (8) heat exchanger (HE) and constant temperature bath inlet and outlet temperatures along with additional fluid flow rates; (9) pump metering level; and (10) overall reservoir temperature. About 90 data acquisition (DAQ) and control points were involved. Some of these are labeled in Fig. 7 as T for thermocouple, TM for multiple thermocouples, I for instrumentation and C for control point. Due to the numerous data points and the volume of data to be monitored in the experiment, much attention was given to the DAQ and the instrumentation system.

Many different data acquisition systems along with compatible software drivers were available commercially. The impetus for increased use of these systems in recent years has been provided by improved instrumentation engineering and advances in computer technology. However, most of these systems are menu-driven and are not capable of performing tasks not included in their menus. An effective way of designing a flexible control, instrumentation and data acquisition system is to interface general “can” commercially available software with custom-written ones so the system can perform the desired tasks.

This work involved the design and development of an instrumentation, control, and data acquisition system that were utilized in implementing the experiments. The commercial data

acquisition software used was LABVIEW which provides a graphical programming environment for custom-written programs.

3.2 SYSTEM CONFIGURATION

The system configuration is shown in Fig. 9. The controller is a basic Pentium II, 330 MHz personal computer (PC), that operates under the Microsoft disk operating system (MS DOS) in a WINDOWS environment. The computer was configured to have a printer port, a serial bus (RS 232), a parallel bus (GPIB), data acquisition boards furnished by National Instruments, mouse driver, timer cards, a hard disk of several (200) megabytes and memory of over 20 megabytes employing 32-bit addressing. The GPIB bus and the RS232 bus were used to access and control the power supply, pumps and valves which regulate flow of liquid in the flow loop. The overall system comprises five subsystems: data acquisition (DAQ) implemented by a data acquisition card; direct access memory (DAM) which provides high-speed transfer of acquired data to the host computer; control was effected by a digital/analog input module; and communications was provided via the GPIB bus and post-data processing which is accomplished using a resident software.

3.2.1 Data Acquisition

Referring to Fig. 9, a front-end signal conditioning chassis houses a variety of signal conditioning and instrumentation modules. These include typically three 32-differential input channel multiplexers. Together these multiplexers have the capability of receiving up to ninety-six (96) analog signal inputs from the thermocouples, pressure sensors, flow sensors, voltages, currents, insulation level sensors and power measuring devices. Also, they have a software-controllable gain of 1, 2, 5, 10, 20, 50, 100, 200, 500, ... 2,000 which is channel-independent and can be selected depending on the range levels of the input signals to amplify all the signals. From the front end signal conditioning system, the data signals were communicated in a multiplexed fashion on to a single plug-in multifunction input/output (DAQ) board in either the signal conditioning chassis or if preferred in the computer.

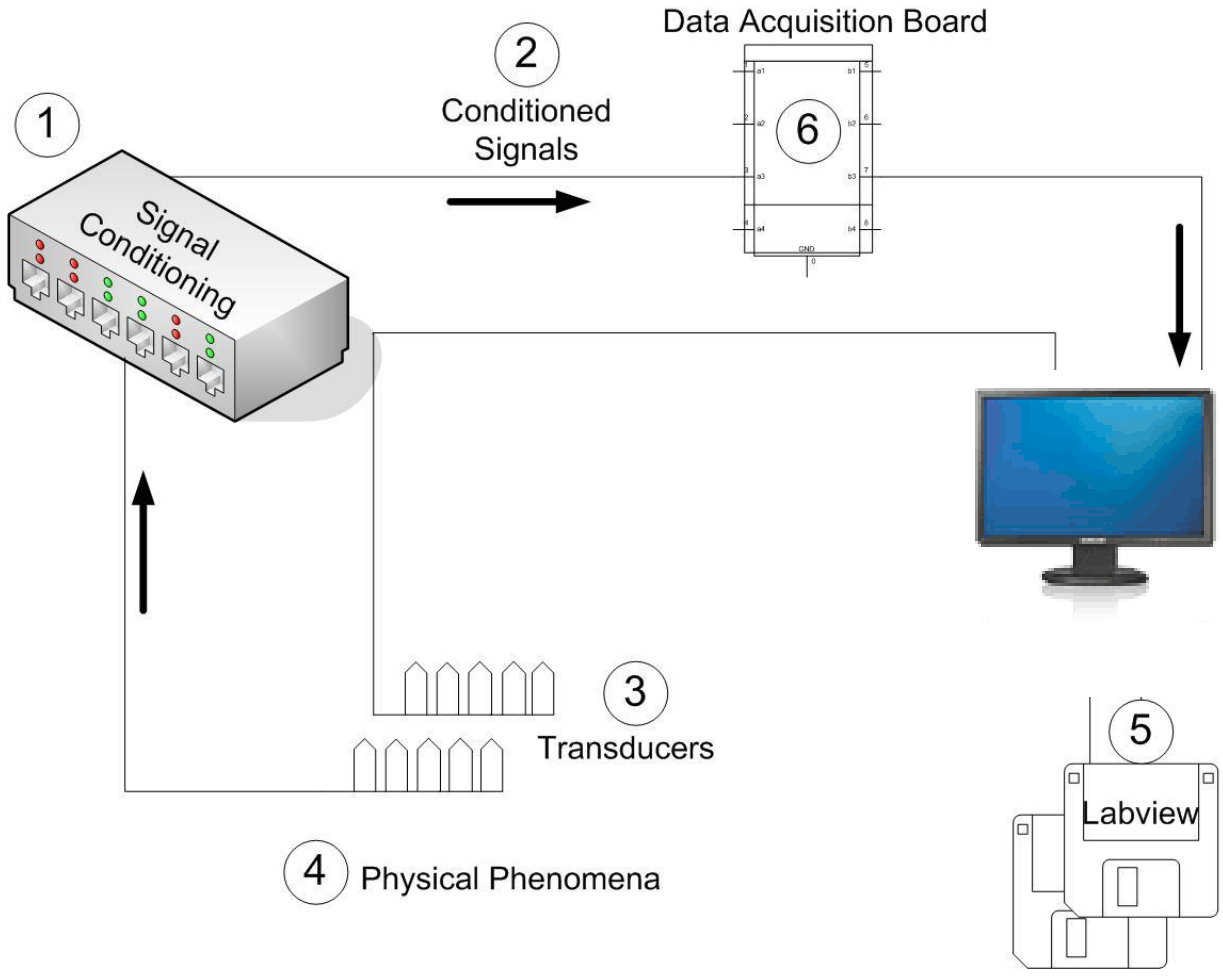

Figure 9: System Configuration

The multifunction input/output (DAQ) board was a 16 single-ended or 8 differential channels board. It acquires data at a rate of up to 100 kilohertz and, like the multiplexer units, has a software selectable gain from 0.5 to 100 depending on the input signal voltage range. This DAQ board also controls and monitors the operation of another board (DIO) with a multi-channel digital inputs and 10 channels output. The design was so versatile that it is possible to monitor and control hundreds of signals using the same DAQ board.

A Real Time System Integration (RTSI) bus in the signal conditioning system provided interconnection of timing signals between the boards [36, 37]. This solved the common problem in instrumentation and data acquisition of not being able to synchronize several measuring devices to a common trigger or timing event.

3.2.2 Direct Memory Access

The Direct Memory Access (DMA) was a key feature of the overall system. The DMA board, resident in most modern PCs, enhances data acquisition by using dedicated hardware to transfer data directly from the DAQ board to the host computer random access memory (RAM). Transfer occurs concurrently with acquisition of samples, thus negating the need for large memory capacity on the DAQ board. Another feature of the DMA board is that it de-multiplexes the scanned data channels into separate buffers on the computer. Fifteen out of twenty megabytes of motherboard memory was allocated dynamically for the sample buffers by the software application operating system.

3.2.3 Controlling Functions

The multi-input/output (DIO) channel board was a 32-channel digital inputs/ 10 channels output board which interfaces with the PC DAQ system. The 32 digital inputs to this board were optically isolated. With this module, it is possible to sense the presence of a wide range of AC or DC signals, from digital logic levels up to 240 V AC/DC. Its optical isolation eliminates ground-loop problems thus isolating the host computer from damaging voltages.

Control operations were effected using the digital lines of the DIO board. Since the board will be used to control slow events such as gradual adjustment of DC power supply, operation of pump motors, valves and other such functions, there was no need to condition the digital signals to have high data rates except near CHF.

3.2.4 Instrumentation

The designed system replaced the traditional bench full of instruments with an instrumentation package that takes the output of sensors such as voltages of current shunts and voltage dividers and other transmitters to create instruments and display the readings at 1/2 second update rate. The data can also be logged at the 1/2 second rate, 50 msec rate, or on demand. Furthermore the instrument readings could be used for real-time control at the 1/2 second rate [38].

3.2.5 Software and Programming Environment

The software interface for the DAQ, control and instrumentation system was implemented using LABVIEW, a National Instruments package, which provided a graphical programming environment for development of application-specific software and creation of a graphical user interface and also provides the operating system to run the software.

Under LABVIEW, programs are known as virtual instruments or Vis, and each consists of a front panel and a block diagram. The user interface was implemented with the front panel and use of a mouse and provides a means of input and output through selected controls and indicators. The programmer can choose from various switches, buttons, slides, knobs, graphs, and tables to arrange on the front panel, and then customize them to suit the application. Controls and indicators were configured to represent the desired data types, ranges, and dimensions.

Each of the controls and indicators on the front panel appear as blocks on the block diagram. Functional blocks were selected from a pallet menu to perform such operations as arithmetic functions, file input/output, array manipulation, data acquisition, and post data acquisition processing. Blocks were then wired together to enable data flow from controls through a multitude of functions and programming structures such as loops to control equipment and indicators.

Once the data has been acquired it can be plotted by clicking on the “Plot Results” button on the data acquisition system panel. There were three basic types of plots: statistical distributions, tables, wave forms. Up to six tables could be plotted on a single page.

4.0 DESIGN OF EXPERIMENTAL FLOW LOOP FOR HIGH HEAT FLUX MEASUREMENTS

4.1 INTRODUCTION

A stainless steel flow loop was designed in order to achieve the steady state conditions for the entire high heat flux system. The reader is referred to reference [33, 39, and 40] for discussions of both the scope and anticipated results for the experiments. The flow loop is a closed loop which operates at a pressure range between 0.1 to 4.0 MPa. The temperature, pressure, flow rate and some other major parameters were monitored and measured during the experiment at several different stations. A sketch of the flow loop is shown in Fig. 7. A positive displacement pump controlled the water volume flow rate (up to 1.5 x 10^{-3} m^3/s) through a calibrated flow meter and into the test section. The test section was heated by a direct current through a heater which is not thermally isolated but is electrically isolated from the test section. The hot water leaving the test section will be cooled by a heat exchanger before returning to the reservoir. A deionizing unit, a degassing tank, filter, and accumulator are included in the loop as shown for purification and degassing purposes. The flow loop was designed to deliver an accurate amount of high quality water under restricted and specified conditions to the test section. The closed loop flow circuit and the test section were configured so that fully developed hydrodynamic water flow condition will exist at the inlet of each test section. A pulsation damper was used at the discharge of the positive displacement pump to absorb the pressure peaks between the pump and the back pressure valve. In most cases, there was subcooled flow boiling or single-phase heat transfer occurring in the test section.

4.2 FLOW LOOP COMPONENTS

4.2.1 Pumps:

In order to move a specific volume per unit time of up to 1.55 x 10e-3 m^3/s (0-25 GPM) of water against a positive differential pressure between the pump suction and pump discharge, a displacement controlled volume or metering pump was used. The metering pump is capable of delivering a volume flow rate which is controllable within one percent of the setting. The pump drive mechanism operates on a polar crank principle. The pneumatic capacity control has been installed and adjusted to operate from zero to 100 percent capacity over a specified instrument air pressure range (usually up to 15 psi [103 kPa]).

4.2.2 Piping System:

a. Suction Piping:

The flow loop was designed in such a way that the suction of the pump is flooded by locating the liquid end below the lowest level of the liquid of the water reservoir. This will prevent negative suction pressure conditions which will affect metering accuracy. Seamless stainless steel tubing was chosen because it has a smooth inner surface and can be formed into long, sweeping bends to minimize frictional flow losses and oxidation. Finally, to prevent foreign particles from entering to the pump a strainer was used.

b. Discharge Piping:

The discharge piping has been selected large enough to prevent excessive pressure losses on the discharge stroke of the pump. The piping has been arranged to provide at least 35 kPa (5.0 psi) positive pressure differential between the discharge side and the suction side.

4.2.3 Accumulator (Surge Chamber)

A Pulsation dampener has been used with the back pressure valve in the discharge line to absorb the flow peaks between the pump and the back pressure valve.

4.2.4 Safety Valves

Motor-driven positive displacement pumps can develop tremendous discharge pressures long before a thermal overload device interrupt the motor electrical circuit. To prevent a blocked discharge line from causing damage to the pump, piping, or process equipment, a safety valve was installed in the pump discharge line.

4.2.5 Degasser

In order to reduce water corrosion premature boiling as well as the loads on chemical neutralization and also on ion exchange demineralization, a degasser unit has been used in the flow loop. It is estimated that the unit reduced the oxygen contamination from zero to 7.0 PPB.

4.2.6 Deionization Equipment

Type I organic free ultrapure water with maximum resistivity up to 18.0 mega-ohm-cm and a total organic carbon less than 10.0 PPB was selected to feed the test section with high accuracy, and high quality water.

4.2.7 Filter

During the operation, some precipitated particles such as iron may be found in water. The precipitated particles were trapped or filtered in a line filter containing a 5 micron filter cartridge.

4.2.8 PH Control System

Some small particles such as dissolved iron are colloidal in form and stay in suspension due to its acidic state. It must be oxidized to a neutral or alkaline ph (7.0 or above) environment before it can be trapped or easily filtered. Dissolved iron can be oxidized by chlorination. Oxidation causes it to “group by attraction” or precipitated into a larger form so it can be filtered.

4.2.9 Heat Exchanger

The power which was added continuously to the working fluid (0-250 kW) was removed by a heat exchanger after the test section and before returning to the reservoir. A counter-flow heat exchanger fits the needs of the flow loop. The heat exchanger is a four pass standard BCF and building chilled water was used as the coolant.

4.2.10 Miscellaneous

In addition to the equipment mentioned above, other secondary equipment includes: shut-off valves, regulators, bypass valves, etc. These components provide the system the capability of operating in different modes.

5.0 BUS BAR CONFIGURATION AND SUPPORT FOR A DIRECT CURRENT POWER SUPPLY

5.1 INTRODUCTION

The design, adaptation, and installation of the copper bus bar for power transfer in the high heat flux experiments were completed. One of the key components of the experimental apparatus is the 300 kW power supply which will be used to energize the heaters for the test section. The power supply installation was effected via an alternating current (AC) feeder from the building electrical/mechanical room to the Institute for High Heat Flux Removal Facility. The feeder terminates in a 300.0 kW Silicon-controlled rectifier. Bus bar connections from this equipment carries the required electrical power to the heaters.

In a previous paper [41], details of design of certain important components, particularly the DC side of the power supply, were not reported. One such component is the 10,000 amperes high capacity bus bar. Due to its reliability, copper bus bars were used. This bus system connects the output of the DC power supply to the heaters. Finally, the overall weight of the bus material (4,250 lb) requires that a proper structural support be provided which is both convenient and safe. This part of the report attempts to outline the rationale behind the selection of material, and the configuration for the bus bar system and the supporting structure.

5.2 DESIGN CONSIDERATIONS

5.2.1 Specifications

The specifications for the bus bar system are as follows:

- The bus bar must be capable of carrying safely 10,000 A of direct current at a maximum operating voltage of 30 Volts in an environment with ambient temperatures of not more than 55 degrees Celsius at 90% humidity;
- The effects of thermal expansion on the bus way runs must be considered; and
- The system should incorporate at least two power takeoffs.

5.2.2 Material Selection and Sizing

The materials most commonly used as conductors in electric power equipment are aluminum and copper. Although the electric power industry has had a fair share of problems in learning how to utilize aluminum, transmission and distribution conductors are predominantly aluminum now.

Generally, in power system work, aluminum is used as a substitute for copper because of its low cost and light weight. Therefore, the initial obvious choice of material for the project was aluminum. However, problems associated with the use of aluminum as a conductor which include bus bar connection failures in the utility industry [42], ruled out the use of this material. Hence, copper was selected as the bus bar material.

Usually bus bars are available from electric equipment manufacturers in standard length and thickness of 3.0 m and 6.4 mm, respectively. The width varies depending on the current capacity requirement and, of course, convenience of installation. For this project, a 152.0 mm width bus bar was selected to tie in with the DC power equipment output termination, which is also made of a 152.0 mm by 6.4 mm thick copper bus bar. The DC current carrying capacity of this standard size bar is 3000 A [43]. This requires that at least four such bars be used per pole of the supply to satisfactorily handle the 10,000 A specified current.

Examination of various manufacturer catalogs showed the average cost of a 3.0 mm section of the required bus bar to be about $10,000. Based on this amount, the initial estimate of two runs of 6.0 m bus bar would cost about $40,000. This cost fell outside the budgeted amount for this aspect of the project. It was therefore decided that the bus bar system be fabricated rather than purchasing an already fabricated bus way system from a manufacturer.

5.2.3 Layout and Supporting Structure

The layout of the bus bar system is shown in Fig. 10. The overall weight of the system is 18.9 kN. To avoid putting excessive stress on the roof truss which was not designed to carry such a heavy weight, it was decided that the bus bar be supported by structural steel columns anchored to both the floor and the wall as shown in Figure 10. Five 10 feet by 4 in by 4 in tubular structural steel columns were found to be adequate to handle the entire weight of the bus bar system. A contractor implemented the installation and added additional supports as needed.

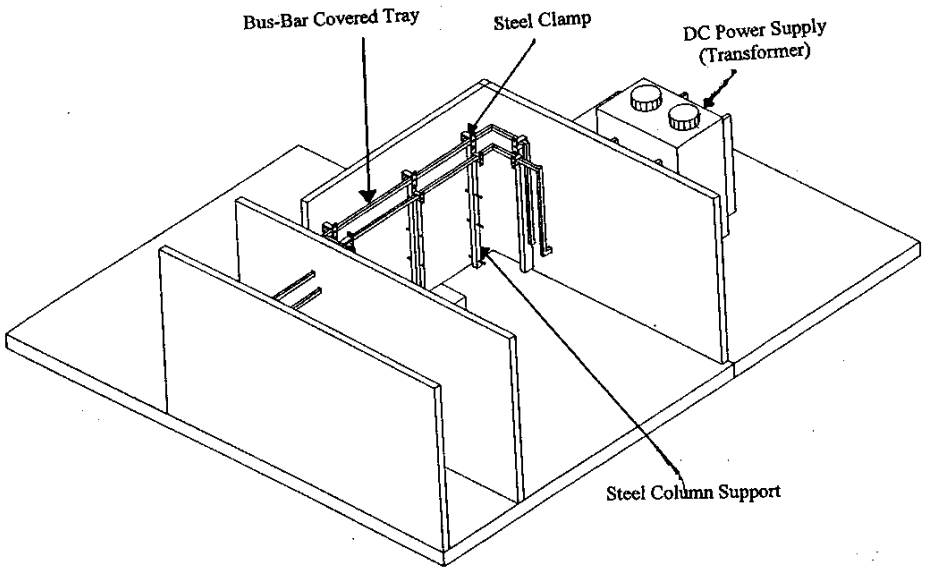

Figure 10: Bus-Bar System Layout.

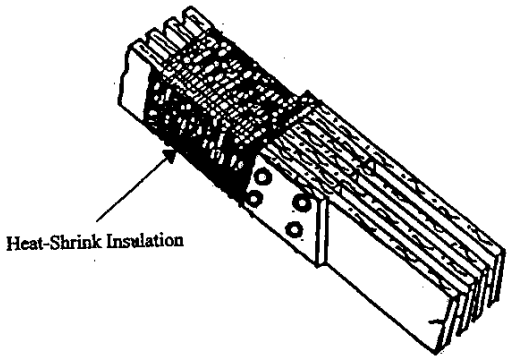

Figure 11: Bus-Bar Construction Detail--Joint.

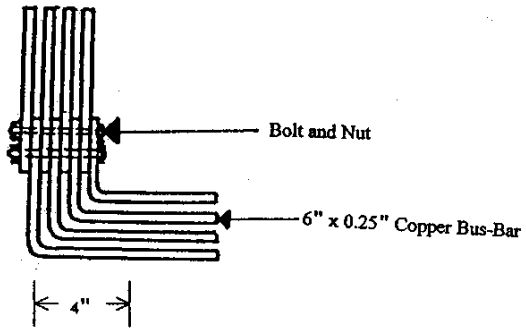

Figure 12: Bus-Bar Construction Detail--Bend.

5.2.4 Fabrication

Because of its large weight, the bus system was fabricated section by section with each section having a maximum length of 3.7 m. Bends, joints and other fabrication details are shown in Figs. 11 and 12. Each section was lifted piece-wise on to the already mounted supporting column. Straps of rectangular steel bars bolted to the sides of the column were used to anchor the system in place to avoid lateral movements.

5.2.5 Safety Consideration

The fabricated bus bar system needed be safe to operating personnel and must provide reliable operation with a minimum of maintenance. To provide these features, a 3M Corporation type BBI-A series heat shrinkable bus bar tubing was used. This tubing is capable of insulating voltages up to 35,000 Volts. This electrical insulating material wraps around each entire pole of the bus bar system which is then placed in a solid steel trough (or tray) and is shown in Figs. 10 and 11. A data acquisition and control system was interfaced with this bus bar system so that should any insulation failure or any electrical short circuit occur--no matter how minor, the system would shut down. This circuit has not been completely implemented. A similar system shut down circuit sensitive to temperature level was designed and tested.

6.0 ANALYSIS OF DISSOLVED OXYGEN

6.1 INTRODUCTION

This section of this report presents an analysis of dissolved oxygen for the High Heat Flux Experiment. This analysis is based on the Henry's Law to calculate the quantity of dissolved oxygen in the water during the experiment. According to this analysis, an alternative design is recommended by using a low price vacuum pump instead of a high price degasifier to remove dissolved oxygen from water in the experiment.

6.2 ANALYSIS

In the design of the high heat flux (HHF) flow loop [44], a degasifier was used to remove oxygen from water. The moles of oxygen dissolved in the water can be evaluated using the following equation,

$$N_{02} = X_{02}\ N_{H_2 0} \tag{6-1}$$

where,

X_{02} is the solubility of oxygen which is a function of the water temperature and the partial pressure of oxygen and,

$N_{H_2 0}$ is the number of moles of water in the system calculated using,

$$N_{H_2 0} = \frac{\rho_{H_2 0}{}^{*} V_{wat}}{m.wt_{H_2 0}} \tag{6-2}$$

where

$\rho_{H_2 0}$ is the density of water,

$m.wt_{H_2 0}$ is the molecular weight of water, and

V_{wat} is the volume of the water.

By Henry's Law, the solubility of a gas is directly proportional to the partial pressure of that gas [45]. Since at the saturation temperature, the solubility of a gas in a liquid equals zero, and since we know the solubility of oxygen in water at 25 ^{0}C and 1 atm only, then the solubility of oxygen in water can be expressed as:

$$X_{02} = X_{02}\,(25\ ^{0}C, 1atm)\ \times \frac{(T(P)_{sat} - T_{wat})P_{02}}{(T_{sat} - 25\ ^{0}C)P_{atm}} \qquad (6\text{-}3)$$

where

P_{02} is partial pressure of oxygen,

X_{02} (25 ^{0}C, 1 atm) is solubility of oxygen in water at 25 ^{0}C and 1 atm ($4.76*10^{-6}$ $\mathrm{Mole}_{0_2} / \mathrm{Mole}_{H_2 0}$ [46]),

P_{atm} is the atmosphere pressure,

T_{wat} is the water temperature, and

$T(P)_{sat}$ is the water saturation temperature as a function of tank pressure P; i.e.,

$$T(P)_{sat} = 373.998*(P)^{0.07144015} - 273.15. \qquad (6\text{-}4)$$

In the equation (6-4), the units of P and $T(P)_{sat}$ are bars and ^{0}C, respectively. Now we can substitute equation (6-4) back into equation (6-3), equation (6-2), and equation (6-1) step by step to get the quantity of dissolved oxygen N_{02}. From equation (6-4), we can find that the saturation temperature can be changed by changing the tank pressure. In equation (6-3), when the saturation temperature equals the water temperature, then

$(T(P)_{sat} - T_{wat}) = 0$, and $X_{0_2} = 0$; hence in equation (1), $N_{0_2} = 0$. (6-5)

6.3 DISCUSSION

Based on this analysis, a vacuum pump can be used to induce boiling in a water tank. After removing the dissolved oxygen, nitrogen should be used to balance the tank pressure up to 14.7 psi. This will keep the pump suction pressure higher than the water saturated pressure. The solubility of nitrogen is $6.73*10^{-6}$ $\mathrm{Mole}_{N_2} / \mathrm{Mole}_{H_2 0}$ *or* $0.427*10^{-3}$ $Mole_{N_2}$ / *litre* at 1 atm and 80 ^{0}C [46]. Since there is no oxygen, the partial pressure of oxygen equals zero. In equation (6-3),

$$P_{0_2} = 0 \qquad \textit{and} \qquad X_{0_2} = 0; \qquad (6\text{-}6)$$

then in equation (6-1),

$$N_{0_2} = 0.$$

This method was used successfully in the experiment, "The Determination of the Reaction Rate Constant for Lithium-Lead and Water Interaction" [47]. The initial gas content of working liquid will be nitrogen. For the HHF flow loop, the volume of dissolved nitrogen can be calculated as noted below.

Nitrogen is an ideal gas and in a closed system, 1 mole gas has 22.4 liter volume at 20 ^{0}C and 1.0 atmosphere. The volume of the dissolved nitrogen [46] is:

$$V_{N_2}(20\,^0C, 1 \text{ amt}) = 0.427\,x10^{-3}\text{mole/liter}\,x\,22.4$$

= 9.5648 x 10^{-3} (liter nitrogen/liter water).

Based on the state equation,

$$\frac{V_1 P_1}{T_1} = \frac{V_2 P_2}{T_2} \tag{6-7}$$

where

V_1, V_2 are the volume of gas, P_1, P_2 are the pressures of the gas, and T_1, T_2 are the temperatures of gas. Then, the volume of the dissolved nitrogen at 80 ^{0}C and 1 atm is:

$$V_{N_2}(80\,^0C, 1atm) - \frac{9.6x10^{-3}(\text{liter nitrogen/liter water})\,x353K}{293\text{K}} = 1.15 \text{ x } 10^{-2} \text{ (liter nitrogen/liter water)}$$

= 1.15 x 10^{-5} (m^3 nitrogen/liter water). (6-8)

From this calculation, the volume of dissolved nitrogen is less than the results of experiment performed by Biney [47]. Some researchers (see reference [48]) investigated subcooled vertical flow boiling and found that if the volume of dissolved nitrogen was as much as 3.5*10^{-3} m^3 nitrogen/liter water, the critical heat flux (CHF) can be reduced by as much as 25%. Buchberg et al. dissolved 9.0*10^{-4} m^3 nitrogen/liter water into water at 13.8 MPa, and found that the CHF was not always reduced. However, some data resulted in substantial reduction in the CHF [48].

7.0 HEATER DESIGN FOR DIFFERENT TEST SECTION CONFIGURATIONS

7.1 INTRODUCTION

As is the case with power transfer and interface components, design of test section configurations for high heat flux experiments directly affected the heater design. This section of the report highlights the selection of graphite as the heater material and its geometric configuration for the test sections. Also discussed is the attachment of the heater and insulation to the test configurations. Finally, the two completed test section configurations are reviewed.

7.2 CONSTRAINTS AND REQUIREMENTS

The heaters for the test sections should satisfy the following design requirements: (1) the material must withstand temperatures well above 650.0 ^{0}C; (2) the resistivity of the material must be very high (above 100.0 μΩ-cm); (3) it must support a maximum power handling capacity of 250.0 kW; (4) it must be electrically insulated with a dielectric material; and (5) the insulator heater must be able to attach to each unique test section design configuration.

7.3 TEST CONFIGURATIONS

Two test section configurations were of interest. The designs include: (1) the circular tube, and (2) the monoblock. Other configurations for future research include the latter configurations with a helical coil insert.

7.3.1 Monoblock Heater

As its name implies, the monoblock it consists of a rectangular block with a cylindrical hole passing through its center along the length-wise axis of the block. The heater initial configuration for the monoblock is shown in Fig. 13. The fluid of choice (typically, water) flows through a pipe at a high mass flow rate. Above the test section is the heater with its bus bar configuration. The graphite heater extends over the entire test section area. The graphite was manufactured in the shape of a rectangle with two levels of thickness (the details are given later). The middle section has one thickness and each end is considerably thicker.

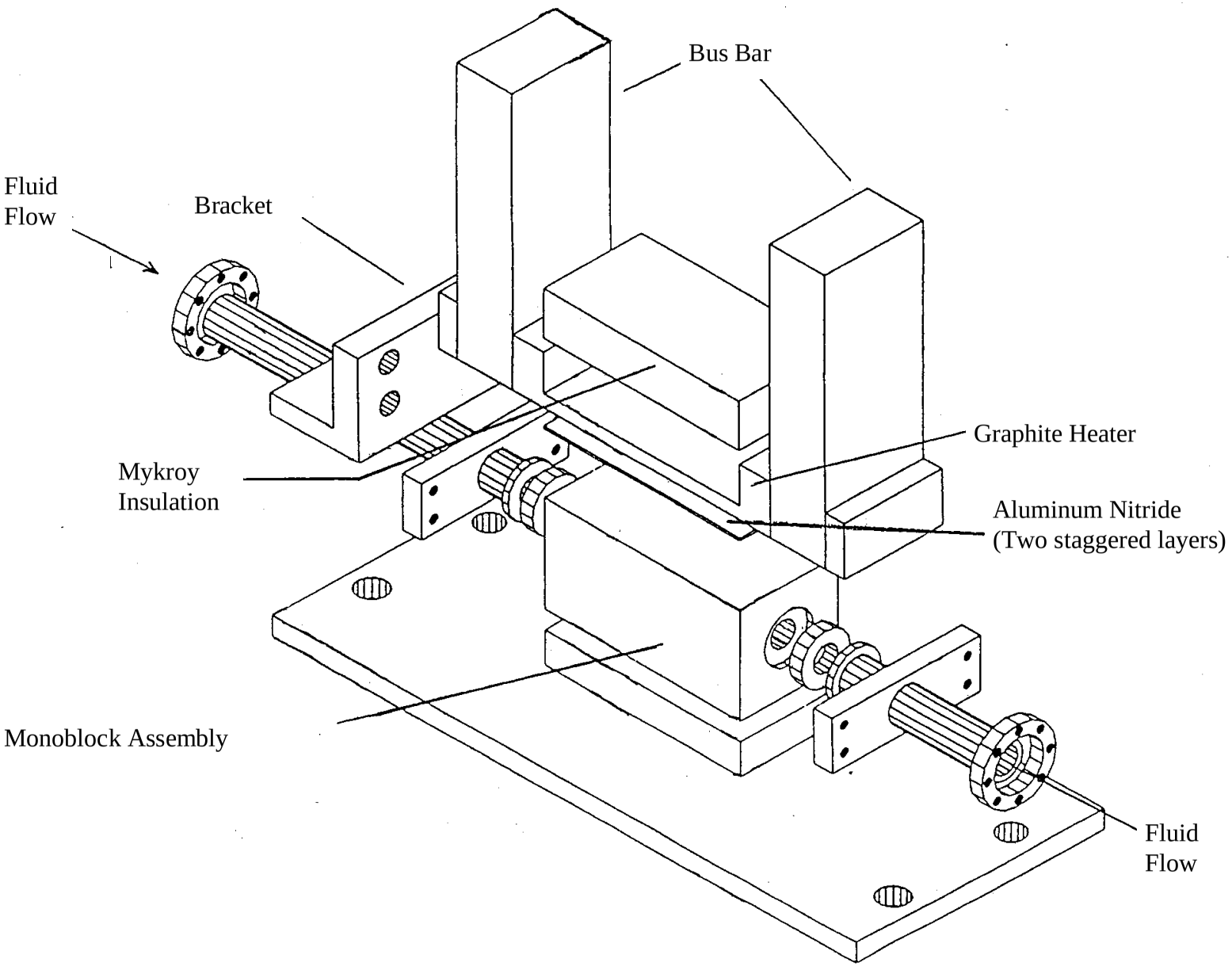

Figure 13: Typical Monoblock Test Section Configuration for Heater Interface.

Between the heater and the test section is a dielectric material, aluminum nitride (AlN) which is used as an electrical insulator with good thermal conductivity properties. It has a rectangular cross section and fits between the heater and the monoblock test section. The bus bars extend from above, down toward the test section and are connected to either end of the heater. The use of two specially designed support brackets act as a brace when placed near the upstream and downstream portions of the test section.

When a block of homogeneous and isotropic material is free to expand in all directions and if this block is heated uniformly, its sides will increase in length. If the temperature difference along a rod of length L is ΔT, its length is found to increase by an amount

$$\Delta L = L\beta\Delta T \tag{7-1}$$

where,

ΔL = change in length

ΔT = change in temperature

β = thermal coefficient of linear expansion.

The value of β depends on the material and temperature range of interest. The thermal expansion is important in that too much expansion could crack or damage the heater [49, 50] AlN.

7.3.2 Circular Heater Shell

The circular heater shell is the second heater design. Fig. 14 shows the conceptual heater design. It is a half circular tube shell with thick ends. This was later subdivided (in the circular direction) into five strip heaters with the same length as the circular tube shell heater. The heater material was manufactured to rest exactly next to the dielectric layer. The dielectric was placed between the heater and the copper flow channel. The AlN insulation was manufactured in thin strips to rest exactly over the outer surface of the circular tube. The outer surface of the circular copper tube (test section) has straight, flat sections on which the AlN was placed. The bus bars were placed on the ends of the heater as in the case of the monoblock heater.

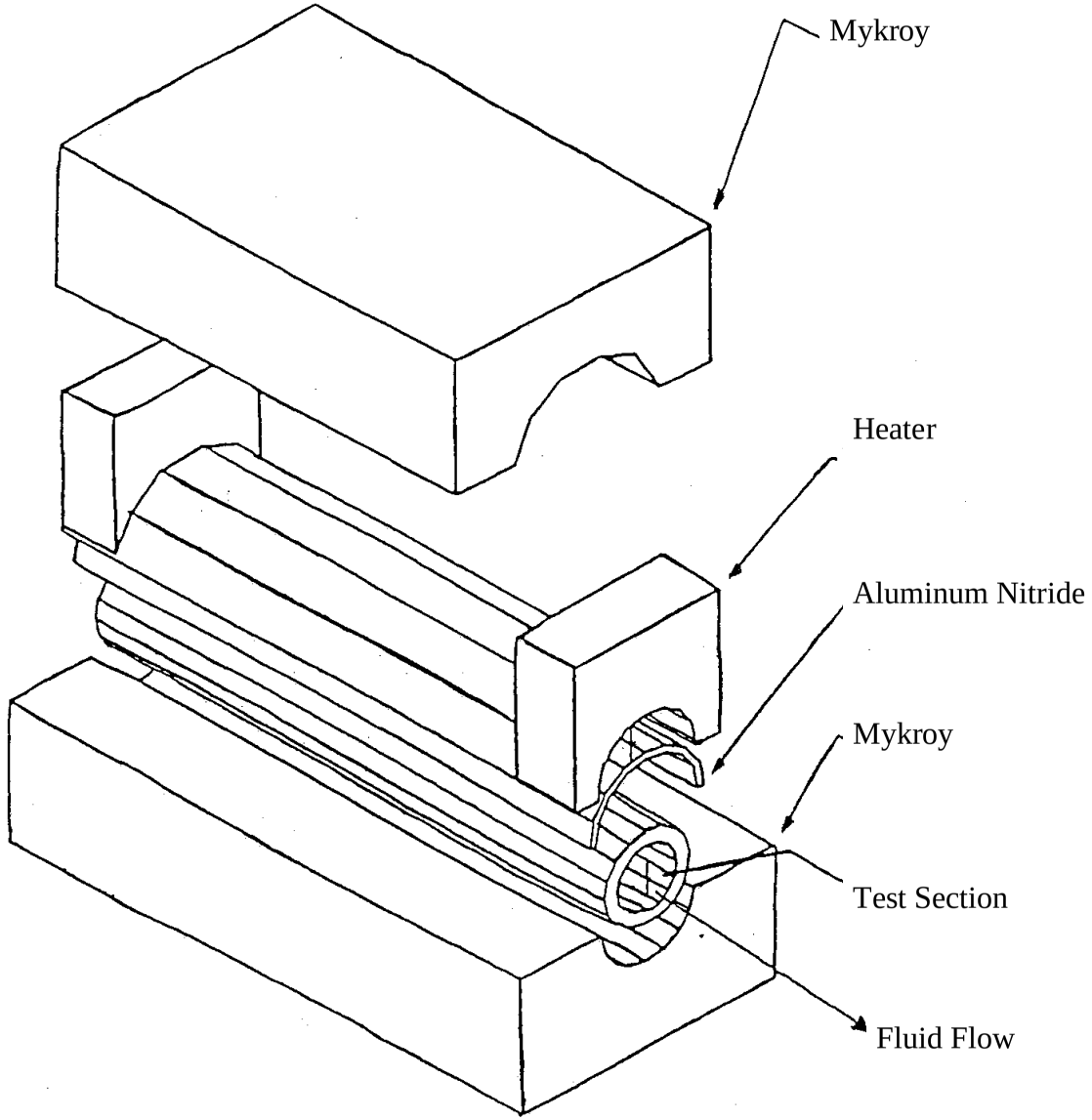

Figure 14: Circular Heater Shell Conceptual Configuration for the High Heat Flux Experiments.

8.0 INTERFACE MECHANISM CONCEPTUAL DESIGN FOR THE TEST SECTION

8.1 INTRODUCTION

The interface between the electrical terminal and the test section is one of the most important concerns of the Institute of High Heat Flux Removal (IHHFR) Experiments. Due to the intricate test section design configuration and restrictions on some of the properties of its associated component materials (material brittleness), it is impossible to use bolts or other lugs for connecting the heater to the electrical bus bar. Therefore, a special design was needed to accomplish the connections. This portion of the report presents the conceptual design concept of the interface mechanism. In this design, external adjustable bolts furnish the required contact pressure between the test section heater and the bus-bar. The graphical presentation of the design is also included.

The IHHFR Facility was designed to study advanced high heat flux removal mechanisms for application in plasma-facing components for fusion reactors. It consists of a flow loop, test section, and electrical equipment and instrumentation. In order to reach high heat fluxes in the test section flow channel, a heater has been designed which will accommodate up to 250 kW of power. The bus-bar carries a high current (up to 10,000.0 amp) to the heater (see Fig. 15). The thermal expansion, which is caused by the temperature gradient, may generate extra pressure. In order to avoid any heat flow to the interface which will cause excessive thermal expansion, some restrictions are described in the next section.

8.2 REQUIREMENTS AND LIMITATIONS

The following are requirements and limitations for the heater:

a. The heater must remain homogenous in order to generate uniform heat;

b. There is limited space in the test section for attachment;

c. Uniform pressure should be generated at the interface area between heater and bus-bar;

d. Uniform thermal conductivity is required between the heater, aluminum nitride, and

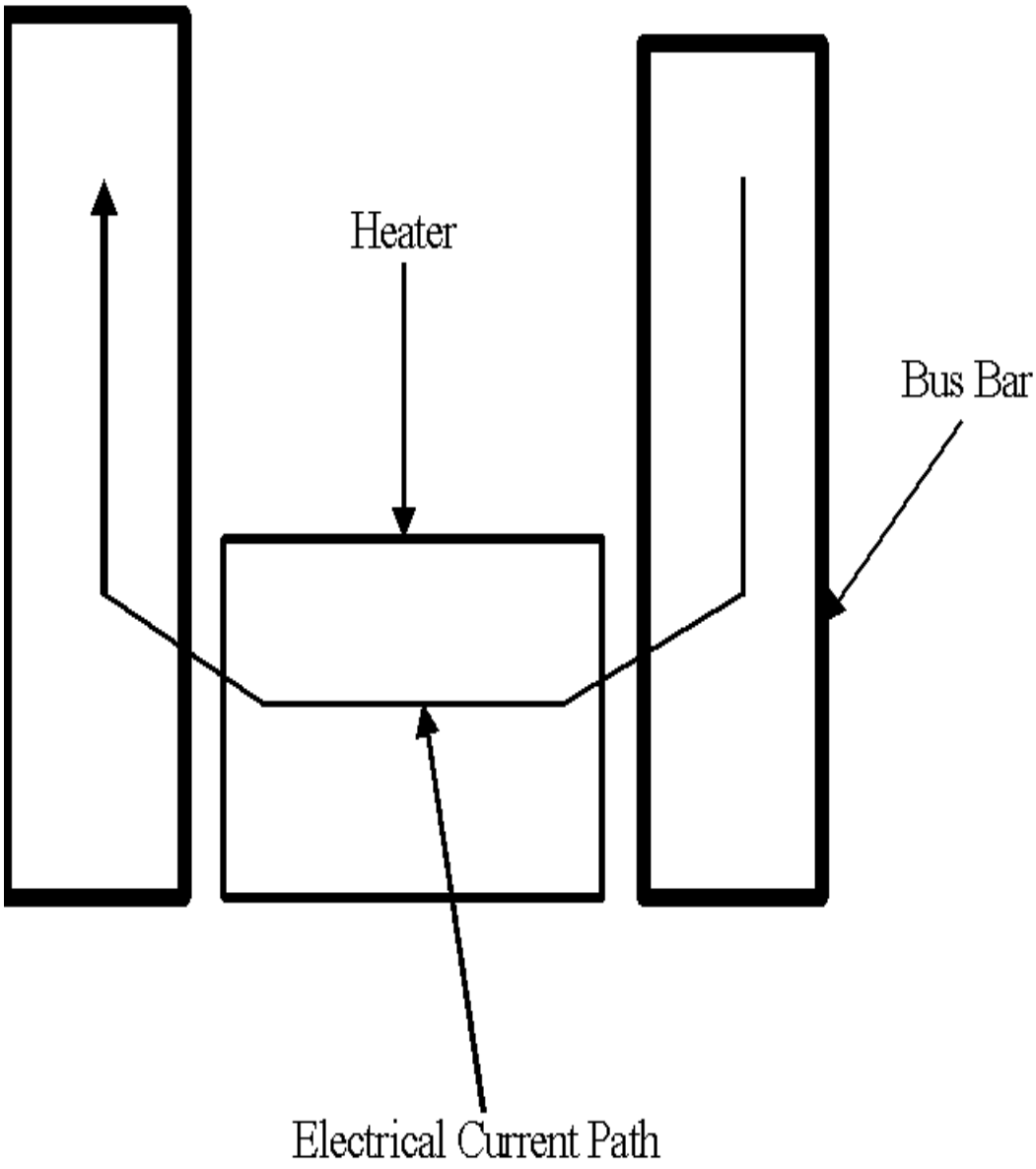

Figure 15

the test section;

e. Thermal expansion should be compensated for and should not have an adverse effect on the pressure between the bus-bar and the heater. Due to brittleness of the heater, excessive pressure could damage the component;

f. The design should have capability to handle different heater configurations for different test sections; and

g. The heater should be easy to install, simple, and low cost.

8.2.1 Mechanical Integrity

The heater was made out of graphite and the bus bar was copper. Further, the heater was electrically insulated from the test section with a very good electric insulator (aluminum nitride, AlN) which has excellent heat conducting properties. The quality of the joint between the heater and bus-bar was improved by optimizing the interface geometry and smoothness of the faces. Because AlN is not a thermal insulator and because it is thin in the present experimental setup, the corresponding thermal resistance for this layer is 3.0×10^{-6} m^2K/W. This value is only slightly greater than the thermal resistance associated with the copper test section.

8.2.2 Effect of Thermal Expansion

The phenomenon of transferring energy to the high temperature heater region from the low temperature bus-bar region is one of the main concerns in the design (Refer to Fig. 15). This phenomena will cause the thermal expansion in both the horizontal and vertical directions in all components. Since the experiment will be conducted at different ranges of power from 0-250 kW, thermal expansion will be progressive as the power increases.

8.3 PRELIMINARY IDEAS

Many different ideas were considered. Among them, three possibilities are presented.

8.3.1. Bolted Configuration

In Fig. 16, the heater is attached to the bus-bar by using several bolts. For the following reason this design was not implemented: 1) bolt will change the characteristics of the heater, 2) it is impossible to apply uniform pressure between graphite and heater, 3) there is not enough room for bolts, and 4) due to the material brittleness and weight of bus-bar, installation was too difficult.

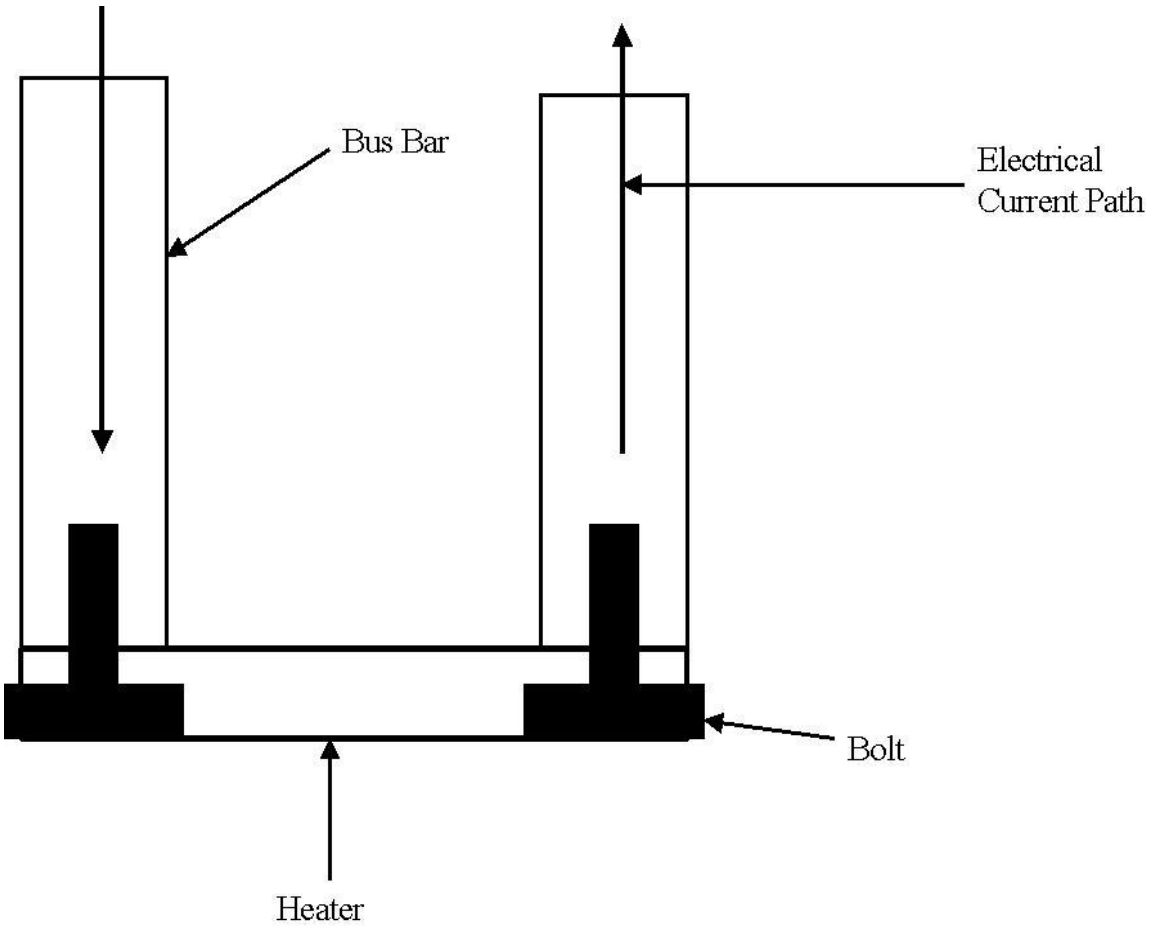

Figure 16

8.3.2. External Bracket

In the external bracket configuration, the bus-bar would be forced against the heater by using several brackets (Fig. 17). The extended bolts would apply the desired pressure between the heater and the bus-bar. The pressure could be adjusted before operation. Since the temperature would change during the experiment (based on the desired power), the pressure also would change due to the thermal expansion. Since the thermal expansivity of copper is relatively high (Mean Coefficient of Thermal Expansion between room temperature and 950 ^{o}C is 19 - 22 x 10^{-6} m/m ^{o}C), serious damage to the heater is possible. For this reason, this design was accepted with precaution. If the increase in pressure is uniform and does not exceed a critical limit, there could be an enhanced thermal contact.

8.3.3 External Bracket with a Compression Spring

In the last design, the geometry was simulated such that thermal expansion was compensated for with special springs in both the horizontal and vertical directions (see Figs. 18 and 19). These springs will absorb the thermal expansion to some extent and will prevent large increase in the pressure between the different components. The pressure range may be adjusted by changing the position of compression nuts. The details of this design are shown in Fig. 18. The mechanism to interface the test section heater to the electric power supply bus-bar has been designed, and the details of this design are shown in Figs. 19 and 20. The unique features of this design are: (1) thermal expansion will not change the pressure between different components, (2) the heater is easy to install, and (3) no bolt will be needed to connect the bus-bar to the heater.

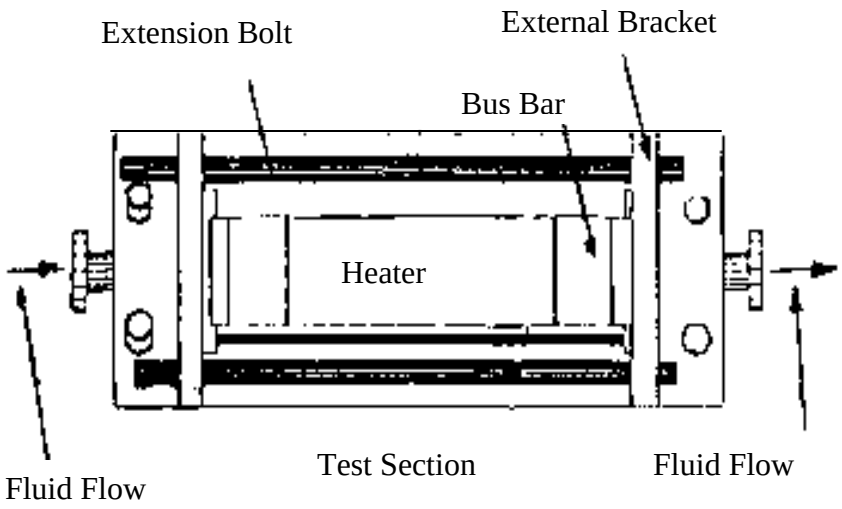

Figure 17: (Top View) Conceptual Heater/Test Section Assembly

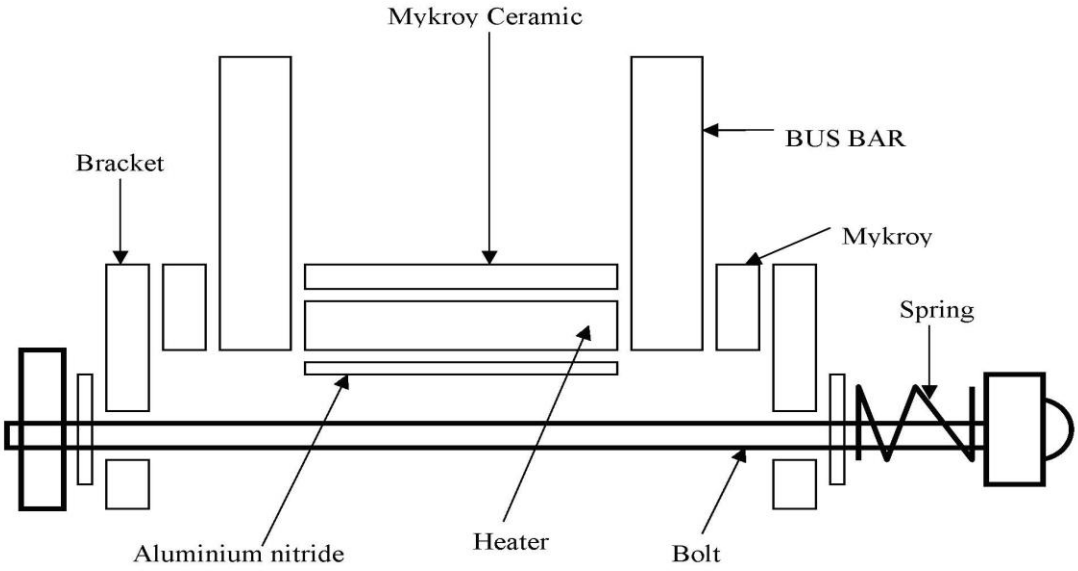

Figure 18: (Side View) Conceptual Heater/Bus Bar Assembly

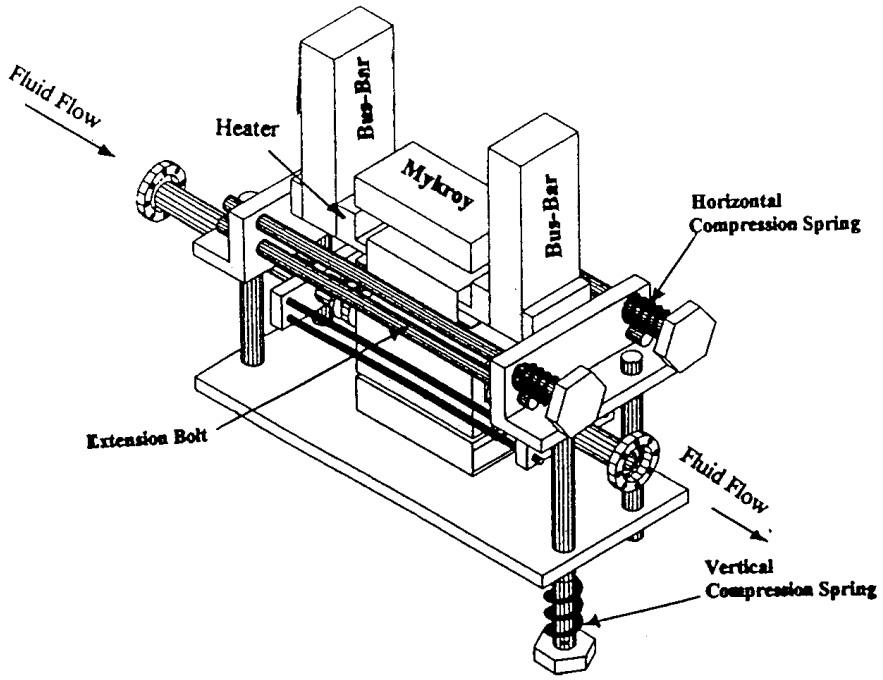

Figure 19: Monoblock Heater Bus-Bar Interface with a Compression Spring.

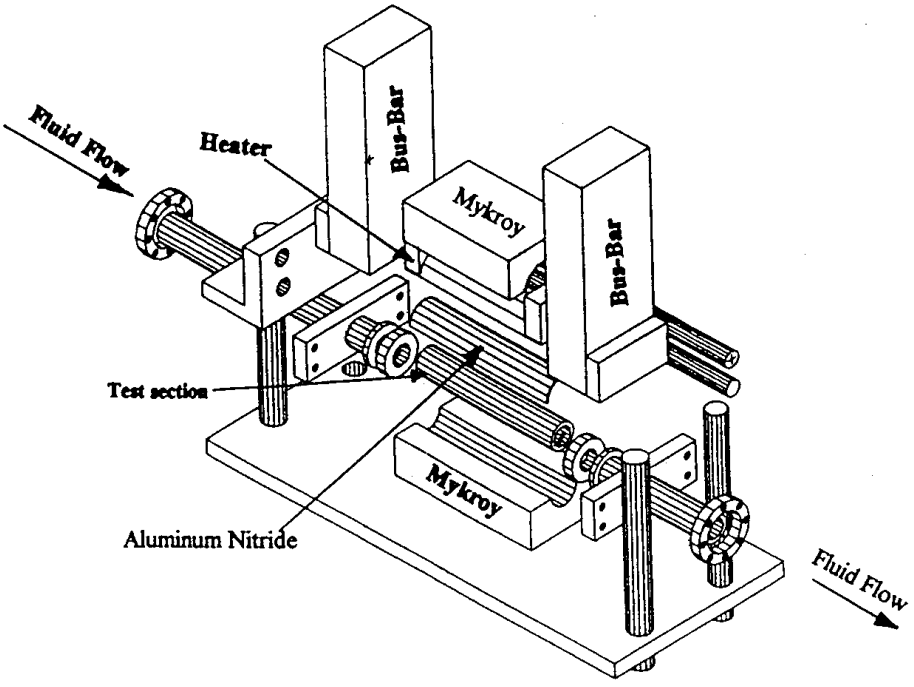

Figure 20: High Heat Flux Experimental Assembly with External Brackets for the Cylindrical Test Section.

9.0 A TEST SECTION FOR MEASUREMENTS OF THREE-DIMENSIONAL, LOCAL FLOW BOILING HEAT FLUX

9.1 INTRODUCTION

The Thermal Science Research Center (TSRC) at Prairie View A&M University has developed a new and unique high heat flux testing facility [51] which is part of the Institute for High Heat Flux Removal (IHHFR). The facility is operational and several speciality bus bars, test sections, and heater designs have been completed, constructed and tested. Although degassed and deionized water is the working fluid, the facility can be expanded to accommodate other working fluids.

The IHHFR is focusing on interdisciplinary applications as it relates to high heat flux engineering issues and problems which arise due to engineering systems being miniaturized, optimized, or requiring increased high heat flux performance.

The test section configurations examined were non-uniformly heated cylindrical-like and monoblock test sections with a circular 10.0 mm diameter coolant channel bored through the center. The theoretical or idealization of the cylindrical-like test section is a circular cylinder with half (-90 degrees to +90 degrees) of its outside boundary subjected to a uniform heat flux and the remaining half insulated. The actual cross-section configuration of this test-section is shown in Fig. 21. Because it was not practical to fabricate a cylindrical shell resistive heater to heat a circular cylinder from one side, five flat faces were machined to convert the theoretical circular cylinder into the cross-section shown in Fig. 21. This latter configuration was heated with five flat resistive graphite heaters. Both types of test sections were 200.0 mm long; and, the heated length was between 180.0 and 200.0 mm (depending on the heater design). Water was the coolant. The inlet water temperature could be set at any level in the range of 26.0 ^{0}C to 130.0 ^{0}C and the exit pressure could be set at any level in the range from 0.4 MPa to 4.0 MPa. Thermocouples (TC) were placed at forty-eight locations inside the solid cylindrical-like or monoblock test section. Typical thermocouple wells for twelve such locations are shown in Fig. 21. For each of four axial stations, three thermocouples were embedded at four circumferential locations (0, 45, 135, and 180 degrees, where 0 degrees corresponds to that portion of the axis of

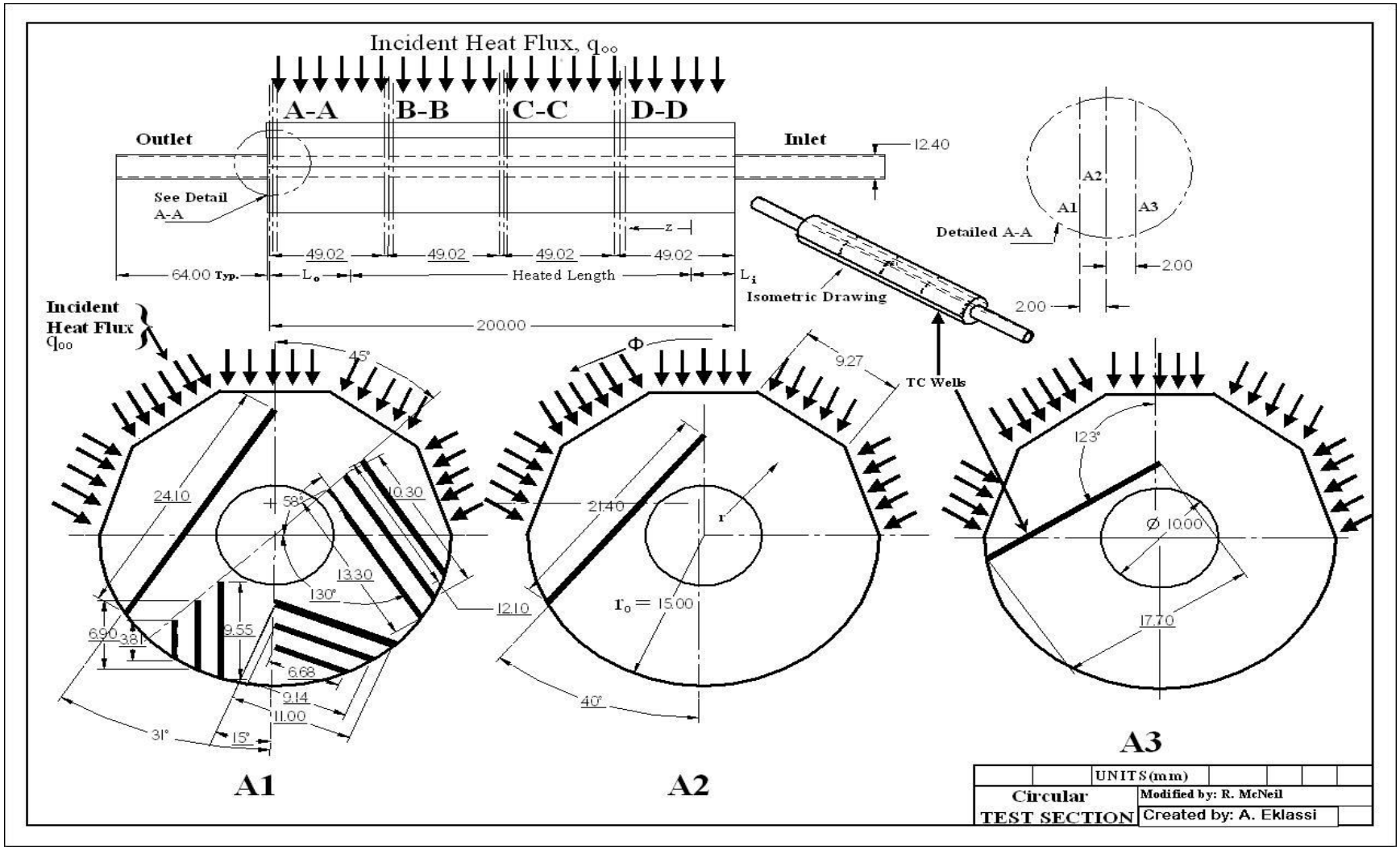

Figure 21: Test Section Used for Local Temperature and Heat Transfer Measurements. Water Flows Through the 10.0 mm Diameter Channel. The Thermocouples (TC) Wells are Solid Black Lines with Specified Lengths and Angles. Note: At $\phi = 0$ degrees, the Single TC Shown in Plane A3 Should be Switched with the Corresponding TC in Plane A1.

symmetry close to the heated surface) in the wall of the test section. Finally, the mass velocity could be set at any level in the range from 0.6 to 10.0 Mg/m^2s.

9.2 TEST SECTION DESCRIPTION

In order to avoid the excess costs associated with using electron- or ion-beams to produce the non-uniform heat flux, the new facility was developed which will allow three-dimensional conjugate heat transfer measurements and two-dimensional local subcooled flow boiling heat flux and related critical heat flux measurements using a DC power source.

As noted, there were two basic test sections (TS) employed: (1) A circular-like cylindrical TS, and (2) A monoblock TS. The TSs were fabricated from Type AL-15 Glidcop Grade Copper, manufactured by OMG Americas. Since the test sections were identical as far as TC placement with the exception of their cross section, a detailed description will only be given for the circular-like TS as shown in Fig. 21. Isometric and longitudinal side views are shown in Fig. 21. The flow inlet and exit are indicated in the latter view. Also shown in the latter view are four axial stations labeled A-A, B-B, C-C, and D-D, which are axial locations where TC wells exist for local in-depth wall temperature measurements. The purpose of the four axial locations was to obtain an estimate of the axial distribution of TS wall temperature for a given applied heat flux. Since the geometry of the TC wells is identical at all four primary axial stations, a detail description will be given for only one axial station. For example, the A-A axial stations have twelve (12) TC wells, with ten (10) wells in plane A1 and one each in planes A2 and A3 which are axially displaced upstream from plane A1 by 2.0 mm and 4.0 mm, respectively.

The TCs at station A-A resulted in both radial and circumferential distributions of the wall temperature. Hence, a combination of all axial stations produced a three-dimensional distribution of the TS wall temperature as a function of the applied heat flux and the water flow regime which varied from single-phase flow at the TS inlet to a possible two-phase flow at the exit.

9.3 TEST SECTION HEATER

This section highlights the selection of graphite as the heater material and its applied geometric configuration for the test sections. The heater material is graphite grade G-20, which is produced by Graphite Engineering Inc. The heaters for the test sections should satisfy the following design requirements: (1) the material must withstand temperatures above 650.0 ^0C; (2) the resitivity of the material must be very high (above 100.0 $\mu\Omega$-cm); (3) it must support a

maximum power handling capacity of 250.0 kW; (4) it must be electrically insulated with a dielectric material with a high thermal conductivity; and (5) the insulator and heater must be able to attach to each unique test section design configuration. Figure 20 and 22 show the conceptual heater design. It is a half cylindrical tube shell with thick ends. For the final (or actual) heater configuration, this cylindrical heater shell was later subdivided (in the circular direction) into five flat strip heaters with the same axial length as the circular tube shell heater. The heater material was manufactured to rest exactly next to the similarly shaped aluminum nitride (AlN) dielectric layer. The dielectric was placed between the heater and copper test section. The AlN electrical insulation was manufactured in thin flat strips to rest exactly over the outer surface of the circular tube. The outer surface of the circular copper test section was machined and its final form has five straight, flat sections on half of the circumferential section (see Fig. 21) on which the AlN is placed. The remaining half of the outside boundary of the test section remained circular. Bus bars were placed on the ends of the heater as is illustrated in Figs. 20 and 22. The exact configuration is presented below (see Figures 32 and 33).

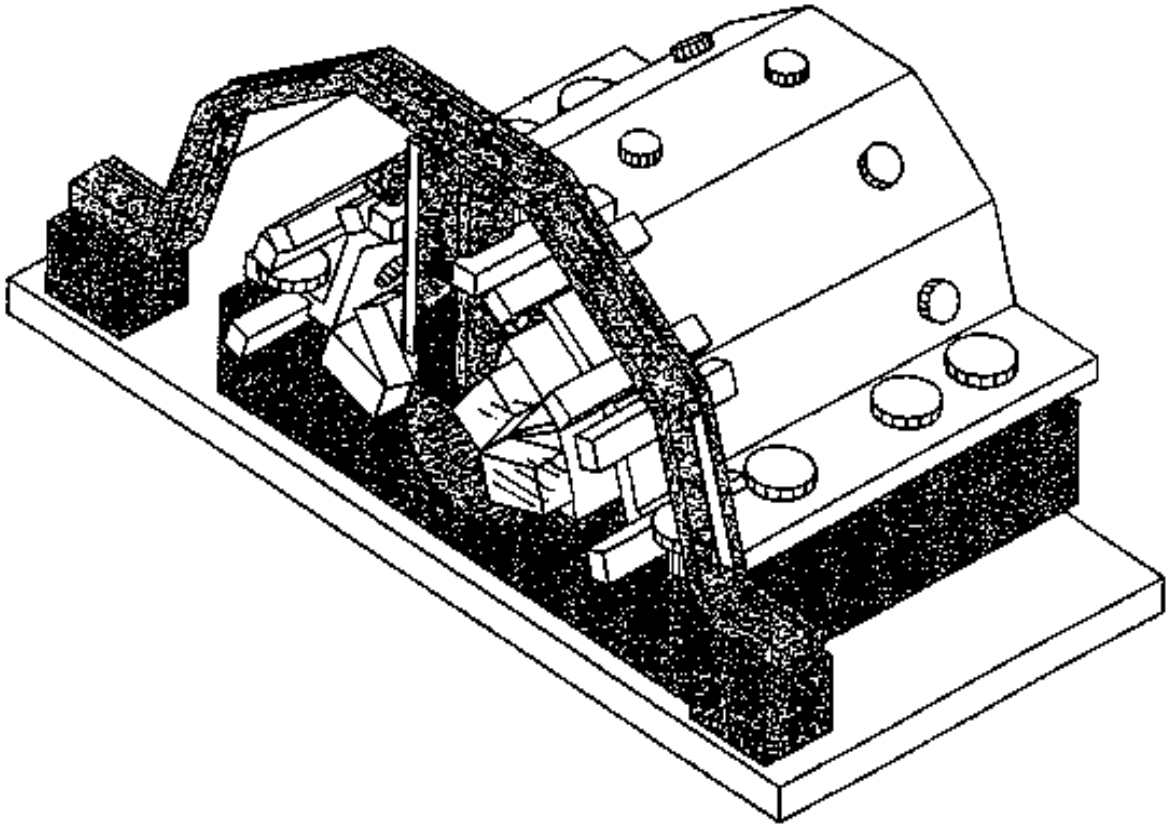

Figure 22: Test Section Assembly with Heaters and conceptual Holding Fixture (see Figs. 21 and 20 for Component Labeling and Details.

10.0 MEASUREMENTS OF THREE-DIMENSIONAL, LOCAL TEMPERATURE FOR A SINGLE-SIDE HEATED (SSH) CYLINDRICAL TS

10.1 INTRODUCTION

Plasma-facing components for fusion reactors and high heat flux heat sinks for aerodynamic applications, are usually subjected to a peripherally non-uniform heat flux. The test section (TS) configuration under study for this work in the IHHFR consists (see Fig. 21) of a partially circular-like cross-section with an inside circular 10.0 mm coolant channel bored through the center. The test section: (1) has no additional interfacing layers between the TS outside and inside boundaries through which the incident heat passes, and (2) was machined from a solid Glidcop Copper block. The main section of the TS was 30.0 mm in nominal outside diameter and 200.0 mm long. The TS was subjected to a constant heat flux on one side only. Water was the coolant. The inlet water temperature was held near 26.0 ^{0}C and the exit pressure was maintained at 0.207 MPa (T_{sat} = 121.3 ^{0}C). Thermocouples (0.5 mm O.D., stainless steel sheathed, Type-J) were placed at forty-eight locations inside the solid TS. For each of four axial stations, three thermocouples were embedded at three radial and four circumferential locations (0, 45, 135, and 180 degrees, where 0 degrees corresponds to that portion of the axis of symmetry close to the heated surface). The mass velocity was 0.59 Mg/m^{2}s. For these conditions, the basic fluid flow is a turbulent (Re = 6,900) and highly developing flow with a reciprocal Graetz number (Gz^{-1}) of 4.5 x 10^{-4}.

For brevity in this section, a detail description of the test facility (etc.) is given in the next section of this report. The thermocouples were calibrated to within 0.2 ^{0}C.

International efforts are vigorously proceeding in the investigation of heat transfer and related CHF in one-side-heated flow channels. Some examples of recent one-side heating efforts include: (1) the international round-robin monoblock CHF swirl-flow tests by Youchison, Schlosser, Escourbiac, Ezato, Akiba, and Baxi [52]; (2) CHF in multiple square channels by Akiba, Ezato, Sato, Suzuki, and Hatono [53]; (3) CHF comparison of an attached-fin hypervapotron and porous coated surface by Youchison, Nygren, Griegoriev, and Driemeyer [54]; (4) CHF enhancements due to wire inserts by Youchison, Cadden, Driemeyer, and Willie [55]; (5) post-CHF with and without swirl flow in a monoblock by Marshall [4]; (6) CHF data base of JAERI by Boscary, Araki, and Akiba [21,22]; (7) post-CHF enhancement factors by

Marshall, Watson, McDonald, and Youchison [6]; (8) CHF peaking factor empirical correlations by Inasaka and Nariari [28], and Akiba et. al. [17]; (9) CHF correlation modification to account for peripheral non-uniform heating by Celata, Cumo, and Mariani [56]; (10) comparison of one-side heating with uniform heating by Boyd [30]; (11) single- and two-phase subcooled flow boiling heat transfer in smooth and swirl tubes by Araki et. al. [57]; (12) smooth tube heat transfer, CHF and post-CHF by Becker et. al. [58]; and (13) turbulent heat transfer analysis by Gartner et. al. [59].

Conjugate heat transfer modeling [60-62] has proved useful in forming baselines and identifying important parameters affecting peaking factors (PFs) and data reduction for the spectrum of high heat fluxes found in a wide variety of applications. For various applications requiring different fluids, the results show the following:

1. the coexistence of three flow boiling regimes inside an one-side heated (OSH) circular geometry (for water only),
2. the correlational dependence of the inside wall heat flux and temperature (fluid independent), and
3. inaccuracies that could arise in some data reduction procedures (fluid independent).

However, for plasma facing component (PFC) applications in fusion reactors, work to expand conjugate heat transfer analyses from simple circular and complex geometries to PFC geometries is still needed for consistently predicting PFs for OSH channels.

10.2 TEST SECTION (TS)

The TSs were fabricated from Type AL-15 Glidcop Grade Copper. A detailed description of the TS is shown in Fig. 21. The overall length of the TS, including the inlet and outlet reduced diameter sections, was 328.0 mm. The main section of the TS (available for heating) was 200.0 mm long with a nominal outside diameter of 30.0 mm and an inside diameter of 10.0 mm. For these tests, the actual directly heated length, L, was 180.0 mm. In Fig. 21, isometric and longitudinal side views are shown.

10.3 RESULTS

Design of robust plasma-facing components (PFCs) must be based on accurate three-dimensional conjugate flow boiling analyses and optimizations of the PFC local wall temperature, and hence on the local flow boiling regime variations. Such analyses must have three-dimensional data as a basis for comparison, assessment, and flow boiling correlation

adaptation for localized boiling. As an initial part of an effort to begin to provide such data, selected steady-state results are presented for the above-noted conditions for the: (1) three-dimensional variations of the TS wall temperature as functions of the circumferential (ϕ), radial (r), and heated axial (Z) coordinates; (2) outside steady-state heat flux as a function of the local wall temperature; and, (3) occurrence of pre- and post-CHF. The three-dimensional variations in the local wall temperature will be discussed first.

10.3.1 Local 3-D Variations

The circumferential variations in the channel wall temperature are presented in Figs. 23a and 23b for four levels of the net, outside, single-side heat flux, q_o. Figures 23a and 23b show such variations close to the inside fluid-solid boundary and the outside (partially heated) boundary, respectively. Comparing the two sets of plots, one observes two very different circumferential wall temperature variations near the two boundaries. Since there are only four circumferential (ϕ = 0 corresponds to the heated side of the plane of symmetry) locations for each set of measurements, these distributions will not show the exact local circumferential slopes but the quantitative trends at the four locations are evident. As one would expect, the wall temperature approaches the fluid temperature in Fig. 23a (near the fluid/solid boundary) as ϕ approaches 180.0 degrees. However, the locus of the data in Fig. 23b (near the outside partially heated boundary) displays approximately the correct boundary condition of a zero circumferential temperature gradient as ϕ approaches 180.0 degrees but differs from the profile near the fluid/solid boundary. In both cases, the temperature is almost constant between ϕ = 45.0 and 135.0 degrees. This is due to the relatively large thickness of the test section. For smaller TS thicknesses, the variation would be greater. In the limit of ϕ approaching 180.0 degrees in Fig. 23b, the wall temperature is well above the fluid temperature and increases as q_o increases.

Figure 24 displays the radial temperature profiles at ϕ = 45.0 degrees and shows small variations with respect to r and some values of ϕ. This is of course contrasted with larger radial variations as displayed by comparing Figs. 23a and 23b at other values of ϕ.

Finally, Fig. 25 shows the remaining portion of the three-dimensional variations via the axial wall temperature profiles which include the three downstream-most axial stations. For this experimental case, the heater length (L) was 180.0 mm long (in the axial direction) and was placed symmetrically on the test section (200.00 mm long). This means that there are 10.0 mm

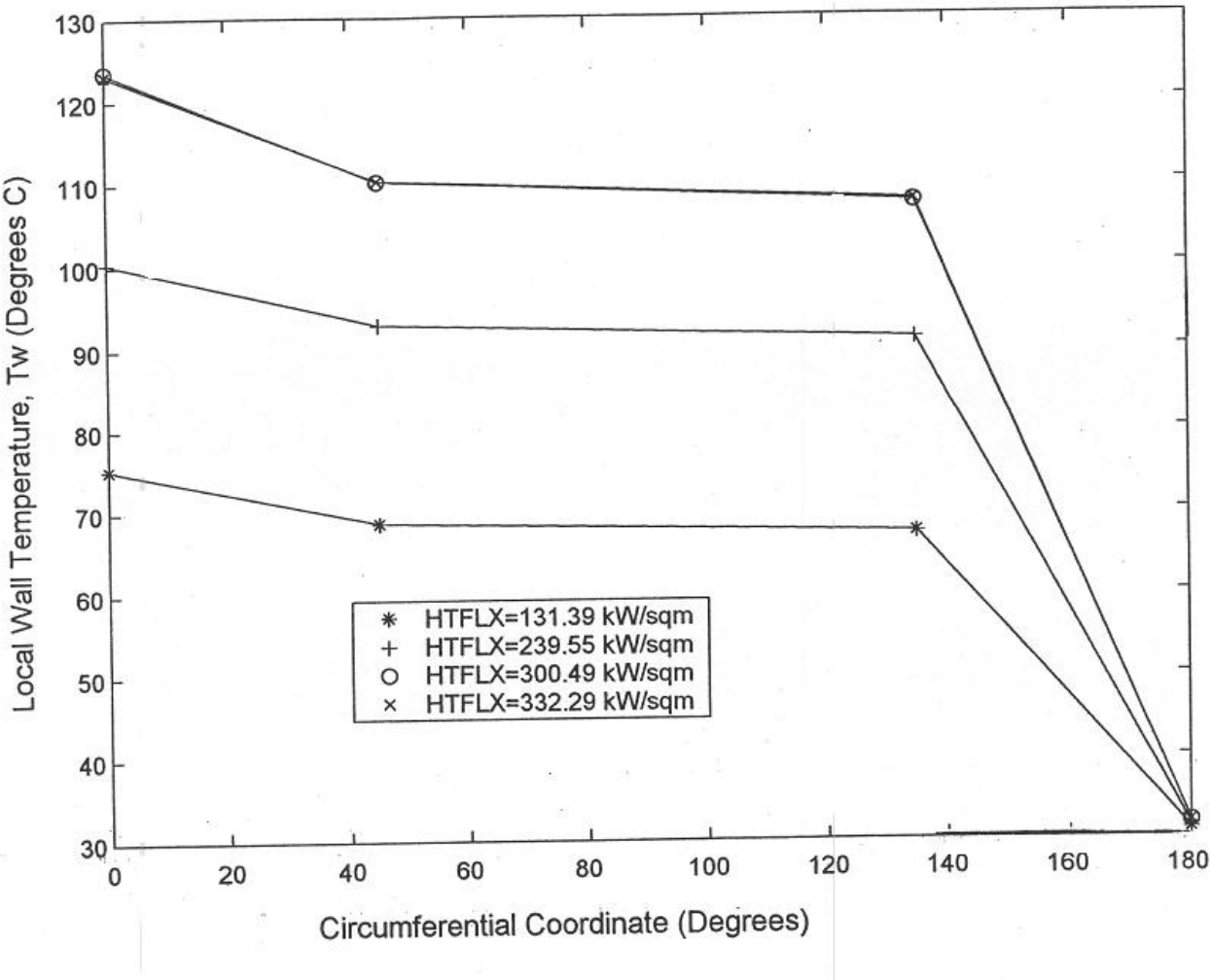

Figure 23a: Circumferential Wall Temperature Profile for the Flow Channel Close to the Fluid/Solid Boundary as a Function of Net Incident Heat Flux, at $Z=Z_4=186.0$ mm ($L_i=L_o=10.0$ mm).

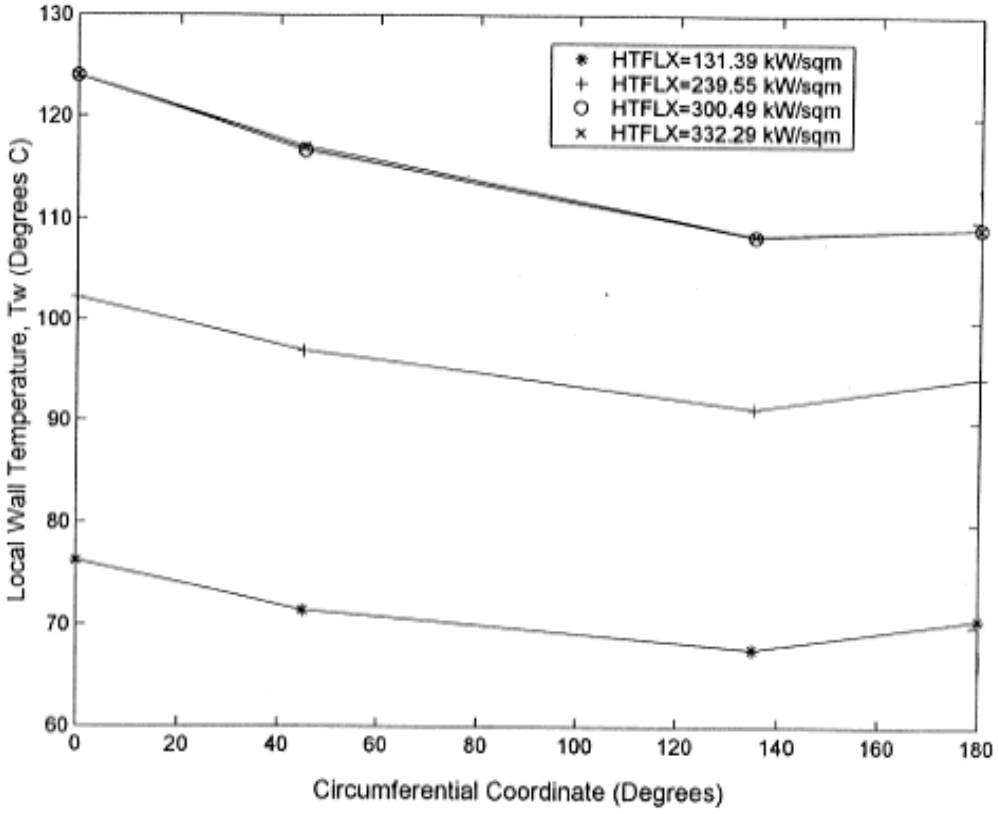

Figure 23b: Circumferential Wall Temperature Profile for the Flow Channel Close to the Heated Boundary (i.e. Away from the Fluid/Solid Boundary) as a Function Of the Net Incident heat Flux ($L_i = L_o = 10.0$ mm).

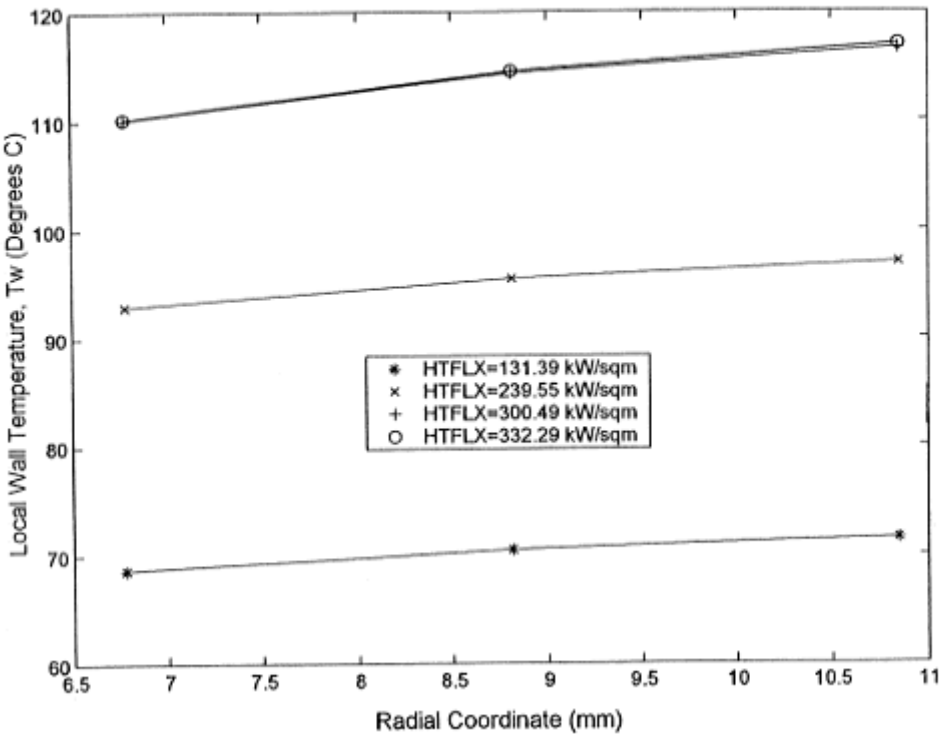

Figure 24: Radial Wall Temperature Profile for the Flow Channel at ϕ = 45.0 degrees and Z = Z_4 = 186.0 mm as a Function of the Net Incident Heat Flux (L_i = L_o = 10.0 mm).

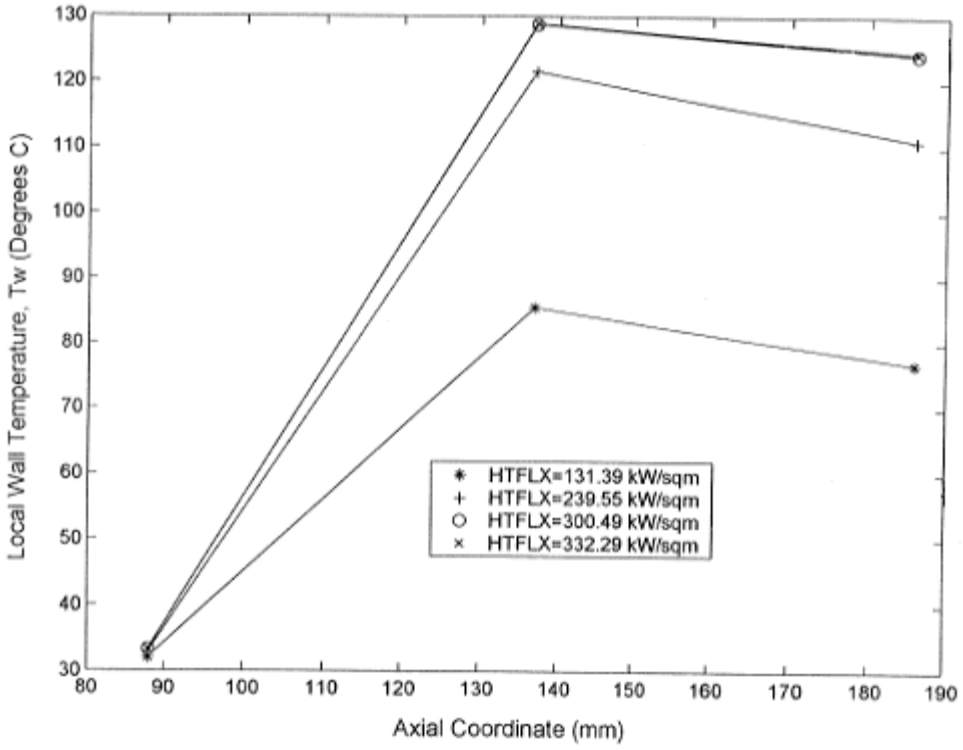

Figure 25: Axial Wall Temperature Profile for the Flow Channel at ϕ = 0.0 degrees, and r = 8.23 mm (Close to the Heated Boundary) as a Function of the Net Incident Heat Flux ($L_i = L_o$ = 10.0 mm).

long unheated (i.e., unheated directly) portions on each end (i.e., $L_i = L_o$ = 10.0 mm) of the test section. The curves shown in Fig. 25 are for test section locations along the axis of symmetry (ϕ = 0.0 degrees) and close to the heated boundary (r = 8.23 mm).

Finally in Figs. 23 through 25, the curves for the highest two heat fluxes almost overlap. This overlap is due to the fact that the onset of fully-developed boiling regime heat flux has been exceeded thereby causing the wall temperature to be virtually unchanged as the heat flux increases and as long as the CHF is not exceeded.

10.3.2 Outside Heat Flux/Wall Temperature Relationship

Two cases are presented here which show the relationship, at different radii, between the net, outside incident heat flux and the local wall temperature. The two cases involve different placements of the heater (i.e., different L_i) relative to the geometric length of the test section. Although not identical, this relationship between q_o and T_w would be directly related to the 2-D local boiling curve if the radius at which this relationship was considered was equal to the inside radius of the flow channel. This work will eventually lead to the latter. For this first case in Fig. 26, the steady-state heat flux/wall temperature relationship is presented: (1) for the axis of symmetry with ϕ = 0.0 degrees; (2) for axial locations of Z = 133.0, 135.0, and 137.0 mm (nominally, Z = Z_3 = 137.0 mm or cross section B-B in Fig. 21; (3) for radii of 12.67, 10.54, and 8.23 mm, respectively; and, (4) with the 180.0 mm (= L) heater placed symmetrically along the axial 200.0 mm test section length with 10.0 mm (= L_i = L_o) of unheated length at the upstream and downstream ends of the test section. For each curve (or radial coordinate) shown, the two left-most data points show the relationship when single-phase convection exists in the flow channel. Beyond this second data point for each radius, the slope of each curve changes denoting an onset of partial nucleate boiling. Finally and beyond the third data point (from the left), one observes a progressive increase of the slope of the q_o vs T_w curves in Fig. 26 as the radius decreases or as the inside fluid-wall boundary is approached. This denotes the region of fully developed nucleate flow boiling in the flow channel.

The second case is presented in Fig. 27 and applies for the following conditions: (1) the 180.0 mm (= L) heater placed asymmetrically along the axial 200.00 mm test section length, with a 4.0 mm (= L_o) unheated length at the downstream end of the test section, and a 16.0 mm (= L_i) unheated length at the upstream end of the test section; (2) the axis of symmetry with ϕ = 0.0 degrees; (3) axial locations of Z = 133.0, 135.0, and 137.00 mm (nominally, Z = Z_3 = 137.0 mm axial station); and (4) radii of 12.67, 10.54, and 8.23 mm, respectively. These curves are more complete than those for the first case in that they not only show the previously mentioned three flow regimes (single-phase, partially nucleate boiling, and fully developed flow boiling) but an apparent local critical heat flux (CHF) occurred and is displayed in Fig. 27 between the right-most pair of data points on each curve. The occurrence of a local dryout is denoted by a decrease in the slopes of the curves between the two right-most points as compared to the curve's slope just to the left of these two points. The normal temperature escalation, which accompanies

CHF in uniformly heated tubes, is absent due to the single-side-heated flow channel geometry and the resulting three-dimensional conjugate heat transfer (which is absent in the uniformly heated cases). This escalation may occur when a global CHF is reached [52]. The reduction in the slope at the upper part of each curve in Fig. 27 suggests a stable entry into the local post-dryout regime (at ϕ = 0.0 degrees and Z = Z_3 = 137.0 mm).

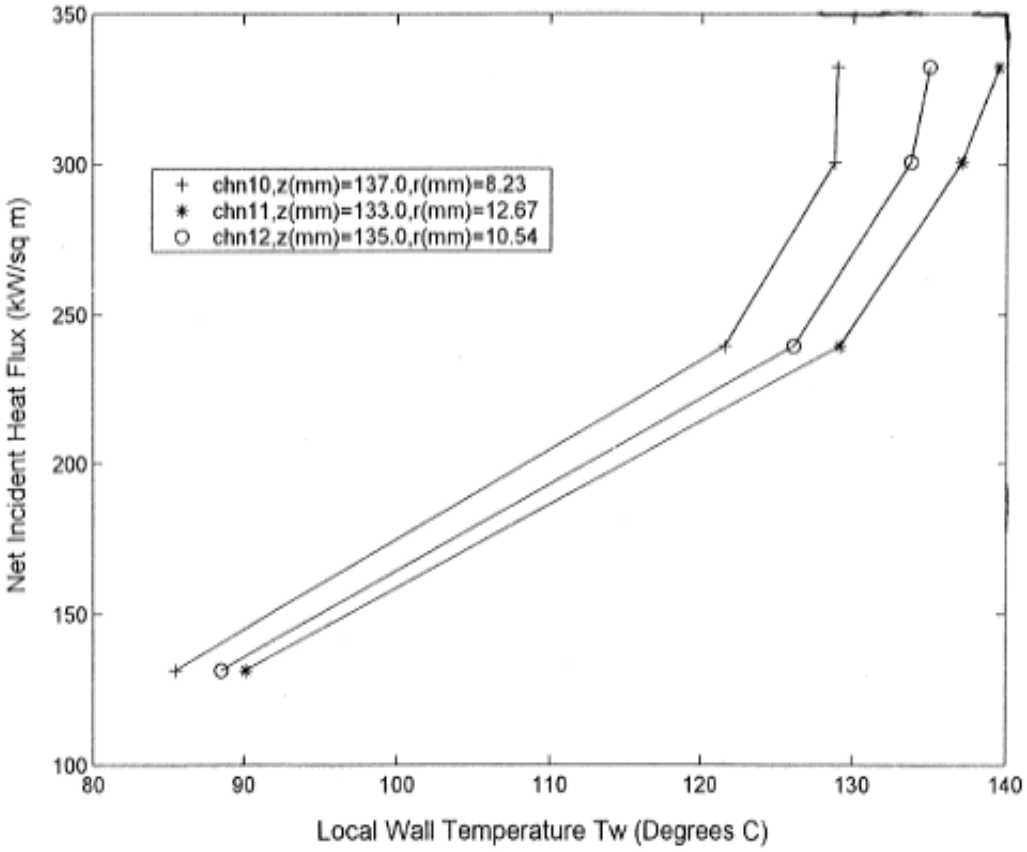

Figure 26: Steady State Net Incident Heat Flux as a Function of the Local Flow Channel Wall Temperature at ϕ = 0.0 degrees and for Specified Axial Locations (Near Z_3 = 137.0 mm) and with Heaters Symmetrically (L_i = L_o = 10.0 mm) Placed with Respect to the Axial Direction (i.e., 10.0 mm of Unheated Flow Channel Both Upstream and Downstream of the Heaters).

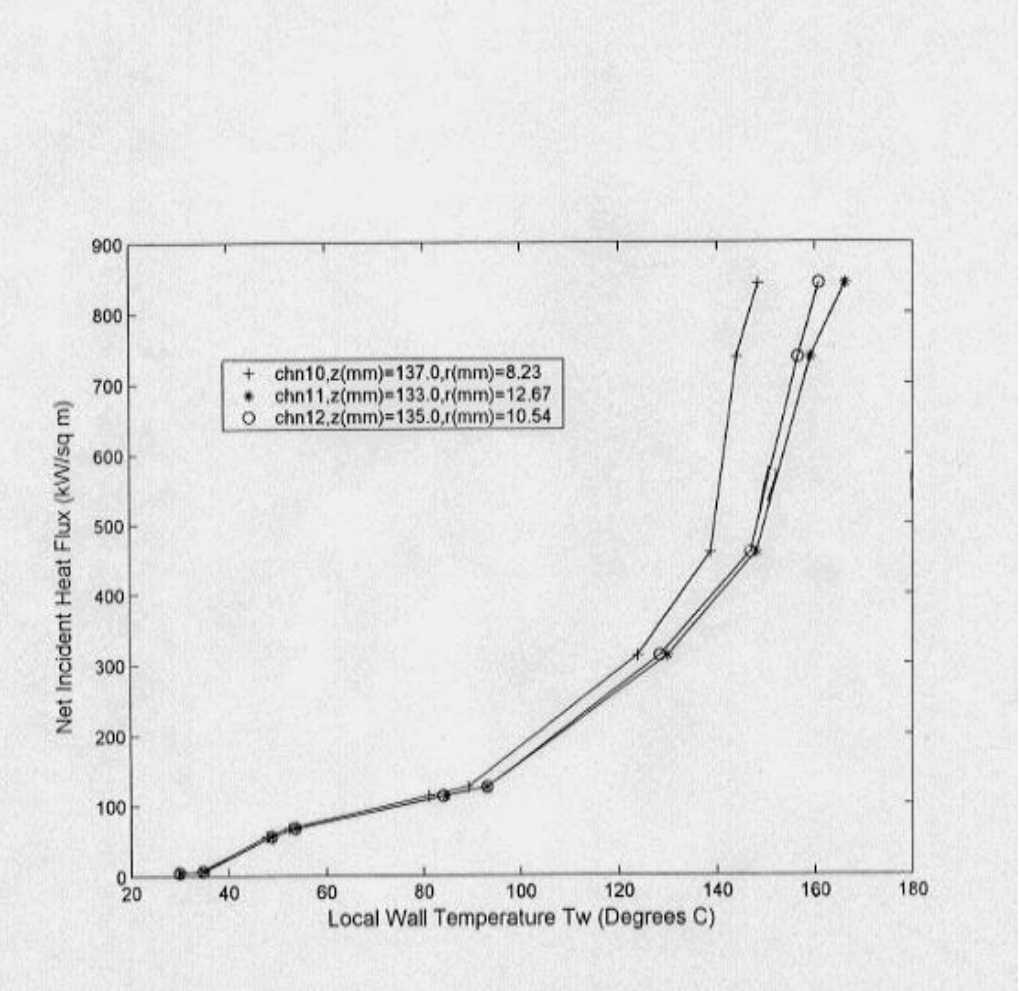

Figure 27: Steady State Net Incident Heat Flux as a Function of the Local Flow Channel Wall Temperature at ϕ = 0.0 degrees and for Specified Axial Locations (Near Z_3) and with Heaters Asymmetrically Placed with Respect to the Axial Direction with L_o = 4.0 mm and L_i = 16.0 mm of Unheated Flow Channel Downstream and Upstream of the Heaters, Respectively.

11.0 A NEW FACILITY FOR MEASUREMENTS OF THREE-DIMENSIONAL, LOCAL FLOW BOILING HEAT FLUX

11.1 BACKGROUND

In the development of plasma-facing components (PFC) for fusion reactors and high heat flux heat sinks (or components) for aerodynamic applications, the components are usually subjected to a peripherally non-uniform heat flux. Even if the applied heat flux is uniform in the axial direction (which is unlikely), both intuition and recent investigations have clearly shown that both the local heat flux and the eventual critical heat flux (CHF) in this three-dimensional (3-D) case will differ significantly from similar quantities found in the voluminous body of data for uniformly heated flow channels. Although this latter case has been used in the past as an estimate for the former case, more study has become necessary to examine the three-dimensional temperature and heat flux distributions and related CHF. Work thus far has shown that the non-uniform peripheral heat flux condition enhances CHF in some cases and CHF can be enhanced significantly by the inclusion of heat flux spreaders in TS [30].

The configurations under study for this work consists of: (1) a non-uniformly heated cylindrical-like test section with a circular coolant channel bored through the center, and (2) a monoblock which is a square cross-section parallelepiped with a circular drilled flow channel through the center line along its length. The theoretical or idealization of the cylindrical-like test section would be a circular cylinder with half (-90^0 degrees to 90^0 degrees) of its outside boundary subjected to a uniform heat flux and the remaining half insulated. For the monoblock, a uniform heat flux is applied to one of the outside surfaces and the remaining surfaces are insulated. The outside diameter of the cylindrical-like test section was 30.0 mm and its length was 200.0 mm. The monoblock square has lengths 30.0 mm. The inside diameter of the flow channel for both types of test sections is 10.0 mm. Water is the coolant. The inlet water temperature can be set at any level in the range from 26.0 ^{0}C to 130.0 ^{0}C and the exit pressure can be set at any level in the range from 0.4 MPa to 4.0 MPa. Thermocouples are placed at forty-eight locations inside the solid cylindrical-like or monoblock test section. For each of four axial stations, three thermocouples are embedded at four circumferential locations (0, 45, 135, and 180 degrees, where 0 degrees corresponds to that portion of the axis of symmetry closet to the heated

surface) in the wall of the test section. Finally, the mass velocity can be set at any level in the range from 0.6 to 10.0 Mg/m^2s.

11.2 OVERVIEW AND SUMMARY

The TSRC at Prairie View A&M University has developed a new and unique high heat flux testing facility which is part of the IHHFR.

In the development of plasma-facing components (PFCs), many investigators have been studying the effect of a single-side applied heat flux on the onset of local coolant boiling and the eventual critical heat flux (CHF). Although encouraging results have been obtained in characterizing peaking factors for local two-dimensional boiling curves and critical heat flux, addition experimental data and theoretical model development are needed to validate the applicability to PFCs and local two-dimensional boiling curve prediction. Both these and related issues will affect the flow boiling correlation and data reduction associated with the development of PFCs for fusion reactors and other physical problems that are dependent on conjugate heat transfer modeling in the heat flux spectrum of applications--which range from micro- to mega-heat flux levels.

One of the most critical technological needs to ensure the reliability of fusion reactor operation in the twenty-first century is the ability to accommodate the high heat fluxes generated near the PFCs. Accordingly, it is essential to have the ability to accurately predict the local heat transfer throughout the coolant channels of PFCs. The maximum value of the local heat flux, which allows a safe channel wall temperature much below the wall melting temperature when water is the coolant, is below the CHF. An applied heat flux that is greater than the CHF may (will for uniformly heated channels [Bergles, [8]; Boyd, [48,11]; Celata and Cumo, [2]; Gaspari and Cattadori, [3]; Groeneveld, [9]; Marshall, [27,4]; Marhall, Watson, et al., [6]; Maulbetsch and Griffith, [10]; Schlosser, [5]; Tolubinskiy and Matorin, [7]; and Youchison, et al., [52,1]) cause local channel wall melting (burnout). It has been demonstrated that among the important parameters affecting the reliable correlation and prediction of the CHF are:

1. flow regime and flow parameters;
2. the applied heat flux profile; and
3. peaking factors for one-side heated (OSH) PFC geometries relative to uniformly heated geometries (UHG).

Although the capability of consistently predicting the local flow boiling curve has been demonstrated for UHG, this capability must be extended to more complex OSH PFC gemoetries (see Fig. 21).

Accurate peaking factor (PF) determination depends on the ability to both accurately predict the flow boiling curve for simple geometries and account for the complications in the prototype due to geometry and other effects. In this report, the PF is defined as the ratio of the inside wall peak heat flux for an OSH geometry to the inside wall peak heat flux for an UHG, with the same flow conditions. Many papers have been published reporting either new flow boiling correlations (e.g., Boyd and Meng, [12]), or assessments (e.g. Katto, [16]) and modifications of previously developed CHF correlations. Generally, there appears to be good confidence in predicting flow boiling for uniformly heated (UH) circular channels with or without twisted tapes. However, all PFCs involve OSH monoblock-like flow channels like that shown in Fig. 21. This poses the following question: How can the UHG data be used for the OSH channels? The answer to this question lies in the existence of PFs. The intent of many ongoing investigations is to use the PFs along with the UHG data to compute accurate conditions for heat transfer and CHF in OSH channels.

International efforts (e.g., Akiba et al., [17]; Araki et al., [19,18]; Baxi et al., [20]; Boscary et al., [21,22]; Boyd et al., [23]; Boyd and Meng, [24]; Escourbiac and Schlosser, [25]; Falter and Thompson, [26]; Marshall et al. [27]; Inasaka and Nariari, [28]; TORE SUPRA team, [29]; and Youchison et al, [1]) are ongoing to produce enough OSH data to determine the appropriate functional representations for the PFs. It has been demonstrated previously by Boyd [30] that the PF is dependent at least on: (a) the channel geometry, (b) incident heat flux profile, and (c) a characteristic Biot number. Although the PF has been defined and characterized for simple OSH geometries, few if any unified comparisons have been made with data. Several authors (e.g., Akiba et al., [17]; and Inasaka and Nariari, [28]) have proposed empirical PF correlations, but these have not been proven to be consistently applicable for the full range of flow parameters and the wide range of PFC geometries.

The descriptions of each aspect of the new facility were given in Sections 2.0 through 9.0; and, (1) a photo gallery of the facility is presented in Appendix “A”, (2) the developed TS Power Measurement System is summarized in Appendix “B” (A TSRC Student Internship), and (3) the design and installation of the Monoblokc TS helical wire insert is given in Appendix “C”

(A TSRC Student Internship). The IHHFR Facility produced OSH flow channel 3-D conjugate heat transfer data with thermally developing single-phase and two-phase flow conditions. This data sets the stage for validation and verification of applicable correlations and computational fluid dynamics and heat transfer codes.

12.0 PATENT DEVELOPMENT

TAMUS 1920: A Local Wall Heat Flux/Temperature (WHFT) Meter for Convective Flow

Applications

- Plasma Facing Components in Fusion Reactors
- Heat Sinks for Electronics
- Power Generation
- Oil, Gas, and Chemical Process Industries
- Aircraft and Aerospace
- Automotive
- Safety
- Medical Equipment
- Heating and Air Conditioning Systems
- Assessment tool for computational fluid dynamics (CFD) in computer codes

Abstract

Traditional heat transfer analysis includes approximating single-side-heated coolant channels with an equivalent uniformly heated channel. However, this technique may not apply in all cases. Single side heating effects are being considered in final designs and, hence, new and convenient methods are needed to correlate these two configurations. Questions pertaining to the correlation and optimization include: What is the parametric heat flux distribution on a channel interior wall that is subjected to single side exterior heating? and: What changes in channel design will result in greater accommodation of heat flux for single-side-heated configurations?

Researchers at the Thermal Science Research Center at Prairie View A&M University have developed a new device and method to measure the local wall heat flux and temperature at the inaccessible inside cylindrical boundary of a tube or pipe containing any flowing fluid and an externally applied heat source. The non-penetrating instrument provides for continuous measurement of the inside 2-dimensional wall heat flux and temperature. It can be used, for example, to determine convective heat transfer coefficients, monitor process conditions related to safety and efficiency, and assist in fluid dynamics and heat transfer computer simulations and analysis.

The advantages and unique features of this thermal measurement technique are:

- Non-invasive: the meter device attaches inline to the tube or pipe
- Able to assess analytical software for turbulent and multi-phase fluid flows
- Allows for 2-dimensional thermal measurement independent of the fluid
- Suitable for a wide range of fluid dynamic environments
- No effect on fluid flow instrumentation and measurement

Inventors

Dr. Ronald D. Boyd, Mr. Ali Ekhlassi, Mr. Penrose Cofie
All of Thermal Science Research Center (http://i2i.pvamu.edu/index.asp?page=tsrc)
Prairie View A&M University

Contact

R. Page Heller
Senior Licensing Manager

US006824305B1

(12) **United States Patent**
Boyd et al.

(10) **Patent No.: US 6,824,305 B1**
(45) **Date of Patent: Nov. 30, 2004**

(54) **LOCAL WALL HEAT FLUX/TEMPERATURE METER FOR CONVECTIVE FLOW AND METHOD OF UTILIZING SAME**

(75) Inventors: **Ronald D. Boyd**, Spring, TX (US); **Ali Ekhlassi**, Tomball, TX (US); **Penrose Cofie**, Houston, TX (US)

(73) Assignee: **The Texas A & M University System**, College Station, TX (US)

(*) Notice: Subject to any disclaimer, the term of this patent is extended or adjusted under 35 U.S.C. 154(b) by 0 days.

(21) Appl. No.: **10/641,826**

(22) Filed: **Aug. 15, 2003**

Related U.S. Application Data

(60) Provisional application No. 60/404,246, filed on Aug. 16, 2002.

(51) **Int. Cl.**[7] **G01K 17/00**; G01K 3/06

(52) **U.S. Cl.** **374/29**; 374/30; 374/44; 374/15

(58) **Field of Search** 374/29, 30, 44, 374/137, 134, 110, 112, 15, 135, 45

(56) **References Cited**

U.S. PATENT DOCUMENTS

3,263,485	A *	8/1966	Mahmoodi	374/44
6,331,075	B1 *	12/2001	Amer et al.	374/44
6,487,866	B1 *	12/2002	Fesmire et al.	62/51.1
6,497,509	B2 *	12/2002	Merzliakov et al.	374/44
6,742,926	B1 *	6/2004	Fesmire et al.	374/45
2003/0196778	A1 *	10/2003	Kobayashi et al.	165/41

OTHER PUBLICATIONS

Boyd, et al., "Similarities and Differences Between Single-Side and Uniform Heating for Fusion Applications–I: Uniform Heat Flux," Fusion Technology, vol. 25, 1994, pp. 411–418, Jul., 1994.

Problems #1 & #2 from Final Exam of MCEG 5153 (1 page), Thermal Science Research Center, College of Engineering, A&M University, Prairie View, TX, Fall, 1996.

Boyd, Sr., et al., "*Single–Side Heated Monoblock, High Heat Flux Removal Using Water Subcooled Turbulent Flow Boiling*", Journal of Heat Transfer, ASME, Thermal Science Research Center, College of Engineering, A&M University, Prairie View, TX, Feb. 2004, vol. 126 (5 pages).

Boyd, Sr. et al., "*Conjugate Heat Transfer Measurements In A Single–Side Heated Circular Flow Channel Under Turbulent, Subcooled Flow Boiling Conditions*", presented at the Twelfth International Heat Transfer Conference, Gremble, France, Aug. 18–23, 2002 (6 pages).

* cited by examiner

Primary Examiner—Gail Verbitsky
(74) *Attorney, Agent, or Firm*—Baker Botts L.L.P.

(57) **ABSTRACT**

According to one embodiment of the invention, a method includes providing a conduit having a fluid flowing therethrough, disposing a plurality of temperature measurement devices inside a wall of the conduit, positioning at least some of the temperature measurement devices proximate an inside surface of the wall of the conduit, positioning at least some of the temperature measurement devices at different radial positions at the same circumferential location within the wall, measuring a plurality of temperatures of the wall with respective ones of the temperature measurement devices to obtain a three-dimensional temperature topology of the wall, determining the temperature dependent thermal conductivity of the conduit, and determining a multi-dimensional thermal characteristic of the inside surface of the wall of the conduit based on extrapolation of the three-dimensional temperature topology and the temperature dependent thermal conductivities.

36 Claims, 15 Drawing Sheets

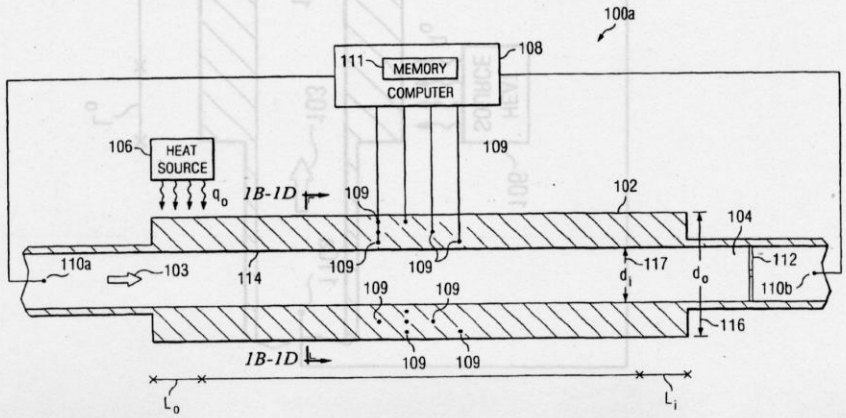

13.0 CONJUGATE HEAT TRANSFER MEASUREMENTS IN A NON-UNIFORMLY HEATED CIRCULAR FLOW CHANNEL UNDER FLOW BOILING CONDITIONS

Because conjugate heat transfer involving thermal solid conduction/thermally developing single-phase and two-phase convection is the primary heat flux removal mechanism in high heat flux applications, this section will extend the 3-D data presentation for the experimental case presented in Section 10.0. Recall that the lengths L_i and L_o shown in Fig. 21 are variable lengths whose sum must equal 20.0 mm for a given experimental setup.

The relationship between the steady state, net incident outside wall heat flux and the locally measured test section wall temperature is presented in Fig. 28 and applies for the following conditions: (1) the 180.0 mm (= L) heater placed asymmetrically along the axial 200.00 mm test section length, with a 4.0 mm (= L_o) unheated length at the downstream end of the test section, and a 16.0 mm (= L_i) unheated length at the upstream end of the test section; (2) the inside and outside flow channel diameters were 10.0 mm and 30.0 mm respectively; (3) ϕ = 0.0 degrees at the heated side of the axis of symmetry; (4) axial locations of Z = 143.0, 145.0, and 147.00 mm (nominally, Z = Z_3 = 147.0 mm axial station); and (5) radii of 12.191, 9.881, and 8.057 mm, respectively. For the results reported below, the test conditions used for the mass velocity, and exit pressure were 0.59 Mg/m^2s, and 0.207 MPa (T_{sat} = 121.3 ^0C), respectively.

These curves in Fig. 28 are complete in that they not only show evidence of an influence from the three basic subcooled flow boiling regimes prior to critical heat flux (single-phase, partially nucleate boiling, and fully developed flow boiling); but, an apparent local critical heat flux (CHF) occurred and is displayed near point "C" in Fig. 28 between the right-most pair of data points on the curve which corresponds to the smallest radius (r = 8.057 mm) with the asterisk (*) data points. For each curve (or radial coordinate) shown in Fig. 28, the six left-most data points show the relationship when single-phase convection exists in the flow channel; i.e., up to point "A." Beyond point "A" for each radius, the slope of each curve changes--denoting an onset of partial nucleate boiling which extends up to point "B." Finally and beyond point "B" (from left to right), one observes a progressive increase of the slope of the q_o vs T_w curves in Fig. 28 as the radius decreases or as the inside fluid-solid boundary is approached. This denotes the region of fully developed nucleate flow boiling in the flow channel and extends to point "C".

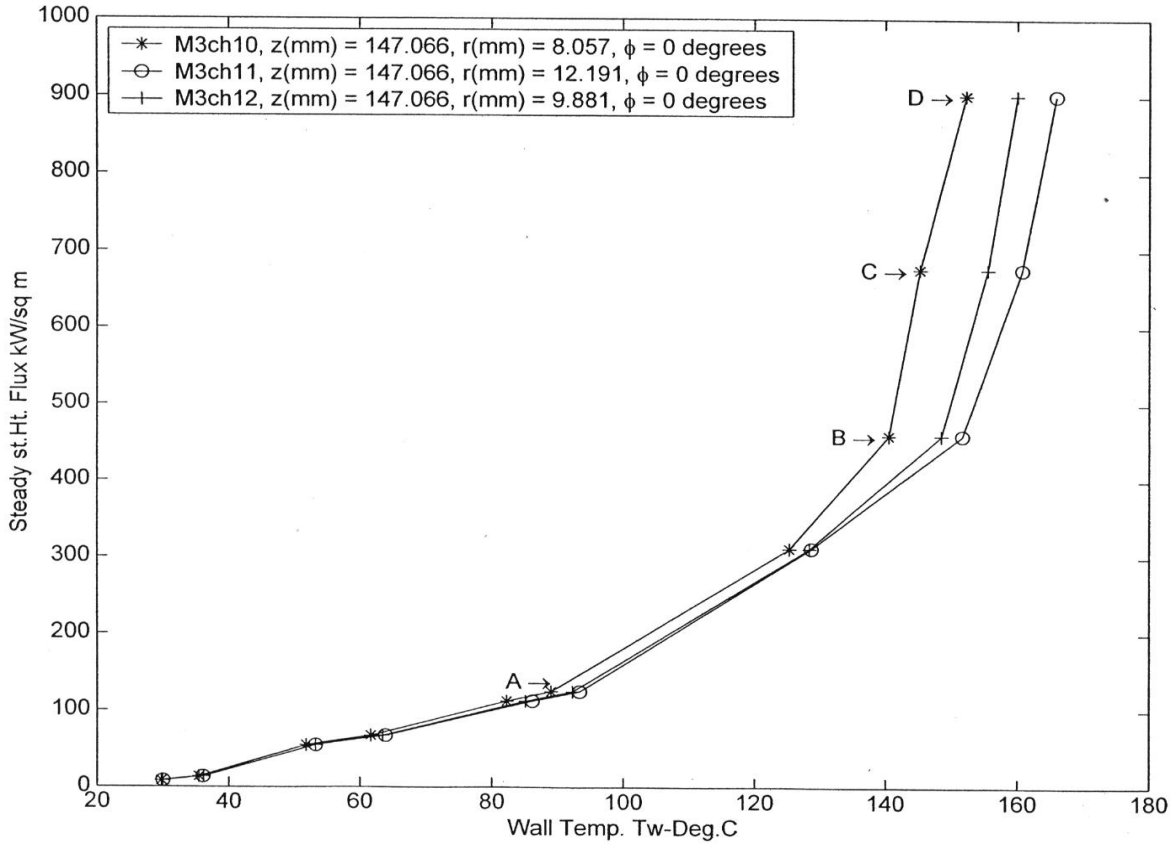

Figure 28: Steady-State net Incident Heat Flux as a Function of the Local Flow Channel Wall Temperature at $\phi = 0.0^0$ and for Specified Axial Locations (near $Z = Z_3 = 147.0$ mm) and Heaters Asymmetrically Placed with Respect to the Axial Direction with $L_o = 4.0$ mm and $L_i = 16.0$ mm of Unheated Flow Channel Downstream and Upstream of the Heaters, Respectively.

The possible occurrence of a local CHF is denoted by a decrease in the slope of the left-most curve with asterisk (*) data points which corresponds to the smallest radius shown (8.057 mm). The reduction in the slope at the upper part of this curve in Fig. 28 suggests a stable entry into the local post-CHF regime at $\phi = 0.0$ degrees and $Z = Z_3 = 147.0$ mm occurred and is displayed between points "C" and "D". As the heat flux was increased above that at point "C," a loud hammer-like sound also began. The normal temperature escalation, which accompanies CHF in

uniformly heated tubes, is absent due to the single-side heated flow channel and the resulting three-dimensional conjugate heat transfer (which is absent in the uniformly heated cases). This escalation may occur when a global CHF is reached [52].

Since Fig. 28 does not display the actual boiling curves, the above designations are preliminary. Future funded work should be devoted to extending and using all related measured data for the flow conditions applicable to Fig. 28 to produce the local boiling curves (inside flow channel wall local heat flux as a function of the inside local wall temperature).

The circumferential variations in the channel wall temperature are presented in Figs. 29a and 29b for seven levels of the outside, single-side heat flux, q_o. Figures 29a and 29b show such variations close to the inside fluid-solid boundary and the outside (partially heated) boundaries, respectively. Comparing the two sets of plots, one observes two very different circumferential wall temperature variations near the two boundaries. Since there are only four circumferential locations for each set of measurements, these distributions will not show the exact local circumferential slopes but the quantitative trends at the four locations are evident. As one would expect, the wall temperature approaches the fluid temperature in Fig. 29a (near the fluid/solid boundary) as ϕ approaches 180.0 degrees. However, the locus of the data in Fig. 29b (near the outside partially heated boundary) displays approximately the correct boundary condition of a zero circumferential temperature gradient as ϕ approaches 180.0 degrees but differs [as it should] from the profile near the fluid/solid boundary. In both cases, the temperature is almost constant between ϕ = 45.0 and 135.0 degrees. This is due to the relatively large thickness of the test section. For smaller TS wall thicknesses, the variation would be greater [30]. In the limit of ϕ approaching 180.0 degrees in Fig. 29b, the wall temperature is well above the fluid temperature and increases as q_o increases.

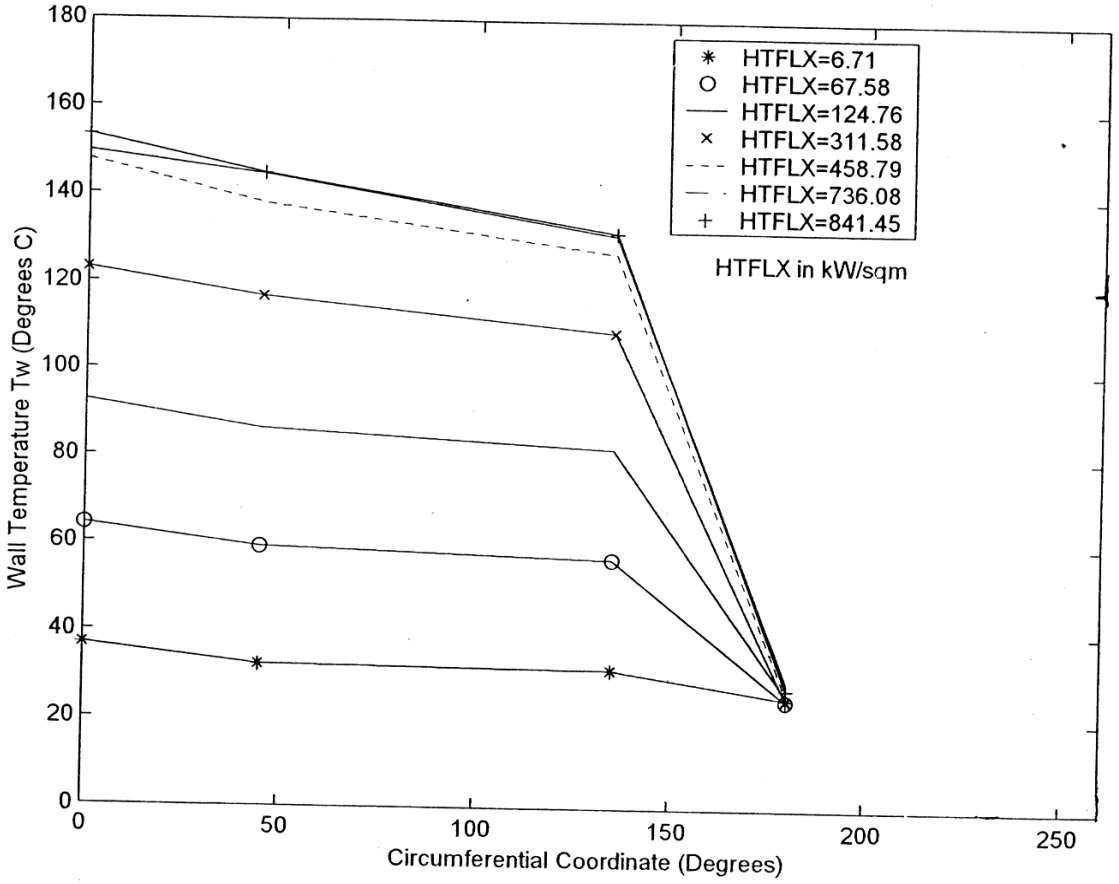

Figure 29a: Circumferential Wall Temperature Profile from the thermocouples Nearest to the Fluid/Solid Boundary as a Function of Net Incident Heat Flux, at Z = Z_4 = 196.0 mm (L_o = 4.0 mm, and L_i = 16.0 mm).

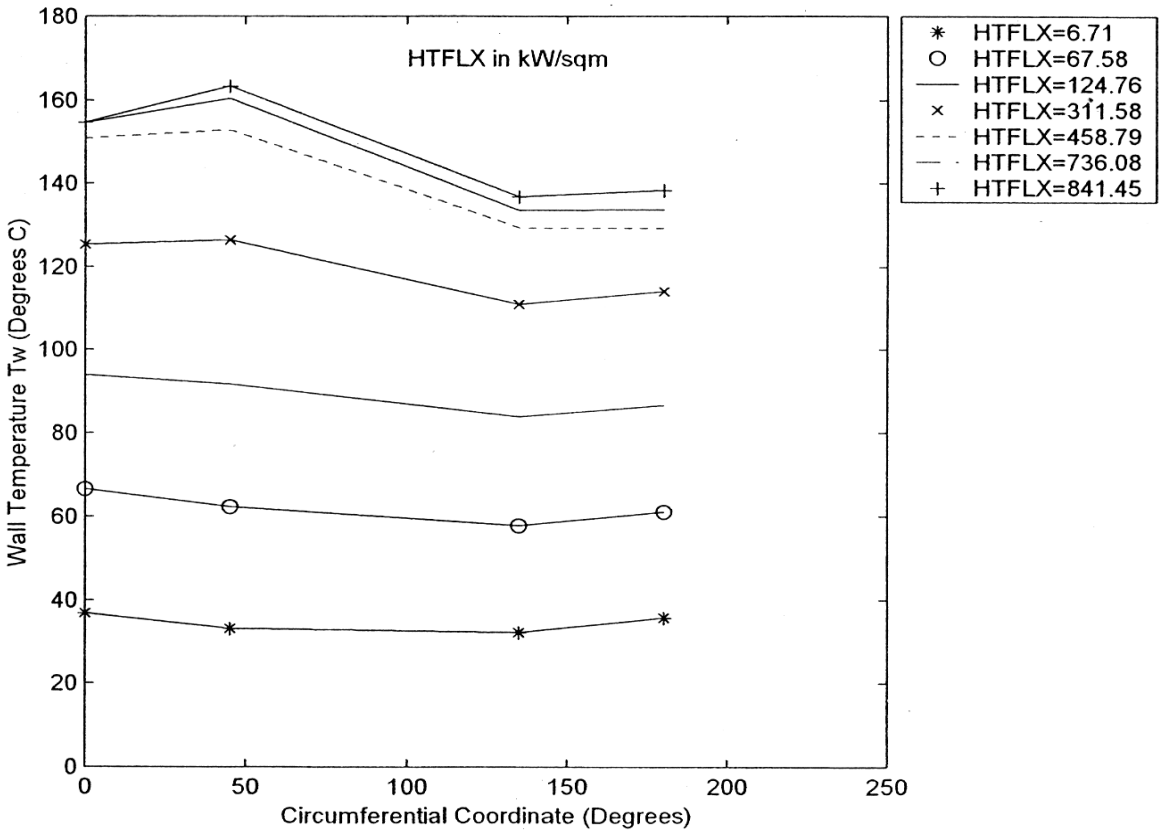

Figure 29b: Circumferential Wall Temperature Profile From the Thermocouples Nearest to the Heated Boundary (i.e., away from the fluid/solid boundary) as a Function of the Net Incident Heat Flux (L_o = 4.0 mm, and L_i = 16.0 mm).

Figure 30 displays the radial temperature profiles at ϕ = 45.0 degrees and shows small variations with respect to r and some values of ϕ. This is of course contrasted with larger radial variations as displayed by comparing Figs. 29a and 29b at other values of ϕ. These radial temperature profiles may be useful in estimating the local heat flux and wall temperature on the inside flow channel surface.

Finally, Fig. 31 shows the remaining portion of the variations via the axial wall temperature profiles which include the three downstream-most axial stations. For this experiment, the heater length (L) was 180.0 mm long (in the axial direction) and was placed asymmetrically on the test section (200.00 mm long). There was 16.0 mm (= L_i) of unheated (i.e., directly unheated) test section upstream of the heater and near the inlet, and 4.0 mm (= L_o) of unheated (i.e., directly unheated) test section downstream of the heater near the outlet. This resulted in the downstream portion of the heater being at the same downstream axial location as the thermocouple in plane A1 of Fig. 21. As a result, the thermocouples at the downstream most axial location are in the same axial plane as the downstream end of the heater. The curves shown in Fig. 31 are for test section locations along the heated portion of the axis of symmetry (ϕ = 0.0 degrees) and close to the heated boundary (r = 12.191 mm). This axial wall temperature profile along the heated boundary and at ϕ = 0.0 degrees shows that the wall temperature in the axial direction decreases (see Fig. 31) at higher powers due to the heat removal effect of the subcooled water flowing in the channel. However for the same value of ϕ (= 0 degrees) but close to the fluid-channel wall boundary, additional profiles reveal a steady increase in the wall temperature at most power levels. Although small, axial variations occurred at all power levels. These variations would increase for test section wall and prototypic PFC substrate thicknesses smaller than the 10.0 mm nominal value for the present case.

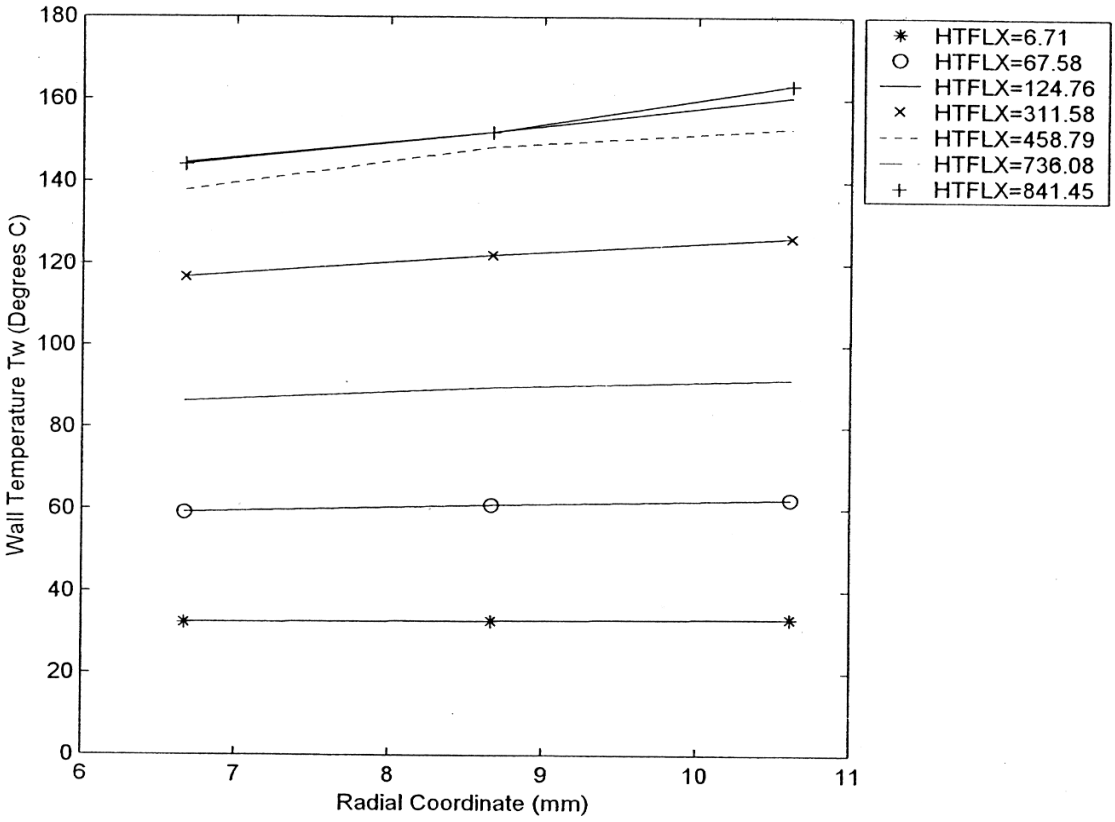

Figure 30: Radial Wall Temperature Profile for the Flow Channel at $\phi = 45.0^0$ and $Z = Z_4 = 196.0$ mm as a Function of the Net Incident Heat Flux ($L_o = 4.0$ mm, and $L_i = 16.0$ mm).

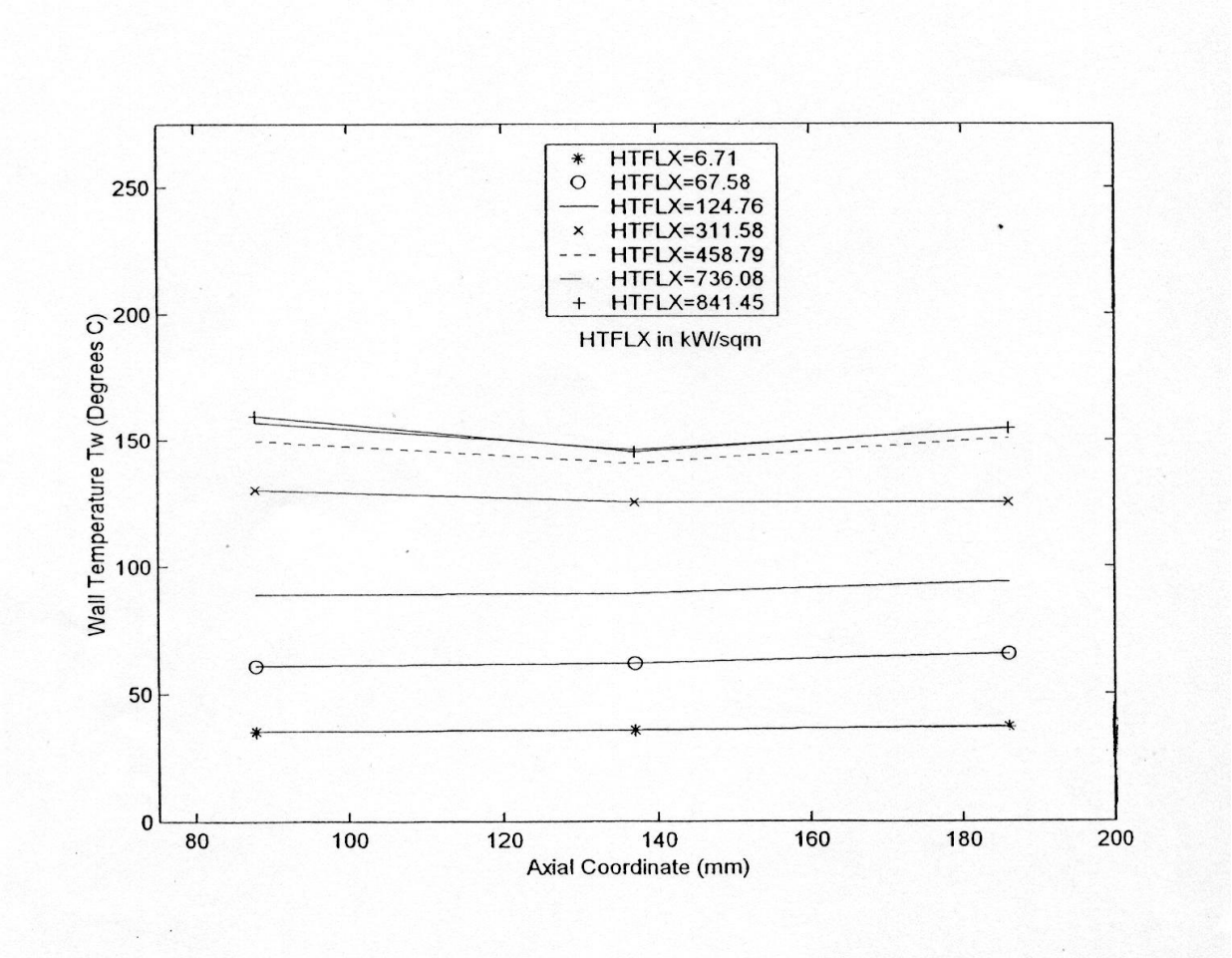

Figure 31: Axial Wall Temperature Profiles From the TCs at $\phi = 0.0^0$, and r = 12.191 mm (close to the heated boundary) as a Function of the Net Incident Heat Flux (L_o = 4.0 mm, and L_i = 16.0 mm).

14.0 HIGH HEAT FLUX REMOVAL DATA BASE FOR SUBCOOLED FLOW BOILING IN A SINGLE-SIDE HEATED CIRCULAR CHANNEL

14.1 INTRODUCTION

Since plasma-facing component (PFC) and electronic heat sink (EHS) design requirements, goals and objectives are evolving, the development of an experimental conjugate multi-dimensional, flow boiling data base will provide the basis for CFD comparisons, flow boiling correlation modifications, and adaptations which include single-side heating effects for detail PFC and EHS flow channel and substrate design studies. This will lead to cost-effective and robust designs. Many papers have been published reporting either new or modified flow boiling correlations. Generally, there appears to be good confidence in predicting water flow boiling for uniformly heated circular channels with or without twisted tapes. However, all PFCs and EHSs involve single-side heated flow channels and hence depend on at least two-dimensional, and in some cases three-dimensional, conjugate data and analysis for new or modified flow boiling or single-phase correlations with two- and possibly three-dimensional influences. Although high heat flux removal designs and related innovations and improvements have been proposed for the PFCs in the International Thermonuclear Experimental Reactor (ITER) via the Engineering Design Activity by many investigators [63-76], additional divertor and PFC development and certification are ongoing for several new machines [71, 77, 78]. One principal machine concept being considered is the fusion ignition research experiment (FIRE). As noted by Ulrickson et al. [77], the primary focus of the FIRE program is an understanding of the plasma dominated by alpha heating. However, they also emphasized that a key issue of the FIRE design is high heat flux removal from the outer divertor or PFC. Nygren [79] and Chappuis et al. [80] summarized prior experiences which may improve PFC functionality. Finally, Rödig et al. [81] compared existing electron beam test facilities used in testing HHFR components.

Fundamental HHFR research involving single-side heated flow channels is evolving. Boscary et al. [82] reported success in: (1) developing a dimensional analysis of the critical heat flux (CHF) in terms of five dimensionless groups, and (2) introducing enhancement factors for single-side heating relative to uniform heating. Further, Boscary et al. [83] detected CHF via an infrared camera and noted that their data was “reasonably well” predicted by the sublayer dryout model of Celata et al. Inasaka and Nariari [84] estimated the inside wall heat flux for single-side

irradiated flow channels with twisted tapes. Celata et al. [85, 86] proposed CHF models which apply to both uniformly-heated and single-side heated channels with and without swirl flow. Liu, Nariai, and Inasaka [87]: (1) reported a CHF model based on liquid layer dryout; (2) made comparisons with a large data bank; (3) displayed parametric trends with respect to several parameters; and, (4) alluded to the model being adaptable to single-side heated flow channels with water, nitrogen and freon-113. Further, Celata et al. [88, 89]: (1) made flow visualizations of water subcooled flow boiling, and (2) obtained bubble and hot spot dimensions as a function of thermal-hydraulic test conditions.

The optimized design of single-side heated PFCs and EHSs is dependent on using conjugate heat transfer to find the local distribution of inside wall heat flux on the flow channels of the component or heat sink cooling substrate. For the present physical configuration involving a single-side heated cylindrical-like flow channel with internal forced flow, the local inside wall heat flux and other fundamental convective/flow boiling quantities were obtained from selectively chosen local wall temperatures close to the inside boundary of the flow channel. To this end, three-dimensional thermal measurements for a one-side heated cylindrical-like test section were made. The resulting local wall temperature data were reduced using a theoretical analysis developed by Boyd et al. [90, 91] to produce the circumferential and radial distributions. The following fundamental inside channel wall convective and flow boiling thermal quantities were deduced from local channel wall temperature measurements: (1) inside wall heat flux distribution, (2) inside wall temperature distributions, and (3) local heat transfer coefficient.

14.2 ANALYSIS

The test section was designed and based on a theoretical analysis of the two-dimensional (radial, r, and circumferential, ϕ), wall temperature distribution in a solid circular tube (with inside and outside radii, r_i and r_o) with internal forced convective flow and: (1) subjected to an external heat flux (q_o) over one-half of the outside perimeter, and (2) with the remaining half of the perimeter insulated. This circular tube is referred to as the "theoretical circular cylinder." For a constant inside mean heat transfer coefficient (h_m), the dimensionless two-dimensional wall temperature distribution is

$$T^*(R,\phi) = \frac{T(r,\phi) - T_b}{\left(\frac{q_o r_o}{k}\right)} = \frac{1}{2}\left(\frac{1}{Bi} + \ln R\right) + \sum_{n=1}^{\infty} \frac{2\sin n\left(\phi + \frac{\pi}{2}\right)}{\pi n^2} \frac{R^n}{R_o^n} \frac{\left(1 - Bi_n R^{-2n}\right)}{\left(1 + Bi_n R_o^{-2}\right)}, \tag{14-1}$$

where n = 1, 3, 5, 7, …; $R = \frac{r}{r_i}; R_o = \frac{r_o}{r_i}$; q_o is the externally applied heat flux; k is the wall thermal conductivity; Bi is the Biot number, ($r_i h_m/k$); $\phi = 0$ at the heated part of the plane of symmetry; and,

$$Bi_n = \frac{Bi - n}{Bi + n}. \tag{14-2}$$

The corresponding dimensionless inside wall heat flux is

$$\frac{q_i(\phi)}{q_o} R_0^{-1} = \frac{1}{2} + \sum_{n=1}^{\infty} \frac{4\sin n\left(\phi + \frac{\pi}{2}\right)}{\pi n\, R_o^n} \left[\frac{Bi}{(Bi + n) + (Bi - n)R_o^{-2n}}\right]. \tag{14-3}$$

The nominal cross-sectional dimensions for the experimental test section were based on a value of R_o of 3.0. The actual value for the inside diameter of the test section was selected to be 10.0 mm, which corresponds to typical values used for flow channels in fusion reactor divertors. The resulting values of r_i and r_o make it physically practical to have a test section thick enough to make local wall temperature measurements. One result of the analysis is that multi-dimensional wall effects will be negligible for: (1) Bi ≤ 0.01 when $R_o \geq 1.34$, and (2) Bi ≤ 0.001 when R_o = 1.04. For these two extrema, the resulting inside channel wall heat flux will not vary in the circumferential direction. For the present experiment, the Bi is anticipated to be of the order of 0.2, which will result in significant circumferential variations of the inside channel wall heat flux. Therefore, the above equations for $T(r, \phi)$ and $q_i(\phi)$ will be applied at a given axial location using the local bulk fluid temperature (T_b (z)) to reduce the measurements of local wall temperature.

The locally measured wall temperature is used in equation (14-1) to produce a value of B_i, which is hence forth referred to as Bi_c and is then used in equation (14-1) for R = 1 and

equation (14-3) to obtain corresponding values of the tube inside wall temperature (T_i) and heat flux (q_i), respectively. The subscript "c" is used here to denote this quantity, Bi_c, not as a characterizing Biot number but as a correlation parameter which facilitates extrapolating the measurement over the small distance to the inside boundary. The result will be circumferential distributions at a given axial location; i.e. T_i (ϕ, z) and q_i (ϕ, z). Although time would not permit, this postulation can be tested using all of the measured local data.

Because it was not practical to fabricate a semi-circular shell resistive heater to facilitate the single-side heating, five flat faces were machined on to the external surface of the "theoretical circular cylinder" to form the cross-section of the actual test section (See Figs. 32 and 33). This configuration was heated with five flat resistive graphite heaters. Although a larger number of heaters would have provided a better approximation, the practical complications of heater installation and stability would have increased. To compensate for this limitation, the test section thickness was chosen to be large, with $R_o = 3.0$.

Calorimetric measurements were used to measure the actual power transferred to the flowing water. The actual power transferred to the water is given in terms of inlet and outlet specific enthalpies by

$$P_a = \dot{m}\left(h_{outlet} - h_{inlet}\right), \tag{14-4}$$

where $\dot{m}$ is the mass flow rate. The actual external, net heat flux is given by

$$q_o = \frac{P_a}{5\,A_H}, \tag{14-5}$$

where A_H is the surface area (180.0 mm x 9.04 mm; i.e., L_H x w) of one of the heaters, L_H is the heater length and w is the heater width.

The local axial bulk fluid temperature is determined from the thermodynamics tables as the temperature corresponding to the following value of the local axial bulk fluid specific enthalpy,

$$h_b(z) = h_{inlet} + \frac{5.0\,q_o\,z\,w}{\dot{m}}. \tag{14-6}$$

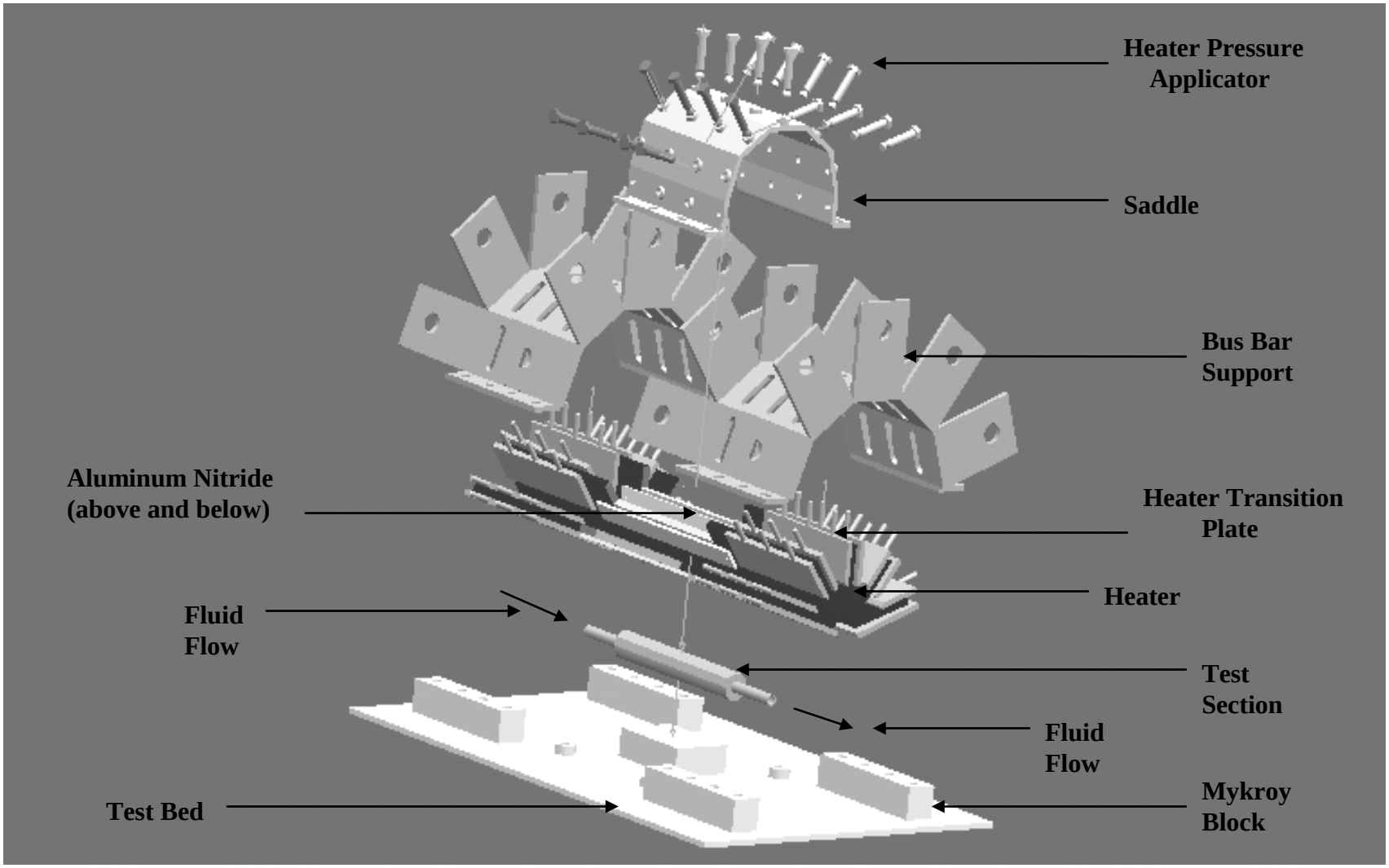

Figure 32: Test Section and Expanded Test Assembly Used for High Heat Flux Removal with Subcooled Flow Boiling in a Single-Side Heated Flow Channel.

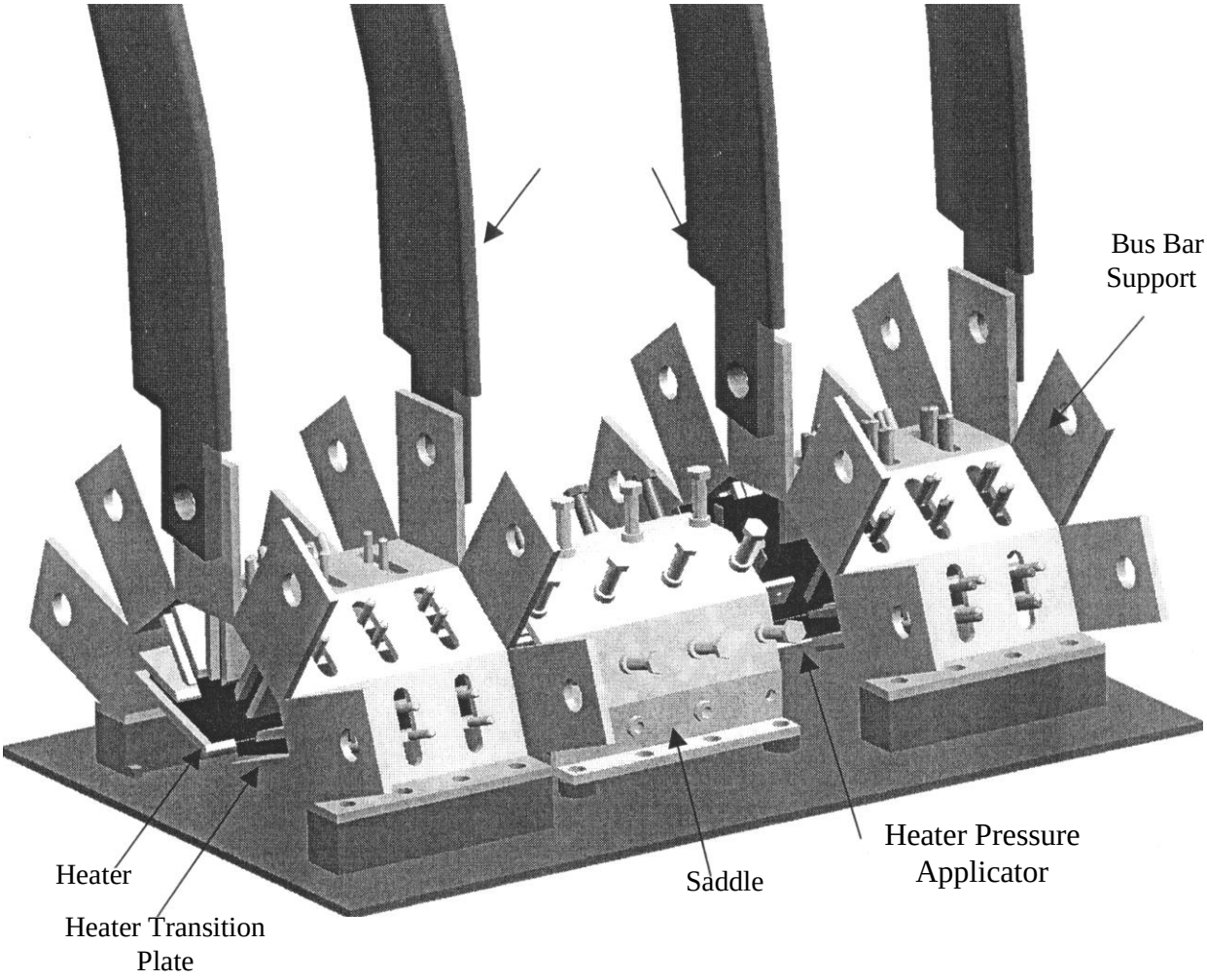

Figure 33: Test Section Assembly with Heaters and Flexible Power Bus Bars Used for High Heat Flux Removal with Subcooled Flow Boiling in a Single-Side Heated Circular Flow Channel.

In an effort to collapse the measured data on to a single curve, additional definitions of the dimensionless temperature and inside wall heat flux were obtained from eqs. (14-1) and (14-3) as follows:

$$\theta_T = \frac{T^* - \frac{1}{2}\left(\frac{1}{Bi_c} + \ln R\right)}{\frac{2}{\pi}\frac{R}{R_o}\frac{\left(1 - Bi_{nc}\big|_{n=1} R^{-2}\right)}{\left(1 + Bi_{nc}\big|_{n=1} R_o^{-2}\right)}}, \tag{14-7}$$

$$\theta_q = \frac{\frac{q_i}{q_o} - \frac{R_o}{2}}{\frac{4}{\pi}\frac{Bi_c}{\left[\left(Bi_c + 1\right) + \left(Bi_c - 1\right)R_o^{-2}\right]}}, \text{ and } Bi_{nc} = \frac{Bi_c - n}{Bi_c + n}. \tag{14-8}$$

Inspection of the reduced data trends indicates that for a given value of Reynolds number, Bi_c is related to q_o $(r_o - r_i)/k$, ϕ, and z. Equations (14-7) and (14-8) can be used to express the measured data in a further dimensionless form for the temperature (θ_T) and the inside wall heat flux (θ_q). Although time would not permit, the resulting data can be examined to see if it collapse on to a single curve using local values of $T_b(z)$ with the theoretical reduced forms of eqs (14-7) and (14-8); i.e.,

$$\theta_T = \sin\left(\phi + \frac{\pi}{2}\right) + \sum_{n=3}^{\infty} \frac{\sin\ n\left(\phi + \frac{\pi}{2}\right)\ R^{n-1}}{n^2\ R_o^{n-1}} \frac{\left(1 - Bi_n R^{-2n}\right)}{\left(1 + Bi_n R_o^{-2n}\right)} \frac{\left(1 + Bi_{nc}\big|_{n=1}\ R_o^{-2}\right)}{\left(1 - Bi_{nc}\big|_{n=1}\ R^{-2}\right)}, \tag{14-9}$$

$$\theta_q = \sin\left(\phi + \frac{\pi}{2}\right) + \sum_{n=3}^{\infty} \frac{\sin\ n\left(\phi + \frac{\pi}{2}\right)}{n\ R_o^{n-1}} \frac{\left(Bi_c + 1\right) + \left(Bi_c - 1\right) R_o^{-2}\ Bi}{\left(Bi + n\right) + \left(Bi - n\right) R_o^{-2n}\ Bi_c}, \tag{14-10}$$

where n = 3, 5, 7, … .

14.3 TEST CONDITIONS

The configuration under study (see Fig. 32) consists of a non-uniformly heated cylindrical-like test section with a circular coolant channel bored through the center. The theoretical or idealization of the cylindrical-like test section would be a circular cylinder with half (-90 degrees to +90 degrees) of its outside boundary subjected to a uniform heat flux and the remaining half insulated. The test conditions and geometric specifications were identical to those

presented in Section 13.0. A post-test inspection of the test section was made to verify the positioning and embedded depths of each of the forty-eight test section TCs. Based on a post-test examination of the test section and measurements, a revised test matrix resulted which included thirty-one (31) test section channel wall TCs.

14.4 TEST SECTION ASSEMBLY

As shown in Fig. 32, the test section assembly is a unique design and allows flow through the test section, heating from one side, and secure positioning of both the test section and heaters. The saddle was used to: (1) secure the position of the heaters relative to the test section; and (2) increase the contact pressure between the heater, the aluminum nitride, and the outside surface of the test section. The latter function of the saddle is essential in reducing the thermal contact resistance between each of these layers.

The saddle and the test section were electrically isolated from the heater by a 0.5 mm thick layer of aluminum nitride. The complete assembly of all components in Fig. 32 is shown in Fig. 33. The mykroy shown serves both as a support for the assembly and as electrical and thermal barriers between the bus bar support and the test bed. Also shown in Fig. 33 are the heater connections to the bus bar support via the heater transition plates. A set of flexible bus bars were used to transfer the electrical current from the rigid copper bus bars to the bus bar support, to the transition plate, and then to the heaters (see Fig. 33).

14.5 TYPICAL RESULTS

High heat flux removal experiments of a single-side heated circular-like flow channel with internal convection have resulted in two-dimensional distributions of the inside flow channel wall temperature, heat flux and heat transfer coefficient. Results are presented with water as the fluid for flow conditions ranging from single-phase to fully- developed flow boiling. Boiling curves, dimensionless representations, and tabulated reduced data are presented. A tabulation of the locally-measured (three-dimensional) channel wall temperatures is in Table I. This data contains the effects of conjugate heat transfer with turbulent and flow boiling.

14.5.1 FLOW CHANNEL INSIDE WALL TEMPERATURE

Figure 34 shows the circumferential distribution of the inside flow channel wall temperature (T_i) at radial locations midway between the heated boundary and the fluid-solid (cooling) boundaries. The plot is for a net incident outside heat flux of q_o = 728.3 kW/m^2. For this outside single-side heat flux, the inside wall heat flux is near 1,368.0 kW/m^2 at z = 192.1

TABLE I: Three-Dimensional Local Circular-Like Flow Channel Wall Temperature Measurements as a Function of the Net Single-Side Outside (or Inciednt) Heat Flux

Net Incident Heat Flux (kW/m^2)	Thermocouple Well Identification (Channel Number/Module Number)			Test Section Coordinates					Local Wall Thermocouple Temperature, T_w (^oC)		
	Axial Coordinate Correction*, D			Circumferential (Degrees)	Radial (mm)			Axial (mm) *	Close to Fluid/Solid Boundary	Intermediate	Close to Heated Boundary
	D = 0 mm	D = 2 mm	D = 4 mm								
	D3 (CH6/3)	D2 (CH5/3)	D1 (CH4/3)	0	7.204	10.269	12.797	45.022+D	29.089	29.23	-
	D6 (CH9/3)	D5 (CH8/3)	D4 (CH7/3)	0	7.512	10.670	12.318	94.044+D	-	28.971	-
	D9 (CH12/3)	D8 (CH11/3)	D7 (CH10/3)	0	8.057	9.881	12.191	143.066+D	30.087	30.477	-
	D12 (CH15/3)	D11(CH14/3)	D10 (CH13/3)	0	8.542	10.966	12.405	192.088+D	30.131	30.323	30.361
	B1 (CH12/2)	B2 (CH13/2)	B3 (CH14/2)	45	7.110	8.843	10.820	49.022	**	**	**
	B4 (CH15/2	B5 (CH16/2)	B6 (CH17/2)	45	7.296	9.215	10.845	98.044	**	-	**
	B7 (CH18/2)	B8 (CH31/2)	B9 (CH0/3)	45	6.565	8.631	10.893	147.066	-	26.058	29.828
	B10 (CH21/2)	B11 (CH22/2)	B12 (CH23/2)	45	5.956	8.946	11.081	196.088	-	**	26.346
6.6581	A1 (CHO/2)	A2 (CH1/2)	A3 (CH2/2)	135	7.328	9.322	11.892	49.022	**	**	-
	A4(CH3/2)	A5 (CH4/2)	A6 (CH5/2)	135	6.901	9.259	12.189	98.044	**	-	**
	A7 (CH7/2)	A8 (CH8/2)	A9 (CH6/2)	135	6.722	9.176	11.784	147.066	-	**	**
	A10 (CH9/2)	A11 (CH10/2)	A12 (CH11/2)	135	6.641	9.079	12.168	196.088	**	-	-
	C3 (CH26/2)	C2 (CH25/2)	C1 (CH24/2)	180	7.328	9.318	11.494	49.022	**	**	**
	C6 (CH28/2)	C5 (CH27/2)	C4 (CH29/2)	180	7.328	9.269	11.533	98.044	**	-	-
	C9 (CH20/2)	C8 (CH19/2)	C7 (CH30/2)	180	7.078	8.963	11.378	147.066	**	-	-
	C12(CH3/3)	C11 (CH1/3)	C10 (CH16/3)	180	7.141	9.015	11.358	196.088	-	29.666	29.686
	D3 (CH6/3)	D2 (CH5/3)	D1 (CH4/3)	0	7.204	10.269	12.797	45.022+D	34.616	34.609	-
	D6 (CH9/3)	D5 (CH8/3)	D4 (CH7/3)	0	7.512	10.670	12.318	94.044+D	-	35.634	-
	D9 (CH12/3)	D8 (CH11/3)	D7 (CH10/3)	0	8.057	9.881	12.191	143.066+D	36.399	36.607	-
	D12 (CH15/3)	D11(CH14/3)	D10 (CH13/3)	0	8.542	10.966	12.405	192.088+D	36.614	36.989	36.92
	B1 (CH12/2)	B2 (CH13/2)	B3 (CH14/2)	45	7.110	8.843	10.820	49.022	30.698	30.751	30.853
	B4 (CH15/2	B5 (CH16/2)	B6 (CH17/2)	45	7.296	9.215	10.845	98.044	30.849	-	31.496
	B7 (CH18/2)	B8 (CH31/2)	B9 (CH0/3)	45	6.565	8.631	10.893	147.066	-	32.46	36.242
	B10 (CH21/2)	B11 (CH22/2)	B12 (CH23/2)	45	5.956	8.946	11.081	196.088	-	33.139	33.257
18.529	A1 (CHO/2)	A2 (CH1/2)	A3 (CH2/2)	135	7.328	9.322	11.892	49.022	30.073	**	-
	A4(CH3/2)	A5 (CH4/2)	A6 (CH5/2)	135	6.901	9.259	12.189	98.044	30.879	-	31.387
	A7 (CH7/2)	A8 (CH8/2)	A9 (CH6/2)	135	6.722	9.176	11.784	147.066	-	31.724	32.28
	A10 (CH9/2)	A11 (CH10/2)	A12 (CH11/2)	135	6.641	9.079	12.168	196.088	31.869	-	-
	C3 (CH26/2)	C2 (CH25/2)	C1 (CH24/2)	180	7.328	9.318	11.494	49.022	30.337	30.21	30.082
	C6 (CH28/2)	C5 (CH27/2)	C4 (CH29/2)	180	7.328	9.269	11.533	98.044	30.869	-	-
	C9 (CH20/2)	C8 (CH19/2)	C7 (CH30/2)	180	7.078	8.963	11.378	147.066	31.581	-	-
	C12(CH3/3)	C11 (CH1/3)	C10 (CH16/3)	180	7.141	9.015	11.358	196.088	-	35.712	35.714
	D3 (CH6/3)	D2 (CH5/3)	D1 (CH4/3)	0	7.204	10.269	12.797	45.022+D	37.618	37.719	-
	D6 (CH9/3)	D5 (CH8/3)	D4 (CH7/3)	0	7.512	10.670	12.318	94.044+D	-	38.42	-
	D9 (CH12/3)	D8 (CH11/3)	D7 (CH10/3)	0	8.057	9.881	12.191	143.066+D	40.227	40.482	-
	D12 (CH15/3)	D11(CH14/3)	D10 (CH13/3)	0	8.542	10.966	12.405	192.088+D	40.204	40.245	40.454
	B1 (CH12/2)	B2 (CH13/2)	B3 (CH14/2)	45	7.110	8.843	10.820	49.022	34.036	33.82	34.08
	B4 (CH15/2	B5 (CH16/2)	B6 (CH17/2)	45	7.296	9.215	10.845	98.044	34.204	-	35.029
	B7 (CH18/2)	B8 (CH31/2)	B9 (CH0/3)	45	6.565	8.631	10.893	147.066	-	36.136	39.813
	B10 (CH21/2)	B11 (CH22/2)	B12 (CH23/2)	45	5.956	8.946	11.081	196.088	-	36.139	36.614
26.6562	A1 (CHO/2)	A2 (CH1/2)	A3 (CH2/2)	135	7.328	9.322	11.892	49.022	32.795	26.759	-
	A4(CH3/2)	A5 (CH4/2)	A6 (CH5/2)	135	6.901	9.259	12.189	98.044	33.905	-	33.965
	A7 (CH7/2)	A8 (CH8/2)	A9 (CH6/2)	135	6.722	9.176	11.784	147.066	-	34.511	35.029
	A10 (CH9/2)	A11 (CH10/2)	A12 (CH11/2)	135	6.641	9.079	12.168	196.088	34.708	-	-
	C3 (CH26/2)	C2 (CH25/2)	C1 (CH24/2)	180	7.328	9.318	11.494	49.022	33.223	32.985	32.905
	C6 (CH28/2)	C5 (CH27/2)	C4 (CH29/2)	180	7.328	9.269	11.533	98.044	34.086	-	-
	C9 (CH20/2)	C8 (CH19/2)	C7 (CH30/2)	180	7.078	8.963	11.378	147.066	34.851	-	-
	C12(CH3/3)	C11 (CH1/3)	C10 (CH16/3)	180	7.141	9.015	11.358	196.088	-	38.711	38.728
	D3 (CH6/3)	D2 (CH5/3)	D1 (CH4/3)	0	7.204	10.269	12.797	45.022+D	49.614	49.773	-
	D6 (CH9/3)	D5 (CH8/3)	D4 (CH7/3)	0	7.512	10.670	12.318	94.044+D	-	50.908	-
	D9 (CH12/3)	D8 (CH11/3)	D7 (CH10/3)	0	8.057	9.881	12.191	143.066+D	53.663	53.944	-
	D12 (CH15/3)	D11(CH14/3)	D10 (CH13/3)	0	8.542	10.966	12.405	192.088+D	54.995	55.876	55.783
	B1 (CH12/2)	B2 (CH13/2)	B3 (CH14/2)	45	7.110	8.843	10.820	49.022	45.505	45.777	46.36
	B4 (CH15/2	B5 (CH16/2)	B6 (CH17/2)	45	7.296	9.215	10.845	98.044	46.08	-	47.407
	B7 (CH18/2)	B8 (CH31/2)	B9 (CH0/3)	45	6.565	8.631	10.893	147.066	-	49.786	53.538
	B10 (CH21/2)	B11 (CH22/2)	B12 (CH23/2)	45	5.956	8.946	11.081	196.088	-	51.617	52.439
54.1654	A1 (CHO/2)	A2 (CH1/2)	A3 (CH2/2)	135	7.328	9.322	11.892	49.022	44.152	37.377	-
	A4(CH3/2)	A5 (CH4/2)	A6 (CH5/2)	135	6.901	9.259	12.189	98.044	45.69	-	45.725
	A7 (CH7/2)	A8 (CH8/2)	A9 (CH6/2)	135	6.722	9.176	11.784	147.066	-	47.803	48.307
	A10 (CH9/2)	A11 (CH10/2)	A12 (CH11/2)	135	6.641	9.079	12.168	196.088	48.22	-	-
	C3 (CH26/2)	C2 (CH25/2)	C1 (CH24/2)	180	7.328	9.318	11.494	49.022	44.102	44.142	44.093
	C6 (CH28/2)	C5 (CH27/2)	C4 (CH29/2)	180	7.328	9.269	11.533	98.044	45.543	-	-
	C9 (CH20/2)	C8 (CH19/2)	C7 (CH30/2)	180	7.078	8.963	11.378	147.066	47.63	-	-
	C12(CH3/3)	C11 (CH1/3)	C10 (CH16/3)	180	7.141	9.015	11.358	196.088	-	52.374	52.278

***Axial Coordinate Correction applies only to thermocouple well identification with "D" labels (e.g., D-1 through D-12).**

TABLE I: Three-Dimensional Local Circular-Like Flow Channel Wall Temperature Measurements as a Function of the Net Single-Side Outside (or Incident) Heat Flux (continued)

Net Incident Heat Flux (kW/m^2)	Thermocouple Well Identification (Channel Number/Module Number)			Test Section Coordinates					Local Wall Thermocouple Temperature, T_w (^oC)		
	Axial Coordinate Correction*, D			Circumferential (Degrees)	Radial (mm)			Axial (mm) *	Close to Fluid/Solid Boundary	Intermediate	Close to Heated Boundary
	D = 0 mm	D = 2 mm	D = 4 mm								
	D3 (CH6/3)	D2 (CH5/3)	D1 (CH4/3)	0	7.204	10.269	12.797	45.022+D	57.952	58.252	-
	D6 (CH9/3)	D5 (CH8/3)	D4 (CH7/3)	0	7.512	10.670	12.318	94.044+D	-	60.178	-
	D9 (CH12/3)	D8 (CH11/3)	D7 (CH10/3)	0	8.057	9.881	12.191	143.066+D	63.334	63.647	-
	D12 (CH15/3)	D11(CH14/3)	D10 (CH13/3)	0	8.542	10.966	12.405	192.088+D	63.889	65.126	64.809
	B1 (CH12/2)	B2 (CH13/2)	B3 (CH14/2)	45	7.110	8.843	10.820	49.022	53.252	53.988	54.585
	B4 (CH15/2	B5 (CH16/2)	B6 (CH17/2)	45	7.296	9.215	10.845	98.044	54.449	-	56.478
	B7 (CH18/2)	B8 (CH31/2)	B9 (CH0/3)	45	6.565	8.631	10.893	147.066	-	59.231	63.329
	B10 (CH21/2)	B11 (CH22/2)	B12 (CH23/2)	45	5.956	8.946	11.081	196.088	-	60.918	62.031
61.866	A1 (CHO/2)	A2 (CH1/2)	A3 (CH2/2)	135	7.328	9.322	11.892	49.022	52.185	40.371	-
	A4(CH3/2)	A5 (CH4/2)	A6 (CH5/2)	135	6.901	9.259	12.189	98.044	40.371	-	54.29
	A7 (CH7/2)	A8 (CH8/2)	A9 (CH6/2)	135	6.722	9.176	11.784	147.066	-	56.581	56.914
	A10 (CH9/2)	A11 (CH10/2)	A12 (CH11/2)	135	6.641	9.079	12.168	196.088	56.335	-	-
	C3 (CH26/2)	C2 (CH25/2)	C1 (CH24/2)	180	7.328	9.318	11.494	49.022	51.484	51.635	51.565
	C6 (CH28/2)	C5 (CH27/2)	C4 (CH29/2)	180	7.328	9.269	11.533	98.044	53.818	-	-
	C9 (CH20/2)	C8 (CH19/2)	C7 (CH30/2)	180	7.078	8.963	11.378	147.066	56.371	-	-
	C12(CH3/3)	C11 (CH1/3)	C10 (CH16/3)	180	7.141	9.015	11.358	196.088	-	60.576	60.428
	D3 *(CH6/3)	D2 (CH5/3)	D1 (CH4/3)	0	7.204	10.269	12.797	45.022+D	76.832	77.121	-
	D6 (CH9/3)	D5 (CH8/3)	D4 (CH7/3)	0	7.512	10.670	12.318	94.044+D	-	82.423	-
	D9 (CH12/3)	D8 (CH11/3)	D7 (CH10/3)	0	8.057	9.881	12.191	143.066+D	85.846	86.437	-
	D12 (CH15/3)	D11(CH14/3)	D10 (CH13/3)	0	8.542	10.966	12.405	192.088+D	82.751	84.618	84.245
	B1 (CH12/2)	B2 (CH13/2)	B3 (CH14/2)	45	7.110	8.843	10.820	49.022	71.897	72.669	73.801
	B4 (CH15/2	B5 (CH16/2)	B6 (CH17/2)	45	7.296	9.215	10.845	98.044	74.806	-	78.408
	B7 (CH18/2)	B8 (CH31/2)	B9 (CH0/3)	45	6.565	8.631	10.893	147.066	-	81.424	85.479
	B10 (CH21/2)	B11 (CH22/2)	B12 (CH23/2)	45	5.956	8.946	11.081	196.088	-	80.185	81.791
104.0506	A1 (CHO/2)	A2 (CH1/2)	A3 (CH2/2)	135	7.328	9.322	11.892	49.022	68.81	46.468	-
	A4(CH3/2)	A5 (CH4/2)	A6 (CH5/2)	135	6.901	9.259	12.189	98.044	74.051	-	74.171
	A7 (CH7/2)	A8 (CH8/2)	A9 (CH6/2)	135	6.722	9.176	11.784	147.066	-	76.641	77.49
	A10 (CH9/2)	A11 (CH10/2)	A12 (CH11/2)	135	6.641	9.079	12.168	196.088	74.092	-	-
	C3 (CH26/2)	C2 (CH25/2)	C1 (CH24/2)	180	7.328	9.318	11.494	49.022	68.505	68.624	68.619
	C6 (CH28/2)	C5 (CH27/2)	C4 (CH29/2)	180	7.328	9.269	11.533	98.044	73.804	-	-
	C9 (CH20/2)	C8 (CH19/2)	C7 (CH30/2)	180	7.078	8.963	11.378	147.066	76.639	-	-
	C12(CH3/3)	C11 (CH1/3)	C10 (CH16/3)	180	7.141	9.015	11.358	196.088	-	78.399	78.848
	D3 (CH6/3)	D2 (CH5/3)	D1 (CH4/3)	0	7.204	10.269	12.797	45.022+D	83.937	84.343	-
	D6 (CH9/3)	D5 (CH8/3)	D4 (CH7/3)	0	7.512	10.670	12.318	94.044+D	-	88.283	-
	D9 (CH12/3)	D8 (CH11/3)	D7 (CH10/3)	0	8.057	9.881	12.191	143.066+D	93.286	93.656	-
	D12 (CH15/3)	D11(CH14/3)	D10 (CH13/3)	0	8.542	10.966	12.405	192.088+D	93.492	94.886	94.165
	B1 (CH12/2)	B2 (CH13/2)	B3 (CH14/2)	45	7.110	8.843	10.820	49.022	77.805	79.107	80.329
	B4 (CH15/2	B5 (CH16/2)	B6 (CH17/2)	45	7.296	9.215	10.845	98.044	80.125	-	83.758
	B7 (CH18/2)	B8 (CH31/2)	B9 (CH0/3)	45	6.565	8.631	10.893	147.066	-	88.193	92.234
	B10 (CH21/2)	B11 (CH22/2)	B12 (CH23/2)	45	5.956	8.946	11.081	196.088	-	89.849	91.951
122.3466	A1 (CHO/2)	A2 (CH1/2)	A3 (CH2/2)	135	7.328	9.322	11.892	49.022	75.365	53.159	-
	A4(CH3/2)	A5 (CH4/2)	A6 (CH5/2)	135	6.901	9.259	12.189	98.044	79.586	-	79.607
	A7 (CH7/2)	A8 (CH8/2)	A9 (CH6/2)	135	6.722	9.176	11.784	147.066	-	83.546	83.889
	A10 (CH9/2)	A11 (CH10/2)	A12 (CH11/2)	135	6.641	9.079	12.168	196.088	82.263	-	-
	C3 (CH26/2)	C2 (CH25/2)	C1 (CH24/2)	180	7.328	9.318	11.494	49.022	74.861	74.869	74.967
	C6 (CH28/2)	C5 (CH27/2)	C4 (CH29/2)	180	7.328	9.269	11.533	98.044	79.05	-	-
	C9 (CH20/2)	C8 (CH19/2)	C7 (CH30/2)	180	7.078	8.963	11.378	147.066	82.849	-	-
	C12(CH3/3)	C11 (CH1/3)	C10 (CH16/3)	180	7.141	9.015	11.358	196.088	-	86.738	86.737
	D3 (CH6/3)	D2 (CH5/3)	D1 (CH4/3)	0	7.204	10.269	12.797	45.022+D	124.868	123.525	-
	D6 (CH9/3)	D5 (CH8/3)	D4 (CH7/3)	0	7.512	10.670	12.318	94.044+D	-	133.206	-
	D9 (CH12/3)	D8 (CH11/3)	D7 (CH10/3)	0	8.057	9.881	12.191	143.066+D	128.825	131.093	-
	D12 (CH15/3)	D11(CH14/3)	D10 (CH13/3)	0	8.542	10.966	12.405	192.088+D	115.424	119.155	120.052
	B1 (CH12/2)	B2 (CH13/2)	B3 (CH14/2)	45	7.110	8.843	10.820	49.022	117.808	120.063	122.739
	B4 (CH15/2	B5 (CH16/2)	B6 (CH17/2)	45	7.296	9.215	10.845	98.044	120.331	-	125.63
	B7 (CH18/2)	B8 (CH31/2)	B9 (CH0/3)	45	6.565	8.631	10.893	147.066	-	122.07	128.087
	B10 (CH21/2)	B11 (CH22/2)	B12 (CH23/2)	45	5.956	8.946	11.081	196.088	-	116.34	117.348
225.2877	A1 (CHO/2)	A2 (CH1/2)	A3 (CH2/2)	135	7.328	9.322	11.892	49.022	110.978	67.269	-
	A4(CH3/2)	A5 (CH4/2)	A6 (CH5/2)	135	6.901	9.259	12.189	98.044	117.299	-	118.148
	A7 (CH7/2)	A8 (CH8/2)	A9 (CH6/2)	135	6.722	9.176	11.784	147.066	-	115.61	116.529
	A10 (CH9/2)	A11 (CH10/2)	A12 (CH11/2)	135	6.641	9.079	12.168	196.088	105.237	-	-
	C3 (CH26/2)	C2 (CH25/2)	C1 (CH24/2)	180	7.328	9.318	11.494	49.022	108.993	109.012	107.726
	C6 (CH28/2)	C5 (CH27/2)	C4 (CH29/2)	180	7.328	9.269	11.533	98.044	116.831	-	-
	C9 (CH20/2)	C8 (CH19/2)	C7 (CH30/2)	180	7.078	8.963	11.378	147.066	114.181	-	-
	C12(CH3/3)	C11 (CH1/3)	C10 (CH16/3)	180	7.141	9.015	11.358	196.088	-	110.412	109.622

***Axial Coordinate Correction applies only to thermocouple well identifications with "D" labels (e.g., D-1 through D-12)**

TABLE I: Three-Dimensional Local Circular-Like Flow Channel Wall Temperature Measurements as a Function of the Net Single-Side Outside (or Incident) Heat Flux (continued)

Net Incident Heat Flux (kW/m^2)	Thermocouple Well Identification (Channel Number/Module Number)			Test Section Coordinates					Local Wall Thermocouple Temperature, T_w (^oC)		
	Axial Coordinate Correction*, D			Circumferential (Degrees)	Radial (mm)			Axial (mm) *	Close to Fluid/Solid Boundary	Intermediate	Close to Heated Boundary
	D = 0 mm	D = 2 mm	D = 4 mm								
	D3 (CH6/3)	D2 (CH5/3)	D1 (CH4/3)	0	7.204	10.269	12.797	45.022+D	128.624	127.855	-
	D6 (CH9/3)	D5 (CH8/3)	D4 (CH7/3)	0	7.512	10.670	12.318	94.044+D	-	130.811	-
	D9 (CH12/3)	D8 (CH11/3)	D7 (CH10/3)	0	8.057	9.881	12.191	143.066+D	131.692	134.327	-
	D12 (CH15/3)	D11(CH14/3)	D10 (CH13/3)	0	8.542	10.966	12.405	192.088+D	124.611	130.475	129.614
	B1 (CH12/2)	B2 (CH13/2)	B3 (CH14/2)	45	7.110	8.843	10.820	49.022	120.171	123.773	125.316
	B4 (CH15/2	B5 (CH16/2)	B6 (CH17/2)	45	7.296	9.215	10.845	98.044	119.715	-	124.559
	B7 (CH18/2)	B8 (CH31/2)	B9 (CH0/3)	45	6.565	8.631	10.893	147.066	-	126.956	131.689
	B10 (CH21/2)	B11 (CH22/2)	B12 (CH23/2)	45	5.956	8.946	11.081	196.088	-	125.027	130.421
294.3267	A1 (CHO/2)	A2 (CH1/2)	A3 (CH2/2)	135	7.328	9.322	11.892	49.022	115.073	79.236	-
	A4(CH3/2)	A5 (CH4/2)	A6 (CH5/2)	135	6.901	9.259	12.189	98.044	115.141	-	118.382
	A7 (CH7/2)	A8 (CH8/2)	A9 (CH6/2)	135	6.722	9.176	11.784	147.066	-	118.566	119.416
	A10 (CH9/2)	A11 (CH10/2)	A12 (CH11/2)	135	6.641	9.079	12.168	196.088	112.771	-	-
	C3 (CH26/2)	C2 (CH25/2)	C1 (CH24/2)	180	7.328	9.318	11.494	49.022	113.033	114.541	115.051
	C6 (CH28/2)	C5 (CH27/2)	C4 (CH29/2)	180	7.328	9.269	11.533	98.044	116.526	-	-
	C9 (CH20/2)	C8 (CH19/2)	C7 (CH30/2)	180	7.078	8.963	11.378	147.066	118.239	-	-
	C12(CH3/3)	C11 (CH1/3)	C10 (CH16/3)	180	7.141	9.015	11.358	196.088	-	116.917	117.103
	D3 *(CH6/3)	D2 (CH5/3)	D1 (CH4/3)	0	7.204	10.269	12.797	45.022+D	138.708	140.254	-
	D6 (CH9/3)	D5 (CH8/3)	D4 (CH7/3)	0	7.512	10.670	12.318	94.044+D	-	141.282	-
	D9 (CH12/3)	D8 (CH11/3)	D7 (CH10/3)	0	8.057	9.881	12.191	143.066+D	145.403	149.272	-
	D12 (CH15/3)	D11(CH14/3)	D10 (CH13/3)	0	8.542	10.966	12.405	192.088+D	138.446	143.376	142.627
	B1 (CH12/2)	B2 (CH13/2)	B3 (CH14/2)	45	7.110	8.843	10.820	49.022	132.432	136.517	141.105
	B4 (CH15/2	B5 (CH16/2)	B6 (CH17/2)	45	7.296	9.215	10.845	98.044	130.909	-	143.684
	B7 (CH18/2)	B8 (CH31/2)	B9 (CH0/3)	45	6.565	8.631	10.893	147.066	-	143.226	151.406
	B10 (CH21/2)	B11 (CH22/2)	B12 (CH23/2)	45	5.956	8.946	11.081	196.088	-	139.251	144.796
417.9938	A1 (CHO/2)	A2 (CH1/2)	A3 (CH2/2)	135	7.328	9.322	11.892	49.022	120.579	86.643	-
	A4(CH3/2)	A5 (CH4/2)	A6 (CH5/2)	135	6.901	9.259	12.189	98.044	123.131	-	125.453
	A7 (CH7/2)	A8 (CH8/2)	A9 (CH6/2)	135	6.722	9.176	11.784	147.066	-	129.05	125.988
	A10 (CH9/2)	A11 (CH10/2)	A12 (CH11/2)	135	6.641	9.079	12.168	196.088	122.314	-	-
	C3 (CH26/2)	C2 (CH25/2)	C1 (CH24/2)	180	7.328	9.318	11.494	49.022	122.006	122.788	122.084
	C6 (CH28/2)	C5 (CH27/2)	C4 (CH29/2)	180	7.328	9.269	11.533	98.044	123.409	-	-
	C9 (CH20/2)	C8 (CH19/2)	C7 (CH30/2)	180	7.078	8.963	11.378	147.066	126.596	-	-
	C12(CH3/3)	C11 (CH1/3)	C10 (CH16/3)	180	7.141	9.015	11.358	196.088	-	127.199	127.989
	D3 (CH6/3)	D2 (CH5/3)	D1 (CH4/3)	0	7.204	10.269	12.797	45.022+D	142.206	147.701	-
	D6 (CH9/3)	D5 (CH8/3)	D4 (CH7/3)	0	7.512	10.670	12.318	94.044+D	-	147.916	-
	D9 (CH12/3)	D8 (CH11/3)	D7 (CH10/3)	0	8.057	9.881	12.191	143.066+D	147.715	153.076	-
	D12 (CH15/3)	D11(CH14/3)	D10 (CH13/3)	0	8.542	10.966	12.405	192.088+D	145.78	149.926	151.532
	B1 (CH12/2)	B2 (CH13/2)	B3 (CH14/2)	45	7.110	8.843	10.820	49.022	139.107	141.815	146.943
	B4 (CH15/2	B5 (CH16/2)	B6 (CH17/2)	45	7.296	9.215	10.845	98.044	138.144	-	146.022
	B7 (CH18/2)	B8 (CH31/2)	B9 (CH0/3)	45	6.565	8.631	10.893	147.066	-	146.736	155.484
	B10 (CH21/2)	B11 (CH22/2)	B12 (CH23/2)	45	5.956	8.946	11.081	196.088	-	147.12	155.015
469.6313	A1 (CHO/2)	A2 (CH1/2)	A3 (CH2/2)	135	7.328	9.322	11.892	49.022	126.079	96.65	-
	A4(CH3/2)	A5 (CH4/2)	A6 (CH5/2)	135	6.901	9.259	12.189	98.044	127.765	-	128.967
	A7 (CH7/2)	A8 (CH8/2)	A9 (CH6/2)	135	6.722	9.176	11.784	147.066	-	131.61	133.564
	A10 (CH9/2)	A11 (CH10/2)	A12 (CH11/2)	135	6.641	9.079	12.168	196.088	127.05	-	-
	C3 (CH26/2)	C2 (CH25/2)	C1 (CH24/2)	180	7.328	9.318	11.494	49.022	125.095	128.83	128.033
	C6 (CH28/2)	C5 (CH27/2)	C4 (CH29/2)	180	7.328	9.269	11.533	98.044	128.297	-	-
	C9 (CH20/2)	C8 (CH19/2)	C7 (CH30/2)	180	7.078	8.963	11.378	147.066	131.772	-	-
	C12(CH3/3)	C11 (CH1/3)	C10 (CH16/3)	180	7.141	9.015	11.358	196.088	-	130.884	133.215
	D3 (CH6/3)	D2 (CH5/3)	D1 (CH4/3)	0	7.204	10.269	12.797	45.022+D	145.325	152.358	-
	D6 (CH9/3)	D5 (CH8/3)	D4 (CH7/3)	0	7.512	10.670	12.318	94.044+D	-	155.083	-
	D9 (CH12/3)	D8 (CH11/3)	D7 (CH10/3)	0	8.057	9.881	12.191	143.066+D	155.286	160.621	-
	D12 (CH15/3)	D11(CH14/3)	D10 (CH13/3)	0	8.542	10.966	12.405	192.088+D	152.277	160.397	153.826
	B1 (CH12/2)	B2 (CH13/2)	B3 (CH14/2)	45	7.110	8.843	10.820	49.022	140.289	145.955	155.013
	B4 (CH15/2	B5 (CH16/2)	B6 (CH17/2)	45	7.296	9.215	10.845	98.044	140.659	-	155.101
	B7 (CH18/2)	B8 (CH31/2)	B9 (CH0/3)	45	6.565	8.631	10.893	147.066	-	153.943	163.554
	B10 (CH21/2)	B11 (CH22/2)	B12 (CH23/2)	45	5.956	8.946	11.081	196.088	-	154.019	160.598
503.1049	A1 (CHO/2)	A2 (CH1/2)	A3 (CH2/2)	135	7.328	9.322	11.892	49.022	133.337	114.605	-
	A4(CH3/2)	A5 (CH4/2)	A6 (CH5/2)	135	6.901	9.259	12.189	98.044	135.109	-	137.233
	A7 (CH7/2)	A8 (CH8/2)	A9 (CH6/2)	135	6.722	9.176	11.784	147.066	-	137.222	140.221
	A10 (CH9/2)	A11 (CH10/2)	A12 (CH11/2)	135	6.641	9.079	12.168	196.088	133.525	-	-
	C3 (CH26/2)	C2 (CH25/2)	C1 (CH24/2)	180	7.328	9.318	11.494	49.022	131.873	133.219	130.186
	C6 (CH28/2)	C5 (CH27/2)	C4 (CH29/2)	180	7.328	9.269	11.533	98.044	134.906	-	-
	C9 (CH20/2)	C8 (CH19/2)	C7 (CH30/2)	180	7.078	8.963	11.378	147.066	135.744	-	-
	C12(CH3/3)	C11 (CH1/3)	C10 (CH16/3)	180	7.141	9.015	11.358	196.088	-	136.131	133.02

***Axial Coordinate Correction applies only to thermocouple well identifications with "D" labels (e.g., D-1 through D-12)**

TABLE I: Three-Dimensional Local Circular-Like Flow Channel Wall Temperature Measurements as a Function of the Net Single-Side Outside (or Incident) Heat Flux (continued)

Net Incident Heat Flux (kW/m^2)	Thermocouple Well Identification (Channel Number/Module Number)			Test Section Coordinates					Local Wall Thermocouple Temperature, T_w (^oC)		
	Axial Coordinate Correction*, D			Circumferential (Degrees)	Radial (mm)			Axial (mm) *	Close to Fluid/Solid Boundary	Intermediate	Close to Heated Boundary
	D = 0 mm	D = 2 mm	D = 4 mm								
728.3243	D3 (CH6/3)	D2 (CH5/3)	D1 (CH4/3)	0	7.204	10.269	12.797	45.022+D	158.761	160.682	-
	D6 (CH9/3)	D5 (CH8/3)	D4 (CH7/3)	0	7.512	10.670	12.318	94.044+D	-	162.324	-
	D9 (CH12/3)	D8 (CH11/3)	D7 (CH10/3)	0	8.057	9.881	12.191	143.066+D	160.056	166.416	-
	D12 (CH15/3)	D11(CH14/3)	D10 (CH13/3)	0	8.542	10.966	12.405	192.088+D	156.763	164.731	159.269
	B1 (CH12/2)	B2 (CH13/2)	B3 (CH14/2)	45	7.110	8.843	10.820	49.022	155.242	157.747	160.745
	B4 (CH15/2	B5 (CH16/2)	B6 (CH17/2)	45	7.296	9.215	10.845	98.044	147.414	-	161.584
	B7 (CH18/2)	B8 (CH31/2)	B9 (CH0/3)	45	6.565	8.631	10.893	147.066	-	161.413	171.564
	B10 (CH21/2)	B11 (CH22/2)	B12 (CH23/2)	45	5.956	8.946	11.081	196.088	-	160.452	169.248
	A1 (CHO/2)	A2 (CH1/2)	A3 (CH2/2)	135	7.328	9.322	11.892	49.022	139.643	129.414	-
	A4(CH3/2)	A5 (CH4/2)	A6 (CH5/2)	135	6.901	9.259	12.189	98.044	138.947	-	142.386
	A7 (CH7/2)	A8 (CH8/2)	A9 (CH6/2)	135	6.722	9.176	11.784	147.066	-	143.244	142.328
	A10 (CH9/2)	A11 (CH10/2)	A12 (CH11/2)	135	6.641	9.079	12.168	196.088	137.995	-	-
	C3 (CH26/2)	C2 (CH25/2)	C1 (CH24/2)	180	7.328	9.318	11.494	49.022	137.981	136.648	139.455
	C6 (CH28/2)	C5 (CH27/2)	C4 (CH29/2)	180	7.328	9.269	11.533	98.044	138.39	-	-
	C9 (CH20/2)	C8 (CH19/2)	C7 (CH30/2)	180	7.078	8.963	11.378	147.066	139.126	-	-
	C12(CH3/3)	C11 (CH1/3)	C10 (CH16/3)	180	7.141	9.015	11.358	196.088	-	141.508	137.824

***Axial Coordinate Correction applies only to thermocouple well identifications with "D" labels (e.g., D-1 through D-12)**

Circumferential Inside Temperature Profile Between Fluid and Heated Boundary
At Z=Z1, Z2, Z3, Z4
High Incident Heat Flux q_o = 728.3 kW/m^2

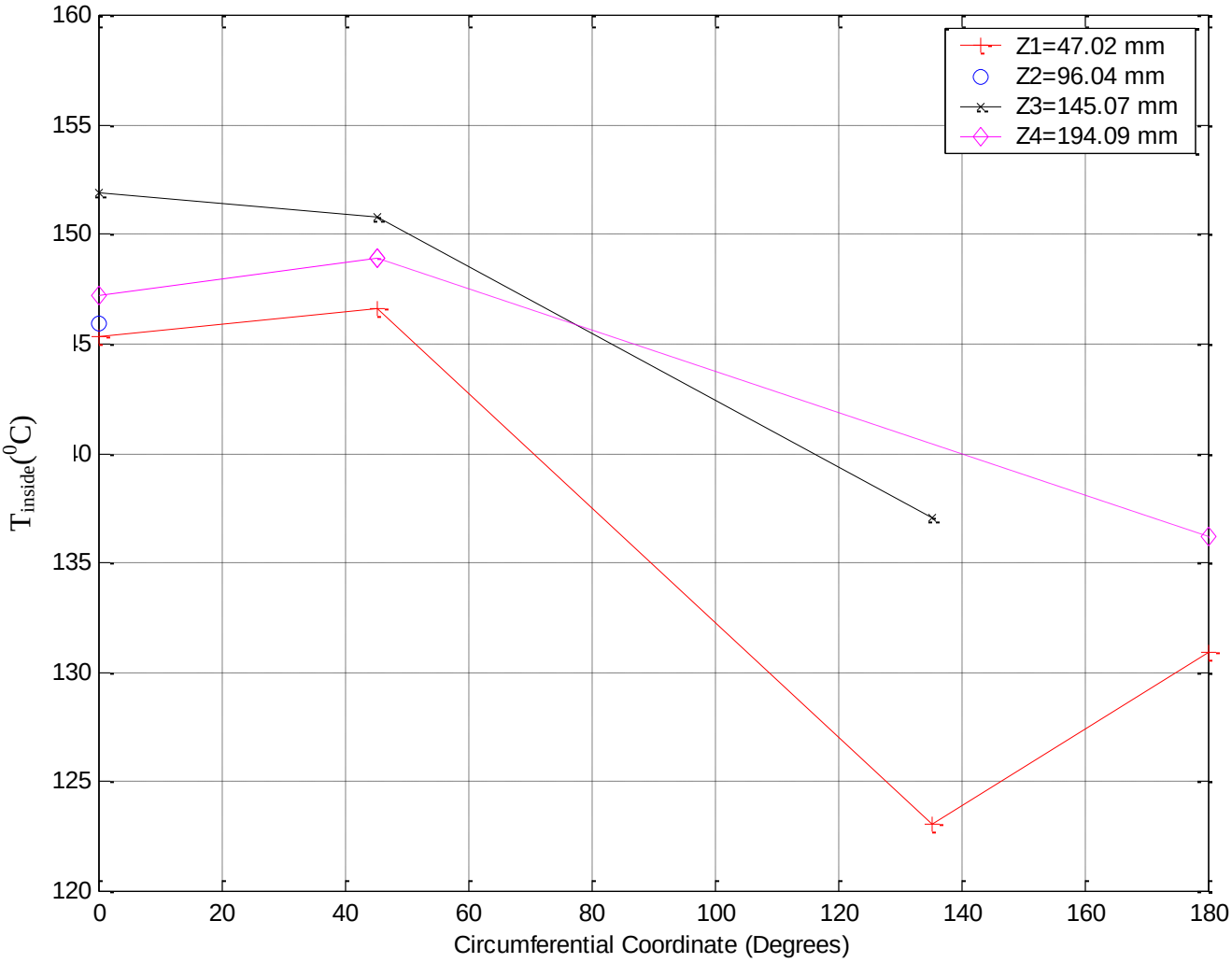

Figure 34: Circumferential Variation of the Inside Circular-Like Test Section Flow Channel Wall Temperature T_i at Different Axial Locations and Derived from Measurements Made at Radial Locations About Midway (see Table II) Between the Heated and Cooled Boundaries for an Outside (or incident) Single-Side Heat Flux of 728.3 KW/m^2.

mm, and ϕ = 0.0 degrees. At ϕ = 0.0 degrees, T_i increases slightly with z up to the third down-stream axial station (z = 143.1 mm) and then decreases as the channel exit was approached. As can be seen, the slope of the inside wall temperature profile is near zero at ϕ = 0.0 degrees. Since there were at most only four circumferential measurement locations, the circumferential data serve as a guide for the detail distribution. Data interpretation improves when the fact that the slope of the T_i-profile must also be zero at ϕ = 180.0 degrees. It should be noted that a dotted line is used in all plots between data points to indicate that there is a missing data point entry between those two points which could have otherwise help to better define the variation between those two points. For example at $z = z_4$ in Figure 34, a dotted line connecting the right-most data points indicates that a missing data point entry is between those two points. If that entry was not missing, more definition in the circumferential variation would have existed and could have been used possibly to verify the zero-slope condition and better display the variation in T_i as ϕ = 180.0 degrees is approached. This can be illustrated further by the data at $z = z_1$, where all four circumferential data entries are present. While the zero-slope condition at ϕ = 0.0 degrees is apparent, a similar condition at ϕ = 180.0 degrees is only realized when it is realized that the shown right-most two data points represents bounds for the physical profile as 180.0 degrees is approached. Data similar to the above inside wall temperature data was generated at twelve additional levels of q_o and its presented in Table II. It should be noted that each point in Fig.34 is for a slightly different radial location. The exact radial and other coordinate location for each point is also contained in Table II.

The non-dimensional form of T_i is T^* and is presented in Fig. 35. The non-dimensionalization reverses the relative magnitudes of the ordinate (compare Figs. 34 and 35). The representation puts the data points in a form that would be conducive for comparisons with other conjugate heat transfer/flow boiling measurements and predictive tools.

TABLE II: Two-Dimensional, Local Circular-Like Flow Channel Inside Wall Temperature as a Function of the Net Single-Side Outside (or Incident) Heat Flux (k=365.0 W/mK)

Net Incident Heat Flux (kW/m^2)	Thermocouple Well Identification (Channel Number/Module Number)			Test Section Coordinates					Inside Temperature, T_i (^oC)		
	Axial Coordinate Correction*, D			Circumferential (Degrees)	Radial (mm)			Axial (mm) *	Close to Fluid/Solid Boundary	Intermediate	Close to Heated Boundary
	D = 0 mm	D = 2 mm	D = 4 mm								
	D3 (CH6/3)	D2 (CH5/3)	D1 (CH4/3)	0	7.204	10.269	12.797	45.022+D	29.03	29.1	-
	D6 (CH9/3)	D5 (CH8/3)	D4 (CH7/3)	0	7.512	10.670	12.318	94.044+D	-	28.82	-
	D9 (CH12/3)	D8 (CH11/3)	D7 (CH10/3)	0	8.057	9.881	12.191	143.066+D	30.01	30.35	-
	D12 (CH15/3)	D11(CH14/3)	D10 (CH13/3)	0	8.542	10.966	12.405	192.088+D	30.04	30.18	29.62
	B1 (CH12/2)	B2 (CH13/2)	B3 (CH14/2)	45	7.110	8.843	10.820	49.022	**	**	**
	B4 (CH15/2	B5 (CH16/2)	B6 (CH17/2)	45	7.296	9.215	10.845	98.044	**	-	**
	B7 (CH18/2)	B8 (CH31/2)	B9 (CH0/3)	45	6.565	8.631	10.893	147.066	-	26.48	30.18
	B10 (CH21/2)	B11 (CH22/2)	B12 (CH23/2)	45	5.956	8.946	11.081	196.088	-	**	29.68
6.6581	A1 (CHO/2)	A2 (CH1/2)	A3 (CH2/2)	135	7.328	9.322	11.892	49.022	**	**	-
	A4(CH3/2)	A5 (CH4/2)	A6 (CH5/2)	135	6.901	9.259	12.189	98.044	**	-	**
	A7 (CH7/2)	A8 (CH8/2)	A9 (CH6/2)	135	6.722	9.176	11.784	147.066	-	**	**
	A10 (CH9/2)	A11 (CH10/2)	A12 (CH11/2)	135	6.641	9.079	12.168	196.088	**	-	-
	C3 (CH26/2)	C2 (CH25/2)	C1 (CH24/2)	180	7.328	9.318	11.494	49.022	**	**	**
	C6 (CH28/2)	C5 (CH27/2)	C4 (CH29/2)	180	7.328	9.269	11.533	98.044	**	-	-
	C9 (CH20/2)	C8 (CH19/2)	C7 (CH30/2)	180	7.078	8.963	11.378	147.066	**	-	-
	C12(CH3/3)	C11 (CH1/3)	C10 (CH16/3)	180	7.141	9.015	11.358	196.088	-	29.61	26.17
	D3 (CH6/3)	D2 (CH5/3)	D1 (CH4/3)	0	7.204	10.269	12.797	45.022+D	34.45	34.24	-
	D6 (CH9/3)	D5 (CH8/3)	D4 (CH7/3)	0	7.512	10.670	12.318	94.044+D	-	35.24	-
	D9 (CH12/3)	D8 (CH11/3)	D7 (CH10/3)	0	8.057	9.881	12.191	143.066+D	36.18	36.27	-
	D12 (CH15/3)	D11(CH14/3)	D10 (CH13/3)	0	8.542	10.966	12.405	192.088+D	36.36	36.58	36.43
	B1 (CH12/2)	B2 (CH13/2)	B3 (CH14/2)	45	7.110	8.843	10.820	49.022	30.54	30.48	30.46
	B4 (CH15/2	B5 (CH16/2)	B6 (CH17/2)	45	7.296	9.215	10.845	98.044	30.68	-	31.1
	B7 (CH18/2)	B8 (CH31/2)	B9 (CH0/3)	45	6.565	8.631	10.893	147.066	-	32.21	35.86
18.529	B10 (CH21/2)	B11 (CH22/2)	B12 (CH23/2)	45	5.956	8.946	11.081	196.088	-	32.86	32.85
	A1 (CHO/2)	A2 (CH1/2)	A3 (CH2/2)	135	7.328	9.322	11.892	49.022	29.96	**	-
	A4(CH3/2)	A5 (CH4/2)	A6 (CH5/2)	135	6.901	9.259	12.189	98.044	30.77	-	31.18
	A7 (CH7/2)	A8 (CH8/2)	A9 (CH6/2)	135	6.722	9.176	11.784	147.066	-	31.56	32.08
	A10 (CH9/2)	A11 (CH10/2)	A12 (CH11/2)	135	6.641	9.079	12.168	196.088	31.78	-	-
	C3 (CH26/2)	C2 (CH25/2)	C1 (CH24/2)	180	7.328	9.318	11.494	49.022	30.23	30.05	29.9
	C6 (CH28/2)	C5 (CH27/2)	C4 (CH29/2)	180	7.328	9.269	11.533	98.044	30.75	-	-
	C9 (CH20/2)	C8 (CH19/2)	C7 (CH30/2)	180	7.078	8.963	11.378	147.066	31.48	-	-
	C12(CH3/3)	C11 (CH1/3)	C10 (CH16/3)	180	7.141	9.015	11.358	196.088	-	35.55	35.52
	D3 (CH6/3)	D2 (CH5/3)	D1 (CH4/3)	0	7.204	10.269	12.797	45.022+D	37.38	37.19	-
	D6 (CH9/3)	D5 (CH8/3)	D4 (CH7/3)	0	7.512	10.670	12.318	94.044+D	-	37.85	-
	D9 (CH12/3)	D8 (CH11/3)	D7 (CH10/3)	0	8.057	9.881	12.191	143.066+D	39.91	39.99	-
	D12 (CH15/3)	D11(CH14/3)	D10 (CH13/3)	0	8.542	10.966	12.405	192.088+D	39.84	39.66	39.75
	B1 (CH12/2)	B2 (CH13/2)	B3 (CH14/2)	45	7.110	8.843	10.820	49.022	33.82	33.43	33.52
	B4 (CH15/2	B5 (CH16/2)	B6 (CH17/2)	45	7.296	9.215	10.845	98.044	33.96	-	34.46
	B7 (CH18/2)	B8 (CH31/2)	B9 (CH0/3)	45	6.565	8.631	10.893	147.066	-	35.77	39.25
	B10 (CH21/2)	B11 (CH22/2)	B12 (CH23/2)	45	5.956	8.946	11.081	196.088	-	35.74	36.03
26.6562	A1 (CHO/2)	A2 (CH1/2)	A3 (CH2/2)	135	7.328	9.322	11.892	49.022	32.63	26.56	-
	A4(CH3/2)	A5 (CH4/2)	A6 (CH5/2)	135	6.901	9.259	12.189	98.044	33.75	-	33.66
	A7 (CH7/2)	A8 (CH8/2)	A9 (CH6/2)	135	6.722	9.176	11.784	147.066	-	34.26	34.73
	A10 (CH9/2)	A11 (CH10/2)	A12 (CH11/2)	135	6.641	9.079	12.168	196.088	34.58	-	-
	C3 (CH26/2)	C2 (CH25/2)	C1 (CH24/2)	180	7.328	9.318	11.494	49.022	33.06	32.76	32.64
	C6 (CH28/2)	C5 (CH27/2)	C4 (CH29/2)	180	7.328	9.269	11.533	98.044	33.92	-	-
	C9 (CH20/2)	C8 (CH19/2)	C7 (CH30/2)	180	7.078	8.963	11.378	147.066	34.7	-	-
	C12(CH3/3)	C11 (CH1/3)	C10 (CH16/3)	180	7.141	9.015	11.358	196.088	-	38.48	38.45
	D3 (CH6/3)	D2 (CH5/3)	D1 (CH4/3)	0	7.204	10.269	12.797	45.022+D	49.12	48.7	-
	D6 (CH9/3)	D5 (CH8/3)	D4 (CH7/3)	0	7.512	10.670	12.318	94.044+D	-	49.75	-
	D9 (CH12/3)	D8 (CH11/3)	D7 (CH10/3)	0	8.057	9.881	12.191	143.066+D	53	52.94	-
	D12 (CH15/3)	D11(CH14/3)	D10 (CH13/3)	0	8.542	10.966	12.405	192.088+D	54.25	54.69	54.34
	B1 (CH12/2)	B2 (CH13/2)	B3 (CH14/2)	45	7.110	8.843	10.820	49.022	45.05	44.98	45.22
	B4 (CH15/2	B5 (CH16/2)	B6 (CH17/2)	45	7.296	9.215	10.845	98.044	45.59	-	46.26
	B7 (CH18/2)	B8 (CH31/2)	B9 (CH0/3)	45	6.565	8.631	10.893	147.066	-	49.04	52.4
	B10 (CH21/2)	B11 (CH22/2)	B12 (CH23/2)	45	5.956	8.946	11.081	196.088	-	50.81	51.26
54.1654	A1 (CHO/2)	A2 (CH1/2)	A3 (CH2/2)	135	7.328	9.322	11.892	49.022	43.8	36.87	-
	A4(CH3/2)	A5 (CH4/2)	A6 (CH5/2)	135	6.901	9.259	12.189	98.044	45.39	-	45.11
	A7 (CH7/2)	A8 (CH8/2)	A9 (CH6/2)	135	6.722	9.176	11.784	147.066	-	47.3	47.7
	A10 (CH9/2)	A11 (CH10/2)	A12 (CH11/2)	135	6.641	9.079	12.168	196.088	47.95	-	-
	C3 (CH26/2)	C2 (CH25/2)	C1 (CH24/2)	180	7.328	9.318	11.494	49.022	43.76	43.66	43.53
	C6 (CH28/2)	C5 (CH27/2)	C4 (CH29/2)	180	7.328	9.269	11.533	98.044	45.21	-	-
	C9 (CH20/2)	C8 (CH19/2)	C7 (CH30/2)	180	7.078	8.963	11.378	147.066	47.32	-	-
	C12(CH3/3)	C11 (CH1/3)	C10 (CH16/3)	180	7.141	9.015	11.358	196.088	-	51.91	51.72

***Axial Coordinate Correction applies only to thermocouple well identifications with "D" labels (e.g., D-1 through D-12)**

TABLE II: Two-Dimensional, Local Circular-Like Flow Channel Inside Wall Temperature as a Function of the Net Single-Side Outside (or Incident) Heat Flux (k=365.0 W/mK) (continued)

Net Incident Heat Flux (kW/m^2)	Thermocouple Well Identification (Channel Number/Module Number)			Test Section Coordinates					Inside Temperature, T_i (^oC)		
	Axial Coordinate Correction*, D			Circumferential (Degrees)	Radial (mm)			Axial (mm) *	Close to Fluid/Solid Boundary	Intermediate	Close to Heated Boundary
	D = 0 mm	D = 2 mm	D = 4 mm								
	D3 (CH6/3)	D2 (CH5/3)	D1 (CH4/3)	0	7.204	10.269	12.797	45.022+D	57.4	57.03	-
	D6 (CH9/3)	D5 (CH8/3)	D4 (CH7/3)	0	7.512	10.670	12.318	94.044+D	-	58.87	-
	D9 (CH12/3)	D8 (CH11/3)	D7 (CH10/3)	0	8.057	9.881	12.191	143.066+D	62.58	62.5	-
	D12 (CH15/3)	D11(CH14/3)	D10 (CH13/3)	0	8.542	10.966	12.405	192.088+D	63.03	63.76	63.16
	B1 (CH12/2)	B2 (CH13/2)	B3 (CH14/2)	45	7.110	8.843	10.820	49.022	52.74	53.09	53.29
	B4 (CH15/2	B5 (CH16/2)	B6 (CH17/2)	45	7.296	9.215	10.845	98.044	53.89	-	55.18
	B7 (CH18/2)	B8 (CH31/2)	B9 (CH0/3)	45	6.565	8.631	10.893	147.066	-	58.38	62.03
	B10 (CH21/2)	B11 (CH22/2)	B12 (CH23/2)	45	5.956	8.946	11.081	196.088	-	60	60.69
61.866	A1 (CHO/2)	A2 (CH1/2)	A3 (CH2/2)	135	7.328	9.322	11.892	49.022	51.79	39.8	-
	A4(CH3/2)	A5 (CH4/2)	A6 (CH5/2)	135	6.901	9.259	12.189	98.044	40.03	-	53.58
	A7 (CH7/2)	A8 (CH8/2)	A9 (CH6/2)	135	6.722	9.176	11.784	147.066	-	56.01	56.22
	A10 (CH9/2)	A11 (CH10/2)	A12 (CH11/2)	135	6.641	9.079	12.168	196.088	56.02	-	-
	C3 (CH26/2)	C2 (CH25/2)	C1 (CH24/2)	180	7.328	9.318	11.494	49.022	51.1	51.08	50.93
	C6 (CH28/2)	C5 (CH27/2)	C4 (CH29/2)	180	7.328	9.269	11.533	98.044	53.43	-	-
	C9 (CH20/2)	C8 (CH19/2)	C7 (CH30/2)	180	7.078	8.963	11.378	147.066	56.02	-	-
	C12(CH3/3)	C11 (CH1/3)	C10 (CH16/3)	180	7.141	9.015	11.358	196.088	-	60.04	59.78
	D3 *(CH6/3)	D2 (CH5/3)	D1 (CH4/3)	0	7.204	10.269	12.797	45.022+D	75.93	75.08	-
	D6 (CH9/3)	D5 (CH8/3)	D4 (CH7/3)	0	7.512	10.670	12.318	94.044+D	-	80.24	-
	D9 (CH12/3)	D8 (CH11/3)	D7 (CH10/3)	0	8.057	9.881	12.191	143.066+D	84.61	84.53	-
	D12 (CH15/3)	D11(CH14/3)	D10 (CH13/3)	0	8.542	10.966	12.405	192.088+D	81.32	82.34	81.5
	B1 (CH12/2)	B2 (CH13/2)	B3 (CH14/2)	45	7.110	8.843	10.820	49.022	71.05	71.18	71.65
	B4 (CH15/2	B5 (CH16/2)	B6 (CH17/2)	45	7.296	9.215	10.845	98.044	73.89	-	76.24
	B7 (CH18/2)	B8 (CH31/2)	B9 (CH0/3)	45	6.565	8.631	10.893	147.066	-	80.01	83.31
	B10 (CH21/2)	B11 (CH22/2)	B12 (CH23/2)	45	5.956	8.946	11.081	196.088	-	78.66	79.55
104.0506	A1 (CHO/2)	A2 (CH1/2)	A3 (CH2/2)	135	7.328	9.322	11.892	49.022	68.15	45.52	-
	A4(CH3/2)	A5 (CH4/2)	A6 (CH5/2)	135	6.901	9.259	12.189	98.044	73.48	-	73
	A7 (CH7/2)	A8 (CH8/2)	A9 (CH6/2)	135	6.722	9.176	11.784	147.066	-	75.69	76.34
	A10 (CH9/2)	A11 (CH10/2)	A12 (CH11/2)	135	6.641	9.079	12.168	196.088	73.59	-	-
	C3 (CH26/2)	C2 (CH25/2)	C1 (CH24/2)	180	7.328	9.318	11.494	49.022	67.88	67.72	67.56
	C6 (CH28/2)	C5 (CH27/2)	C4 (CH29/2)	180	7.328	9.269	11.533	98.044	73.18	-	-
	C9 (CH20/2)	C8 (CH19/2)	C7 (CH30/2)	180	7.078	8.963	11.378	147.066	76.06	-	-
	C12(CH3/3)	C11 (CH1/3)	C10 (CH16/3)	180	7.141	9.015	11.358	196.088	-	77.52	77.79
	D3 (CH6/3)	D2 (CH5/3)	D1 (CH4/3)	0	7.204	10.269	12.797	45.022+D	82.82	81.89	-
	D6 (CH9/3)	D5 (CH8/3)	D4 (CH7/3)	0	7.512	10.670	12.318	94.044+D	-	85.67	-
	D9 (CH12/3)	D8 (CH11/3)	D7 (CH10/3)	0	8.057	9.881	12.191	143.066+D	91.77	91.36	-
	D12 (CH15/3)	D11(CH14/3)	D10 (CH13/3)	0	8.542	10.966	12.405	192.088+D	91.77	92.16	90.89
	B1 (CH12/2)	B2 (CH13/2)	B3 (CH14/2)	45	7.110	8.843	10.820	49.022	76.76	77.31	77.74
	B4 (CH15/2	B5 (CH16/2)	B6 (CH17/2)	45	7.296	9.215	10.845	98.044	78.99	-	81.16
	B7 (CH18/2)	B8 (CH31/2)	B9 (CH0/3)	45	6.565	8.631	10.893	147.066	-	86.48	89.62
	B10 (CH21/2)	B11 (CH22/2)	B12 (CH23/2)	45	5.956	8.946	11.081	196.088	-	88.01	89.27
122.3466	A1 (CHO/2)	A2 (CH1/2)	A3 (CH2/2)	135	7.328	9.322	11.892	49.022	74.55	52.03	-
	A4(CH3/2)	A5 (CH4/2)	A6 (CH5/2)	135	6.901	9.259	12.189	98.044	78.87	-	78.19
	A7 (CH7/2)	A8 (CH8/2)	A9 (CH6/2)	135	6.722	9.176	11.784	147.066	-	82.38	82.49
	A10 (CH9/2)	A11 (CH10/2)	A12 (CH11/2)	135	6.641	9.079	12.168	196.088	81.63	-	-
	C3 (CH26/2)	C2 (CH25/2)	C1 (CH24/2)	180	7.328	9.318	11.494	49.022	74.09	73.77	73.69
	C6 (CH28/2)	C5 (CH27/2)	C4 (CH29/2)	180	7.328	9.269	11.533	98.044	78.27	-	-
	C9 (CH20/2)	C8 (CH19/2)	C7 (CH30/2)	180	7.078	8.963	11.378	147.066	82.12	-	-
	C12(CH3/3)	C11 (CH1/3)	C10 (CH16/3)	180	7.141	9.015	11.358	196.088	-	85.67	85.45
	D3 (CH6/3)	D2 (CH5/3)	D1 (CH4/3)	0	7.204	10.269	12.797	45.022+D	122.9	119	-
	D6 (CH9/3)	D5 (CH8/3)	D4 (CH7/3)	0	7.512	10.670	12.318	94.044+D	-	128.4	-
	D9 (CH12/3)	D8 (CH11/3)	D7 (CH10/3)	0	8.057	9.881	12.191	143.066+D	126.1	126.9	-
	D12 (CH15/3)	D11(CH14/3)	D10 (CH13/3)	0	8.542	10.966	12.405	192.088+D	112.3	114.1	114
	B1 (CH12/2)	B2 (CH13/2)	B3 (CH14/2)	45	7.110	8.843	10.820	49.022	115.9	116.8	118
	B4 (CH15/2	B5 (CH16/2)	B6 (CH17/2)	45	7.296	9.215	10.845	98.044	118.3	-	120.9
	B7 (CH18/2)	B8 (CH31/2)	B9 (CH0/3)	45	6.565	8.631	10.893	147.066	-	118.9	123.3
	B10 (CH21/2)	B11 (CH22/2)	B12 (CH23/2)	45	5.956	8.946	11.081	196.088	-	113	112.4
225.2877	A1 (CHO/2)	A2 (CH1/2)	A3 (CH2/2)	135	7.328	9.322	11.892	49.022	109.5	65.23	-
	A4(CH3/2)	A5 (CH4/2)	A6 (CH5/2)	135	6.901	9.259	12.189	98.044	116	-	115.6
	A7 (CH7/2)	A8 (CH8/2)	A9 (CH6/2)	135	6.722	9.176	11.784	147.066	-	113.5	114
	A10 (CH9/2)	A11 (CH10/2)	A12 (CH11/2)	135	6.641	9.079	12.168	196.088	104.1	-	-
	C3 (CH26/2)	C2 (CH25/2)	C1 (CH24/2)	180	7.328	9.318	11.494	49.022	107.6	107	105.4
	C6 (CH28/2)	C5 (CH27/2)	C4 (CH29/2)	180	7.328	9.269	11.533	98.044	115.4	-	-
	C9 (CH20/2)	C8 (CH19/2)	C7 (CH30/2)	180	7.078	8.963	11.378	147.066	112.9	-	-
	C12(CH3/3)	C11 (CH1/3)	C10 (CH16/3)	180	7.141	9.015	11.358	196.088	-	108.5	107.3

***Axial Coordinate Correction applies only to thermocouple well identifications with "D" labels (e.g., D-1 through D-12)**

TABLE II: Two-Dimensional, Local Circular-Like Flow Channel Inside Wall Temperature as a Function of the Net Single-Side Outside (or Incident) Heat Flux (k=365.0 W/mK) (continued)

Net Incident Heat Flux (kW/m^2)	Thermocouple Well Identification (Channel Number/Module Number)			Test Section Coordinates					Inside Temperature, T_i (^oC)		
	Axial Coordinate Correction*, D			Circumferential (Degrees)	Radial (mm)			Axial (mm) *	Close to Fluid/Solid Boundary	Intermediate	Close to Heated Boundary
	D = 0 mm	D = 2 mm	D = 4 mm								
	D3 (CH6/3)	D2 (CH5/3)	D1 (CH4/3)	0	7.204	10.269	12.797	45.022+D	125.9	121.9	-
	D6 (CH9/3)	D5 (CH8/3)	D4 (CH7/3)	0	7.512	10.670	12.318	94.044+D	-	124.5	-
	D9 (CH12/3)	D8 (CH11/3)	D7 (CH10/3)	0	8.057	9.881	12.191	143.066+D	128	128.8	-
	D12 (CH15/3)	D11(CH14/3)	D10 (CH13/3)	0	8.542	10.966	12.405	192.088+D	120.4	123.8	121.7
	B1 (CH12/2)	B2 (CH13/2)	B3 (CH14/2)	45	7.110	8.843	10.820	49.022	117.7	119.5	119.1
	B4 (CH15/2	B5 (CH16/2)	B6 (CH17/2)	45	7.296	9.215	10.845	98.044	117	-	118.3
	B7 (CH18/2)	B8 (CH31/2)	B9 (CH0/3)	45	6.565	8.631	10.893	147.066	-	122.8	125.4
	B10 (CH21/2)	B11 (CH22/2)	B12 (CH23/2)	45	5.956	8.946	11.081	196.088	-	120.6	123.9
294.3267	A1 (CHO/2)	A2 (CH1/2)	A3 (CH2/2)	135	7.328	9.322	11.892	49.022	113.2	76.59	-
	A4(CH3/2)	A5 (CH4/2)	A6 (CH5/2)	135	6.901	9.259	12.189	98.044	113.5	-	115.1
	A7 (CH7/2)	A8 (CH8/2)	A9 (CH6/2)	135	6.722	9.176	11.784	147.066	-	115.9	116.1
	A10 (CH9/2)	A11 (CH10/2)	A12 (CH11/2)	135	6.641	9.079	12.168	196.088	111.3	-	-
	C3 (CH26/2)	C2 (CH25/2)	C1 (CH24/2)	180	7.328	9.318	11.494	49.022	111.2	112	112.1
	C6 (CH28/2)	C5 (CH27/2)	C4 (CH29/2)	180	7.328	9.269	11.533	98.044	114.7	-	-
	C9 (CH20/2)	C8 (CH19/2)	C7 (CH30/2)	180	7.078	8.963	11.378	147.066	116.6	-	-
	C12(CH3/3)	C11 (CH1/3)	C10 (CH16/3)	180	7.141	9.015	11.358	196.088	-	114.4	114.2
	D3 *(CH6/3)	D2 (CH5/3)	D1 (CH4/3)	0	7.204	10.269	12.797	45.022+D	134.9	131.8	-
	D6 (CH9/3)	D5 (CH8/3)	D4 (CH7/3)	0	7.512	10.670	12.318	94.044+D	-	132.2	-
	D9 (CH12/3)	D8 (CH11/3)	D7 (CH10/3)	0	8.057	9.881	12.191	143.066+D	140.1	141.3	-
	D12 (CH15/3)	D11(CH14/3)	D10 (CH13/3)	0	8.542	10.966	12.405	192.088+D	132.4	133.9	131.2
	B1 (CH12/2)	B2 (CH13/2)	B3 (CH14/2)	45	7.110	8.843	10.820	49.022	128.9	130.3	132.2
	B4 (CH15/2	B5 (CH16/2)	B6 (CH17/2)	45	7.296	9.215	10.845	98.044	127	-	134.7
	B7 (CH18/2)	B8 (CH31/2)	B9 (CH0/3)	45	6.565	8.631	10.893	147.066	-	137.3	142.4
	B10 (CH21/2)	B11 (CH22/2)	B12 (CH23/2)	45	5.956	8.946	11.081	196.088	-	132.9	135.5
417.9938	A1 (CHO/2)	A2 (CH1/2)	A3 (CH2/2)	135	7.328	9.322	11.892	49.022	117.9	82.97	-
	A4(CH3/2)	A5 (CH4/2)	A6 (CH5/2)	135	6.901	9.259	12.189	98.044	120.9	-	120.8
	A7 (CH7/2)	A8 (CH8/2)	A9 (CH6/2)	135	6.722	9.176	11.784	147.066	-	125.3	121.4
	A10 (CH9/2)	A11 (CH10/2)	A12 (CH11/2)	135	6.641	9.079	12.168	196.088	120.3	-	-
	C3 (CH26/2)	C2 (CH25/2)	C1 (CH24/2)	180	7.328	9.318	11.494	49.022	119.5	119.2	117.9
	C6 (CH28/2)	C5 (CH27/2)	C4 (CH29/2)	180	7.328	9.269	11.533	98.044	120.9	-	-
	C9 (CH20/2)	C8 (CH19/2)	C7 (CH30/2)	180	7.078	8.963	11.378	147.066	124.3	-	-
	C12(CH3/3)	C11 (CH1/3)	C10 (CH16/3)	180	7.141	9.015	11.358	196.088	-	123.8	123.9
	D3 (CH6/3)	D2 (CH5/3)	D1 (CH4/3)	0	7.204	10.269	12.797	45.022+D	137.8	138.1	-
	D6 (CH9/3)	D5 (CH8/3)	D4 (CH7/3)	0	7.512	10.670	12.318	94.044+D	-	137.6	-
	D9 (CH12/3)	D8 (CH11/3)	D7 (CH10/3)	0	8.057	9.881	12.191	143.066+D	141.8	144	-
	D12 (CH15/3)	D11(CH14/3)	D10 (CH13/3)	0	8.542	10.966	12.405	192.088+D	138.9	139.1	138.6
	B1 (CH12/2)	B2 (CH13/2)	B3 (CH14/2)	45	7.110	8.843	10.820	49.022	135.1	134.8	136.9
	B4 (CH15/2	B5 (CH16/2)	B6 (CH17/2)	45	7.296	9.215	10.845	98.044	133.7	-	135.9
	B7 (CH18/2)	B8 (CH31/2)	B9 (CH0/3)	45	6.565	8.631	10.893	147.066	-	140.1	145.3
	B10 (CH21/2)	B11 (CH22/2)	B12 (CH23/2)	45	5.956	8.946	11.081	196.088	-	139.9	144.5
469.6313	A1 (CHO/2)	A2 (CH1/2)	A3 (CH2/2)	135	7.328	9.322	11.892	49.022	123.2	92.56	-
	A4(CH3/2)	A5 (CH4/2)	A6 (CH5/2)	135	6.901	9.259	12.189	98.044	125.2	-	123.8
	A7 (CH7/2)	A8 (CH8/2)	A9 (CH6/2)	135	6.722	9.176	11.784	147.066	-	127.4	128.5
	A10 (CH9/2)	A11 (CH10/2)	A12 (CH11/2)	135	6.641	9.079	12.168	196.088	124.8	-	-
	C3 (CH26/2)	C2 (CH25/2)	C1 (CH24/2)	180	7.328	9.318	11.494	49.022	122.3	124.9	123.4
	C6 (CH28/2)	C5 (CH27/2)	C4 (CH29/2)	180	7.328	9.269	11.533	98.044	125.5	-	-
	C9 (CH20/2)	C8 (CH19/2)	C7 (CH30/2)	180	7.078	8.963	11.378	147.066	129.2	-	-
	C12(CH3/3)	C11 (CH1/3)	C10 (CH16/3)	180	7.141	9.015	11.358	196.088	-	127.1	128.7
	D3 (CH6/3)	D2 (CH5/3)	D1 (CH4/3)	0	7.204	10.269	12.797	45.022+D	140.6	142	-
	D6 (CH9/3)	D5 (CH8/3)	D4 (CH7/3)	0	7.512	10.670	12.318	94.044+D	-	144.1	-
	D9 (CH12/3)	D8 (CH11/3)	D7 (CH10/3)	0	8.057	9.881	12.191	143.066+D	148.9	150.9	-
	D12 (CH15/3)	D11(CH14/3)	D10 (CH13/3)	0	8.542	10.966	12.405	192.088+D	144.9	148.8	139.9
	B1 (CH12/2)	B2 (CH13/2)	B3 (CH14/2)	45	7.110	8.843	10.820	49.022	135.9	138.4	144.2
	B4 (CH15/2	B5 (CH16/2)	B6 (CH17/2)	45	7.296	9.215	10.845	98.044	135.9	-	144.2
	B7 (CH18/2)	B8 (CH31/2)	B9 (CH0/3)	45	6.565	8.631	10.893	147.066	-	146.8	152.7
	B10 (CH21/2)	B11 (CH22/2)	B12 (CH23/2)	45	5.956	8.946	11.081	196.088	-	146.3	149.4
503.1049	A1 (CHO/2)	A2 (CH1/2)	A3 (CH2/2)	135	7.328	9.322	11.892	49.022	130.2	110.1	-
	A4(CH3/2)	A5 (CH4/2)	A6 (CH5/2)	135	6.901	9.259	12.189	98.044	132.4	-	131.7
	A7 (CH7/2)	A8 (CH8/2)	A9 (CH6/2)	135	6.722	9.176	11.784	147.066	-	132.8	134.8
	A10 (CH9/2)	A11 (CH10/2)	A12 (CH11/2)	135	6.641	9.079	12.168	196.088	131.1	-	-
	C3 (CH26/2)	C2 (CH25/2)	C1 (CH24/2)	180	7.328	9.318	11.494	49.022	128.9	129	125.3
	C6 (CH28/2)	C5 (CH27/2)	C4 (CH29/2)	180	7.328	9.269	11.533	98.044	132	-	-
	C9 (CH20/2)	C8 (CH19/2)	C7 (CH30/2)	180	7.078	8.963	11.378	147.066	133	-	-
	C12(CH3/3)	C11 (CH1/3)	C10 (CH16/3)	180	7.141	9.015	11.358	196.088	-	132.2	128.3

***Axial Coordinate Correction applies only to thermocouple well identifications with "D" labels (e.g., D-1 through D-12)**

TABLE II: Two-Dimensional, Local Circular-Like Flow Channel Inside Wall Temperature as a Function of the Net Single-Side Outside (or Incident) Heat Flux (k=365.0 W/mK)
(continued)

Net Incident Heat Flux (kW/m^2)	Thermocouple Well Identification (Channel Number/Module Number)			Test Section Coordinates					Inside Temperature, T_i (^oC)		
	Axial Coordinate Correction*, D			Circumferential (Degrees)	Radial (mm)			Axial (mm) *	Close to Fluid/Solid Boundary	Intermediate	Close to Heated Boundary
	D = 0 mm	D = 2 mm	D = 4 mm								
728.3243	D3 (CH6/3)	D2 (CH5/3)	D1 (CH4/3)	0	7.204	10.269	12.797	45.022+D	151.8	145.3	-
	D6 (CH9/3)	D5 (CH8/3)	D4 (CH7/3)	0	7.512	10.670	12.318	94.044+D	-	145.9	-
	D9 (CH12/3)	D8 (CH11/3)	D7 (CH10/3)	0	8.057	9.881	12.191	143.066+D	150.4	151.9	-
	D12 (CH15/3)	D11(CH14/3)	D10 (CH13/3)	0	8.542	10.966	12.405	192.088+D	145.5	147.2	138.2
	B1 (CH12/2)	B2 (CH13/2)	B3 (CH14/2)	45	7.110	8.843	10.820	49.022	148.7	146.6	144.8
	B4 (CH15/2	B5 (CH16/2)	B6 (CH17/2)	45	7.296	9.215	10.845	98.044	140.3	-	145.6
	B7 (CH18/2)	B8 (CH31/2)	B9 (CH0/3)	45	6.565	8.631	10.893	147.066	-	150.8	155.4
	B10 (CH21/2)	B11 (CH22/2)	B12 (CH23/2)	45	5.956	8.946	11.081	196.088	-	148.9	152.5
	A1 (CHO/2)	A2 (CH1/2)	A3 (CH2/2)	135	7.328	9.322	11.892	49.022	135.2	123.1	-
	A4(CH3/2)	A5 (CH4/2)	A6 (CH5/2)	135	6.901	9.259	12.189	98.044	135.2	-	134.7
	A7 (CH7/2)	A8 (CH8/2)	A9 (CH6/2)	135	6.722	9.176	11.784	147.066	-	137.1	134.9
	A10 (CH9/2)	A11 (CH10/2)	A12 (CH11/2)	135	6.641	9.079	12.168	196.088	134.8	-	-
	C3 (CH26/2)	C2 (CH25/2)	C1 (CH24/2)	180	7.328	9.318	11.494	49.022	133.9	130.9	132.7
	C6 (CH28/2)	C5 (CH27/2)	C4 (CH29/2)	180	7.328	9.269	11.533	98.044	134.4	-	-
	C9 (CH20/2)	C8 (CH19/2)	C7 (CH30/2)	180	7.078	8.963	11.378	147.066	135.5	-	-
	C12(CH3/3)	C11 (CH1/3)	C10 (CH16/3)	180	7.141	9.015	11.358	196.088	-	136.2	131.6

***Axial Coordinate Correction applies only to thermocouple well identifications with "D" labels (e.g., D-1 through D-12)**

Circumferential Dimensionless Temperature Profiles Between the Fluid and Heated Boundary
At Z=Z1, Z2, Z3, Z4
High Incident Heat Flux, q_o = 728.3 kW/m^2

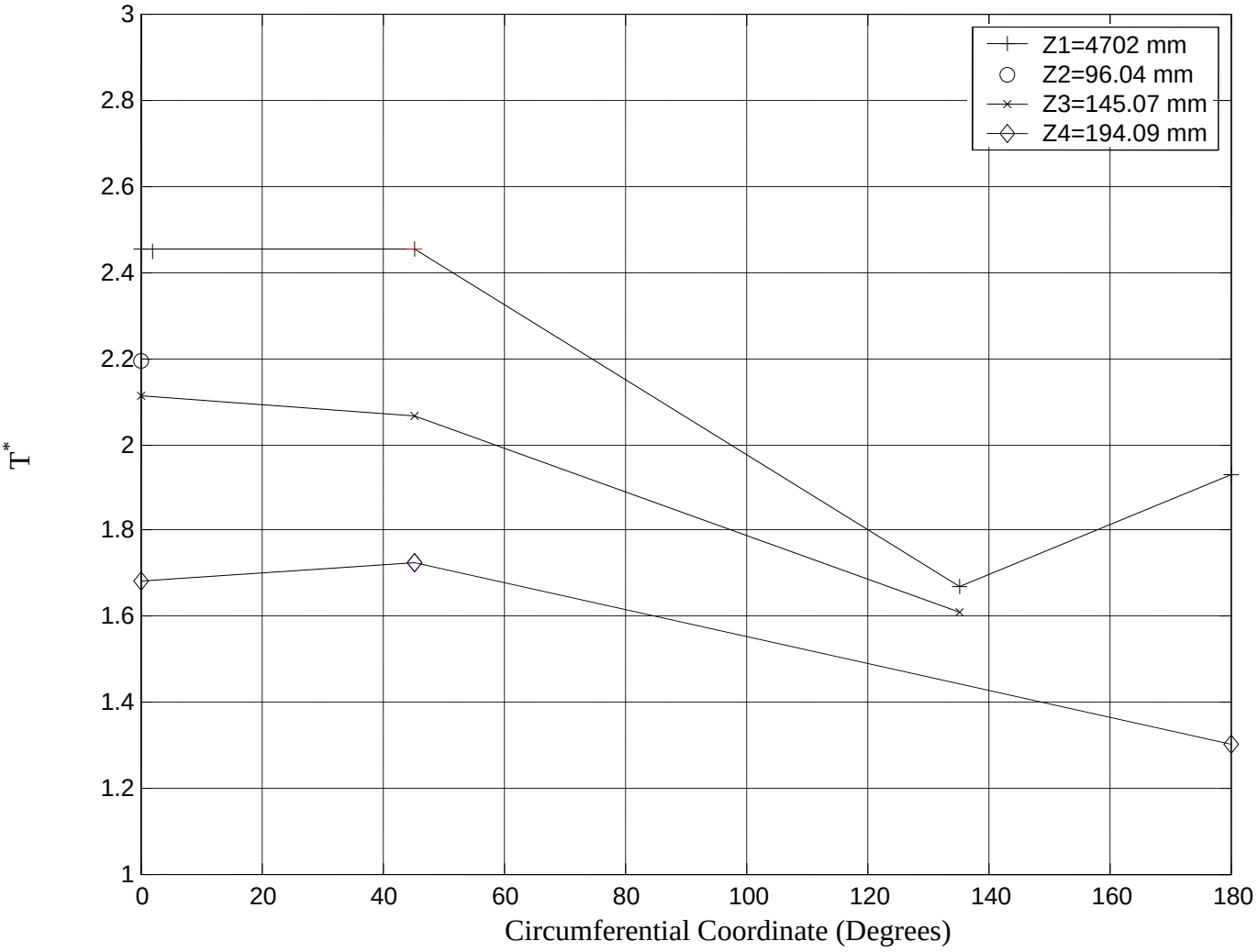

Figure 35: Circumferential Variation of the Inside Circular Like Test Section Flow Channel Dimensionless Wall Temperature (T^*) at Different Axial Locations and Derived from Measurements Made at Radial Locations About Midway (see Table II) Between the Heated and Cooled Boundaries for an Outside (or incident) Single-Side Heat Flux of 728.3 kW/m^2

14.5.2 FLOW CHANNEL INSIDE WALL HEAT FLUX

The data representing the circumferential, inside wall heat flux (q_i) profile is shown in Fig. 36 for the above noted conditions. The variations with respect to ϕ are substantial and can be seen to be amenable to the zero slope conditions at ϕ = 0.0 and 180.0 degrees. At ϕ = 0.0 degrees, q_i increases with z. All thirty-one thermocouple well data were reduced to produce values of q_i. For a given value of ϕ and z, the thermocouple wells closest to the heated boundary resulted in higher values of q_i than the other two locations close to the fluid. It is believed that those wells closest to the fluid boundary will result in better estimates of q_i. Reduced data for q_i at thirteen levels of q_o are tabulated in Table III from each of the thirty-one measurements. The reduced data for q_i and T_i and the data for T (r, ϕ, z) form an evolving conjugate heat transfer data-base with influences of turbulence, developing flow, single-side heating, single-phase flow, and flow boiling. The corresponding values of the local (axial) bulk fluid (water) temperature are contained in Table IV. The representation of the inside heat flux in dimensionless form is given in Fig. 37.

14.6 LOCAL BOILING CURVES

Two-dimensional (circumferential and axial), local boiling curves are presented for subcooled water flow boiling in a single-side heated circular flow channel. Although a complete compilation of all the reduced data is contained in Tables II and III, examples of the 2-D boiling curves are shown in Figs. 38 through 41. The boiling curves in Fig. 38 is for a nominal axial coordinate of $z = z_3 = 143.07$ mm.

The quantitative differences in the circumferential (ϕ) variations of the boiling curve are shown in Fig. 38 for ϕ varying from 0.0 degrees to 180.0 degrees. The highest two heat fluxes (right-most pair of points) at 0.0 degrees indicate a fully developed boiling regime exists; and as ϕ increases, the slope of the boiling curve at similar points decreases which indicates that a region of less and less flow boiling exists. Although these trends exist at all axial locations, the circumferential variations did change for different values of z.

The axial variations can be discerned by comparing Figs. 38 through 41. As one would expect, the superheat (i.e., $T_i - T_{sat}$) and the above noted slopes at all circumferential locations decreased with z. As z decreases from z_3 = 143.07 mm (Fig. 38) to a nominal axial location of $z = z_2$ = 94.04 mm (Fig. 39), there is a change in the polarity of the relative superheat for ϕ = 0.0 degrees and 45.0 degrees at the highest heat fluxes. As z decreases further to 45.0 mm (Fig. 40),

the polarity remains unchanged and the absolute value of the differences in relative superheat increases. However if z increases from z_3 to $z = z_4 = 192.09$ mm (Fig. 41), the polarity does not change; but, the differences in the absolute value of the relative superheat increase. The above noted differences may be due to a redistribution of the flow and/or heat transfer. At values of q_i above those shown in Figs. 38 through 41, a loud hammer-like sound occurred and increased in amplitude as the heat flux was increased.

Circumferential Inside Heat Flux Profiles Between the Fluid and Heated Boundary
At Z = Z1, Z2, Z3, Z4
High Incident Heat Flux, q_o = 728.3 kW/m^2

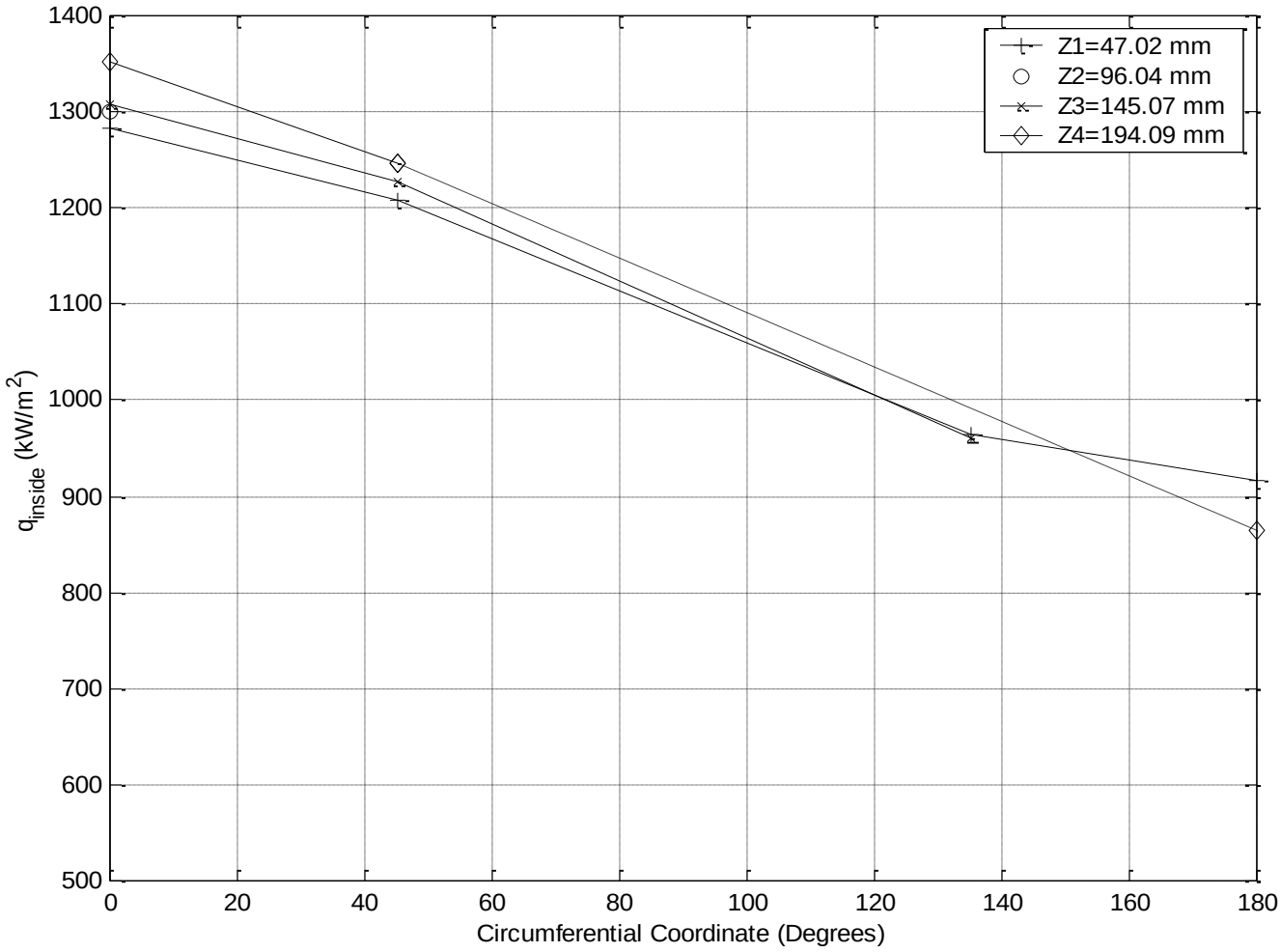

Figure 36: Circumferential Variation of the Inside Circular-Like Test Section Flow Channel Wall Heat Flux (q_i) at Different Axial Locations and Derived from Measurements Made at Radial Locations About Midway (see Table II) Between the Heated and Cooled Boundaries for an Outside (or incident) Single-Side Heat Flux of 728.3 kW/m^2.

TABLE III: Two-Dimensional, Local Circular-Like Flow Channel Inside Heat Flux as a Function of the Net Single-Side Outside (or Incident) Heat Flux (k=365.0 W/mK)

Net Incident Heat Flux (kW/m^2)	Thermocouple Well Identification (Channel Number/Module Number)			Test Section Coordinates					Inside Heat Flux (kW/m^2)		
	Axial Coordinate Correction*, D			Circumferential (Degrees)	Radial (mm)			Axial (mm) *	Close to Fluid/Solid Boundary	Intermediate	Close to Heated Boundary
	D = 0 mm	D = 2 mm	D = 4 mm								
	D3 (CH6/3)	D2 (CH5/3)	D1 (CH4/3)	0	7.204	10.269	12.797	45.022+D	10.39	10.38	-
	D6 (CH9/3)	D5 (CH8/3)	D4 (CH7/3)	0	7.512	10.670	12.318	94.044+D	-	10.43	-
	D9 (CH12/3)	D8 (CH11/3)	D7 (CH10/3)	0	8.057	9.881	12.191	143.066+D	10.31	10.28	-
	D12 (CH15/3)	D11(CH14/3)	D10 (CH13/3)	0	8.542	10.966	12.405	192.088+D	10.31	10.3	10.3
	B1 (CH12/2)	B2 (CH13/2)	B3 (CH14/2)	45	7.110	8.843	10.820	49.022	**	**	**
	B4 (CH15/2	B5 (CH16/2)	B6 (CH17/2)	45	7.296	9.215	10.845	98.044	**	-	**
	B7 (CH18/2)	B8 (CH31/2)	B9 (CH0/3)	45	6.565	8.631	10.893	147.066	-	11.49	10.21
	B10 (CH21/2)	B11 (CH22/2)	B12 (CH23/2)	45	5.956	8.946	11.081	196.088	-	**	13.64
6.6581	A1 (CHO/2)	A2 (CH1/2)	A3 (CH2/2)	135	7.328	9.322	11.892	49.022	**	**	-
	A4(CH3/2)	A5 (CH4/2)	A6 (CH5/2)	135	6.901	9.259	12.189	98.044	**	-	**
	A7 (CH7/2)	A8 (CH8/2)	A9 (CH6/2)	135	6.722	9.176	11.784	147.066	-	**	**
	A10 (CH9/2)	A11 (CH10/2)	A12 (CH11/2)	135	6.641	9.079	12.168	196.088	**	-	-
	C3 (CH26/2)	C2 (CH25/2)	C1 (CH24/2)	180	7.328	9.318	11.494	49.022	**	**	**
	C6 (CH28/2)	C5 (CH27/2)	C4 (CH29/2)	180	7.328	9.269	11.533	98.044	**	-	-
	C9 (CH20/2)	C8 (CH19/2)	C7 (CH30/2)	180	7.078	8.963	11.378	147.066	**	-	-
	C12(CH3/3)	C11 (CH1/3)	C10 (CH16/3)	180	7.141	9.015	11.358	196.088	-	9.646	9.647
	D3 (CH6/3)	D2 (CH5/3)	D1 (CH4/3)	0	7.204	10.269	12.797	45.022+D	28.96	28.99	-
	D6 (CH9/3)	D5 (CH8/3)	D4 (CH7/3)	0	7.512	10.670	12.318	94.044+D	-	28.88	-
	D9 (CH12/3)	D8 (CH11/3)	D7 (CH10/3)	0	8.057	9.881	12.191	143.066+D	28.8	28.8	-
	D12 (CH15/3)	D11(CH14/3)	D10 (CH13/3)	0	8.542	10.966	12.405	192.088+D	28.81	28.79	28.8
	B1 (CH12/2)	B2 (CH13/2)	B3 (CH14/2)	45	7.110	8.843	10.820	49.022	29.14	29.16	29.16
	B4 (CH15/2	B5 (CH16/2)	B6 (CH17/2)	45	7.296	9.215	10.845	98.044	29.16	-	29.05
	B7 (CH18/2)	B8 (CH31/2)	B9 (CH0/3)	45	6.565	8.631	10.893	147.066	-	28.86	28.46
18.529	B10 (CH21/2)	B11 (CH22/2)	B12 (CH23/2)	45	5.956	8.946	11.081	196.088	-	28.79	28.79
	A1 (CHO/2)	A2 (CH1/2)	A3 (CH2/2)	135	7.328	9.322	11.892	49.022	26.41	**	-
	A4(CH3/2)	A5 (CH4/2)	A6 (CH5/2)	135	6.901	9.259	12.189	98.044	26.57	-	26.66
	A7 (CH7/2)	A8 (CH8/2)	A9 (CH6/2)	135	6.722	9.176	11.784	147.066	-	26.69	26.78
	A10 (CH9/2)	A11 (CH10/2)	A12 (CH11/2)	135	6.641	9.079	12.168	196.088	26.69	-	-
	C3 (CH26/2)	C2 (CH25/2)	C1 (CH24/2)	180	7.328	9.318	11.494	49.022	25.8	25.73	25.66
	C6 (CH28/2)	C5 (CH27/2)	C4 (CH29/2)	180	7.328	9.269	11.533	98.044	25.92	-	-
	C9 (CH20/2)	C8 (CH19/2)	C7 (CH30/2)	180	7.078	8.963	11.378	147.066	26.08	-	-
	C12(CH3/3)	C11 (CH1/3)	C10 (CH16/3)	180	7.141	9.015	11.358	196.088	-	26.77	26.76
	D3 (CH6/3)	D2 (CH5/3)	D1 (CH4/3)	0	7.204	10.269	12.797	45.022+D	41.76	41.8	-
	D6 (CH9/3)	D5 (CH8/3)	D4 (CH7/3)	0	7.512	10.670	12.318	94.044+D	-	41.74	-
	D9 (CH12/3)	D8 (CH11/3)	D7 (CH10/3)	0	8.057	9.881	12.191	143.066+D	41.51	41.51	-
	D12 (CH15/3)	D11(CH14/3)	D10 (CH13/3)	0	8.542	10.966	12.405	192.088+D	41.56	41.58	41.57
	B1 (CH12/2)	B2 (CH13/2)	B3 (CH14/2)	45	7.110	8.843	10.820	49.022	41.61	41.69	41.67
	B4 (CH15/2	B5 (CH16/2)	B6 (CH17/2)	45	7.296	9.215	10.845	98.044	41.65	-	41.55
	B7 (CH18/2)	B8 (CH31/2)	B9 (CH0/3)	45	6.565	8.631	10.893	147.066	-	41.39	41.01
26.6562	B10 (CH21/2)	B11 (CH22/2)	B12 (CH23/2)	45	5.956	8.946	11.081	196.088	-	41.44	41.39
	A1 (CHO/2)	A2 (CH1/2)	A3 (CH2/2)	135	7.328	9.322	11.892	49.022	38.25	31.14	-
	A4(CH3/2)	A5 (CH4/2)	A6 (CH5/2)	135	6.901	9.259	12.189	98.044	38.42	-	38.4
	A7 (CH7/2)	A8 (CH8/2)	A9 (CH6/2)	135	6.722	9.176	11.784	147.066	-	38.45	38.53
	A10 (CH9/2)	A11 (CH10/2)	A12 (CH11/2)	135	6.641	9.079	12.168	196.088	38.45	-	-
	C3 (CH26/2)	C2 (CH25/2)	C1 (CH24/2)	180	7.328	9.318	11.494	49.022	37.47	37.37	37.33
	C6 (CH28/2)	C5 (CH27/2)	C4 (CH29/2)	180	7.328	9.269	11.533	98.044	37.63	-	-
	C9 (CH20/2)	C8 (CH19/2)	C7 (CH30/2)	180	7.078	8.963	11.378	147.066	37.75	-	-
	C12(CH3/3)	C11 (CH1/3)	C10 (CH16/3)	180	7.141	9.015	11.358	196.088	-	38.36	38.36
	D3 (CH6/3)	D2 (CH5/3)	D1 (CH4/3)	0	7.204	10.269	12.797	45.022+D	84.92	85	-
	D6 (CH9/3)	D5 (CH8/3)	D4 (CH7/3)	0	7.512	10.670	12.318	94.044+D	-	84.93	-
	D9 (CH12/3)	D8 (CH11/3)	D7 (CH10/3)	0	8.057	9.881	12.191	143.066+D	84.55	84.57	-
	D12 (CH15/3)	D11(CH14/3)	D10 (CH13/3)	0	8.542	10.966	12.405	192.088+D	84.47	84.43	84.48
	B1 (CH12/2)	B2 (CH13/2)	B3 (CH14/2)	45	7.110	8.843	10.820	49.022	84.08	84.1	84.07
	B4 (CH15/2	B5 (CH16/2)	B6 (CH17/2)	45	7.296	9.215	10.845	98.044	84.1	-	84.01
	B7 (CH18/2)	B8 (CH31/2)	B9 (CH0/3)	45	6.565	8.631	10.893	147.066	-	83.74	83.42
	B10 (CH21/2)	B11 (CH22/2)	B12 (CH23/2)	45	5.956	8.946	11.081	196.088	-	83.62	83.58
54.1654	A1 (CHO/2)	A2 (CH1/2)	A3 (CH2/2)	135	7.328	9.322	11.892	49.022	78.44	76.9	-
	A4(CH3/2)	A5 (CH4/2)	A6 (CH5/2)	135	6.901	9.259	12.189	98.044	78.57	-	78.54
	A7 (CH7/2)	A8 (CH8/2)	A9 (CH6/2)	135	6.722	9.176	11.784	147.066	-	78.73	78.78
	A10 (CH9/2)	A11 (CH10/2)	A12 (CH11/2)	135	6.641	9.079	12.168	196.088	78.73	-	-
	C3 (CH26/2)	C2 (CH25/2)	C1 (CH24/2)	180	7.328	9.318	11.494	49.022	76.93	72.86	72.83
	C6 (CH28/2)	C5 (CH27/2)	C4 (CH29/2)	180	7.328	9.269	11.533	98.044	77.1	-	-
	C9 (CH20/2)	C8 (CH19/2)	C7 (CH30/2)	180	7.078	8.963	11.378	147.066	77.38	-	-
	C12(CH3/3)	C11 (CH1/3)	C10 (CH16/3)	180	7.141	9.015	11.358	196.088	-	73.81	73.79

***Axial Coordinate Correction applies only to thermocouple well identifications with "D" labels (e.g., D-1 through D-12)**

TABLE III: Two-Dimensional, Local Circular-Like Flow Channel Inside Heat Flux as a Function of the Net Single-Side Outside (or Incident) Heat Flux (k=365.0 W/mK) (continued)

Net Incident Heat Flux (kW/m^2)	Thermocouple Well Identification (Channel Number/Module Number)			Test Section Coordinates					Inside Heat Flux (kW/m^2)		
	Axial Coordinate Correction*, D			Circumferential (Degrees)	Radial (mm)			Axial (mm) *	Close to Fluid/Solid Boundary	Intermediate	Close to Heated Boundary
	D = 0 mm	D = 2 mm	D = 4 mm								
61.866	D3 (CH6/3)	D2 (CH5/3)	D1 (CH4/3)	0	7.204	10.269	12.797	45.022+D	96.39	96.44	-
	D6 (CH9/3)	D5 (CH8/3)	D4 (CH7/3)	0	7.512	10.670	12.318	94.044+D	-	96.31	-
	D9 (CH12/3)	D8 (CH11/3)	D7 (CH10/3)	0	8.057	9.881	12.191	143.066+D	96.01	96.02	-
	D12 (CH15/3)	D11(CH14/3)	D10 (CH13/3)	0	8.542	10.966	12.405	192.088+D	96.03	95.97	96.02
	B1 (CH12/2)	B2 (CH13/2)	B3 (CH14/2)	45	7.110	8.843	10.820	49.022	95.5	95.46	95.44
	B4 (CH15/2	B5 (CH16/2)	B6 (CH17/2)	45	7.296	9.215	10.845	98.044	95.45	-	95.33
	B7 (CH18/2)	B8 (CH31/2)	B9 (CH0/3)	45	6.565	8.631	10.893	147.066	-	95.13	94.88
	B10 (CH21/2)	B11 (CH22/2)	B12 (CH23/2)	45	5.956	8.946	11.081	196.088	-	95.06	95.02
	A1 (CHO/2)	A2 (CH1/2)	A3 (CH2/2)	135	7.328	9.322	11.892	49.022	90.17	88.11	-
	A4(CH3/2)	A5 (CH4/2)	A6 (CH5/2)	135	6.901	9.259	12.189	98.044	87.95	-	90.27
	A7 (CH7/2)	A8 (CH8/2)	A9 (CH6/2)	135	6.722	9.176	11.784	147.066	-	90.41	90.43
	A10 (CH9/2)	A11 (CH10/2)	A12 (CH11/2)	135	6.641	9.079	12.168	196.088	90.35	-	-
	C3 (CH26/2)	C2 (CH25/2)	C1 (CH24/2)	180	7.328	9.318	11.494	49.022	88.66	88.66	88.63
	C6 (CH28/2)	C5 (CH27/2)	C4 (CH29/2)	180	7.328	9.269	11.533	98.044	88.89	-	-
	C9 (CH20/2)	C8 (CH19/2)	C7 (CH30/2)	180	7.078	8.963	11.378	147.066	89.13	-	-
	C12(CH3/3)	C11 (CH1/3)	C10 (CH16/3)	180	7.141	9.015	11.358	196.088	-	89.49	89.47
104.0506	D3 *(CH6/3)	D2 (CH5/3)	D1 (CH4/3)	0	7.204	10.269	12.797	45.022+D	162.6	162.7	-
	D6 (CH9/3)	D5 (CH8/3)	D4 (CH7/3)	0	7.512	10.670	12.318	94.044+D	-	162.2	-
	D9 (CH12/3)	D8 (CH11/3)	D7 (CH10/3)	0	8.057	9.881	12.191	143.066+D	161.8	161.8	-
	D12 (CH15/3)	D11(CH14/3)	D10 (CH13/3)	0	8.542	10.966	12.405	192.088+D	162.3	162.2	162.3
	B1 (CH12/2)	B2 (CH13/2)	B3 (CH14/2)	45	7.110	8.843	10.820	49.022	160.7	160.7	160.6
	B4 (CH15/2	B5 (CH16/2)	B6 (CH17/2)	45	7.296	9.215	10.845	98.044	160.5	-	160.3
	B7 (CH18/2)	B8 (CH31/2)	B9 (CH0/3)	45	6.565	8.631	10.893	147.066	-	160.1	159.8
	B10 (CH21/2)	B11 (CH22/2)	B12 (CH23/2)	45	5.956	8.946	11.081	196.088	-	160.3	160.2
	A1 (CHO/2)	A2 (CH1/2)	A3 (CH2/2)	135	7.328	9.322	11.892	49.022	151.5	146.6	-
	A4(CH3/2)	A5 (CH4/2)	A6 (CH5/2)	135	6.901	9.259	12.189	98.044	151.9	-	151.8
	A7 (CH7/2)	A8 (CH8/2)	A9 (CH6/2)	135	6.722	9.176	11.784	147.066	-	151.9	152
	A10 (CH9/2)	A11 (CH10/2)	A12 (CH11/2)	135	6.641	9.079	12.168	196.088	151.6	-	-
	C3 (CH26/2)	C2 (CH25/2)	C1 (CH24/2)	180	7.328	9.318	11.494	49.022	149	148.9	148.9
	C6 (CH28/2)	C5 (CH27/2)	C4 (CH29/2)	180	7.328	9.269	11.533	98.044	149.6	-	-
	C9 (CH20/2)	C8 (CH19/2)	C7 (CH30/2)	180	7.078	8.963	11.378	147.066	149.8	-	-
	C12(CH3/3)	C11 (CH1/3)	C10 (CH16/3)	180	7.141	9.015	11.358	196.088	-	149.8	149.8
122.3466	D3 (CH6/3)	D2 (CH5/3)	D1 (CH4/3)	0	7.204	10.269	12.797	45.022+D	191.8	192	-
	D6 (CH9/3)	D5 (CH8/3)	D4 (CH7/3)	0	7.512	10.670	12.318	94.044+D	-	191.6	-
	D9 (CH12/3)	D8 (CH11/3)	D7 (CH10/3)	0	8.057	9.881	12.191	143.066+D	191	191	-
	D12 (CH15/3)	D11(CH14/3)	D10 (CH13/3)	0	8.542	10.966	12.405	192.088+D	191.2	191.1	191.3
	B1 (CH12/2)	B2 (CH13/2)	B3 (CH14/2)	45	7.110	8.843	10.820	49.022	189.5	189.5	189.4
	B4 (CH15/2	B5 (CH16/2)	B6 (CH17/2)	45	7.296	9.215	10.845	98.044	189.4	-	189.2
	B7 (CH18/2)	B8 (CH31/2)	B9 (CH0/3)	45	6.565	8.631	10.893	147.066	-	188.8	188.5
	B10 (CH21/2)	B11 (CH22/2)	B12 (CH23/2)	45	5.956	8.946	11.081	196.088	-	188.7	188.6
	A1 (CHO/2)	A2 (CH1/2)	A3 (CH2/2)	135	7.328	9.322	11.892	49.022	177.6	172.4	-
	A4(CH3/2)	A5 (CH4/2)	A6 (CH5/2)	135	6.901	9.259	12.189	98.044	178	-	177.9
	A7 (CH7/2)	A8 (CH8/2)	A9 (CH6/2)	135	6.722	9.176	11.784	147.066	-	178.2	178.2
	A10 (CH9/2)	A11 (CH10/2)	A12 (CH11/2)	135	6.641	9.079	12.168	196.088	178	-	-
	C3 (CH26/2)	C2 (CH25/2)	C1 (CH24/2)	180	7.328	9.318	11.494	49.022	174.4	174.4	174.4
	C6 (CH28/2)	C5 (CH27/2)	C4 (CH29/2)	180	7.328	9.269	11.533	98.044	174.9	-	-
	C9 (CH20/2)	C8 (CH19/2)	C7 (CH30/2)	180	7.078	8.963	11.378	147.066	175.3	-	-
	C12(CH3/3)	C11 (CH1/3)	C10 (CH16/3)	180	7.141	9.015	11.358	196.088	-	175.6	175.6
225.2877	D3 (CH6/3)	D2 (CH5/3)	D1 (CH4/3)	0	7.204	10.269	12.797	45.022+D	354.6	354.6	-
	D6 (CH9/3)	D5 (CH8/3)	D4 (CH7/3)	0	7.512	10.670	12.318	94.044+D	-	354.1	-
	D9 (CH12/3)	D8 (CH11/3)	D7 (CH10/3)	0	8.057	9.881	12.191	143.066+D	354.9	354.8	-
	D12 (CH15/3)	D11(CH14/3)	D10 (CH13/3)	0	8.542	10.966	12.405	192.088+D	358.9	358.4	358.5
	B1 (CH12/2)	B2 (CH13/2)	B3 (CH14/2)	45	7.110	8.843	10.820	49.022	349.4	349.3	349.1
	B4 (CH15/2	B5 (CH16/2)	B6 (CH17/2)	45	7.296	9.215	10.845	98.044	349.5	-	349.1
	B7 (CH18/2)	B8 (CH31/2)	B9 (CH0/3)	45	6.565	8.631	10.893	147.066	-	349.7	349.1
	B10 (CH21/2)	B11 (CH22/2)	B12 (CH23/2)	45	5.956	8.946	11.081	196.088	-	351.1	351.2
	A1 (CHO/2)	A2 (CH1/2)	A3 (CH2/2)	135	7.328	9.322	11.892	49.022	326.4	312.9	-
	A4(CH3/2)	A5 (CH4/2)	A6 (CH5/2)	135	6.901	9.259	12.189	98.044	326.9	-	326.8
	A7 (CH7/2)	A8 (CH8/2)	A9 (CH6/2)	135	6.722	9.176	11.784	147.066	-	326.2	326.3
	A10 (CH9/2)	A11 (CH10/2)	A12 (CH11/2)	135	6.641	9.079	12.168	196.088	324.2	-	-
	C3 (CH26/2)	C2 (CH25/2)	C1 (CH24/2)	180	7.328	9.318	11.494	49.022	319.8	319.7	319.3
	C6 (CH28/2)	C5 (CH27/2)	C4 (CH29/2)	180	7.328	9.269	11.533	98.044	320.9	-	-
	C9 (CH20/2)	C8 (CH19/2)	C7 (CH30/2)	180	7.078	8.963	11.378	147.066	319.8	-	-
	C12(CH3/3)	C11 (CH1/3)	C10 (CH16/3)	180	7.141	9.015	11.358	196.088	-	318.1	317.8

***Axial Coordinate Correction applies only to thermocouple well identifications with "D" labels (e.g., D-1 through D-12)**

TABLE III: Two-Dimensional, Local Circular-Like Flow Channel Inside Heat Flux as a Function of the Net Single-Side Outside (or Incident) Heat Flux (k=365.0 W/mK) (continued)

Net Incident Heat Flux (kW/m^2)	Thermocouple Well Identification (Channel Number/Module Number)			Test Section Coordinates					Inside Heat Flux (kW/m^2)		
	Axial Coordinate Correction*, D			Circumferential (Degrees)	Radial (mm)			Axial (mm) *	Close to Fluid/Solid Boundary	Intermediate	Close to Heated Boundary
	D = 0 mm	D = 2 mm	D = 4 mm								
	D3 (CH6/3)	D2 (CH5/3)	D1 (CH4/3)	0	7.204	10.269	12.797	45.022+D	470.6	472.1	-
	D6 (CH9/3)	D5 (CH8/3)	D4 (CH7/3)	0	7.512	10.670	12.318	94.044+D	-	472.4	-
	D9 (CH12/3)	D8 (CH11/3)	D7 (CH10/3)	0	8.057	9.881	12.191	143.066+D	472.3	472.1	-
	D12 (CH15/3)	D11(CH14/3)	D10 (CH13/3)	0	8.542	10.966	12.405	192.088+D	477	475.5	476.6
	B1 (CH12/2)	B2 (CH13/2)	B3 (CH14/2)	45	7.110	8.843	10.820	49.022	461.9	461.5	461.5
	B4 (CH15/2	B5 (CH16/2)	B6 (CH17/2)	45	7.296	9.215	10.845	98.044	463	-	462.6
	B7 (CH18/2)	B8 (CH31/2)	B9 (CH0/3)	45	6.565	8.631	10.893	147.066	-	462.3	461.7
294.3267	B10 (CH21/2)	B11 (CH22/2)	B12 (CH23/2)	45	5.956	8.946	11.081	196.088	-	463.9	462.9
	A1 (CHO/2)	A2 (CH1/2)	A3 (CH2/2)	135	7.328	9.322	11.892	49.022	421.8	406.1	-
	A4(CH3/2)	A5 (CH4/2)	A6 (CH5/2)	135	6.901	9.259	12.189	98.044	421.1	-	421.5
	A7 (CH7/2)	A8 (CH8/2)	A9 (CH6/2)	135	6.722	9.176	11.784	147.066	-	420.8	420.9
	A10 (CH9/2)	A11 (CH10/2)	A12 (CH11/2)	135	6.641	9.079	12.168	196.088	418.4	-	-
	C3 (CH26/2)	C2 (CH25/2)	C1 (CH24/2)	180	7.328	9.318	11.494	49.022	410.7	411	411
	C6 (CH28/2)	C5 (CH27/2)	C4 (CH29/2)	180	7.328	9.269	11.533	98.044	410.7	-	-
	C9 (CH20/2)	C8 (CH19/2)	C7 (CH30/2)	180	7.078	8.963	11.378	147.066	410.2	-	-
	C12(CH3/3)	C11 (CH1/3)	C10 (CH16/3)	180	7.141	9.015	11.358	196.088	-	407.8	407.7
	D3 *(CH6/3)	D2 (CH5/3)	D1 (CH4/3)	0	7.204	10.269	12.797	45.022+D	682.1	684.1	-
	D6 (CH9/3)	D5 (CH8/3)	D4 (CH7/3)	0	7.512	10.670	12.318	94.044+D	-	687	-
	D9 (CH12/3)	D8 (CH11/3)	D7 (CH10/3)	0	8.057	9.881	12.191	143.066+D	684.8	684.1	-
	D12 (CH15/3)	D11(CH14/3)	D10 (CH13/3)	0	8.542	10.966	12.405	192.088+D	694.2	693.1	695.7
	B1 (CH12/2)	B2 (CH13/2)	B3 (CH14/2)	45	7.110	8.843	10.820	49.022	664.1	663.5	662.8
	B4 (CH15/2	B5 (CH16/2)	B6 (CH17/2)	45	7.296	9.215	10.845	98.044	667.1	-	663.7
	B7 (CH18/2)	B8 (CH31/2)	B9 (CH0/3)	45	6.565	8.631	10.893	147.066	-	664.6	662.6
417.9938	B10 (CH21/2)	B11 (CH22/2)	B12 (CH23/2)	45	5.956	8.946	11.081	196.088	-	669	667.7
	A1 (CHO/2)	A2 (CH1/2)	A3 (CH2/2)	135	7.328	9.322	11.892	49.022	589.6	564.4	-
	A4(CH3/2)	A5 (CH4/2)	A6 (CH5/2)	135	6.901	9.259	12.189	98.044	588.8	-	588.8
	A7 (CH7/2)	A8 (CH8/2)	A9 (CH6/2)	135	6.722	9.176	11.784	147.066	-	588.6	586.8
	A10 (CH9/2)	A11 (CH10/2)	A12 (CH11/2)	135	6.641	9.079	12.168	196.088	583.6	-	-
	C3 (CH26/2)	C2 (CH25/2)	C1 (CH24/2)	180	7.328	9.318	11.494	49.022	571	570.9	570.1
	C6 (CH28/2)	C5 (CH27/2)	C4 (CH29/2)	180	7.328	9.269	11.533	98.044	568.8	-	-
	C9 (CH20/2)	C8 (CH19/2)	C7 (CH30/2)	180	7.078	8.963	11.378	147.066	567.8	-	-
	C12(CH3/3)	C11 (CH1/3)	C10 (CH16/3)	180	7.141	9.015	11.358	196.088	-	563.9	564
	D3 (CH6/3)	D2 (CH5/3)	D1 (CH4/3)	0	7.204	10.269	12.797	45.022+D	778.8	778.7	-
	D6 (CH9/3)	D5 (CH8/3)	D4 (CH7/3)	0	7.512	10.670	12.318	94.044+D	-	784.1	-
	D9 (CH12/3)	D8 (CH11/3)	D7 (CH10/3)	0	8.057	9.881	12.191	143.066+D	785.1	783.1	-
	D12 (CH15/3)	D11(CH14/3)	D10 (CH13/3)	0	8.542	10.966	12.405	192.088+D	794.3	794.3	795.2
	B1 (CH12/2)	B2 (CH13/2)	B3 (CH14/2)	45	7.110	8.843	10.820	49.022	752.7	752.8	751.7
	B4 (CH15/2	B5 (CH16/2)	B6 (CH17/2)	45	7.296	9.215	10.845	98.044	756.7	-	755.4
	B7 (CH18/2)	B8 (CH31/2)	B9 (CH0/3)	45	6.565	8.631	10.893	147.066	-	756.2	753
	B10 (CH21/2)	B11 (CH22/2)	B12 (CH23/2)	45	5.956	8.946	11.081	196.088	-	759.9	756.8
469.6313	A1 (CHO/2)	A2 (CH1/2)	A3 (CH2/2)	135	7.328	9.322	11.892	49.022	655.9	628.1	-
	A4(CH3/2)	A5 (CH4/2)	A6 (CH5/2)	135	6.901	9.259	12.189	98.044	653.9	-	653
	A7 (CH7/2)	A8 (CH8/2)	A9 (CH6/2)	135	6.722	9.176	11.784	147.066	-	651.8	652.5
	A10 (CH9/2)	A11 (CH10/2)	A12 (CH11/2)	135	6.641	9.079	12.168	196.088	645.7	-	-
	C3 (CH26/2)	C2 (CH25/2)	C1 (CH24/2)	180	7.328	9.318	11.494	49.022	629.9	632	630.8
	C6 (CH28/2)	C5 (CH27/2)	C4 (CH29/2)	180	7.328	9.269	11.533	98.044	627.9	-	-
	C9 (CH20/2)	C8 (CH19/2)	C7 (CH30/2)	180	7.078	8.963	11.378	147.066	626.2	-	-
	C12(CH3/3)	C11 (CH1/3)	C10 (CH16/3)	180	7.141	9.015	11.358	196.088	-	618.2	620
	D3 (CH6/3)	D2 (CH5/3)	D1 (CH4/3)	0	7.204	10.269	12.797	45.022+D	842.6	841.4	-
	D6 (CH9/3)	D5 (CH8/3)	D4 (CH7/3)	0	7.512	10.670	12.318	94.044+D	-	845.3	-
	D9 (CH12/3)	D8 (CH11/3)	D7 (CH10/3)	0	8.057	9.881	12.191	143.066+D	846.1	844.1	-
	D12 (CH15/3)	D11(CH14/3)	D10 (CH13/3)	0	8.542	10.966	12.405	192.088+D	858.4	853.4	866.8
	B1 (CH12/2)	B2 (CH13/2)	B3 (CH14/2)	45	7.110	8.843	10.820	49.022	812.9	811.2	807.6
	B4 (CH15/2	B5 (CH16/2)	B6 (CH17/2)	45	7.296	9.215	10.845	98.044	817.3	-	811.2
	B7 (CH18/2)	B8 (CH31/2)	B9 (CH0/3)	45	6.565	8.631	10.893	147.066	-	813.5	809.5
	B10 (CH21/2)	B11 (CH22/2)	B12 (CH23/2)	45	5.956	8.946	11.081	196.088	-	818.3	815.8
503.1049	A1 (CHO/2)	A2 (CH1/2)	A3 (CH2/2)	135	7.328	9.322	11.892	49.022	700.5	684.2	-
	A4(CH3/2)	A5 (CH4/2)	A6 (CH5/2)	135	6.901	9.259	12.189	98.044	698.2	-	697.7
	A7 (CH7/2)	A8 (CH8/2)	A9 (CH6/2)	135	6.722	9.176	11.784	147.066	-	694.2	695.8
	A10 (CH9/2)	A11 (CH10/2)	A12 (CH11/2)	135	6.641	9.079	12.168	196.088	687.8	-	-
	C3 (CH26/2)	C2 (CH25/2)	C1 (CH24/2)	180	7.328	9.318	11.494	49.022	671.2	671.3	667.5
	C6 (CH28/2)	C5 (CH27/2)	C4 (CH29/2)	180	7.328	9.269	11.533	98.044	668.4	-	-
	C9 (CH20/2)	C8 (CH19/2)	C7 (CH30/2)	180	7.078	8.963	11.378	147.066	663.3	-	-
	C12(CH3/3)	C11 (CH1/3)	C10 (CH16/3)	180	7.141	9.015	11.358	196.088	-	654.8	649.2

***Axial Coordinate Correction applies only to thermocouple well identifications with "D" labels (e.g., D-1 through D-12)**

TABLE III: Two-Dimensional, Local Circular-Like Flow Channel Inside Heat Flux as a Function of the Net Single-Side Outside (or Incident) Heat Flux (k=365.0 W/mK) (continued)

Net Incident Heat Flux (kW/m^2)	Thermocouple Well Identification (Channel Number/Module Number)			Test Section Coordinates					Inside Heat Flux (kW/m^2)		
	Axial Coordinate Correction*, D			Circumferential (Degrees)	Radial (mm)			Axial (mm) *	Close to Fluid/Solid Boundary	Intermediate	Close to Heated Boundary
	D = 0 mm	D = 2 mm	D = 4 mm								
728.3243	D3 (CH6/3)	D2 (CH5/3)	D1 (CH4/3)	0	7.204	10.269	12.797	45.022+D	1268	1282	-
	D6 (CH9/3)	D5 (CH8/3)	D4 (CH7/3)	0	7.512	10.670	12.318	94.044+D	-	1301	-
	D9 (CH12/3)	D8 (CH11/3)	D7 (CH10/3)	0	8.057	9.881	12.191	143.066+D	1311	1308	-
	D12 (CH15/3)	D11(CH14/3)	D10 (CH13/3)	0	8.542	10.966	12.405	192.088+D	1358	1352	1396
	B1 (CH12/2)	B2 (CH13/2)	B3 (CH14/2)	45	7.110	8.843	10.820	49.022	1207	1209	1212
	B4 (CH15/2	B5 (CH16/2)	B6 (CH17/2)	45	7.296	9.215	10.845	98.044	1231	-	1222
	B7 (CH18/2)	B8 (CH31/2)	B9 (CH0/3)	45	6.565	8.631	10.893	147.066	-	1227	1219
	B10 (CH21/2)	B11 (CH22/2)	B12 (CH23/2)	45	5.956	8.946	11.081	196.088	-	1247	1239
	A1 (CHO/2)	A2 (CH1/2)	A3 (CH2/2)	135	7.328	9.322	11.892	49.022	981.7	964.1	-
	A4(CH3/2)	A5 (CH4/2)	A6 (CH5/2)	135	6.901	9.259	12.189	98.044	971.4	-	970.8
	A7 (CH7/2)	A8 (CH8/2)	A9 (CH6/2)	135	6.722	9.176	11.784	147.066	-	960.9	956.8
	A10 (CH9/2)	A11 (CH10/2)	A12 (CH11/2)	135	6.641	9.079	12.168	196.088	938.4	-	-
	C3 (CH26/2)	C2 (CH25/2)	C1 (CH24/2)	180	7.328	9.318	11.494	49.022	922.5	916.3	920.1
	C6 (CH28/2)	C5 (CH27/2)	C4 (CH29/2)	180	7.328	9.269	11.533	98.044	907.9	-	-
	C9 (CH20/2)	C8 (CH19/2)	C7 (CH30/2)	180	7.078	8.963	11.378	147.066	889.4	-	-
	C12(CH3/3)	C11 (CH1/3)	C10 (CH16/3)	180	7.141	9.015	11.358	196.088	-	865.5	847.8

***Axial Coordinate Correction applies only to thermocouple well identifications with "D" labels (e.g., D-1 through D-12)**

TABLE IV: Local (Axial) Variation of the Bulk Fluid (Water) Flowing Inside a Single-Side Heated Circular-Like Test Section with Respect to the Net Single-Side Outside (or Incident) Heat Flux

Net Incident Heat Flux (kW/m^2)	Thermocouple Well Identification (Channel Number/Module Number)			Test Section Coordinates					Local Bulk Fluid Temperature, T_b (^0C)		
				Circumferential (Degrees)	Radial (mm)			Axial (mm) *	Axial Coordinate Correction*, D		
									D = 0 mm	D = 2 mm	D = 4 mm
6.6581	D3 (CH6/3)	D2 (CH5/3)	D1 (CH4/3)	0	7.204	10.269	12.797	45.022+D	25.8846	25.8878	25.8909
	D6 (CH9/3)	D5 (CH8/3)	D4 (CH7/3)	0	7.512	10.670	12.318	94.044+D	25.9615	25.9646	25.9678
	D9 (CH12/3)	D8 (CH11/3)	D7 (CH10/3)	0	8.057	9.881	12.191	143.066+D	26.0384	26.0415	26.0447
	D12 (CH15/3)	D11(CH14/3)	D10 (CH13/3)	0	8.542	10.966	12.405	192.088+D	26.1153	26.1184	26.1216
	B1 (CH12/2)	B2 (CH13/2)	B3 (CH14/2)	45	7.110	8.843	10.820	49.022	-	-	25.8909
	B4 (CH15/2	B5 (CH16/2)	B6 (CH17/2)	45	7.296	9.215	10.845	98.044	-	-	25.9678
	B7 (CH18/2)	B8 (CH31/2)	B9 (CH0/3)	45	6.565	8.631	10.893	147.066	-	-	26.0447
	B10 (CH21/2)	B11 (CH22/2)	B12 (CH23/2)	45	5.956	8.946	11.081	196.088	-	-	26.1216
	A1 (CHO/2)	A2 (CH1/2)	A3 (CH2/2)	135	7.328	9.322	11.892	49.022	-	-	25.8909
	A4(CH3/2)	A5 (CH4/2)	A6 (CH5/2)	135	6.901	9.259	12.189	98.044	-	-	25.9678
	A7 (CH7/2)	A8 (CH8/2)	A9 (CH6/2)	135	6.722	9.176	11.784	147.066	-	-	26.0447
	A10 (CH9/2)	A11 (CH10/2)	A12 (CH11/2)	135	6.641	9.079	12.168	196.088	-	-	26.1216
	C3 (CH26/2)	C2 (CH25/2)	C1 (CH24/2)	180	7.328	9.318	11.494	49.022	-	-	25.8909
	C6 (CH28/2)	C5 (CH27/2)	C4 (CH29/2)	180	7.328	9.269	11.533	98.044	-	-	25.9678
	C9 (CH20/2)	C8 (CH19/2)	C7 (CH30/2)	180	7.078	8.963	11.378	147.066	-	-	26.0447
	C12(CH3/3)	C11 (CH1/3)	C10 (CH16/3)	180	7.141	9.015	11.358	196.088	-	-	26.1216
18.529	D3 (CH6/3)	D2 (CH5/3)	D1 (CH4/3)	0	7.204	10.269	12.797	45.022+D	25.9905	25.9993	26.008
	D6 (CH9/3)	D5 (CH8/3)	D4 (CH7/3)	0	7.512	10.670	12.318	94.044+D	26.2045	26.2131	26.222
	D9 (CH12/3)	D8 (CH11/3)	D7 (CH10/3)	0	8.057	9.881	12.191	143.066+D	26.4185	26.4272	26.4359
	D12 (CH15/3)	D11(CH14/3)	D10 (CH13/3)	0	8.542	10.966	12.405	192.088+D	26.6325	26.6412	26.6499
	B1 (CH12/2)	B2 (CH13/2)	B3 (CH14/2)	45	7.110	8.843	10.820	49.022	-	-	26.008
	B4 (CH15/2	B5 (CH16/2)	B6 (CH17/2)	45	7.296	9.215	10.845	98.044	-	-	26.222
	B7 (CH18/2)	B8 (CH31/2)	B9 (CH0/3)	45	6.565	8.631	10.893	147.066	-	-	26.4359
	B10 (CH21/2)	B11 (CH22/2)	B12 (CH23/2)	45	5.956	8.946	11.081	196.088	-	-	26.6499
	A1 (CHO/2)	A2 (CH1/2)	A3 (CH2/2)	135	7.328	9.322	11.892	49.022	-	-	26.008
	A4(CH3/2)	A5 (CH4/2)	A6 (CH5/2)	135	6.901	9.259	12.189	98.044	-	-	26.222
	A7 (CH7/2)	A8 (CH8/2)	A9 (CH6/2)	135	6.722	9.176	11.784	147.066	-	-	26.4359
	A10 (CH9/2)	A11 (CH10/2)	A12 (CH11/2)	135	6.641	9.079	12.168	196.088	-	-	26.6499
	C3 (CH26/2)	C2 (CH25/2)	C1 (CH24/2)	180	7.328	9.318	11.494	49.022	-	-	26.008
	C6 (CH28/2)	C5 (CH27/2)	C4 (CH29/2)	180	7.328	9.269	11.533	98.044	-	-	26.222
	C9 (CH20/2)	C8 (CH19/2)	C7 (CH30/2)	180	7.078	8.963	11.378	147.066	-	-	26.4359
	C12(CH3/3)	C11 (CH1/3)	C10 (CH16/3)	180	7.141	9.015	11.358	196.088	-	-	26.6499
26.6562	D3 (CH6/3)	D2 (CH5/3)	D1 (CH4/3)	0	7.204	10.269	12.797	45.022+D	25.9617	25.9743	25.9868
	D6 (CH9/3)	D5 (CH8/3)	D4 (CH7/3)	0	7.512	10.670	12.318	94.044+D	26.2696	26.2821	26.2947
	D9 (CH12/3)	D8 (CH11/3)	D7 (CH10/3)	0	8.057	9.881	12.191	143.066+D	26.5774	26.59	26.6025
	D12 (CH15/3)	D11(CH14/3)	D10 (CH13/3)	0	8.542	10.966	12.405	192.088+D	26.8852	26.8978	26.9104
	B1 (CH12/2)	B2 (CH13/2)	B3 (CH14/2)	45	7.110	8.843	10.820	49.022	-	-	25.9868
	B4 (CH15/2	B5 (CH16/2)	B6 (CH17/2)	45	7.296	9.215	10.845	98.044	-	-	26.2947
	B7 (CH18/2)	B8 (CH31/2)	B9 (CH0/3)	45	6.565	8.631	10.893	147.066	-	-	26.6025
	B10 (CH21/2)	B11 (CH22/2)	B12 (CH23/2)	45	5.956	8.946	11.081	196.088	-	-	26.9104
	A1 (CHO/2)	A2 (CH1/2)	A3 (CH2/2)	135	7.328	9.322	11.892	49.022	-	-	25.9868
	A4(CH3/2)	A5 (CH4/2)	A6 (CH5/2)	135	6.901	9.259	12.189	98.044	-	-	26.2947
	A7 (CH7/2)	A8 (CH8/2)	A9 (CH6/2)	135	6.722	9.176	11.784	147.066	-	-	26.6025
	A10 (CH9/2)	A11 (CH10/2)	A12 (CH11/2)	135	6.641	9.079	12.168	196.088	-	-	26.9104
	C3 (CH26/2)	C2 (CH25/2)	C1 (CH24/2)	180	7.328	9.318	11.494	49.022	-	-	25.9868
	C6 (CH28/2)	C5 (CH27/2)	C4 (CH29/2)	180	7.328	9.269	11.533	98.044	-	-	26.2947
	C9 (CH20/2)	C8 (CH19/2)	C7 (CH30/2)	180	7.078	8.963	11.378	147.066	-	-	26.6025
	C12(CH3/3)	C11 (CH1/3)	C10 (CH16/3)	180	7.141	9.015	11.358	196.088	-	-	26.9104
54.1654	D3 (CH6/3)	D2 (CH5/3)	D1 (CH4/3)	0	7.204	10.269	12.797	45.022+D	26.2935	26.319	26.3445
	D6 (CH9/3)	D5 (CH8/3)	D4 (CH7/3)	0	7.512	10.670	12.318	94.044+D	26.919	26.9445	26.9701
	D9 (CH12/3)	D8 (CH11/3)	D7 (CH10/3)	0	8.057	9.881	12.191	143.066+D	27.5445	27.5701	27.5956
	D12 (CH15/3)	D11(CH14/3)	D10 (CH13/3)	0	8.542	10.966	12.405	192.088+D	28.1701	28.1956	28.2211
	B1 (CH12/2)	B2 (CH13/2)	B3 (CH14/2)	45	7.110	8.843	10.820	49.022	-	-	26.3445
	B4 (CH15/2	B5 (CH16/2)	B6 (CH17/2)	45	7.296	9.215	10.845	98.044	-	-	26.9701
	B7 (CH18/2)	B8 (CH31/2)	B9 (CH0/3)	45	6.565	8.631	10.893	147.066	-	-	27.5956
	B10 (CH21/2)	B11 (CH22/2)	B12 (CH23/2)	45	5.956	8.946	11.081	196.088	-	-	28.2211
	A1 (CHO/2)	A2 (CH1/2)	A3 (CH2/2)	135	7.328	9.322	11.892	49.022	-	-	26.3445
	A4(CH3/2)	A5 (CH4/2)	A6 (CH5/2)	135	6.901	9.259	12.189	98.044	-	-	26.9701
	A7 (CH7/2)	A8 (CH8/2)	A9 (CH6/2)	135	6.722	9.176	11.784	147.066	-	-	27.5956
	A10 (CH9/2)	A11 (CH10/2)	A12 (CH11/2)	135	6.641	9.079	12.168	196.088	-	-	28.2211
	C3 (CH26/2)	C2 (CH25/2)	C1 (CH24/2)	180	7.328	9.318	11.494	49.022	-	-	26.3445
	C6 (CH28/2)	C5 (CH27/2)	C4 (CH29/2)	180	7.328	9.269	11.533	98.044	-	-	26.9701
	C9 (CH20/2)	C8 (CH19/2)	C7 (CH30/2)	180	7.078	8.963	11.378	147.066	-	-	27.5956
	C12(CH3/3)	C11 (CH1/3)	C10 (CH16/3)	180	7.141	9.015	11.358	196.088	-	-	28.2211

***Axial Coordinate Correction applies only to thermocouple well identifications with "D" labels (e.g., D-1 through D-12)**

TABLE IV: Local (Axial) Variation of the Bulk Fluid (Water) Flowing Inside a Single-Side Heated Circular-Like Test Section with Respect to the Net Single-Side Outside (or Incident) Heat Flux (continued)

Net Incident Heat Flux (kW/m^2)	Thermocouple Well Identification (Channel Number/Module Number)			Test Section Coordinates					Local Bulk Fluid Temperature, T_b (^0C)		
				Circumferential (Degrees)	Radial (mm)			Axial (mm) *	Axial Coordinate Correction*, D		
									D = 0 mm	D = 2 mm	D = 4 mm
	D3 (CH6/3)	D2 (CH5/3)	D1 (CH4/3)	0	7.204	10.269	12.797	45.022+D	26.8502	26.8793	26.9085
	D6 (CH9/3)	D5 (CH8/3)	D4 (CH7/3)	0	7.512	10.670	12.318	94.044+D	27.5646	27.5938	27.6229
	D9 (CH12/3)	D8 (CH11/3)	D7 (CH10/3)	0	8.057	9.881	12.191	143.066+D	28.2791	28.3082	28.3374
	D12 (CH15/3)	D11(CH14/3)	D10 (CH13/3)	0	8.542	10.966	12.405	192.088+D	28.9935	29.0227	29.0518
	B1 (CH12/2)	B2 (CH13/2)	B3 (CH14/2)	45	7.110	8.843	10.820	49.022	-	-	26.9085
	B4 (CH15/2	B5 (CH16/2)	B6 (CH17/2)	45	7.296	9.215	10.845	98.044	-	-	27.6229
	B7 (CH18/2)	B8 (CH31/2)	B9 (CH0/3)	45	6.565	8.631	10.893	147.066	-	-	28.3374
	B10 (CH21/2)	B11 (CH22/2)	B12 (CH23/2)	45	5.956	8.946	11.081	196.088	-	-	29.0518
61.866	A1 (CHO/2)	A2 (CH1/2)	A3 (CH2/2)	135	7.328	9.322	11.892	49.022	-	-	26.9085
	A4(CH3/2)	A5 (CH4/2)	A6 (CH5/2)	135	6.901	9.259	12.189	98.044	-	-	27.6229
	A7 (CH7/2)	A8 (CH8/2)	A9 (CH6/2)	135	6.722	9.176	11.784	147.066	-	-	28.3374
	A10 (CH9/2)	A11 (CH10/2)	A12 (CH11/2)	135	6.641	9.079	12.168	196.088	-	-	29.0518
	C3 (CH26/2)	C2 (CH25/2)	C1 (CH24/2)	180	7.328	9.318	11.494	49.022	-	-	26.9085
	C6 (CH28/2)	C5 (CH27/2)	C4 (CH29/2)	180	7.328	9.269	11.533	98.044	-	-	27.6229
	C9 (CH20/2)	C8 (CH19/2)	C7 (CH30/2)	180	7.078	8.963	11.378	147.066	-	-	28.3374
	C12(CH3/3)	C11 (CH1/3)	C10 (CH16/3)	180	7.141	9.015	11.358	196.088	-	-	29.0518
	D3 *(CH6/3)	D2 (CH5/3)	D1 (CH4/3)	0	7.204	10.269	12.797	45.022+D	28.0476	28.0966	28.1456
	D6 (CH9/3)	D5 (CH8/3)	D4 (CH7/3)	0	7.512	10.670	12.318	94.044+D	29.2492	29.2982	29.3473
	D9 (CH12/3)	D8 (CH11/3)	D7 (CH10/3)	0	8.057	9.881	12.191	143.066+D	30.451	30.5001	30.5491
	D12 (CH15/3)	D11(CH14/3)	D10 (CH13/3)	0	8.542	10.966	12.405	192.088+D	31.6532	31.7023	31.7513
	B1 (CH12/2)	B2 (CH13/2)	B3 (CH14/2)	45	7.110	8.843	10.820	49.022	-	-	28.1456
	B4 (CH15/2	B5 (CH16/2)	B6 (CH17/2)	45	7.296	9.215	10.845	98.044	-	-	29.3473
	B7 (CH18/2)	B8 (CH31/2)	B9 (CH0/3)	45	6.565	8.631	10.893	147.066	-	-	30.5491
104.0506	B10 (CH21/2)	B11 (CH22/2)	B12 (CH23/2)	45	5.956	8.946	11.081	196.088	-	-	31.7513
	A1 (CHO/2)	A2 (CH1/2)	A3 (CH2/2)	135	7.328	9.322	11.892	49.022	-	-	28.1456
	A4(CH3/2)	A5 (CH4/2)	A6 (CH5/2)	135	6.901	9.259	12.189	98.044	-	-	29.3473
	A7 (CH7/2)	A8 (CH8/2)	A9 (CH6/2)	135	6.722	9.176	11.784	147.066	-	-	30.5491
	A10 (CH9/2)	A11 (CH10/2)	A12 (CH11/2)	135	6.641	9.079	12.168	196.088	-	-	31.7513
	C3 (CH26/2)	C2 (CH25/2)	C1 (CH24/2)	180	7.328	9.318	11.494	49.022	-	-	28.1456
	C6 (CH28/2)	C5 (CH27/2)	C4 (CH29/2)	180	7.328	9.269	11.533	98.044	-	-	29.3473
	C9 (CH20/2)	C8 (CH19/2)	C7 (CH30/2)	180	7.078	8.963	11.378	147.066	-	-	30.5491
	C12(CH3/3)	C11 (CH1/3)	C10 (CH16/3)	180	7.141	9.015	11.358	196.088	-	-	31.7513
	D3 (CH6/3)	D2 (CH5/3)	D1 (CH4/3)	0	7.204	10.269	12.797	45.022+D	31.4322	31.4899	31.5476
	D6 (CH9/3)	D5 (CH8/3)	D4 (CH7/3)	0	7.512	10.670	12.318	94.044+D	32.8458	32.9035	32.9612
	D9 (CH12/3)	D8 (CH11/3)	D7 (CH10/3)	0	8.057	9.881	12.191	143.066+D	34.2594	34.3171	34.3748
	D12 (CH15/3)	D11(CH14/3)	D10 (CH13/3)	0	8.542	10.966	12.405	192.088+D	35.673	35.7307	35.7884
	B1 (CH12/2)	B2 (CH13/2)	B3 (CH14/2)	45	7.110	8.843	10.820	49.022	-	-	31.5476
	B4 (CH15/2	B5 (CH16/2)	B6 (CH17/2)	45	7.296	9.215	10.845	98.044	-	-	32.9612
	B7 (CH18/2)	B8 (CH31/2)	B9 (CH0/3)	45	6.565	8.631	10.893	147.066	-	-	34.3748
122.3466	B10 (CH21/2)	B11 (CH22/2)	B12 (CH23/2)	45	5.956	8.946	11.081	196.088	-	-	35.7884
	A1 (CHO/2)	A2 (CH1/2)	A3 (CH2/2)	135	7.328	9.322	11.892	49.022	-	-	31.5476
	A4(CH3/2)	A5 (CH4/2)	A6 (CH5/2)	135	6.901	9.259	12.189	98.044	-	-	32.9612
	A7 (CH7/2)	A8 (CH8/2)	A9 (CH6/2)	135	6.722	9.176	11.784	147.066	-	-	34.3748
	A10 (CH9/2)	A11 (CH10/2)	A12 (CH11/2)	135	6.641	9.079	12.168	196.088	-	-	35.7884
	C3 (CH26/2)	C2 (CH25/2)	C1 (CH24/2)	180	7.328	9.318	11.494	49.022	-	-	31.5476
	C6 (CH28/2)	C5 (CH27/2)	C4 (CH29/2)	180	7.328	9.269	11.533	98.044	-	-	32.9612
	C9 (CH20/2)	C8 (CH19/2)	C7 (CH30/2)	180	7.078	8.963	11.378	147.066	-	-	34.3748
	C12(CH3/3)	C11 (CH1/3)	C10 (CH16/3)	180	7.141	9.015	11.358	196.088	-	-	35.7884
	D3 (CH6/3)	D2 (CH5/3)	D1 (CH4/3)	0	7.204	10.269	12.797	45.022+D	35.7706	35.8768	35.983
	D6 (CH9/3)	D5 (CH8/3)	D4 (CH7/3)	0	7.512	10.670	12.318	94.044+D	38.3736	38.4798	38.5859
	D9 (CH12/3)	D8 (CH11/3)	D7 (CH10/3)	0	8.057	9.881	12.191	143.066+D	40.977	41.0832	41.1895
	D12 (CH15/3)	D11(CH14/3)	D10 (CH13/3)	0	8.542	10.966	12.405	192.088+D	43.5812	43.6875	43.7937
	B1 (CH12/2)	B2 (CH13/2)	B3 (CH14/2)	45	7.110	8.843	10.820	49.022	-	-	35.983
	B4 (CH15/2	B5 (CH16/2)	B6 (CH17/2)	45	7.296	9.215	10.845	98.044	-	-	38.5859
	B7 (CH18/2)	B8 (CH31/2)	B9 (CH0/3)	45	6.565	8.631	10.893	147.066	-	-	41.1895
	B10 (CH21/2)	B11 (CH22/2)	B12 (CH23/2)	45	5.956	8.946	11.081	196.088	-	-	43.7937
225.2877	A1 (CHO/2)	A2 (CH1/2)	A3 (CH2/2)	135	7.328	9.322	11.892	49.022	-	-	35.983
	A4(CH3/2)	A5 (CH4/2)	A6 (CH5/2)	135	6.901	9.259	12.189	98.044	-	-	38.5859
	A7 (CH7/2)	A8 (CH8/2)	A9 (CH6/2)	135	6.722	9.176	11.784	147.066	-	-	41.1895
	A10 (CH9/2)	A11 (CH10/2)	A12 (CH11/2)	135	6.641	9.079	12.168	196.088	-	-	43.7937
	C3 (CH26/2)	C2 (CH25/2)	C1 (CH24/2)	180	7.328	9.318	11.494	49.022	-	-	35.983
	C6 (CH28/2)	C5 (CH27/2)	C4 (CH29/2)	180	7.328	9.269	11.533	98.044	-	-	38.5859
	C9 (CH20/2)	C8 (CH19/2)	C7 (CH30/2)	180	7.078	8.963	11.378	147.066	-	-	41.1895
	C12(CH3/3)	C11 (CH1/3)	C10 (CH16/3)	180	7.141	9.015	11.358	196.088	-	-	43.7937

***Axial Coordinate Correction applies only to thermocouple well identifications with "D" labels (e.g., D-1 through D-12)**

TABLE IV: Local (Axial) Variation of the Bulk Fluid (Water) Flowing Inside a Single-Side Heated Circular-Like Test Section with Respect to the Net Single-Side Outside (or Incident) Heat Flux (continued)

Net Incident Heat Flux (kW/m^2)	Thermocouple Well Identification (Channel Number/Module Number)			Test Section Coordinates					Local Bulk Fluid Temperature, T_b (^oC)		
				Circumferential (Degrees)	Radial (mm)			Axial (mm) *	Axial Coordinate Correction*, D		
									D = 0 mm	D = 2 mm	D = 4 mm
	D3 (CH6/3)	D2 (CH5/3)	D1 (CH4/3)	0	7.204	10.269	12.797	45.022+D	41.79	41.9288	42.0676
	D6 (CH9/3)	D5 (CH8/3)	D4 (CH7/3)	0	7.512	10.670	12.318	94.044+D	45.1923	45.3311	45.4699
	D9 (CH12/3)	D8 (CH11/3)	D7 (CH10/3)	0	8.057	9.881	12.191	143.066+D	48.5946	48.7334	48.8722
	D12 (CH15/3)	D11(CH14/3)	D10 (CH13/3)	0	8.542	10.966	12.405	192.088+D	51.995	52.1336	52.2723
	B1 (CH12/2)	B2 (CH13/2)	B3 (CH14/2)	45	7.110	8.843	10.820	49.022	-	-	42.0676
	B4 (CH15/2	B5 (CH16/2)	B6 (CH17/2)	45	7.296	9.215	10.845	98.044	-	-	45.4699
	B7 (CH18/2)	B8 (CH31/2)	B9 (CH0/3)	45	6.565	8.631	10.893	147.066	-	-	48.8722
294.3267	B10 (CH21/2)	B11 (CH22/2)	B12 (CH23/2)	45	5.956	8.946	11.081	196.088	-	-	52.2723
	A1 (CHO/2)	A2 (CH1/2)	A3 (CH2/2)	135	7.328	9.322	11.892	49.022	-	-	42.0676
	A4(CH3/2)	A5 (CH4/2)	A6 (CH5/2)	135	6.901	9.259	12.189	98.044	-	-	45.4699
	A7 (CH7/2)	A8 (CH8/2)	A9 (CH6/2)	135	6.722	9.176	11.784	147.066	-	-	48.8722
	A10 (CH9/2)	A11 (CH10/2)	A12 (CH11/2)	135	6.641	9.079	12.168	196.088	-	-	52.2723
	C3 (CH26/2)	C2 (CH25/2)	C1 (CH24/2)	180	7.328	9.318	11.494	49.022	-	-	42.0676
	C6 (CH28/2)	C5 (CH27/2)	C4 (CH29/2)	180	7.328	9.269	11.533	98.044	-	-	45.4699
	C9 (CH20/2)	C8 (CH19/2)	C7 (CH30/2)	180	7.078	8.963	11.378	147.066	-	-	48.8722
	C12(CH3/3)	C11 (CH1/3)	C10 (CH16/3)	180	7.141	9.015	11.358	196.088	-	-	52.2723
	D3 *(CH6/3)	D2 (CH5/3)	D1 (CH4/3)	0	7.204	10.269	12.797	45.022+D	46.1326	46.3297	46.5268
	D6 (CH9/3)	D5 (CH8/3)	D4 (CH7/3)	0	7.512	10.670	12.318	94.044+D	50.9635	51.1604	51.3573
	D9 (CH12/3)	D8 (CH11/3)	D7 (CH10/3)	0	8.057	9.881	12.191	143.066+D	55.7906	55.9876	56.1845
	D12 (CH15/3)	D11(CH14/3)	D10 (CH13/3)	0	8.542	10.966	12.405	192.088+D	60.6169	60.8136	61.0103
	B1 (CH12/2)	B2 (CH13/2)	B3 (CH14/2)	45	7.110	8.843	10.820	49.022	-	-	46.5268
	B4 (CH15/2	B5 (CH16/2)	B6 (CH17/2)	45	7.296	9.215	10.845	98.044	-	-	51.3573
	B7 (CH18/2)	B8 (CH31/2)	B9 (CH0/3)	45	6.565	8.631	10.893	147.066	-	-	56.1845
	B10 (CH21/2)	B11 (CH22/2)	B12 (CH23/2)	45	5.956	8.946	11.081	196.088	-	-	61.0103
417.9938	A1 (CHO/2)	A2 (CH1/2)	A3 (CH2/2)	135	7.328	9.322	11.892	49.022	-	-	46.5268
	A4(CH3/2)	A5 (CH4/2)	A6 (CH5/2)	135	6.901	9.259	12.189	98.044	-	-	51.3573
	A7 (CH7/2)	A8 (CH8/2)	A9 (CH6/2)	135	6.722	9.176	11.784	147.066	-	-	56.1845
	A10 (CH9/2)	A11 (CH10/2)	A12 (CH11/2)	135	6.641	9.079	12.168	196.088	-	-	61.0103
	C3 (CH26/2)	C2 (CH25/2)	C1 (CH24/2)	180	7.328	9.318	11.494	49.022	-	-	46.5268
	C6 (CH28/2)	C5 (CH27/2)	C4 (CH29/2)	180	7.328	9.269	11.533	98.044	-	-	51.3573
	C9 (CH20/2)	C8 (CH19/2)	C7 (CH30/2)	180	7.078	8.963	11.378	147.066	-	-	56.1845
	C12(CH3/3)	C11 (CH1/3)	C10 (CH16/3)	180	7.141	9.015	11.358	196.088	-	-	61.0103
	D3 (CH6/3)	D2 (CH5/3)	D1 (CH4/3)	0	7.204	10.269	12.797	45.022+D	55.761	55.9823	56.2035
	D6 (CH9/3)	D5 (CH8/3)	D4 (CH7/3)	0	7.512	10.670	12.318	94.044+D	61.1828	61.4038	61.6247
	D9 (CH12/3)	D8 (CH11/3)	D7 (CH10/3)	0	8.057	9.881	12.191	143.066+D	66.5993	66.8204	67.0414
	D12 (CH15/3)	D11(CH14/3)	D10 (CH13/3)	0	8.542	10.966	12.405	192.088+D	72.0148	72.2355	72.4563
	B1 (CH12/2)	B2 (CH13/2)	B3 (CH14/2)	45	7.110	8.843	10.820	49.022	-	-	56.2035
	B4 (CH15/2	B5 (CH16/2)	B6 (CH17/2)	45	7.296	9.215	10.845	98.044	-	-	61.6247
	B7 (CH18/2)	B8 (CH31/2)	B9 (CH0/3)	45	6.565	8.631	10.893	147.066	-	-	67.0414
469.6313	B10 (CH21/2)	B11 (CH22/2)	B12 (CH23/2)	45	5.956	8.946	11.081	196.088	-	-	72.4563
	A1 (CHO/2)	A2 (CH1/2)	A3 (CH2/2)	135	7.328	9.322	11.892	49.022	-	-	56.2035
	A4(CH3/2)	A5 (CH4/2)	A6 (CH5/2)	135	6.901	9.259	12.189	98.044	-	-	61.6247
	A7 (CH7/2)	A8 (CH8/2)	A9 (CH6/2)	135	6.722	9.176	11.784	147.066	-	-	67.0414
	A10 (CH9/2)	A11 (CH10/2)	A12 (CH11/2)	135	6.641	9.079	12.168	196.088	-	-	72.4563
	C3 (CH26/2)	C2 (CH25/2)	C1 (CH24/2)	180	7.328	9.318	11.494	49.022	-	-	56.2035
	C6 (CH28/2)	C5 (CH27/2)	C4 (CH29/2)	180	7.328	9.269	11.533	98.044	-	-	61.6247
	C9 (CH20/2)	C8 (CH19/2)	C7 (CH30/2)	180	7.078	8.963	11.378	147.066	-	-	67.0414
	C12(CH3/3)	C11 (CH1/3)	C10 (CH16/3)	180	7.141	9.015	11.358	196.088	-	-	72.4563
	D3 (CH6/3)	D2 (CH5/3)	D1 (CH4/3)	0	7.204	10.269	12.797	45.022+D	61.5288	61.7655	62.0022
	D6 (CH9/3)	D5 (CH8/3)	D4 (CH7/3)	0	7.512	10.670	12.318	94.044+D	67.3317	67.5685	67.8053
	D9 (CH12/3)	D8 (CH11/3)	D7 (CH10/3)	0	8.057	9.881	12.191	143.066+D	73.1318	73.3682	73.6047
	D12 (CH15/3)	D11(CH14/3)	D10 (CH13/3)	0	8.542	10.966	12.405	192.088+D	78.9224	79.1585	79.3946
	B1 (CH12/2)	B2 (CH13/2)	B3 (CH14/2)	45	7.110	8.843	10.820	49.022	-	-	62.0022
	B4 (CH15/2	B5 (CH16/2)	B6 (CH17/2)	45	7.296	9.215	10.845	98.044	-	-	67.8053
	B7 (CH18/2)	B8 (CH31/2)	B9 (CH0/3)	45	6.565	8.631	10.893	147.066	-	-	73.6047
503.1049	B10 (CH21/2)	B11 (CH22/2)	B12 (CH23/2)	45	5.956	8.946	11.081	196.088	-	-	79.3946
	A1 (CHO/2)	A2 (CH1/2)	A3 (CH2/2)	135	7.328	9.322	11.892	49.022	-	-	62.0022
	A4(CH3/2)	A5 (CH4/2)	A6 (CH5/2)	135	6.901	9.259	12.189	98.044	-	-	67.8053
	A7 (CH7/2)	A8 (CH8/2)	A9 (CH6/2)	135	6.722	9.176	11.784	147.066	-	-	73.6047
	A10 (CH9/2)	A11 (CH10/2)	A12 (CH11/2)	135	6.641	9.079	12.168	196.088	-	-	79.3946
	C3 (CH26/2)	C2 (CH25/2)	C1 (CH24/2)	180	7.328	9.318	11.494	49.022	-	-	62.0022
	C6 (CH28/2)	C5 (CH27/2)	C4 (CH29/2)	180	7.328	9.269	11.533	98.044	-	-	67.8053
	C9 (CH20/2)	C8 (CH19/2)	C7 (CH30/2)	180	7.078	8.963	11.378	147.066	-	-	73.6047
	C12(CH3/3)	C11 (CH1/3)	C10 (CH16/3)	180	7.141	9.015	11.358	196.088	-	-	79.3946

***Axial Coordinate Correction applies only to thermocouple well identifications with "D" labels (e.g., D-1 through D-12)**

TABLE IV: Local (Axial) Variation of the Bulk Fluid (Water) Flowing Inside a Single-Side Heated Circular-Like Test Section with Respect to the Net Single-Side Outside (or Incident) Heat Flux

(continued)

Net Incident Heat Flux (kW/m^2)	Thermocouple Well Identification (Channel Number/Module Number)			Test Section Coordinates					Local Bulk Fluid Temperature, T_b (^0C)		
				Circumferential (Degrees)	Radial (mm)			Axial (mm) *	Axial Coordinate Correction*, D		
									D = 0 mm	D = 2 mm	D = 4 mm
728.3243	D3 (CH6/3)	D2 (CH5/3)	D1 (CH4/3)	0	7.204	10.269	12.797	45.022+D	71.4786	71.821	73.1633
	D6 (CH9/3)	D5 (CH8/3)	D4 (CH7/3)	0	7.512	10.670	12.318	94.044+D	79.8626	80.2044	80.5461
	D9 (CH12/3)	D8 (CH11/3)	D7 (CH10/3)	0	8.057	9.881	12.191	143.066+D	88.233	88.5742	88.9154
	D12 (CH15/3)	D11(CH14/3)	D10 (CH13/3)	0	8.542	10.966	12.405	192.088+D	96.5868	96.927	97.2672
	B1 (CH12/2)	B2 (CH13/2)	B3 (CH14/2)	45	7.110	8.843	10.820	49.022	-	-	73.1633
	B4 (CH15/2	B5 (CH16/2)	B6 (CH17/2)	45	7.296	9.215	10.845	98.044	-	-	80.5461
	B7 (CH18/2)	B8 (CH31/2)	B9 (CH0/3)	45	6.565	8.631	10.893	147.066	-	-	88.9154
	B10 (CH21/2)	B11 (CH22/2)	B12 (CH23/2)	45	5.956	8.946	11.081	196.088	-	-	97.2672
	A1 (CHO/2)	A2 (CH1/2)	A3 (CH2/2)	135	7.328	9.322	11.892	49.022	-	-	73.1633
	A4(CH3/2)	A5 (CH4/2)	A6 (CH5/2)	135	6.901	9.259	12.189	98.044	-	-	80.5461
	A7 (CH7/2)	A8 (CH8/2)	A9 (CH6/2)	135	6.722	9.176	11.784	147.066	-	-	88.9154
	A10 (CH9/2)	A11 (CH10/2)	A12 (CH11/2)	135	6.641	9.079	12.168	196.088	-	-	97.2672
	C3 (CH26/2)	C2 (CH25/2)	C1 (CH24/2)	180	7.328	9.318	11.494	49.022	-	-	73.1633
	C6 (CH28/2)	C5 (CH27/2)	C4 (CH29/2)	180	7.328	9.269	11.533	98.044	-	-	80.5461
	C9 (CH20/2)	C8 (CH19/2)	C7 (CH30/2)	180	7.078	8.963	11.378	147.066	-	-	88.9154
	C12(CH3/3)	C11 (CH1/3)	C10 (CH16/3)	180	7.141	9.015	11.358	196.088	-	-	97.2672

***Axial Coordinate Correction applies only to thermocouple well identifications with "D" labels (e.g., D-1 through D-12)**

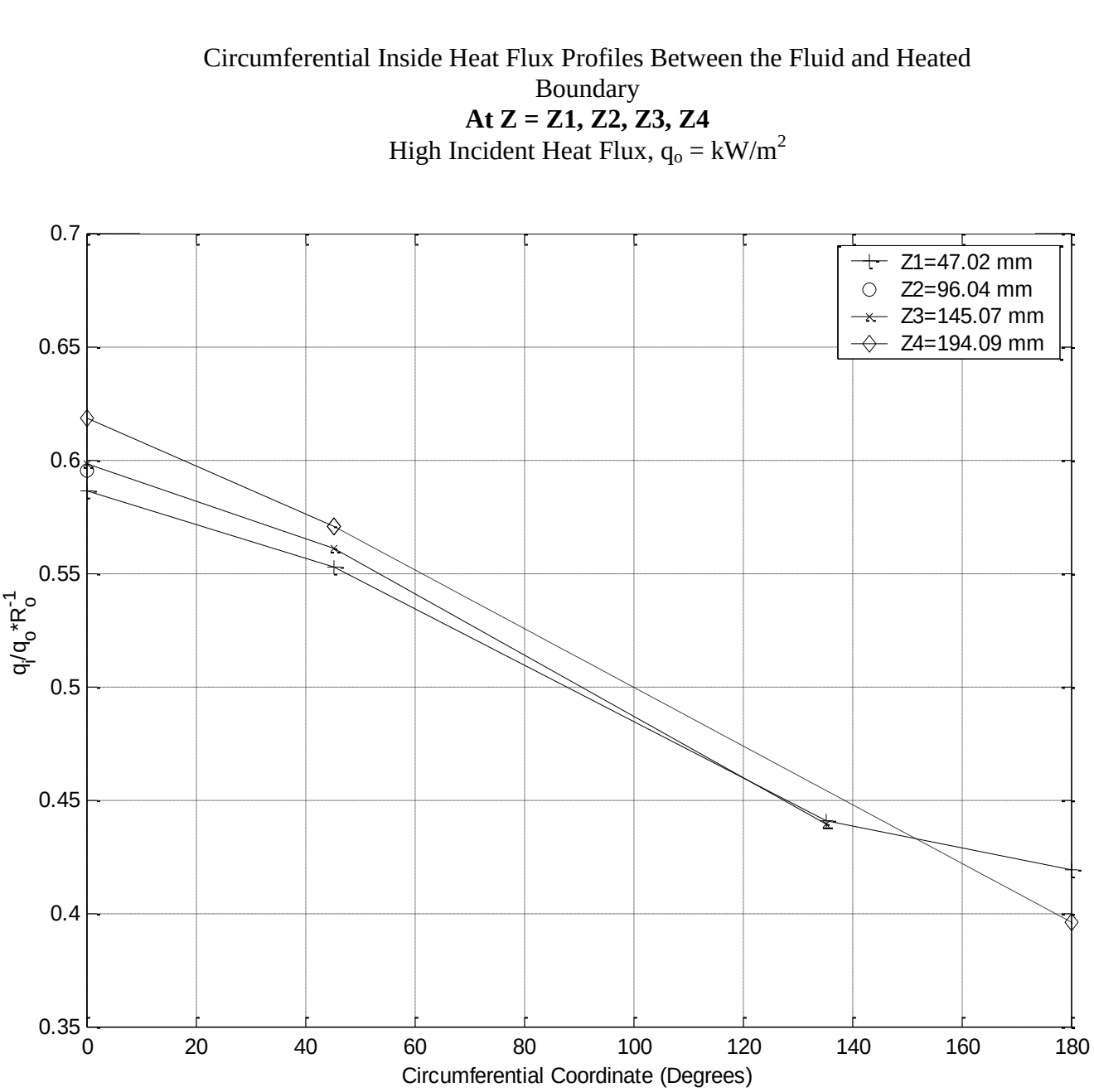

Figure 37: Cirrcumferential Variation of the Inside Circular-Like Test Section Flow Channel Dimensionless Wall Heat Flux ($q_i/q_o*R_o^{-1}$) at Different Axial Locations and Derived from Measurements Made at Radial Locations About Midway (see Table II) Between the Heated and Cooled Boundaries for an Outside (or incident) Single-Side Heat Flux of 728.3 kW/m^2.

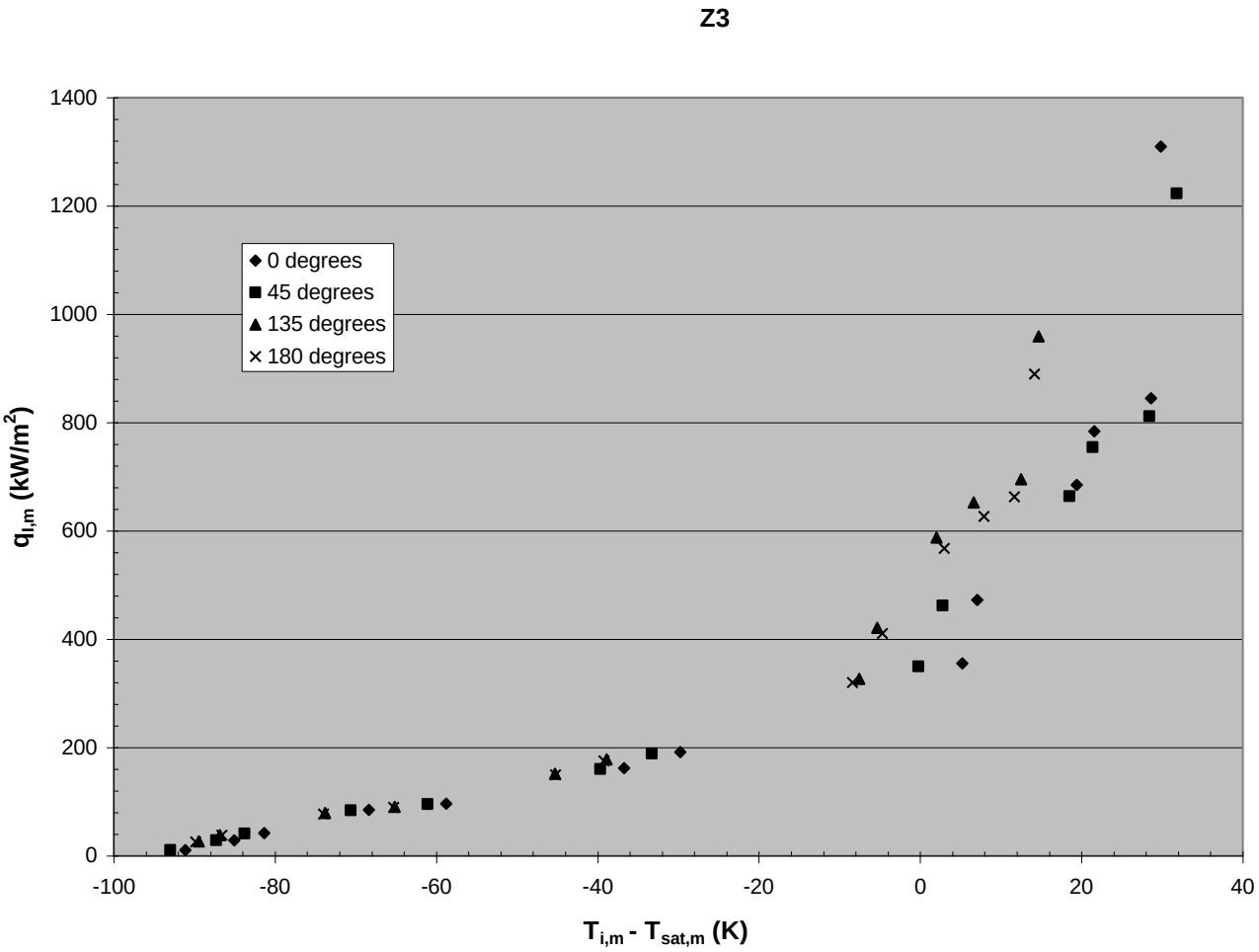

Figure 38: Local (2-D) Boiling Curves at Z=Z3=143.07 mm as a Function of the Circumferential Coordinate wit ϕ = 0.0 and 180.0 Degrees Corresponding to the Heated and Cooled Portions, Respectively, of the Plane of Symmetry of the Circular-Like Test Section.

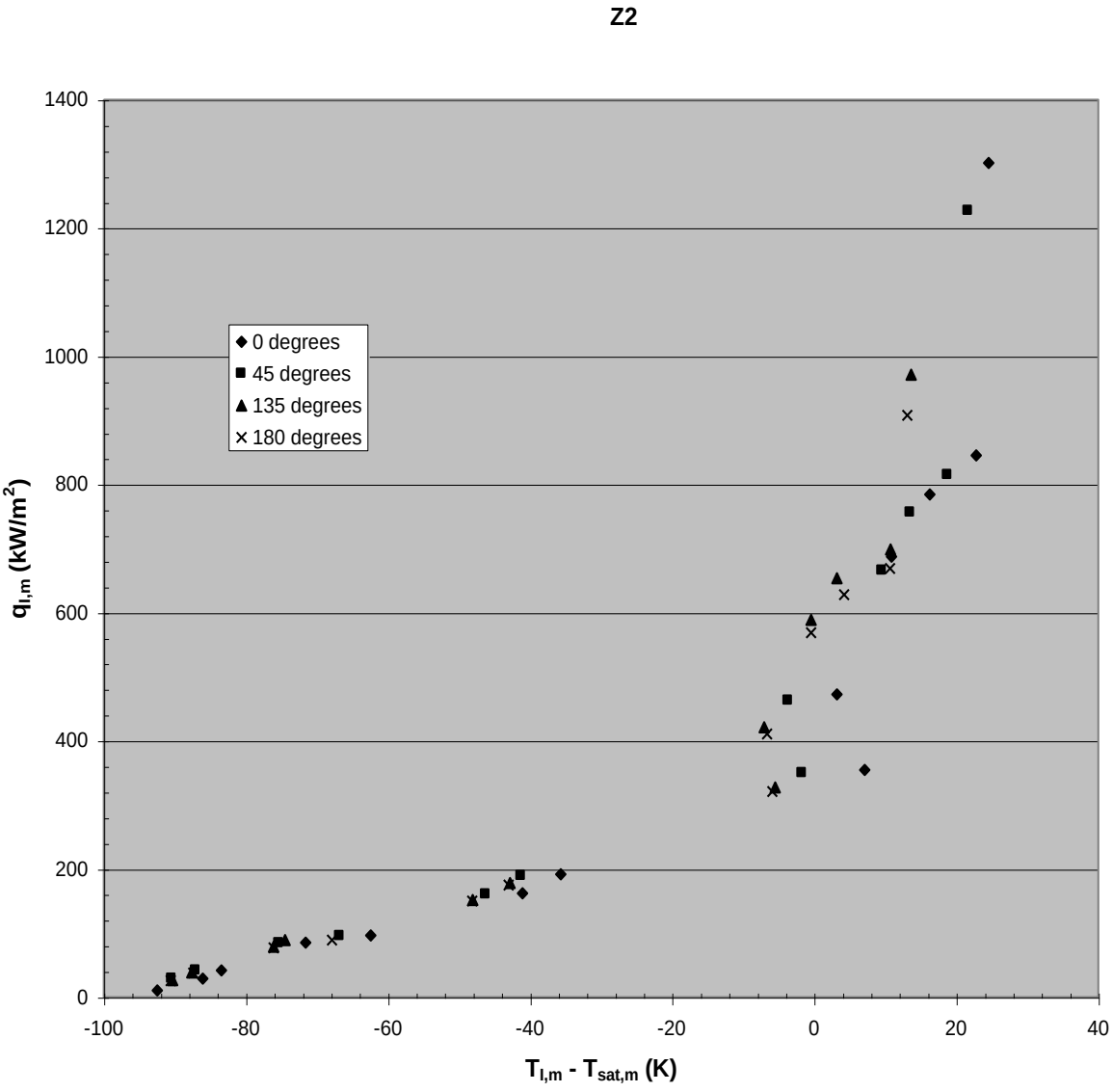

Figure 39: Local (2-D) Boiling Curves at Z=Z2=94.04 mm as a Function of the Circumferential Coordinate with ϕ = 0.0 and 180.0 Degrees Corresponding to the Heated and Cooled Portions, Respectively, of the Plane of Symmetry of the Circular-Like Test Section.

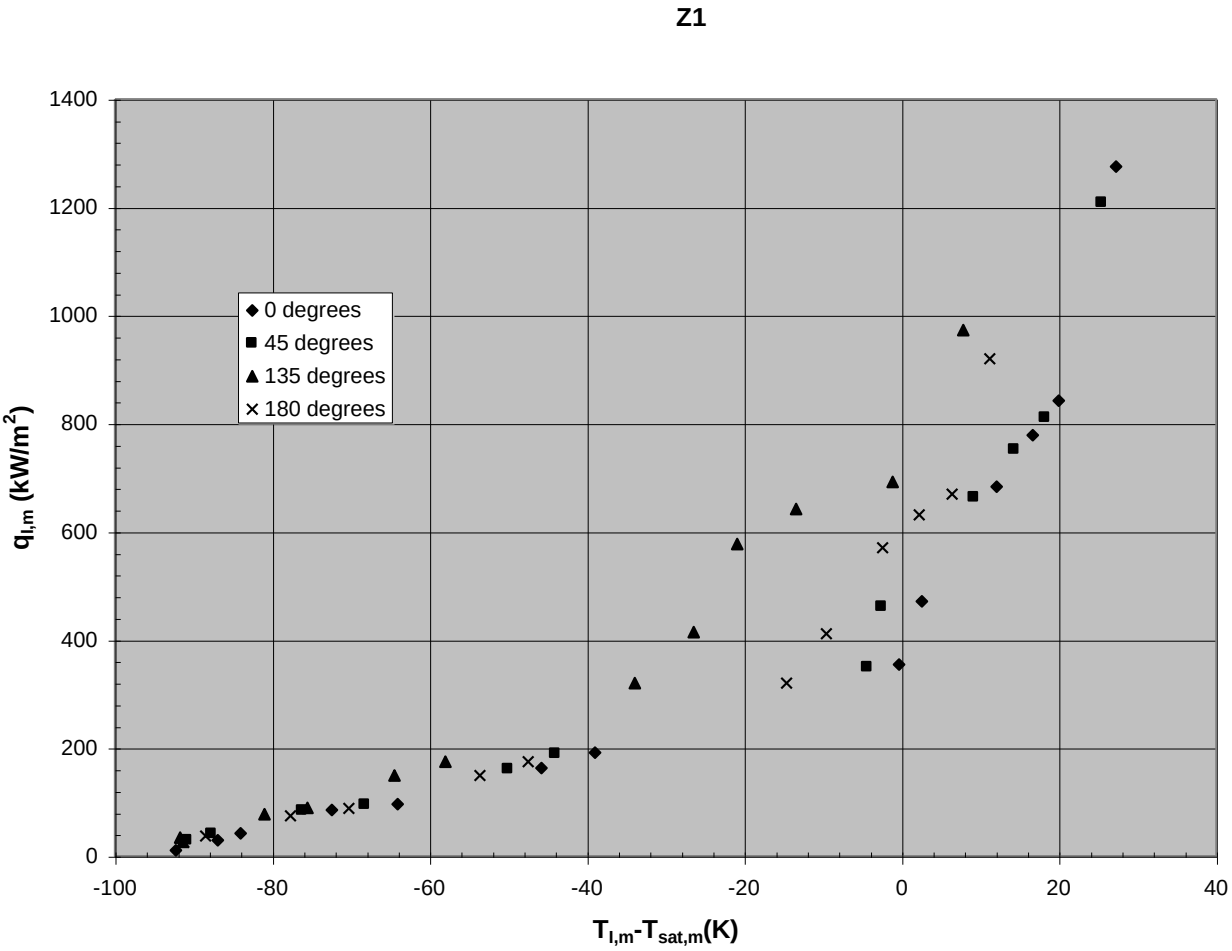

Figure 40 Local (2-D) Boiling Curve at Z=Z1=45.02 mm as a Function of the Circumferential Coordinate with ϕ = 0.0 and 180.0 Degrees Corresponding to the Heated and Cooled Portions, Respectively, of the Plane of Symmetry of the Circular-Like Test Section.

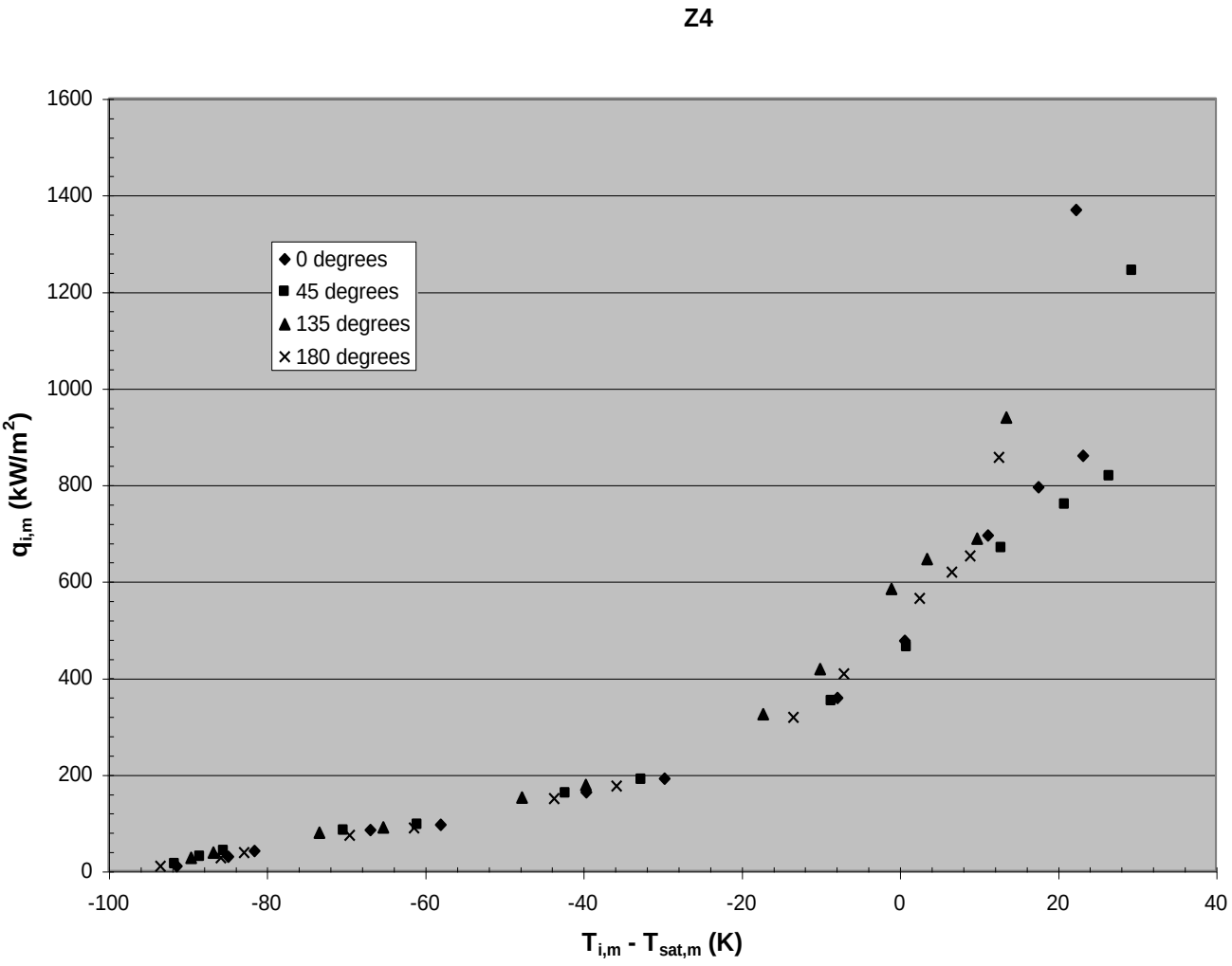

Figure 41: Local (2-D) Boiling Curve at Z=Z4=192.09 mm as a Function of the Circumferential Coordinate with ϕ = 0.0 and 180.0 Degrees Corresponding to the Heated and Cooled Portions, Respectively, of the Plane of Symmetry of the Circular-Like Test Section.

15.0 HIGH HEAT FLUX REMOVAL DATA FOR A SINGLE-SIDE HEATED MONOBLOCK USING FLOW BOILING

15.1 BACKGROUND

The robust design of one-side-heated plasma-facing components and other high heat flux components is dependent on knowing the local distribution of inside wall heat flux in the flow channels. The local inside wall heat flux can be obtained from selectively chosen local plasma-facing component wall temperatures close to the inside boundary of the flow channel. To this end, three-dimensional thermal measurements for a one-side-heated monoblock were made and show: (1) the three-dimensional variation of the wall temperature close to both the heated and fluid-solid surface boundaries, (2) the resultant effects of mass velocity on the 3-D wall temperature/outside heat flux relationship, and (3) the occurrence of local critical heat flux and local post-critical heat flux. The monoblock has a 180.0 mm heated length, has a 10.0 mm inside diameter, and has a square cross-section with 30.0 mm nominal outside surfaces.

15.2 INTRODUCTION

The test section configuration under study for this work, consists of a square cross-section monoblock with an inside circular 10.0 mm diameter coolant channel bored through the center. The outside square sides are 30.0 mm. The main section of the monoblock is 200.0 mm long. The monoblock is subjected to a constant heat flux on one side only. Water is the coolant. The inlet water temperature is held near 26.0 ^{0}C and the exit pressure is maintained at 0.207 MPa (T_{sat} = 121.3 ^{0}C). Thermocouples (0.5 mm O.D., stainless steel sheathed, Type-J) were placed in forty-eight thermal well locations inside the solid Glidcop Copper monoblock. For each of four axial stations, three thermocouples were embedded at three radial and four circumferential locations (0, 45, 135, and 180 degrees, where 0 degrees corresponds to that portion of the axis of symmetry close to the heated surface). The mass velocity was 1.18 Mg/m^{2}s.

In addition to the technical literature given in Section 10.1, Nygren [72] presented an extensive review on actively cooled plasma-facing components.

15.3 MONOBLOCK TEST SECTION

The monoblock test sections (see Fig. 42) were fabricated from Type AL-15 Glidcop Grade Copper. The overall length of the test section, including the inlet and outlet reduced diameter sections, was 328.0 mm.

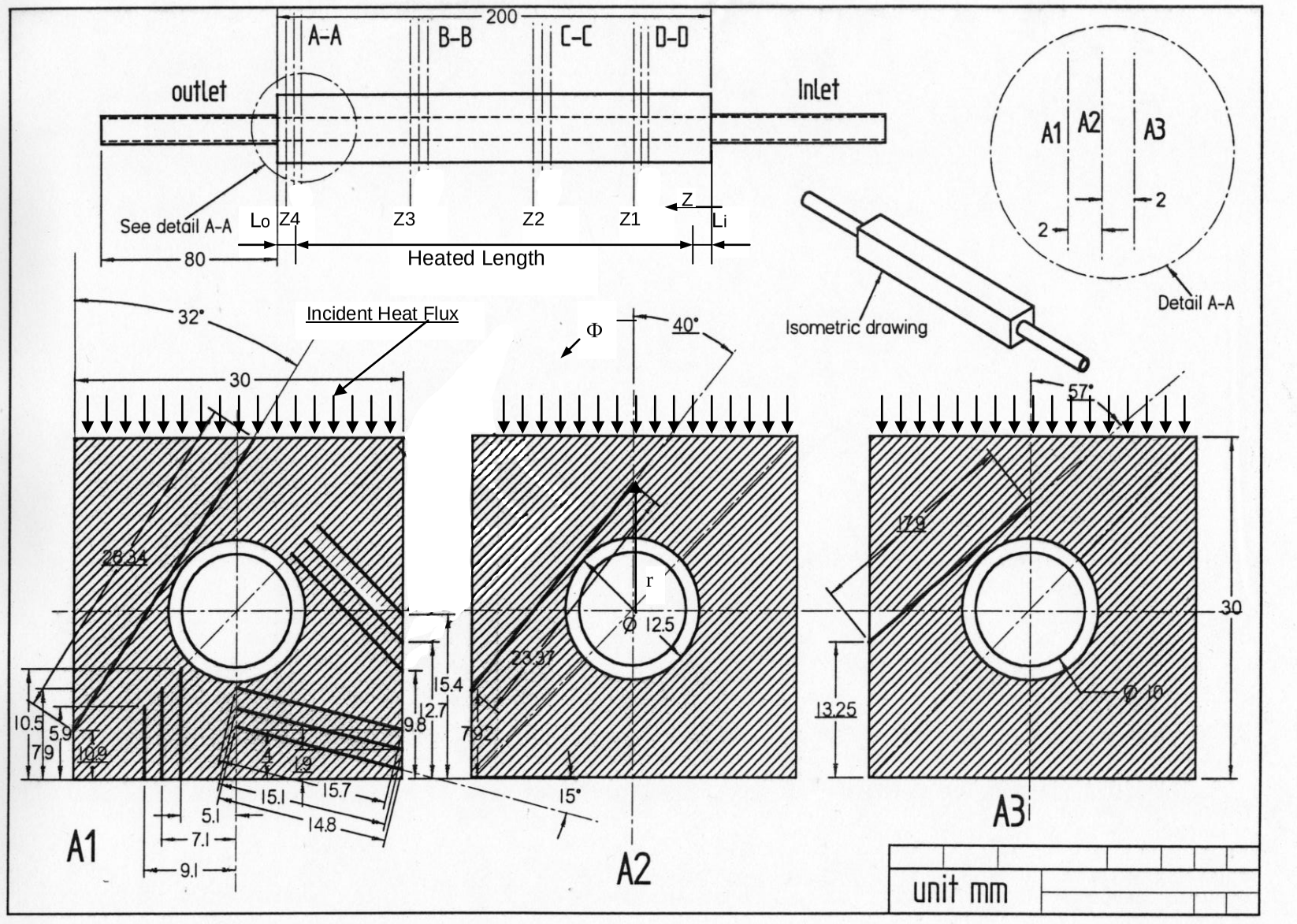

Figure 42: Monoblock Test Section Used for Local Temperature and Heat Transfer Measurements. Water Flows Through the 10.0 mm Diameter Channel. The Thermocouple (TC) Wells are the Solid Black Lines with Specified Lengths and Angles. The Outer Concentric Circle Around the 10.0 mm Inner Diameter channel Should Not Appear in the Shown Sections But Has Been Added to Show the Outside Diameter of the Channel Near the Inlet and Exit.

The main section of the monoblock test section (available for heating) is 200.0 mm long with a nominal outside surface width of the square cross section monoblock of 30.0 mm and an inside diameter of 10.0 mm. For these tests, the actual directly heated length, L, was 180.0 mm. In Fig. 42, isometric and longitudinal side views are shown. The flow channel inlet and exit are indicated in the latter view. Also shown in the latter view are four axial stations labeled A-A, B-B, C-C, and D-D, which are axial locations where thermocouple (TC) wells exist for local in-depth wall temperature measurements. The purpose of the four axial locations is to obtain an estimate of the axial distribution of the monoblock test section wall temperature for a given applied heat flux. Since the geometry of the TC wells is identical at all four primary axial stations, a detail description will be given for only one axial station. For example, the A-A axial station has twelve (12) TC wells, with ten (10) wells in plane A1 and one each in planes A2 and A3 which are axially displaced upstream from plane A1 by 2.0 mm and 4.0 mm, respectively.

The TCs at station A-A will give both radial and circumferential distributions of the local wall temperature. Hence, a combination of all axial stations will produce a three-dimensional distribution of the monoblock test section local wall temperature as a function of the applied heat flux and the water flow regime which will vary from single-phase at the monoblock test section inlet to subcooled pre- and post-CHF near the exit. The applied heat flux comes from a DC power supply which provides resistive heating to the monoblock test section via one, grade G-20 graphite flat heater which is placed over a 1.0 mm thick aluminum nitride layer which in turn rests on the monoblock test section shown in Fig. 42. As noted above, the power supply feeds the heater element (see Fig. 43) in the experimental set-up through a copper bus duct/cabling (bus bar) system [51].

15.4 RESULTS

15.4.1 Three-Dimensional Variations

The circumferential variations in the channel wall temperature are presented in Figs. 44a and 44b for eight levels of the net, outside, single-side heat flux, q_o. Figures 44a and 44b show such variations close to the outside (partially heated) boundary and the inside fluid-solid boundary, respectively. Comparing the two sets of plots, one observes two very different circumferential wall temperature variations near the two boundaries. Since there are only four circumferential locations for each set of measurements, these distributions will not show the exact local circumferential slopes but the quantitative trends at the four locations are evident. The locus of

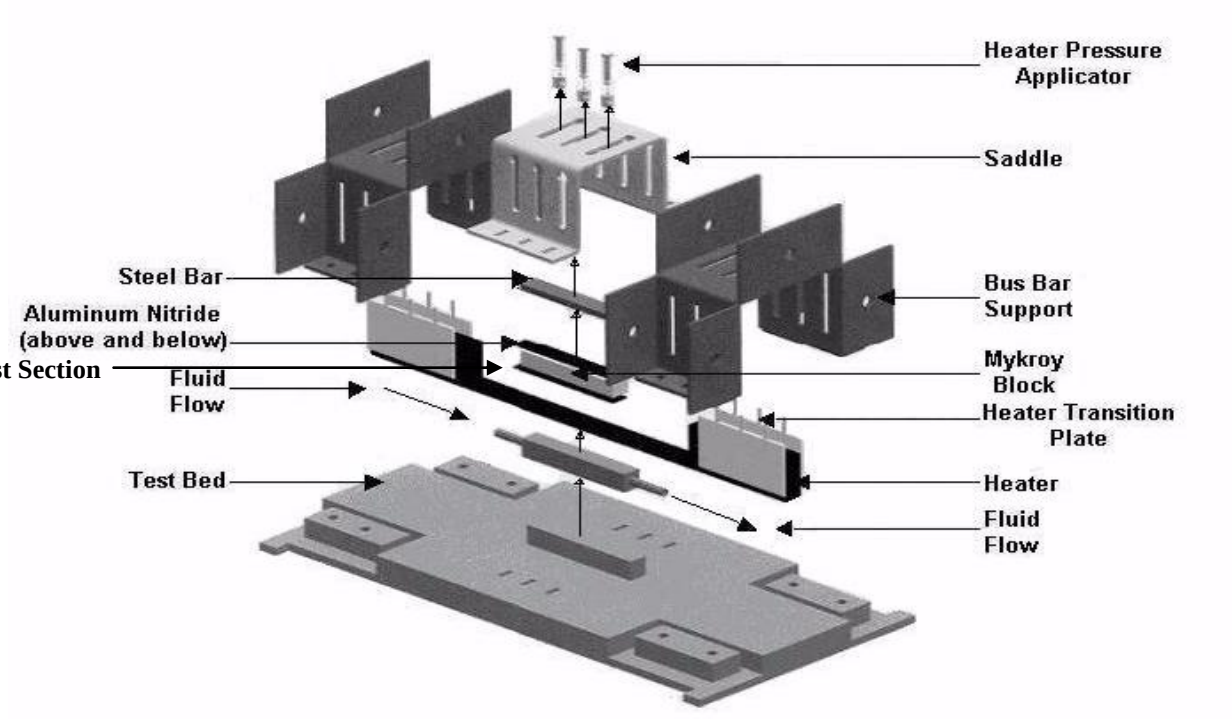

(a)

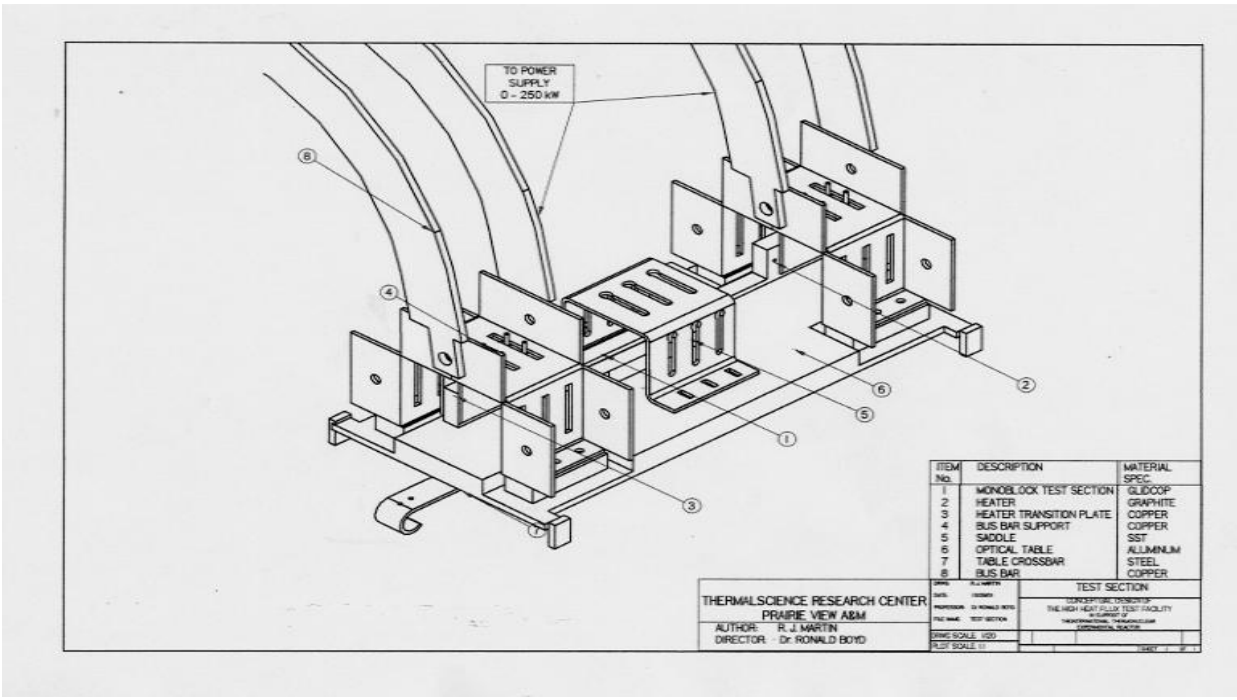

(b)

Figure 43: (a) High Heat Flux Monoblock Test Section Expanded Assembly, (b) Monoblock Test Section Assembly with Heater, Flexible Bus Bars, and Test Bed (see Figures 43 and 44a for component labeling and additional details).

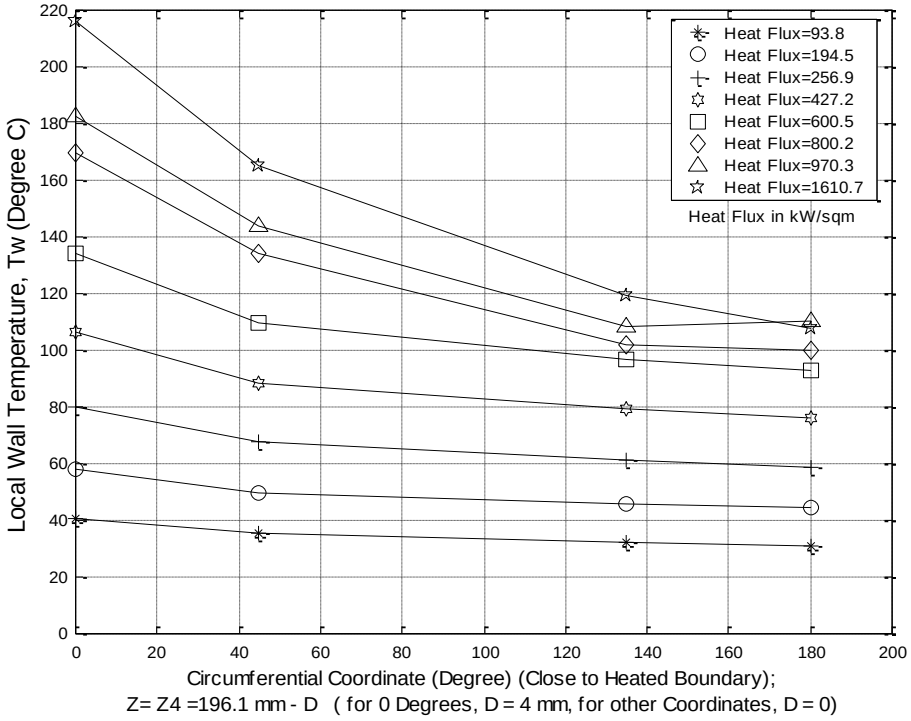

(a)

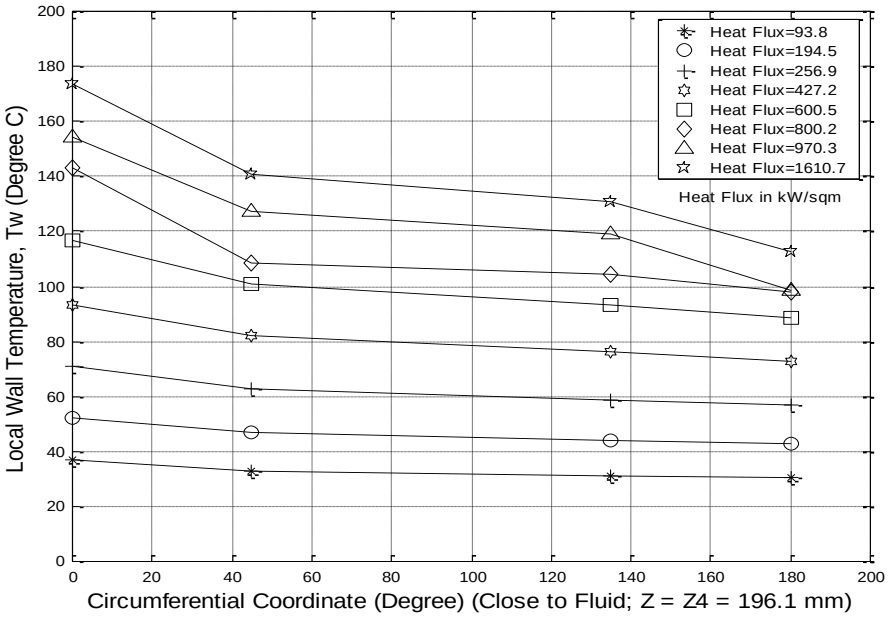

(b)

Figure 44: The Flow Conditions Included G = 1.18 Mg/m^2s, P_{exit} = 0.207 MPa, and $T_{b_{inlet}}$ = 26.0 ^{0}C. (a) Circumferential Monoblock Wall Temperature Profile from the Thermocouples Nearest to the Heated Boundary (i.e., away from the fluid/solid boundary) as a Function of the Net Incident Heat Flux at Z = Z_4 = 196.1 mm. (b) Circumferential Monoblock Wall Temperature Profile from the thermocouples Nearest to the Fluid/Solid boundary as a Function of Net Incident Heat Flux, at Z = Z_4 = 196.1 mm (L_i = 16.0 mm and L_o = 4.0 mm).

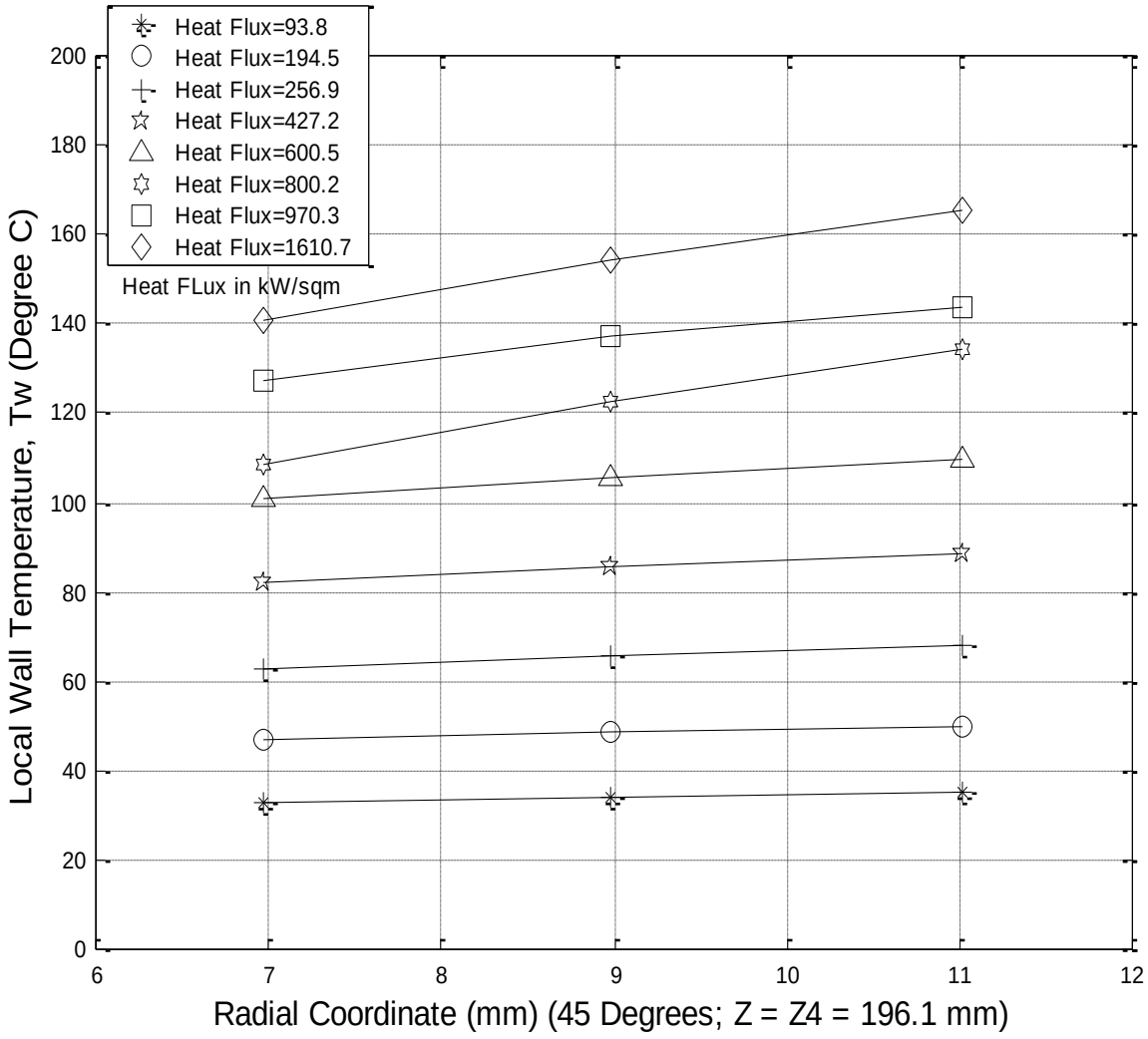

Figure 45: Radial Wall Temperature Profile for the Monoblock Flow Channel at ϕ = 45.0 Degrees and Z = Z_4 = 196.1 mm as a Function of the Net Incident Heat Flux (L_i = 16.0 mm and L_o = 4.0 mm). The Flow Conditions Included G = 1.18 Mg/m^{2}s, P_{exit} = 0.207 MPa, and $T_{b_{inlet}}$ = 26.0 ^{0}C.

the data in Fig. 44a (near the outside partially heated boundary) displays approximately the correct boundary condition of a zero circumferential temperature gradient as ϕ approaches 180.0 degrees but differs from the profile near the fluid/solid boundary. In Fig. 44b which shows the local circumferential monoblock wall temperature variation close to the fluid-solid boundary, the temperature is almost constant between ϕ = 45.0 and 135.0 degrees. This is due to the relatively large thickness of the test section in some cases and due to localized boiling in other cases. For smaller TS thicknesses, the variation would be greater in regions where a phase change is not occurring. In the limit of ϕ approaching 180.0 degrees in Figs. 44a and 44b, the wall temperature is well above the fluid temperature and increases as q_o increases.

Figure 45 displays the radial temperature profiles at ϕ = 45.0 degrees and shows small variations with respect to r. This is of course contrasted with larger radial variations as displayed by comparing Figs. 44a and 44b at for example, ϕ = 0 degrees.

Finally, Fig.46 shows the remaining portion of the three-dimensional variations via the axial wall temperature profiles which include the four axial stations. For this work, the heater length (L) was 180.0 mm long (in the axial direction) and was placed asymmetrically on test section (200.0 mm long). More specifically, there was a 4.0 mm (= L_o) unheated portion (i.e., unheated directly) at the down-stream most part of the square monoblock test section; and, there was a 16.0 mm (= L_i) unheated portion (i.e., unheated directly) at the up-stream most part of the monoblock test section. The curves shown in Fig. 46 are for monoblock test section locations along the axis of symmetry (ϕ = 0.0 degrees) and close the heated boundary.

15.4.2 Net Incident Heat Flux/Wall Temperature Relationship

Two cases are presented here which show the effects at two different levels of mass velocity on the relationship between the net incident (outside) monoblock heat flux (q_o) and the local wall temperature (T_w). Although not identical, this relationship between q_o and T_w would be directly related to the 2-D local boiling curve if the radius at which this relationship was considered was equal to the inside radius of the flow channel. This will be completed in future work. In Fig. 47, the steady-state incident heat flux/wall temperature relationship is presented: (1) for the axis of symmetry with ϕ = 0.0 degrees; (2) for axial locations of Z = 143.1, 145.1, and 147.1 mm (nominally, Z = Z_3 = 147.1 mm or cross section B-B in Fig. 42); and, (3) for radii of 12.82, 10.62, and 7.95 mm, respectively.

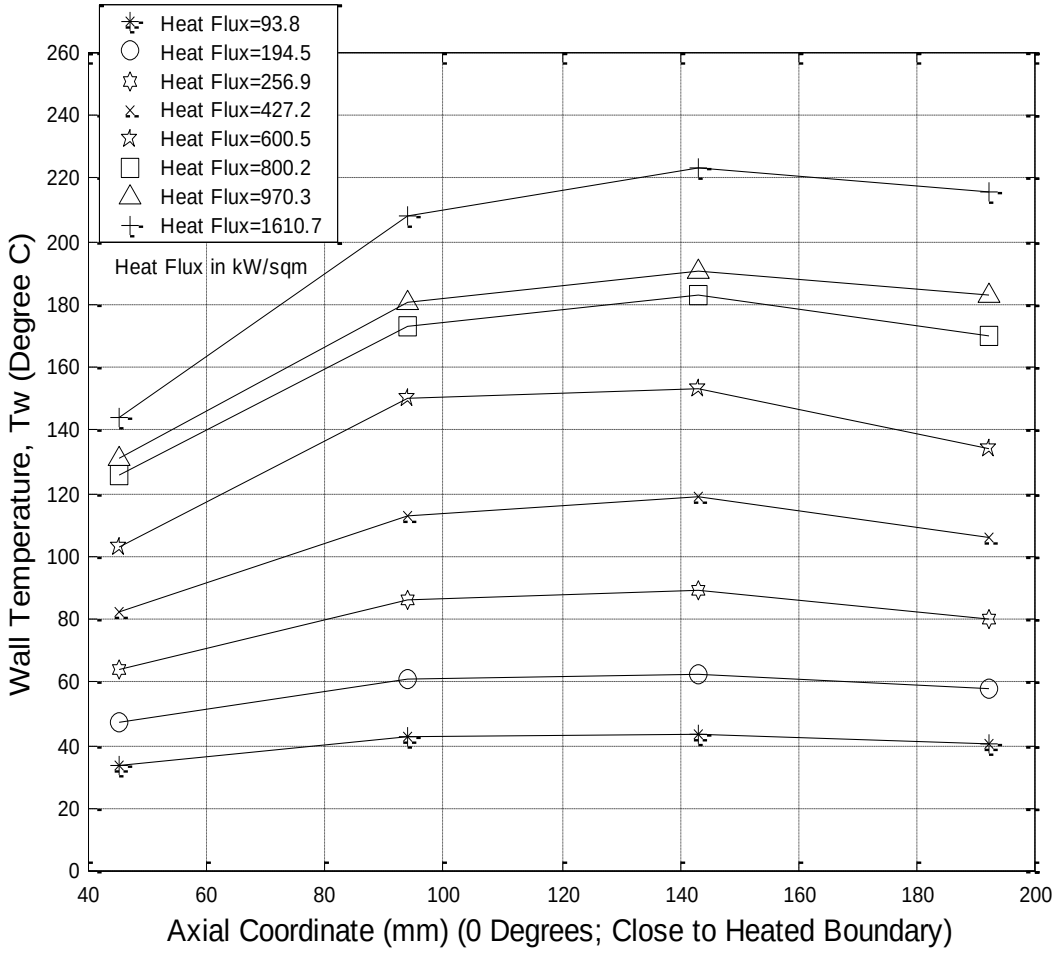

Figure 46: Monoblock Axial Wall Temperature Profiles From the Thermocouples at ϕ = 0.0 Degrees (Close to the Heated Boundary) as a Function of the Net Incident Heat Flux. The Flow Conditions Included G = 1.18 Mg/m^{2}s, P_{exit} = 0.207 MPa, and $T_{b_{inlet}}$ = 26.0 ^{0}C.

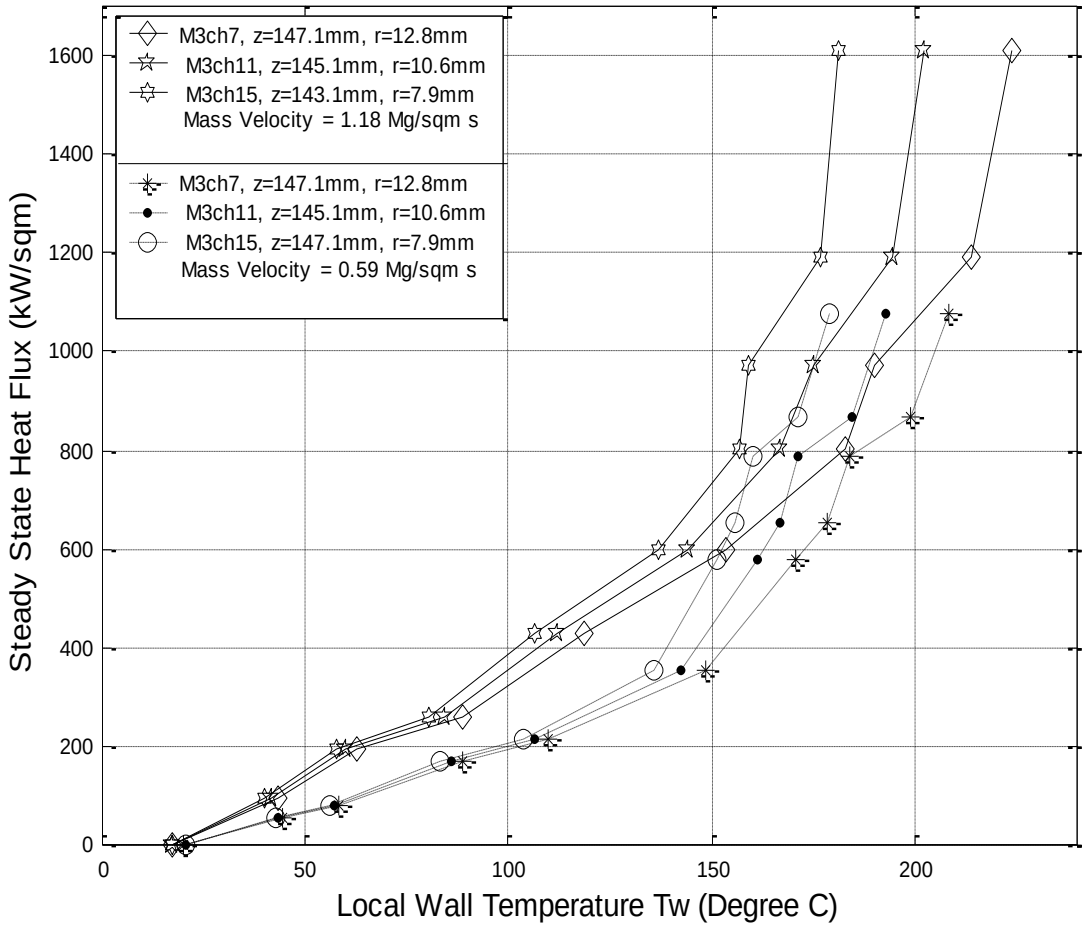

Figure 47: Steady State Net Incident Heat Flux as a Function of the Local Flow Monoblock Channel Wall Temperature at ϕ = 0.0 degrees and For Specified Axial and Radial Locations (Near Z_3) and Heaters Asymmetrically Placed With Respect to the Axial Direction with L_o = 4.0 mm and L_i = 16.0 mm of Unheated Flow Channel Both Upstream of the Heaters, Respectively. Other Flow Conditions Included P_{exit} = 0.207 MPa, and $T_{b_{inlet}}$ = 26.0 ^{0}C.

16.0 SINGLE-SIDE HEATED MONOBLOCK, HIGH HEAT FLUX REMOVAL USING WATER SUBCOOLED TURBULENT FLOW BOILING

16.1 BACKGROUND

Plasma-facing components for fusion reactors and other high heat flux heat sinks are subjected to a peripherally non-uniform heat flux. The monoblock test section under study is a single-side heated square cross-section heat sink with a circular coolant channel bored through the center. The heated length of the test section is 180 mm. The inside diameter and outside square sides are 10 mm and 30 mm, respectively. It was subjected to a constant heat flux on one side of the outside surfaces, and the remaining portion was not heated. The results consist of three-dimensional wall temperature distributions and a display of two-dimensional quasi-boiling curves. These results are among the first full set of three-dimensional wall temperature measurements for a single-side heated monoblock flow channel which contains the effects of conjugate heat transfer for turbulent, and subcooled flow boiling. In the single-phase region, good predictability resulted when the thermal hydraulic diameter was used. Comparisons are made with water flow in a single-side heated circular cylinder.

16.2 INTRODUCTION

Since plasma-facing component (PFC) design requirements and goals are evolving, the development of an experimental conjugate multi-dimensional, flow boiling data base will provide the basis for flow boiling correlation modification and adaptation as well as computational fluid dynamic code validation. This would include single-side heating effects as well as subcooled turbulent flow boiling effects. The results: (1) would be used for detail PFC and other high heat flux heat sink (HHFHS) flow channel and substrate design studies, and (2) would lead to cost-effective and robust designs. The optimized design of single-side heated PFCs and HHFHS is dependent on using conjugate heat transfer to find the local distribution of inside channel wall temperature and heat flux.

Conjugate heat transfer modeling [60, 62] has proven useful in forming baselines and identifying important parameters affecting peaking factors and data reduction for the spectrum of high heat fluxes found in a wide variety of applications. For various applications requiring different fluids, the results show the following: (1) the coexistence of three flow boiling regimes at some axial locations inside the single-side heated flow channel, (2) the correlational

dependence of the inside wall heat flux and temperature (fluid independent), and (3) inaccuracies that could arise in some data reduction procedures (fluid independent). However, for PFC and other HHFHS (e.g., in rocket engines, boilers, and electronic components) applications, work is still needed to expand conjugate heat transfer analyses from simple circular and complex geometries [21, 84] to prototypic geometries. This will lead to improved predictability of peaking factors and prototypic conditions.

16.3 MONOBLOCK TEST SECTION

The configuration under study consists of a single-side heated monoblock (with square outside surfaces) test section with a circular coolant channel bored through the center. A detailed description of the test section is shown in Fig. 42 and given in Section 15.3.

The mass velocity, exit pressure, and exit water subcooling range used for the present case were 0.59 Mg/m^2s, 0.207 MPa (T_{sat} = 121.3 ^0C), and 55 to 101 ^0C, respectively. Type-J thermocouples were used and calibrated to within ± 0.1 ^0C with a precision calibrator. For these conditions, the basic fluid flow is a turbulent (Re = 9,400) and highly developing flow with a reciprocal Graetz number (Gz^{-1}) less than 3.3×10^{-4}.

16.4 RESULTS

Robust PFC and HHFHS designs must be based on accurate three-dimensional conjugate flow boiling analyses and optimizations of the local wall temperature and hence on the local flow boiling regime variations. Such analyses must have 3-D data as a basis for comparison, assessment, and flow boiling correlation adaptation for localize boiling. As an initial part of an effort to begin to provide such data, selected results are presented for the above noted conditions for the: (1) 3-D variations of the wall temperature as functions of the circumferential (ϕ), radial (r), and axial (Z) coordinates; and, (2) net incident steady-state heat flux as a function of the local wall temperature (2-D quasi-boiling curves). The net incident heat flux relationship with the locally measured wall temperature will be discussed first.

16.4.1 Incident Heat Flux/Wall Temperature Relationship

Experimental results show the relationship between the incident heat flux (q_o) and the wall temperature (T_w) at different 3-D coordinates. As noted above, this relationship between q_o and T_w would be directly related to the two-dimensional local boiling curve if the radius at which this relationship was considered was equal to the inside radius of the flow channel. The present work will lead eventually to the development of these two-dimensional boiling curves.

16.4.1.1 Single-Side Heated Monoblock

The relationship between the steady state, net incident heat flux and the local wall temperature is presented in Fig. 48 for Z = Z_4. These solid curves connecting the data are complete in that they show evidence of an influence from the three basic subcooled flow boiling regimes (partially nucleate boiling, fully developed flow boiling, and local film boiling) of the boiling curve. Measured data are shown for three radial locations (r = 8.0, 10.8, and 12.9 mm) and are used to extrapolate the local inside (r = 5 mm) wall temperature of the coolant channel. Both the saturation temperature and the temperature for the onset of nucleate boiling (T_{ONB2}) are shown [92]. Further, Petukhov's [93] correlation was used for the single-phase heat transfer predictions at the inside boundary of the coolant channel. For the single-side heated geometry predictions, all fluid properties were evaluated at the local bulk temperature; and, the thermal hydraulic [12] diameter (D_T) was used in the Nusselt number. D_T is defined as $a_a \cdot D_i$, where a_a is a constant which accounts for single-side heating effects (a_a = 1.2 for the monoblock and 2.0 for the circular cylinder). Good agreement occurs except near ONB.

One observes a progressive increase of the slope of the q_o vs T_w curves in Fig. 48 as the radius decreases or as the inside fluid-solid boundary is approached. The set of three data points on each curve beyond ONB denotes possible […since these locations are not at r_i] entry into the region of fully developed nucleate flow boiling. The occurrence of a significant boiling event at ϕ = 0 degree and Z = Z_4 (which is nominally 196.1 mm) is denoted by a decrease in the slope of the curves beyond these points as q_o increases further. The reduction in the slope suggests an as yet undetermined event. As the heat flux was increased further, a loud hammer-like sound also began and increased in amplitude as the heat flux was further increased. In addition, moderate local wall temperature fluctuations (about 10 ^{0}C) begin with a modest increase in the incident heat flux (850 to 870 kW/m^2). These periodic fluctuations increased in magnitude to about 18.0 ^{0}C as q_o was increased beyond 1.0 MW/m^2. It is interesting to note that these periodic steady conditions resulted in an increase in the slope of the $T_w - q_o$ curve and hence resulted in locally stable, steady, periodic conditions in which the local mean and peak wall temperatures were almost constant.

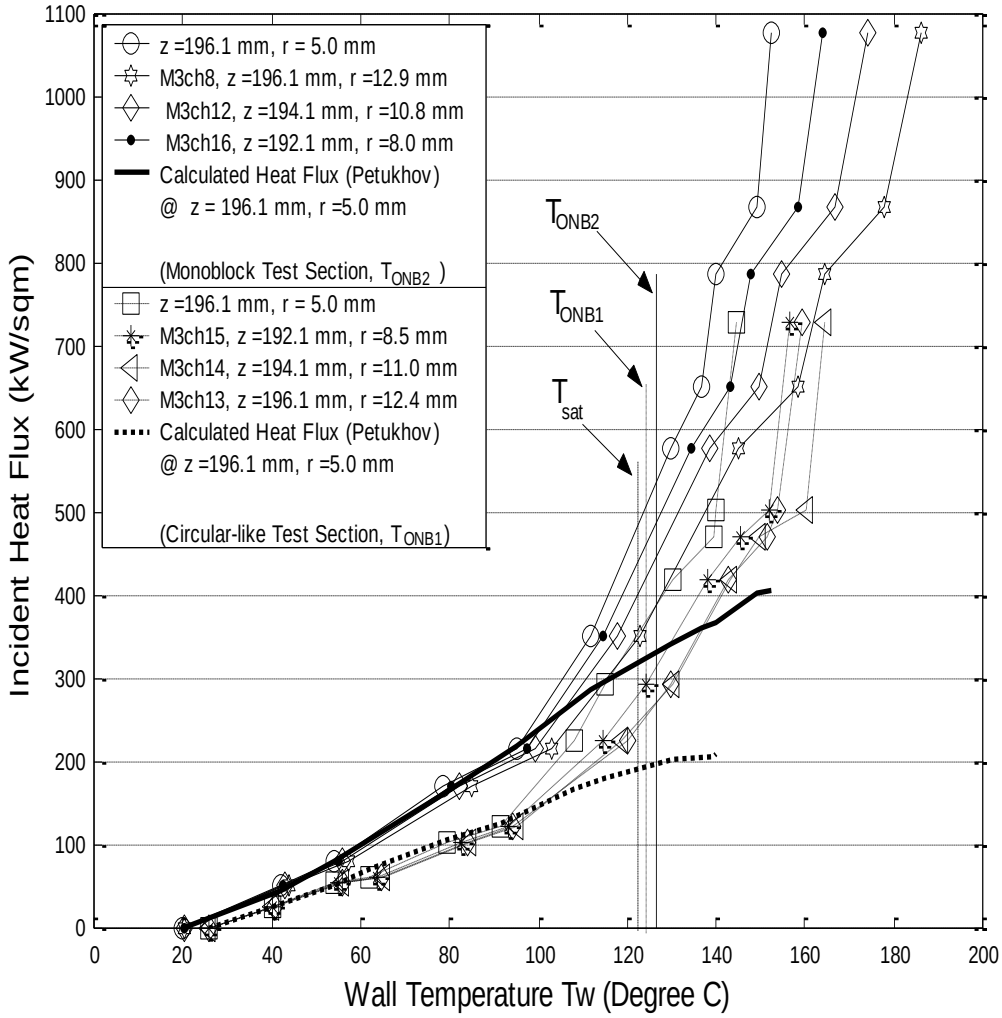

Figure 48: Measured 2-D Quasi-Boiling Curves for the Single-Side Heated Monoblock and Single Side Heated Circular Test Sections at ϕ = 0 Degree and for Specified Axial Locations (near Z = Z_4 = 196.1 mm) with G = 0.59 Mg/m^{2}s and P_{exit} = 0.27 MPa.

16.4.1.2 Comparisons With the Single-Side Heated Circular Tube

Figure 48 shows a comparison of two single-side heated geometries: (1) a monoblock test section heated on one of its four (4) outside surfaces, and (2) a "circular-like" (approximating a circular tube) test section heated on one-half of its outside circumference. For this comparison, the mass velocity was 0.59 Mg/m^2s and the measurements were made near the end of the heated length of the test sections. The cross-sectional aspect ratio (R_o) for the single-side heated monoblock test section is defined as the ratio of the heated width to the inside diameter of the flow channel. R_o for the single-side heated "circular-like" tube is the ratio of the outside diameter to the inside diameter. For both geometries, R_o is 3. It should be noted that R_o is neither a peaking factor nor a similarity parameter for this comparison. Rather, it is used in the present work only: (1) for convenience of design, and (2) to demonstrate the obvious difference which has not been always apparent to some investigators. As expected at a given level of heat flux, the wall temperatures in the circular-like test section are typically higher than those in the monoblock test section. Correspondingly at a given power level, the local monoblock test section wall temperature is higher than that for the circular tube. As can be seen, there is also good agreement between the data for both configurations and single-phase predictions except near ONB.

16.4.1.3 Three-Dimensional Variations for a Single-Side Heated Monoblock

The circumferential variations of the wall temperature are presented in Figs. 49a and 49b for ten levels of the net incident heat flux, q_o. These figures show such variations close to the inside fluid-solid boundary and the outside (partially heated) boundaries, respectively. Comparing the two sets of plots, one observes that the circumferential wall temperature variations are basically similar except at the highest heat flux. However, there is a larger variation near the partially heated boundary. Since there are only four circumferential locations for each set of measurements, these distributions will not show the exact local circumferential slopes but the quantitative trends at the four locations are evident. The locus of the data in Fig. 49a displays approximately the correct boundary condition of a zero circumferential temperature gradient as ϕ approaches 180 degrees for most levels of q_o. The zero temperature gradient is not directly apparent at $\phi = 0$ degree from the lines (used only for convenient data point identification) connecting the data points. However, this data is amenable to this boundary condition; and, the data interpretation improves when this condition is used. Close to the fluid-

solid boundary, the temperature is almost constant between ϕ = 135 and 180 degrees. As ϕ increases, the local wall temperature decreases sharply and then gradually decreases as expected. The gradual decrease is due to the large value of R_o. As R_o decreases, this circumferential variation will increase [30].

At all heat flux levels, the temperature variations between ϕ = 0 and 45 degrees are usually much less for the circular tube than for the monoblock. This implies that for a given heat flux level above that needed for local boiling, a larger portion of the single-side heated circular tube inside wall experiences boiling in the circumferential direction than the single-side heated monoblock. Figure 50 displays the radial temperature profiles at ϕ = 45 degrees and shows significant variations with respect to r. As can be seen by comparing Figs. 49a and 49b at identical values of q_o, the radial variation at ϕ = 0 degree is larger than at other circumferential locations. These radial temperature profiles may be useful in estimating the local heat flux and wall temperature on the inside flow channel surface.

Finally, Fig. 51 shows the remaining portion of the 3-D variations via the axial wall temperature profiles. The curves are for test section locations along the heated portion of the axis of symmetry (ϕ = 0 degree) and close to the heated boundary. This local axial wall temperature profile shows that the wall temperature in the axial direction increases with the axial coordinate up to the third axial station (Z = Z_3 = 147.1 mm), beyond which the local wall temperature decreases. Although small, axial variations occurred between Z_2 (= 98 mm) and Z_3 (= 147.1 mm) at all power levels. These variations will increase for monoblock test section wall and prototypic PFC substrate thicknesses smaller than the 10 mm nominal value for the present case.

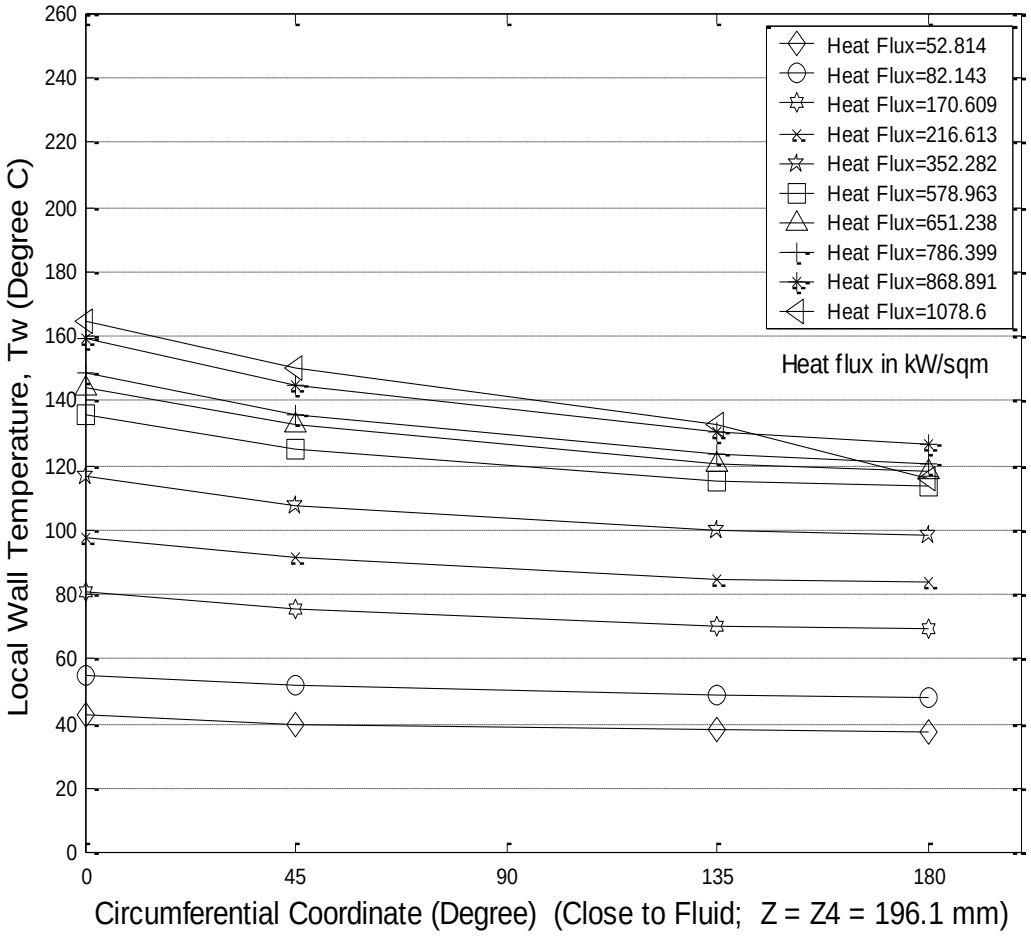

Figure 49a: Monoblock Circumferential Wall Temperature Profile from the Thermocouples Nearest to the Fluid/Solid Boundary as a Function of Net Incident Heat Flux, at $Z = Z_4 = 196.1$ mm with $G = 0.59$ Mg/m^{2}s and $P_{exit} = 0.27$ MPa.

.

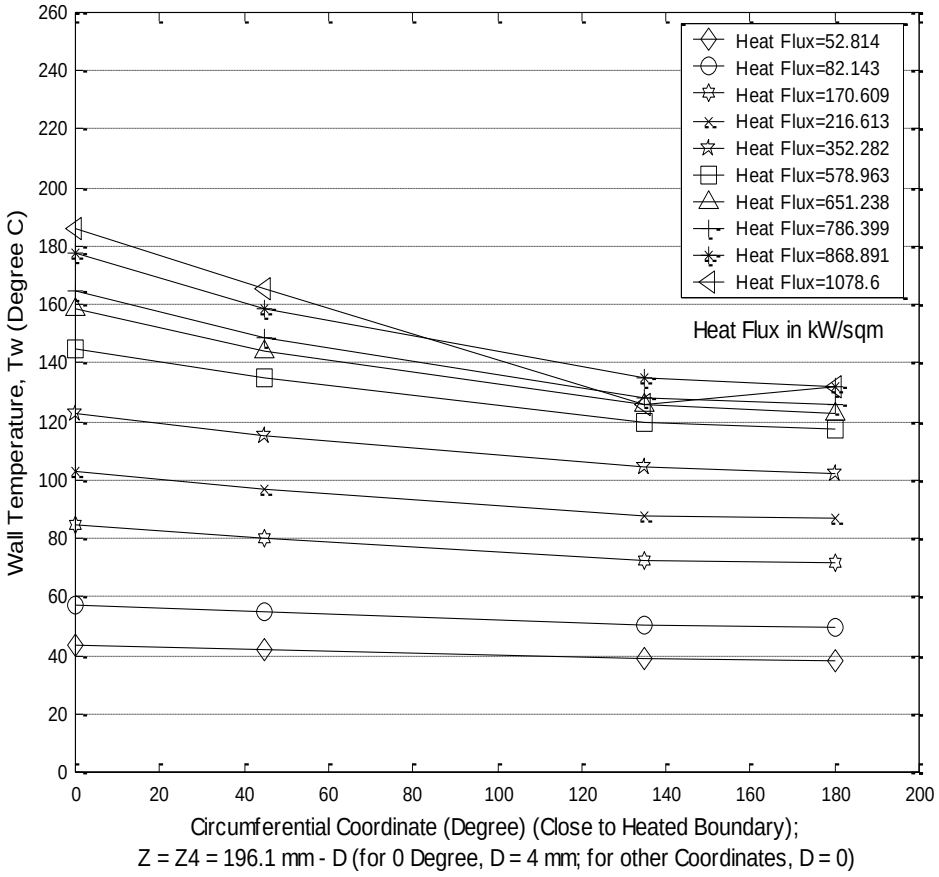

Figure 49b: Monoblock Circumferential Wall Temperature Profile from the Thermocouples Nearest to the Heated Boundary (i.e., away from the fluid/solid boundary) as a Function of the Net Incident Heat Flux with G = 0.59 Mg/m^2s and P_{exit} = 0.27 MPa.

.

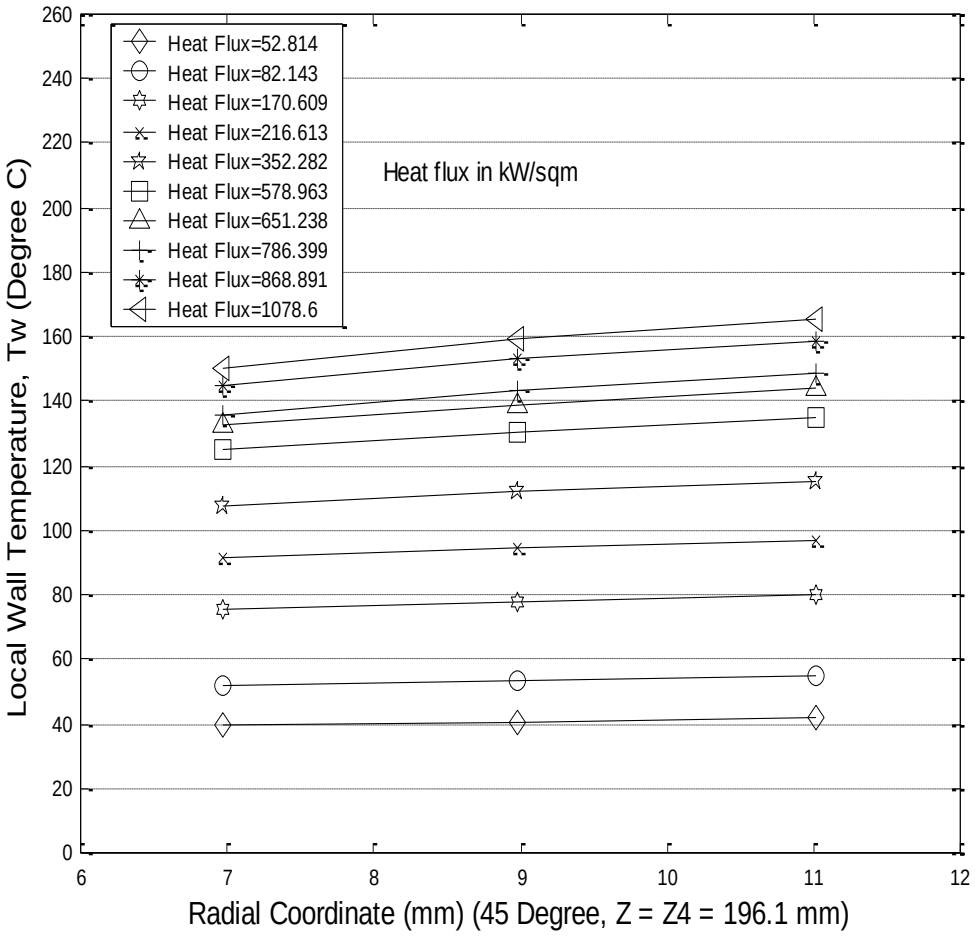

Figure 50: Monoblock Radial Wall Temperature Profile for the Flow Channel at ϕ = 45 Degrees and Z = Z_4 = 196.1 mm as a Function of the Net Incident Heat Flux with G = 0.59 Mg/m^2s and P_{exit} = 0.27 MPa.

.

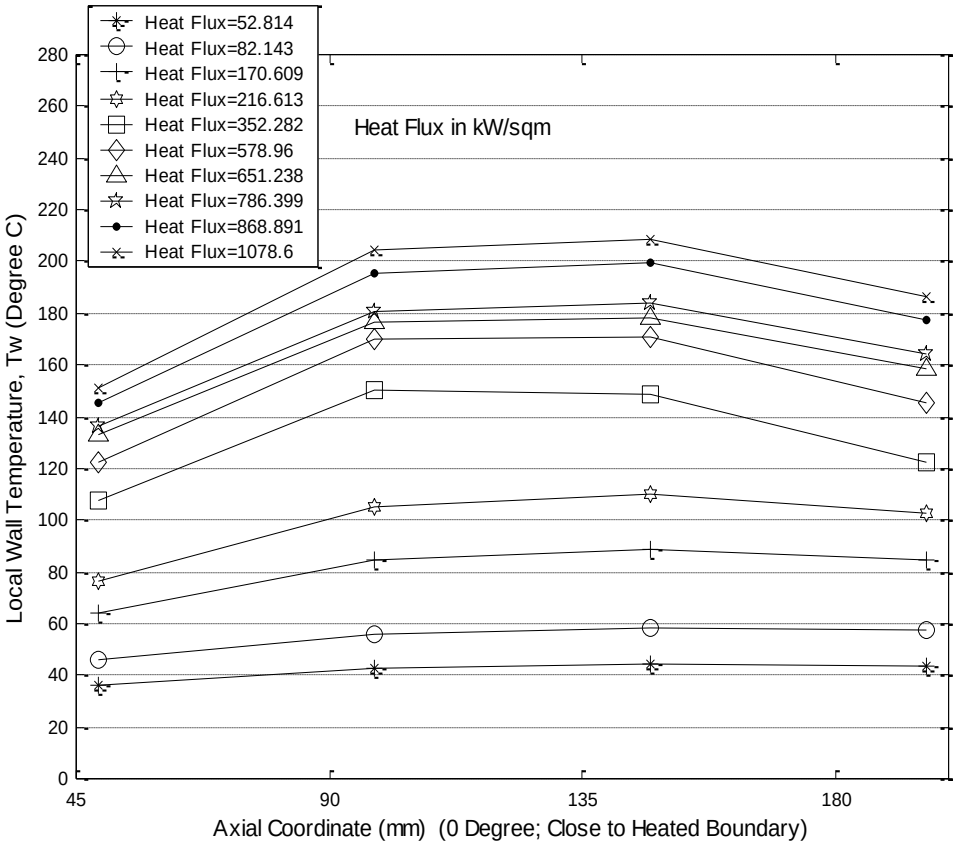

Figure 51: Monoblock Axial Wall Temperature Profiles from the TCs at ϕ = 0 Degree, and Close to the Heated Boundary as a Function of the Net Incident Heat Flux with G = 0.59 Mg/m^2s and P_{exit} = 0.27 MPa.

17.0 CONJUGATE HEAT TRANSFER DATA BASE AND MEASUREMENT DETAILS FOR ONE-SIDE HEATED CIRCULAR CYLINDRICAL AND MONOBLOCK FLOW CHANNELS

17.1 INTROUCTION

Flow boiling has been widely applied in modern industries such as power plants, optical and electronic systems, chemical process plants, nuclear facilities, etc. Over the years, many uniform wall heat flux and uniform wall temperature single-phase and flow boiling correlations have been developed [94-110]. As more and more non-uniform heat fluxes are involved in advanced applications (like plasma-facing components for the next generation fusion reactors, rocket engines, electronic heat sinks, space control systems, etc.), it is necessary to understand the non-uniform or single-side heating effect on the resultant inside flow channel heat flux and temperature distributions. Further, the heat transfer in the heated substrate sometimes cannot be decoupled from the heat transfer in the flowing fluid. Hence, this coupling of multiple heat transfer modes (i.e., substrate conduction and fluid flow boiling) in multiple media is called conjugate heat transfer. Since the primary motivation for the present work is high heat flux removal from single-side heated flow channels for plasma facing components (PFCs), conjugate heat transfer including flow boiling is important. Since a limited data base [62, 101-102] exists, an additional flow boiling data base with multi-dimensional conjugate heat transfer for non-uniformly heated channels becomes essential to providing the basis for: (1) the optimized and robust design of PFCs, (2) computational fluid dynamics (CFD) validation and comparisons, and (3) single-phase and flow boiling correlation assessment, and if need be modification. The present work is a part of an effort to: (1) make three-dimensional (3-D) local wall temperature measurements as a function of the net outside (or incident) heat flux for non-uniform heated circular cylinder and single-side heated monoblock test sections, (2) determine the 2-D inside flow channel wall temperature distribution, and (3) make qualitative estimates of the 2-D inside flow channel wall heat flux distribution and related boiling curve. In this secition a more detail description of test adjustments, preparation, and assembly (etc.) is given.

17.2 STEADY-STATE EXPERIMENTAL SYSTEM

17.2.1 EXPERIMENTAL INVESTIGATION

The objective of the present work was to conduct steady-state flow boiling experiments in a horizontal flow channel with water as a flowing fluid. The purposes of this experimental

investigation were to: (1) measure the local three-dimensional (3-D) wall temperature distributions for a given net applied heat flux; (2) use the wall temperature measurements to extrapolate the 2-D temperature distribution on the inside wall of the flow channel; (3) estimate the 2-D inside channel wall heat flux distribution; (4) calculate the heat transfer coefficient variation; and, (5) make comparisons of the wall temperature distributions for different flow rates, different exit fluid pressures and as a function of heat flux.

The primary parameters measured during the experiment were: (1) flow rate, (2) exit fluid pressure, (3) local wall temperature, (4) inlet and outlet fluid temperatures, and (5) power input on the test section. Since the complete experimental system is described in Section 11.0 and elsewhere [90], only a summary and other details will be given here.

17.2.2 FLOW LOOP

17.2.2.1 Flow Loop Description and Adjustments

The experimental flow loop was constructed of stainless steel tubing. This loop is a closed flow loop and the exit flow pressure can be operated between 0.1 MPa to 4.0 MPa; and, the mass flow velocity can be set between 0.2 Mg/m²·s to 15 Mg/ m²·s. After the preheater and other controls have been installed, the inlet water flow rate was set. A sketch of the flow loop is shown in Figure 7. The flow loop was designed to deliver an accurate amount of high quality water to the test section. The dionized and degassed water, which is stored in a reservoir, is pumped into the heated copper test section. A damper is connected to the pump to reduce the flow oscillations. The test section is heated by a direct current through a graphite heater which is electrically isolated from the test section. The maximum power available is 300.0 kW. The power system is connected directly from a main 750 kVA power substation via a 480/277 volt, 3-phase feeder. The power supply feeds heater elements in an experimental set-up through a copper bus cabling (bus bar) system. The inlet water temperature, exit flow pressure, flow rate and other major parameters were monitored and measured during the experiment.

17.2.2.2 Test Section (TS) Description

The monoblock and circular cylindrical test sections were fabricated from Type AL-15 Glidcop Grade copper. This grade of copper along with other high temperature grades is candidates for the basic structure of plasma-facing components. The overall length of the test section (TS), including the inlet and outlet reduced diameter sections, is 360.0 mm. The main part of the TSs (available for heating) is 200.0 mm long with an inside diameter of 10.0 mm. The

monoblock TS has a square cross section of 30.0 mm and the circular TS has a circular cross section of outside diameter of 30.0 mm. As shown in Figure 52, the heat flux was applied to the top surface of the monoblock. For the circular TS (see Figure 21) the heat flux was applied to the top half of the TS via five flat heaters [90]. In the present work, the actual directly heated length was 180.0 mm. Forty-eight thermocouples were placed in axial, circumferential and radial locations in either TS (see Figures 52 and 21 and Tables V and VI). The purpose of the four axial locations is to obtain axial temperature distributions for a given applied heat flux. There are three different planes (e.g., planes A1, A2, and A3 in Figures 52 and 21) with embedded thermocouples (TCs) for each nominal (e.g., planes A1, A2, and A3 are displaced 2.0 mm from each other) axial location. In Figures 52 and 21, the A-A axial location has twelve (12) TC wells, with ten (10) wells in plane A1 and one each in planes A2 and A3 which are axially located upstream from the plane A1 by 2.0 mm and 4.0 mm, respectively. The TCs at each axial location gave both radial (three locations for each circumferential location) and circumferential (0, 45, 135, and 180 degrees, for each axial location, where 0 degree correspond to that portion of the plane of symmetry close to the heated surface; See Figures 52 and 21) local wall temperature distributions. The axial, radial, and circumferential local wall temperatures provided a 3-D wall temperature distribution for both monoblock and circular test sections as a function of the applied heat flux and other flow parameters.

17.2.2.3 Instrumentation

In the present experimental setup, forty-eight Type-J micro-thermocouples (0.5 mm in diameter) were embedded into the test section and were used to make measurements of wall temperatures. Other experimental parameters that require accurate control and monitoring are: (1) water flow rates; (2) fluid exit pressure; (3) power supply voltage and current; (4) water quality, which include ph, resistivity, and gas content; (5) pump metering level; (6) overall reservoir temperature; and, (7) test section electrical insulation. Data acquisition LABVIEW software provided a graphical programming environment for data recording. The data could be logged at the ½ second rate, 50.0 msec rate, or on demand.

Table V: Thermocouple Measuring Tip 3-D Geometric Coordinates for the Monoblock Test Section (TS).

Thermocouple Well Identification			Test Section Coordinates					
Axial Coordinate Correction*, D			Circumferential	Radial r (mm)			Axial z (mm)	
D = 4 mm	D = 2 mm	D = 0 mm	ϕ (Degrees)	Close to Fluid/Solid Boundary	Intermediate	Close to Outside Boundary		
TC(Channel/Module)	TC(Channel/Module)	TC(Channel/Module)						
TC45(CH13/3)	TC41(CH9/3)	TC37(CH5/3)	0	7.960	10.854	13.031	z1	49.022-D
TC46(CH14/3)	TC42(CH10/3)	TC38(CH6/3)	0	7.987	10.873	12.881	z2	98.044-D
TC47(CH15/3)	TC43(CH11/3)	TC39(CH7/3)	0	7.946	10.621	12.817	z3	147.066-D
TC48(CH16/3)	TC44(CH12/3)	TC40(CH8/3)	0	8.042	10.815	12.860	z4	196.088-D
TC25(CH24/2)	TC29(CH28/2)	TC33(CH0/3)	45	6.961	8.971	11.005	z1	49.022
TC26(CH25/2)	TC30(CH29/2)	TC34(CH1/3)	45	6.966	8.974	11.012	z2	98.044
TC27(CH26/2)	TC31(CH30/2)	TC35(CH3/3)	45	6.967	8.975	11.005	z3	147.066
TC28(CH27/2)	TC32(CH31/2)	TC36(CH4/3)	45	6.969	8.973	11.011	z4	196.088
TC1(CH0/2)	TC5(CH4/2)	TC9(CH8/2)	135	6.700	9.831	12.856	z1	49.022
TC2(CH1/2)	TC6(CH5/2)	TC10(CH9/2)	135	6.634	9.902	12.856	z2	98.044
TC3(CH2/2)	TC7(CH6/2)	TC11(CH10/2)	135	6.667	9.902	12.910	z3	147.066
TC4(CH3/2)	TC8(CH7/2)	TC12(CH11/2)	135	6.634	9.919	12.892	z4	196.088
TC13(CH12/2)	TC17(CH16/2)	TC21(CH20/2)	180	6.981	9.021	11.019	z1	49.022
TC14(CH13/2)	TC18(CH17/2)	TC22(CH21/2)	180	6.981	8.964	10.984	z2	98.044
TC15(CH14/2)	TC19(CH18/2)	TC23(CH22/2)	180	7.008	9.059	10.951	z3	147.066
TC16(CH15/2)	TC20(CH19/2)	TC24(CH23/2)	180	6.751	9.066	10.951	z4	196.088

Table VI: Thermocouple Wall Geometric Specification for Circular Test Section.

Thermocouple Well Identification			Test Section Coordinates					
Axial Coordinate Correction*, D			Circumferential	Radial r (mm)			Axial z (mm)	
D = 4 mm	D = 2 mm	D = 0 mm	ϕ (Degrees)	Close to Fluid/Solid Boundary	Intermediate	Close to Outside Boundary		
TC(Channel/Module)	TC(Channel/Module)	TC(Channel/Module)						
D3 (CH6/3)	D2 (CH5/3)	D1 (CH4/3)	0	7.204	10.269	12.797	z1	49.022-D
D6 (CH9/3)	D5 (CH8/3)	D4 (CH7/3)	0	7.512	10.670	12.318	z2	98.044-D
D9 (CH12/3)	D8 (CH11/3)	D7 (CH10/3)	0	8.057	9.881	12.191	z3	147.066-D
D12 (CH15/3)	D11(CH14/3)	D10 (CH13/3)	0	8.542	10.966	12.405	z4	196.088-D
B1 (CH12/2)	B2 (CH13/2)	B3 (CH14/2)	45	7.110	8.843	10.820	z1	49.022
B4 (CH15/2	B5 (CH16/2)	B6 (CH17/2)	45	7.296	9.215	10.845	z2	98.044
B7 (CH18/2)	B8 (CH31/2)	B9 (CH0/3)	45	6.565	8.631	10.893	z3	147.066
B10 (CH21/2)	B11 (CH22/2)	B12 (CH23/2)	45	5.956	8.946	11.081	z4	196.088
A1 (CH0/2)	A2 (CH1/2)	A3 (CH2/2)	135	7.328	9.322	11.892	z1	49.022
A4(CH3/2)	A5 (CH4/2)	A6 (CH5/2)	135	6.901	9.259	12.189	z2	98.044
A7 (CH7/2)	A8 (CH8/2)	A9 (CH6/2)	135	6.722	9.176	11.784	z3	147.066
A10 (CH9/2)	A11 (CH10/2)	A12 (CH11/2)	135	6.641	9.079	12.168	z4	196.088
C3 (CH26/2)	C2 (CH25/2)	C1 (CH24/2)	180	7.328	9.318	11.494	z1	49.022
C6 (CH28/2)	C5 (CH27/2)	C4 (CH29/2)	180	7.328	9.269	11.533	z2	98.044
C9 (CH20/2)	C8 (CH19/2)	C7 (CH30/2)	180	7.078	8.963	11.378	z3	147.066
C12 (CH3/3)	C11 (CH1/3)	C10 (CH16/3)	180	7.14	9.015	11.358	Z4	196.088

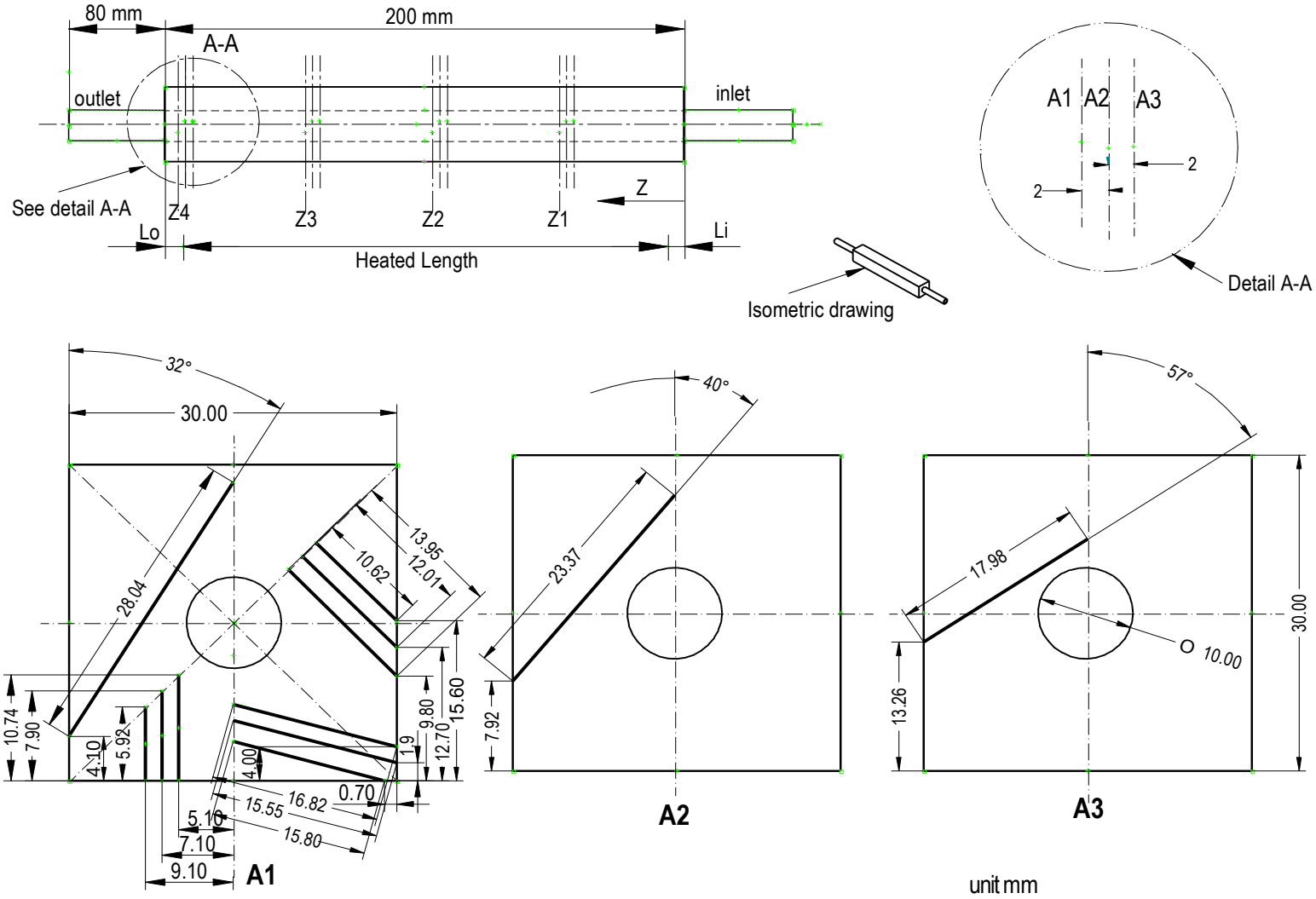

Figure 52: Monoblock Test Section Used for Local Temperature and Heat Transfer Measurements. Water Flows Through the 10.0 mm Diameter Channel. The Thermocouple (TC) Wells are the Solid Black Lines with Specified Lengths and Angles.

17.2.3 TEST PREPARATIONS AND ASSEMBLY

17.2.3.1 Test Preparation:

- Forty-eight thermocouples were calibrated with a precision calibrator to within 0.1 ºC.
- Heater Transition Plate and Test Section (see Figure 43a) were cleaned using 91% alcohol.
- Conductive grease was applied to the Heater Transition Plates and Bus Bars (see Figure 43a) around the holes which were used to connect the resistive heater to the electrical power supply via the bus bar supports.
- The flow rate and exit flow pressure were adjusted to the magnitudes which the test required (see the Flow Matrix in Tables VII and VIII).
- The damper pressure was regulated to minimize the TS exit pressure fluctuations.

17.2.3.2 Assembly (see Figure 43a):

- Electrical cables were connected to the bus bar.
- Aluminum Nitride (AlN), whose width and length are the same as the test sections', is put on the test section.
- The heater was placed on top of the AlN and aligned for the required values of L_o and L_i.
- Two pieces of Mykroy Block were fixed on the top side of each thick end of the heater by applying bolts from the bus bars support (typically, the torque on these bolts is near 25.0 in-lbs (2.82 N-m).
- A piece of Mykroy Block, which has a length which is slightly less than the thin portion of the heater and the same width as the test section, was put on the heater (thin portion).

In order to apply pressure on the heater efficiently, two stainless steel bars, which have same size as the last mykroy block, were applied on top of the mykroy block.

- The Saddle was put above the Test Section and fixed on the Test Bed.
- A small amount of pressure was applied using the heater pressure applicators to the steel bars, the mykroy block, and hence the heater.
- After everything on the heater was aligned, more pressure was applied using each pressure applicator in small increments up to the desired test level.

Table VII: Flow Matrix For Monoblock Test Section (TS #5)

Test #	Volume Flow Rate	Mass Velocity G	Exit Pressure Pexit	Saturated Temp. (C)	L_i (mm)	L_o (mm)	Highest Power Supply Components		Torque on T.S. (In Pounds)	Pressure on T.S. (MPa)	Torque on Heater Ends (In Pounds)	Pressure on Heater Ends (MPa)	Comments
	Gal/min	Mg/sqm s	MPa				Voltage (Volt)	Current (Amp.)					
1	0.75	0.59	0.207	121.04	16.0	4.0	10.1	1298	55	37.5	30	20.4	
2	1.5	1.18	0.207	121.04	16.0	4.0	8.7	1059	55	37.5	30	20.4	Unfinished test, according to heater problem
3	1.5	1.18	0.207	121.04	16.0	4.0	6.8	343	55	37.5	30	20.4	Unfinished test, according to heater problem
4	1.5	1.18	0.207	121.04	16.0	4.0	10.2	1464	55	37.5	30	20.4	The largest difference value between inlet water temp. and outlet water temp. was picked for the highest heat flux.
5	1.5	1.18	0.207	121.04	16.0	4.0	8.0	1190	55	37.5	30	20.4	Unfinished test, according to heater problem
6	1.5	1.18	0.207	121.04	16.0	4.0	10.3	1593	55	37.5	30	20.4	
7	4.0	3.15	0.572	156.94	16.0	4.0	11.1	1701	120	81.8	30	20.4	
8	8.1	6.49	1.190	186.88	10.0	10.0	8.7	1150	120	81.8	30	20.4	Unfinished test, according to heater problem and program problem
9	8.1	6.49	1.190	186.88	10.0	10.0	11.3	1745	120	81.8	30	20.4	Unfinished test, according to heater problem
10	8.1	6.49	1.190	186.88	10.0	10.0	6.8	449	100	68.2	50	34.1	Unfinished test, according to heater problem and program problem
11	10.0	8.01	1.499	198.25	10.0	10.0	9.6	1233	100	68.2	30	20.4	Unfinished test, according to heater problem and program problem
12	9.5	7.61	1.190	186.88	10.0	10.0	12.9	1948	120	81.8	20	13.6	Thermal compound was applied between TS and aluminum nitrid also between aluminum nitrid and heater
13	9.5	7.61	1.190	186.88	10.0	10.0	12.8	1832	120	81.8	20	13.6	Thermal compound was applied between TS and aluminum nitrid also between aluminum nitrid and heater
14	8.0	6.41	0.709	165.49	10.0	10.0	14.0	1062	80	54.5			No thermal compound was applied. *Thin heater*
15	8.0	6.41	0.726	166.41	10.0	10.0	11.6	1757	100	68.2	50	34.1	No thermal compound was applied.
16	6.0	4.8	0.460	148.7	10.0	10.0			90	61.3			

Table VIII: Flow Matrix For Circular Test Section

Test #	Volume Flow Rate	Mass Velocity G	Exit Pressure Pexit	Saturated Temp. (C)	L_i (mm)	L_o (mm)	Highest Power Supply Components		Torque on T.S. (MPa)	Pressure on T.S. (MPa)	Torque on "Turkey" (In Pounds)	Pressure on "Turkey" (MPa)	Comments
	Gal/min	Mg/sqm s	MPa				Voltage (Volt)	Current (Amp.)					
17	0.75	0.59	0.207	121.04	10.0	10.0	3.9	982.0					
18	0.75	0.59	0.207	121.04	10.0	10.0	5.5	1638.0					Continuation of Test 17
19	0.75	0.59	0.207	121.04	10.0	10.0	6.0	1712.0					Continuation of Test 17
20	0.75	0.59	0.207	121.04	16.0	4.0	6.5	2114.0					Thermal & Electrical Insulators installed up and downstream of the TS
21	0.75	0.59	0.563	156.38	16.0	4.0	7.0	2262.0					
22	0.75	0.59	0.932	176.85	16.0	4.0	7.8	2616.0					

- Typically, the testing torque level was near 100.00 in-lbs (11.29 N-m) which transfers a vertically applied force or a total quasi-uniform pressure of 68.15 MPa from each applicator to the heater.
- Heater Transition Plates were fixed on the heater by applying bolts to plate clamps.
- There can be no electrical continuity between saddle, the two bus bar support, the test bed or the test section. The experiment cannot proceed until the discontinuities are assured.

17.2.4 TEST SECTION GEOMETRIC CHARACTERIZATION

17.2.4.1 Monoblock Test Section

Figure 53 shows one axial location for TC wells for all four circumferential locations. Since the TC well in Figure F1 is the one which is closest to the vertical centerline, it is defined as being located at 0 degree. The TC well at the location in Figure F2 is defined as being located at 45 degrees. The TC well at the locations in Figure F3 and F4 are defined as being located at 135 and 180 degrees, respectively. The radial coordinate is the distance from the flow channel axial centerline to the bottom of the TC wells at the given circumferential location. The radial coordinates were computed from precision TC well lengths supplied by the TS manufacturer (and later verified). A procedure similar to that used by Northcutt [111] was used.

17.2.4.2 Circular Test Section

A similar method was used to define the circumferential and radial coordinates for the circular test section; these specifications were determined by Northcutt [111]. An important correction was made for the parameter D (see Table VI).

17.2.5 EXPERIMENTAL PROCEDURE AND DATA ACQUISITION

17.2.5.1 Experimental Procedure

The procedure described below were the steps for running a test:

1. Assemble the test section and make sure no electrical continuity existed between test section and heater.
2. The entire water system was turned on one hour before the test started.
3. The flow loop was checked for leaks.
4. The flow rate was adjusted for the required rate.
5. Adjust the damper to keep the flow pressure stable.
6. Adjust the exit flow pressure valve to obtain the required flow pressure.

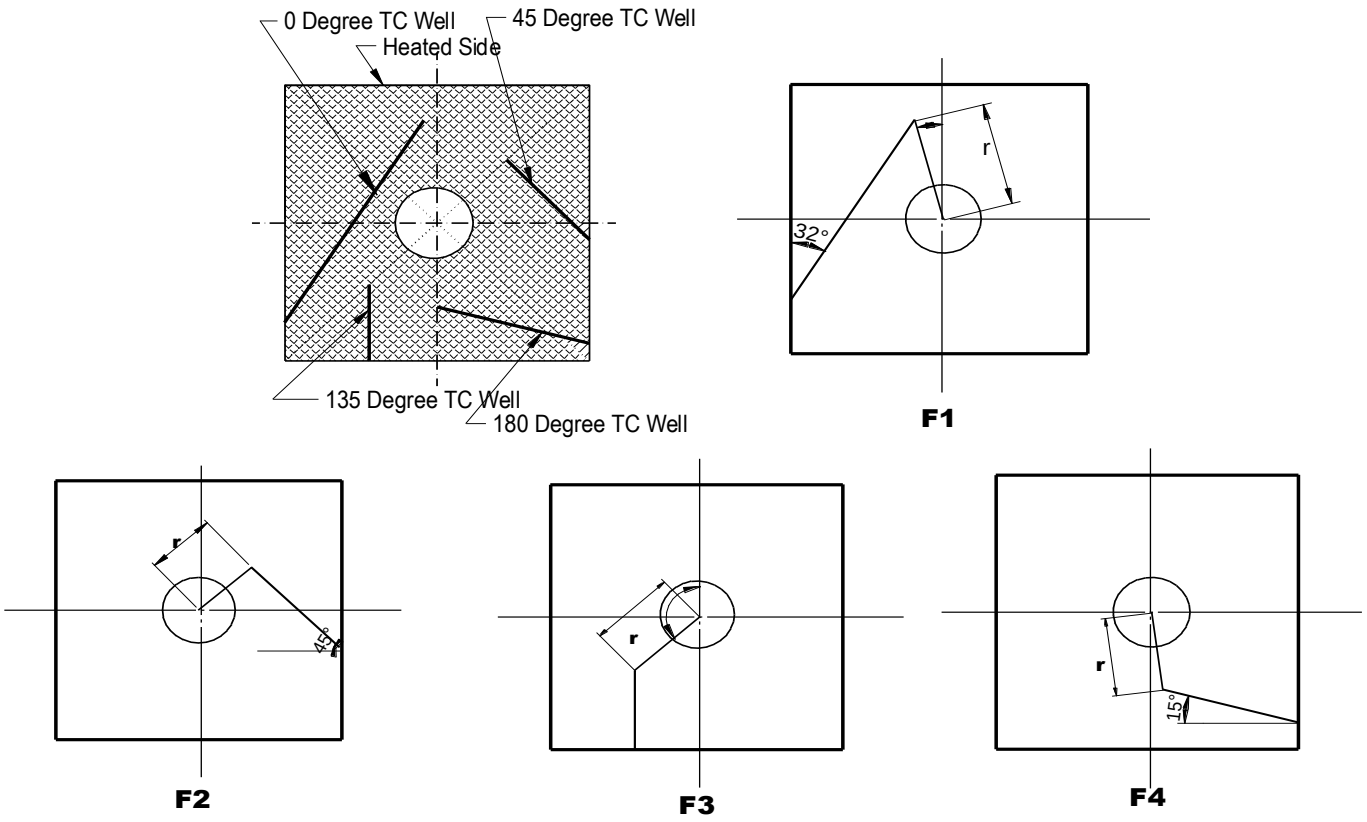

Figure 53: Cross Section of the Monoblock Test Section.

7. The data acquisition system on the computer was turned on and the scan rate was adjusted to the required rate for the test.
8. The data acquisition upper temperature limit was set for accurate TC responses.
9. Record the initial local wall temperature before the power was turned on.
10. Manually record the flow rate (since the flow rate is not in the data acquisition system).
11. The power to the heater was turned on, and then slowly increased to the first voltage (and current) level.

12. In the data acquisition system, all the temperatures of the thermocouple were monitored. Due to the amount of the thermocouples, more attention was paid to some particular channels. For example, the channels at 0 degree which are close to heated boundary and close to fluid where constantly monitored. When these thermocouple temperatures become stable, a steady state was assumed, and the data was recorded.
13. The power was successively increased to the higher levels; and, for each level, steady state and intermediate transient (i.e., between each steady states) were recorded.
14. Before the power was increased, the data acquisition upper temperature limit was increased to maintain accurate TC recordings.
15. During portions of the experiment, special or unique sounds may be heard from the flow loop and test section. Also, a glow may be seen on the heater; so paying attention to the heater and listening for flow loop sounds were essential.

17.2.5.2 Data Acquisition

In each test, forty-eight wall temperatures, reservoir and heat exchanger temperatures, the inlet and outlet water temperatures, one exit TS pressure, one inlet TS pressure, the flow rate, power level (i.e. the voltage, current) were recorded. All the recorded data except flow rate, and power supply power (voltage and current) were read and stored in the data acquisition system.

17.2.6 TEST CONDITIONS AND FLOW MATRIX

17.2.6.1 Test Conditions

The monoblock test section was partly heated on the top side of its external square section. The idealization of the monoblock test section would be that it was thermally insulated around the other three unheated outside boundaries. Due to safety factors, the three unheated outside boundaries were exposed to the air. Although it was felt intuitively that the heat losses from the unheated sides were secondary, estimation of these losses showed the losses to be negligible (given below).

In the present work, some experiments were run with the unheated portion length (Lo) = 4.0 mm (see Figure 52) at the downstream end of the test section and unheated portion length (Li) = 16.0 mm at the upstream end of the test section. Some experiments were run with the

graphite heater placed symmetrically on the monoblock test section in the axial direction (Li = Lo = 10.0 mm). The heated TS was cooled by subcooled water flowing in the circular channel with various inlet flow temperatures (from 17 ^{0}C to 90 ^{0}C), mass flow velocities (from 0.59 Mg/m²·s to 8.1 Mg/ m²·s) and exit pressures (from 0.207 MPa to 1.5 MPa).

17.2.6.2 Flow Matrix and the Summary Tables

In the flow matrix (Tables VII and VIII), experimental conditions were detailed for all tests which include four complete tests each for the monoblock and circular test sections as well as other incomplete monoblock TS tests. In the summary tables (Table IX and X), the Reynolds and Prandtl numbers were evaluated at both the film temperature and bulk temperatures; also, the boiling number, onset of nucleate boiling temperature, and onset of fully developed boiling temperature were evaluated at the film temperature. All of the above are listed for all four complete tests for each monoblock and circular test section.

17.2.7 ESTIMATION OF THE MONOBLOCK TS HEAT LOSSES

The monoblock TS heat loss was due to the nature convection, radiation, and conduction (see Fig. 54). The maximum heat loss was estimated to be less than 1.4 % of the total energy transferred to the coolant.

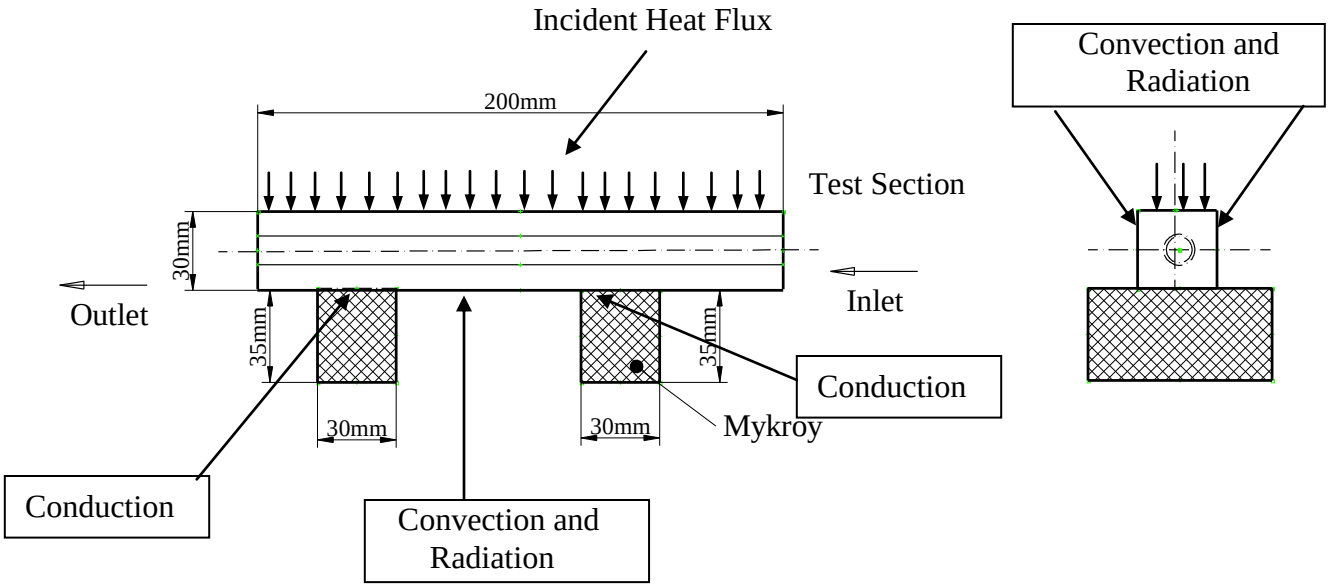

Figure 54: Actual Boundary Condition on Monoblock Test Section.

Table IX: Summary Table for 4 Complete Tests for Monoblock TS #5

Test #	Volume Flow Rate Gal/min	Mass Velocity G Mg/sqm s	Exit Pressure MPA	Saturation Temp (C)	Reynolds Number Evaluated at Bulk Temp.	Reynolds Number Evaluated at Film Temp.	Prandtl Number Evaluated at Bulk Temp.	Prandtl Number Evaluated at Film Temp.	Boiling Number Evaluated at Film Temp.	Tonb @ Tf (C)	Tfdb @ Tf (C)
1	0.75	0.59	0.207	121.04	4900~14700	5000~45000	2.2 ~ 7.0	0.8 ~ 6.8	3.85e-6~9.63e-4	126.35	149.58
4	1.5	1.18	0.207	121.04	9300~24000	9400~72000	2.6 ~ 7.4	0.9 ~ 7.3	1.93e-6~6.17e-4	128.35	153.34
6	1.5	1.18	0.207	121.04	9400~25000	9500~78000	2.4 ~ 7.36	0.9 ~ 7.2	1.93e-6~6.93e-4	128.52	153.59
7	4.0	3.15	0.572	156.94	26000~125000	26000~228000	1.3 ~ 7.1	0.9 ~ 7.1	7.47e-7~5.23e-4	163.98	190.69

Reynolds number, Prandtl number, Boiling number, T_{onb} and T_{fdb} are calculated for Z3, 0 degree location.

Table X: Summary Table for Tests for Circular TS #2

Test #	Volume Flow Rate Gal/min	Mass Velocity G Mg/sqm s	Exit Pressure MPA	Saturation Temp (C)	Reynolds Number Evaluated at Bulk Temp.	Reynolds Number Evaluated at Film Temp.	Prandtl Number Evaluated at Bulk Temp.	Prandtl Number Evaluated at Film Temp.	Boiling Number Evaluated at Film Temp.	Tonb @ Tf (C)	Tfdb @ Tf (C)
23	0.75	0.59	0.207	121.04	4200~10000	4400~29000	2.2 ~ 7.0	0.8 ~ 6.8	3.85e-6~9.63e-4	126.35	149.58
24	0.75	0.59	0.207	121.04	4300~30000	4500~72000	2.6 ~ 7.4	0.9 ~ 7.3	1.93e-6~6.17e-4	128.35	153.34
25	0.75	0.59	0.563	156.38	4000~36000	9500~78000	2.4 ~ 7.36	0.9 ~ 7.2	1.93e-6~6.93e-4	128.52	153.59
26	0.75	0.59	0.932	176.85	3900~14000	26000~228000	1.3 ~ 7.1	0.9 ~ 7.1	7.47e-7~5.23e-4	163.98	190.69

Reynolds number, Prandtl number, Boiling number, Tonb and Tfdb are calculated for Z3, 0 degree location

17.3: EXPERIMENTAL DATA REDUCTION PROCEDURES

17.3.1 OVERVIEW

In the present work, sixteen flow boiling experiments for the monoblock TS were conducted at different flow rates, different exit flow pressures, and different inlet water temperature conditions (see the flow matrix in Table VII). Due to the various reasons (see the comment in Table VII), only four experiments were run to completion. The data from four completed circular TS (see Table VIII) was also analyzed and reduced. In all the experiments, the local wall temperatures were measured at four axial locations, and four circumferential and three radial locations for each axial location. The applied power was varied so that the flow ranged from single-phase to well into the fully-developed, nucleate flow boiling regime. Both unsteady state and steady state data were recorded. As a result, a huge amount of data resulted for each experiment. It was necessary to reduce the data with a minimum amount of analysis. During the calibration of the thermocouples, it was observed that the maximum displayed data acquisition temperature compared best to the calibration temperature. As such, the maximum recorded wall temperatures were used in all reduced data.

During the experiment, the power supply electrical powers (the voltages and currents) were recorded for each steady state heat flux level. Since there were some heat losses between the power supply and the test section, the net incident heat flux (based on the net power transferred to the fluid and the outside heated surface area of the TS) was much less than the actual power input to the heater. The averaged net incident heat flux $\left(q_o^{"}\right)$ was calculated from the average inlet and outlet water temperatures and the outside heated surface area of the test section as follows:

$$q^{"} = \frac{\dot{m}(i_2 - i_1)}{A}, \qquad (17\text{-}1)$$

where $\dot{m}$ is the mass flow rate in kg/s; i_1 and i_2 are the inlet and outlet water enthalpies, respectively; and A_s is the outside heated surface area of the test section, in m^2.

The local (Z location) bulk fluid temperature was calculated from the incident heat flux and the inlet water temperature using and equation similar to equation (14-6) or

$$q_o'' = \frac{\dot{m}(i_l - i_1)}{A_s}$$
$$\Rightarrow i_l = i_1 + \frac{q_o'' \cdot A_s}{\dot{m}} = i_1 + \frac{q_o'' \cdot w \cdot Z}{\dot{m}} \qquad (17\text{-}2)$$

where, i_l is the local bulk enthalpy at the Z location (kJ/kg), *w* is the heated width of the square surface of the test section (m), and Z is the axial distance from the inlet heated point of the test section (m). For the circular test section *w* in equation (17-2) was replaced with $\pi\ r_o$. Then, the local bulk temperature was interpolated from the local bulk enthalpy i_l and used in heat transfer correlations for comparisons with the measured data.

17.3.2 THREE-DIMENSIONAL DATA REDUCTION

The manner in which the steady state data was selected is very important. If the data was selected from the temperature changing period between two different steady power levels, it might show an inaccurate or even a wrong trend.

In order to find out the most representative data from the huge amount of data for each experiment, data reduction approaches were developed and used to estimate the local (2-D) heat transfer coefficient, and the 2-D inside flow channel wall heat flux and wall temperature distributions. To enhance data interpretation, the onset of nucleate boiling wall temperature and the onset of fully developed nucleate boiling wall temperature were computed for all axial and circumferential locations. Data Reduction Approach #1 was the first data reduction method developed. Since some shortcomings were found based on the temperature fluctuations during the quasi-steady state, Data Reduction Approach # 2 was developed and used in this work. Both approaches will be described below.

17.3.2.1 Three-Dimensional Data Reduction Approach #1

Two ways were used to reduce the data for Data Reduction Approach #1. One way (Approach #1.1) was: (1) to select steady state data according to the data print-outs for the steady state local temperature, and (2) go to the data table and find the data line which all or most of the temperatures were the highest temperature during the time period recorded between two power levels. By using this approach, all the steady state temperatures were chosen. This approach was used for Test #1 (see Figures 55 and 56) and Test #4. The advantage of this approach was: it was quick and convenient, and all forty-eight local temperatures could be considered at the same time. The shortcoming to this approach was some steady states might be ignored or missed. As a

note for curiosity at this point, notice the displayed notes in Figure 56 of when sounds were heard from flow loop as the heat flux was increased. It is now felt that some of these sounds are associated with local bubble coalescence.

The other way (Approach #1.2) of selecting steady states was to plot the local wall temperature history (temperature versus time). From the plot, the highest temperatures occurring just before the next power level were chosen for that level's steady state data. The data line number corresponding to the highest temperature was then used for all data at that steady state level. This approach was applied to Test #7 and also to Test #1 (see Figures 57 and 58). The virtue of this approach was all the steady states' data could be found out easily. The disadvantage of this approach was: it was time consuming and not all forty-eight local temperatures could be considered at the same time.

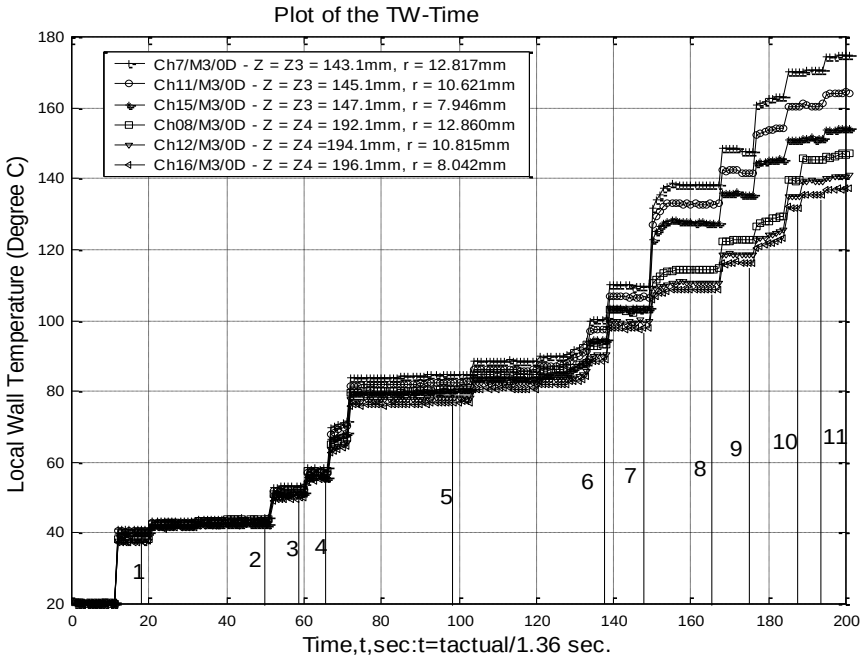

Figure 55: Local Wall Temperature versus Time (Partial History) [First Part] for Test #1 by Approach #1.1 to Selecting Data.

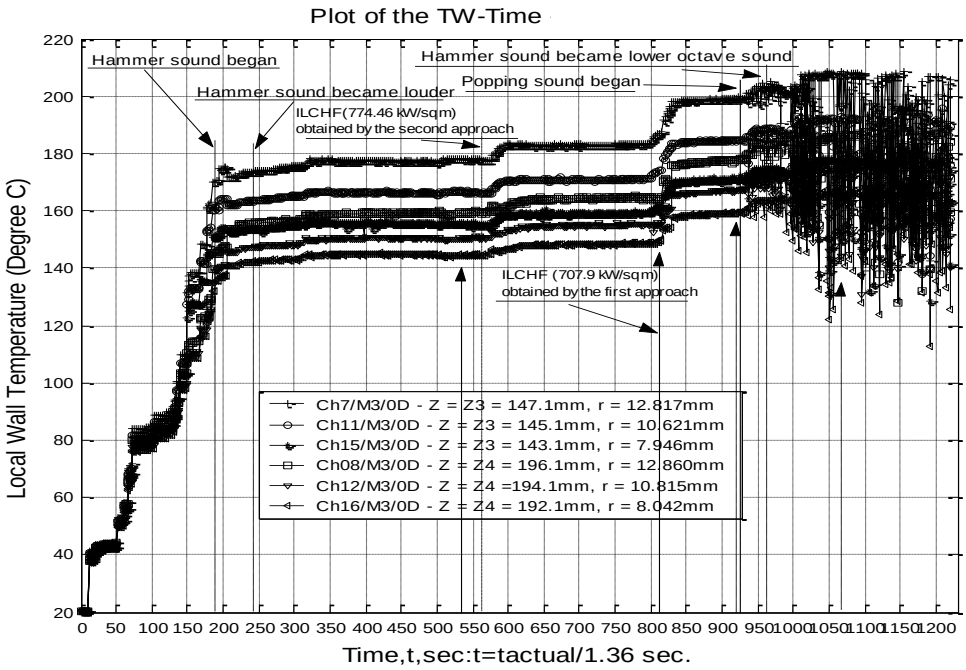

Figure 56: Local Wall Temperature versus Time (Partial History) [Second Part] for Test #1 by Approach #1.1 to Selecting Data.

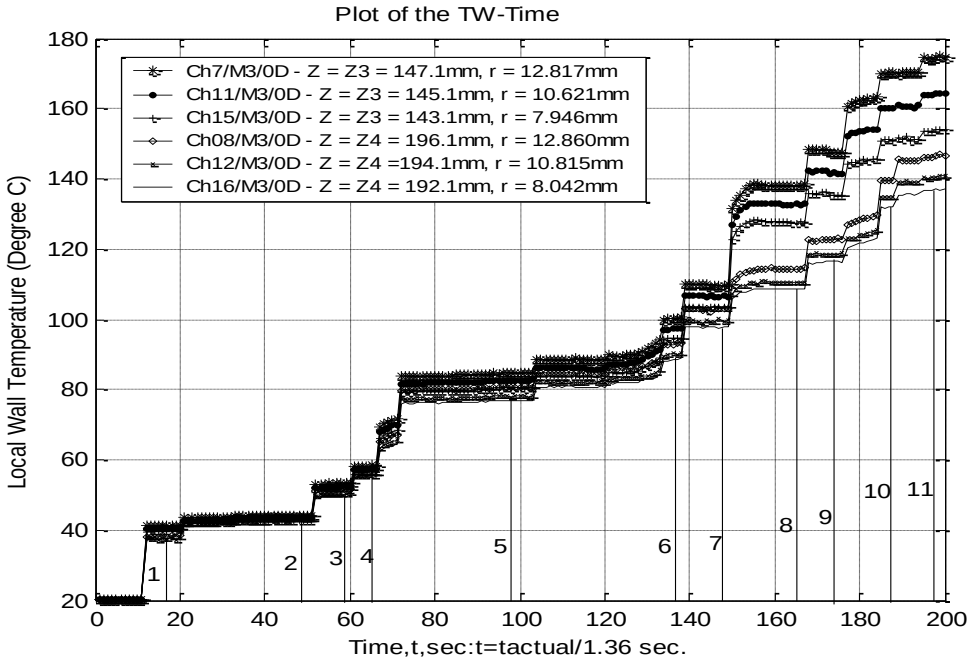

Figure 57: Local Wall Temperature versus Time (Partial History) [First Part] for Test #1 by Approach #1.2 to Selecting Data.

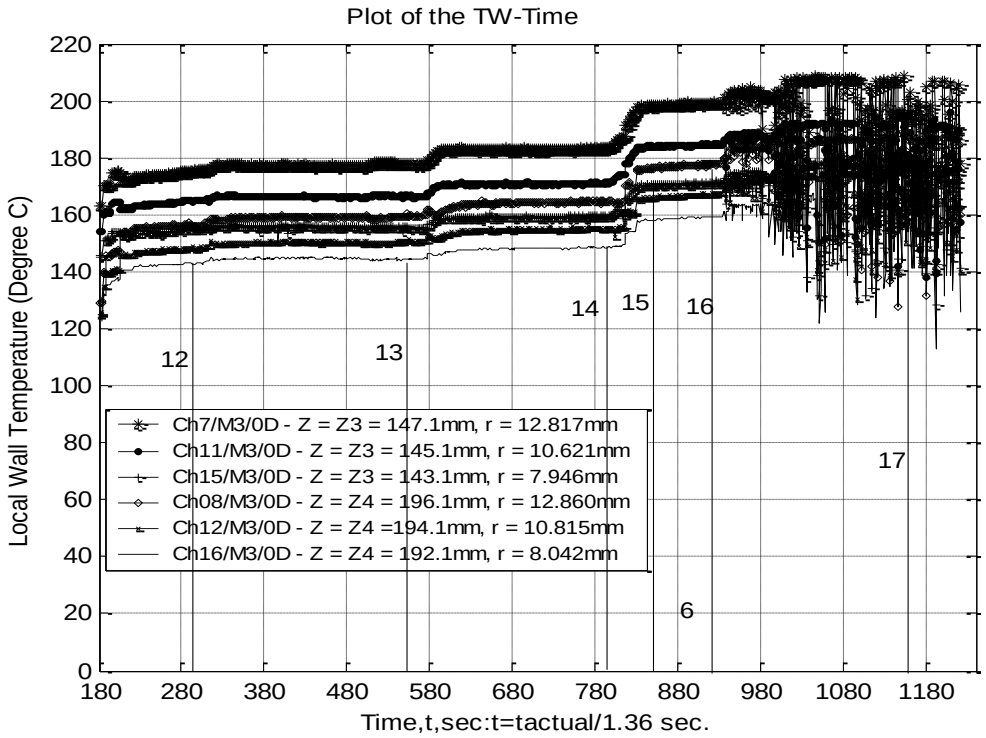

Figure 58: Local Wall Temperature versus Time (Partial History) [Second Part] for Test #1 by Approach #1.2 to Selecting Data.

17.3.2.2 Three-Dimensional Data Reduction Approach #2

Data Reduction Approach #2 was based on steady state identification from: (1) that portion of total incident heat flux (i.e., the average net incident heat flux $\left(q_o^{"}\right)$) which eventually was transferred to the fluid, and (2) the maximum measured wall temperature. During the quasi-steady state, most of the local wall temperatures fluctuated. As a result, it was difficult to choose one data line where all or most channels were at their highest temperature. Consistent with the TC calibration results, this method requires choosing the maximum temperature $\left(Tw_{\max}\right)$ for each channel for that particular steady state. For Test #1, all the data for Z = Z3 and ϕ = 0, 45, 135, and 180 degrees were plotted in Figures 59 through 62. Notice that Approach #2 uses the locus of data formed by a line which is the right-most boundary of the data. As noted above, this boundary (See Figures 59 through 62) was formed by selecting, at each steady state, $Tw_{\max}$ and $q_o^{"}$. Notice from Figures 59 through 62 that one can consistently select this boundary with minimum uncertainty due to judgment. However for inlet and outlet bulk temperatures, the

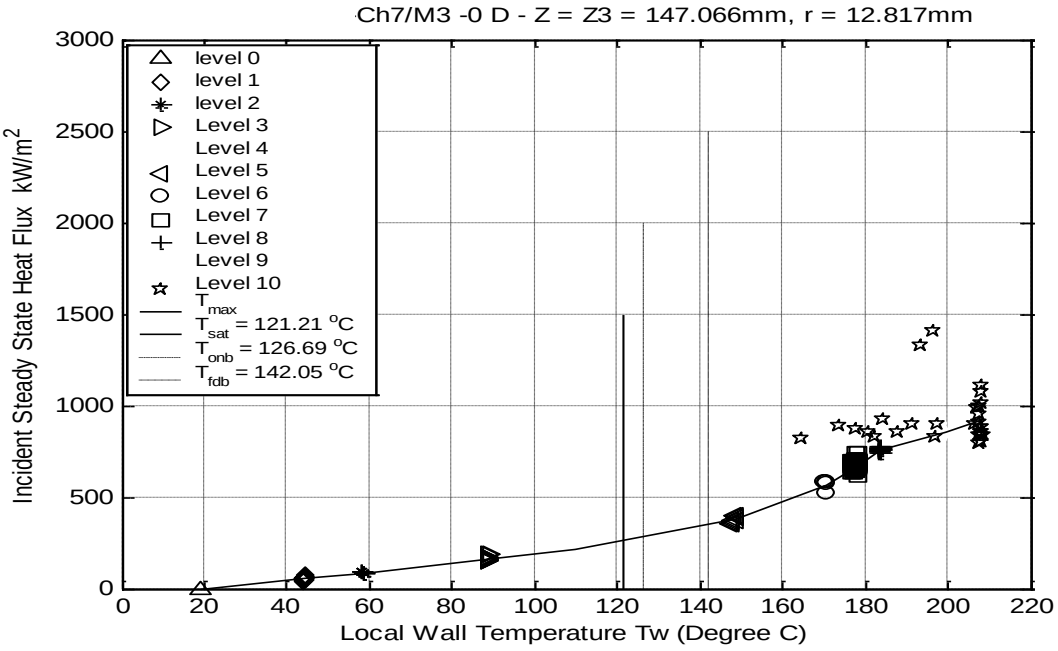

Figure 59: Local Wall Temperature versus Average Net Incident Steady State Heat Flux for Test #1 at 0 Degree, Z3 by Approach #2 to Selecting Data.

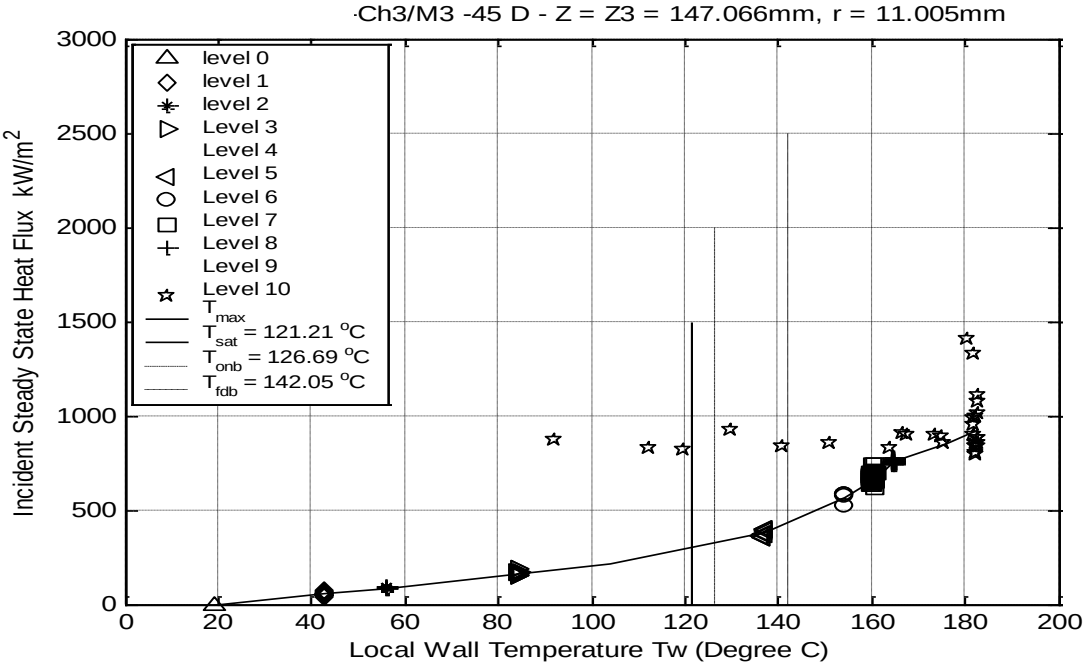

Figure 60: Local Wall Temperature versus Average Net Incident Steady State Heat Flux for Test #1 at 45 Degree, Z3 by Approach #2 to Selecting Data.

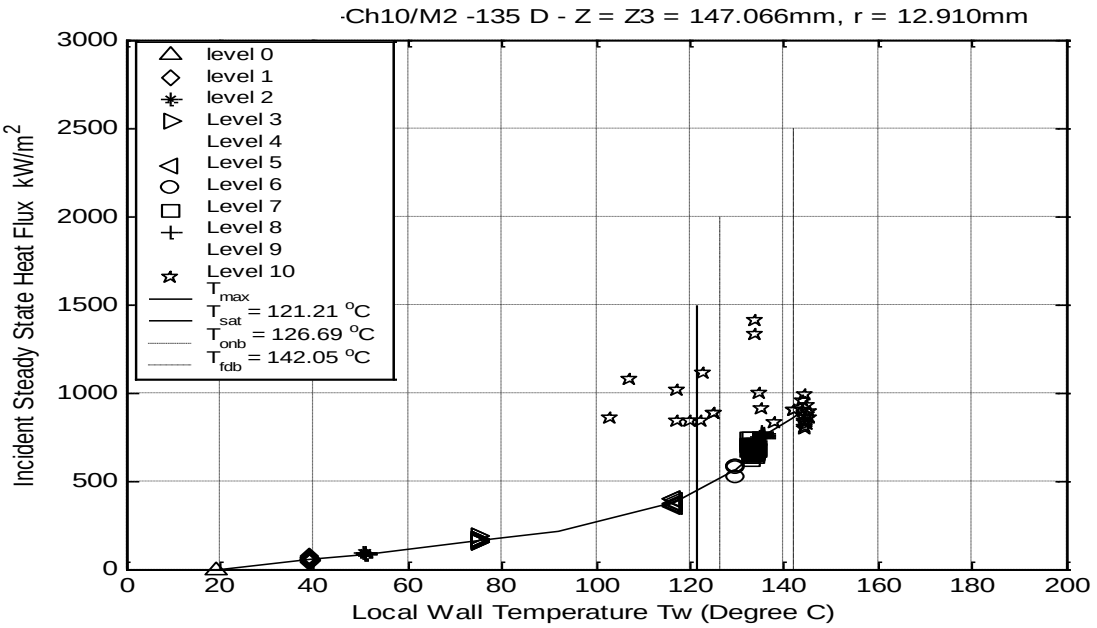

Figure 61: Local Wall Temperature versus Average Net Incident Steady State Heat Flux for Test #1 at 135 Degree, Z3 by Approach #2 to Selecting Data.

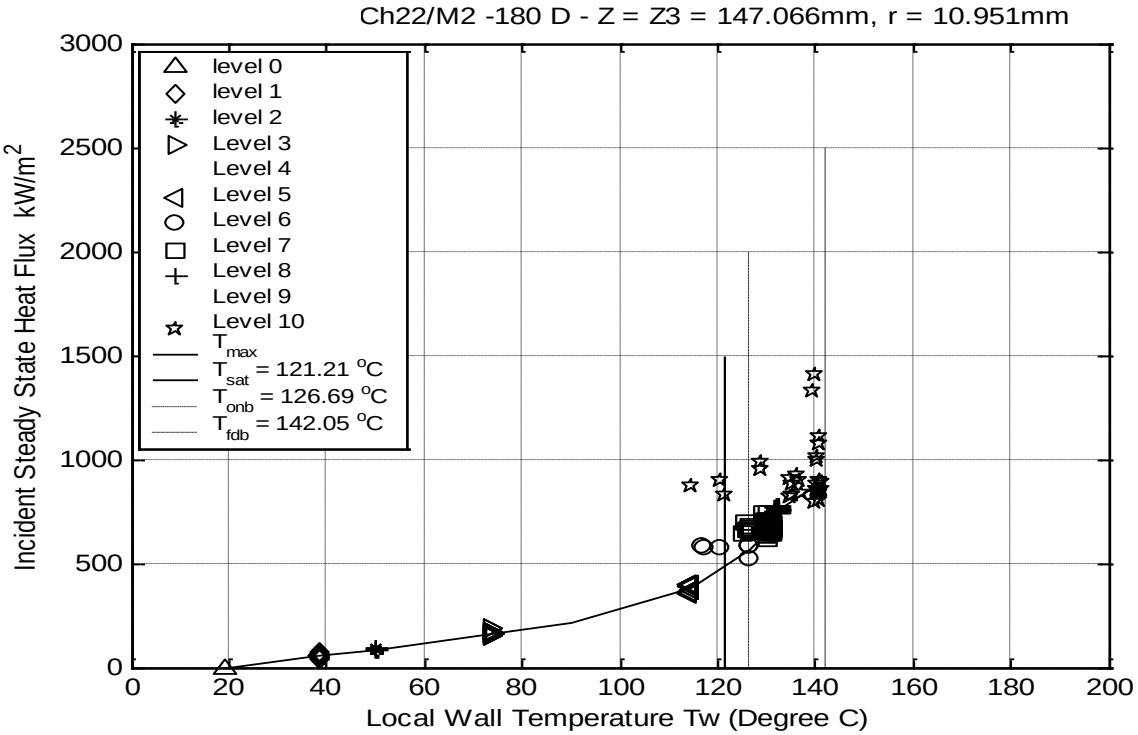

Figure 62: Local Wall Temperature versus Average Net Incident Steady State Heat Flux for Test #1 at 180 Degree, Z3 by Approach #2 to Selecting Data.

average values were used for the inlet and outlet water temperatures to calculate the average net heat flux $\left(q_o^{"}\right)$ transferred to the fluid for each steady state. In the present work, Approach #2 was used for all the data reduction.

17.3.3 DATA CORRECTION DUE TO AXIAL LOCATION

In both the monoblock and circular test sections for each nominal axial location, three different planes have embedded thermocouples (e.g., see planes A1, A2, and A3 in Figures 52 and 43a). At 0 degree for example, the thermocouple which is: (1) close to the fluid is in plane A3 or at an axial location of Z4 – 4 mm, and (2) at the intermediate location is between the TC close to fluid and the TC close to the outside boundary and at an axial location of Z4 – 2 mm (plane A2 in Figures 52 and 21). In Table V, the parameter D is the axial correction distance that is used to correct TC measurements made in e.g. planes A2 or A3 (or similar planes; e.g., planes B2 and B3) to plane A1 (or e.g., B1). In this work, all the data from these two planes (or analogous planes) were corrected to the Z4 location (or other analogous locations, e.g., Z1, Z2 or Z3) using a linear interpolation over a distance of 2 mm or 4 mm between axial TC measurements which are 49 mm apart. So, the correction distance for the axial location is a small percentage (< 8.2 %) of the axial TC separation.

17.3.4 INSIDE WALL TEMPERATURE EXTRAPOLATIONS

Due to the difficulties of putting thermocouples at the flow channel surface, the temperatures at the inside wall were not measured. How to find the inside local wall temperature based on the measured temperatures becomes essential. Using local wall temperature measurements to extrapolate the two-dimensional inside flow channel wall temperature (T_{wi} (ϕ, Z) = T_w ($r = r_i$, ϕ, Z)) was found to be the only simplistic method. Other investigators (e.g., [96, 109]) used an inversed conduction approach to determine T_{wi} (ϕ). However, no investigators have determined T_{wi} (ϕ, Z) which is determined in this work. Since the extrapolation is over less than ~3 mm, it is felt that this approach is satisfactory. After several different extrapolation methods were tested, the method below was found to be the most suitable one.

To summarize, a fifth-order polynomial was used with five unknown constants (a, b, c, d, and e). For given circumferential and axial locations, three local (radial) TC temperature measurements (e.g., T_{w1} @ $r = r_1$, T_{w2} @ $r = r_2$, and T_{w3} @ $r = r_3$) were made (i.e. close to outside boundary, intermediate location and close to the fluid, respectively) and hence provide three conditions for the unknown constants. The remaining two conditions were provided by

computing the two radial temperature slopes $\left(\left.\frac{\partial \mathrm{T}}{\partial r}\right|_{r=r_4} \text{ and } \left.\frac{\partial \mathrm{T}}{\partial r}\right|_{r=r_5} \right)$ at the mid-points (r = r_4 and r = r_5) between the three radial TC measurements. The result is as follows:

$$T_{w1} = a \cdot r_1 + b \cdot r_1^{\,2} + c \cdot r_1^{\,3} + d \cdot r_1^{\,4} + e \cdot r_1^{\,5};$$

$$T_{w2} = a \cdot r_2 + b \cdot r_2^{\,2} + c \cdot r_2^{\,3} + d \cdot r_2^{\,4} + e \cdot r_2^{\,5};$$

$$T_{w3} = a \cdot r_3 + b \cdot r_3^{\,2} + c \cdot r_3^{\,3} + d \cdot r_3^{\,4} + e \cdot r_3^{\,5}; \tag{17-3}$$

$$\left.\frac{\partial T_4}{\partial r_4}\right|_{r_4 = r_1 + \frac{(r_2 - r_1)}{2}} = a + 2 \cdot b \cdot r_4 + 3 \cdot c \cdot r_4^{\,2} + 4 \cdot d \cdot r_4^{\,3} + 5 \cdot e \cdot r_4^{\,4} = \frac{(T_{w2} - T_{w1})}{(r_2 - r_1)}; \tag{17-4}$$

$$\left.\frac{\partial T_5}{\partial r_5}\right|_{r_5 = r_2 + \frac{(r_3 - r_2)}{2}} = a + 2 \cdot b \cdot r_5 + 3 \cdot c \cdot r_5^{\,2} + 4 \cdot e \cdot r_5^{\,3} + 5 \cdot e \cdot r_5^{\,4} = \frac{(T_{w3} - T_{w2})}{(r_3 - r_2)}; \tag{17-5}$$

$$T_{wi} = a \cdot r_i + b \cdot r_i^{\,2} + c \cdot r_i^{\,3} + d \cdot r_i^{\,4} + e \cdot r_i^{\,5};$$

where, T_{w1}, T_{w2}, and T_{w3} were the measured local wall temperatures close to fluid, at the intermediate location, and close to the outside boundary, respectively. Further, r_1, r_2, and r_3 were the radial locations for the thermocouples close to the fluid, at the intermediate location, and close to the outside boundary, respectively. MATLAB programs were developed and used to do all the extrapolations for eight completed tests (four for the monoblock TS and four for the circular TS) in this work.

17.3.5 QUALITATIVE ESTIMATES OF THE INSIDE FLOW CHANNEL WALL HEAT FLUX

The inside flow channel wall heat flux was calculated based on thermal conduction in the monoblock and circular test sections from the measured wall temperatures close to the fluid location and the extrapolated inside flow channel wall temperatures; i.e.,

$$q_i'' = k\frac{\Delta T}{\Delta r} = k\frac{(T_{w1} - T_{wi})}{r_1 - r_i} \tag{17-6}$$

Using a plot from the manufacturer [112] of the Glidcop copper used for the test sections, the following equation was obtained for the temperature dependence of *k*,

$$k = -\frac{3}{25}T + 367.4 \tag{17-7}$$

where, *k* is the thermal conductivity for the test section (W/m·K) and T (in ^{o}C) is the local wall temperature. In equation (17-7), the monoblock test section's thermal conductivity k was evaluated at the mean value of the inside flow channel wall temperature T_{wi} and the measured wall temperature (T_{w1}) close to the fluid location.

From the magnitudes of the k and the difference of T_{w1} and T_{wi} (i.e., ΔT), a relatively small inaccuracy in T_{wi} or T_{w1} will result in a much greater magnitude change for q_i''. At this point, the accuracy of the inside flow channel wall heat flux is decided by the accuracy of the extrapolated data and the measured temperature, $T_{w1.}$

Twelve thermocouples shown in Table XI were located at 0 degree and the four axial locations. Since the inside wall temperature is limited to the extrapolation method, the difference between T_{w1} and T_{wi}, is: (1) 0.76 ^{o}C for the Z_4 (= 196.1 mm) location which was much smaller than 14.06 ^{o}C for the Z_2 (= 98.0 mm) location. This results in a huge difference (88.4 kW/m^2 at Z_4 compare to 1668.9 kW/m^2 at Z_2) for the inside flow channel wall heat flux between two locations. Another practical explanation for the low value of q_i'' at Z_4 is the heater was not directly over (but slightly upstream) the Z_4 location for some tests (see Tables VII and VIII). Further, the corresponding values of ΔT at Z_1 (= 49.0 mm) and Z_3 (= 147.1 mm) are comparable to the value for Z_2.

Table XI: Calculation Examples for Extrapolated Data and Inside Wall Heat Flux for Test #4.

Net Average Incident Heat Flux kW/m² *(Inlet water temp. / Outlet water temp. (˚C))*	Thermocouple Well Identification				Extrapolated Inside Wall Temperature @ Z, T_{wi} (˚C)	Extrapolated Temp. to Z from (˚C)		Measured Wall Temperature @ Z, close to Outside Boundary T_{w3}	Extrapolated Local Thermophysical Results and Properties for Z	
	Axial Coordinate Correction, D			Axial, Z (mm)		Close to Fluid @ Z - 4, T_{w1}	Intermediate @ Z - 2, T_{w2}		Thermal Conductivity k (W/m K)	Inside Heat Flux, q_i (kW/m²)
	D =4mm	D =2mm	D =0mm							
600.5 *(22.169 /30.078)*	TC45	TC41	TC37	49.0-D	107.1	118.75	130.15	102.616	353.85	1392.7
	TC46	*TC42*	*TC38*	*98.0-D*	*120.91*	*135.07*	*144.7*	*150.547*	*352.04*	*1668.9*
	TC47)	TC43	TC39	147.1-D	130.61	136.87	144.15	153.473	351.35	746.59
	TC48	*TC44*	*TC40*	*196.1-D*	*114.17*	*114.93*	*122.4*	*134.249*	*353.65*	*88.355*

17.4 STEADY-STATE EXPERIMENTAL RESULTS

17.4.1 OVERVIEW

In the present work, four monoblock test section experiments were completed and were analyzed along with four circular test section experimental data. In all cases, flow rate, average net incident heat flux $\left(q_o^{"}\right)$, and exit pressure were parameters for these steady state experiments. Local (3-D) wall temperature measurements were made and used to determine the 2-D distributions for the flow channel inside: (1) wall temperature, (2) heat flux, (3) heat transfer coefficient, and (4) $q_o^{"}$ vs $T_{w_{\max}}$ relationship.

In this work, the idealization of the one-side heated monoblock and circular test sections was: (1) a constant heat flux is applied to the top side (e.g. see Figures 52 and 21) of the test section, and (2) the remaining sides (or side) were perfectly insulated. Due to the safety factors, the unheated outside boundary was exposed to the ambient air from each side and to the Mykroy (an insulator; k (1.32 W/mk) and air on the bottom (e.g., see Figure 54). This resulted in heat losses from the TS due to the natural convection, radiation and conduction to the surroundings. In addition, there were energy losses via axial conduction to the flow loop. The total heat losses to the surroundings (neglecting axial conduction) were estimated as follows:

At lower heat fluxes, the total heat loss was the 1.32 percent of $q_o^{"}$; and,

At highest heat fluxes, the total heat loss was the 0.89 percent of $q_o^{"}$.

From the above, the heat losses from the TS to the surroundings were neglected.

17.4.2 THREE-DIMENSIONAL WALL TEMPERATURE DISTRIBUTIONS

17.4.2.1 Circumferential (ϕ) Variations:

17.4.2.1-1 Monoblock Test Section Results

The circumferential wall temperature (Tw) variations for the monoblock test section are presented in Figures 63 and 64. These two figures were based on the data from Test #1 (at mass flow velocity of 0.59 Mg/m2s, and exit flow pressure 0.207 MPa). There were a total of ten levels shown of the one side averaged net incident heat flux $\left(q_o^{"}\right)$. These figures show T_w variations close to fluid boundary and outside heated boundary, respectively; and, they also show the local temperature decreases as the circumferential coordinate increases. The circumferential coordinate measurement locations are defined on Figure 65. Figure 64 ($Z = Z_3$) shows that the 0 degree TC wells were closest to the heated side of the test section and channel 5 in module #3 [see Table V] was closest to the heated side at 0 degrees; but in Figure 66 ($Z = Z_1$), the temperature of a similar channel was lower than that at $\phi = 45$ degrees. So there might have been either something wrong with that channel or end effects may have reduced that temperature. However one must also note that for all circumferential plots, the axial coordinate was constant (i.e., the axial correction was applied); but, the radial coordinate did vary slightly from one circumferential data point to the other. The 180 degree TC wells were the farthest away from the heated side of the test sections. Since there were only four circumferential locations in the test section, the figures do not show the exact local circumferential slopes but the trends for these four locations were evident. Further the actual profiles were enhanced when one used the boundary conditions which requires the slopes of the profiles to be zero at both $\phi = 0$ and 180 degrees.

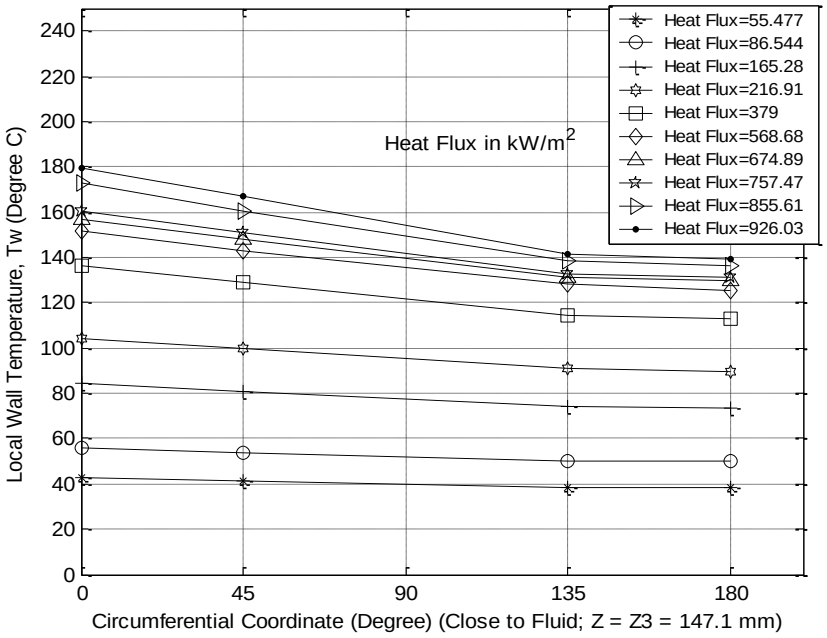

Figure 63: Monoblock Test Section Local Wall Temperature Circumferential Profiles from the Thermocouples Close to the Fluid/Solid Boundary (see Table V) as a Function of the Net Incident Heat Flux, at Z = Z3, with G = 0.59 Mg/m^2s, and P_{exit} = 0.207 MPa (T_{sat} = 121.0 ^oC).

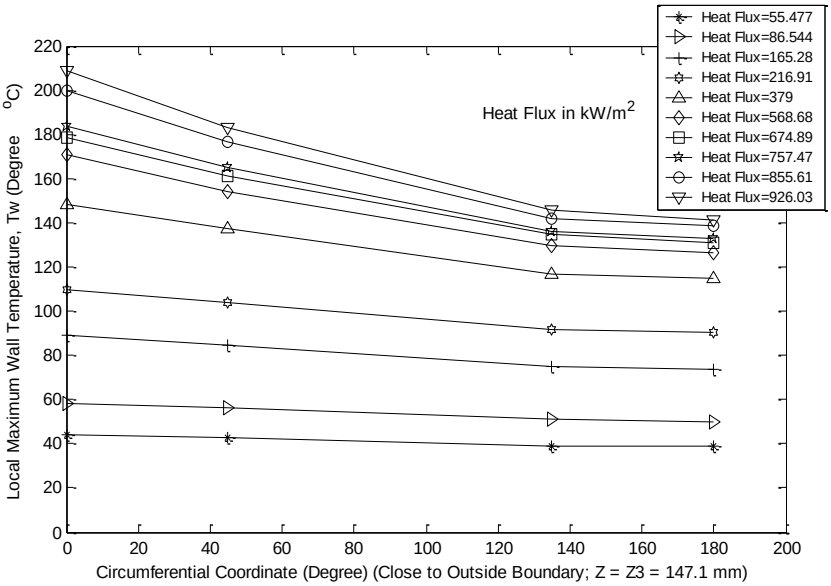

Figure 64: Monoblock Test Section Local Wall Temperature Circumferential Profiles from the Thermocouples Close to the Heated Boundary as a Function of the Net Incident Heat Flux at, Z = Z3 with G = 0.59 Mg/m^2s, and P_{exit} = 0.207 MPa (T_{sat} = 121.0 ˚C).

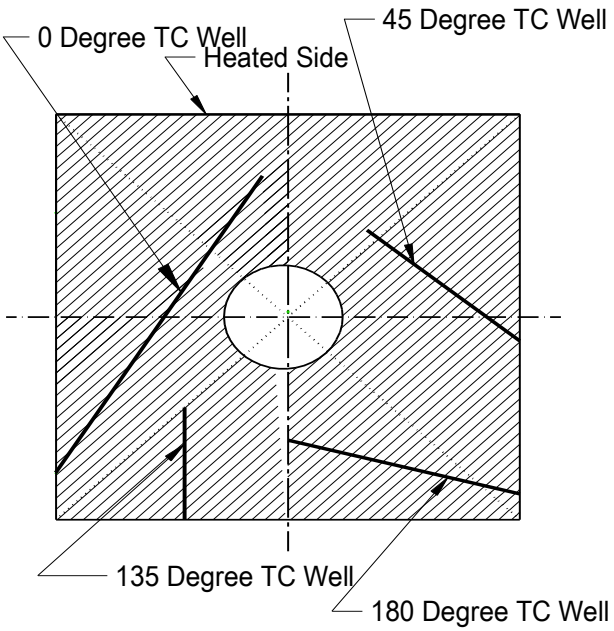

Figure 65: Cross Section of the Monoblock Test Section. See Figure 52 for the Two Additional Cross Sections (e.g. for planes A2 (D = 2 mm) and A3 (D = 4 mm).

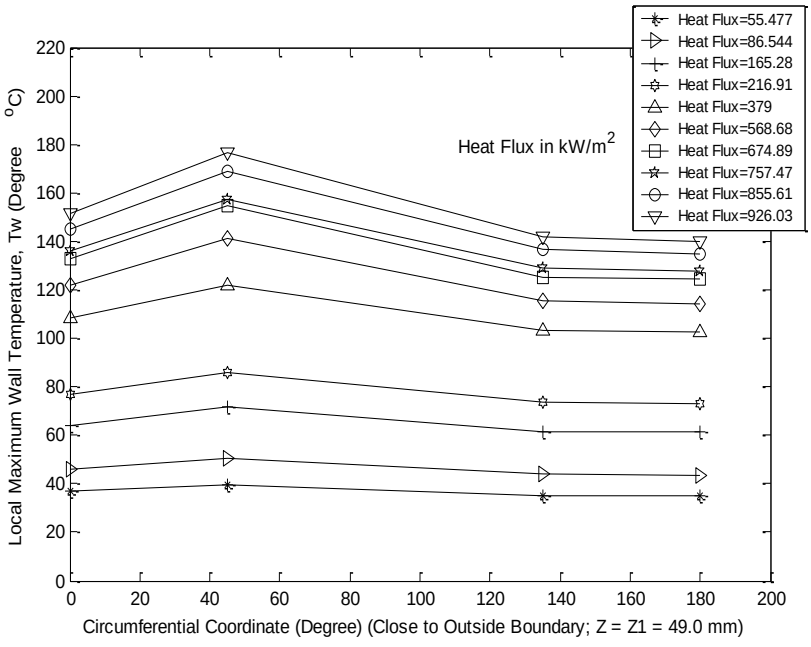

Figure 66: Monoblock Test Section Local Wall Temperature Circumferential Profiles from the Thermocouples Close to the Heated Boundary as a Function of the Net Incident Heat Flux, at Z = Z1 with G = 0.59 Mg/m^{2}s, and P_{exit} = 0.207 MPa (T_{sat} = 121.0 ˚C).

Figures 67 and 68 clearly show the relation between mass velocity and the monoblock circumferential wall temperature variations close to fluid/solid boundary. Figure 67 shows the comparisons for the local wall temperature at different circumferential coordinates for mass velocities of 0.59 Mg/m2·s (Test #1) and 1.18 Mg/m2·s (Test #4). As the mass velocity increases, the temperature differences among the four circumferential locations increases. This is proved in Figure 68. During Test #7 (G = 3.15 Mg/m^2s, P_{exit} = 0.572 MPa and T_{Sat} = 156.9 ˚C), there was a man-made or operational mistake made by those conducting the test in which the temperature limit of Module #2 was not changed as the temperature increased. As a result, all the 45- degree channel temperatures erroneously remained the same when the heat flux exceeded 1220.5 kW/m^2. Consequently, the last five points at ϕ = 45 degree in Figure 68 were not connected to the other points at ϕ = 0 and 135 degrees. Fortunately, the 0 degree thermocouple channels were in Module #3 where the temperature limit was changed.

The relationship between mass velocity and monoblock circumferential wall temperature, at the intermediate and close to outside heated boundary locations have the same trend as the circumferential wall temperature closest to fluid/solid boundary as outlined above. These trends are showed in Figures 69, 70, 71, and 72.

17.4.2.1-2 Circular Test Section Results

The circumferential variation for circular TS is much similar to the one for monoblock TS (e.g., see Figures 23, 44, 49, and 63-72).

17.4.3 Radial Variations

17.4.3-1 Monoblock Test Section Results

Radial local monoblock test section wall temperature variations at ϕ = 0 degree are shown in Figure 73. In all cases, the value of the local wall temperature at r = r_i = 5 mm was extrapolated over a distance of between 1.4 mm and 3.0 mm to the inside wall of the flow channel. The figure shows that small to moderate variations (5 – 25 ^oC) resulted when the radius varied from approximately to 7.95 mm to 12.82 mm which is the radial range for the TC TS wall measurements. As noted, this difference increased as the heat flux increased and became larger (as high as 50 ^oC as G increased) when projected to the inside wall of the test section.

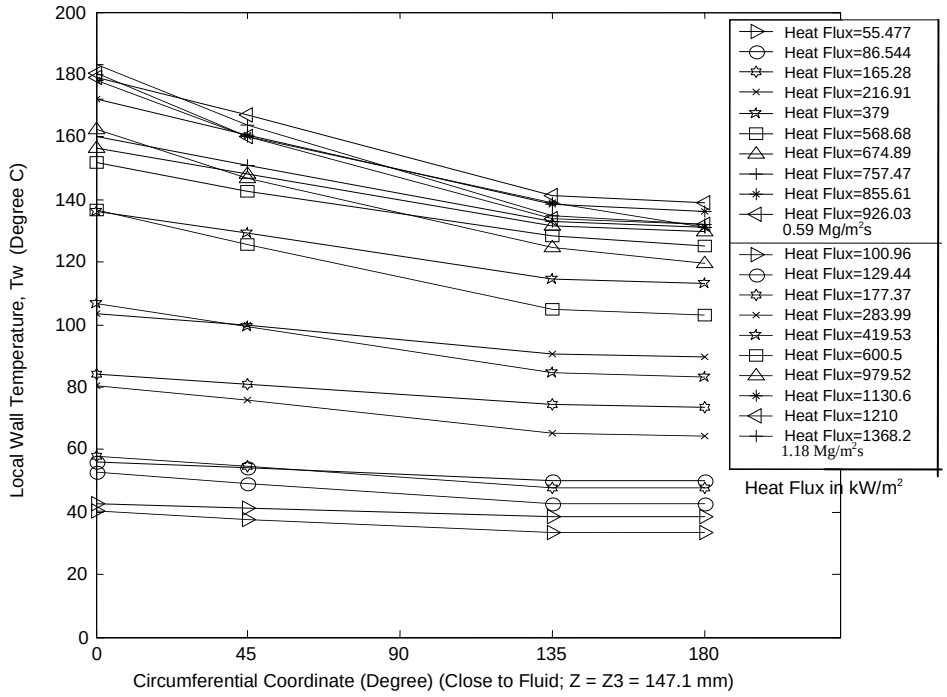

Figure 67: Comparison of the Monoblock Test Section Local Wall Temperature Circumferential Profiles from the Thermocouples Close to the Fluid/Solid Boundary as a Function of the Net Incident Heat Flux, at Z = Z3 with P_{exit} = 0.207 MPa (T_{sat} = 121.0 ˚C) for Different Mass Velocities (for G = 0.59 Mg/m^{2}s and 1.18 Mg/m^{2}s).

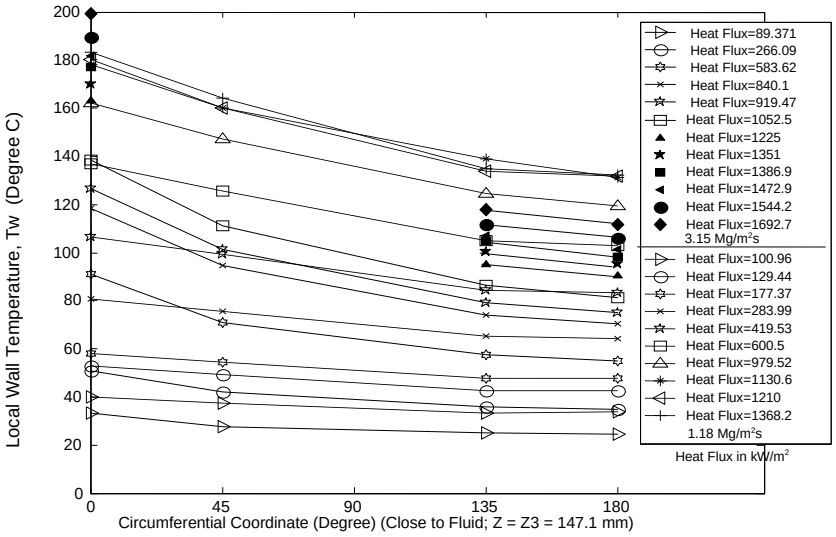

Figure 68: Comparison of the Monoblock Test Section Wall Temperature Circumferential Profile from the Thermocouples Close to the Fluid/Solid Boundary as a Function of the Net Incident Heat Flux, at Z = Z3 for Different Mass Velocities: G = 3.15 Mg/m^{2}s with P_{exit} = 0.572 MPa (T_{sat} = 156.9 ˚C) and for G = 1.18 Mg/m^{2}s with P_{exit} = 0.207 MPa (T_{sat} = 121.0 ˚C).

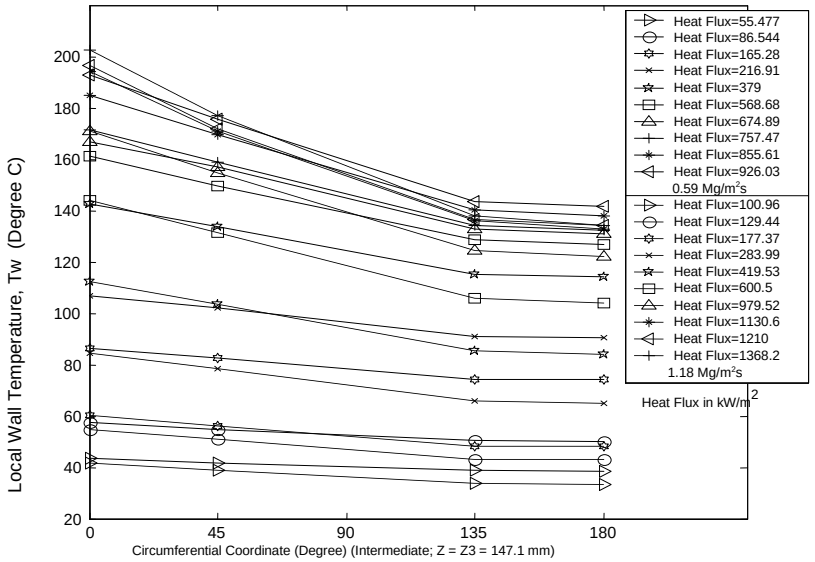

Figure 69: The Comparison of the Monoblock Test Section Local Wall Temperature Circumferential Profiles from the Intermediate Thermocouples as a Function of the Net Incident Heat Flux, at Z = Z3 with P_{exit} = 0.207 MPa, (T_{sat} = 121.0 ˚C) for Different Mass Velocities (for G = 0.59 Mg/m^{2}s and 1.18 Mg/m^{2}s).

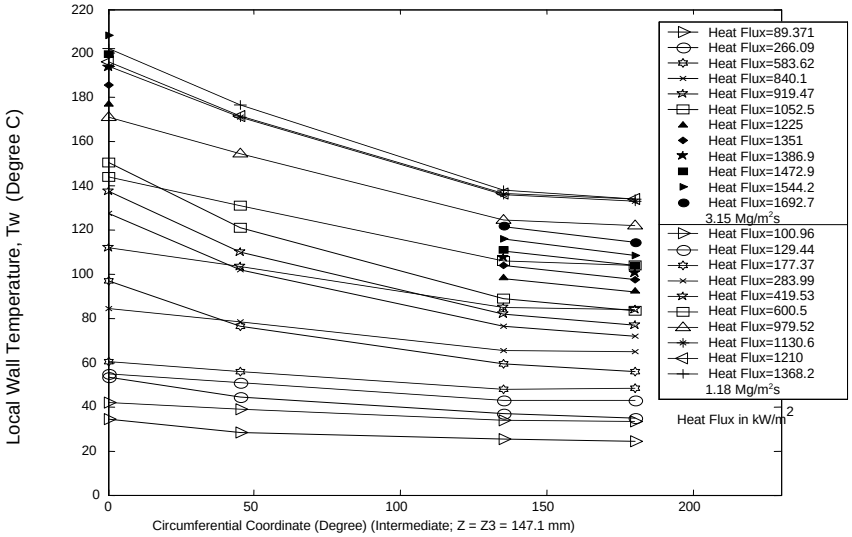

Figure 70: The Comparison of the Monoblock Test Section Wall Temperature Circumferential Profile from the Intermediate Thermocouples as a Function of the Net Incident Heat Flux, at Z = Z3 for Different Mass Flow Velocities: for G = 3.15 Mg/m^{2}s with P_{exit} = 0.572 MPa (T_{sat} = 156.9 ˚C) and for G = 1.18 Mg/m^{2}s with P_{exit} = 0.207 MPa (T_{sat} = 121.0 ˚C).

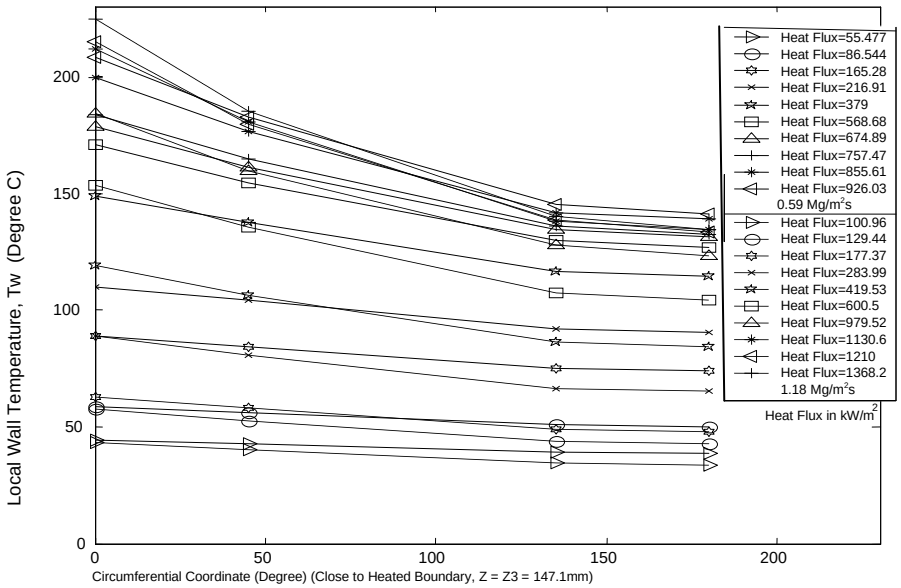

Figure 71: The Comparison of the Monoblock Test Section Wall Temperature Circumferential Profile from the Thermocouples Close to the Outside Heated Boundary as a Function of the Net Incident Heat Flux, at Z = Z3 with P_{exit} = 0.207 MPa, (T_{sat} = 121.0 ˚C) for Different Mass Flow Velocities (for G = 0.59 Mg/m^{2}s and 1.18 Mg/m^{2}s).

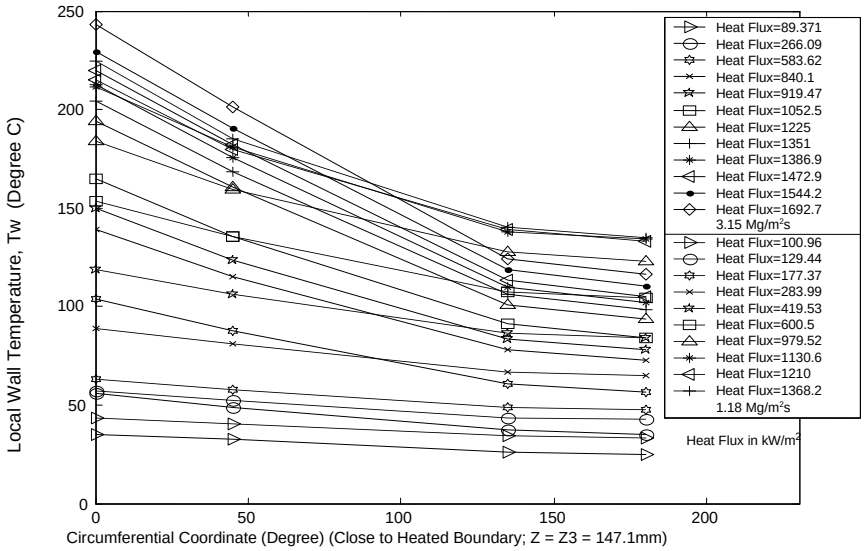

Figure 72: The Comparison of the MonoblockTest Section Wall Temperature Circumferential Profile from the Thermocouples Close to the Outside Heated Boundary as a Function of the Net Incident Heat Flux, at Z = Z3 with P_{exit} = 0.207 MPa, (T_{sat} = 121.0 ˚C) for Different Mass Flow Velocities: for G = 3.15 Mg/m^{2}s with P_{exit} = 0.572 MPa (T_{sat} = 156.9 ˚C) and for G = 1.18 Mg/m^{2}s with P_{exit} = 0.207 MPa (T_{sat} = 121.0 ˚C).

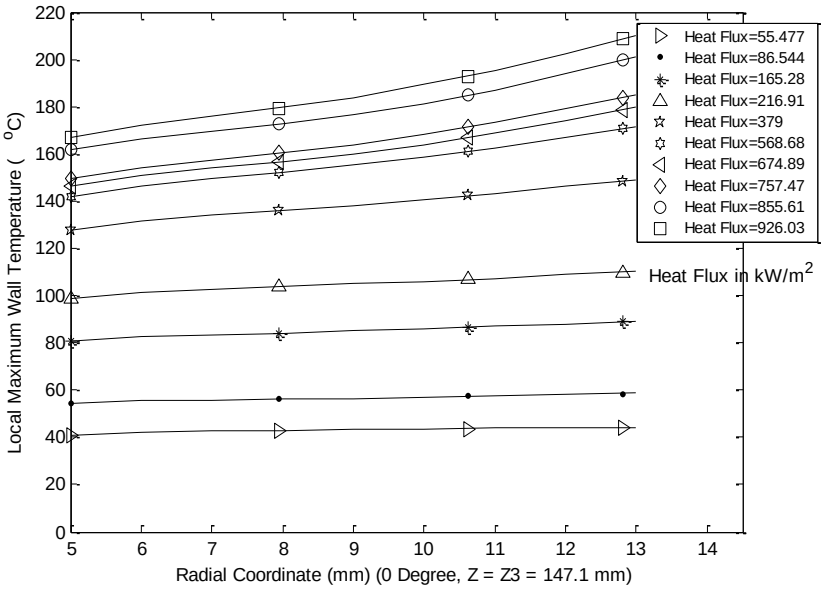

Figure 73: Radial Wall Temperature Profiles for the Monoblock Test Section Flow Channel at ϕ = 0 degree and Z = Z3 = 147.1 mm as a Function of the Net Incident Heat Flux (G = 0.59 Mg/m^2s, P_{exit} = 0.207 MPa, and T_{sat} = 121.0 ˚C).

Further results showing the relation between mass velocity and radial variations are shown in Figures 74 through 75. Figure 74 shows that relation when the mass velocities are at 0.59 Mg/m^2s and 1.18 Mg/m^2s. As expected, the radial variation increased with the mass velocity. This is further shown in Figure 75 where the mass flow velocities are at 3.15 Mg/m^2s and 1.18 Mg/m^2s; but here, the exit pressures were different.

17.4.3.2 Circular Test Section Results

For circular TS, the radial variation is similar to the one for monoblock TS. Figure 76 shows the variation in the radial profile for two different exit pressures (P_{exit} = 0.207 and 0.563 MPa).

17.4.4 AXIAL VARIATIONS

17.4.4.1 Monoblock Test Section Results

Local monoblock test section wall temperature measurements were made at four axial locations (See Figure 52). For all the experiments, the same heater was used. Its length (L) was 180.0 mm (in axial direction) and was placed on the test section (200.0 mm long). There was a

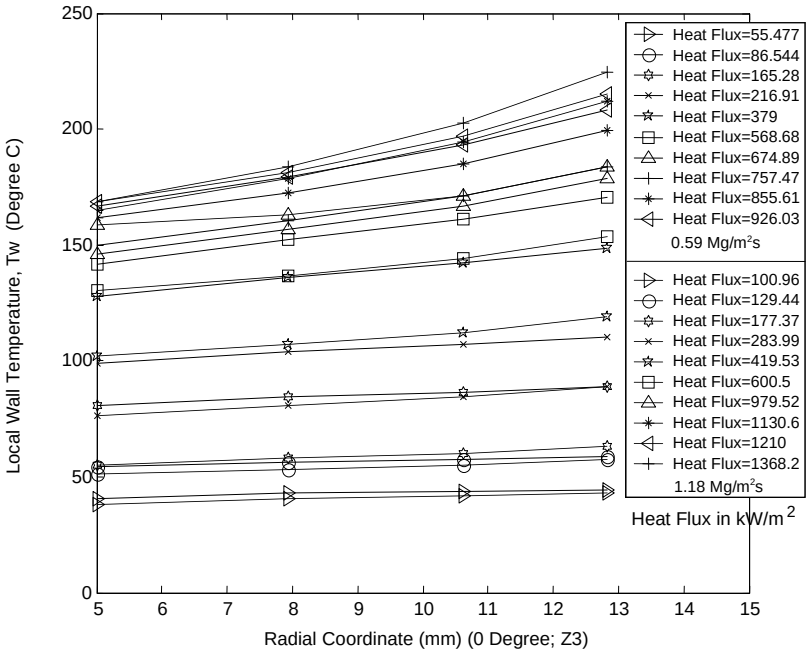

Figure 74: Radial Wall Temperature Profiles for the Monoblock Test Section Flow Channel at ϕ = 0 degree and Z = Z3 = 147.1 mm as a Function of the Net Incident Heat Flux with P_{exit} = 0.207 MPa, (T_{sat} = 121.0 ˚C) at Different Mass Velocities (for G = 0.59 Mg/m^{2}s and 1.18 Mg/m^{2}s).

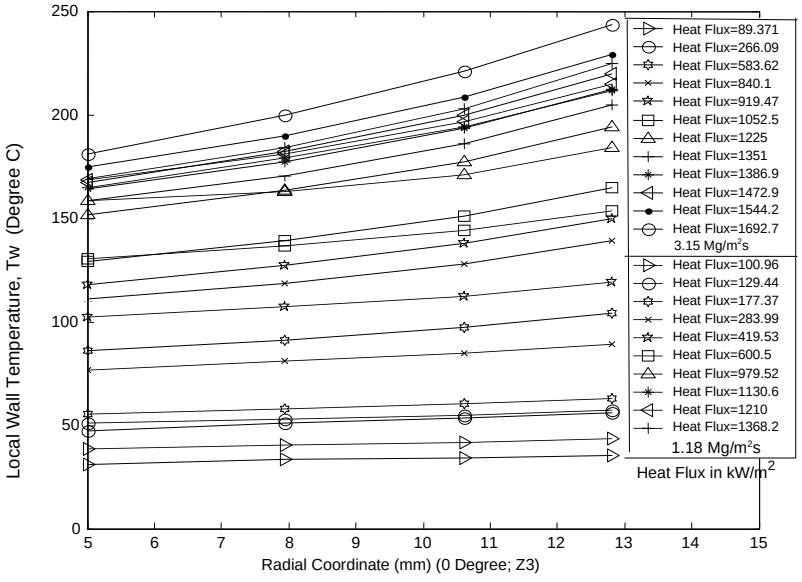

Figure 75: Radial Wall Temperature Profiles for the Monoblock Test Section Flow Channel at ϕ = 0 degree and Z = Z3 =147.1 mm as a Function of the Net Incident Heat Flux at Different Mass Velocities: for G = 3.15 Mg/m^{2}s, with P_{exit} = 0.572 MPa (T_{sat} = 156.9 ˚C) and G = 1.18 Mg/m^{2}s, with P_{exit} = 0.207 MPa (T_{sat} = 121.0 ˚C).

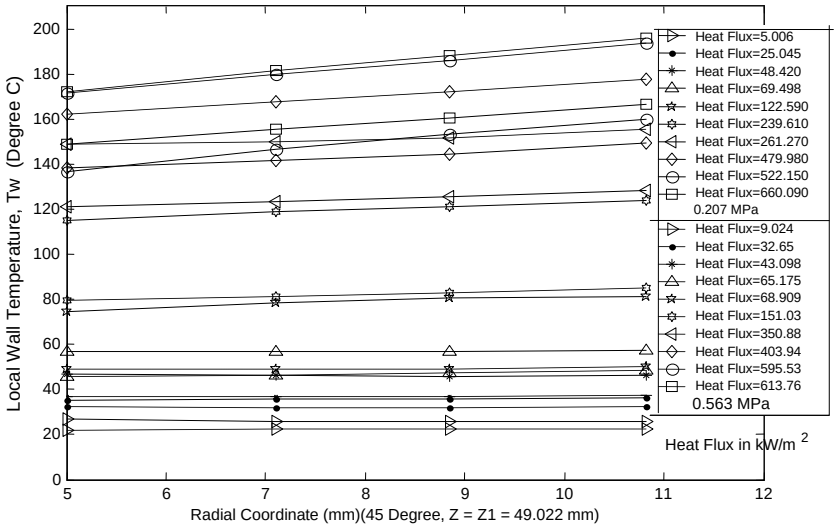

Figure 76: Radial Wall Temperature Profiles for the Circular Test Section Flow Channel at ϕ = 45 degree, G = 0.59 Mg/m^{2}s, and Z = Z1 as a Function of the Average Net Incident Heat Flux at Different Exit Pressures: for P_{exit} = 0.207 MPa (T_{sat} = 121.0 ˚C) and P_{exit} = 0.563 MPa (T_{sat} = 156.4 ˚C).

4.0 mm (= Lo) unheated portion at the down-stream end of the test section and a 16.0 mm (=Li) unheated portion at the up-stream end. Figure 77 shows the axial local wall temperature variations (at 0 degree, close to fluid boundary for a mass velocity of 0.59 Mg/m2s and exit pressure of 0.207 MPa).

In all cases shown in Figures 78 through 83, the local wall temperature at all axial locations decreased as the mass velocity increased. From Figures 78 and 79 however, no clear relation can be proved between mass velocity and axial wall temperature difference variations close to the outside boundary. Figure 78 shows the axial distribution for mass velocities of 0.59 Mg/m^{2}s and 1.18 Mg/m^{2}s.

As noted above, data reduction Approach #2 was used to determine the average net incident heat flux as a function of measured maximum flow channel local wall temperature for the single-side heated monoblock test section and was plotted for all forty-eight channels for all the completed tests.

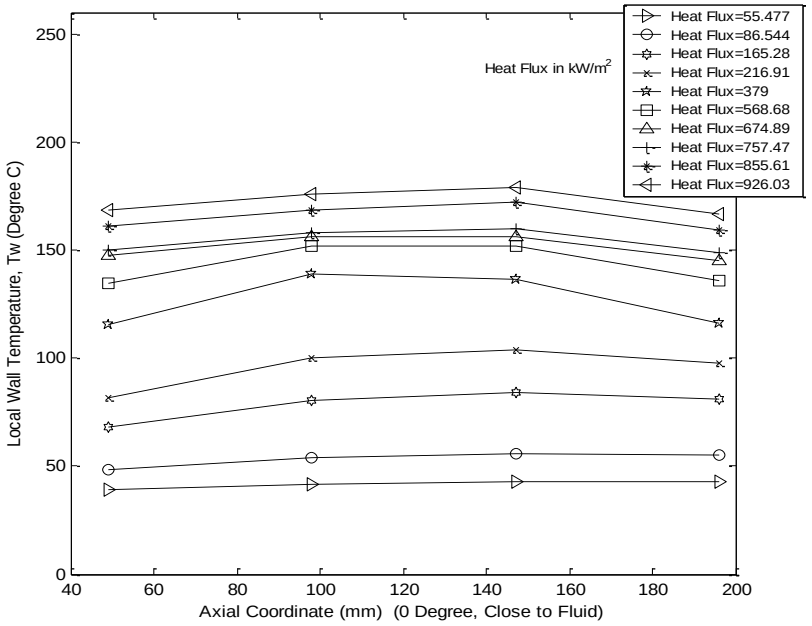

Figure 77: MonoblockTest Section Local Axial Wall Temperature Profiles for the Thermocouples at ϕ = 0 degree, Close to Outside Heated Boundary as a Function of the Net Incident Heat Flux (G = 0.59 Mg/m^{2}s with P_{exit} = 0.207 MPa, and T_{sat} = 121.0 ˚C).

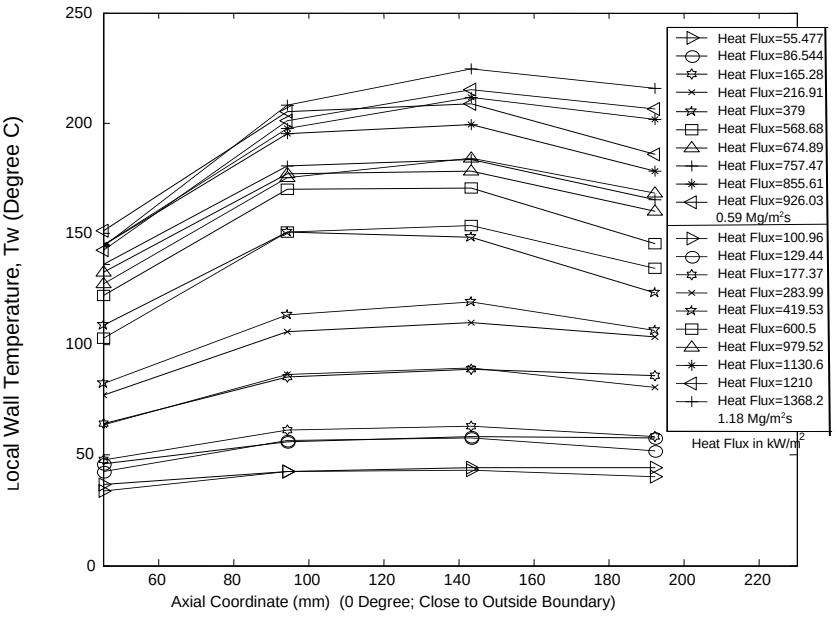

Figure 78: Monoblock Test Section Local Axial Wall Temperature Profiles for the Thermocouples at ϕ = 0 degree, Close to Outside Heated Boundary as a Function of the Net Incident Heat Flux with P_{exit} = 0.207 MPa, and T_{sat} = 121.0 ˚C at Different Mass Flow Velocities (for G = 0.59 Mg/m^{2}s and 1.18 Mg/m^{2}s).

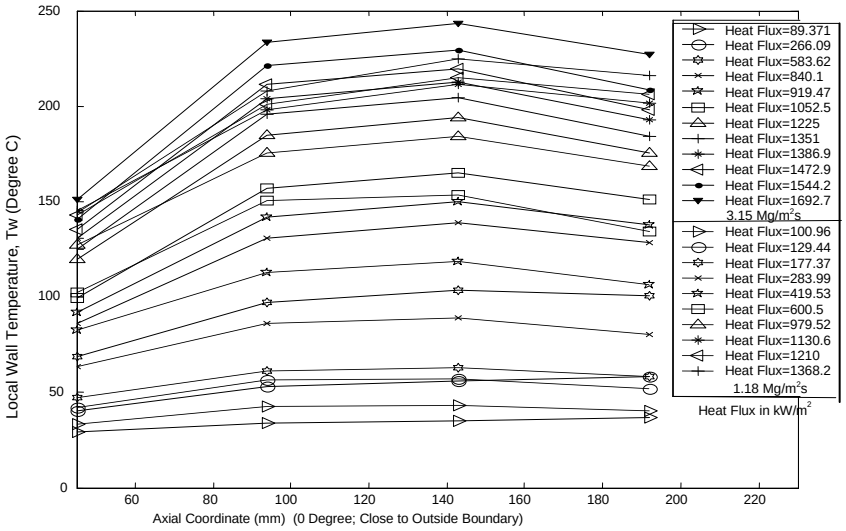

Figure 79: Monoblock Test Section Local Axial Wall Temperature Profiles for the Thermocouples at ϕ = 0 degree, Close to Outside Heated Boundary as a Function of the Net Incident Heat Flux at Different Mass Velocities: for G = 3.15 Mg/m^{2}s with P_{exit} = 0.572 MPa (T_{sat} = 156.9 C) and G = 1.18 Mg/m^{2}s with P_{exit} = 0.207 MPa (T_{sat} = 121.0 ˚C).

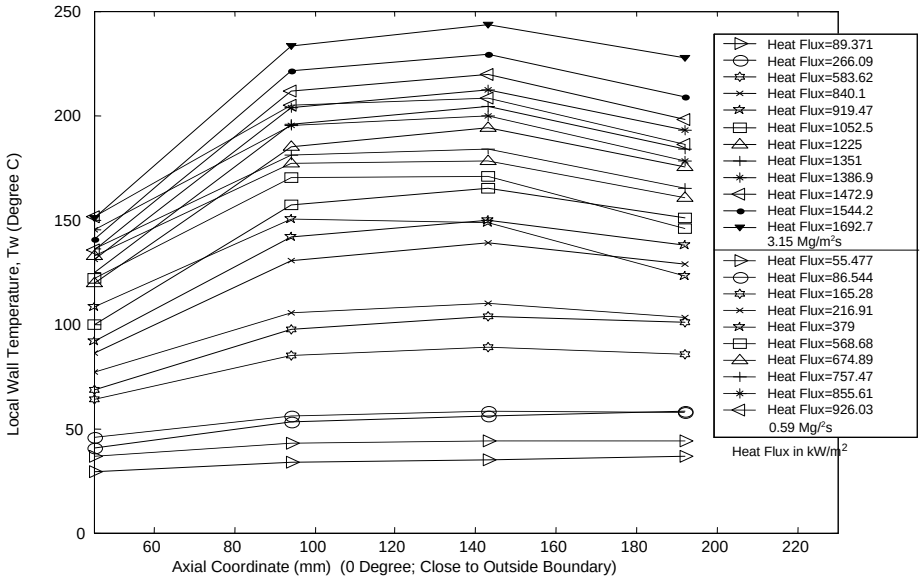

Figure 80: Monoblock Test Section Local Axial Wall Temperature Profiles for the Thermocouples at ϕ = 0 degree, Close to Outside Heated Boundary as a Function of the Net Incident Heat Flux at Different Mass Velocities: for G = 3.15 Mg/m^{2}s with P_{exit} = 0.572 MPa (T_{sat} = 156.9 ˚C) and G = 0.59 Mg/m^{2}s with P_{exit} = 0.207 MPa (T_{sat} = 121.0 ˚C).

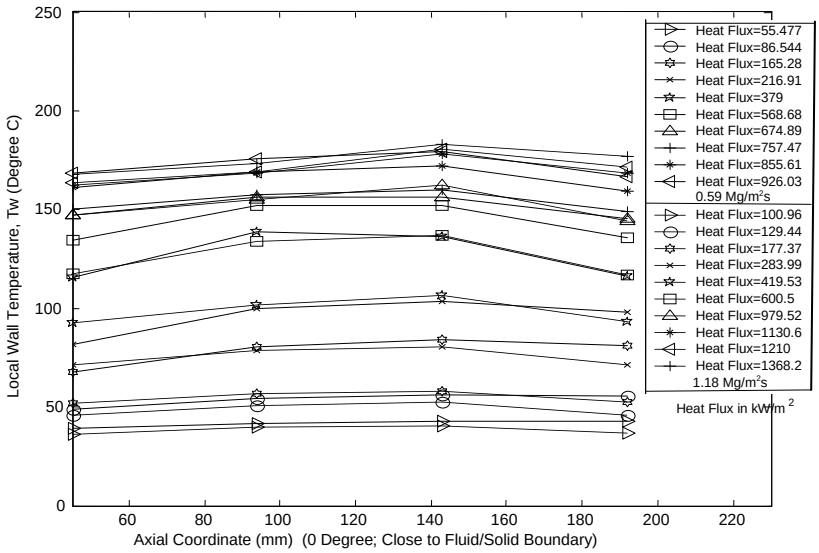

Figure 81: Monoblock Test Section Local Axial Wall Temperature Profiles for the Thermocouples at ϕ = 0 degree, Close to Fluid/Solid Boundary as a Function of the Net Incident Heat Flux with P_{exit} = 0.207 MPa, T_{sat} = 121.0 ˚C at Different Mass Flow Velocities (G = 0.59 Mg/m^2s and 1.18 Mg/m^2s).

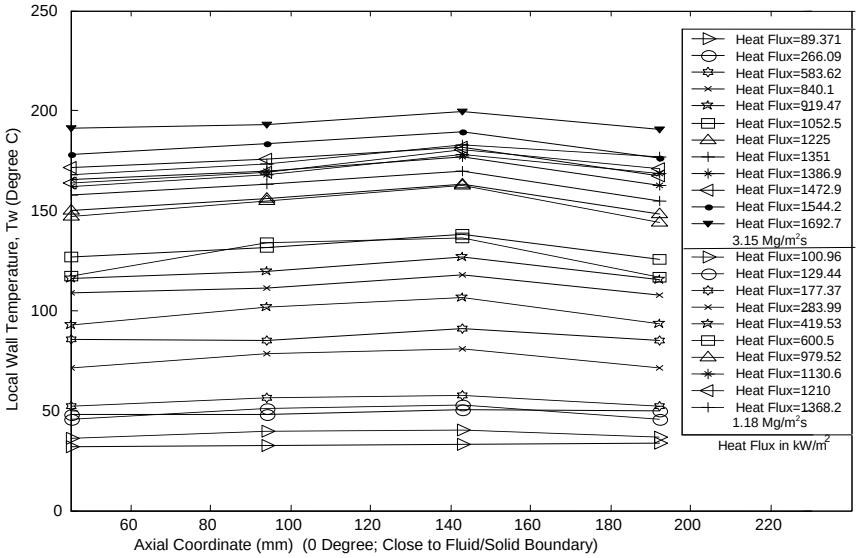

Figure 82: Monoblock Test Section Local Axial Wall Temperature Profiles for the Thermocouples at ϕ = 0 degree, Close to Fluid/Solid Boundary as a Function of the Net Incident Heat Flux at Different Mass Velocities: for G = 3.15 Mg/m^2s with P_{exit} = 0.572 MPa (T_{sat} = 156.9 ˚C) and G = 1.18 Mg/m^2s with P_{exit} = 0.207 MPa (T_{sat} = 121.0 ˚C).

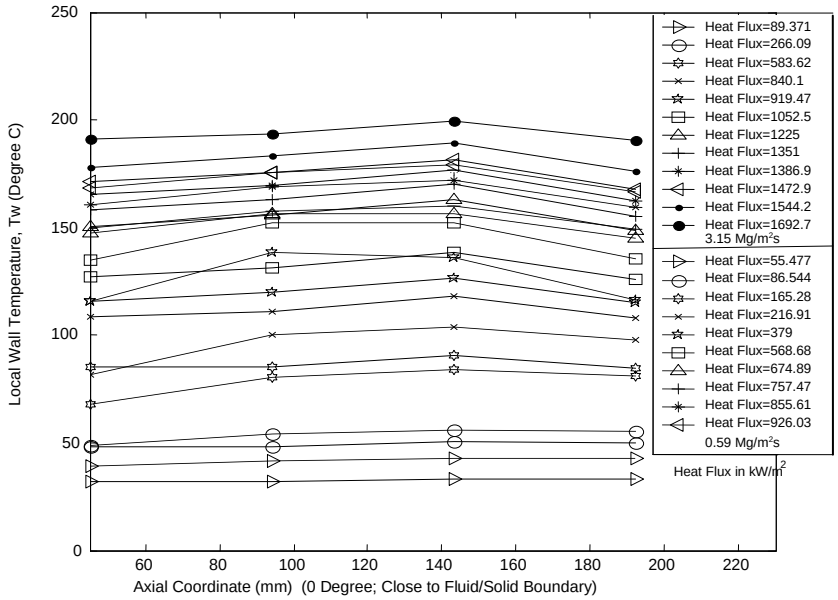

Figure 83: Monoblock Test Section Local Axial Wall Temperature Profiles for the Thermocouples at ϕ = 0 degree, Close to Fluid/Solid Boundary as a Function of the Net Incident Heat Flux at Different Mass Velocities: for G = 3.15 Mg/m^{2}s with P_{exit} = 0.572 MPa (T_{sat} = 156.9 ˚C) and G = 0.59 Mg/m^{2}s with P_{exit} = 0.207 MPa (T_{sat} = 121.0 ˚C).

17.4.4.2 Circular Test Section Results

Similar to the monoblock test section, thermocouples were placed at four different axial locations in the circular test section. For each test, five (5) new heaters were fixed on the test section. As a result, the contact between the heaters and the test section may not have been uniform. This may have resulted in different trends on axial wall temperature for different tests.

17.4.5 MEASURED 3-D RELATIONSHIP BETWEEN $q_o^{"}$ and Tw_{max} USING DATA REDUCTION APPROACH #2

17.4.5.1 Monoblock Test Results

All the figures shown below are the measured maximum local wall temperatures (Tw_{max}) as a function of the averaged net incident heat flux $\left(q_o^{"}\right)$ for the four axial locations. They are presented in the following order: ϕ = 0 degree (close to fluid, intermediate, close to outside boundary), ϕ = 45 degree (close to fluid, intermediate, close to outside boundary), ϕ = 135 degree (close to fluid, intermediate, close to outside boundary), and ϕ = 180 degree (close to fluid, intermediate, close to outside boundary). In all the figures (Figures 84 through 131) below, the

vertical dotted line shows the saturation temperature. Note: for Test #7, at ϕ = 45 degree, only the lower 6 heat flux levels are represented here due to the bad data for the other heat flux levels at this location.

17.4.5.2 Circular Test Section

For the circular test section, some channel data were eliminated for many reasons. Although no figures are presented here, similar 3-D flow channel wall temperature distributions (i.e., similar to those for monoblock) resulted.

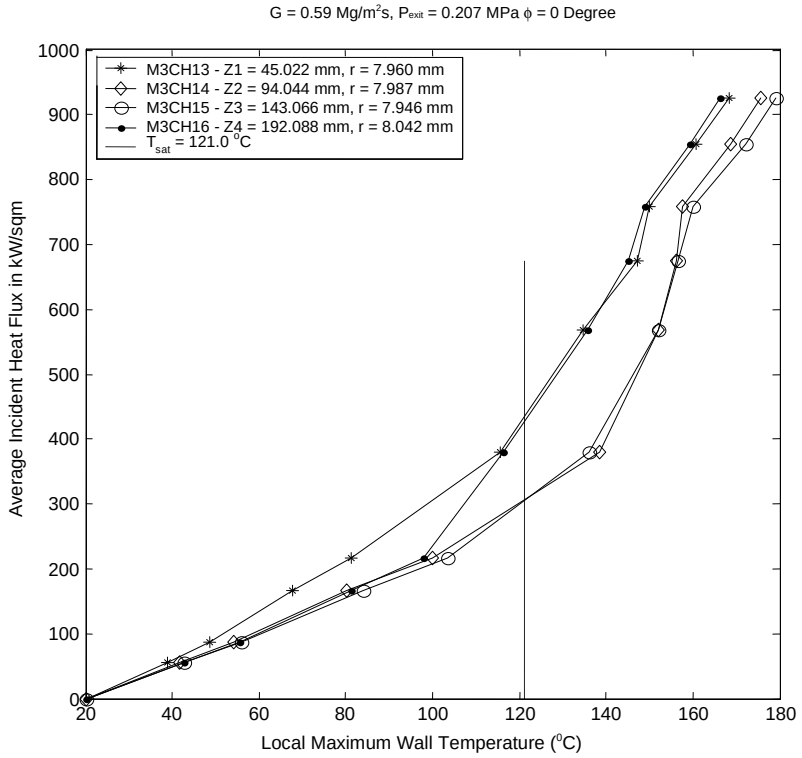

Figure 84: Measured Maximum Local Wall Temperature Axial Variation as a Function of the Average Incident Heat Flux for a Single-Side Heated Monoblock for ϕ = 0 Degree, Close to Fluid Boundary Location (for Test #1: G = 0.59 Mg/m^{2}s, with P_{exit} = 0.207 MPa, and T_{sat} = 121.0 ˚C).

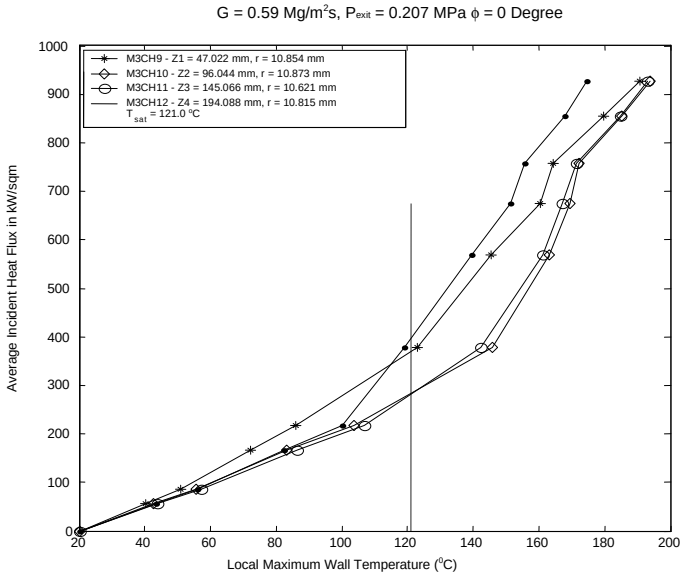

Figure 85: Measured Maximum Local Wall Temperature Axial Variation as a Function of the Average Incident Net Heat Flux for a Single-Side Heated Monoblock for ϕ = 0 Degree, Intermediate Location (Test #1: G = 0.59 Mg/m^{2}s, with P_{exit} = 0.207 MPa, and T_{sat} = 121.0 ˚C).

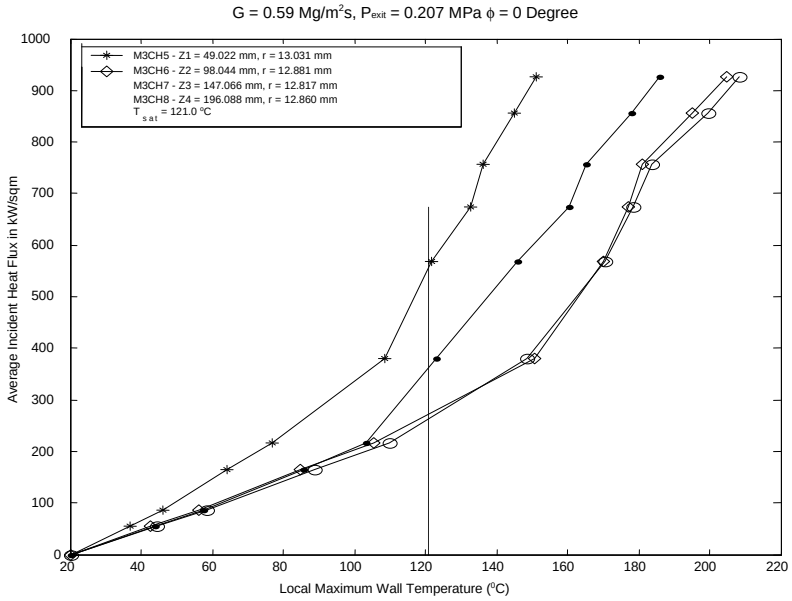

Figure 86: Measured Maximum Local Wall Temperature Axial Variation as a Function of the Average Incident Net Heat Flux for a Single-Side Heated Monoblock for ϕ = 0 Degree, Close to Outside Boundary Location (Test #1: G = 0.59 Mg/m^{2}s, with P_{exit} = 0.207 MPa, and T_{sat} = 121.0 ˚C).

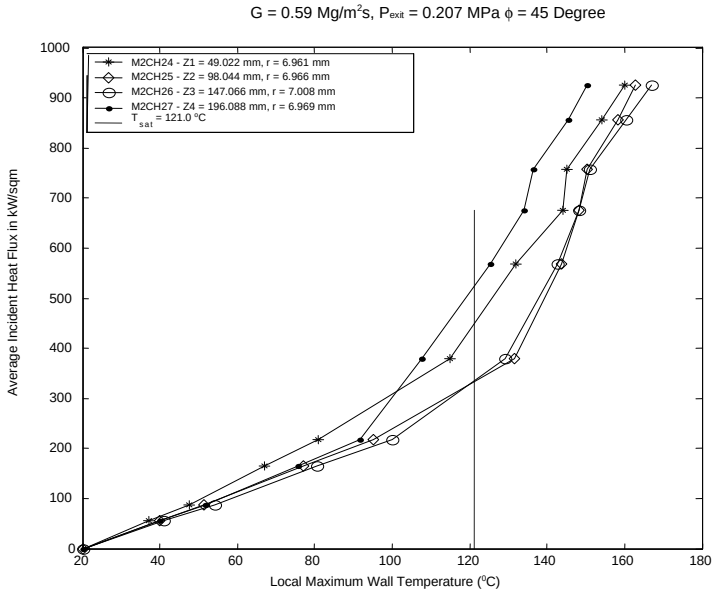

Figure 87: Measured Maximum Local Wall Temperature Axial Variation as a Function of the Average Incident Net Heat Flux for a Single-Side Heated Monoblock for ϕ = 45 Degree, Close to Fluid Boundary Location (for Test #1: G = 0.59 Mg/m^{2}s, with P_{exit} = 0.207 MPa, and T_{sat} = 121.0 ˚C).

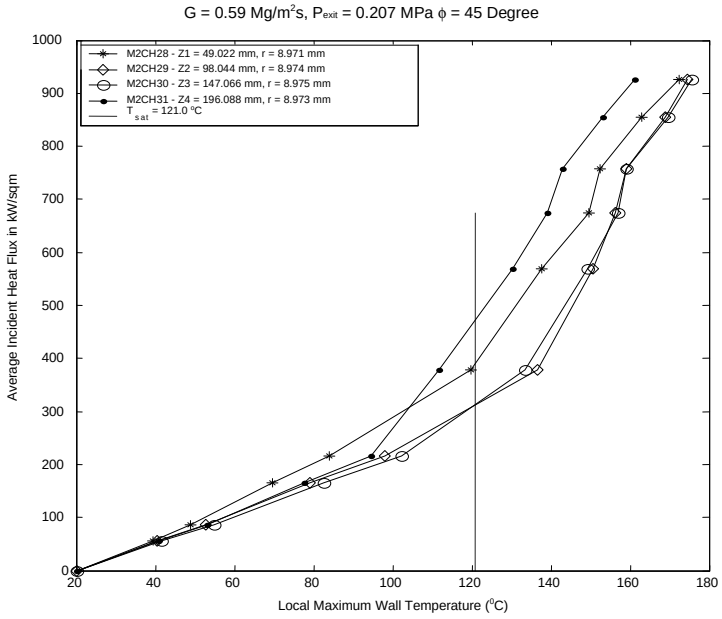

Figure 88: Measured Maximum Local Wall Temperature Axial Variation as a Function of the Average Incident Net Heat Flux for a Single-Side Heated Monoblock for ϕ = 45 Degree, Intermediate Location (for Test #1: G = 0.59 Mg/m^{2}s, with P_{exit} = 0.207 MPa, and T_{sat} = 121.0 ˚C).

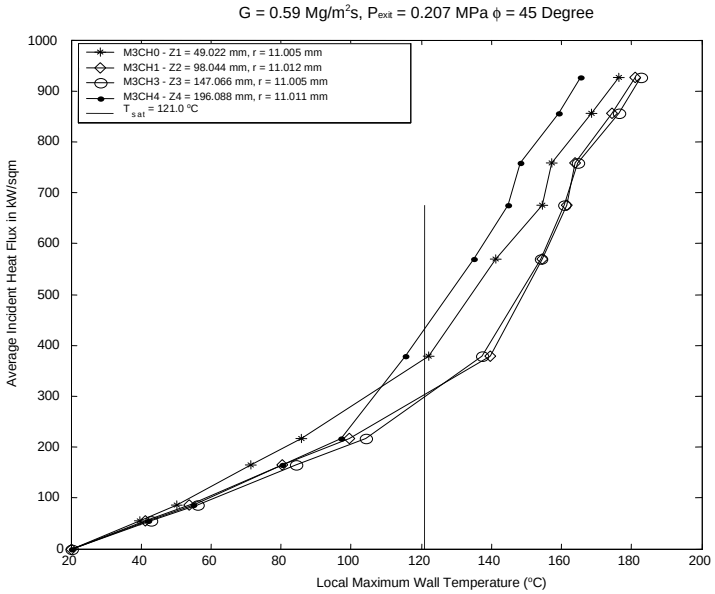

Figure 89: Measured Maximum Local Wall Temperature Axial Variation as a Function of the Average Incident Net Heat Flux for a Single-Side Heated Monoblock for ϕ = 45 Degree, Close to Outside Boundary Location (for Test #1: G = 0.59 Mg/m^{2}s, with P_{exit} = 0.207 MPa, and T_{sat} = 121.0 ˚C).

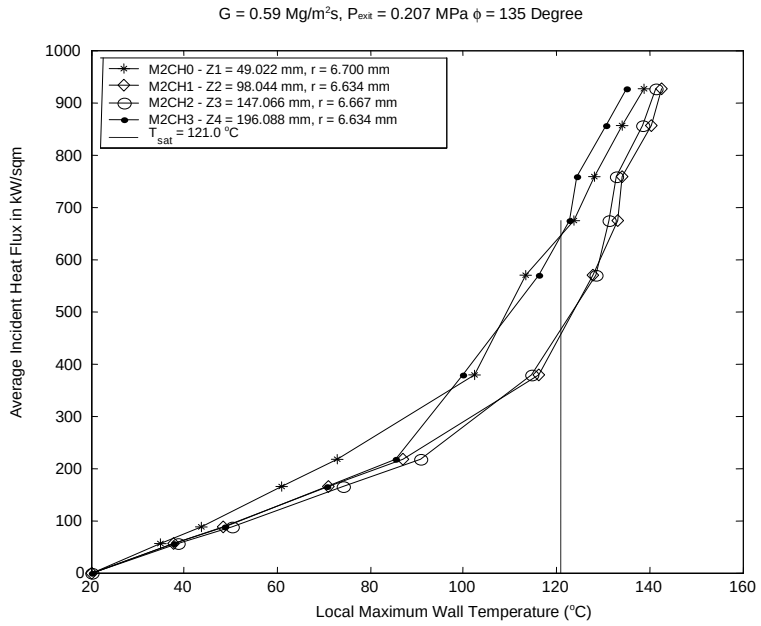

Figure 90: Measured Maximum Local Wall Temperature Axial Variation as a Function of the Average Incident Net Heat Flux for a Single-Side Heated Monoblock for ϕ = 135 Degree, Close to Fluid Boundary Location (for Test #1: G = 0.59 Mg/m^{2}s, with P_{exit} = 0.207 MPa, and T_{sat} = 121.0 ˚C).

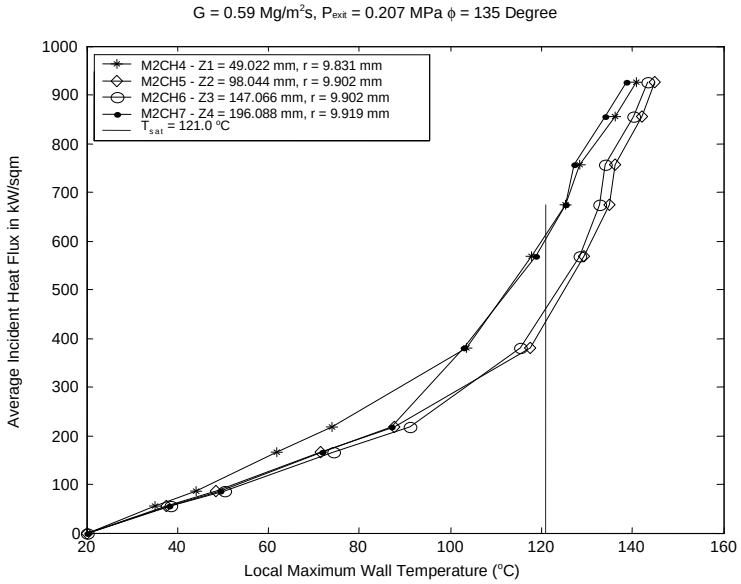

Figure 91: Measured Maximum Local Wall Temperature Axial Variation as a Function of the Average Incident Net Heat Flux for a Single-Side Heated Monoblock for ϕ = 135 Degree, Intermediate Location (for Test #1: G = 0.59 Mg/m^{2}s, with P_{exit} = 0.207 MPa, and T_{sat} = 121.0 ˚C).

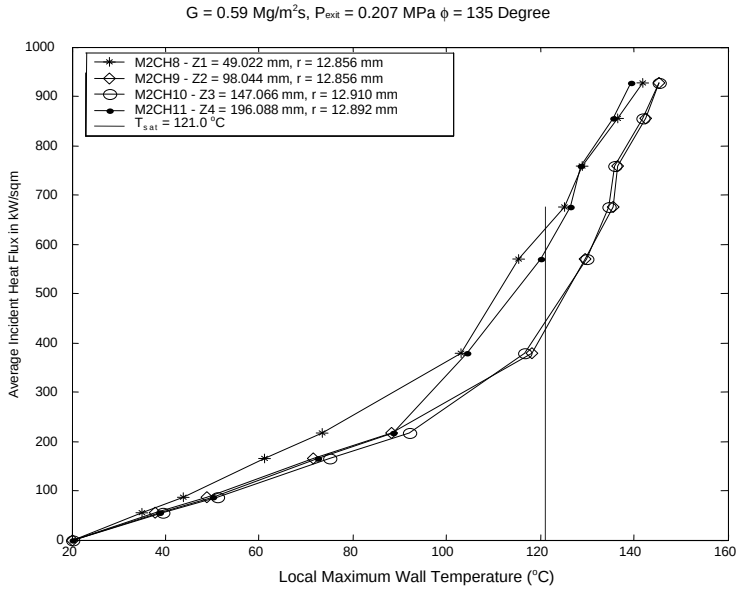

Figure 92: Measured Maximum Local Wall Temperature Axial Variation as a Function of the Average Incident Net Heat Flux for a Single-Side Heated Monoblock for ϕ = 135 Degree, Close to Outside Boundary Location (for Test #1: G = 0.59 Mg/m^{2}s, with P_{exit} = 0.207 MPa, and T_{sat} = 121.0 ˚C).

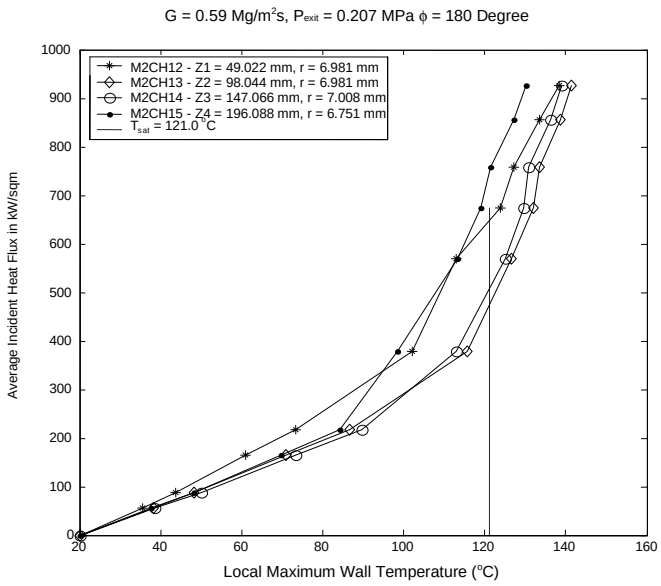

Figure 93: Measured Maximum Local Wall Temperature Axial Variation as a Function of the Average Incident Net Heat Flux for a Single-Side Heated Monoblock for ϕ = 180 Degree, Close to Fluid Boundary Location (for Test #1: G = 0.59 Mg/m^{2}s, with P_{exit} = 0.207 MPa, and T_{sat} = 121.0 ˚C).

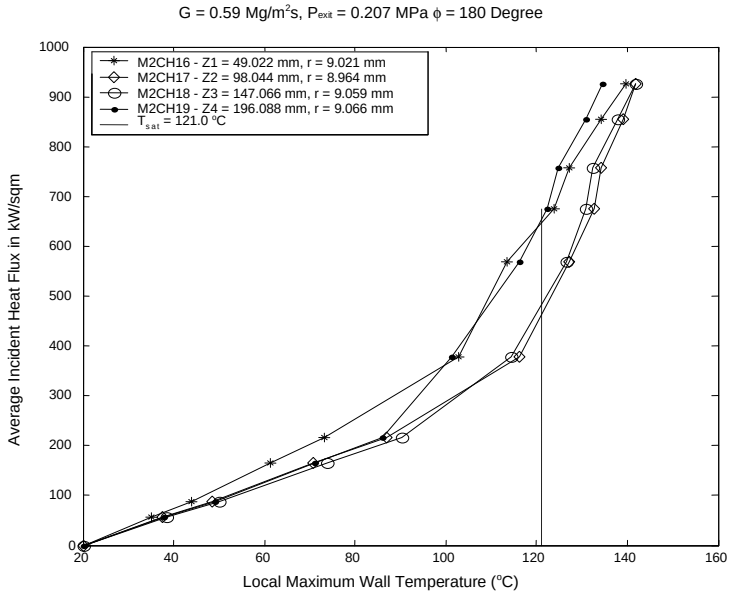

Figure 94: Measured Maximum Local Wall Temperature Axial Variation as a Function of the Average Incident Net Heat Flux for a Single-Side Heated Monoblock for ϕ = 180 Degree, Intermediate Location (for Test #1: G = 0.59 Mg/m^{2}s, with P_{exit} = 0.207 MPa, and T_{sat} = 121.0 ˚C).

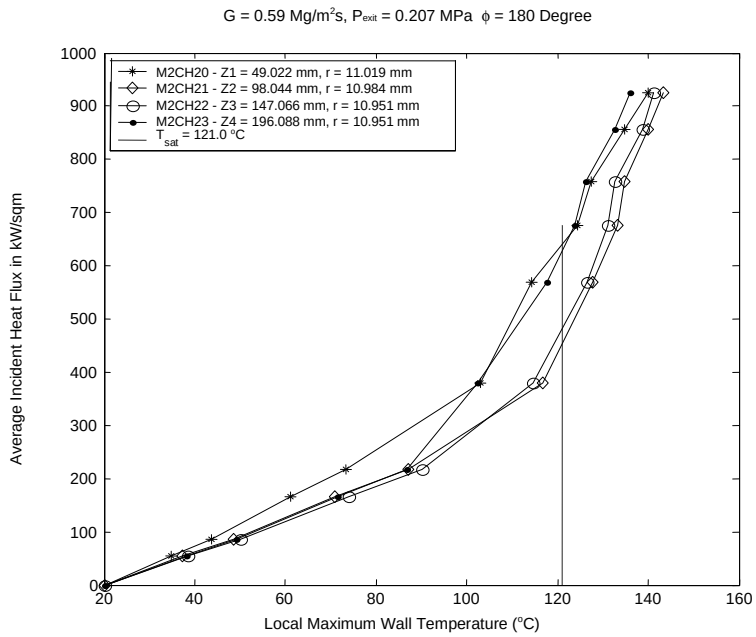

Figure 95: Measured Maximum Local Wall Temperature Axial Variation as a Function of the Average Incident Net Heat Flux for a Single-Side Heated Monoblock for ϕ = 180 Degree, Close to Outside Boundary Location (for Test #1: G = 0.59 Mg/m^{2}s, with P_{exit} = 0.207 MPa, and T_{sat} = 121.0 ˚C).

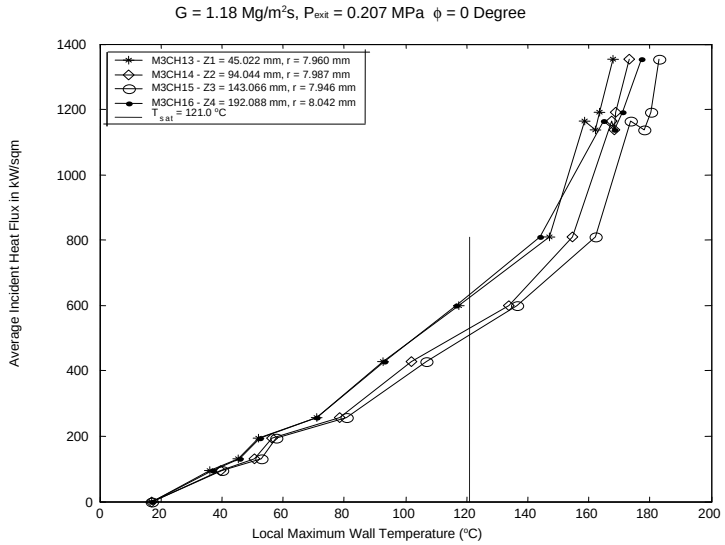

Figure 96: Measured Maximum Local Wall Temperature Axial Variation as a Function of the Average Incident Net Heat Flux for a Single-Side Heated Monoblock for ϕ = 0 Degree, Close to Fluid Boundary Location (for Test #4: G = 1.18 Mg/m^{2}s, with P_{exit} = 0.207 MPa, and T_{sat} = 121.0 ˚C).

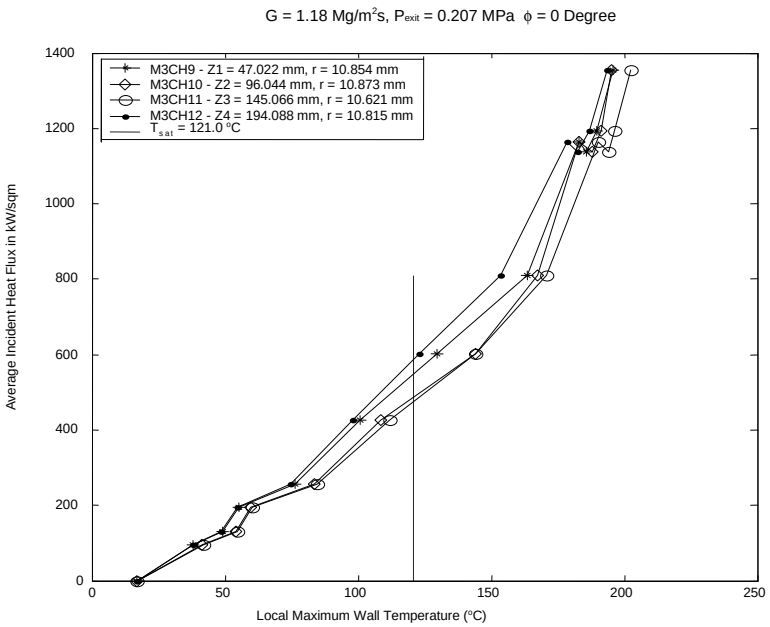

Figure 97: Measured Maximum Local Wall Temperature Axial Variation as a Function of the Average Incident Net Heat Flux for a Single-Side Heated Monoblock for ϕ= 0 Degree, Intermediate Location (for Test #4: G = 1.18 Mg/m^{2}s, with P_{exit} = 0.207 MPa, and T_{sat} = 121.0 ˚C).

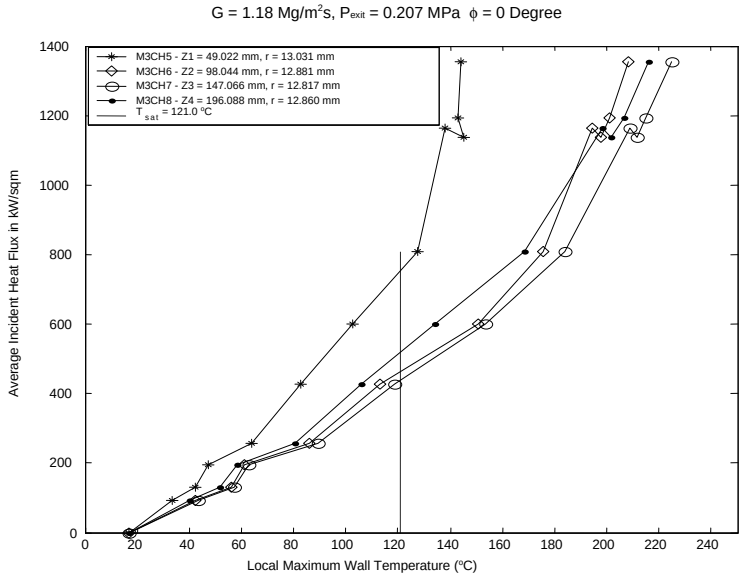

Figure 98: Measured Maximum Local Wall Temperature Axial Variation as a Function of the Average Incident Net Heat Flux for a Single-Side Heated Monoblock for ϕ = 0 Degree, Close to Outside Boundary Location (for Test #4: G = 1.18 Mg/m^{2}s, with P_{exit} = 0.207 MPa, and T_{sat} = 121.0 ˚C).

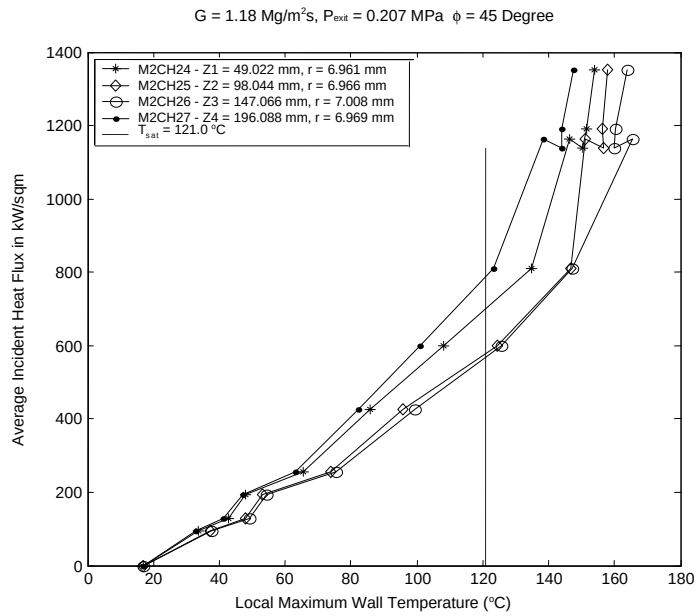

Figure 99: Measured Maximum Local Wall Temperature Axial Variation as a Function of the Average Incident Net Heat Flux for a Single-Side Heated Monoblock for ϕ = 45 Degree, Close to Fluid Boundary Location (for Test #4: G = 1.18 Mg/m^{2}s, with P_{exit} = 0.207 MPa, and T_{sat} = 121.0 ˚C)**.**

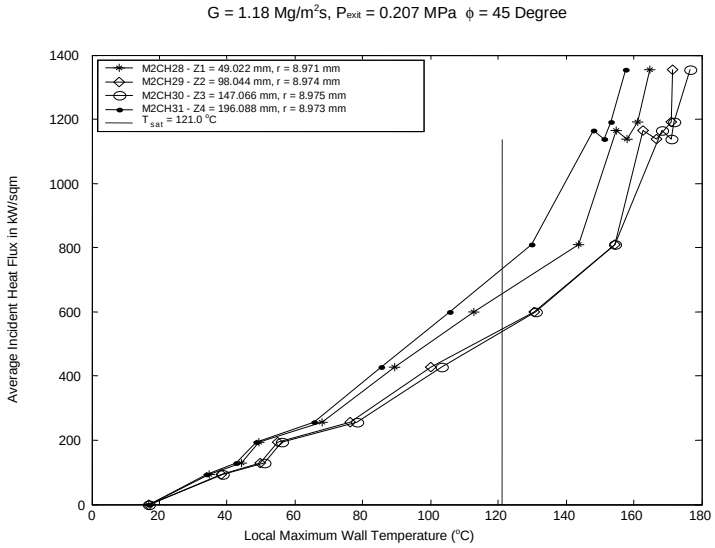

Figure 100: Measured Maximum Local Wall Temperature Axial Variation as a Function of the Average Incident Net Heat Flux for a Single-Side Heated Monoblock for ϕ = 45 Degree, Intermediate Location (for Test #4: G = 1.18 Mg/m^{2}s, with P_{exit} = 0.207 MPa, and T_{sat} = 121.0 ˚C).

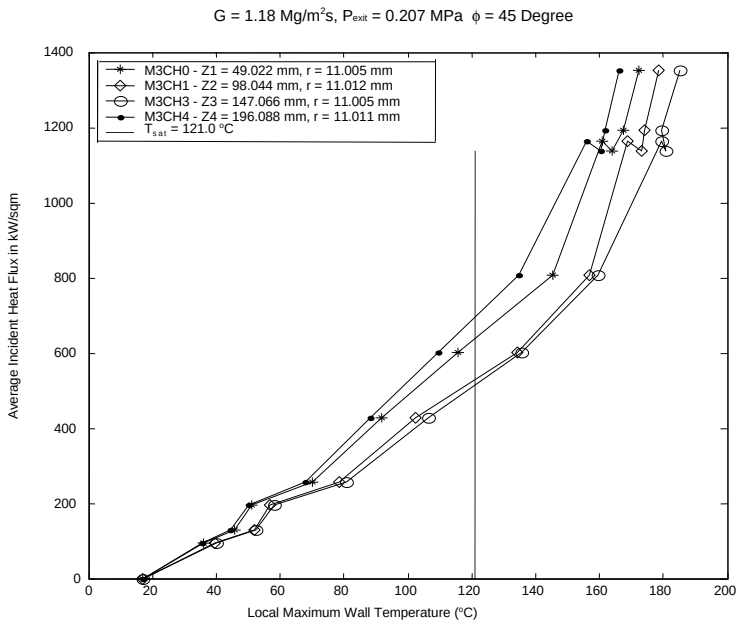

Figure 101: Measured Maximum Local Wall Temperature Axial Variation as a Function of the Average Incident Net Heat Flux for a Single-Side Heated Monoblock for ϕ = 45 Degree, Close to Outside Boundary Location (for Test #4: G = 1.18 Mg/m^{2}s, with P_{exit} = 0.207 MPa, and T_{sat} = 121.0 ˚C).

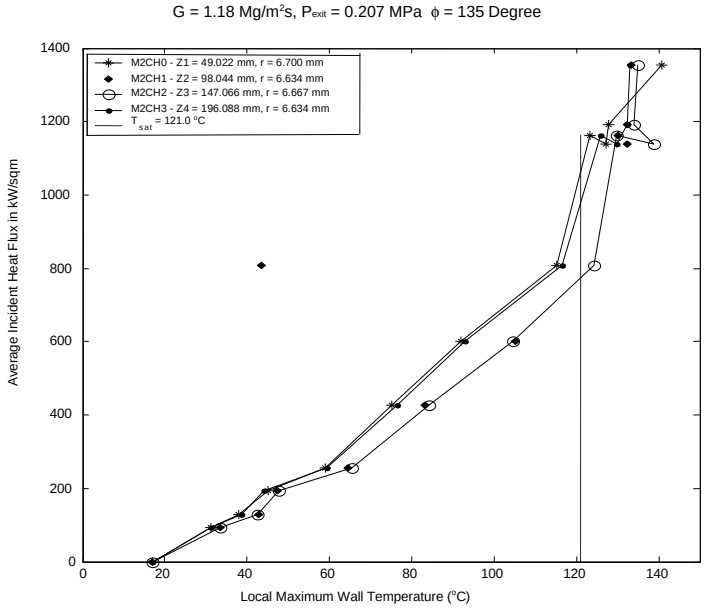

Figure 102: Measured Maximum Local Wall Temperature Axial Variation as a Function of the Average Incident Net Heat Flux for a Single-Side Heated Monoblock for ϕ = 135 Degree, Close to Fluid Boundary Location (for Test #4: G = 1.18 Mg/m^{2}s, with P_{exit} = 0.207 MPa, and T_{sat} = 121.0 ˚C).

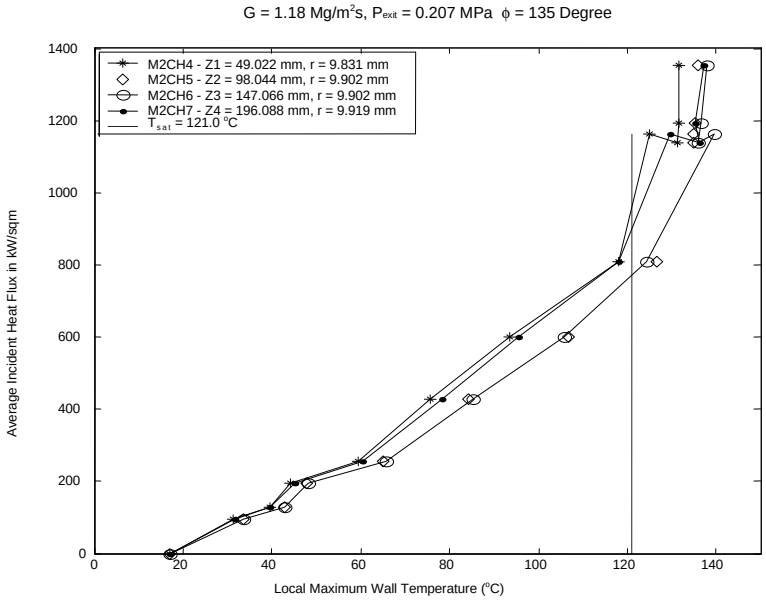

Figure 103: Measured Maximum Local Wall Temperature Axial Variation as a Function of the Average Incident Net Heat Flux for a Single-Side Heated Monoblock for ϕ = 135 Degree, Intermediate Location (for Test #4: G = 1.18 Mg/m^{2}s, with P_{exit} = 0.207 MPa, and T_{sat} = 121.0 ˚C).

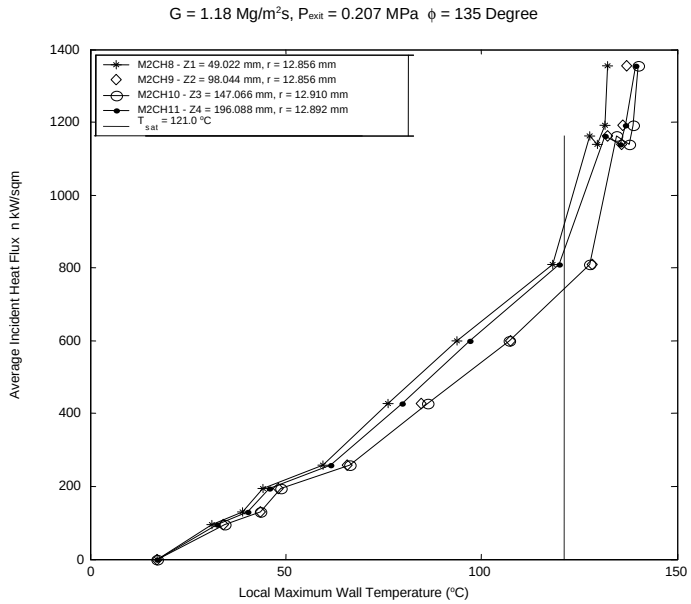

Figure 104: Measured Maximum Local Wall Temperature Axial Variation as a Function of the Average Incident Net Heat Flux for a Single-Side Heated Monoblock for ϕ = 135 Degree, Close to Outside Boundary Location (for Test #4: G = 1.18 Mg/m^{2}s, with P_{exit} = 0.207 MPa, and T_{sat} = 121.0 ˚C).

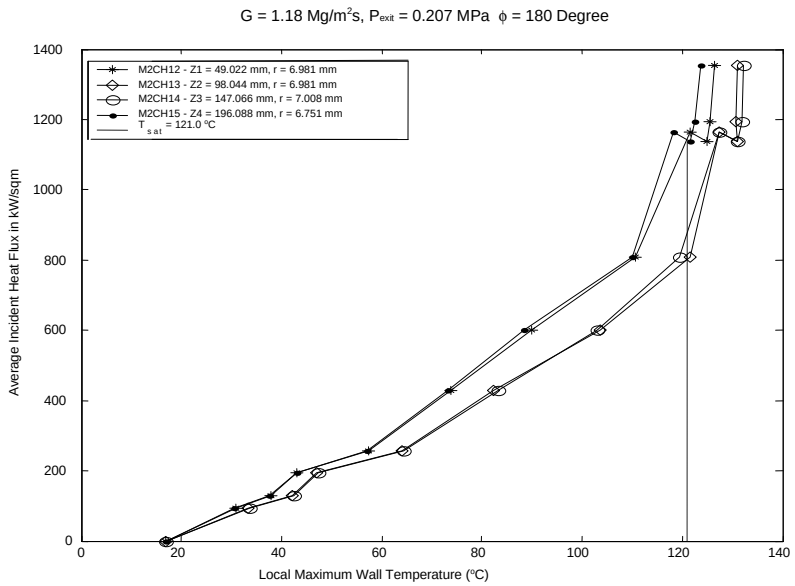

Figure 105: Measured Maximum Local Wall Temperature Axial Variation as a Function of the Average Incident Net Heat Flux for a Single-Side Heated Monoblock for ϕ = 180 Degree, Close to Fluid Boundary Location (for Test #4: G = 1.18 Mg/m^{2}s, with P_{exit} = 0.207 MPa, and T_{sat} = 121.0 ˚C).

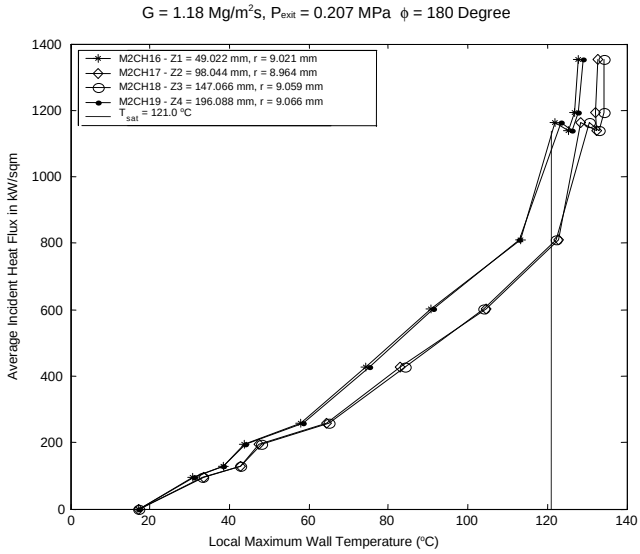

Figure 106: Measured Maximum Local Wall Temperature Axial Variation as a Function of the Average Incident Net Heat Flux for a Single-Side Heated Monoblock for ϕ = 180 Degree, Intermediate Location (for Test #4: G = 1.18 Mg/m^{2}s, with P_{exit} = 0.207 MPa, and T_{sat} = 121.0 ˚C).

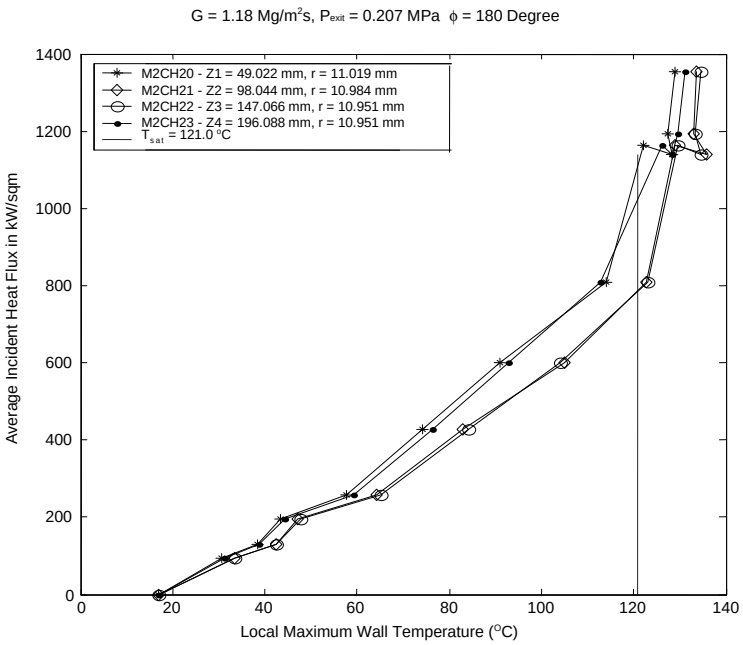

Figure 107: Measured Maximum Local Wall Temperature Axial Variation as a Function of the Average Incident Net Heat Flux for a Single-Side Heated Monoblock for ϕ = 180 Degree, Close to Outside Boundary Location (for Test #4: G = 1.18 Mg/m^{2}s, with P_{exit} = 0.207 MPa, and T_{sat} = 121.0 ˚C).

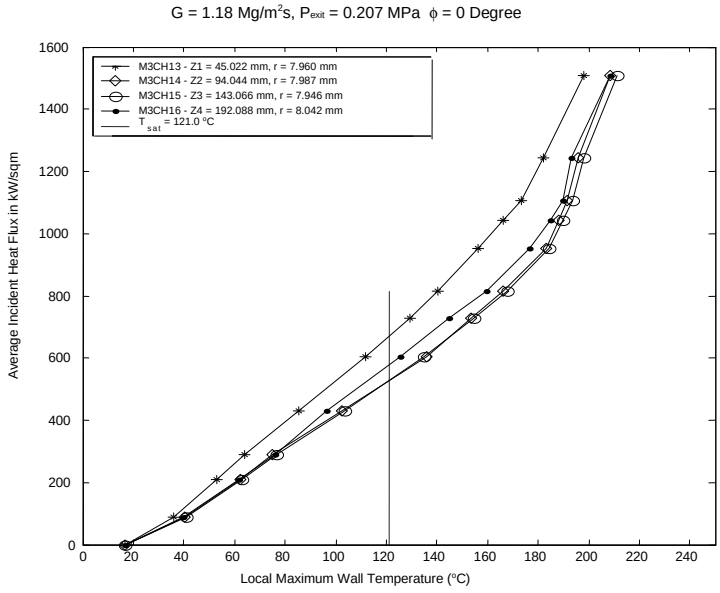

Figure 108: Measured Maximum Local Wall Temperature Axial Variation as a Function of the Average Incident Net Heat Flux for a Single-Side Heated Monoblock for ϕ = 0 Degree, Close to Fluid Boundary Location (for Test #6: G = 1.18 Mg/m^{2}s, with P_{exit} = 0.207 MPa, and T_{sat} = 121.0 ˚C).

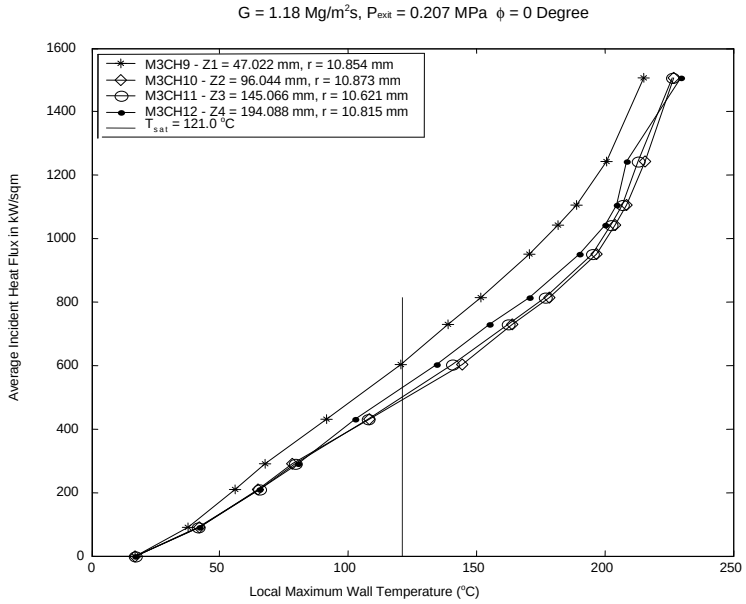

Figure 109: Measured Maximum Local Wall Temperature Axial Variation as a Function of the Average Incident Net Heat Flux for a Single-Side Heated Monoblock for ϕ = 0 Degree, Intermediate Location (for Test #6: G = 1.18 Mg/m^{2}s, with P_{exit} = 0.207 MPa, and T_{sat} = 121.0 ˚C).

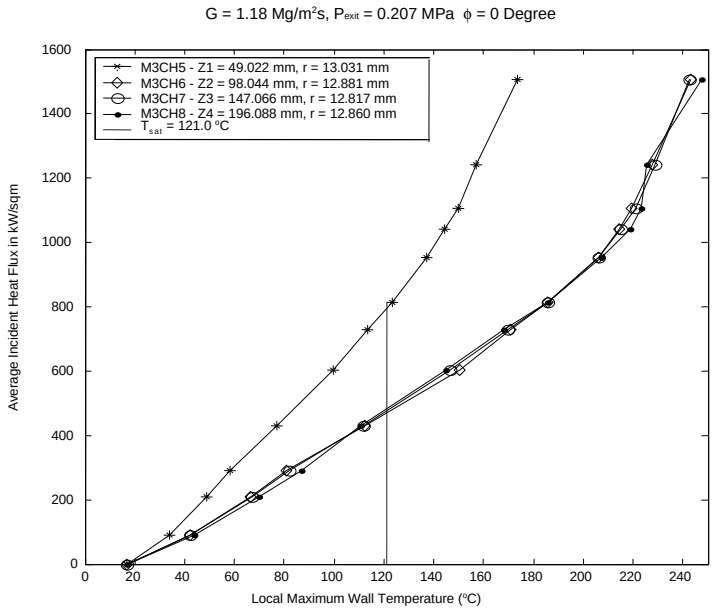

Figure 110: Measured Maximum Local Wall Temperature Axial Variation as a Function of the Average Incident Net Heat Flux for a Single-Side Heated Monoblock for ϕ = 0 Degree, Close to Outside Boundary Location (for Test #6: G = 1.18 Mg/m^{2}s, with P_{exit} = 0.207 MPa, and T_{sat} = 121.0 ˚C).

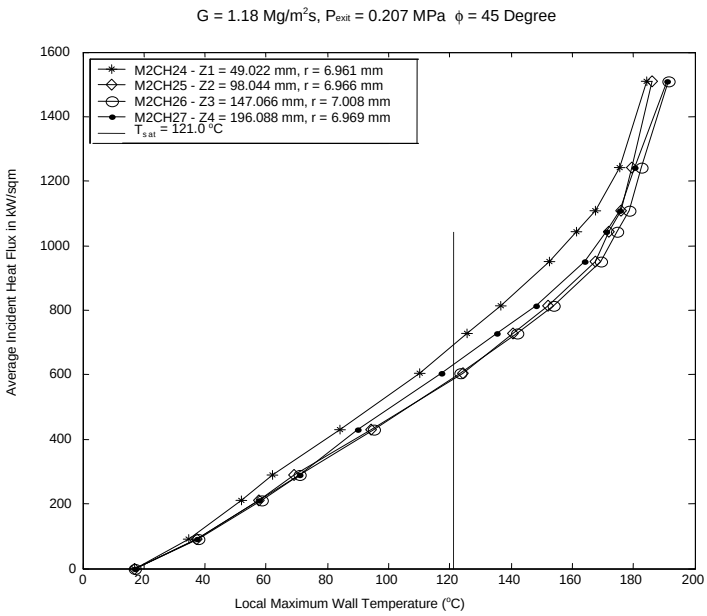

Figure 111: Measured Maximum Local Wall Temperature Axial Variation as a Function of the Average Incident Net Heat Flux for a Single-Side Heated Monoblock for ϕ = 45 Degree, Close to Fluid Boundary Location (for Test #6: G = 1.18 Mg/m^{2}s, with P_{exit} = 0.207 MPa, and T_{sat} = 121.0 ˚C).

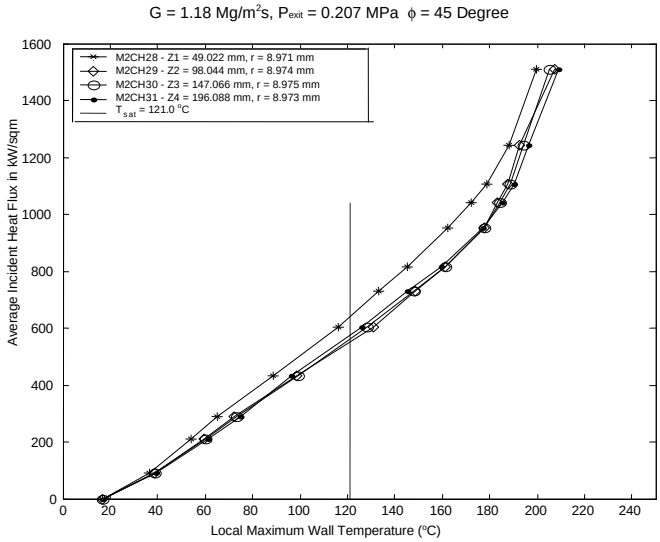

Figure 112: Measured Maximum Local Wall Temperature Axial Variation as a Function of the Average Incident Net Heat Flux for a Single-Side Heated Monoblock for ϕ = 45 Degree, Intermediate Location (for Test #6: G = 1.18 Mg/m^{2}s, with P_{exit} = 0.207 MPa, and T_{sat} = 121.0 ˚C).

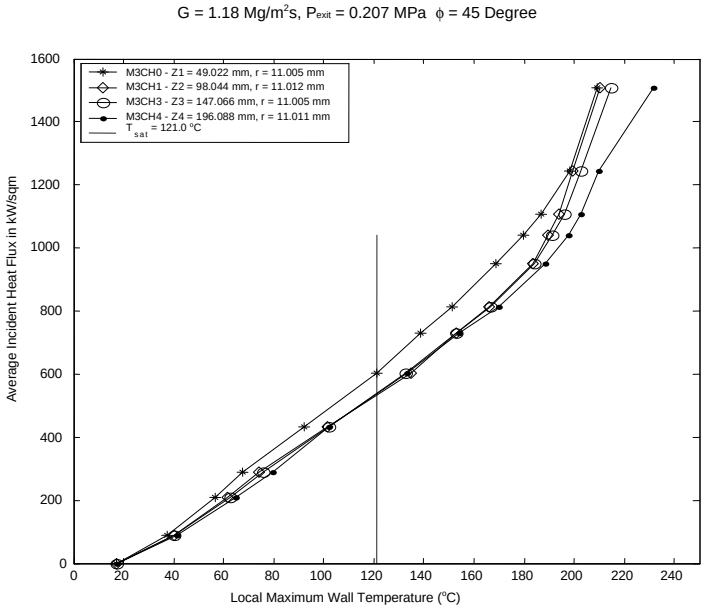

Figure 113: Measured Maximum Local Wall Temperature Axial Variation as a Function of the Average Incident Net Heat Flux for a Single-Side Heated Monoblock for ϕ = 45 Degree, Close to Outside Boundary Location (for Test #6: G = 1.18 Mg/m^{2}s, with P_{exit} = 0.207 MPa, and T_{sat} = 121.0 ˚C).

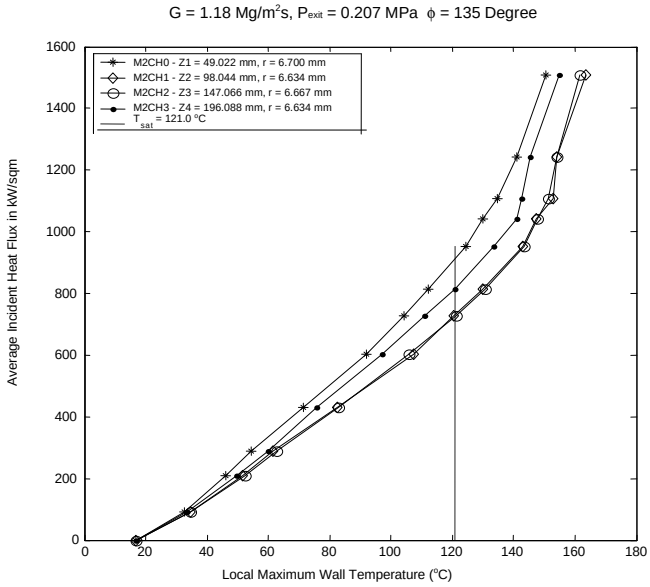

Figure 114: Measured Maximum Local Wall Temperature Axial Variation as a Function of the Average Incident Net Heat Flux for a Single-Side Heated Monoblock for ϕ = 135 Degree, Close to Fluid Boundary Location (for Test #6: G = 1.18 Mg/m^{2}s, with P_{exit} = 0.207 MPa, and T_{sat} = 121.0 ˚C).

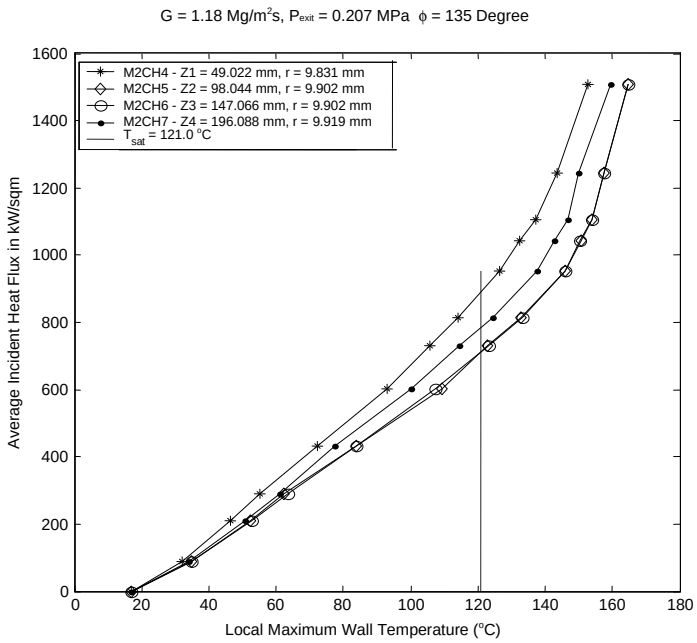

Figure 115: Measured Maximum Local Wall Temperature Axial Variation as a Function of the Average Incident Net Heat Flux for a Single-Side Heated Monoblock for ϕ = 135 Degree, Intermediate Location (for Test #6: G = 1.18 Mg/m^{2}s, with P_{exit} = 0.207 MPa, and T_{sat} = 121.0 ˚C).

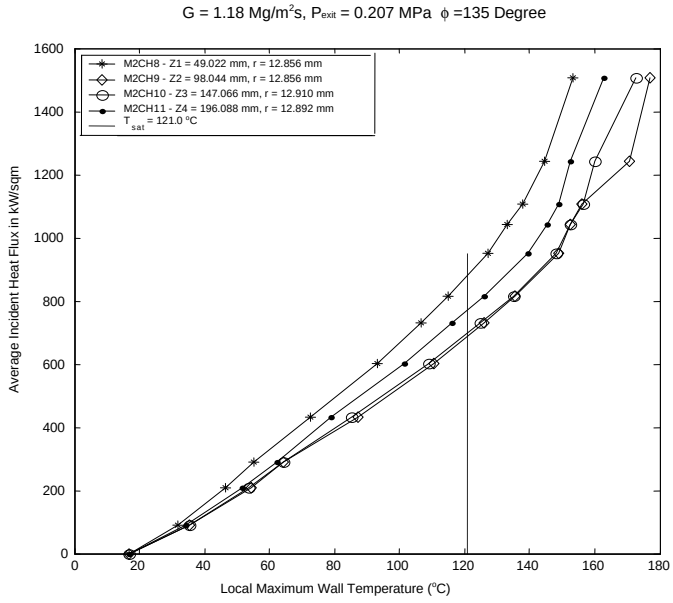

Figure 116: Measured Maximum Local Wall Temperature Axial Variation as a Function of the Average Incident Net Heat Flux for a Single-Side Heated Monoblock for ϕ = 135 Degree, Close to Outside Boundary Location (for Test #6: G = 1.18 Mg/m^{2}s, with P_{exit} = 0.207 MPa, and T_{sat} = 121.0 ˚C**).**

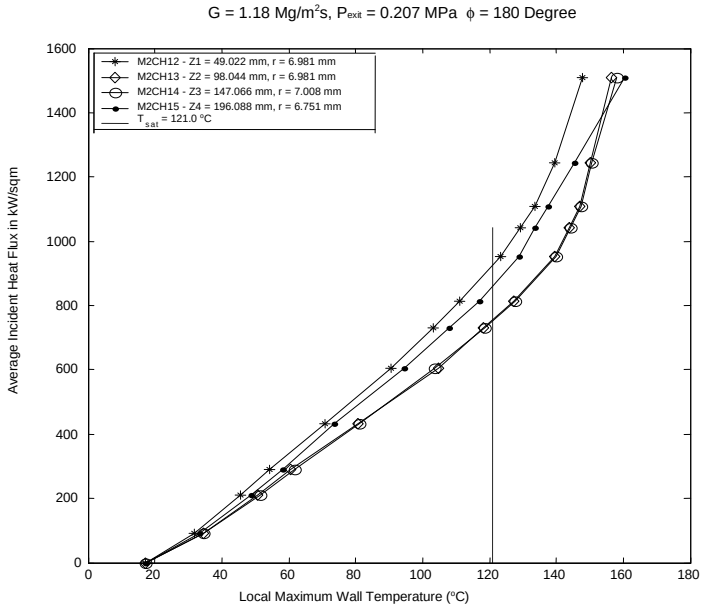

Figure 117: Measured Maximum Local Wall Temperature Axial Variation as a Function of the Average Incident Net Heat Flux for a Single-Side Heated Monoblock for ϕ = 180 Degree, Close to Fluid Boundary Location (for Test #6: G = 1.18 Mg/m^{2}s, with P_{exit} = 0.207 MPa, and T_{sat} = 121.0 ˚C).

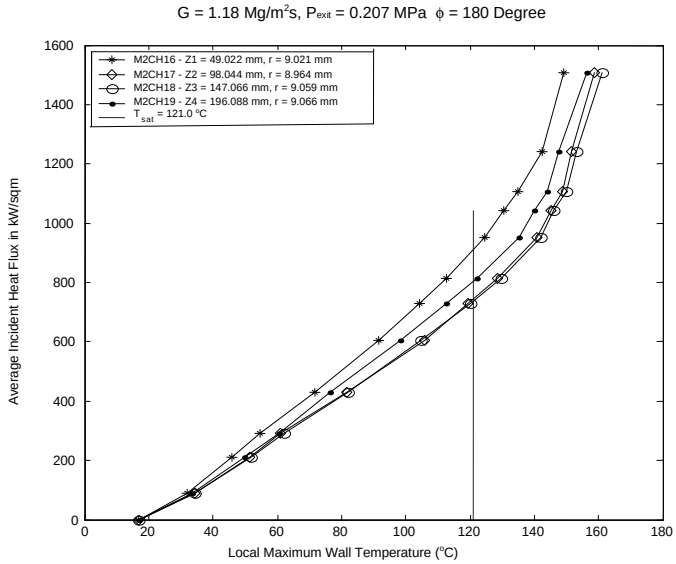

Figure 118: Measured Maximum Local Wall Temperature Axial Variation as a Function of the Average Incident Net Heat Flux for a Single-Side Heated Monoblock for ϕ = 180 Degree, Intermediate Location (for Test #6: G = 1.18 Mg/m^{2}s, with P_{exit} = 0.207 MPa, and T_{sat} = 121.0 ˚C).

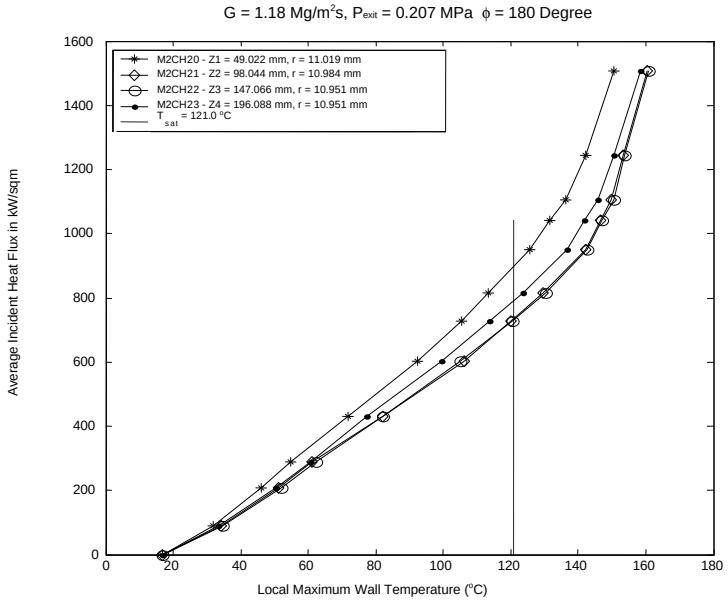

Figure 119: Measured Maximum Local Wall Temperature Axial Variation as a Function of the Average Incident Net Heat Flux for a Single-Side Heated Monoblock for ϕ = 180 Degree, Close to Outside Boundary Location (for Test #6: G = 1.18 Mg/m^{2}s, with P_{exit} = 0.207 MPa, and T_{sat} = 121.0 ˚C).

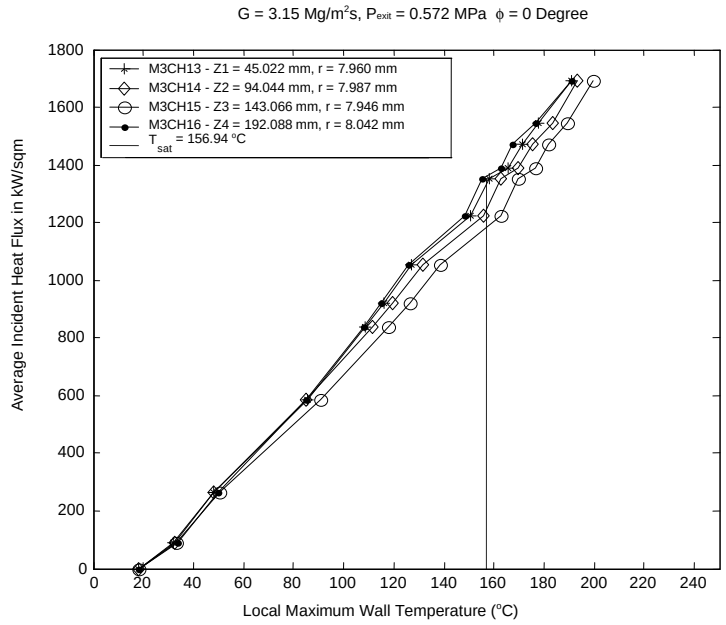

Figure 120: Measured Maximum Local Wall Temperature Axial Variation as a Function of the Average Incident Net Heat Flux for a Single-Side Heated Monoblock for ϕ = 0 Degree, Intermediate Location (for Test #7: G = 3.15 Mg/m^{2}s, with P_{exit} = 0.572 MPa, and T_{sat} = 156.94 ˚C).

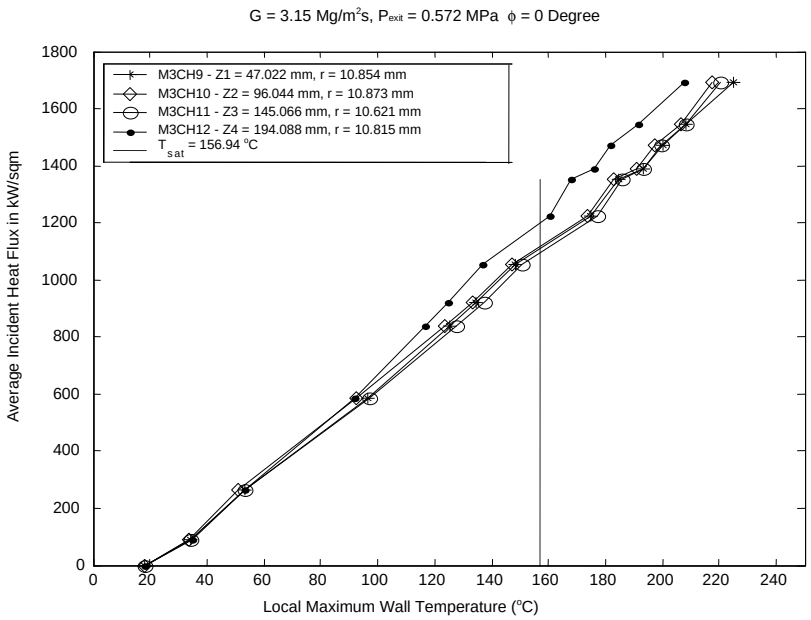

Figure 121: Measured Maximum Local Wall Temperature Axial Variation as a Function of the Average Incident Net Heat Flux for a Single-Side Heated Monoblock for ϕ = 0 Degree, Close to Fluid Boundary Location (for Test #7: G = 3.15 Mg/m^{2}s, with P_{exit} = 0.572 MPa, and T_{sat} = 156.94 ˚C).

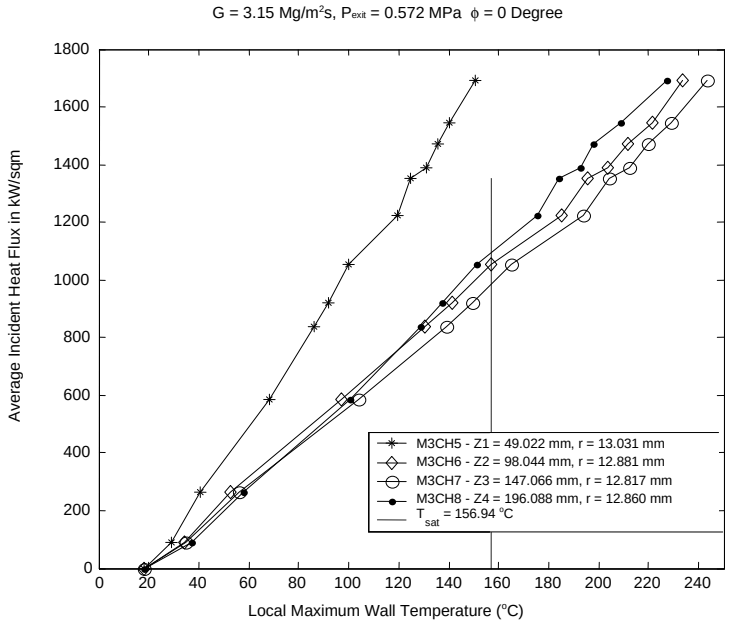

Figure 122: Measured Maximum Local Wall Temperature Axial Variation as a Function of the Average Incident Net Heat Flux for a Single-Side Heated Monoblock for ϕ = 0 Degree, Close to Outside Boundary Location (for Test #7: G = 3.15 Mg/m^{2}s, with P_{exit} = 0.572 MPa, and T_{sat} = 156.94 ˚C).

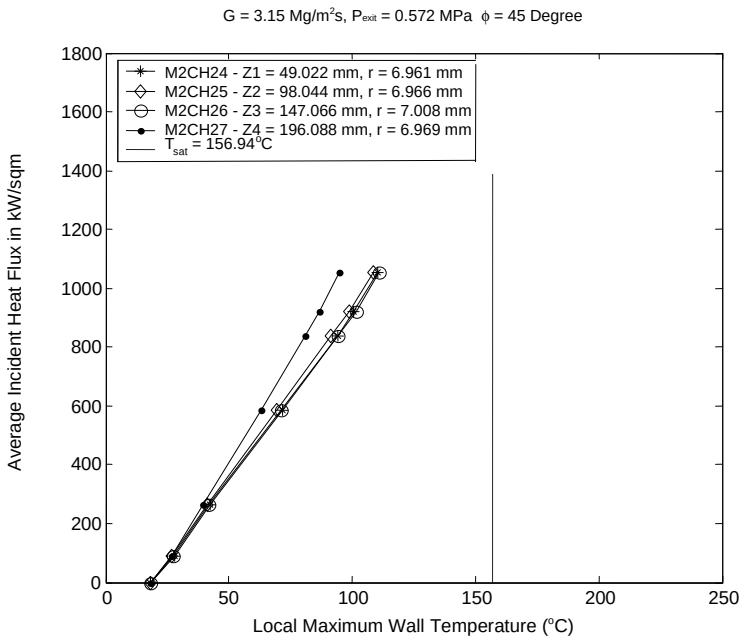

Figure 123: Measured Maximum Local Wall Temperature Axial Variation as a Function of the Average Incident Net Heat Flux for a Single-Side Heated Monoblock for ϕ = 45 Degree, Close to Fluid Boundary Location (for Test #7: G = 3.15 Mg/m^{2}s, with P_{exit} = 0.572 MPa, and T_{sat} = 156.94 ˚C).

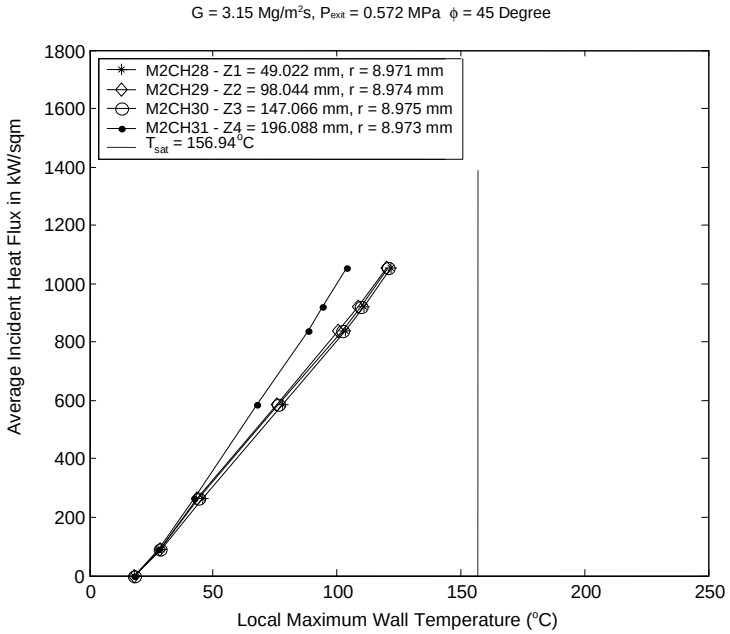

Figure 124: Measured Maximum Local Wall Temperature Axial Variation as a Function of the Average Incident Net Heat Flux for a Single-Side Heated Monoblock for ϕ = 45 Degree, Intermediate Location (for Test #7: G = 3.15 Mg/m^{2}s, with P_{exit} = 0.572 MPa, and T_{sat} = 156.94 ˚C).

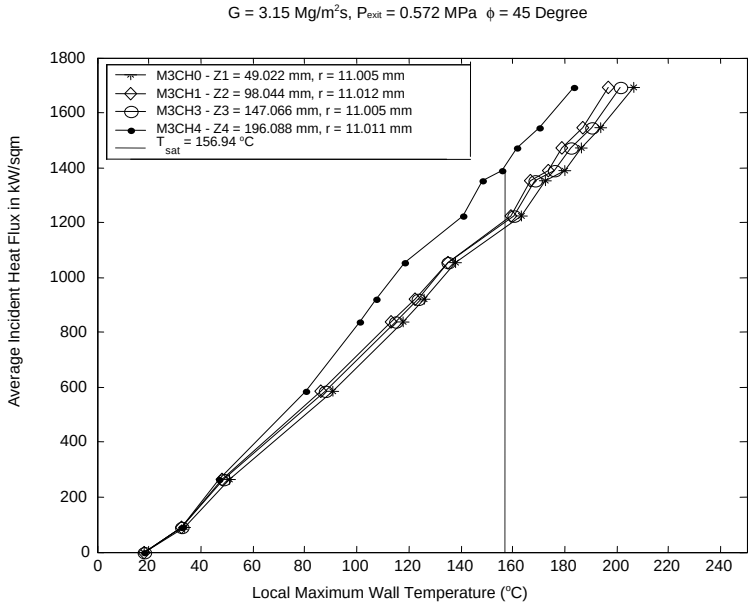

Figure 125: Measured Maximum Local Wall Temperature Axial Variation as a Function of the Average Incident Net Heat Flux for a Single-Side Heated Monoblock for ϕ = 45 Degree, Close to Outside Boundary Location (for Test #7: G = 3.15 Mg/m^{2}s, with P_{exit} = 0.572 MPa, and T_{sat} = 156.94 ˚C).

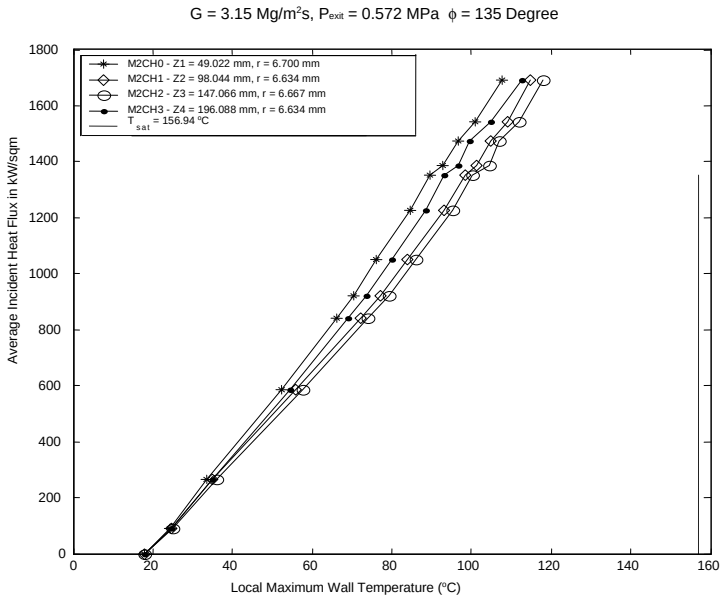

Figure 126: Measured Maximum Local Wall Temperature Axial Variation as a Function of the Average Incident Net Heat Flux for a Single-Side Heated Monoblock for ϕ = 135 Degree, Close to Fluid Boundary Location (for Test #7: G = 3.15 Mg/m^{2}s, with P_{exit} = 0.572 MPa, and T_{sat} = 156.94 ˚C).

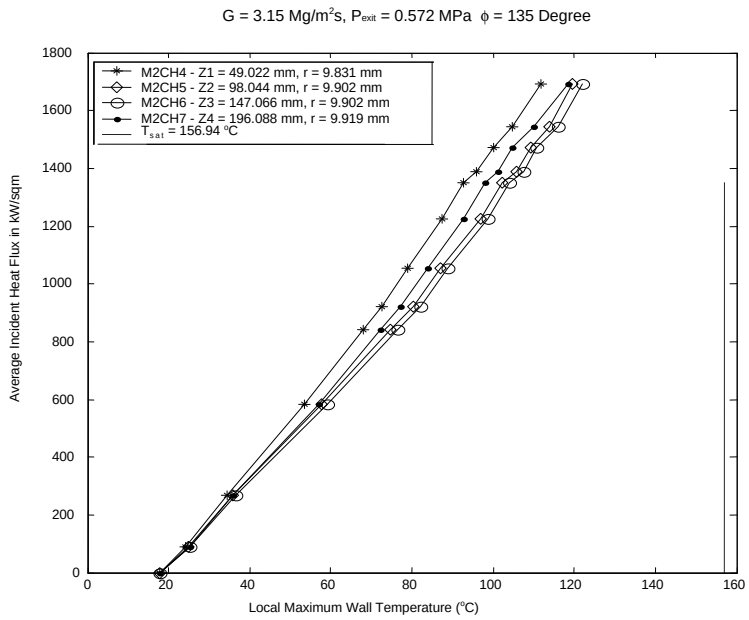

Figure 127: Measured Maximum Local Wall Temperature Axial Variation as a Function of the Average Incident Net Heat Flux for a Single-Side Heated Monoblock for ϕ = 135 Degree, Intermediate Location (for Test #7: G = 3.15 Mg/m^{2}s, with P_{exit} = 0.572 MPa, and T_{sat} = 156.94 ˚C).

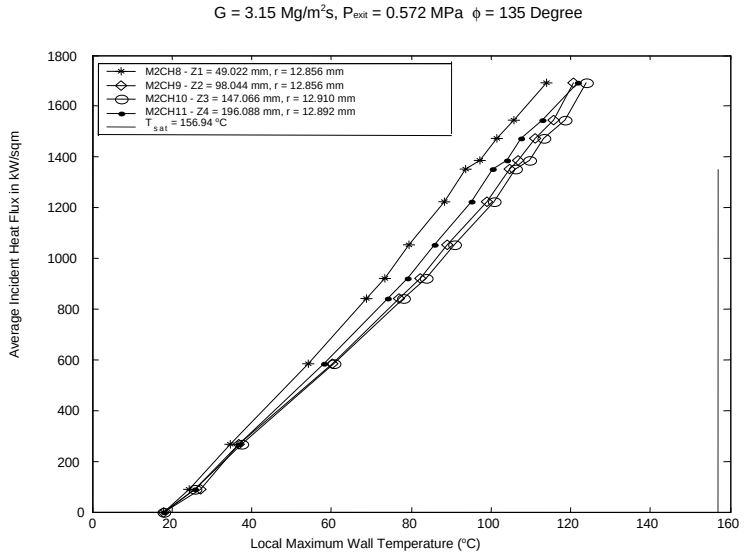

Figure 128: Measured Maximum Local Wall Temperature Axial Variation as a Function of the Average Incident Net Heat Flux for a Single-Side Heated Monoblock for ϕ = 135 Degree, Close to Outside Boundary Location (for Test #7: G = 3.15 Mg/m^{2}s, with P_{exit} = 0.572 MPa, and T_{sat} = 156.94 ˚C).

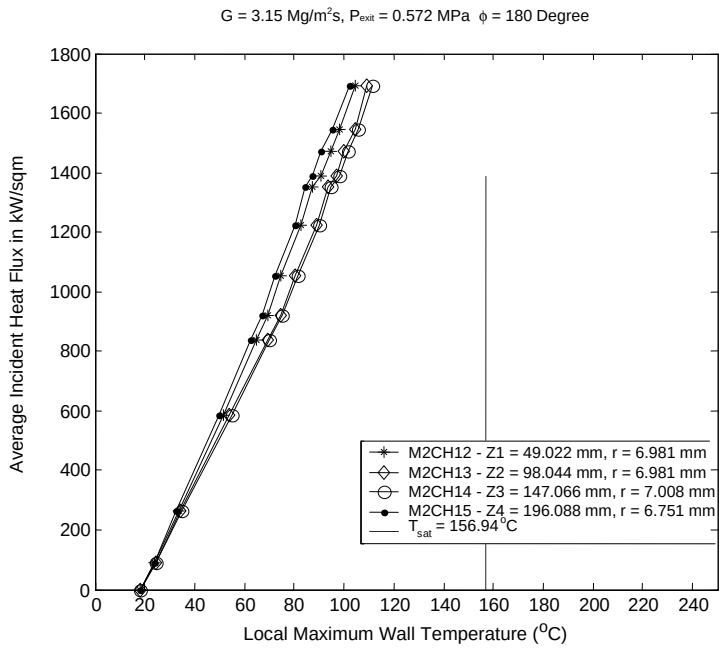

Figure 129: Measured Maximum Local Wall Temperature Axial Variation as a Function of the Average Incident Net Heat Flux for a Single-Side Heated Monoblock for ϕ = 180 Degree, Close to Fluid Boundary Location (for Test #7: G = 3.15 Mg/m^{2}s, with P_{exit} = 0.572 MPa, and T_{sat} = 156.94 ˚C).

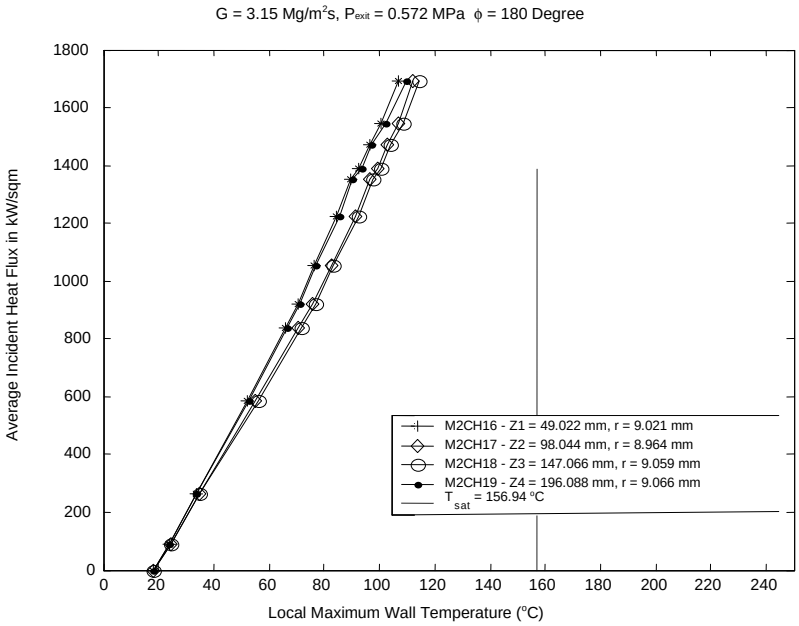

Figure 130: Measured Maximum Local Wall Temperature Axial Variation as a Function of the Average Incident Net Heat Flux for a Single-Side Heated Monoblock for ϕ = 180 Degree, Intermediate Location (for Test #7: G = 3.15 Mg/m^{2}s, with P_{exit} = 0.572 MPa, and T_{sat} = 156.94 ˚C).

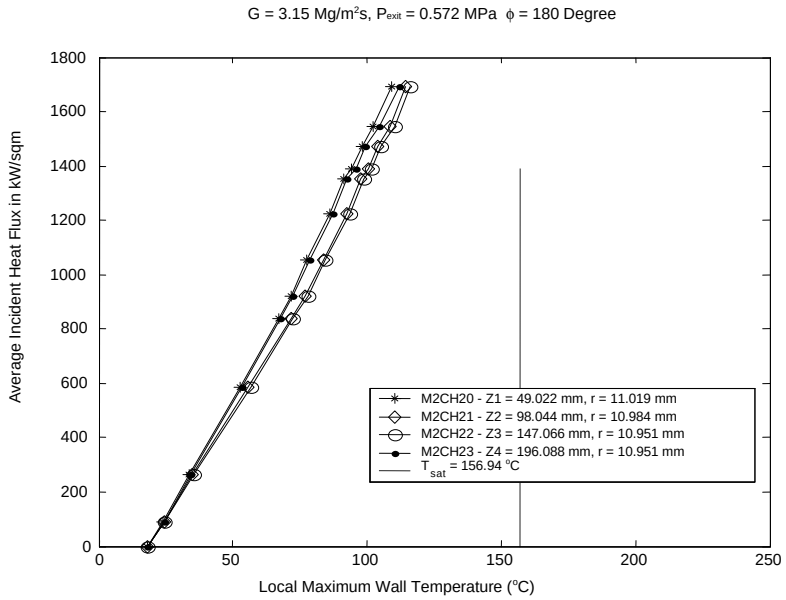

Figure 131: Measured Maximum Local Wall Temperature Axial Variation as a Function of the Average Incident Net Heat Flux for a Single-Side Heated Monoblock for ϕ = 180 Degree, Close to Outside Boundary Location (for Test #7: G = 3.15 Mg/m^{2}s, with P_{exit} = 0.572 MPa, and T_{sat} = 156.94 ˚C).

17.5 EFFECT OF MASS VELOCITY AND EXIT PRESSURE

17.5.1 Monoblock Test Section Results

Figures 132 to 143 show the local flow channel maximum wall temperature (Tw_{max}) distribution at different average net incident heat flux (i.e., $q_o^{"}$) levels for mass velocities of 0.59, 1.18, and 3.15 Mg/m^{2}s for the single-side heated monoblock test section. For the mass velocity of 1.18 Mg/m^{2}s, the data from Test #4 was used.

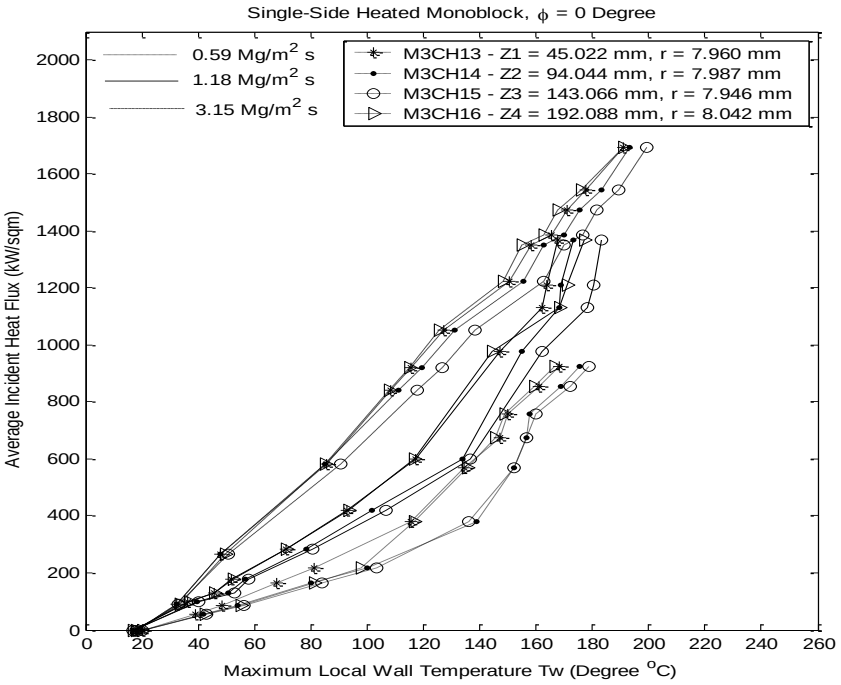

Figure 132: Measured Maximum Local Wall Temperature Axial Variation as a Function of the Average Incident Net Heat Flux for a Single-Side Heated Monoblock for ϕ = 0 Degree, Close to Fluid Boundary Location for Different Mass Velocities.

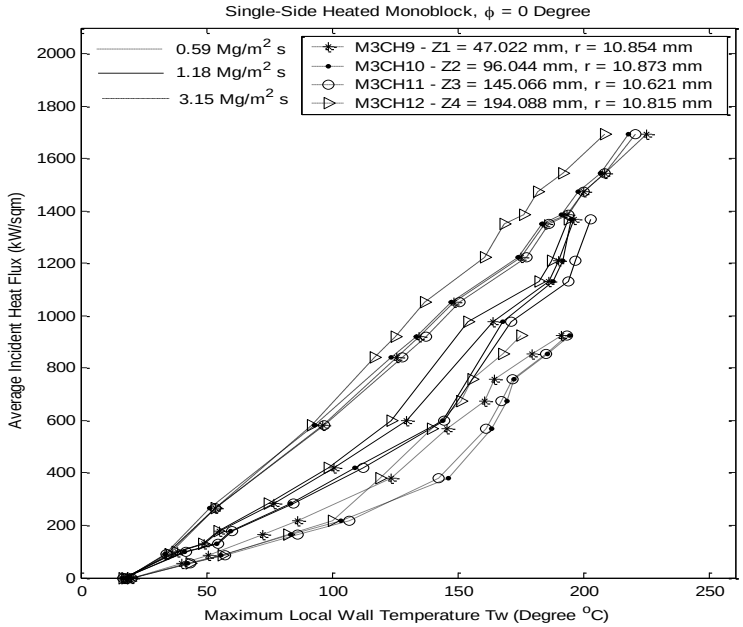

Figure 133: Measured Maximum Local Wall Temperature Axial Variation as a Function of the Average Incident Net Heat Flux for a Single-Side Heated Monoblock for ϕ = 0 Degree, Intermediate Location for Different Mass Velocities.

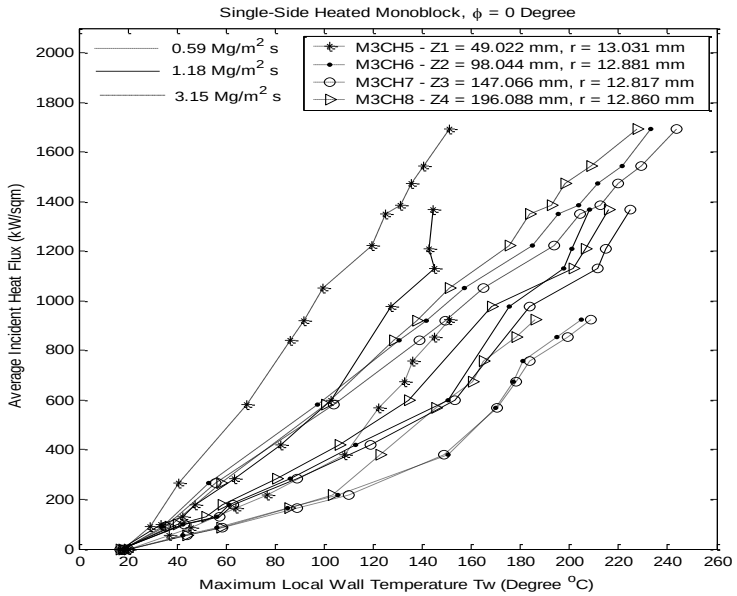

Figure 134: Measured Maximum Local Wall Temperature Axial Variation as a Function of the Average Incident Net Heat Flux for a Single-Side Heated Monoblock for ϕ = 0 Degree, Close to Outside Boundary Location for Different Mass Velocities.

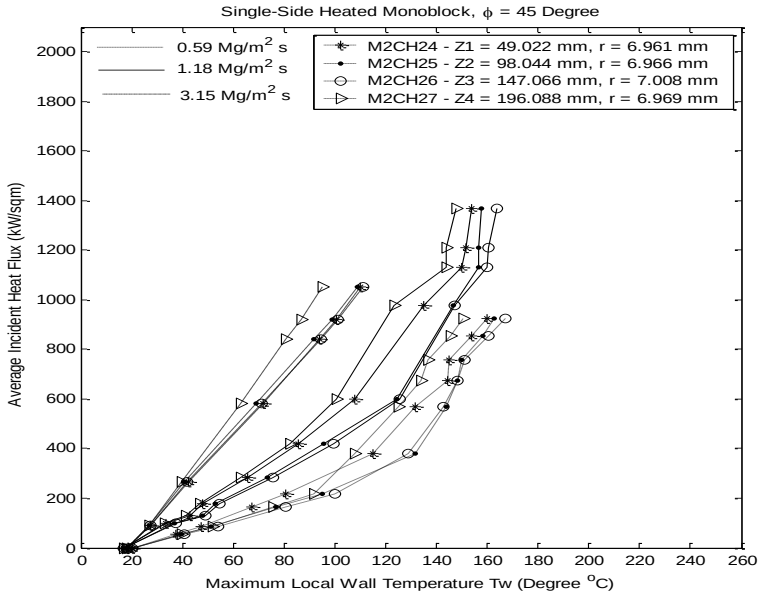

Figure 135: Measured Maximum Local Wall Temperature Axial Variation as a Function of the Average Incident Net Heat Flux for a Single-Side Heated Monoblock for ϕ = 45 Degree, Close to Fluid Boundary Location for Different Mass Velocities.

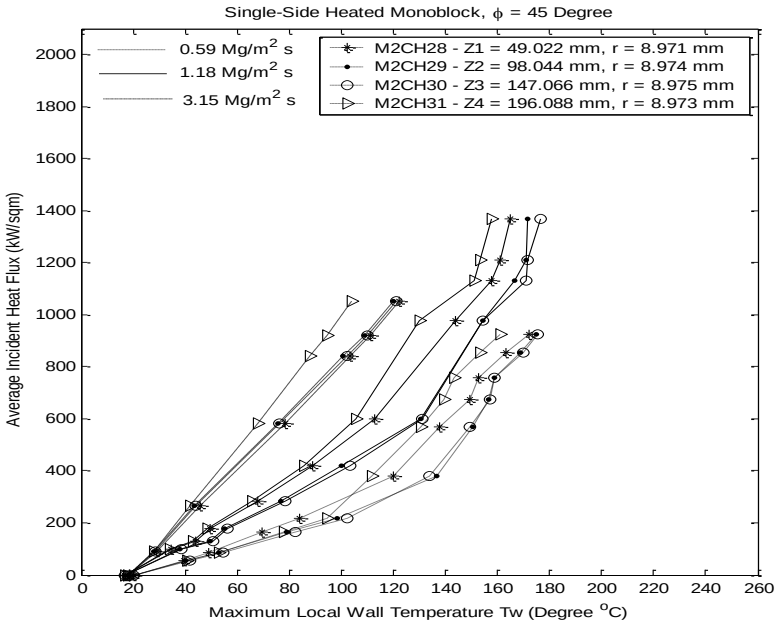

Figure 136: Measured Maximum Local Wall Temperature Axial Variation as a Function of the Average Incident Net Heat Flux for a Single-Side Heated Monoblock for ϕ = 45 Degree, Intermediate Location for Different Mass Velocities.

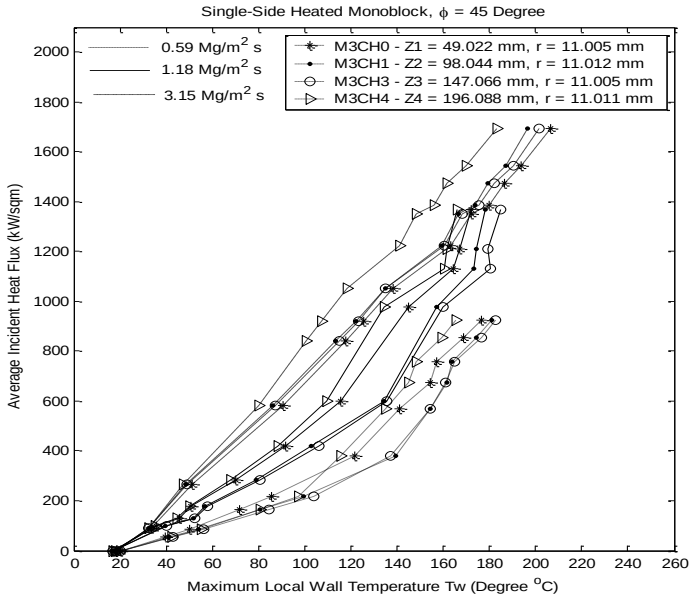

Figure 137: Measured Maximum Local Wall Temperature Axial Variation as a Function of the Average Incident Net Heat Flux for a Single-Side Heated Monoblock for ϕ = 45 Degree, Close to Outside Boundary Location for Different Mass Velocities.

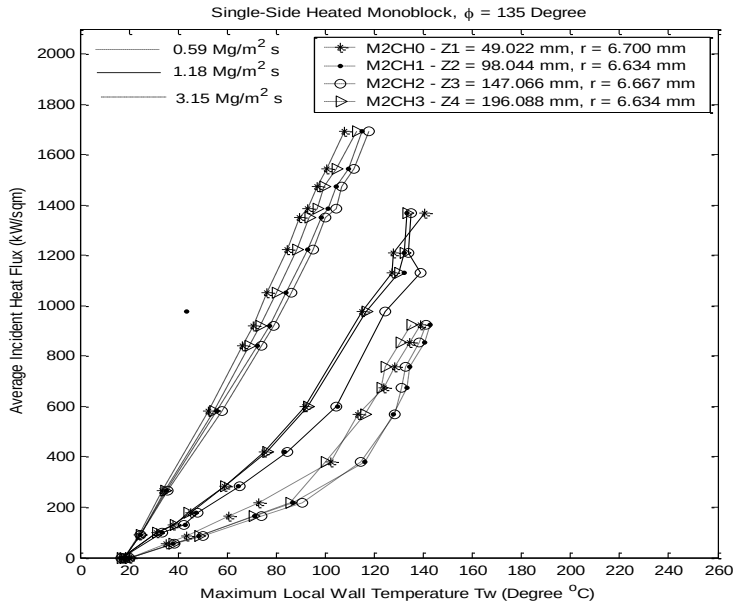

Figure 138: Measured Maximum Local Wall Temperature Axial Variation as a Function of the Average Incident Net Heat Flux for a Single-Side Heated Monoblock for ϕ = 135 Degree, Close to Fluid Boundary Location for Different Mass Velocities.

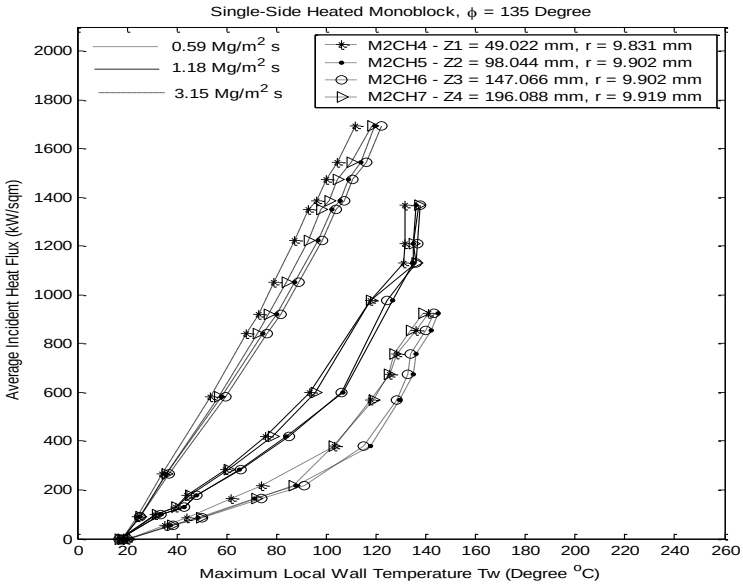

Figure 139: Measured Maximum Local Wall Temperature Axial Variation as a Function of the Average Incident Net Heat Flux for a Single-Side Heated Monoblock for ϕ = 135 Degree, Intermediate Location for Different Mass Velocities.

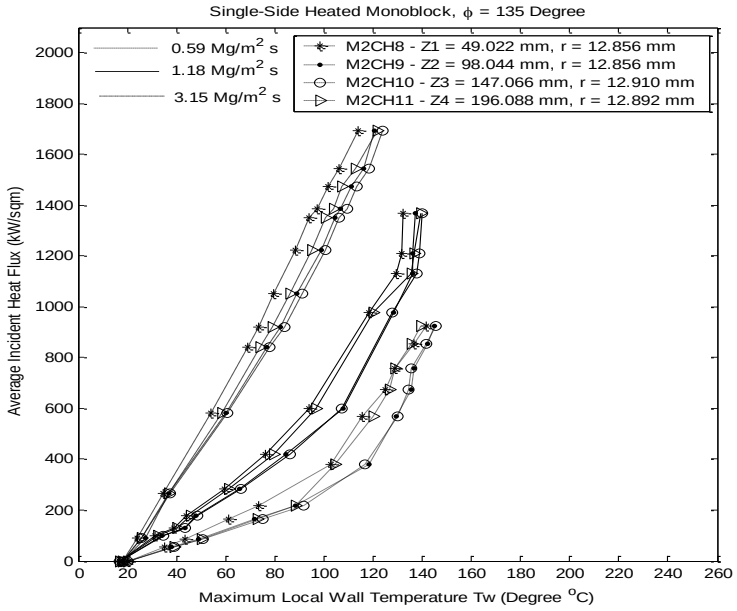

Figure 140: Measured Maximum Local Wall Temperature Axial Variation as a Function of the Average Incident Net Heat Flux for a Single-Side Heated Monoblock for ϕ = 135 Degree, Close to Outside Boundary Location for Different Mass Velocities**.**

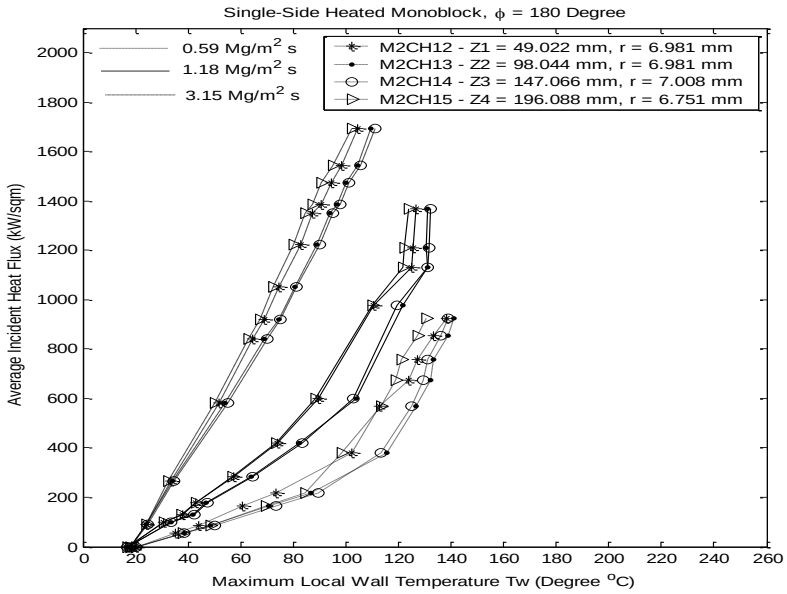

Figure 141: Measured Maximum Local Wall Temperature Axial Variation as a Function of the Average Incident Net Heat Flux for a Single-Side Heated Monoblock for ϕ = 180 Degree, Close to Fluid Boundary Location for Different Mass Velocities.

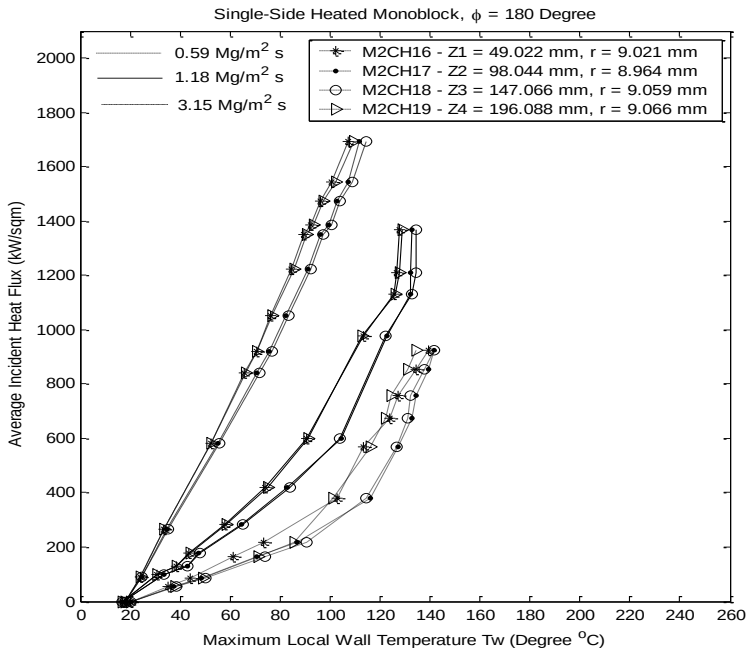

Figure 142: Measured Maximum Local Wall Temperature Axial Variation as a Function of the Average Incident Net Heat Flux for a Single-Side Heated Monoblock for ϕ = 180 Degree, Intermediate Location for Different Mass Velocities.

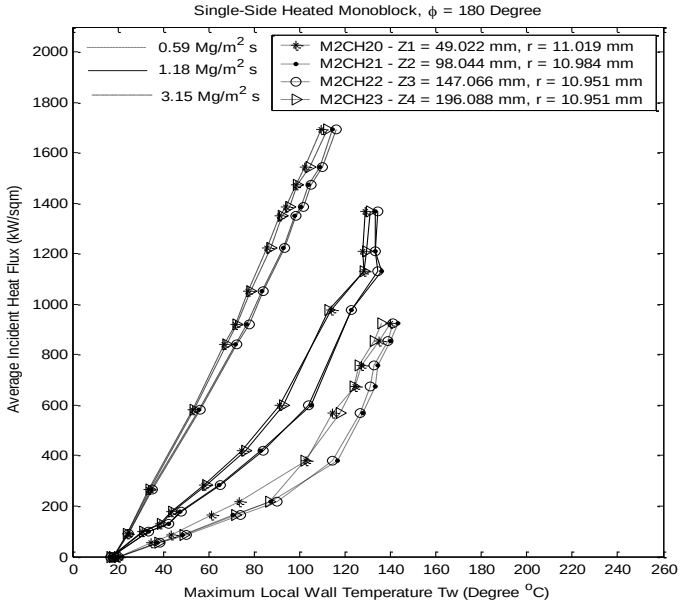

Figure 143: Measured Maximum Local Wall Temperature Axial Variation as a Function of the Average Incident Net Heat Flux for a Single-Side Heated Monoblock for ϕ = 180 Degree, Close to Outside Boundary Location for Different Mass Velocities.

17.5.2 Circular Test Section Results

Figures 144 through 155 show the 3-D effect of exit pressure on the $q_o^{"}$ versus Tw_{max} relationship for the circular test section. The vertical lines shown denote the saturation temperature for the given exit pressure.

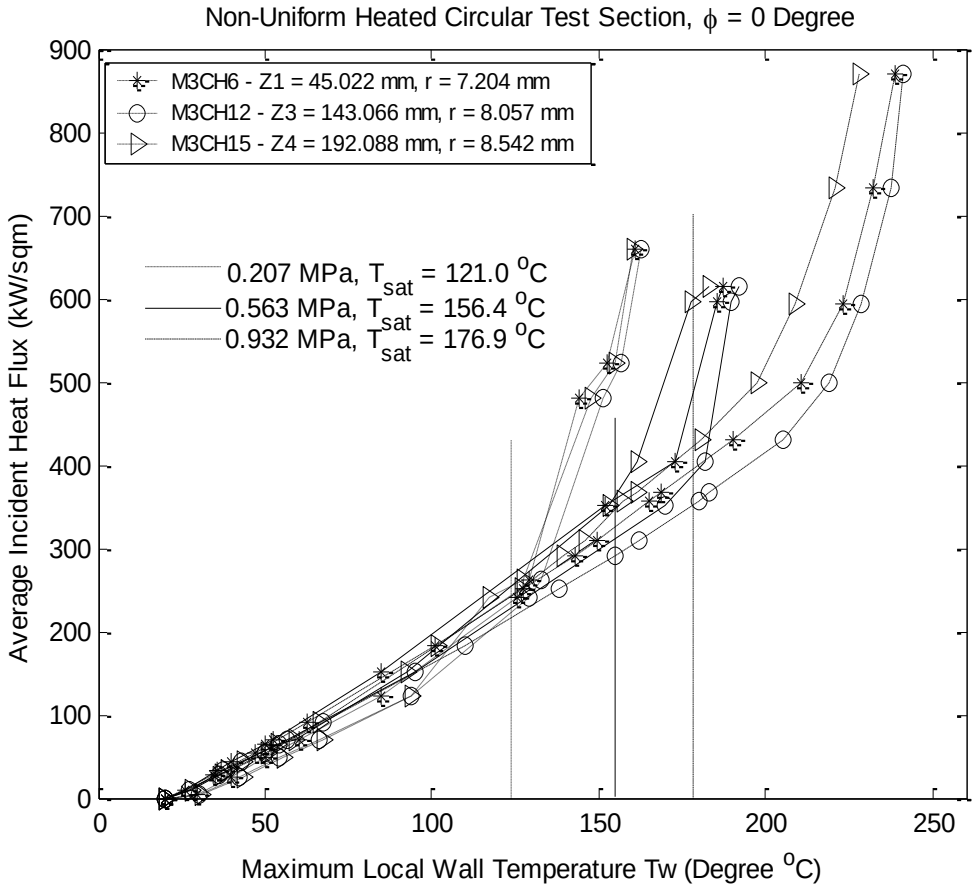

Figure 144: Measured Maximum Local Wall Temperature Axial Variation as a Function of the Average Net Incident Heat Flux for a Non-uniform Heated Circular Test Section for ϕ = 0 Degree, Close to Fluid Location for Different Exit Pressures.

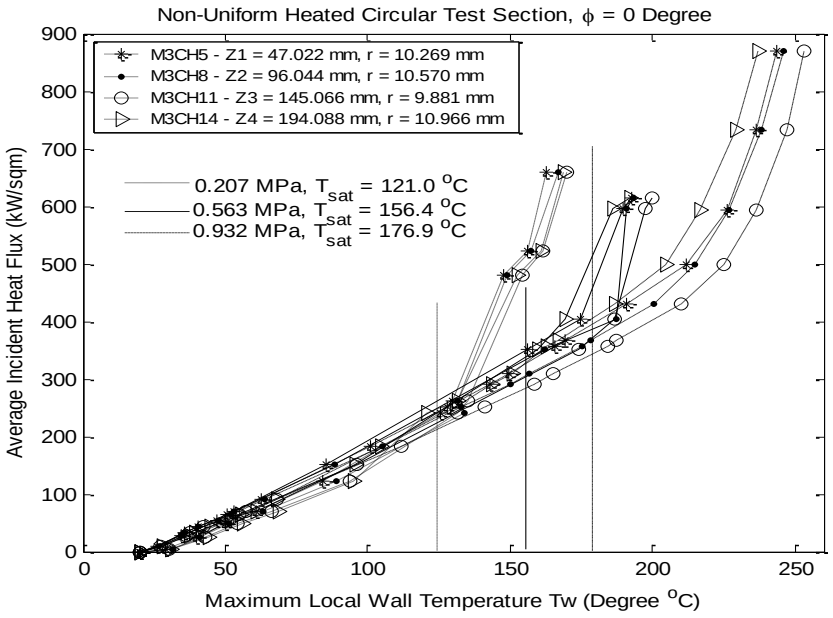

Figure 145: Measured Maximum Local Wall Temperature Axial Variation as a Function of the Average Net Incident Heat Flux for a Non-uniform Heated Circular Test Section for ϕ = 0 Degree, Intermediate Location for Different Exit Pressures.

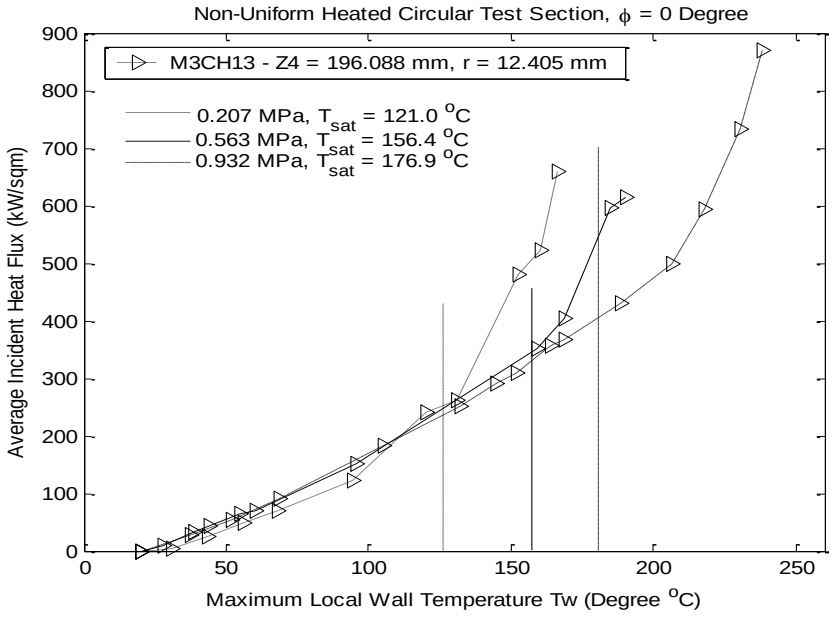

Figure 146: Measured Maximum Local Wall Temperature Axial Variation as a Function of the Average Net Incident Heat Flux for a Non-uniform Heated Circular Test Section for ϕ = 0 Degree, Close to Outside Boundary Location for Different Exit Pressures.

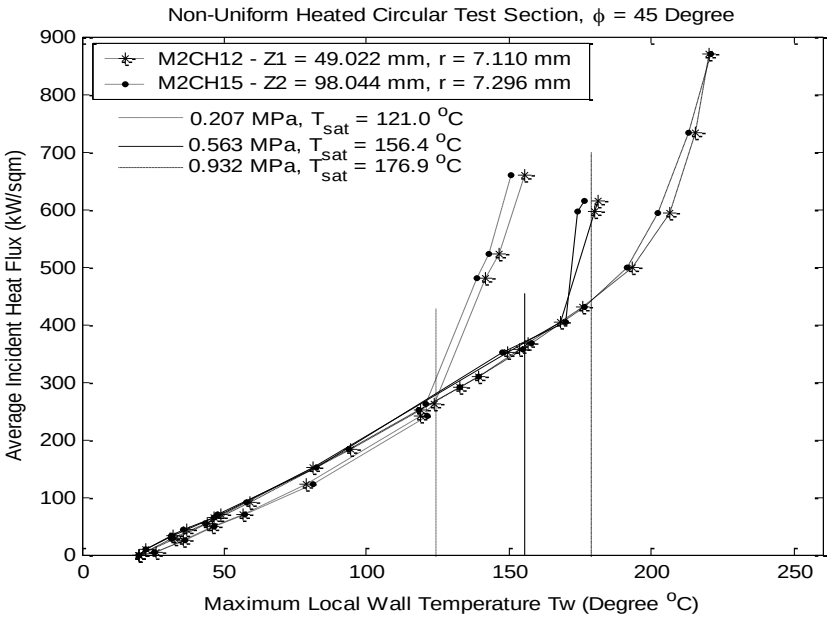

Figure 147: Measured Maximum Local Wall Temperature Axial Variation as a Function of the Average Net Incident Heat Flux for a Non-uniform Heated Circular Test Section for ϕ = 45 Degree, Close to Fluid Location for Different Exit Pressures.

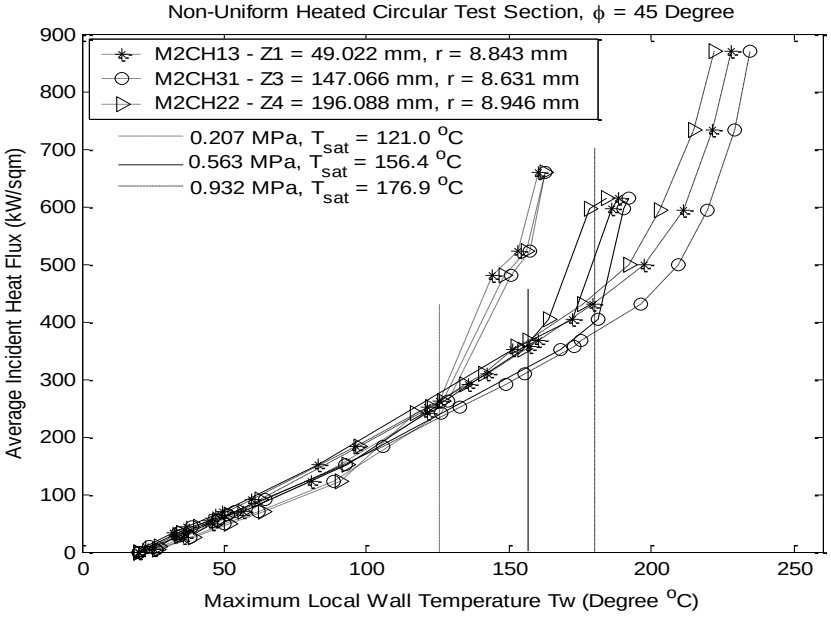

Figure 148: Measured Maximum Local Wall Temperature Axial Variation as a Function of the Average Net Incident Heat Flux for a Non-uniform Heated Circular Test Section for ϕ = 45 Degree, Intermediate Location for Different Exit Pressures.

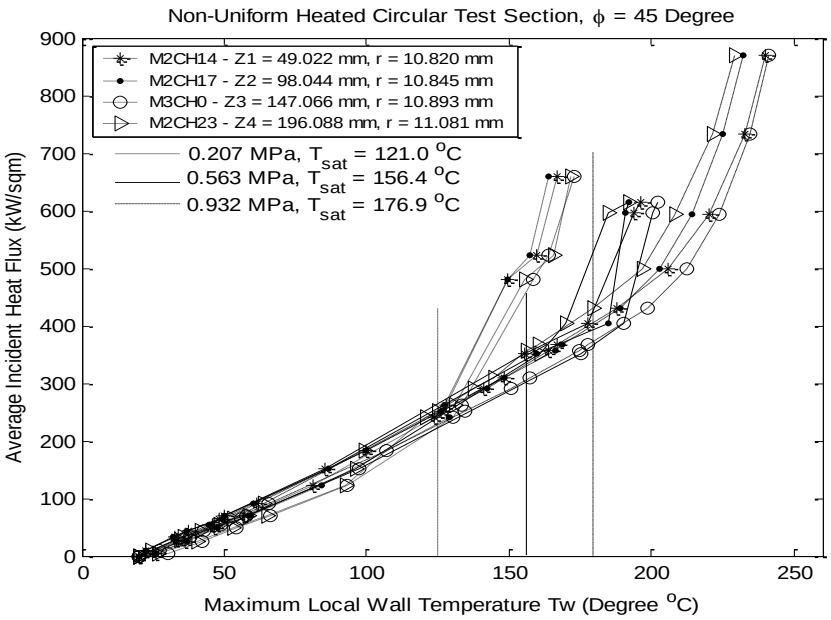

Figure 149: Measured Maximum Local Wall Temperature Axial Variation as a Function of the Average Net Incident Heat Flux for a Non-uniform Heated Circular Test Section for ϕ = 45 Degree, Close to Outside Boundary Location for Different Exit Pressures.

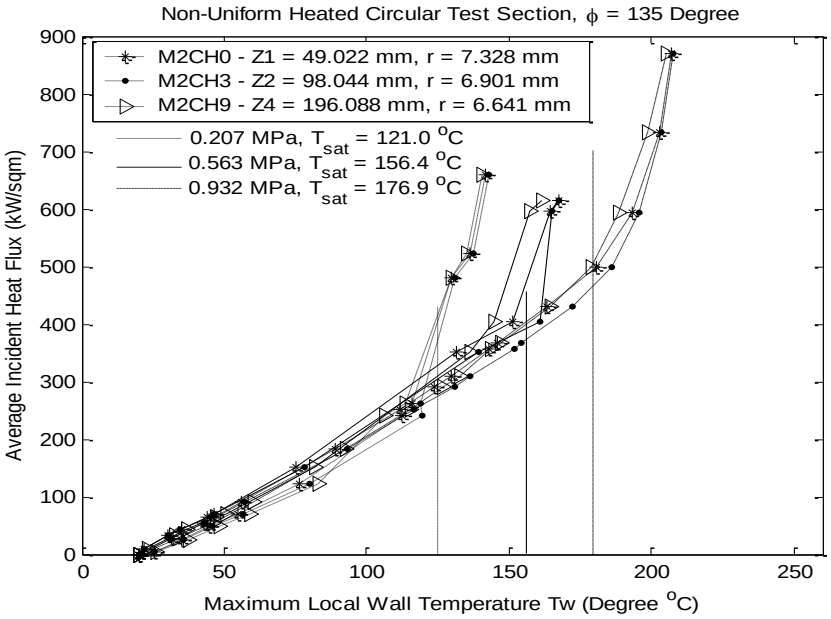

Figure 150: Measured Maximum Local Wall Temperature Axial Variation as a Function of the Average Net Incident Heat Flux for a Non-uniform Heated Circular Test Section for ϕ = 135 Degree, Close to Fluid Location for Different Exit Pressures.

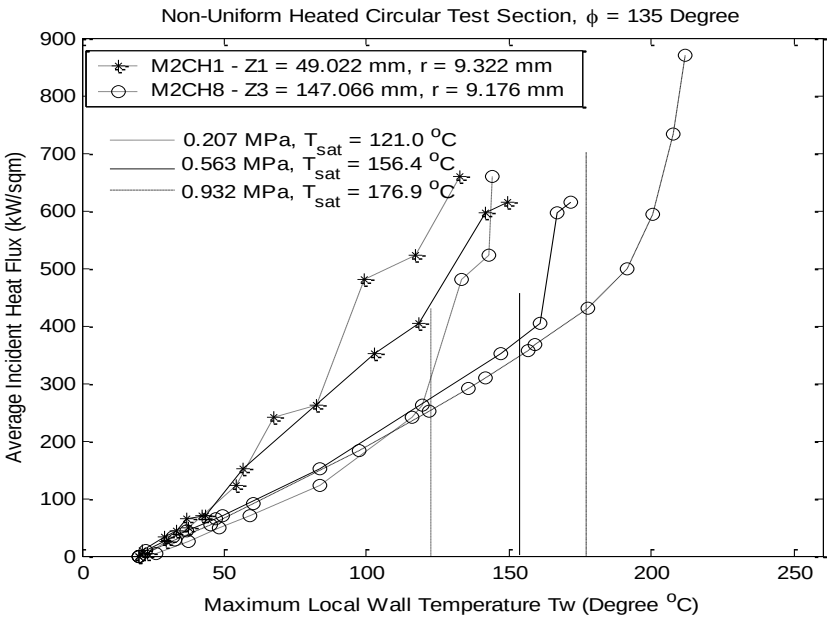

Figure 151: Measured Maximum Local Wall Temperature Axial Variation as a Function of the Average Net Incident Heat Flux for a Non-uniform Heated Circular Test Section for ϕ = 135 Degree, Intermediate Location for Different Exit Pressures.

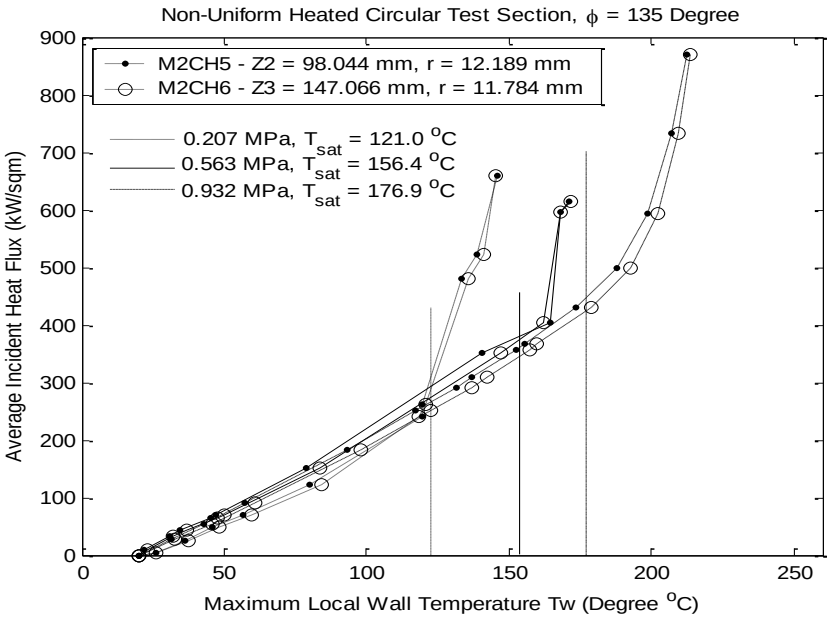

Figure 152: Measured Maximum Local Wall Temperature Axial Variation as a Function of the Average Net Incident Heat Flux for a Non-uniform Heated Circular Test Section for ϕ = 135 Degree, Close to Outside Boundary Location for Different Exit Pressures.

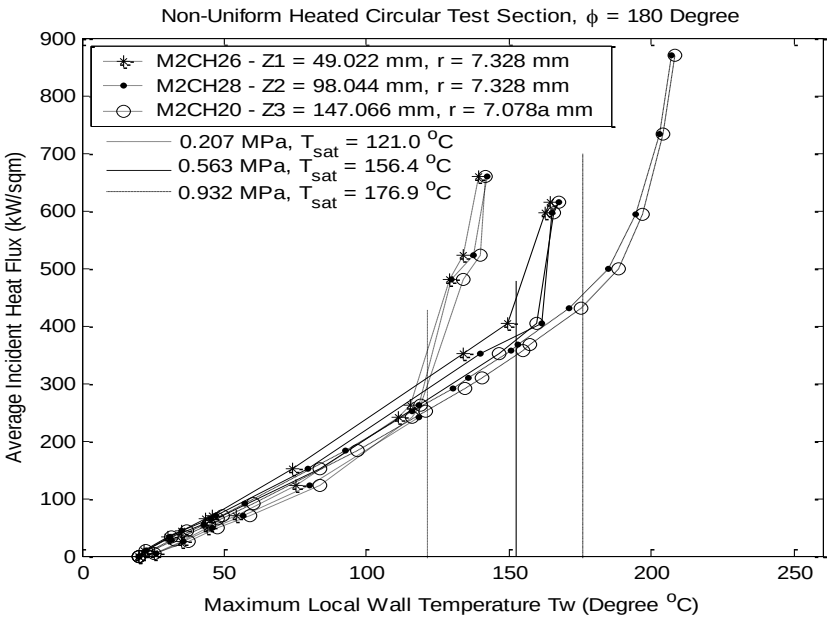

Figure 153: Measured Maximum Local Wall Temperature Axial Variation as a Function of the Average Net Incident Heat Flux for a Non-uniform Heated Circular Test Section for ϕ = 180 Degree, Close to Fluid Location for Different Exit Pressures.

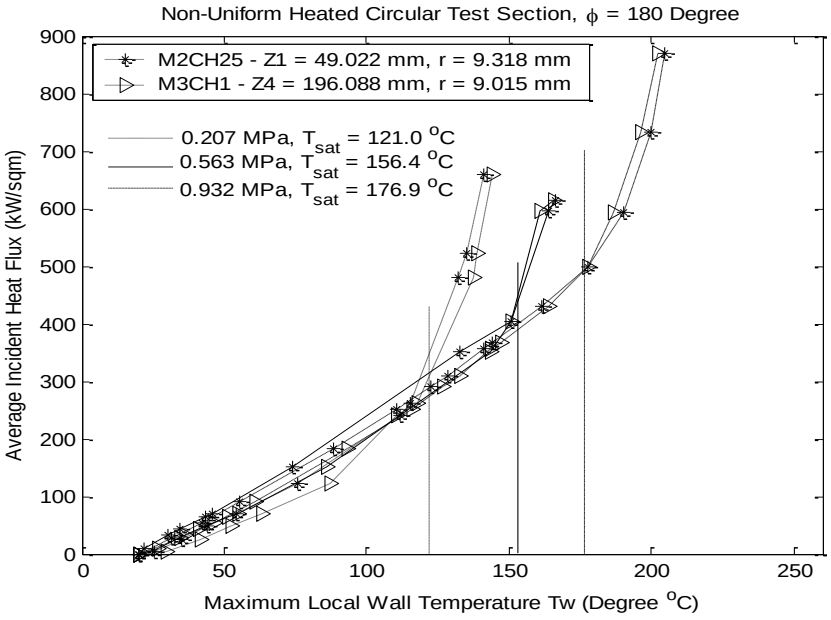

Figure 154: Measured Maximum Local Wall Temperature Axial Variation as a Function of the Average Net Incident Heat Flux for a Non-uniform Heated Circular Test Section for ϕ = 180 Degree, Intermediate Location for Different Exit Pressures.

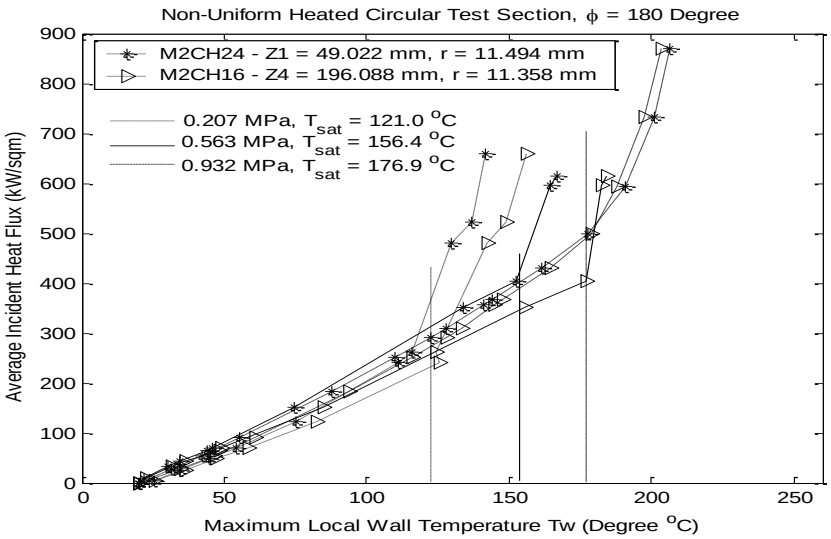

Figure 155: Measured Maximum Local Wall Temperature Axial Variation as a Function of the Average Net Incident Heat Flux for a Non-uniform Heated Circular Test Section for ϕ = 180 Degree, Close to Outside Boundary Location for Different Exit Pressures.

18.0 CONJUGATE HEAT TRANSFER MEASUREMENTS AND 2-D BOILING CURVES FOR WATER FLOW BOILING IN A SINGLE-SIDE HEATED MONOBLOCK FLOW CHANNEL

18.1 INTRODUCTION

Many engineering applications involved conjugate heat transfer in substrates which: (1) are heated from a single side; (2) are cooled via coupled, internal, turbulent single-phase or two-phase flow; and, (3) have peripheral or circumferential heat transfer around the flow channel. Examples include plasma-facing components (PFCs) in fusion reactors, optical heat sinks, electronic heat sinks, protective air transport systems, and space systems. In some high heat flux removal systems, the internally flowing fluid likely may change phase along the length of the flow channel. Engineering feasibility studies and reviews (e.g., [113, 72]) have shown the advantages of and the need for local embedded thermocouple data for characterizing conjugate heat transfer in applications involving single-side heated components with both internal and circumferential cooling. Such data would be invaluable in the future scale-up activity to large-scale components and applications. For optimized and robust system development where single-side heat transfer is involved, it is necessary to measure, understand and, correlate the non-uniform or single-side heating effects on the resultant inside flow channel heat flux and temperature distributions (i.e., the boiling curve).

The objective of the present work was to produce two-dimensional (2-D) boiling curves using steady-state, three-dimensional (3-D), flow boiling and single-phase measurements in a horizontal single-side heated monoblock flow channel with water as a flowing fluid. *It should be noted that the present 2-D boiling curves are among the first that have appeared in the technical literature.* The purposes of this experimental investigation were to: (1) measure the local 3-D wall temperature distributions for a given net applied heat flux; (2) generate 2-D boiling curves; (3) estimate the 2-D inside channel wall heat flux distributions; and, (4) make comparisons between the experimental data and selected correlations from the literature.

Since the complete experimental system is described elsewhere [90], only a summary of the flow parameters will be given. The flow parameters are as follows: 0-3.0 MW/m^2 heat flux, 0.59 - 3.15 Mg/m^2s mass velocity, 0.21 - 0.57 MPa exit pressure, $5 \times 10^3 - 2 \times 10^5$ Reynolds number, and less than 130 ^0C subcooling.

In his review of actively cooled PFCs, Nygren [72] alluded to the importance of monoblock flow channel data from embedded thermocouples. In the case of plasma facing components heated from one side, Araki et al. [113] emphasized the need for a comprehensive database which includes heat transfer around the circumference of flow channels. Using existing uniform heat flux correlations, they compared their data for single-side heated circular cylindrical flow channels (r_i = 5.0 mm) as a function of the incident heat flux and local wall temperature. Using Shah's (Jens and Lottes') and Thom's correlations, a modified inverse conduction analysis was compared favorably with local circumferential temperature variations which were recorded from embedded (in the wall of the flow channel) thermocouples. However, no data were produced for the inside flow channel wall temperature (T_{wi}) and heat flux (q_i). In one case involving a tube without a twisted tape, the local heat transfer coefficient was compared and found to be bracketed by these correlations to within ± 30%. Some form of the modified inverse analysis produced predictions for T_{wi} and q_i; but, the analysis were based on either the Shah or Thom correlation. It should be noted that conventional inverse conduction analyses should be independent of such correlations. Therefore, there is still a need to produce T_{wi} (ϕ, Z) and q_i (ϕ, Z) for single-side heated circular and monoblock flow channels with internal single-phase and flow boiling conditions.

In their study, Araki et al. [102] measured local (r/r_i = 1.3) circumferential channel wall temperature variations in a single-side heated circular flow channel (r_o/r_i = 1.5). One of their objectives was to determine whether existing heat transfer correlations, developed for uniform heating, were applicable for single-side heated circular flow channels in the single-phase and flow boiling regimes. They concluded that existing correlations: (1) could be used in the "non-boiling region," but (2) could not be used in the subcooled flow boiling regimes. Using a correlational form similar to that of the Thom and Jens-Lottes correlations for the subcooled flow boiling fully-developed regime, they proposed a new correlation which fit (± 15%) their single-side heated data base. Consistent with the peaking factor (PF) predictions of Boyd and Meng [24], they found that the PF was less than r_o/r_i.

Based on a modified mixing-length turbulent model and the Davis-Anderson onset of nucleate flow boiling (ONB) criterion, Shim, Soliman, and Sims [114] used a two-dimensional conjugate analysis for annuli with finite thickness fins to successfully predict (to within 13%) ONB data and wall-to-fluid temperature differences. In addition to including variable fluid

properties for their fully-developed (both hydodynamically and thermally) turbulent flow, comparisons were made with smooth annulus data. For these cases: (1) the ratio of outside to inside flow channel radius varied from 1.6 to 80.7, (2) the Reynolds number varied from 10^4 to 10^6, and (3) the Prandtl number varied from 0.7 to 10.0. The ONB was computed as the intersection of two curves formed by the Davis-Anderson criterion and that at the fluid-solid interface from the conjugate analysis. Very good agreement resulted up to a mean velocity of 4.0 m/s. In all cases, the ONB occurred at the center of the root between two fins.

Increasing international attention is being given to single-side heated flow channels which might be used in PFCs and other applications. Using the ABAQUS code and unspecified swirl flow boiling correlations, Youchison et al. [52] obtained good agreement with data for a single-side heated monoblock with internal water flow boiling. Raffray et al. [115] addressed three different coolant systems for single-side heat flux accommodation in future fusion reactor divertor and blanket components. Among other details, they noted that "structural integrity" requires the monoblock pitch to be ≥ 20.0 mm for a 10.0 mm inside diameter flow channels. For this channel size, the PF was estimated to be 1.46 for a pitch of 19.0 mm and 1.6 when the pitch is 24.0 mm. Obviously, PF also depends on the value of $\frac{r_o - r_i}{r_i}$ at $\phi = 0$. Baxi [78] reviewed and summarized important aspects of heat transfer in single-side heated monoblocks used in PFCs which included: (1) a typical variation of the heat transfer coefficient over all subcooled flow boiling regimes, (2) a typical ratio of inside flow channel wall heat flux to the incident heat flux ($\lesssim$ 1.5) for flow channels with swirl tape inserts, and (3) a summary assessment of various heat transfer enhancement techniques. For single-side heated flow channels with swirl tape inserts, Inasaka and Nariai [84] studied the circumferential heat flux variation and developed correlations for single-side heat flux multipliers relative to uniformly heated flow channels. Among many important issues, the design of PFCs depends on resulting thermal stresses which result when composite monoblocks are subjected to heat fluxes from one side [116]. Embedded temperature measurement results will assist in this regard. Razmerov and Molochnikov [117] studied stability of fusion reactor first wall flow channels for inlet and flow conditions recommended by Raffray et al. [115]. Under these conditions, they found that stability became an important issue when the monoblock mass velocity was substantially reduced. It appears that additional work is still needed on stability issues for PFCs.

Izumi et al. [103] studied heat transfer mechanisms based on temperature profiles and bubble motion from a single-side heated copper block on a test section with internal flow boiling but without peripheral or circumferential cooling. Although this and other such studies (e.g., [104]) contain fundamental flow boiling phenomenology, the test sections used significantly differ from the present single-side heated monoblock because of the absence of circumferential heat transfer.

18.2. MONOBLOCK THERMAL BOUNDARY CONDITIONS

The thermophysical configuration for the monoblock test section is shown in Fig. 156. The incident heat flux was applied to a single-side and subcooled water flowed through the channel in the center of the test section. A flow-developing section existed upstream of the heated section such that the flow in the heated section was hydrodynamically fully-developed. The test section was exposed to ambient air on all other surfaces except on the top (where the incident heat flux was applied) and where the mykroy (k = 1.32 W/mK) supports were located on the bottom. This resulted in heat losses from the test section due to the natural convection, radiation and conduction to the surroundings. In addition, there were energy losses via axial conduction to the flow loop. The total rate of heat losses to the surroundings were estimated to be less than 1.5% of the rate of energy transferred to the flowing fluid (i.e, q_o). The averaged net incident heat flux $\left(q_o^{"}\right)$ was computed from the ratio of q_o to the product of L w (=A_s). Thus, $q_o^{"}$ is given by

$$q_o^{"} = \frac{\dot{m}\left(i_2 - i_1\right)}{A_s}, \tag{18-1}$$

where $\dot{m}$ is the mass flow rate in kg/s; i_1 and i_2 are the inlet and outlet water specific enthalpies, respectively; and A_s is the surface area of the test section-heater interface. The local (Z-location) bulk specific enthalpy was calculated from $q_o^{"}$ and the inlet water specific enthalpy using an equation similar to equation (17-2) or

$$i_l = i_1 + \frac{q_o^{"} \cdot w \cdot Z}{\dot{m}}, \tag{18-2}$$

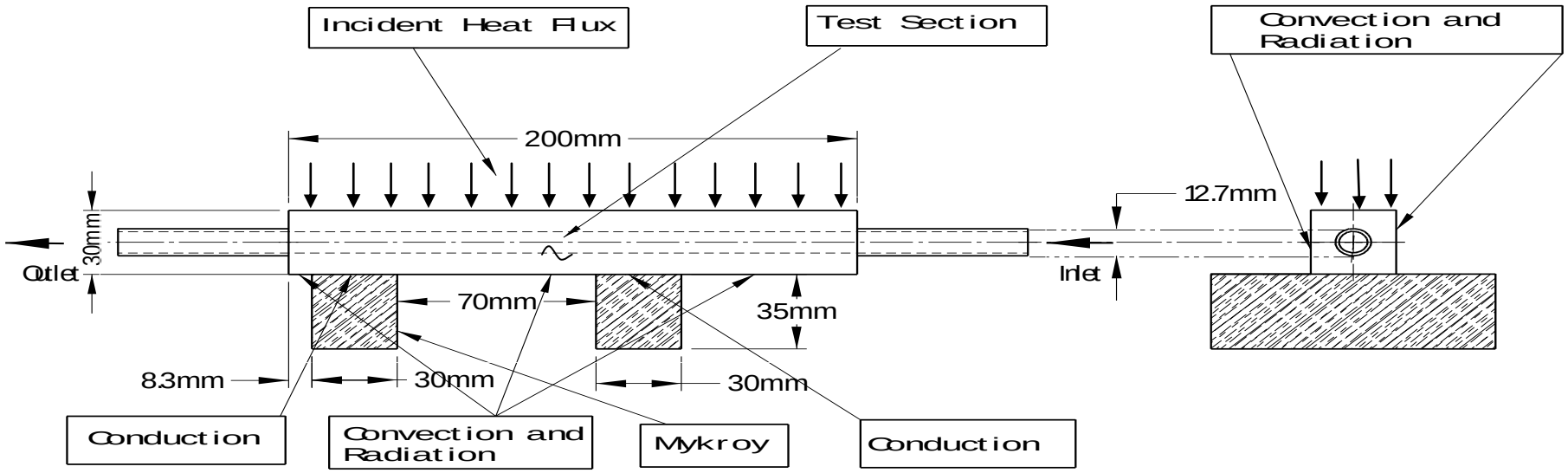

Figure 156: Boundary Conditions for the Monoblock Test Section.

where, i_l is the local bulk specific enthalpy at the Z location, w is the heated width of the test section, and Z is the axial distance from the inlet heated point of the test section. Then, the local bulk temperature was interpolated from thermodynamic data using the local bulk specific enthalpy (i_l). It was used in some heat transfer correlations for comparisons with the measured data.

In the present work, single-side heating effects were accounted for by replacing D_i as the characteristic diameter in some correlations with the thermal-hydraulic flow diameter [60, 118],

$$D_T = a_a \cdot D_i , \tag{18-3}$$

where a_a is parameter, and D_i is the test section inside flow diameter. The quantity D_T was used to: (1) predict the onset nucleated boiling heat flux and fully developed boiling heat flux for the single-side heated test section, and (2) in select boiling curve correlations. It should be noted that D_T was used only in the Reynolds number $\left(\mathrm{Re}_{D_T}\right)$ and the Nusselt number $\left(Nu_{D_T}\right)$.

18.3 RESULTS

The three-dimensional (3-D) temperature distributions were measured as a function of the averaged net incident flux $\left(q_o^{"}\right)$ for the single-side heated monoblock test section which is cooled internally via single-phase convection and flow boiling. All local measurements include effects of conjugate heat transfer with turbulent flow. The measurements were used to radially extrapolate the inside flow channel wall temperature $\left(T_{wi}\right)$ and then determine the inside heat flux ($q_i^{"}$). *To this principal investigator's (PI) knowledge, these results are the first direct representations of 2-D boiling curves for a single-side heated monoblock.* Comparisons with selected correlations from the literature were made.

Since there appears to be few correlations in the literature (e.g., see [102 and 60]) developed for a single side heated flow channel, selected correlations and methodologies (e.g., [102, 62, and 95]), which have been applied to a single side heated flow channel, were compared with the present data. In the Marshall, Youchison, and Caldwallader methodology [62], the following single-phase and subcooled flow boiling correlations were used: (1) Sieder-Tate for the single-phase region, (2) Bergles-Rohsenow for the onset of nucleate boiling, (3) Bergles-Rohsenow for the partial nucleate boiling regime, and (4) Araki et al. [102] for the fully-developed boiling regime. In reporting their correlation for the fully-developed nucleate boiling

regime, Araki et al. used the same correlation to obtain agreement (± 15%) with flow channels with and without a swirl tape insert. Although Marshall, Youchison and Caldwallader used the arithmetic mean bulk temperature based on the inlet and outlet bulk temperatures for their single axial measurement location, the predictions in the present work use the local bulk temperature, T_b (Z) for the multiple axial measurement locations. In the Boyd-Meng methodology [95], the following single-phase and subcooled flow boiling correlations were used: (1) Petukhov for the single-phase regime, (2) Bergles-Rohsenow for the onset of nucleate boiling, (3) Boyd-Meng correlation for the partial nucleate boiling regime, (4) Engelberg-Forster--Greif criterion for the onset of fully-developed boiling, and (5) Shah for the fully-developed boiling regime.

18.3.1 Boiling Curves

The applied power from the test section heater [90] was used to generate the incident heat flux, q''_{oo} (see Figs. 43 and 156). This heat flux was varied so that the test section flow ranged from single-phase to well into the fully-developed, nucleate flow boiling regime. In all cases, flow rate, average net incident heat flux $\left(q''_o\right)$, and exit pressure were parameters for these steady-state experiments. Local (3-D) wall temperature measurements (see Fig. 42) were made and used to determine the 2-D distributions for the flow channel inside: (1) wall temperature, (2) heat flux, and (3) the resulting boiling curves.

From the embedded thermocouples in the single-side heated test section, a set of sixteen (16) inside flow channel wall temperatures $\left(T_{wi}\right)$ and the inside wall heat fluxes $\left(q''_i\right)$ were obtained for different levels of the average net incident heat flux, q''_o. These sets include four axial (Z_1 = 49.02 mm, Z_2 = 98.04 mm, Z_3 = 147.07 mm, and Z_4 = 196.09 mm) and four circumferential (ϕ = 0, 45, 135, and 180 degrees) locations. In Figs. 157a through 157d, the locus of the "star" symbol data points represents the boiling curves (i.e., q''_i vs T_{wi} with T_{sat} shown in the figures) for a mass velocity of 0.59 Mg/m^{2}s and exit pressure of 0.207 MPa at: (1) an axial location of 147.07 mm (about three-quarters downstream of the heated entrance), and (2) the four circumferential locations. The first vertical line denotes the saturation temperature at the exit pressure. The "triangular" symbol data points represent q''_o versus T_{wi}. The ratio of q''_i to q''_o is related to the local peaking factor. To enhance data interpretation, the onset of nucleate boiling (ONB) inside wall temperature and the onset of fully developed nucleate boiling (FDB) inside

wall temperature were computed and displayed in each figure. These are shown as the remaining two vertical lines in Fig. 157.

Initially as T_{wi} increases, $q_i^{"}$ @ ϕ = 0 degree (Fig. 169a) was greater than $q_i^{"}$ @ ϕ = 45 degrees (Fig. 157b). However in the middle to the latter portion of the single-phase region, $q_i^{"}$ @ ϕ = 45 degrees became > $q_i^{"}$ @ ϕ = 0 degrees; and, this continued into the subcooled flow boiling regime. Similar trends occurred at the higher mass velocities of 1.18 and 3.15 Mg/m^{2}s. Further, inspection and comparisons of Figs. 157a through 157d (ϕ = 180 degrees) indicate that the shape of the boiling curve does change as ϕ changes. For example, in Figs. 157b (ϕ = 45 degrees) and 157c (ϕ = 135 degrees), the corresponding values of T_{wi} are quite different for the same value of $q_i^{"}$. Similar results were produced at all axial locations and the three levels of the mass velocity. *These results represent an evolving 2-D conjugate heat transfer and boiling curve data base for a single-side heated monoblock; and hence for the first time, a multi-dimensional boiling curve data base has been measured for a single-side heated monoblock flow channel*.

18.3.2 Data/Correlation Comparisons

The above noted correlations have been used to express a relationship between the inside channel wall heat flux and the inside wall temperature. Although most of the correlations were developed for uniform heat flux, the Araki et al. [102] correlation has been applied to single-side heated flow channel configurations. The single-side heated effect was accounted for in the Boyd-Meng methodology by using D_T (e.g., see [118]) as the characteristic diameter. Since all correlations were developed for thermally and hydrodynamically fully-developed flow, comparisons were made at a down-stream location (Z = Z_3 or Z_3/D_i = 14.7) where these conditions exist. Figures 157a through 157d contain comparisons with the inside heat flux and inside wall temperature (i.e., $q_i^{"}$ vs T_{wi} or "star" symbol) data set at Z = Z_3 = 147.1 mm and G = 0.59 Mg/m^{2}s. There is no agreement or correlation with this data; but there is some correlation at higher mass velocities. Since the correlations for the most part were developed for a uniform heat

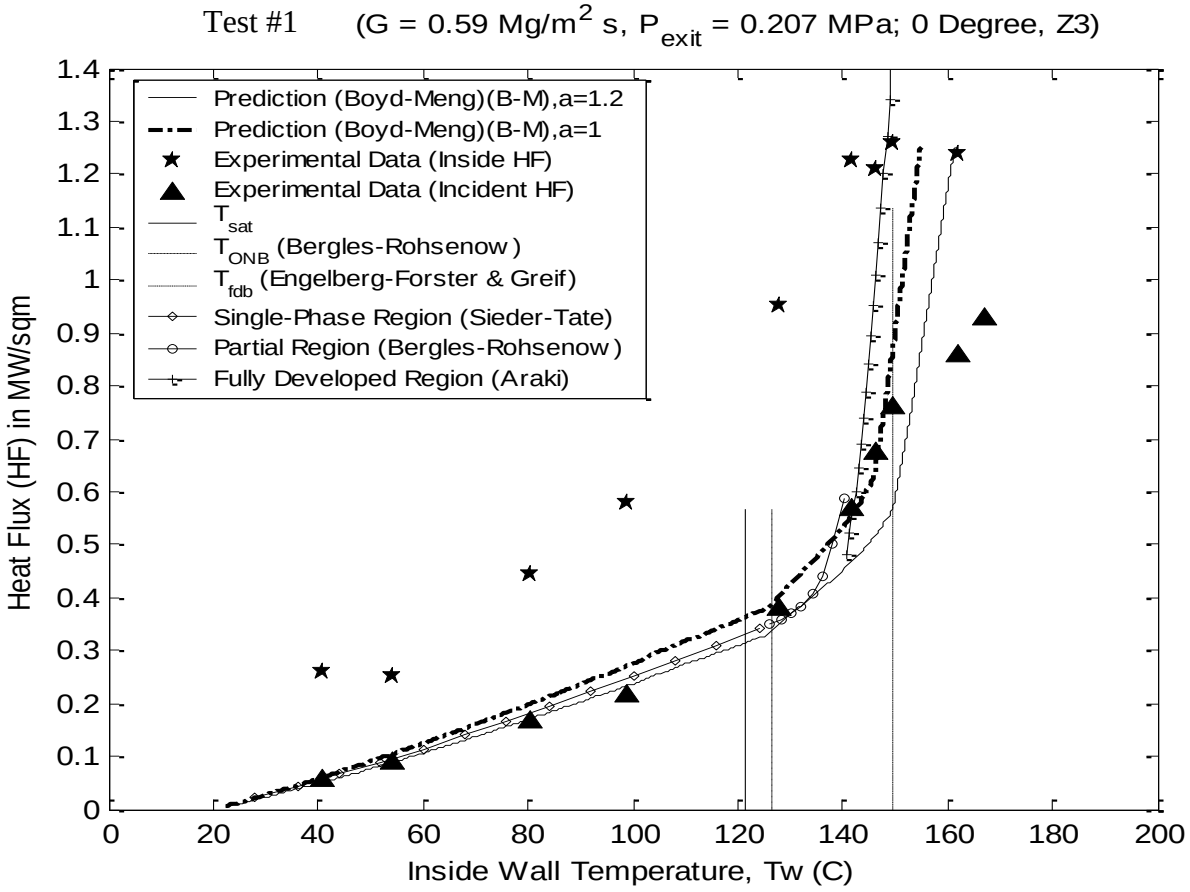

Figure 157a: ϕ = 0 degree [Note: The above parameter, a, should be replaced with the parameter a_a.]

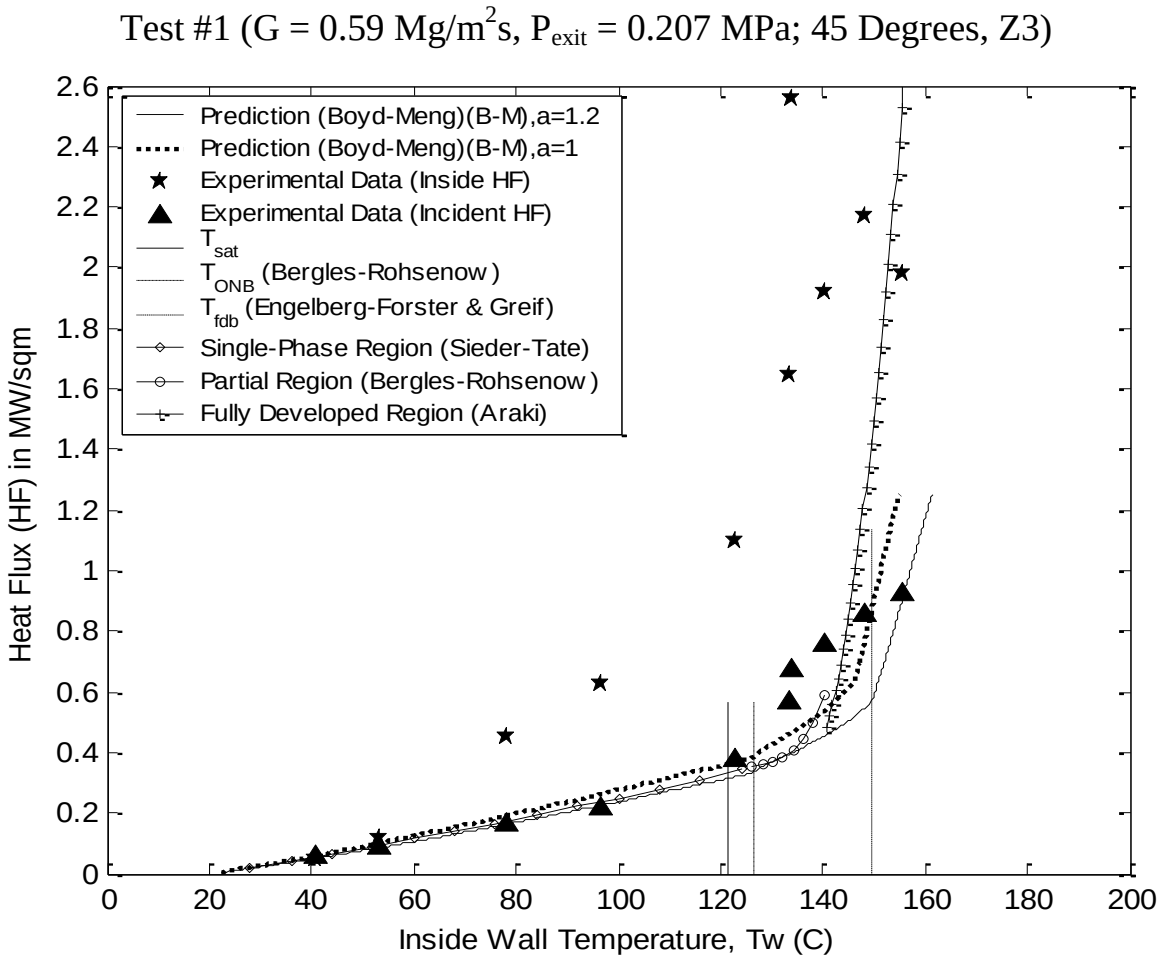

Figure 157b: ϕ = 45 degrees [Note: The above parameter, a, should be replaced with the parameter a_a.]

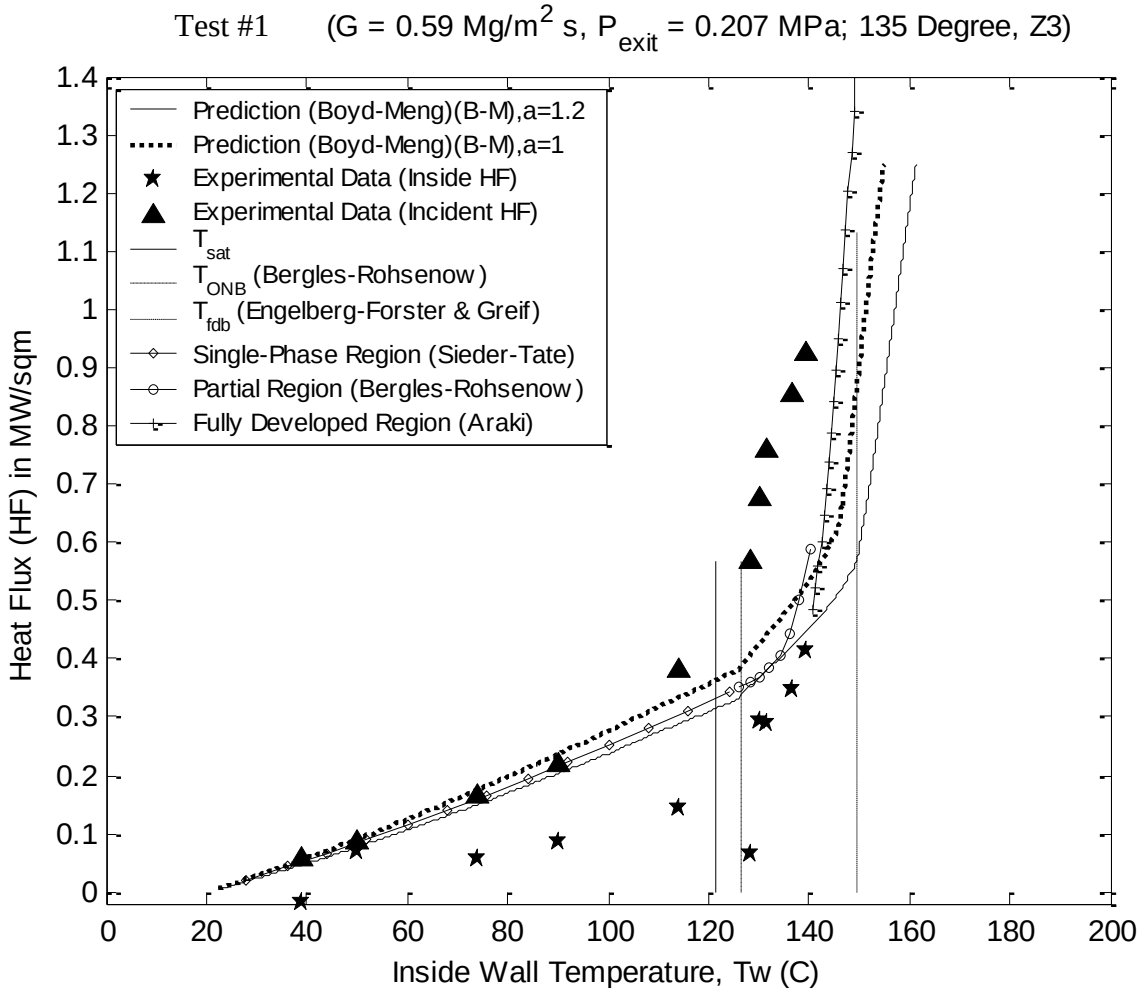

Figure 157c: ϕ = 135 degrees [Note: The above parameter, a, should be replaced with the parameter a_a.]

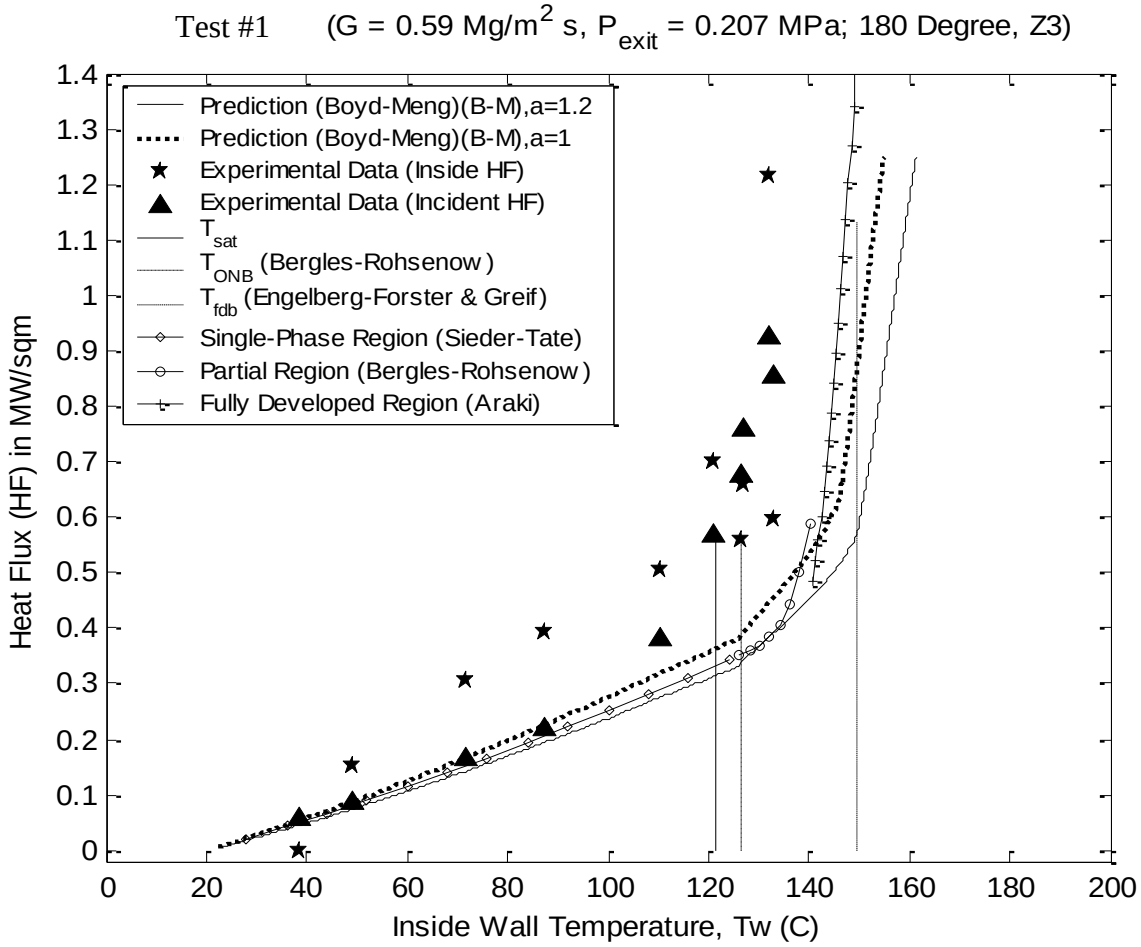

Figure 157d: ϕ = 180 degrees [Note: The above parameter, a, should be replaced with the parameter a_a.]

flux flow channel, this poor correlation is not surprising. However, the correlations are closer to the $q_o^{"}$ vs T_{wi} ("triangular" symbol) data set in many cases.

In the single-phase region for G = 0.59 Mg/m^{2}s, the Sieder-Tate correlation and the Boyd-Meng methodology with a_a = 1.0 characterized the $q_o^{"}$ vs T_{wi} relationship for the data fairly well. For this mass velocity, all correlations under-predicted (e.g., see Fig. 158) the inside heat flux for a given value of T_{wi}; and at the zero degree location for the highest mass velocity (3.15 Mg/m^{2}s), the correlations under-predicted the inside wall heat flux. Figure 158 shows that for ϕ = 0 degree and Z = Z_3, the Boyd-Meng methodology characterizes the entire boiling curve for the highest mass velocity (G = 3.15 Mg/m^{2}s) well when a_a = 1.2. Better characterization was obtained (not shown) when a_a = 1.4. However, additional results show that none of the correlations characterized the $q_i^{"}$ vs T_{wi} data at any circumferential coordinates for the two lowest mass velocities (G = 0.59 and 1.18 Mg/m^{2}s). It is therefore apparent that additional work is needed to either adapt existing correlations or develop new correlations which contain single-side and conjugate heat transfer effects for both the turbulent single-phase and flow boiling regimes.

The flow-developing nature of the $q_i^{"}$ vs T_{wi} and $q_o^{"}$ vs T_{wi} relationships are shown as a function of the axial coordinate in Fig. 159 (Note: inside HF = $q_i^{"}$ and the incident HF = $q_o^{"}$) at the top (i.e., ϕ = 0 degree) of the single-side heated test section. The data base includes similar measurements for other values of ϕ. The local peaking factor (i.e., PF is related to $q_i^{"}/q_o^{"}$) variation is also apparent; and PF is a function of Z, thermal flow developing effects, and the circumferential conjugate heat transfer.

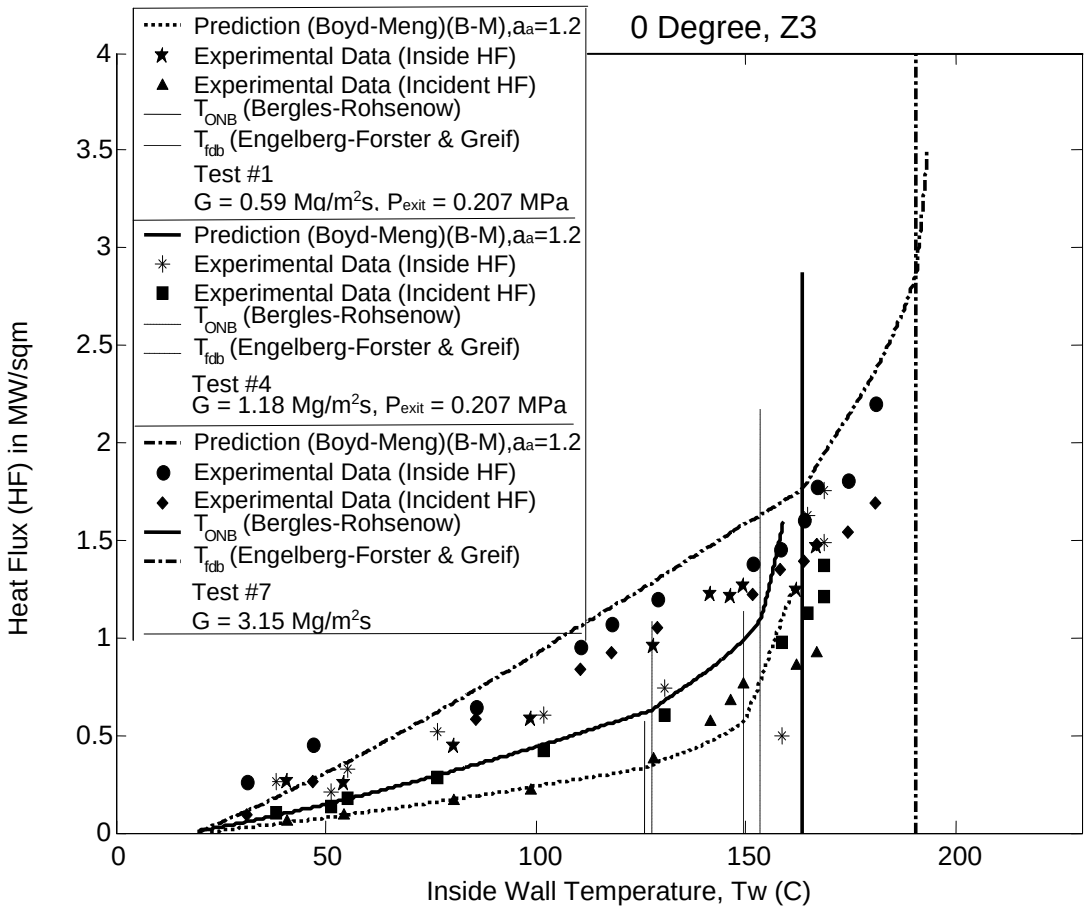

Figure 158: Select Correlation Comparisons and Mass Velocity (G) Dependence on Both the Flow Channel Inside Heat Flux--and Average Net Incident Heat Flux--Inside Wall Temperature Relationships at $\phi = 0^0$ and $Z_3 = 147.1$ mm.

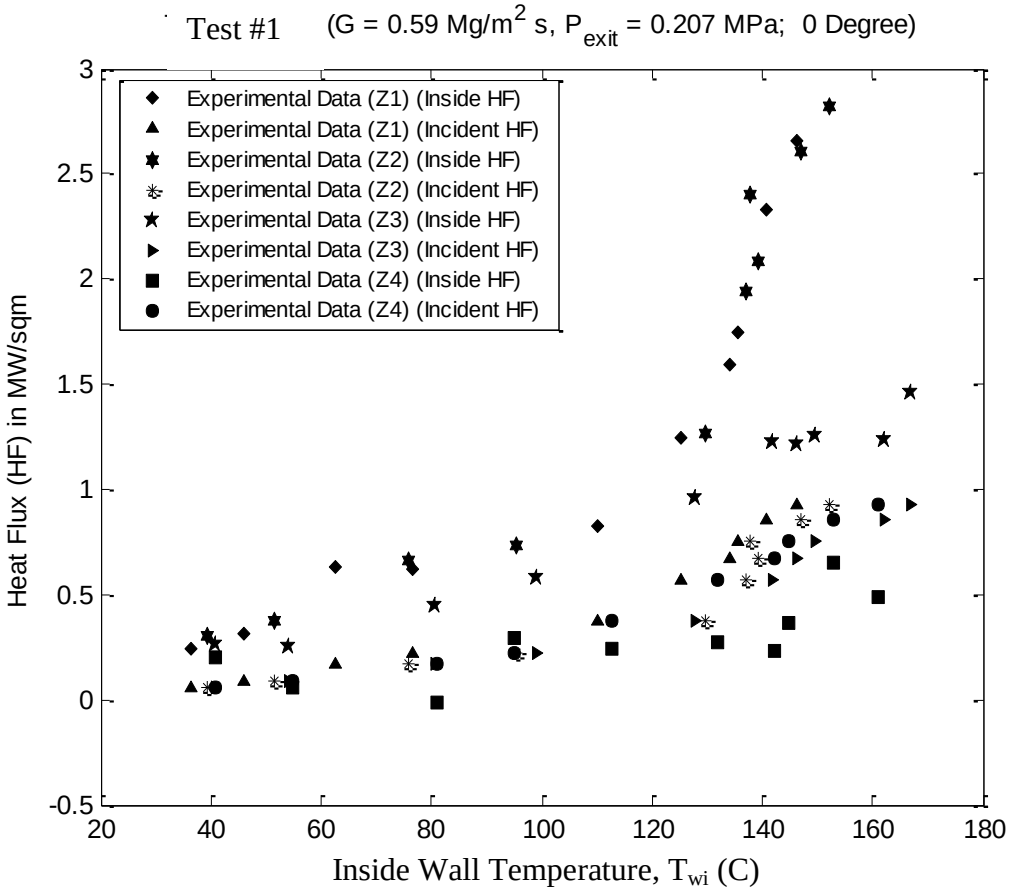

Figure 159: Axial Variation of the $q_i^{"}$ vs T_{wi} and the $q_0^{"}$ vs T_{wi} Relationships at $\phi = 0^0$ for G = 0.59 Mg/m^{2}s, and P_{exit} = 0.207 MPa.

For the first time, a multi-dimensional boiling curve data base has been developed for a single-side heated monoblock flow channel and it includes effects of: (1) conjugate heat transfer; (2) internal turbulent, single-phase flow and flow boiling; and, (3) circumferential heat transfer. From comparisons with selected correlations, good agreement was obtained only on the heated side of the plane of symmetry: (1) for the entire boiling curve at the highest mass velocity (G = 3.2 Mg/m^{2}s) using the Boyd-Meng correlation with D_T = 1.4 D_i; and, (2) for the $q_o^{"}$ vs T_{wi} relationship in the single-phase region only at the lower levels of the mass velocity (G < 1.2 Mg/m^{2}s), and using either the Sieder-Tate correlation and the Petukhov correlation with D_T = 1.2 D_i (slightly better). Clearly, additional correlation development and adaptation is needed.

However, the developed 2-D boiling curve monoblock data base provides a basis for future correlational development so that single-side heating and conjugate heat transfer effects with both circumferential and axial dependence can be correlated. *Finally, these newly measured 2-D boiling curves can now be used to validate those computational fluid dynamics and heat transfer codes which will be used for example in the future high heat flux (HHF) removal design of fusion reactor and aerodynamic HHF components.*

19.0 THREE-DIMENSIONAL (3-D) CONJUGATE HEAT TRANSFER DATA VERIFICATION AND ENHANCEMENT EXAMINATION OF HELICAL WIRE INSERTS

19.1 INTRODUCTION

In the Institute of High Heat Flux Removal (IHHFR), considerable time and effort have been invested in the data base generation and verification of local three-dimensional (3-D) conjugate heat transfer temperature distributions, ($T_w(r, \phi, z)$), and inside flow channel wall heat flux ($q_{wi}(r, \phi, z)$) for two-phase, laminar and turbulent flows. All measurements were made on a developed IHHFR monoblock test section (see Fig. 160). This remains a focus because the resulting data contains the "exact" physical characteristics of multidimensional, two-phase, conjugate heat transfer for laminar and turbulent flows. No approximate or limiting physical turbulent or two-phase models are needed; and hence, the data contains the true thermal physics for the above noted conditions--all which are present in HHFR fusion and other similar HHF components. Previous efforts have been expanded by generating $T(r, \phi, z)$ using embedded thermocouples (see Fig. 161) in a monoblock test section (TS) with a helical wire insert (HWI); and then the HHFR-HWI enhancing results were compared with cases without the helical insert (w/o HWI). Before the HWI data was reduced, an extensive data reduction verification campaign was launched to examine the variation in the data results from independent examiners (IE, IE-1 and IE-2). This comparison proved satisfactory; and $T_w(r, \phi, z)$, $T_{wi}(\phi, z)$, and $q_{wi}(r, \phi, z)$ data were obtained and comparisons were made for monoblocks with HWI and w/o HWI. Here, $T_{wi}(\phi, z)$ is the local inside flow channel wall temperature. Extensive additional facility and TS design, development, manufacture, and measurements were required to produce the above noted data.

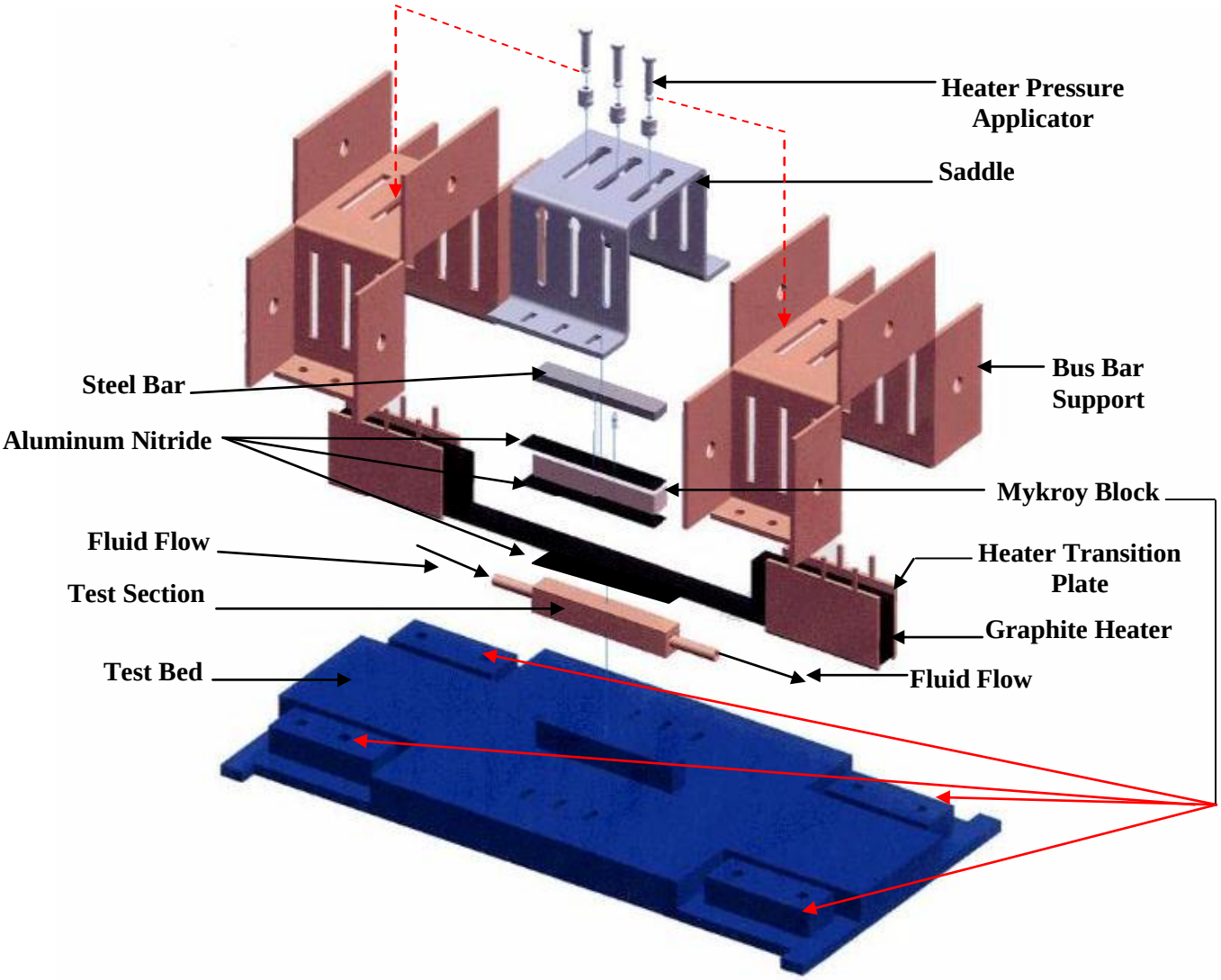

Figure 160: High Heat Flux Monoblock Test Section (TS) Expanded Assembly.

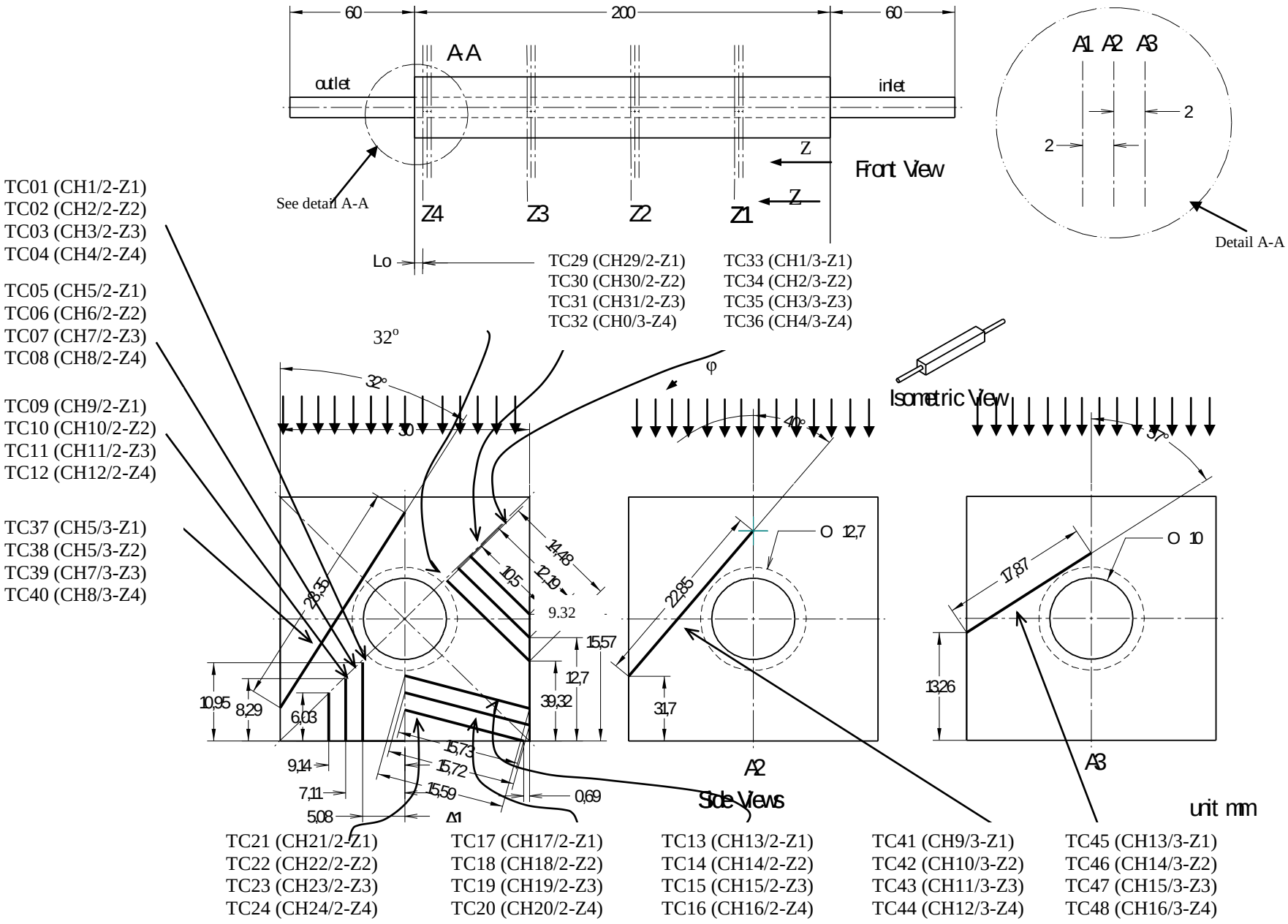

Figure 161: Channel Assignment for the Monoblock Test Section #4 (TS 4) with Helical Wire Insert (HWI) Used for Local Temperature and Heat Transfer Measurements. Thermocouple Wells are the Solid Black Lines with Specified Lengths and Angles. The Heat Flux is Applied to the Top Surface of the Test Section (also see Fig. 160).

19.2 THE IHHFR FACILITY OVERVIEW

The Thermal Science Research Center (TSRC) IHHFR facility [90] is composed of a closed stainless steel water flow loop with two integrated test sections (TS) of monoblock geometry--one with a helical wire insert (HWI) (see Fig. 161) and one w/o HWI (see Fig. 162). Each test section is externally heated (see Fig. 160) from a single side by a grade G-20 graphite flat heater that is electrically, but not thermally, isolated from the test section. The heater is provided by a 300 kW DC, at 30 V power supply. Each of the test sections has 48 stainless steel sheathed type-J thermocouples (calibrated to ± 0.1 ^{o}C with a precision calibrator) embedded in the monoblock walls (e.g. see Fig. 161) configured to provide three radial, four circumferential and four axial temperature measurements as shown in Figs. 161 and 162.

19.2.1 Description of the Test Sections

The monoblock test sections in Figures 161 and 162 were fabricated from AL-15 Glipcop Grade Copper. The test sections are qualitatively identical with the exception of a helical wire insert in TS 4 (Fig. 161), which is not shown in the figure. Each test section was custom fabricated and precision measurements (compare Figs. 161 and 162) of thermocouple (TC) well depths and locations were made for each TS; and, the resulting TC well base locations were verified by three independent examiners (IES). Also, the inlet/outlet reduced diameter lengths differ, which are 80 and 64 mm for TS5 (w/o HWI) and TS 4 (HWI), respectively. The monoblock portion of the test sections are 200 mm in length, with heating lengths of 180 mm. This heating length begins at L_i (shown in the front view of Figs. 161 and 162) and ends at Z = (200-L_o) mm. The overall lengths of the TS 5 and 4 (including the inlet and outlet reduced diameters) are 360 mm, and 328 mm, respectively. The monoblock sides are 30 mm and the 10 mm diameters flow channel bored through the center is typical of fusion reactor divertor water flow channels.

The four axial stations where thermocouples were inserted are labeled Z_4 (Section A-A), Z_3, Z_2, and Z_1 in Figures 161 and 162. For each of these axial stations, there are thermocouples embedded at four circumferential locations; i.e., φ of 0, 45, 135, and 180 deg, where φ = 0 deg originates from the portion of the plane of symmetry close to the heated surface in the wall of the test sections. At each circumferential location, there are three TC measurement points (at each

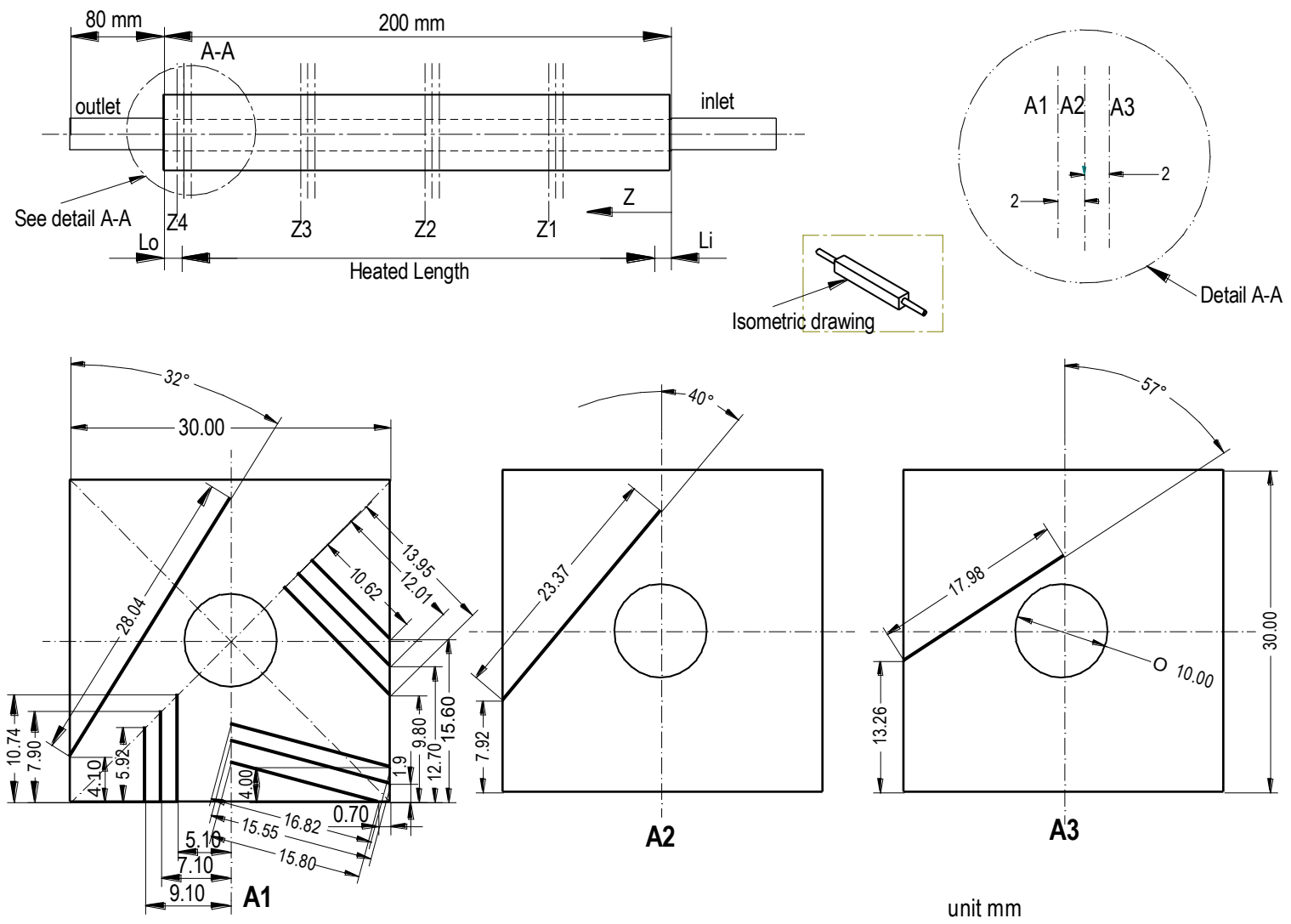

Figure 162: Monoblock Test Section #5 (TS 5) Without Helical Wire Insert (HWI) Used for Local Temperature and Heat transfer Measurements. Thermocouple Wells are the Solid Black Lines with Specified Lengths and Angles. The Heat Flux is Applied to the Top Surface of the Test Section.

well depth) spaced radically at locations: (1) close to the fluid-solid interface (CTF), (2) at an intermediate (INT) location between the fluid and outside boundary, and (3) close to the outside boundary (CTO). Except for the 0 deg circumferential location, the TC wells were drilled in a way such that each one had to be on a separate axial plane to avoid interfering with each other; thus explaining the 2 mm axial spacing in the detail A-A of Figures 161 and 162. The TC well depths measured for TS 5 (Figure 162) are slightly different from those measured for TS 4 (Figure 161).

19.2.2 Helical Wire Insert TS4 Assembly

The Glidcop AL-15 cooper alloy monoblock Test Section #4 (TS4, see Figure 161) was used for the helical wire insert (HWI) installation. The HWI was made of inconel-600; and, it had a wire diameter of 1.0 mm with a helical pitch of 5.0 mm (see Figure 163). After being coated with a brazing flux compound, a thin (0.25 mm) brass (65 Cu-35 Zn; melting point* = 648 ^{o}C--measured in the TSRC) sheet was rolled inside the inside flow section of TS4 and thereby forming an inner brass tube. The HWI was placed into the brass tube. This entire assembly was placed in a vacuum furnace and heated to the melting temperature of the bass. Later, radiographic inspections were made to ensure the integrity of the braze.

19.2.3 New Helical-Flow Test Section and TC Preparation

19.2.3.1 Verification of Hole Depths

The design, implementation, installation, and inspection verification of the helium wire insert installation into Test Section #4 (TS4) was successful and formed the basis for the experimental campaigns. Prior to installation of the thermocouples into TS4 with the helical insert (w/HWI), the TC wells needed to be cleaned and measured to verify the dimensions specified by the manufacturers. During cleaning, loose particles and dirt were discovered within the wells. Well depth measurement inspections were performed by two IE's (IE-3 and IE-4) with an electric caliper for each of the forty-eight (48) TC wells to within -0.012 in. (0.3048 mm) average tolerance of the manufacturer's measurements recorded in Table XI. The following procedure was used for this verification process:

1) A dental cleaning pin was used to scrape out any excess dirt and loose copper in each hole in TS4 shown in Figures 161 and 162. Each hole was inverted during its cleaning to allow the particles to fall out.

---

*The corresponding value for the Glidcop copper is 1083^{0}C.

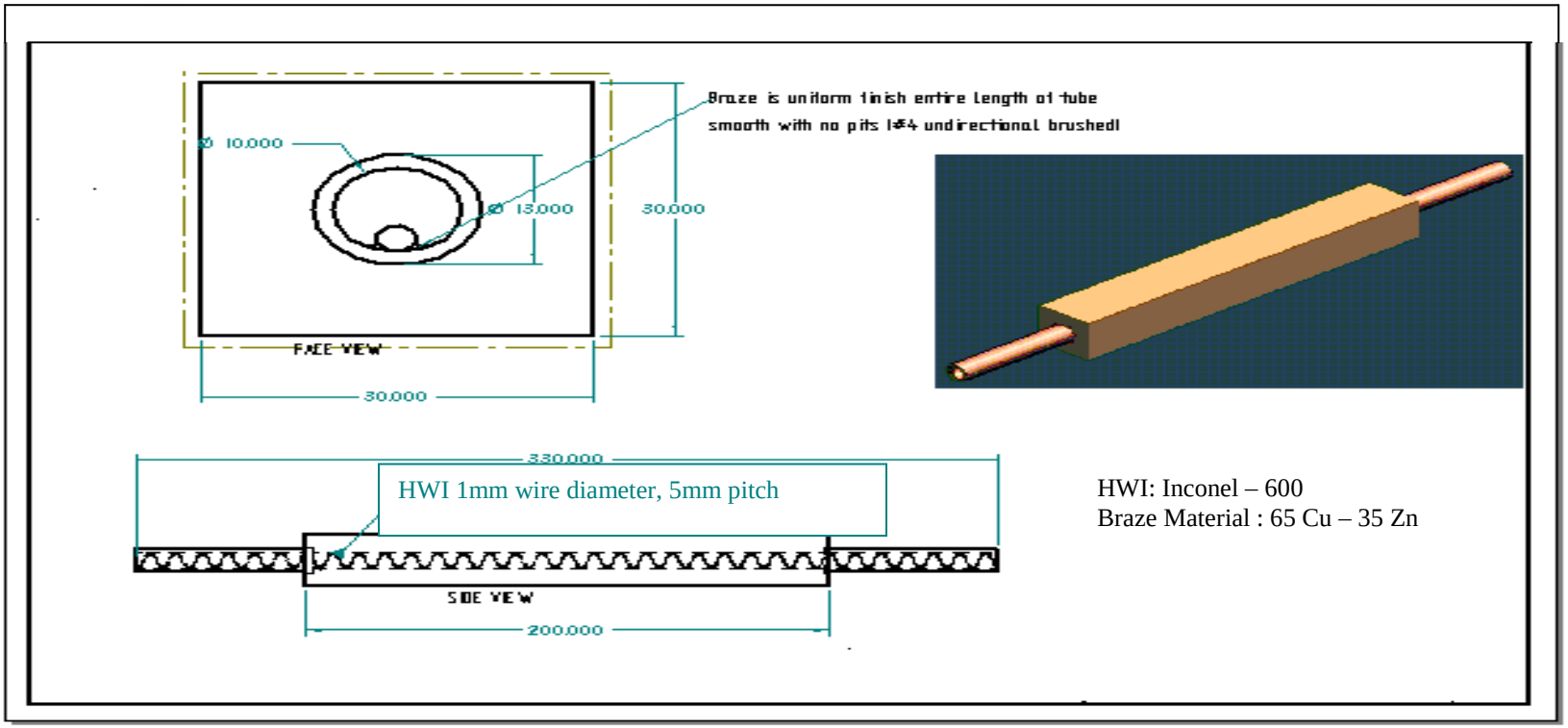

Figure 163: TSRC Monoblock Test Section #4 (TS4) with the Helical Wire Insert (HWI).

Table XI: Hole Depth Measurements Verification for Monoblock Test Section #4 (TS4) (Helical Inserts) – <u>Part I of II</u>

Hole Drilling Angle	TC Well #	Hole Depth Measurements (inches)				
		Manufacturer Measurements	IE-3's Measurements	IE-3's Tolerance	IE-4's Measurements	IE-4's Tolerance
0°	1	0.424	0.42	*-0.004*	0.414	*-0.010*
	2	0.424	0.434	*0.010*	0.425	*0.001*
	3	0.45	0.445	*-0.005*	0.419	*-0.031***
	4	0.426	0.425	*-0.001*	0.419	*-0.007*
	5	0.329	0.322	*-0.007*	0.319	*-0.010*
	6	0.327	0.327	*0.000*	0.315	*-0.012*
	7	0.326	0.319	*-0.007*	0.318	*-0.008*
	8	0.324	0.325	*0.001*	0.304	*-0.020*
	9	0.244	0.238	*-0.006*	0.224	*-0.020*
	10	0.234	0.217	*-0.017*	0.225	*-0.009*
	11	0.235	0.241	*0.006*	0.242	*0.007*
	12	0.237	0.228	*-0.009*	0.212	*-0.025*
15°	13	0.613	0.596	*-0.017*	0.612	*-0.001*
	14	0.615	0.611	*-0.004*	0.612	*-0.003*
	15	0.621	0.611	*-0.010*	0.609	*-0.012*
	16	0.606	0.597	*-0.009*	0.593	*-0.013*
	17	0.633	0.623	*-0.010*	0.632	*-0.001*
	18	0.612	0.6	*-0.012*	0.593	*-0.019*
	19	0.611	0.605	*-0.006*	0.619	*0.008*
	20	0.62	0.623	*0.003*	0.612	*-0.008*
	21	0.614	0.596	*-0.018*	0.599	*-0.015*
	22	0.616	0.614	*-0.002*	0.592	*-0.024*
	23	0.626	0.614	*-0.012*	0.601	*-0.025*
	24	0.621	0.605	*-0.016*	0.653	*0.032***

*** Indicates values tolerances not within ±0.03 inches*.

Table XI: Hole Depth Measurements Verification for Monoblock Test Section #4 (TS4) (Helical Inserts) – <u>Part II of II</u>

Table 1 Continued.

Hole Drilling Angle	TC Well #	Hole Depth Measurements (inches)				
		Manufacturer Measurements	IE-3's Measurements	IE-3's Tolerance	IE-4's Measurements	IE-4's Tolerance
45°	25	0.557	0.524	*-0.033* **	0.258	*-0.299*
	26	0.561	0.557	*-0.004*	0.551	*-0.010*
	27	0.578	0.57	*-0.008*	0.552	*-0.026*
	28	0.584	0.557	*-0.027*	0.557	*-0.027*
	29	0.478	0.455	*-0.023*	0.451	*-0.027*
	30	0.474	0.45	*-0.024*	0.456	*-0.018*
	31	0.481	0.456	*-0.025*	0.472	*-0.009*
	32	0.487	0.464	*-0.023*	0.486	*-0.001*
	33	0.404	0.403	*-0.001*	0.413	*0.009*
	34	0.413	0.39	*-0.023*	0.378	*-0.035* **
	35	0.405	0.382	*-0.023*	0.387	*-0.018*
	36	0.431	0.416	*-0.015*	0.404	*-0.027*
32°	37	1.12	1.113	*-0.007*	1.112	*-0.008*
	38	1.127	1.11	*-0.017*	1.102	*-0.025*
	39	1.109	1.101	*-0.008*	1.102	*-0.007*
	40	1.105	1.106	*0.001*	1.09	*-0.015*
40°	41	0.892	0.907	*0.015*	0.874	*-0.018*
	42	0.901	0.899	*-0.002*	0.881	*-0.020*
	43	0.905	0.907	*0.002*	0.901	*-0.004*
	44	0.9	0.898	*-0.002*	0.878	*-0.022*
57°	45	0.707	0.709	*0.002*	0.701	*-0.006*
	46	0.699	0.701	*0.002*	0.678	*-0.021*
	47	0.703	0.69	*-0.013*	0.686	*-0.017*
	48	0.705	0.702	*-0.003*	0.681	*-0.024*

** *Indicates values tolerances not within ±0.03 inches*.

2) For each hole, alcohol was used to flush out the excess dirt that would not be removed otherwise. This and the previous step were repeated to insure cleanliness of the test section.
3) Beginning with hole #1, a 0.397 mm diameter copper wire was inserted as a verification that future installed TCs would be able to make contact with the bottom of the hole. A permanent marker was used in marking the copper wire at a point aligned with the top edge of the well.
4) Using an electric caliper, the depth was measured and recorded (see Table XI) from the marking to the wire tip (which touched the bottom surface of the hole).
5) The mark on the copper measuring wire was cleaned with alcohol so that the wire could be reused for measuring.
6) Steps 1 thru 5 were repeated for the remaining TC wells in TS4.
7) Steps 1 thru 6 were repeated by IE-3 and IE-4 for independent well depth measurement verification (see Table XII).

19.2.3.2 Thermocouple (TC) Calibration

To account for accuracy of the TS #4 0.508 mm diameter thermocouples (type J grounded) and prior to integrating them into the test section, a calibration was performed using a precision calibrator, the DAQ system and a microprocessor. A selected sample set of the TCs were calibrated for the test section and their temperature responses were measured to within ± 0.2 ^{0}C tolerance using an Omega HH23 microprocessor because the DAQ system for TS #4 had not yet been installed. These TCs were used for all the Z1 and Z2 axial locations. Other pre-calibrated (with CL-750A Omega precision calibrator) thermocouples were measured to within -0.7 ^{0}C using the DAQ system channels and these were mainly used for the Z4 location. All other TCs were placed at the Z3 location. The following summarizes the TC calibration procedures:

1) A CL-750A Omega temperature precision calibrator was activated and set to the desired calibration temperature with a ramp rate of 10 ^{0}C/min. and a hold time of 60 min.
2) The calibrator was allowed at least 10 min. to stabilize.
3) After stabilization, two of the labeled thermocouples were inserted into the two smallest wells of the calibrator allowing 1 min. stabilization time. The two thermocouple male connector ends were then inserted into the T-1 and T-2

Table XII. Thermocouple Measuring Tip 3-D Geometric Coordinates for the Monoblock Test Section #4 (TS 4)

Thermocouple Well Identification			Test Section Coordinates					
Axial Coordinate Correction*, D			Circumferential Φ (Degrees)	Radial, r (mm)			Axial, z (mm)	
D = 4 mm	D = 2 mm	D = 0 mm		Close to Fluid/Solid Boundary	Intermediate	Close to Outside Boundary		
TC#(Channel#/Module#)	TC#(Channel#/Module#)	TC#(Channel#/Module#)						
TC45(13/2)	TC41(9/2)	TC37(5/2)	0	8.029	10.279	13.203	z1	49.022-D
TC46(14/2)	TC42(10/2)	TC38(6/2)	0	7.918	10.449	13.355	z2	98.044-D
TC47(15/2)	TC43(11/2)	TC39(7/2)	0	7.973	10.525	12.967	z3	147.066-D
TC48(16/2)	TC44(12/2)	TC40(8/2)	0	8.001	10.430	12.881	z4	196.088-D
TC25(25/1)	TC29(29/1)	TC33(1/2)	45	6.944	8.973	11.002	z1	49.022
TC26(26/1)	TC30(30/1)	TC34(2/2)	45	6.943	8.975	11.006	z2	98.044
TC27(27/1)	TC31(31/1)	TC35(3/2)	45	6.955	8.973	11.002	z3	147.066
TC28(28/1)	TC32(0/2)	TC36(4/2)	45	6.966	8.973	11.027	z4	196.088
TC1(1/1)	TC5(5/1)	TC9(9/1)	135	6.618	9.740	12.700	z1	49.022
TC2(2/1)	TC6(6/1)	TC10(10/1)	135	6.618	9.774	12.878	z2	98.044
TC3(3/1)	TC7(7/1)	TC11(11/1)	135	6.215	9.792	12.860	z3	147.066
TC4(4/1)	TC8(8/1)	TC12(12/1)	135	6.585	9.827	12.824	z4	196.088
TC13(13/1)	TC17(17/1)	TC21(21/1)	180	6.968	8.935	11.000	z1	49.022
TC14(14/1)	TC18(18/1)	TC22(22/1)	180	6.955	9.058	10.990	z2	98.044
TC15(15/1)	TC19(19/1)	TC23(23/1)	180	6.919	9.064	10.946	z3	147.066
TC16(16/1)	TC20(20/1)	TC24(24/1)	180	7.015	9.008	10.967	z4	196.088

*The axial correction is applied only to the $\phi = 0$ degree locations Close to the Fluid/Solid Boundary (D = 4 mm), Intermediate Location (D = 2 mm), and Close to the Outside Boundary (D = 0 mm)

terminals of the microprocessor. After waiting 1 min. for the microprocessor readings to stabilized, each temperature reading was recorded.

4) Steps 2 & 3 were repeated for the remaining selected thermocouples for the test section.
5) The TS4 inlet and exit 1.588 mm diameter thermocouples, were calibrated to within less than + 0.8 and + 0.9 ^{0}C, respectively; and this time, four trials were performed to account for the accuracy of the calibration process. The results in ^{0}C were as follows:
    a. Inlet TC – (consistent to within – 0.2 ^{0}C).
    b. Exit TC – (consistent to within – 0.1 ^{0}C).

19.3 INTEGRATION OF TCS INTO TS4

The steps involved for installation of the thermocouples into the test section were: (1) ensuring contact between the thermocouples and the desired measurement points (at the bottom of the TC wells), (2) isolating the test section and thermocouples from the assembly table, and (3) permanently positioning the test section. One issue concerning heater assembly installation of the previous test section (TS5) was: the securing brackets used for holding the test section in place would interfere with the heater transition plates; so, these brackets had to be removed during each assembly of the heating system. This allowed the test section to move freely, which might have varied the position of TS5 from test to test. A simple TS securing bracket, shown in Figure 164, was designed and fabricated from stainless steel 1/8″ thick sheet metal (1″ by 8″) to permanently secure the test section to the mounting table as shown in Figure 165.

The thermocouple installation procedure can be outlined as follows:

1) The mykroy blocks (Figure 165, items 2 and 3) were machined using a diamond saw blade to the dimensions specified in Figure 166 as TS support, mounting, insulation, and TC insulation. These blocks were then cleaned with 91% alcohol.
2) The four TC insulation blocks were super-glued onto both sides of each of the two mounting panels in the test bed as shown in Figure 165 (item 3). The purpose of these blocks was to electrically insulate the thermocouple wires from the test bed to prevent any possible interference of the TC readings.

3) The test section mounting blocks were placed on top of these same panels while the test section was stacked on top of them. These two blocks were used to thermally insulate the test bed.
4) The test section was mounted on the 2 mounting blocks, and the brackets were positioned and bolted into the sliding nuts in the grooves of the test bed.
5) Using a permanent marker, the first thermocouple was labeled “48” on its male connector label tab.

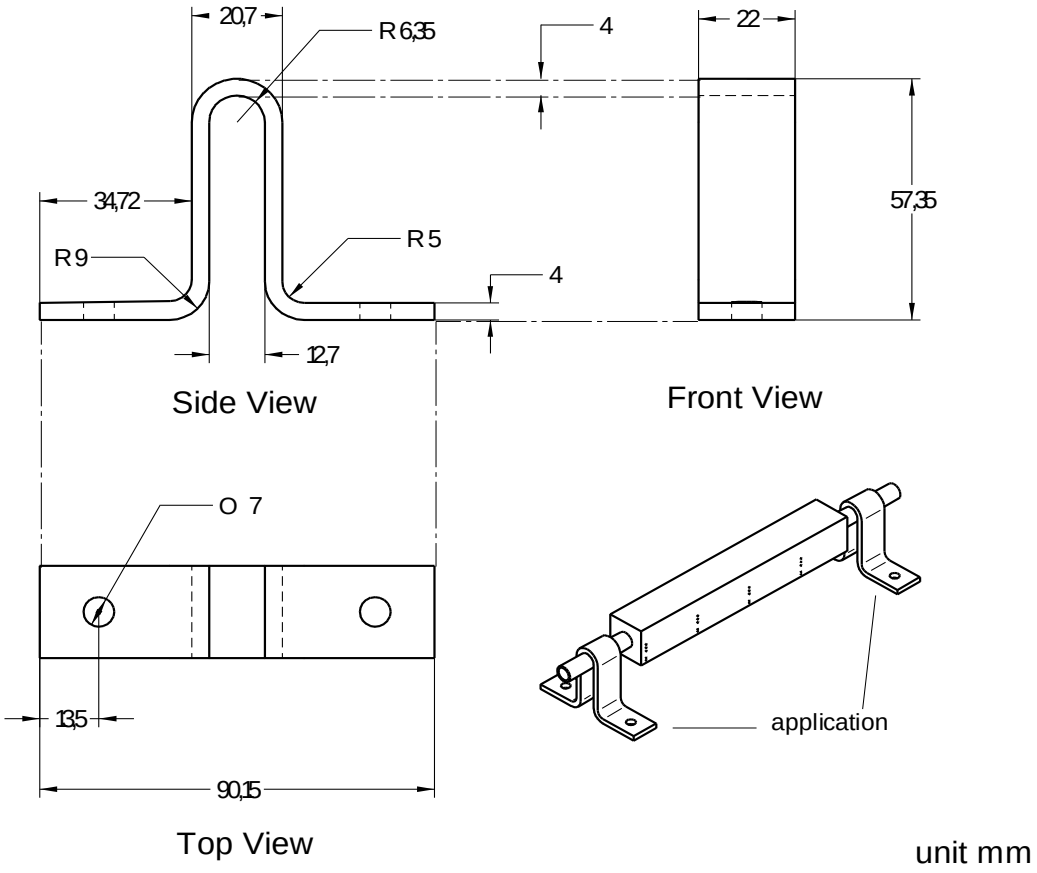

Figure 164: Dimensions and Application of the Test Section Securing Bracket Used for TS4 Installation to Permanently Position the Test Section.

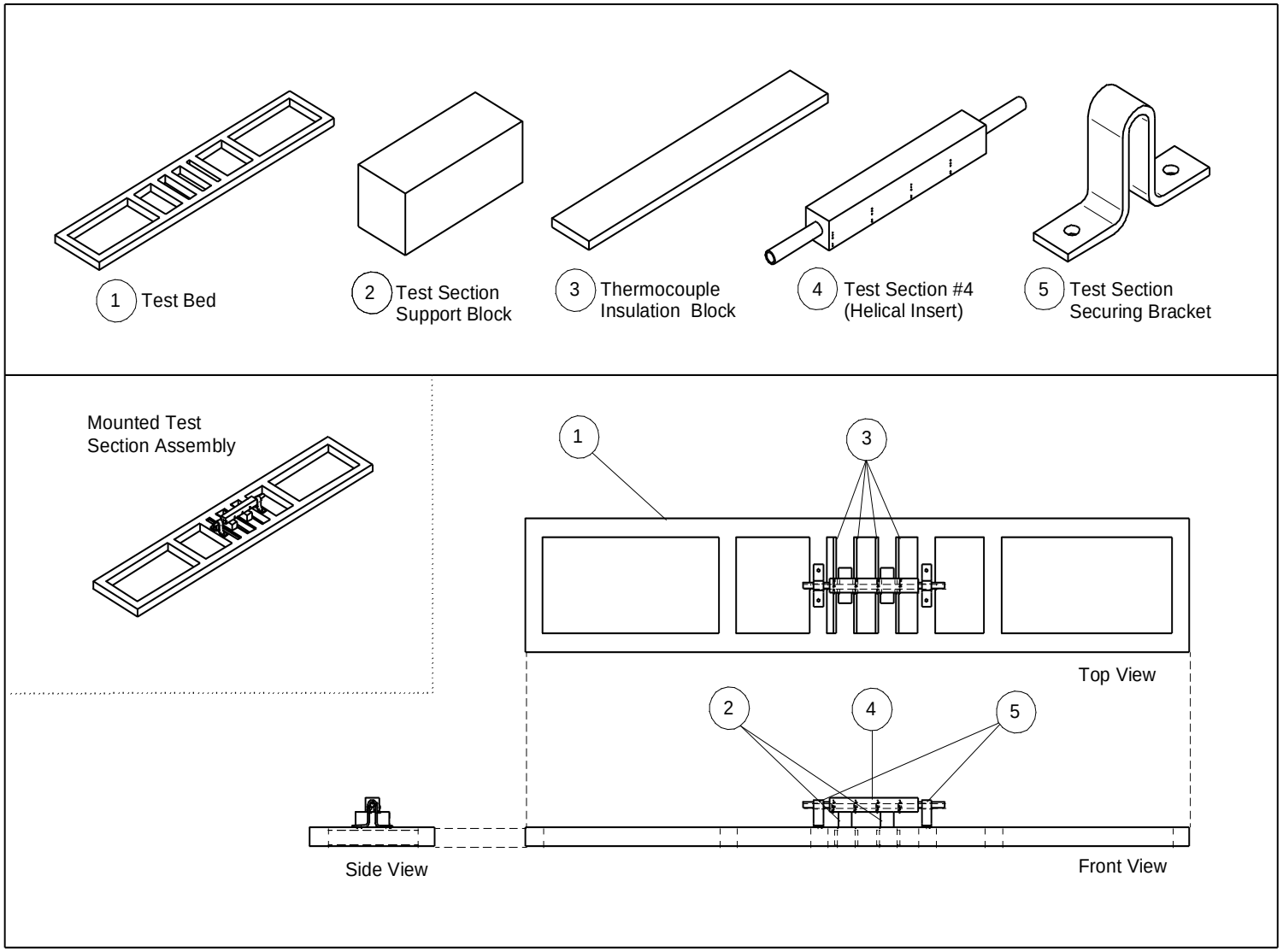

Figure 165: Initial Mounting Diagram of TS4 Installation Process.

Mykroy Block

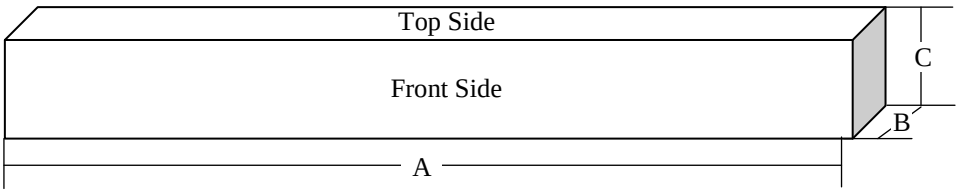

Insulation Use (qty.)	Dimensions (mm)		
	A	B	C
Middle Pressure Applicators (1)	175	30	20
End Pressure Applicators (2)	30	30	32
TS Support and Insulation (2)	35	30	32
TC Insulation (4)	203.2	6.4	31.8
Bus Bar Supp. Mounting (4)	180	32	32
Bus Bar Support Bolting (8)	30	30	32

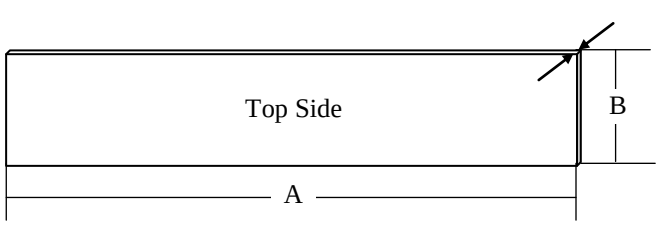

Use (qty.)	Dimensions (mm)	
	A	B
TS Strip 1 (1)	114	30
TS Strip 2 (1)	86	30
Steel Bar Insulation (2)	64	30

Figure 166: Dimensions for Mykroy and Aluminum Nitride Insulations for Monoblock Type Heater Assemblies. TC 48 was then penetrated into the corresponding TC well #48 (see Figures 161 and 167) of the test section until tapping the bottom of the well was reached.

6) The permanent marker was used to mark the thermocouple at the point aligned with the top edge of the well.
7) After removing the TC from the well, the well depth was verified and its tip was dipped in alcohol approximately ½ of a cm and then dipped into a copper micro-particle powder, coating the tip of the TC.
8) The coated TC tip was re-inserted into the same TC well (#48), and pushed down until the mark was re-aligned with the top edge of the well.
9) The un-inserted portion of the TC was bent below the test section at angles greater than 90^0 against the test bed, creating a spring force to stabilize the TC inside the wells.
10) Super glue was applied around the edge of the TC inserted, binding the TC to the well after approximately 30 seconds drying time.
11) The previous steps were repeated for the remaining 11 circumferential TCs and wells at the Z4 location (see Figure 167).
12) Before installing TCs for the next Z location (Z3), the TCs were silicon-glued to the TC insulation located in the test bed on both sides of each of the mounting panels shown in Figure 165 (item 3), allowing at least 24 hrs drying time to hold all twelve Z4 thermocouples in place, while keeping them spring-loaded into the wells.

The previous steps were performed for the remaining TCS and wells at locations Z3, Z2, and Z1 with the exception of the silicon glue application of step 13 being carried out simultaneously for all three locations at the save time.

19.4 PRESSURE TRANSDUCER CALIBRATION

After the test section was integrated into the flow loop, two pressure transducers (24 VDC, 4 to 20 mA) were calibrated to the gage pressures at the inlet and exit locations of the test section. These calibrations were made using a dead weight tester (Amelek Twin Seal Pressure Tester Unit Type: 10-3525) and a Fluke 73III multimeter to read the voltages. Each of the pressure transducers was calibrated at 7 different pressure levels with 4 trials per level. The following procedure was used for this calibration:

1) Positive and negative wires were run between pressure transducer #1 (for the inlet test section flow loop location) and the voltmeter.

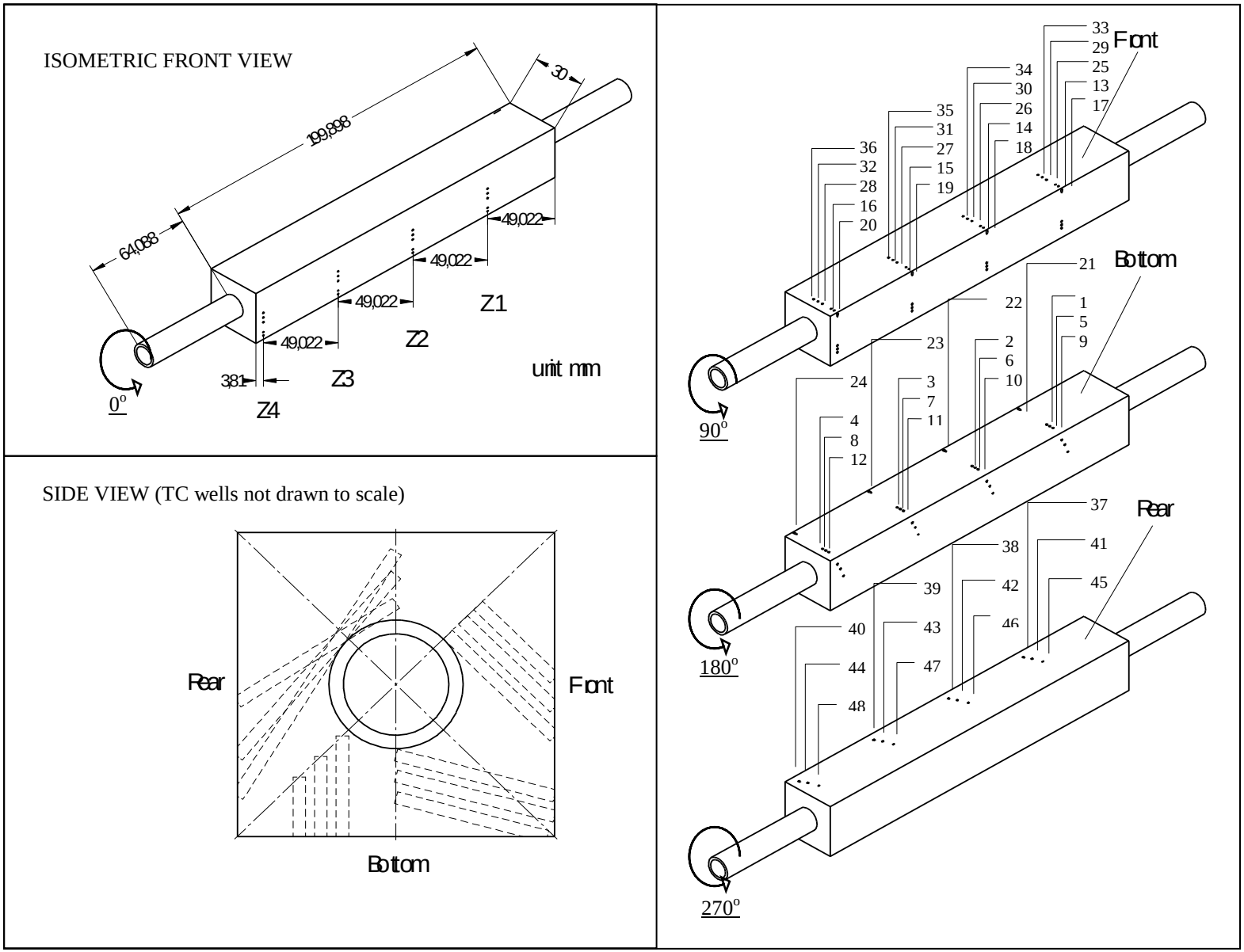

Figure 167: TC Well Locations for Test Section #4 (TS4) Used to Verify Dimensions and Channel Assignment (see Table 2) to the DAQ System.

2) The bolted end of the pressure transducer was screwed into the union nut of the offset pipe assembly.
3) All weights were removed from the tester platform, and the air vent bolt was unscrewed.
4) The calibration unit venire valve was closed as the relief valve was opened to remove any excess pressure.
5) To begin trial #1 of the calibration (no weights added to the platform), the relief valve was screwed shut.
6) The tester handle was pumped slowly and carefully until the platform was hydraulically lifted. The venire valve was then adjusted (screwing and unscrewing), while spinning the platform, until the engraved line on the high pressure platform shaft stabilized in the center of the dead weight cylinder cut out window.
7) The voltage reading for the trial was recorded and steps 4 – 6 were repeated three additional times for the initial pressure level.
8) Calibrations were repeated with the remaining weight levels for the desire pressure ranges to complete pressure transducer #1 calibration.
9) The previous calibration steps were repeated for pressure transducer #2 (for the exit test section flow loop location).

19.5 THERMOCOUPLE AND PRESSURE TRANSDUCER TERMINATION TO THE DAQ SYSTEM

The TC wires include male connectors at their termination ends. The following procedure was used for terminating the TCs and pressure transducers to the DAQ system:

1) A total of 50 insulated wires each were cut approximately 10 ft. long and 2 insulated wires were each cut approximately 2 ft. long from an insulated wire spool and the ends of each wire were spliced using a wire cutter.
2) A female connector was dressed on one end of each of the 50 wires using a small flat head screwdriver.
3) The first DAQ module was opened (disassembled) using a small screwdriver for wire termination.

4) The undressed end of each wire (31 of 50) was braided and terminated to the proper channel (avoiding wire crossing) and each wire was labeled on their female connector tabs the appropriate "TC#" according to Table XIII and Figure 161.
5) The module was reassembled and terminated to the DAQ chassis.
6) Another set of labels including module and channel numbers "M#/CH#" was added on both ends of each wire.
7) The second module TCs were terminated and labeled using steps 3 – 6.
8) Before closing the second module, a total of nine wires (cut approx. 1 ft. long) were spliced and dressed with female connectors to be terminated into channels 19 – 26 for the other TCs shown in Table XIII as TCs #51 - #58.
9) TCs #51-#58 were disconnected from the TS #5 DAQ system module 3 and their ends were dressed with male connectors for convenience so that they could be conveniently plugged into their respective TS4 DAQ system module 2 channels.
10) Step 8 was repeated for the TS5 DAQ system module 3 to allow TCs #51 - #58 to be shared by both DAQ systems.
11) Steps 8-10 were used for all of the pressure and flow rate channels of the TS4 DAQ system Module 3 and the TS5 DAQ system module 4.

19.6 DATA ACQUISITION SYSTEM (DAQ) CALIBRATION

To calibrate the TS4 DAQ system, the temperature precision calibrator form the TC calibrations were used. The up-to-date DAQ system allowed linear calibrations to be made in the system by using a calibrated TC to measure temperatures inside the temperature calibrator for the DAQ system. The calibrator temperature was input as a reference temperature to the DAQ system for the channel of calibration. As this process was performed for five different calibration temperature levels (30, 70, 100, 200, and 300 ^{0}C), the DAQ system produced a linear calibration curve based on the measured temperatures as a function the referenced temperatures. This was done for all of the TC temperature measuring channels of modules 1 and 2 of the TS4 DAQ system.

Table XIII: THERMOCOUPLE (TC) WELL DATA ACQUISITION CHANNEL ASSIGNMENT TEST SECTION #4 (TS 4) (MONOBLOCK - HELICAL INSERT)

Module #1					Module #2					Module #3	
Channel #	**TC Well #**	**Axial Location**	**Radial* Location**	**Circ. Location**	**Channel #**	**TC Well #**	**Axial Location**	**Radial* Location**	**Circ. Location**	**Channel #**	**Location**
0	…….	…….		…….	**0**	32	Z4	INT	45 Deg.	**0**	Bad
1	1	Z1	CTF	135 Deg.	**1**	33	Z1	CTO		**1**	Test Section 5 Outlet Pressure
2	2	Z2			**2**	34	Z2			**2**	High Heat Ex. Exit Pressure
3	3	Z3			**3**	35	Z3			**3**	Pump Exit Pressure
4	4	Z4			**4**	36	Z4			**4**	Tank Exit Pressure
5	5	Z1	INT		**5**	37	Z1	CTO	0 Deg.	**5**	Tank InletPressure
6	6	Z2			**6**	38	Z2			**6**	TS 5 Flow Rate Inlet
7	7	Z3			**7**	39	Z3			**7**	Current
8	8	Z4			**8**	40	Z4			**8**	Voltage
9	9	Z1	CTO		**9**	41	Z1	INT		**9**	Test Section 5 Inlet Pressure
10	10	Z2			**10**	42	Z2			**10**	Test Section 4 Outlet Pressure
11	11	Z3			**11**	43	Z3			**11**	Test Section 4 Inlet Pressure
12	12	Z4			**12**	44	Z4			**12**	
13	13	Z1	CTF	180 Deg.	**13**	45	Z1	CTF		**13**	
14	14	Z2			**14**	46	Z2			**14**	
15	15	Z3			**15**	47	Z3			**15**	
16	16	Z4			**16**	48	Z4			**16**	
17	17	Z1	INT		**17**	49	Test Section Inlet Temp.			**17**	
18	18	Z2			**18**	50	Test Section Exit Temp.			**18**	
19	19	Z3			**19**	51	Low Heat Ex. Outlet Temp.			**19**	
20	20	Z4			**20**	52	Tank Outlet Temp.			**20**	
21	21	Z1	CTO		**21**	53	Water Vapor			**21**	
22	22	Z2			**22**	54	Tank Water			**22**	
23	23	Z3			**23**	55	Pump Outlet Temp			**23**	
24	24	Z4			**24**	56	Chilled Water Outlet Temp.			**24**	
25	25	Z1	CTF	45 Deg.	**25**	57	Chilled Water Inlet Temp.			**25**	
26	26	Z2			**26**	58	High Heat Ex. Outlet Temp.			**26**	
27	27	Z3			**27**					**27**	
28	28	Z4			**28**					**28**	
29	29	Z1	INT		**29**					**29**	
30	30	Z2			**30**					**30**	
31	31	Z3			**31**					**31**	

To calibrate the voltage reading channels of module 3, both the inlet and exit pressure transducers were attached to the dead weight tester and the same weight levels from the earlier calibrations (see previous section) were used so that the voltages of readings of the corresponding weight levels could be used as references inputs to the DAQ system calibration.

19.7 BUS BAR SUPPORTS ALIGNMENT AND ELECTRIC BUS ROUTING

Before aligning the bus bar supports on the test section table, the mykroy blocks listed in Figure 166 had to be machined and installed (see Fig. 165). The different blocks include (see Figure 166): (1) the four mykroy blocks listed as bus bar support mountings, and (2) two mykroy blocks listed as the bus bar support bolting. The blocks were machined to the corresponding dimensions (see Figure 166) with holes drilled centered width-wise through the blocks in axial positions corresponding to the holes at the bottom of the bus bar supports (see Figures 168 and 169). The mykroy bus bar support blocks were used to support the bus bar supports as well as to insulate them from the table. The mykroy bus bar bolting blocks were used to avoid contact between the bolts (used to secure the bus bar supports to the test bed) and the bus bar supports. The alignment of the bus bar supports on the test bed were done with a heater and transition plates installed (see Figures 168 and 169) so that their positions with respect to the test section would yield L_i = 16 mm and L_o = 4 mm (see Figure 162). The main issues concerning this alignment were: (1) verifying that there were no interferences between the transition plates and the test section and (2) verifying that the bus bar support bolts were not in contact with the bus bar supports.

Since the newer test section (TS4) would be farther from the power source than the former (TS5), longer bus bars were needed to terminate the power source to their supports. Each of the eight 3 ft (0.91 m) bus bars used for the TS5 system were replaced with two connecting 5 ft (1.52 m) bus bars totaling 10 ft (3.05m) lengths. This longer length was needed to route these cables above the former test section and on to the latter. Each of the 5 ft (1.52 m) bus bars were covered with heat shrink insulation and joined with a complementary 5 ft (1.52 m)bus bar with conductive grease applied between each contact.

19.8 ACCOUNTING FOR THE HEAT LOSS FROM THE MONOBLOCK TEST SECTION

The heat losses for the monoblock test section were estimated for q''_{oo} from the measured averaged incident heat flux q''_o. Using Figures 168 and 169 as a basis, q''_{oo} was estimated to be

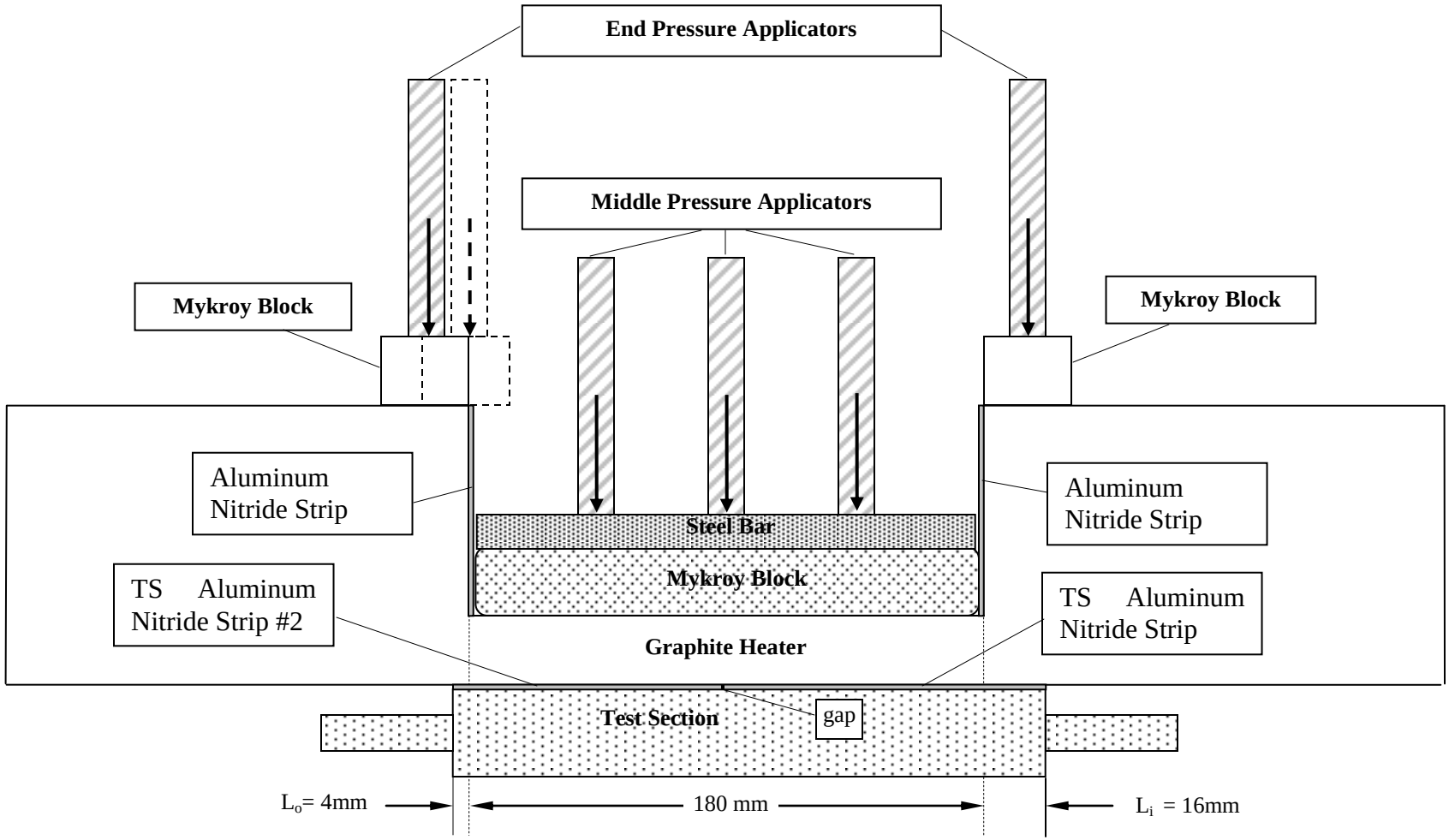

Figure 168: Schematic of the Heater Assembly Procedure for Monoblock Test Sections.

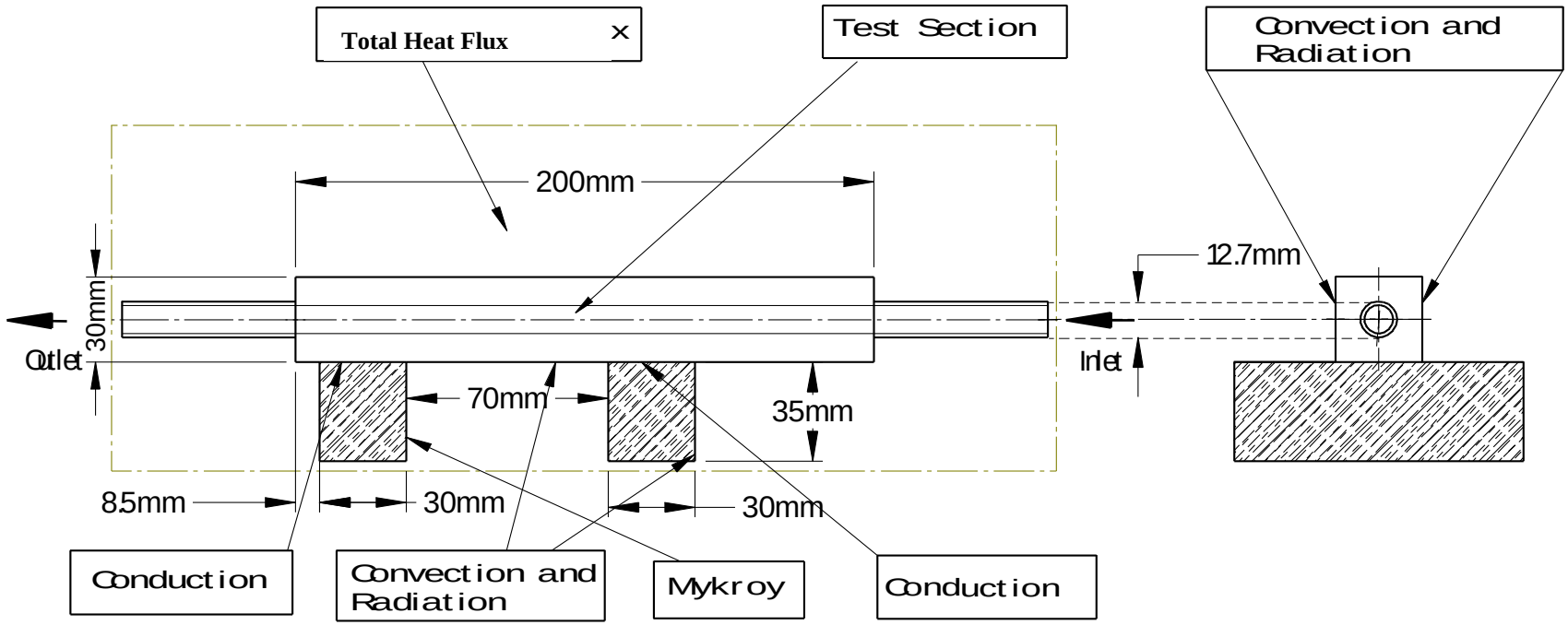

Figure 169: Schematic of Heat Transfer Conditions for the TSRC Monoblock Test Section Setup.

1.0 % higher than $q_o^{''}$. Therefore, this confirms our intuition, prior to the test section installation, that the effect of adding insulation aournd the TS was not absolutely necessary. It was discovered that all of the available blanket insulation would either out-gas and/or was combustible at the higher power TS conditions. This presented safety concerns which we wanted to avoid completely.

19.9 TEST PREPARATION AND ASSEMBLY

Aside from calibrations of the data acquisition (DAQ) system and pressure transducers and other procedures done during the construction of the flow loop system, the main preparation routines for each experiment involved: (1) assembly of the heater system, (2) setting the flow conditions by deionizing the water, stabilizing the flow rate and test section exit pressure and the test section inlet water temperature in the flow loop, and (3) machining and cutting the aluminum nitride and mykroy.

19.9.1 Procedures for Heater System Assembly

A detailed schematic of the procedures used in the monoblock test section heater system assembly of Figure 160 is presented in Figure 165. The procedure is as follows:

- The mykroy blocks and aluminum nitride strips were fabricated to the dimensions specified in Figure 166 using a diamond saw blade. A grinder was used to round the edges of the middle mykroy block. This was needed to prevent the following from occurring when the pressure applicators are torqued: the mykroy could slide into the heater causing cracks to develop in the heater corner.
- The test section, aluminum nitride (AlN) strips, mykroy block and graphite heater were cleaned with 91% alcohol.
- Two complementary aluminum nitride strips were edge-aligned on top of the test section as shown in Figure 169. Two strips are used due to the AlN sheet sides (114 mm) from the manufacturer were less than the 200 mm length of the test section.
- Distance L_i = 16 mm and L_o = 4 mm were pencil marked on the graphite heaters and on the transitions portions to be used for alignment with the test section.
- The graphite heater was place on top of the test section with the L_i and L_o marks aligned with the ends of the test section as illustrated in Figure 168.
- A voltmeter was used to make sure there was no continuity (electrical current) between the graphite heater and the test section.

- Pressure applicators were hand tightened at the test section end locations through the inside bus bar support slots (see Figure 160) to temporarily secure the aligned graphite heater on the test section.
- Both the mykroy block and the steel bar were edge-aligned on top of the graphite heater as shown in Figure 168.
- The saddle was carefully bolted to the test bed around the middle of the assembly with the middle pressure applicator bolts centered (width-wise) over the steel bar.
- Using a torque wrench, torque was iteratively applied to the middle pressure applicator bolts. Beginning with 25 in-lb, the middle bolt was slightly torqued; next, the right bolt was torqued and then the far left bolt of the middle pressure applicators. This iterative torquing process was continued until the torque on all three bolts reached 25 in-lb. The torque iteration process was repeated at 15 in-lb incremented torque wrench settings up to variable torque ratings over 100 in-lb.
- The end pressure applicator bolts were hand tightened and continuity was checked between the saddle and heater and again between the test section and heater using the voltmeter. In some cases, these bolts were torqued up to 60 in-lb; but to reduce the risk of stressing the corners of the heater portion, the left-most heater pressure applicator bolt was shifted to the right (illustrated in Figure 168) to minimize the pressure distribution on unsupported heater areas outside of the test section.
- The heater transition plates were sanded, cleaned with 91% alcohol, and conductive grease was applied to them on the areas where the plates contact the graphite heater and the bus bar supports.
- Each greased heater transition plate was positioned against the heater as in Figure 160 and mildly hand tightened to the top of its prospective bus bar support plate by a locking nut (not shown in Figures), vertically quasi-centered on the plate, and a clamp was used to squeeze the transition plates onto the heater to sustain contact as the plates were snug tightened. This clamp was monitored for interference with the saddle due to the cramped spacing of the system.
- Finally, the transition plate clamp was snug tightened and the absence of continuity was verified between the test section and heater, and between the saddle and heater.

19.9.2 Procedure for Setting the Test Conditions

Setting the test conditions began with deionization the water in the reservoir. During this process, the valves to the test flow loop were closed from the reservoir. The deionization loop valves were then opened and the deionization pump was turned on for at least 3 to 24 hrs to allow the total circulation of the water from the reservoir. The test flow loop valves were reopened and the deionization valves were closed so that the water that was in the test flow loop water during the deionization could be circulated back into the reservoir to complete deionization. The deionization reading of the purified water was typically over 17 MΩ.

19.10 DATA REDUCTION AND EXPERIMENTAL RESULTS

The purpose in reducing the data was to capture the data trends that best represent the physical experiment. To reduce the data, established TSRC methods were used. In order to verify that there would was reasonable and acceptable confidence in the data reduction, two independent examiners (IE) reduced identical data sets. The results are presented below. Measured values such as the heat flux, mass flow rates, saturation temperatures and etc. were calculated during this procedure as well extrapolated inside test section channel wall temperature and heat flux approximations. This approach involves: (1) identifying the steady state data, (2) selecting the maximum temperature values of each steady state level, while (3) using the average inlet and outlet temperature values to calculate heat fluxes for each steady state power level.

19.10.1 Identifying the Steady State Data

As shown in Figures 171 through 173, the raw test data from a TS w/o HWI was plotted vs. the time step and the steady states were identified from the plot's horizontal straight-line trends using the steady state printouts from the test as an aid. For the 1st reduction process, large steady state data spreads (see Figure 172) such as steady state numbers 2, 5, 12, 13, 14, 15, and 17 were purged sparing the smaller data portions toward the ends of the steady state data while all of the transient data was purged from the examination process. The maximum (TS5) or average (TS4) temperature was used as the steady state temperature for every steady state power level line of each channel.

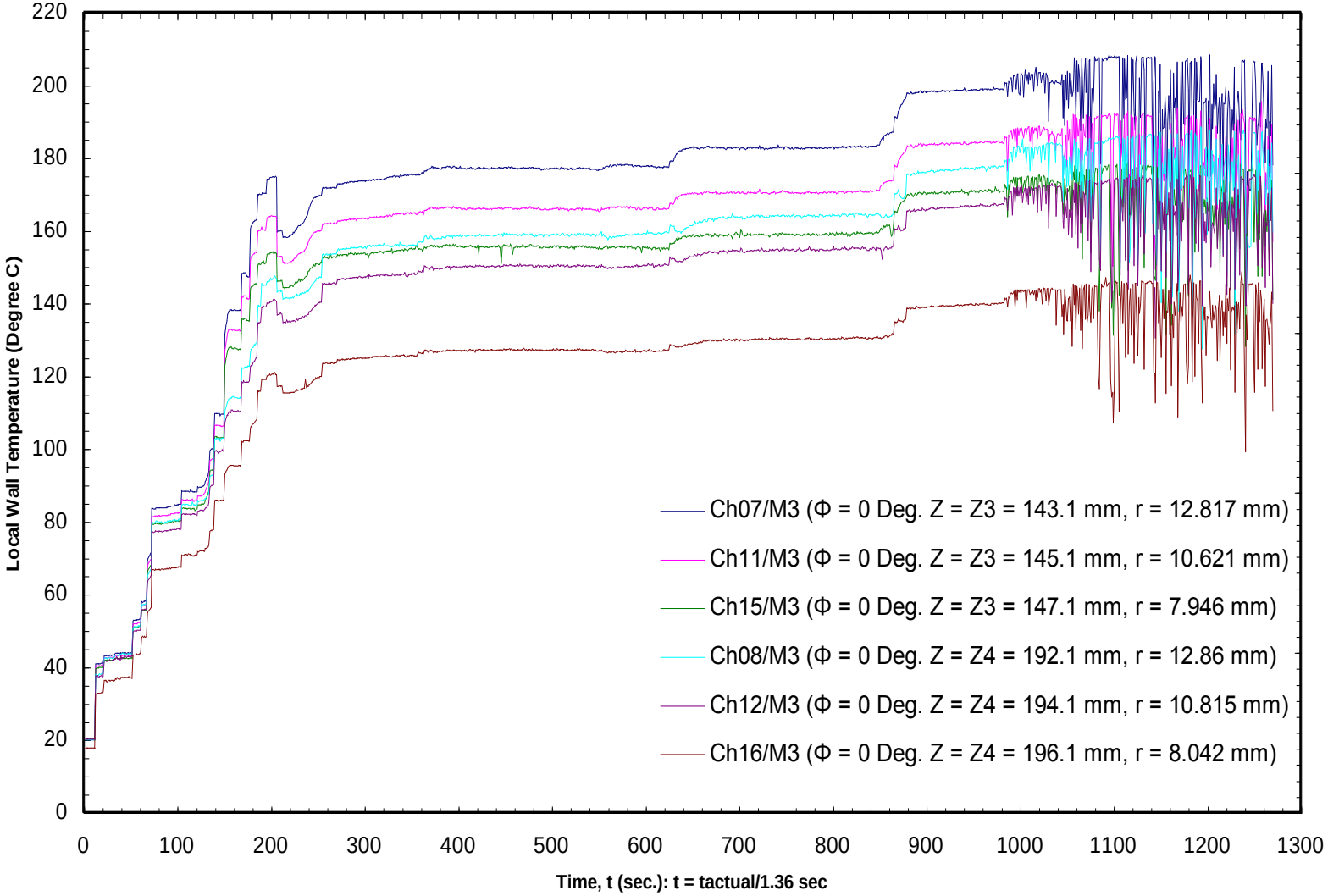

Figure 171: Local Wall Temperature vs. Time for the Following Monoblock w/o HWI Test Conditions: Mass Velocity (G), and Exit Pressure (P_{exit}) are 0.59 Mg/m^2s, and 0.207 MPa, Respectively.

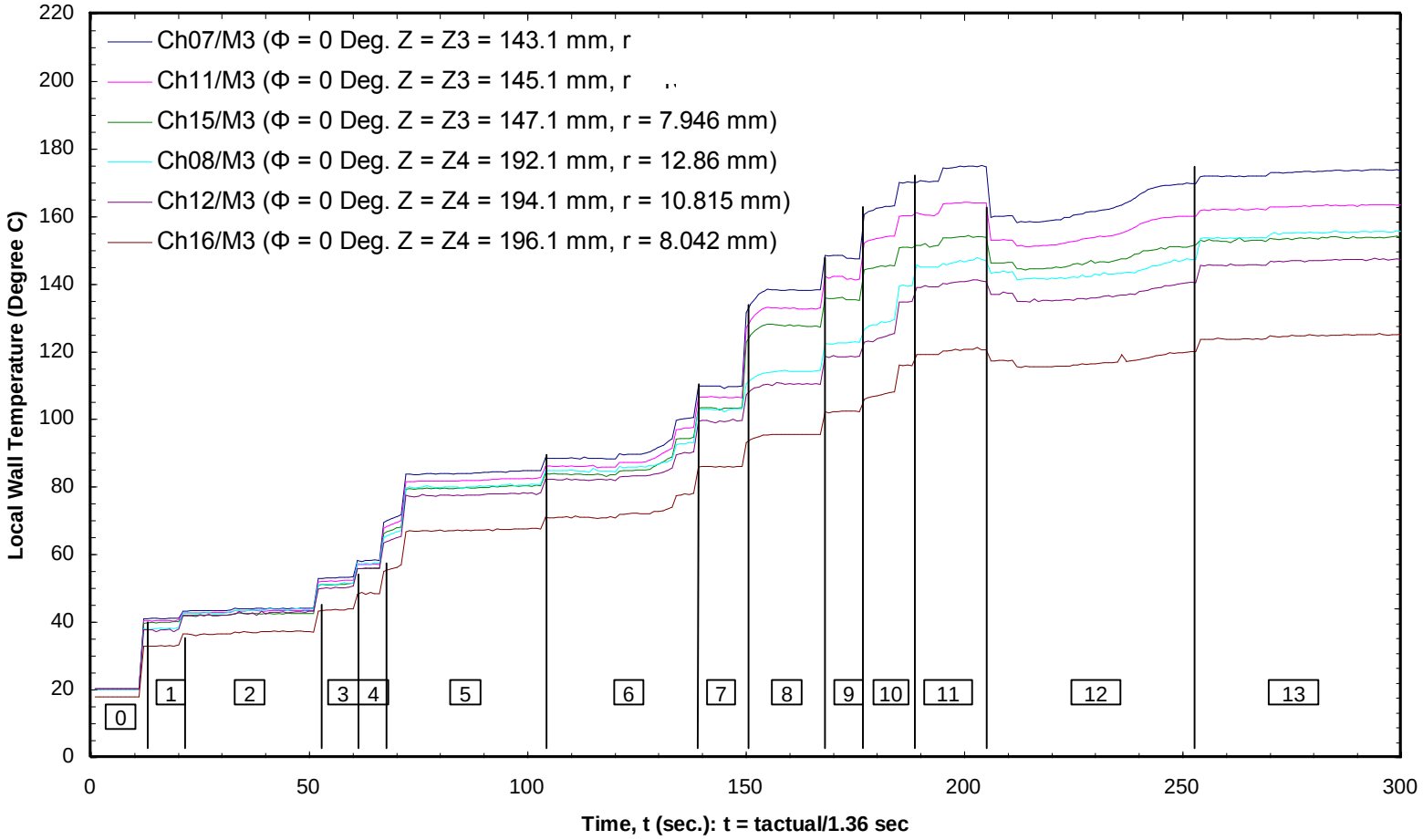

Figure 172: Steady-State Identification (Part I; Times: 0-300) and Local Wall Temperature vs. Time for the Following Monoblock w/o HWI Test Conditions: Mass Velocity (G), and Exit Pressure (P_{exit}) are 0.59 Mg/m^2s, and 0.207 MPa, Respectively.

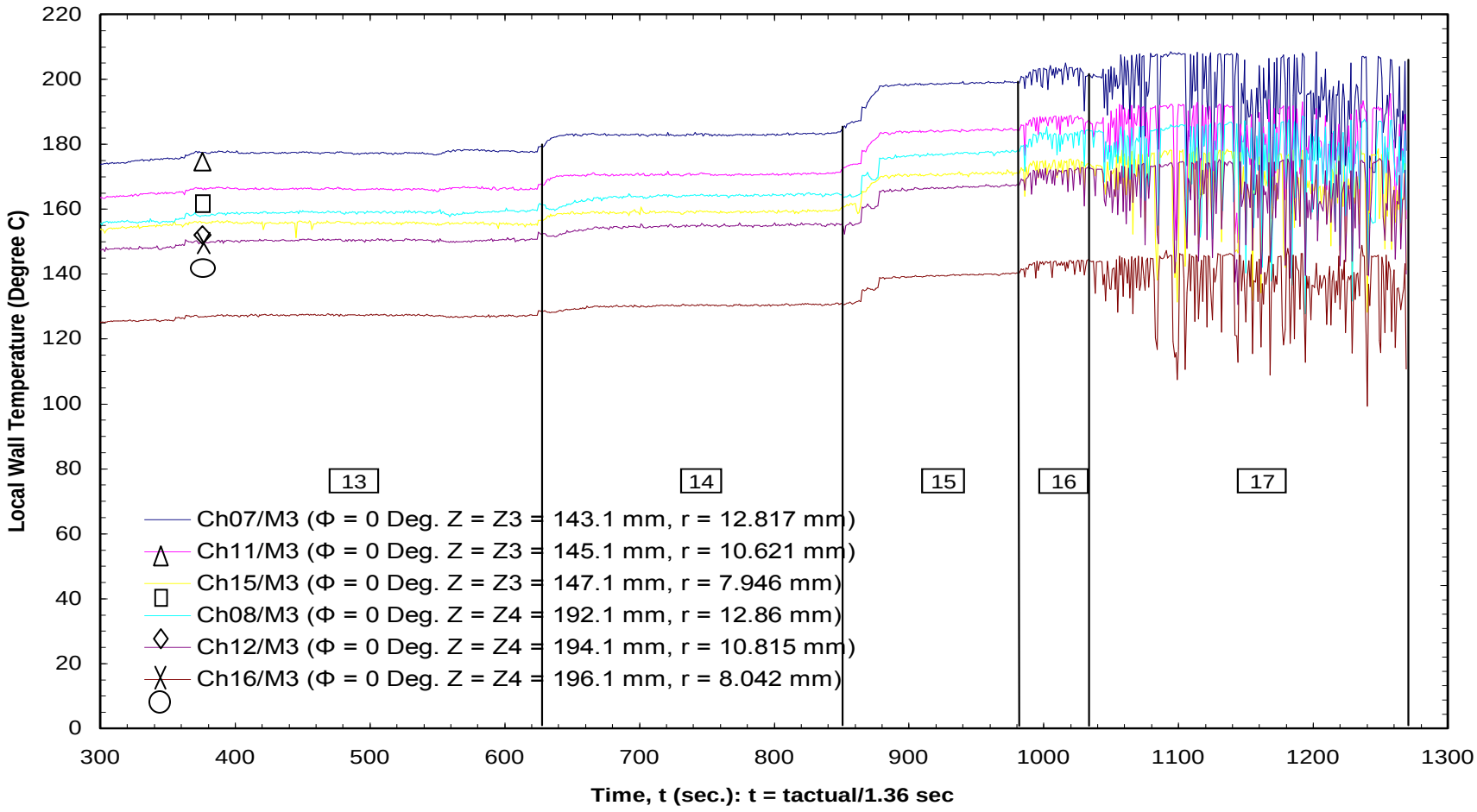

Figure 173: Steady-State Identification (Part II; Times: 300-1300) and Local Wall Temperature vs. Time for the Following Monoblock w/o HI Test Conditions: Mass Velocity (G), and Exit Pressure (P_{exit}) are 0.59 Mg/m^2s, and 0.207 MPa, Respectively.

19.10.2 Experimental Analysis Calculations

Based on the average inlet and exit temperatures for each steady level, heat fluxes were generated using the First Law of Thermodynamics; and, the bulk fluid temperatures at each z location were also computed (see Figure 161). Further, the temperatures at z locations 2 mm (φ = 0, INT) and 4 mm (φ = 0, CTF) away from the general axial locations of Figure 161 (e.g. Planes A2 and A3) were used to obtain interpolated equivalent values at the general z locations (i.e. Z_1, Z_2, Z_3, and Z_4) using the surrounding measurements at other axial locations. This is illustrated in Figure 174. At Z2 and φ = 0 deg, the CTF TC measurement was axially interpolated to Z2 between the Z1 and Z3 CTF measurements. Using the resulting reduced local wall temperature measurements (measurement, and the interpolated INT and CTF measurements) of the respective Z location, the inside wall boundary temperatures was extrapolated using a polynomial equation or a linear equation depending on the radial local wall data trends. The main criteria for linear interpolation were: (1) if the temperature difference between the CTO (close to outside boundary) and INT (interia location) locations was substantially higher than the temperature difference of the INT and CTF locations–causing the polynomial extrapolation to yield an inside wall temperature higher than the CTF (close to the fluid-solid boundary) temperature, and/or (2) if the measured CTO temperature was less than the INT temperature for the upper circumferential locations 0 and 45 deg.

19.10.3 Verification of Benchmarked Experimental Results

A comparison and verification of the results is presented in this section for a benchmarked test involving a monoblock TS w/o HWI (see Figure 162) for the following conditions: G = 0.59 Mg/m^2s, P_{exit} = 0.027 MPa, and T_{sat} = 121.3 ^oC. The identical 3-D, steady state raw data was reduced by two independent examiners, IE-1 and IE-2. The verification results are presented in Figures 175 through 191. Since the heat flux was applied at the top side of the TS (at φ = 0 degrees), this series of plots represents the most critical TC temperature measurements for the monoblock test section. For all cases, there appears to be good agreement between the two IEs. Figures 175 through 177 show a basic comparison of the local wall temperatures measured at the φ = 0 deg location for radial locations CTF, INT, and CTO. It can be seen from the figures that different heat flux levels can be calculated from the same data. This was due to the differences of steady state data spreads used to generate the average inlet and exit

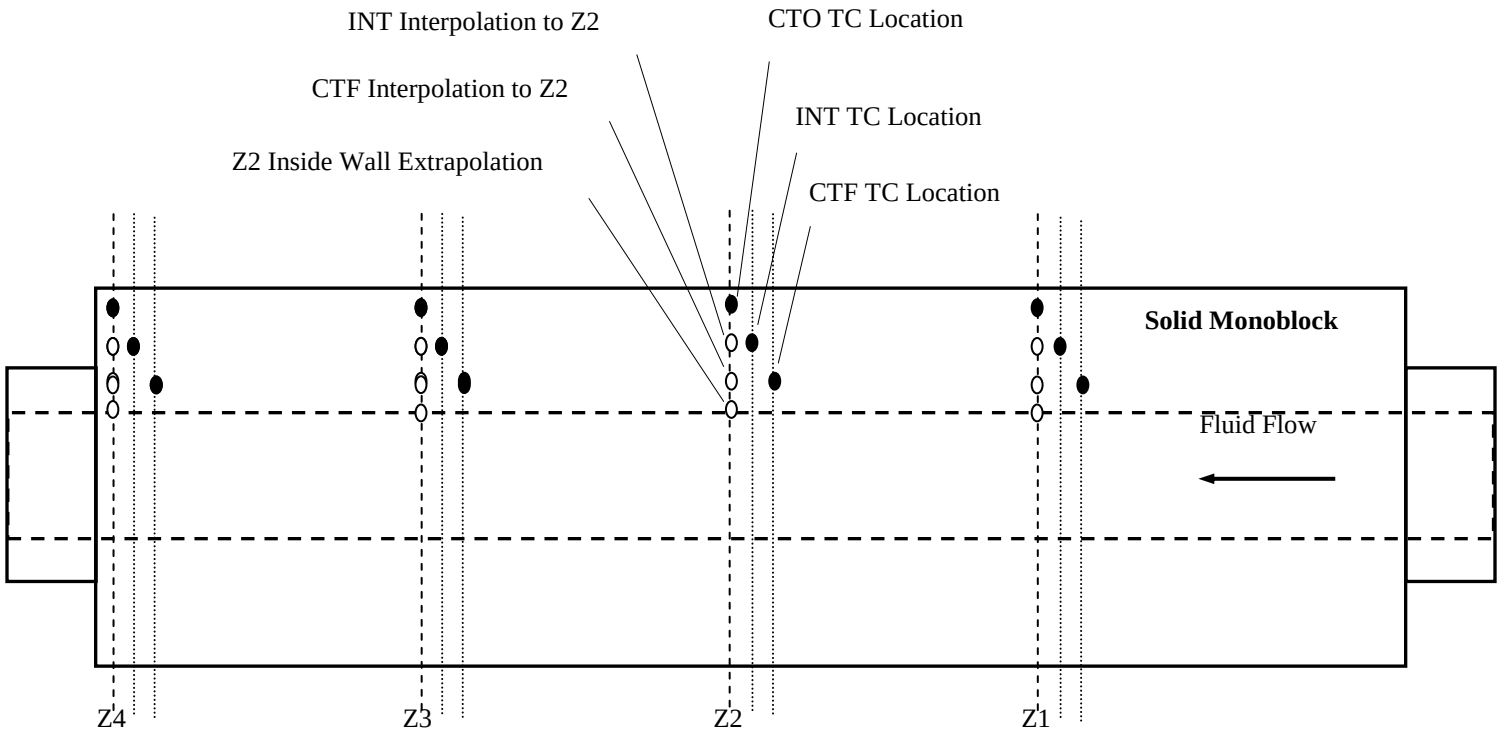

Figure 174: Example of Local and Inside Wall Interpolations and Extrapolations to the General Z Locations for the φ = 0 Degree TC Measurements of the Monoblock TS.

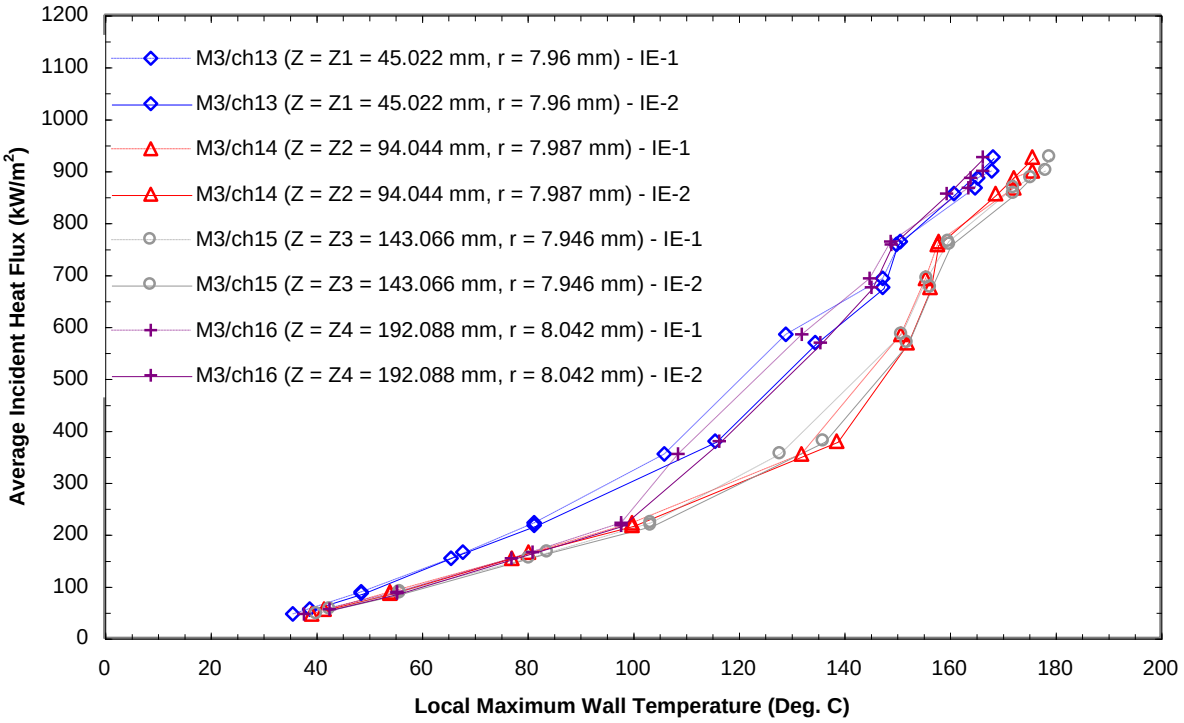

Figure 175: Verification and Comparisons made at Measured Maximum Local Wall Temperature Axial Variation as a Function of the Net Average Incident Heat Flux for the Monoblock Test Section #5 w/o HI for φ = 0, Close to Fluid Boundary Location (G = 0.59 Mg/m^2s, P_{exit} = 0.207 MPa, and T_{sat} = 121.3 ^0C).

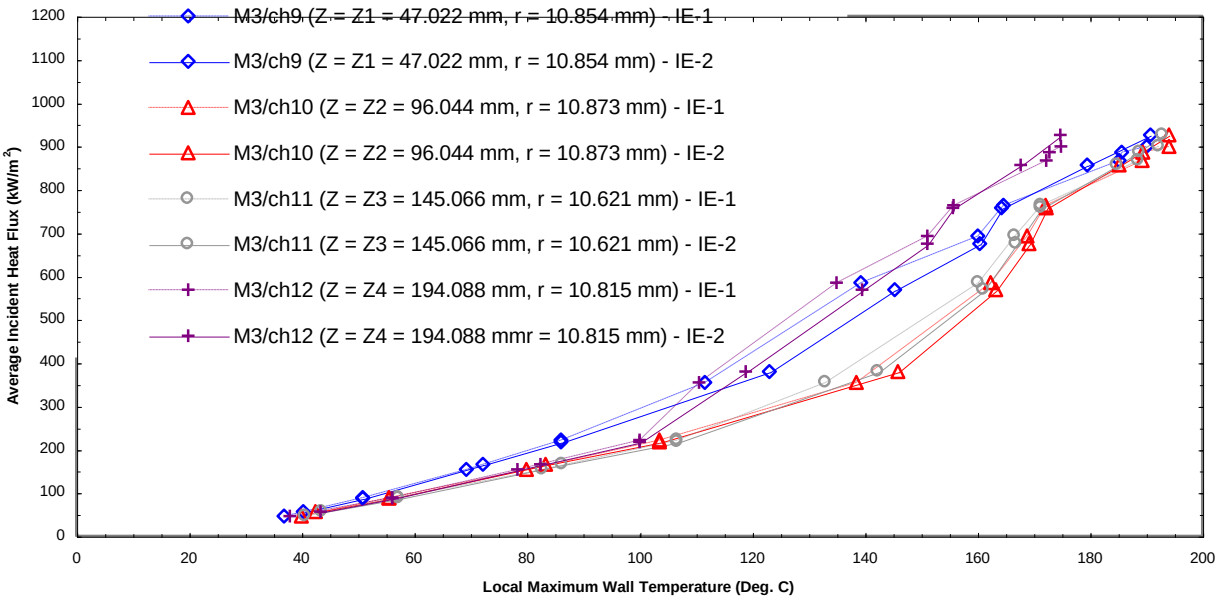

Figure 176: Verfication and Comparisons made at Measrued Maximum Local Wall Temperature Axial Variation as a Function of the Net Average Incident Heat Flux for the Monoblock Test Section #5 w/o HI for for φ = 0, Intermediate Location (G = 0.59 Mg/m^2s, P_{exit} = 0.207 MPa, and T_{sat} = 121.3 ^0C).

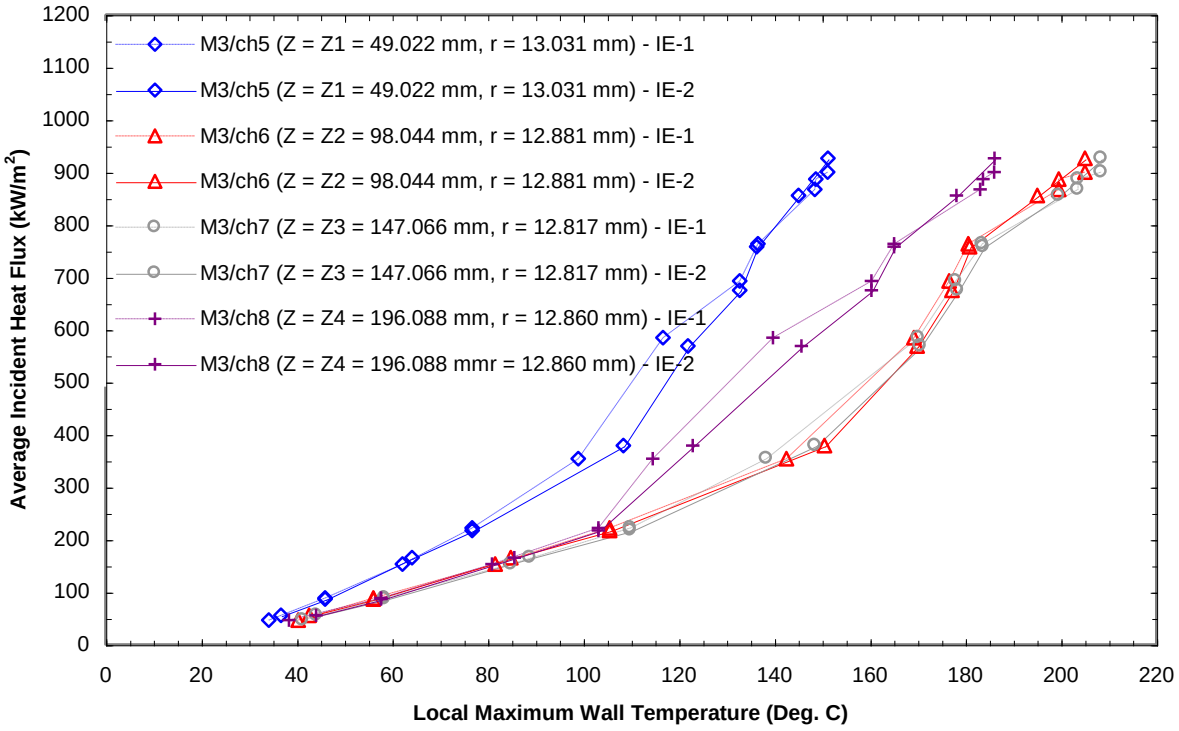

Figure 177: Verification and Comparisons made at Measured Maximum Local Wall Temperature Axial Variation as a Function of the Net Average Incident Heat Flux for the Monoblock Test Section #5 w/o HI for φ = 0, Close to Fluid Boundary Location (G = 0.59 Mg/m^2s, P_{exit} = 0.207 MPa, and T_{sat} = 121.3 ^0C).

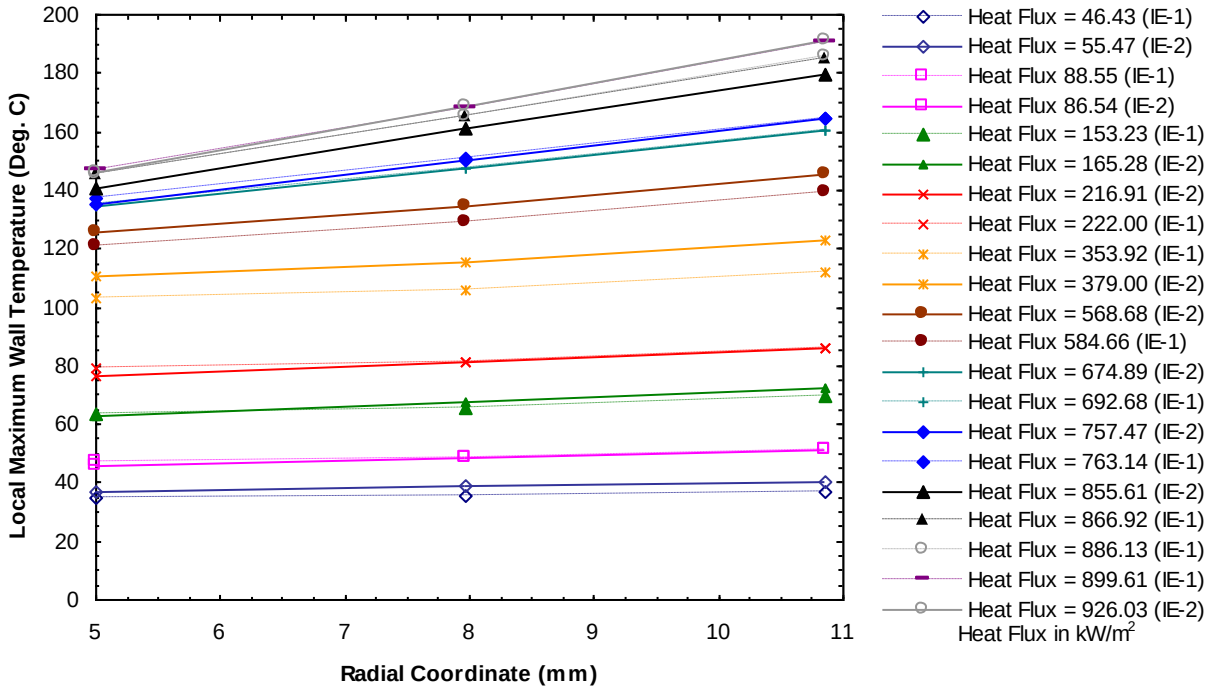

Figure 178: Verification and Comparisons made at Radial Wall Temperature Profiles for the Monoblock Test Section Flow Channel w/o HWI at φ = 0 degree and Z = Z1 = 49.022 mm as a Function of the Net Average Incident Heat Flux for G = 0.59 Mg/m^2s, P_{exit} = 0.207 MPa, and T_{sat} = 121.3 ^0C.

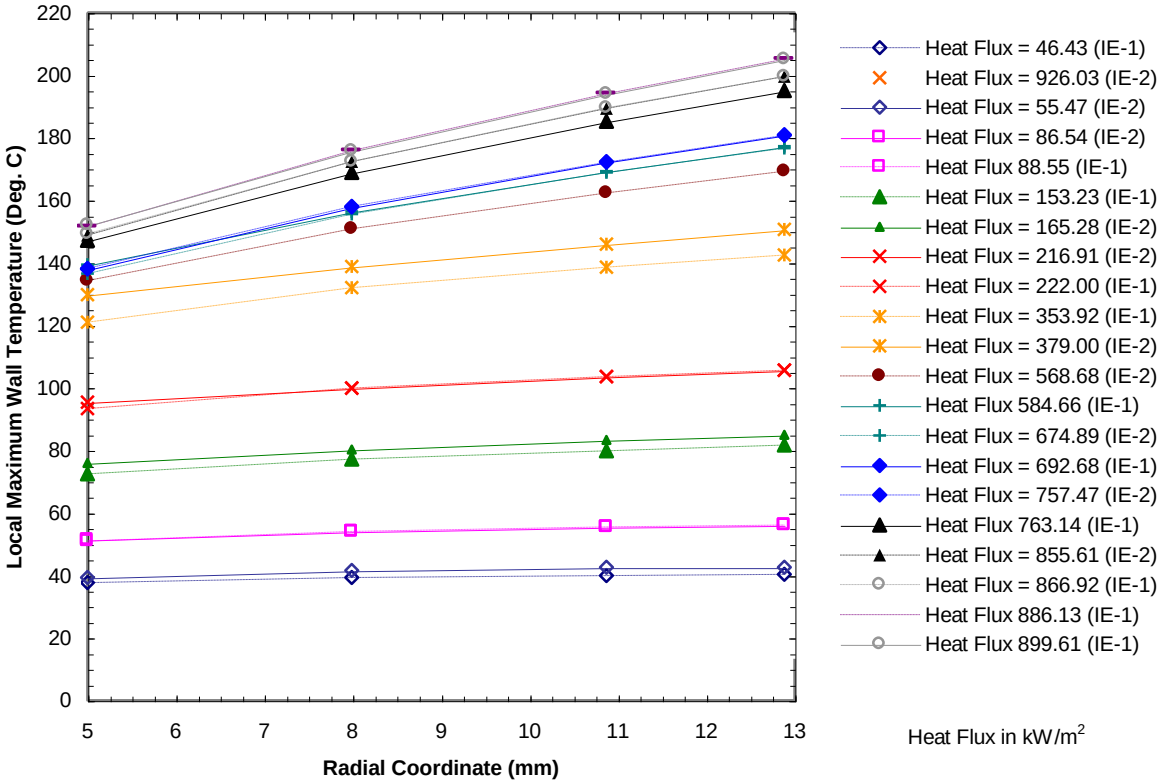

Figure 179: Verification and Comparisons of Radial Wall Temperature Profies for the Monoblock Test Section Flow Channel w/o HI at φ = 0 degrees and Z = Z2 = 98.044 mm as a Function of the Net Average Incident Heat Flux (G = 0.59 Mg.m^{2}s, P_{exit} = 0.207 MPa, and T_{sat} = 121.3 ^{0}C.

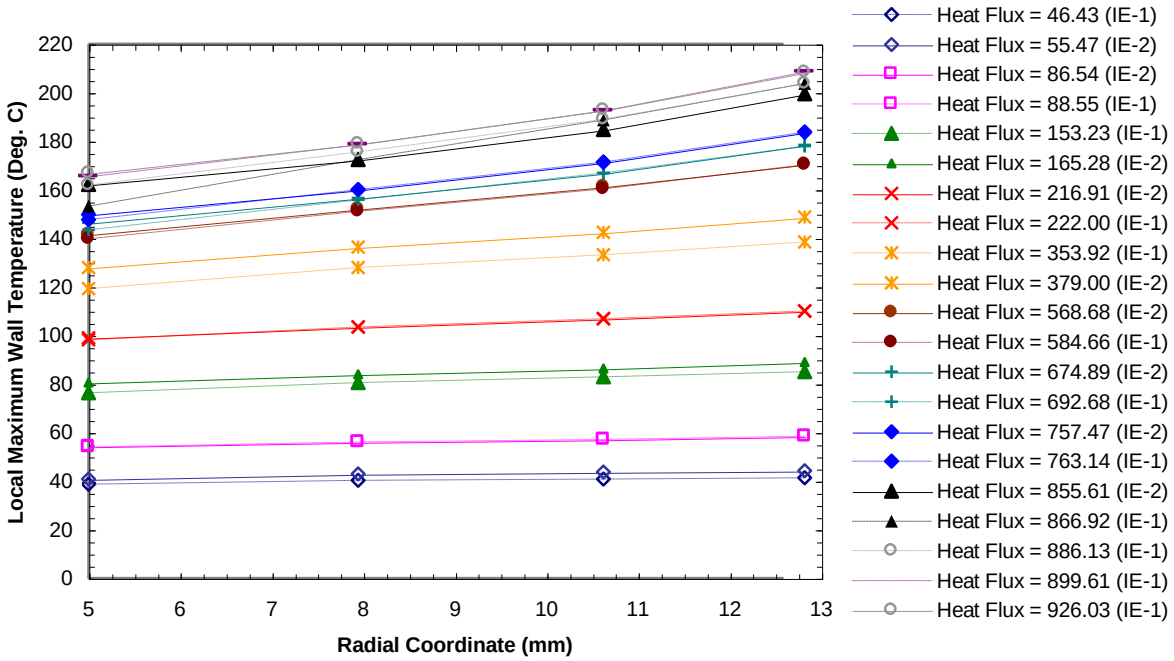

Figure 180: Verification and Comparisons of Radial Wall Temperature Profiles for the Monoblock Test Section Flow Channel w/o HWI at φ = 0 degrees and Z = Z3 = 147.066 mm as a Function of the Net Average Incident Heat Flux (G = 0.59 Mg/m^{2}s, P_{exit} = 0.207 MPa, and T_{sat} = 121.3 ^{0}C).

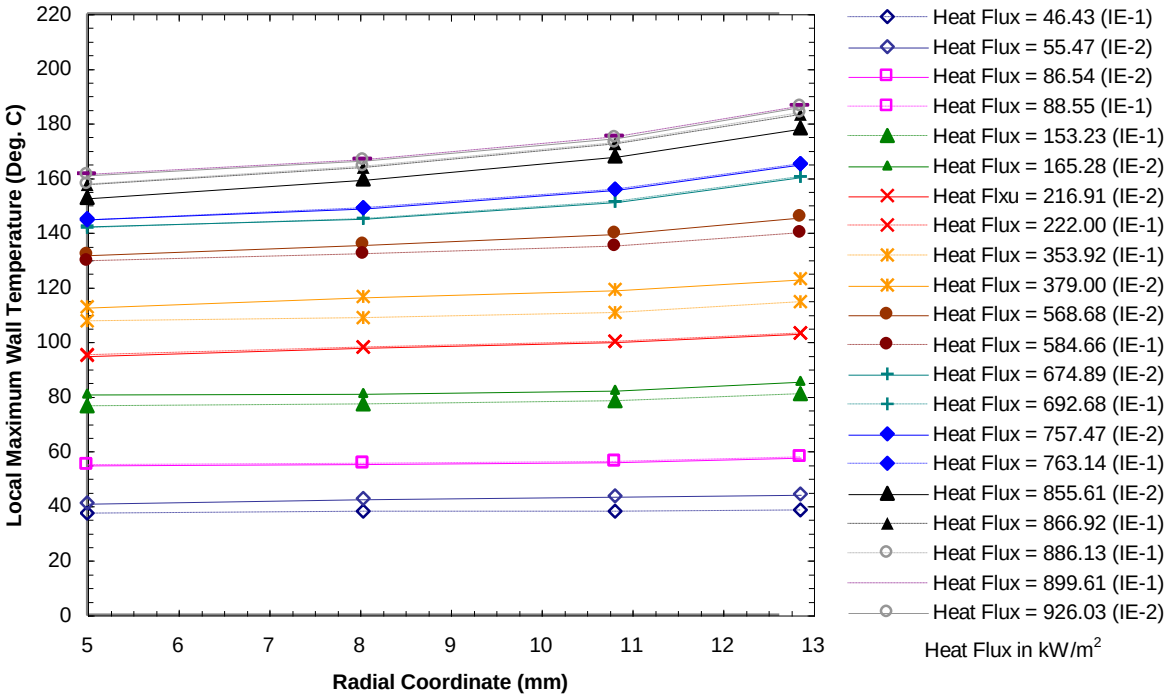

Figure 181: Verification and Comparisons of Radial Wall Temperature Profiles for the Monoblock Test Section Flow Channel w/o HWI at φ = 0 degrees and Z = Z4 = 196.088 mm as a Function of the Net Average Incident Heat Flux (G = 0.59 Mg/m^{2}s, P_{exit} = 0.207 MPa, and T_{sat} = 121.3 ^{0}C).

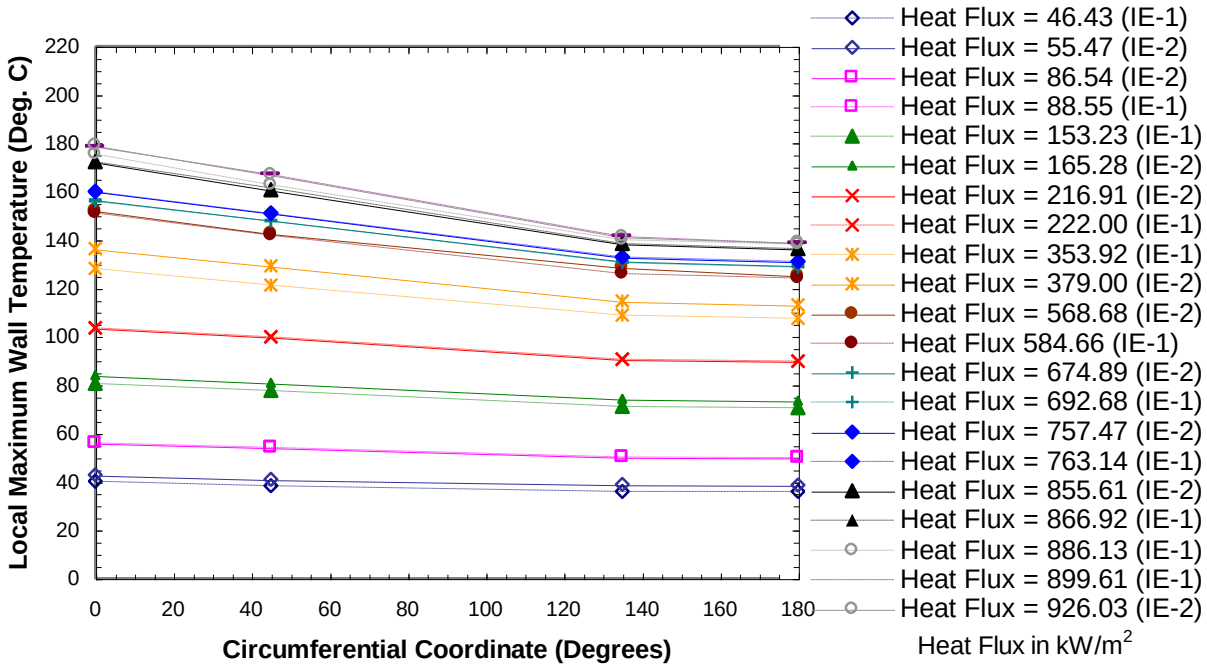

Figure 182: Verification and Comparisons of Circumferential Wall Temperature Profiles for the Monoblock Test Section w/o HWI Thermocouples Close to the Fluid/Solid Boundary as a Function of the Average Net Incident Heat Flux, at Z = Z3 = 147.066 mm (G = 0.59 Mg/m^{2}s, P_{exit} = 0.207 MPa, and T_{sat} = 121.3 ^{0}C

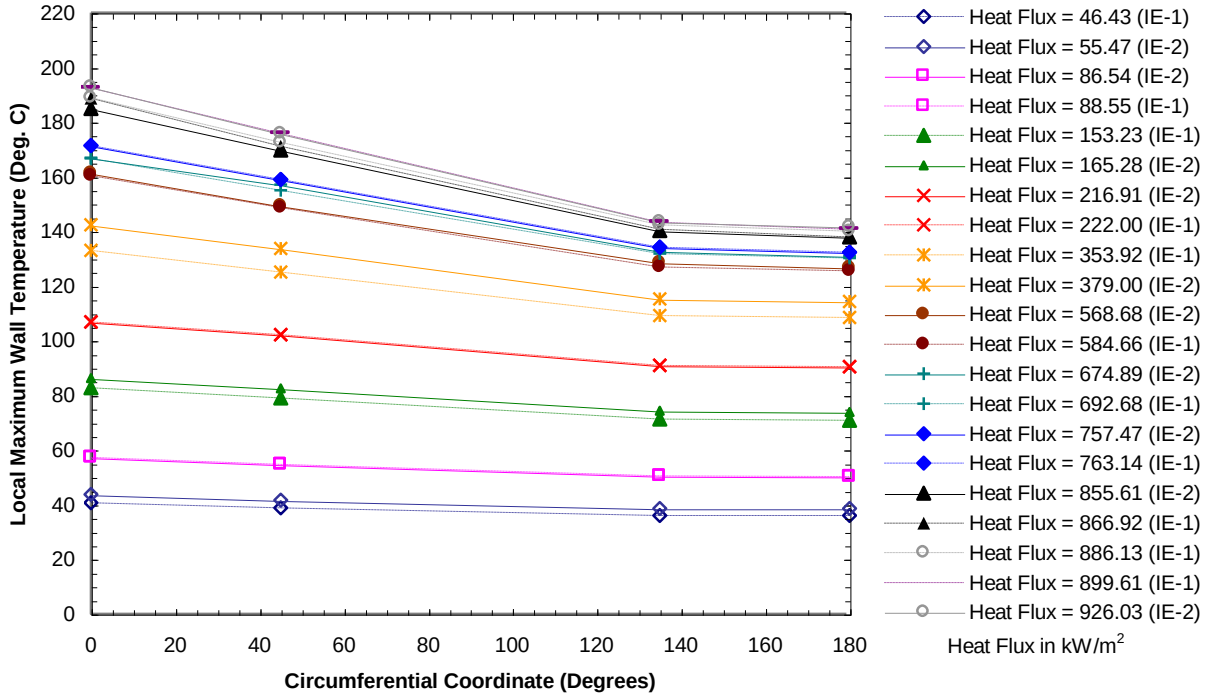

Figure 183: Verification and Comparisons of Circumferential Wall Tempeature Profiles for the Monoblock Test Section w/o HWI Intermediate Thermocouples as a Function of the Average Net Incident Heat Flux, at Z = Z3 = 147.033 mm (G = 0.59 Mg/m^2s, P_{exit} = 0.207 MPa, and T_{sat} = 121.3 ^{0}C.

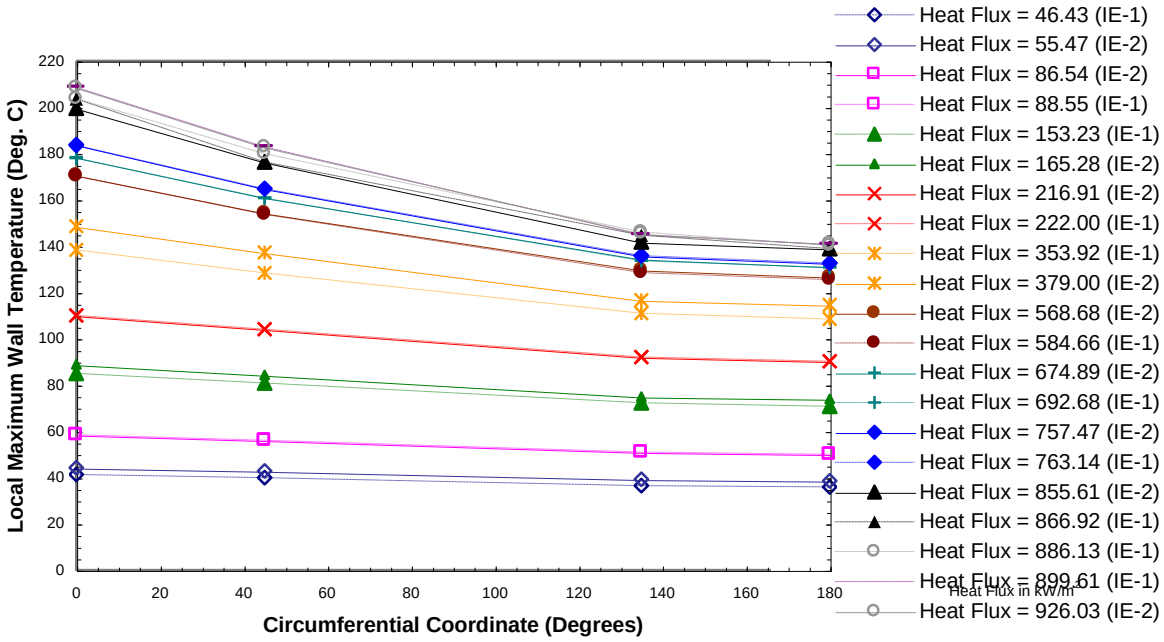

Figure 184: Verification and Comparisons of Circumferential Wall Tempeature Profiles for the Monoblock Test Section w/o HWI Intermediate Thermocouples as a Function of the Average Net Incident Heat Flux, at Z = Z3 = 147.033 mm (G = 0.59 Mg/m^2s, P_{exit} = 0.207 MPa, and T_{sat} = 121.3 ^{0}C.

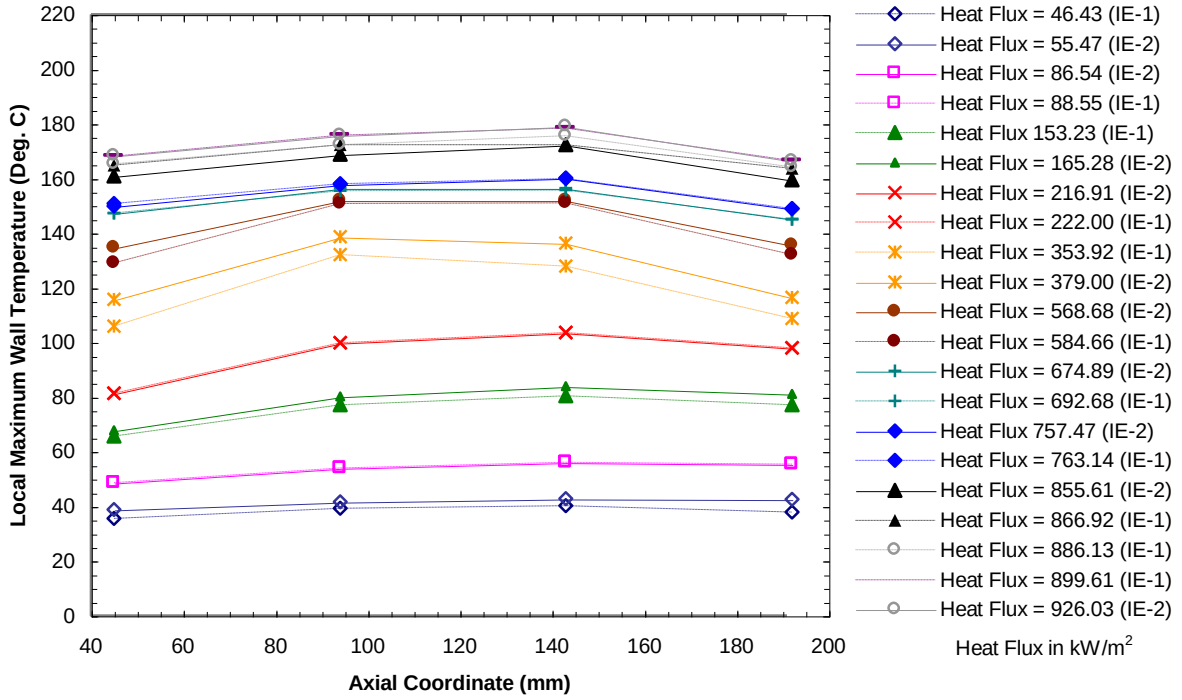

Figure 185: Verification and Comparisons of Axial Wall Temperature Profiles for the Monoblock Test Section w/o HWI Thermocouples at φ = 0 degrees, Close to Fluid Boundary as a Function of the Average Net Incident Heat Flux (G = 0.59 Mg/m^{2}s, P_{exit} = 0.207 MPa, and T_{sat} = 121.3 ^{0}C.

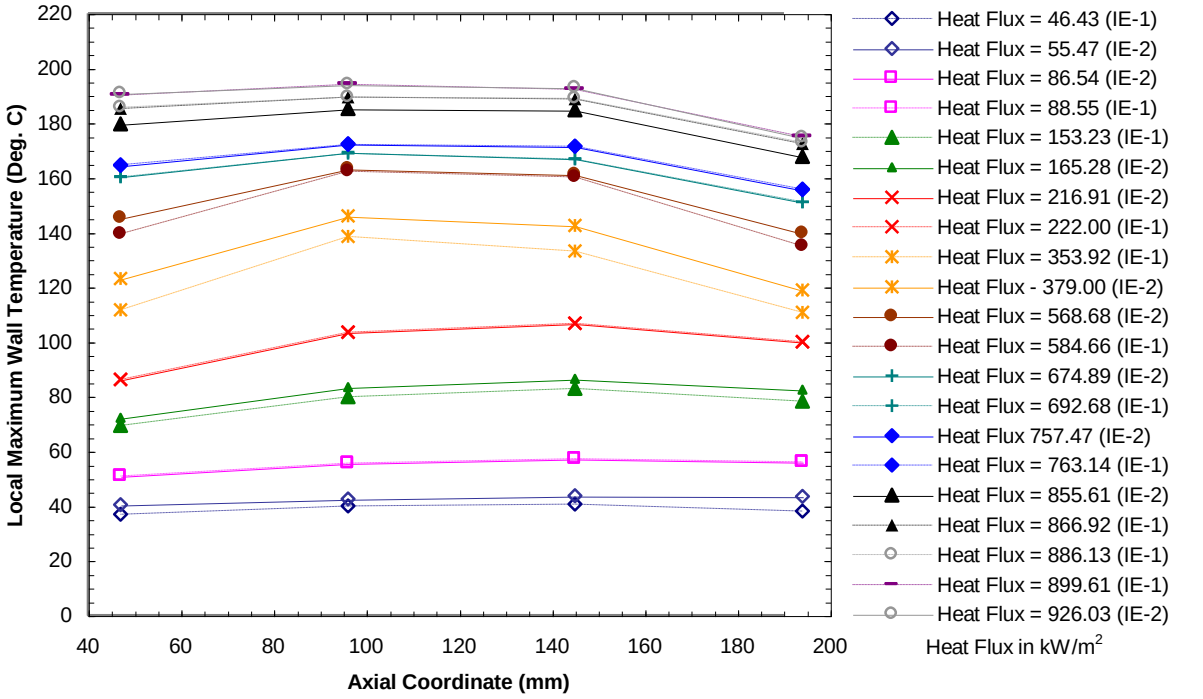

Figure 186: Verification and Comparisons of Axial Wall Temperature Profiles for the Monoblock Test Section w/o HWI Intermediate Thermocouples at φ = 0 Degree as a Function of the Average Net Incident Heat Flux (G = 0.59 Mg/m^{2}s, P_{exit} = 0.207 MPa, and T_{sat} = 121.3 ^{0}C).

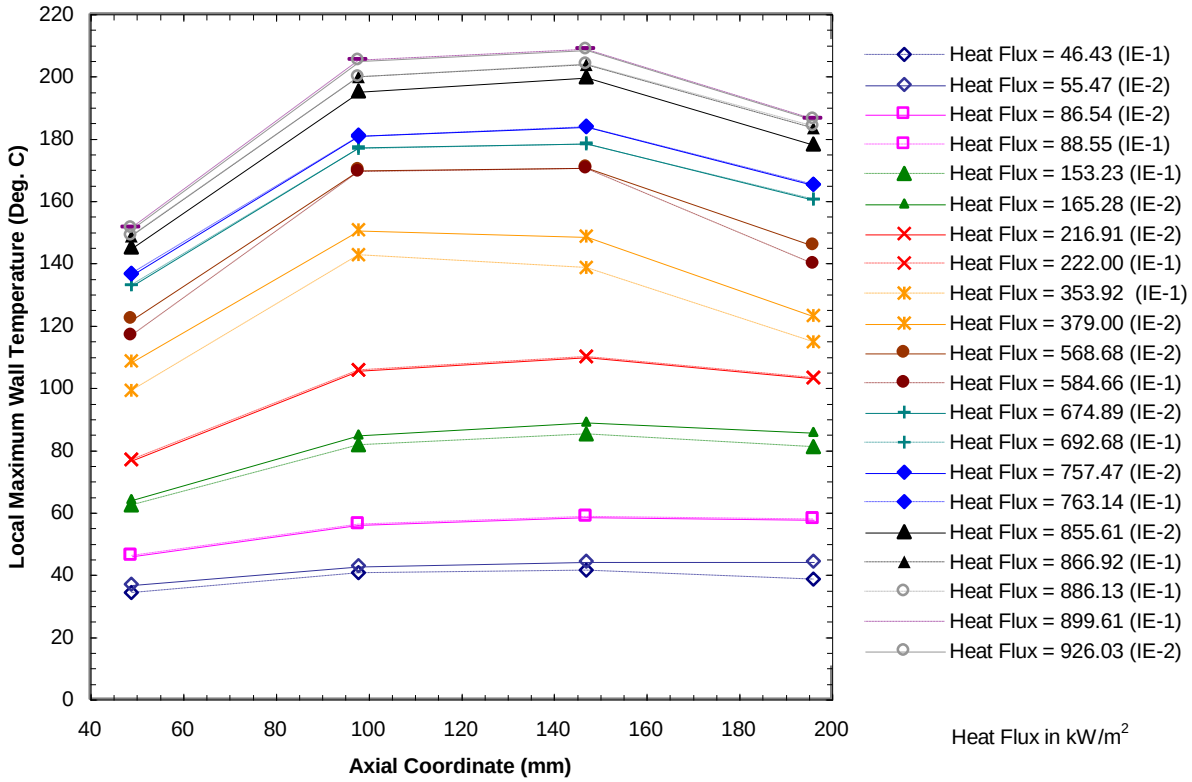

Figure 187: Verification and Comparisons of Axial Wall Temperature Profiles for the Monoblock Test Section w/o HWI Thermocouples at φ = 0 Degree, Close to the Outside Boundary as a Function of the Average Net Incident Heat Flux (G = 0.59 Mg/m^{2}s, P_{exit} = 0.207 MPa, and T_{sat} = 121.3 ^{0}C).

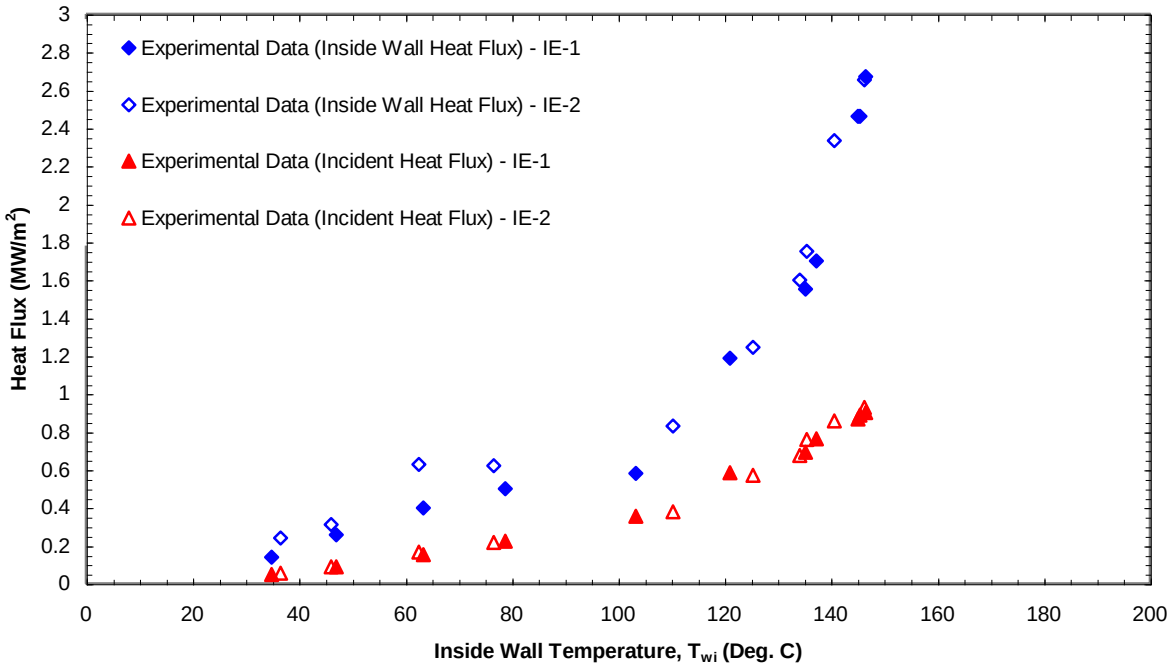

Figure 188: Verification and Comparisons of Inside (2-D Boiling Curve) and Net Average Incident Wall Heat Flux vs the Inside Wall Temperature Profiles for the Monoblock Test Section w/o HWI Thermocouples at φ = 0 Degree and Z = Z1 = 49.022 mm (G = 0.59 Mg/m^{2}s, P_{exit} = 0.207 MPa, and T_{sat} = 121.3 ^{0}C).

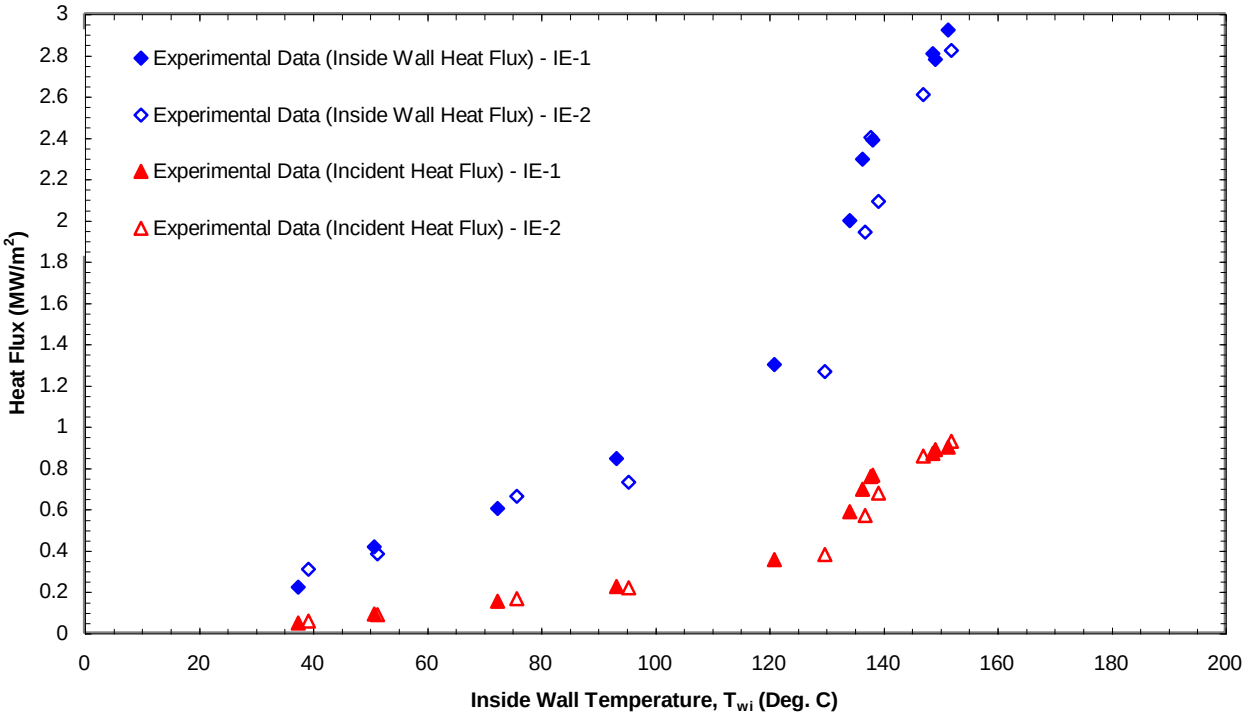

Figure 189: Verification and Comparisons of Inside (2-D Boiling Curve) and Net Average Incident Wall Heat Flux vs the Inside Wall Temperature Profiles for the Monoblock Test Section w/o HWI Thermocouples at φ = 0 Degree and Z = Z2 = 98.044 mm (G = 0.59 Mg/m^{2}s, P_{exit} = 0.207 MPa, and T_{sat} = 121.3 ^{0}C).

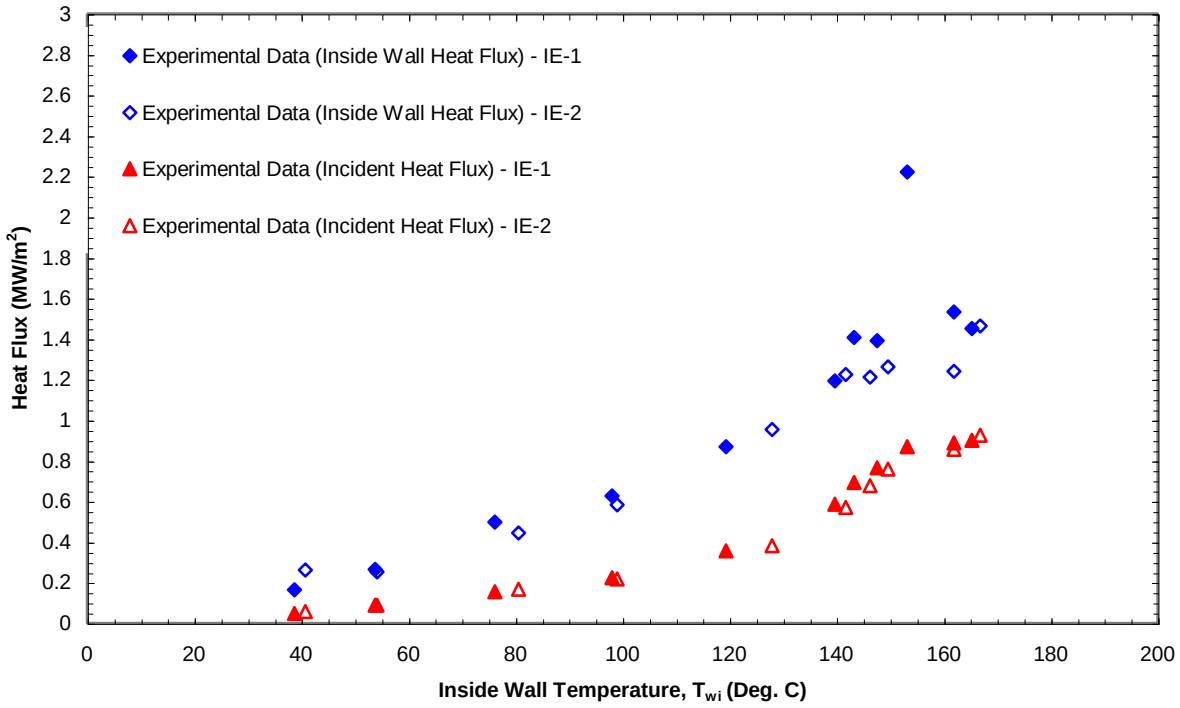

Figure 190: Verification and Comparisons of Inside (2-D Boiling Curve) and Net Average Incident Wall Heat Flux vs the Inside Wall Temperature Profiles for the Monoblock Test Section w/o HWI Thermocouples at φ = 0 Degree and Z = Z3 = 147.066 mm (G = 0.59 Mg/m^{2}s, P_{exit} = 0.207 MPa, and T_{sat} = 121.3 ^{0}C).

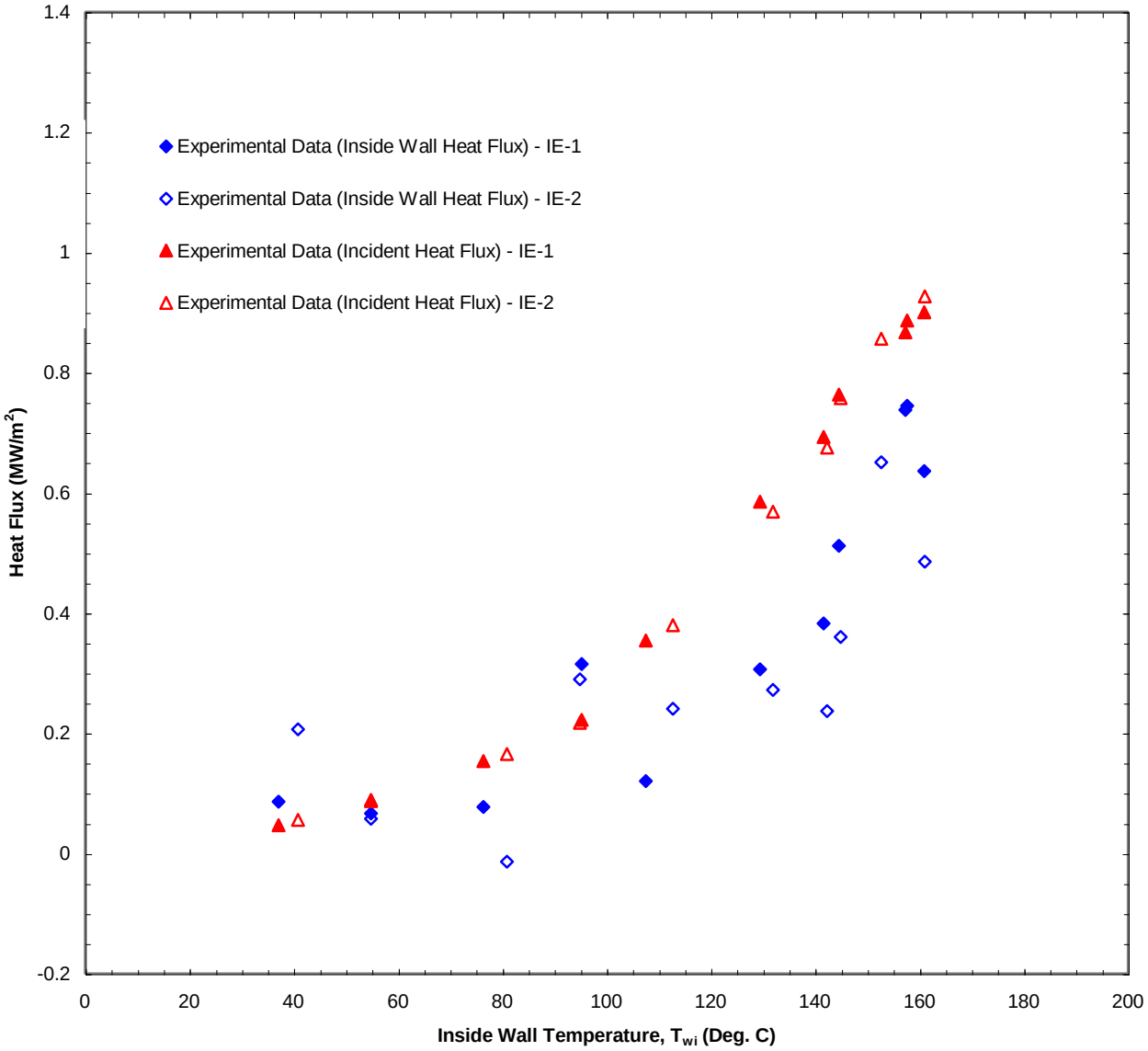

Figure 191: Verification and Comparisons of Inside (2-D Boiling Curve) and Net Average Incident Wall Heat Flux vs the Inside Wall Temperature Profiles for the Monoblock Test Section w/o HWI Thermocouples at φ = 0Degree and Z = Z4 = 196.088 mm (G = 0.59 Mg/m^{2}s, P_{exit} = 0.207 MPa, and T_{sat} = 121.3 ^{0}C).

temperatures. These values varied from one observer to the next unless the exact same steady state data the φ = 0 spreads are used. Figures 178 through 181 show the radial wall temperature distributions of each z location at 0 deg, which include the inside wall temperature extrapolations at the 5 mm radial location. Figures 182 through 184 show the CTF, INT, and CTO circumferential variations at the Z3 location, where the highest temperature of TS5 were typically found to be CTO at the φ = 0 deg. This can be seen from axial temperature distributions of Figures 185 through 187. *Figures 188 through 191 show the inside wall heat flux (2-D boiling curves) vs. temperature profiles, and verifies that the data reduction procedure is consistently reliable. These 2-D boiling curves (data for the other circumferential locations were measured) are among the first multi-dimensional water boiling curves (MDBC) produced in the technical literature. To emphasize their importance: If the MDBC is known, it could be used to both in a thermal conduction code to determine the "real" or physical multi-dimension temperature profile in a HHF component and a validation-verification base-line for CFD codes that are designed to predict conjugate (convective-conduction) heat transfer for thermally developing single- or two-phase laminar and turbulent flows.*

19.10.4 Comparison of Monoblock TS4 (with Helical Wire Insert-HWI) and TS5 (w/o HWI) Experimental Results

The experimental Campaign using the monoblock TS4 with the helical wire insert (HI) had the following conditions: G = 3.2 Mg/m^2s, P_{exit} = 0.572 MPa, T_{sat} = 157 ^oC, L_i = 16.0 mm, L_o = 4.0 mm, and a torque on the TS of 120 in-lbs. This campaign was compared with results obtained using TS5 w/o HWI and under similar flow conditions. As seen in Figures 192 through 208, the helical flow yielded lower 3-D wall temperatures for each heat flux level relative to the non-helical flow.

As before, detail comparisons will be presented here for a major portion of the data for ϕ = 0 degree. Figures 192 through 194 show the basic data comparisons for the average incident heat flux (q''_{oo}) as a function the local flow channel wall temperature at the four axial locations. At comparable levels of q''_{oo}, selected 3-D (r-, ϕ, and z) local wall temperature distributions are shown for the monoblocks with and without the HWI in Figures 195 through 204. For most measurement locations, the effect of the HWI is to reduce $T_w(r, \phi, z)$. Figures 195 through 198 show that for the helical flow test at φ = 0 deg, there are higher radial temperature gradients than for the non-helical flow, and these slopes change with respect to the Z locations. Although the Z1

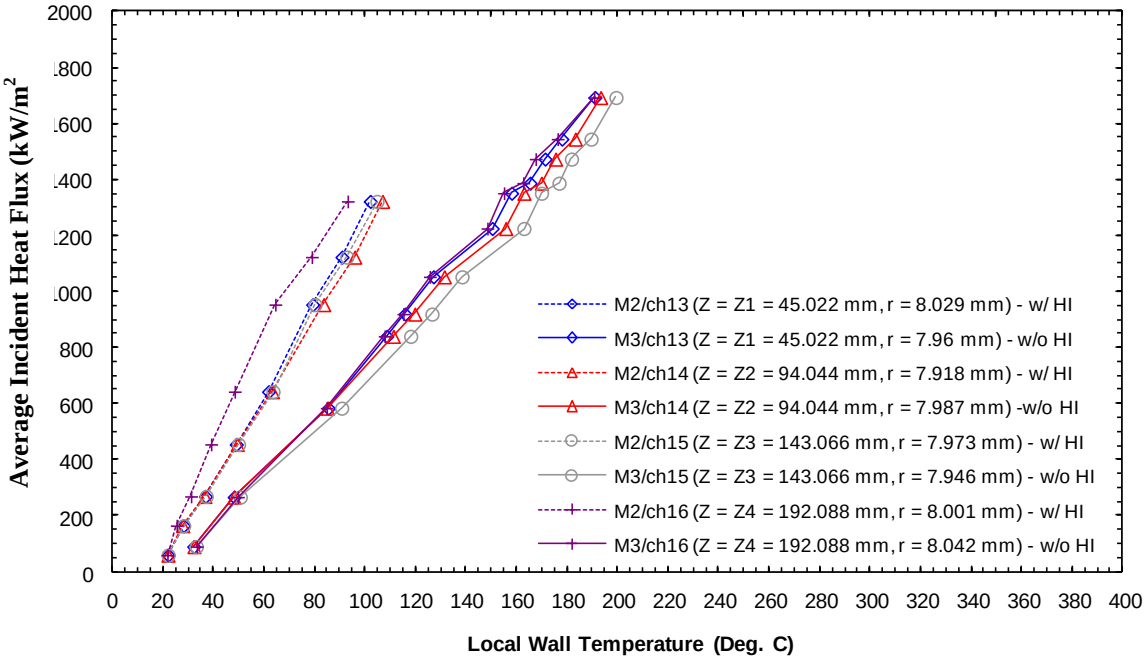

Figure 192: Monoblock w/ HI Comparison to Monoblock w/o HI for Measured Maximum Local Wall Temperature Axial Variation as a Function of the Net Average Incident Heat Flux for φ = 0, Close to Fluid Boundary Location (G = 3.2 Mg/m^{2}s, P_{exit} = 0.572 MPa, and T_{sat} = 157 ^{o}C).

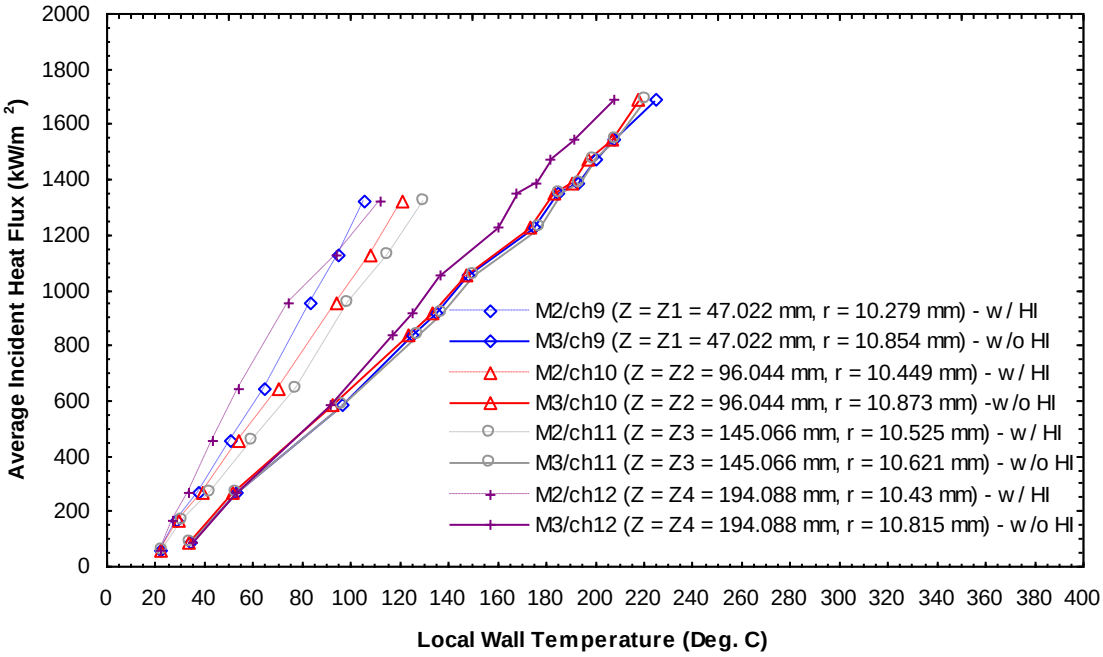

Figure 193: Monoblock w/ HI Comparison to Monoblock w/o HI for Measured Maximum Local Wall Temperature Axial Variation as a Function of the Net Average Incident Heat Flux for φ = 0, Intermediate Location (G = 3.2 Mg/m^{2}s, P_{exit} = 0.572 MPa, and T_{sat} = 157 ^{o}C). P_{exit} = 0.207 MPa, and T_{sat} = 121.3 ^{o}C).

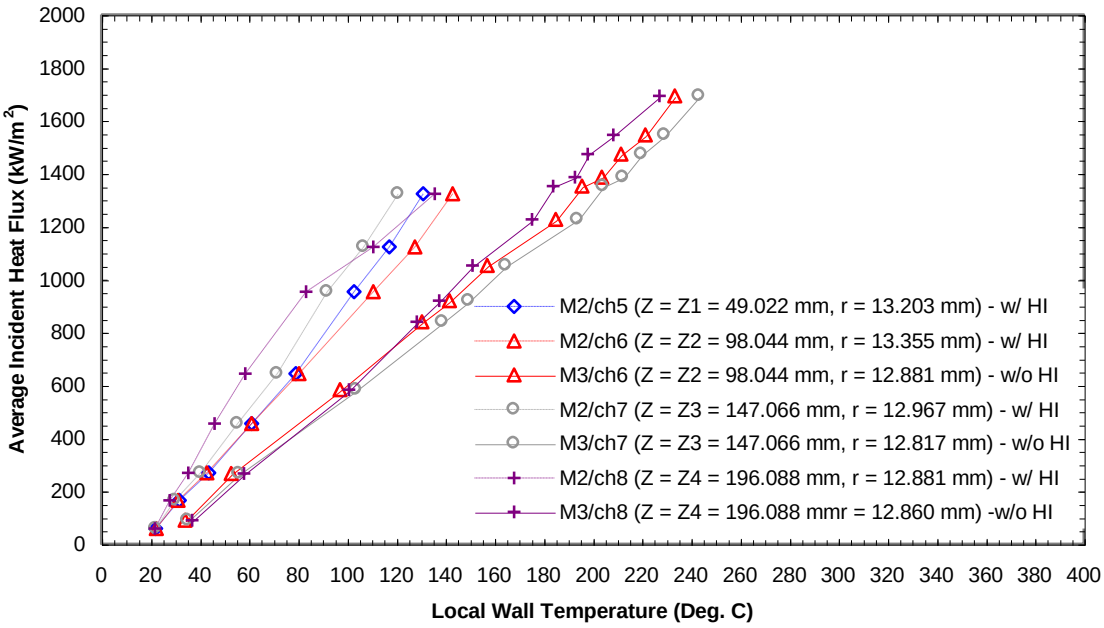

Figure 194: Monoblock w/ HI Comparison to Monoblock w/o HI for Measured Maximum Local Wall Temperature Axial Variation as a Function of the Net Average Incident Heat Flux for φ = 0, Close to the Outside Boundary Location (G = 3.2 Mg/m^{2}s, P_{exit} = 0.572 MPa, and T_{sat} = 157 ^{o}C).

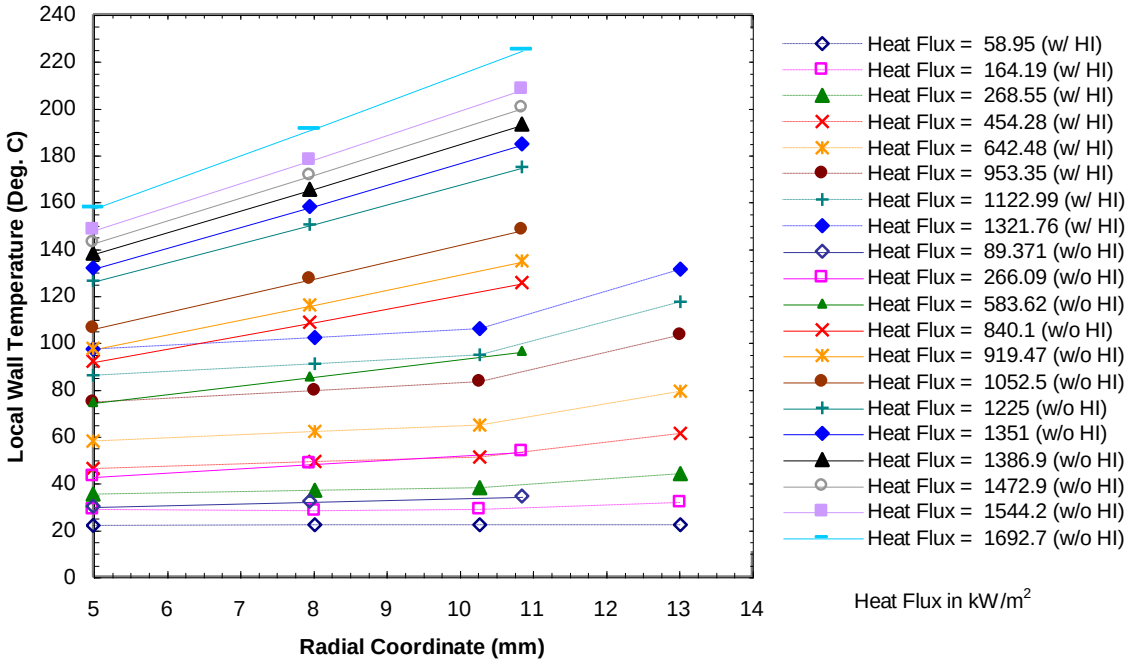

Figure 195: Monoblock w/ HI Comparison to Monoblock w/o HI for Radial Wall Temperature Profiles at φ = 0 deg and Z = Z1 = 49.022 mm as a Function of the Net Average Incident Heat Flux (G = 3.2 Mg/m^{2}s, P_{exit} = 0.572 MPa, and T_{sat} = 157 ^{o}C).

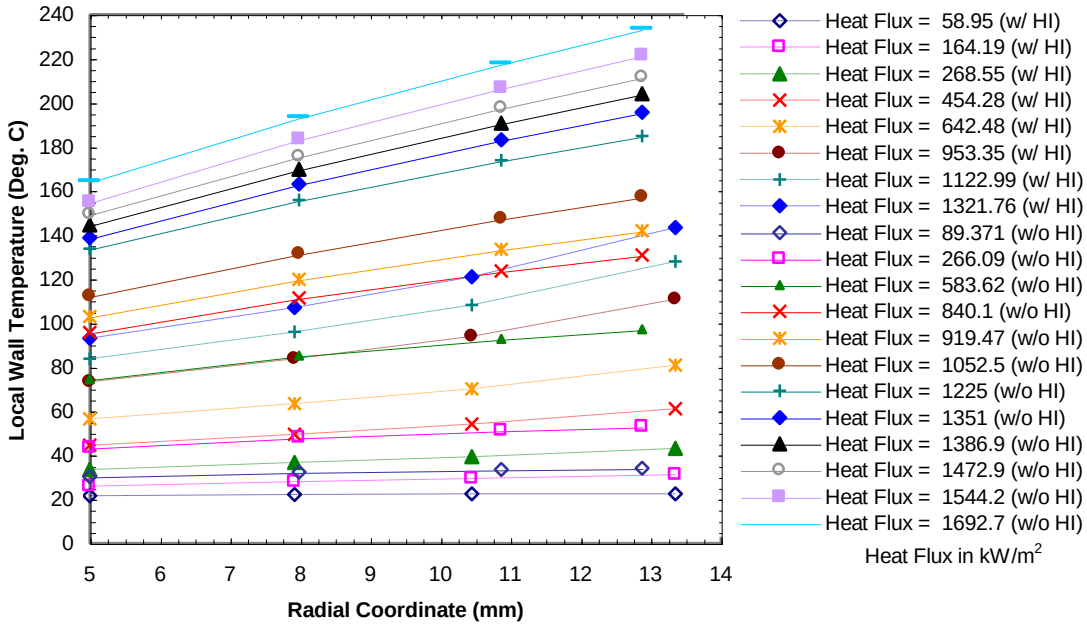

Figure 196: Monoblock w/ HI Comparison to Monoblock w/o HI for Radial Wall Temperature Profiles at φ = 0 deg and Z = Z2 = 98.044 mm as a Function of the Net Average Incident Heat Flux (G = 3.2 Mg/m^{2}s, P_{exit} = 0.572 MPa, and T_{sat} = 157 ^{o}C).

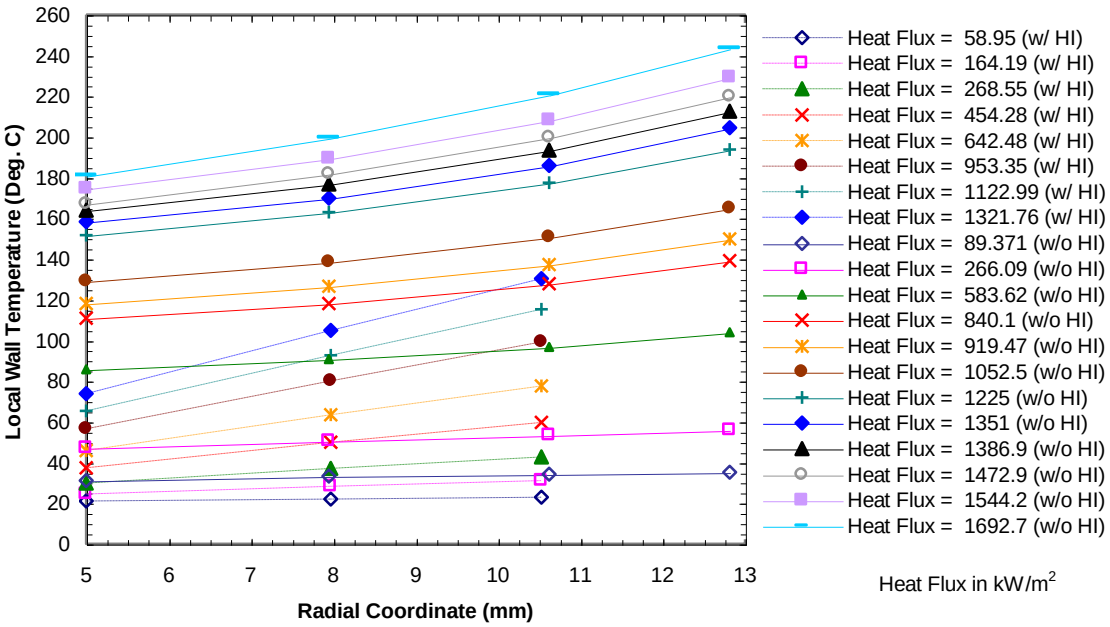

Figure 197: Monoblock w/ HI Comparison to Monoblock w/o HI for Radial Wall Temperature Profiles at φ = 0 deg and Z = Z3 = 147.066 mm as a Function of the Net Average Incident Heat Flux (G = 3.2 Mg/m^{2}s, P_{exit} = 0.572 MPa, and T_{sat} = 157 ^{o}C).

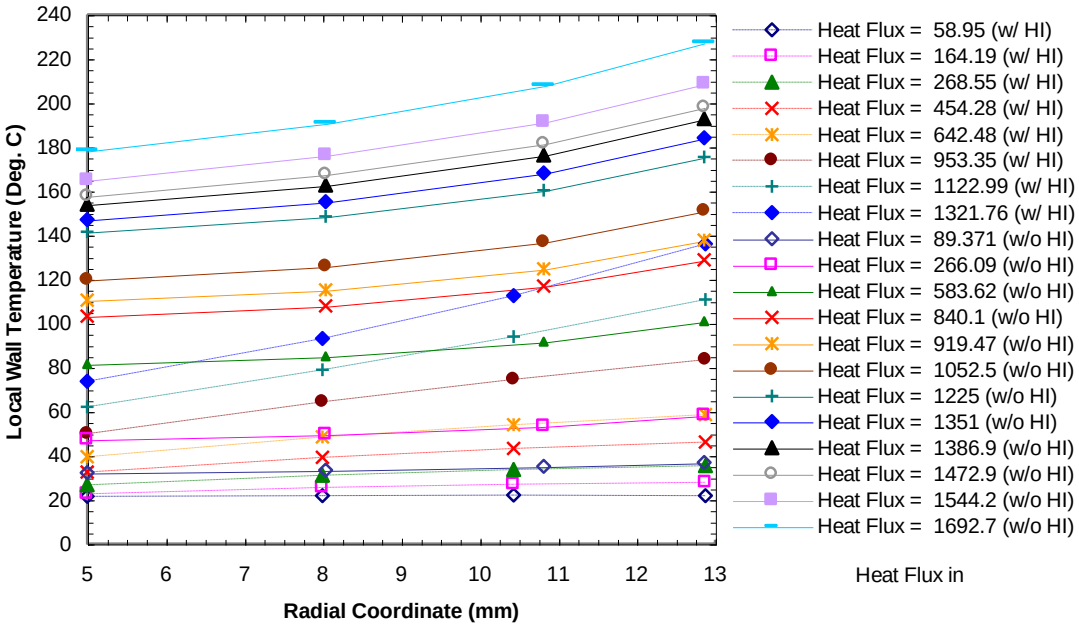

Figure 198: Monoblock w/ HI Comparison to Monoblock w/o HI for Radial Wall Temperature Profiles at φ = 0 deg and Z = Z4 = 196.088 mm as a Function of the Net Average Incident Heat Flux (G = 3.2 Mg/m^{2}s, P_{exit} = 0.572 MPa, and T_{sat} = 157 ^{o}C).

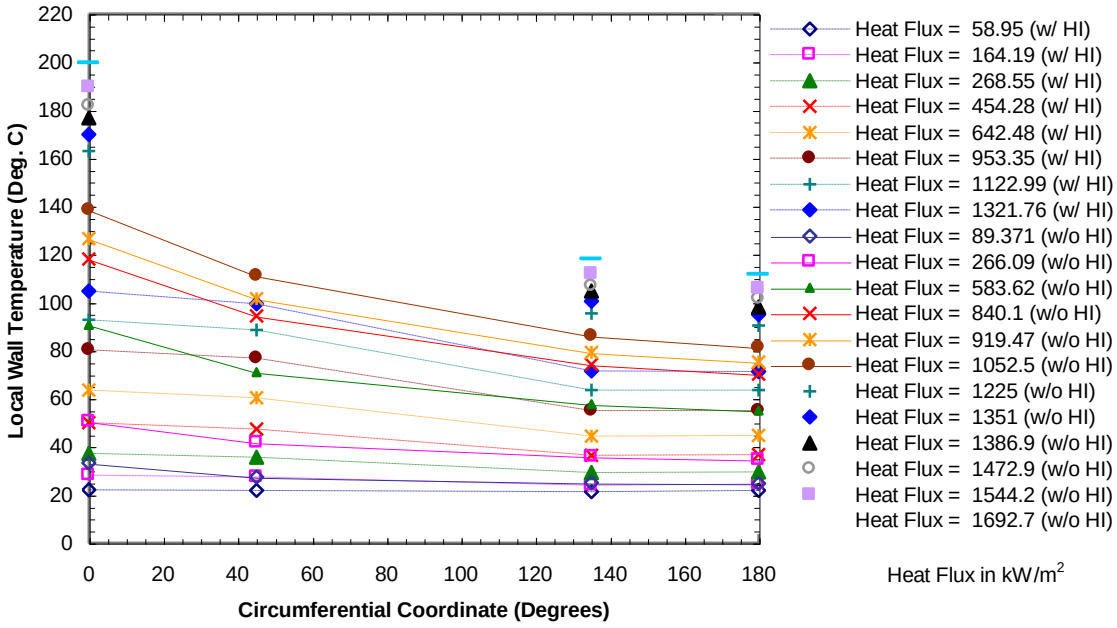

Figure 199: Monoblock w/ HI Comparison to Monoblock w/o HI for Circumferential Wall Temperature Profiles Close to the Fluid/Solid Boundary as a Function of the Average Net Incident Heat Flux, at Z = Z3 = 147.066 mm (G = 3.2 Mg/m^{2}s, P_{exit} = 0.572 MPa, and T_{sat} = 157 ^{o}C).

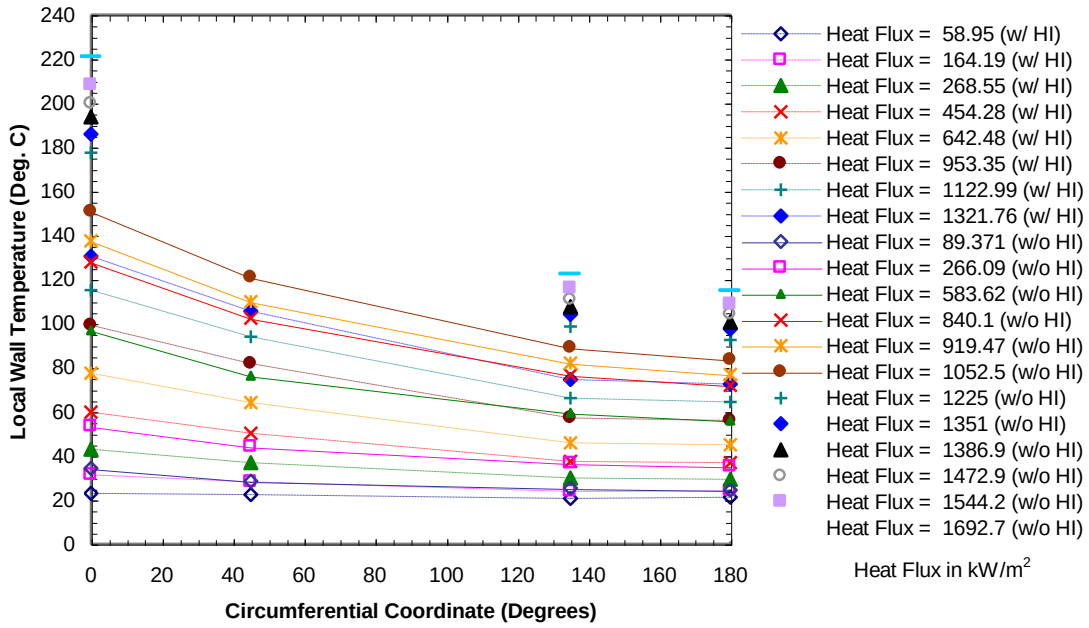

Figure 200: Monoblock w/ HI Comparison to Monoblock w/o HI for Intermediate Circumferential Wall Temperature Profiles as a Function of the Average Net Incident Heat Flux, at Z = Z3 = 147.066 mm (G = 3.2 Mg/m^{2}s, P_{exit} = 0.572 MPa, and T_{sat} = 157 ^{o}C).

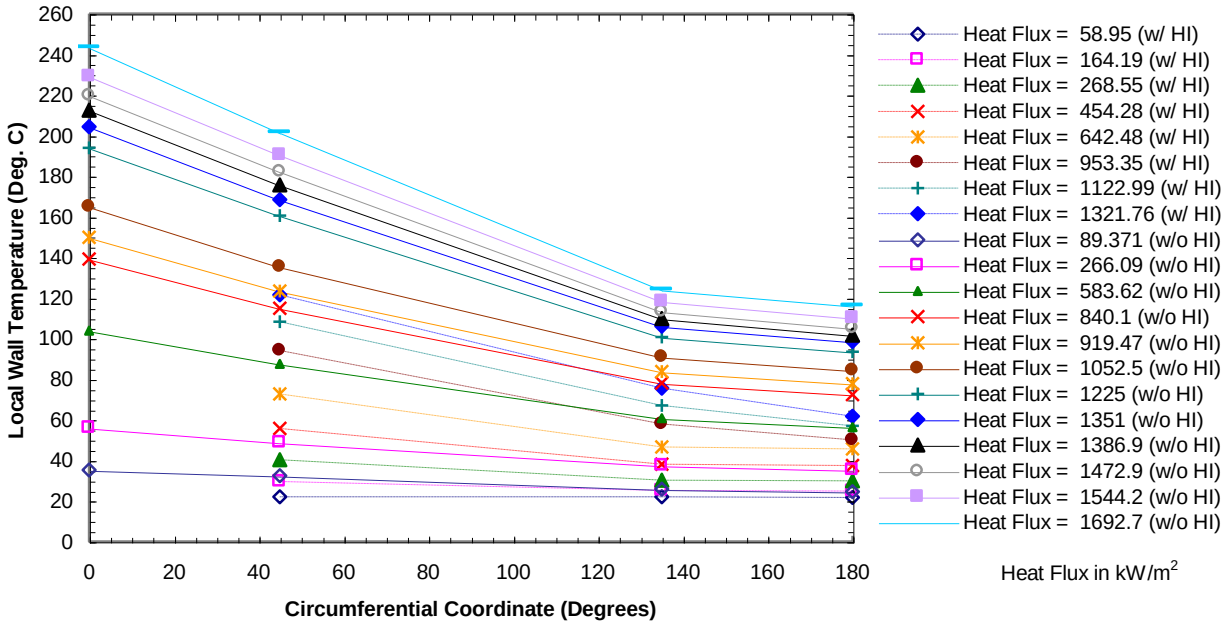

Figure 201: Monoblock w/ HI Comparison to Monoblock w/o HI for Circumferential Wall Temperature Profiles Close to the Outside Boundary as a Function of the Average Net Incident Heat Flux, at Z = Z3 = 147.066 mm (G = 3.2 Mg/m^{2}s, P_{exit} = 0.572 MPa, and T_{sat} = 157 ^{o}C).

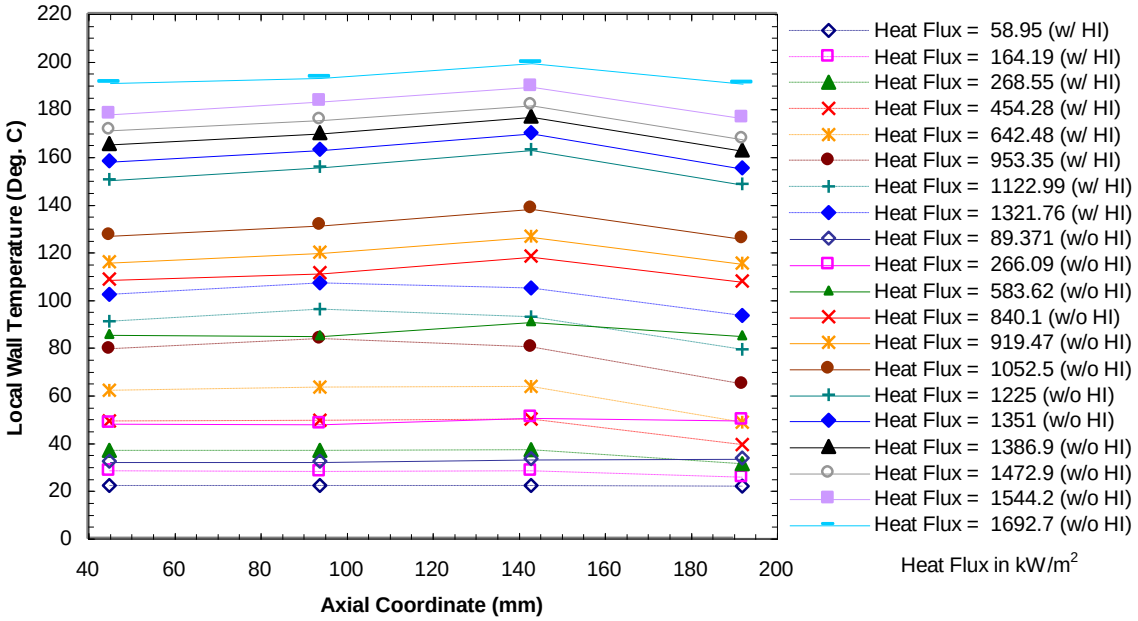

Figure 202: Monoblock w/ HI Comparison to Monoblock w/o HI for Axial Wall Temperatures at φ = 0 Degree, Close to Fluid Boundary as a Function of the Average Net Incident Heat Flux (G = 3.2 Mg/m^{2}s, P_{exit} = 0.572 MPa, and T_{sat} = 157 ^{o}C).

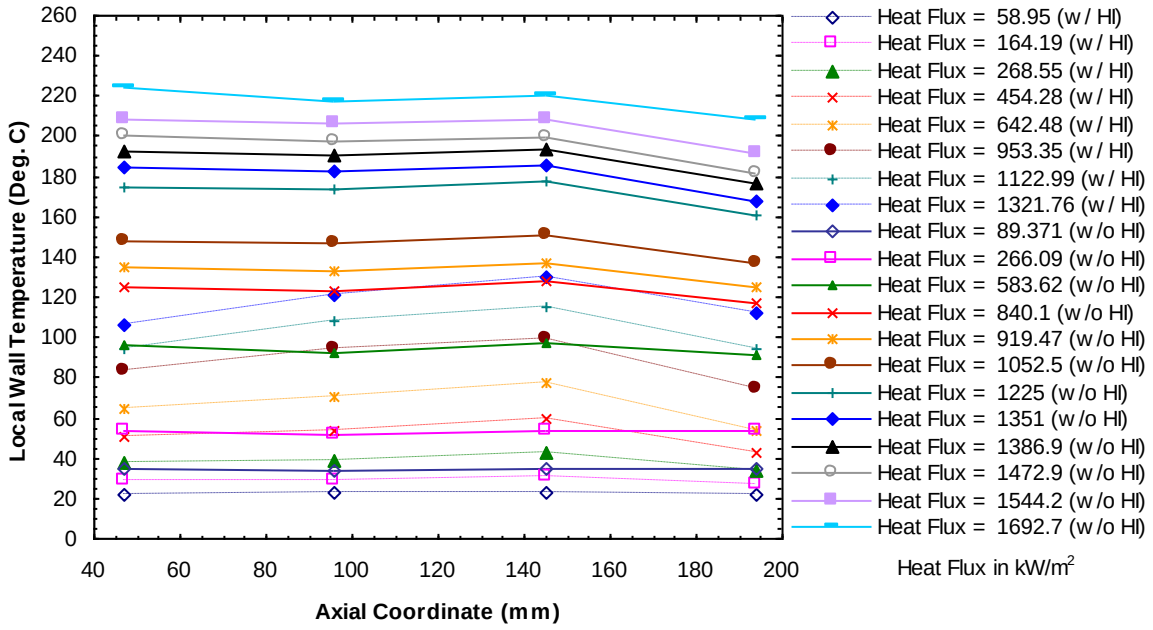

Figure 203: Monoblock w/ HI Comparison to Monoblock w/o HI for Axial Intermediate Wall Temperature Profiles at φ = 0 Degree as a Function of the Average Net Incident Heat Flux (G = 3.2 Mg/m^{2}s, P_{exit} = 0.572 MPa, and T_{sat} = 157 ^{o}C).

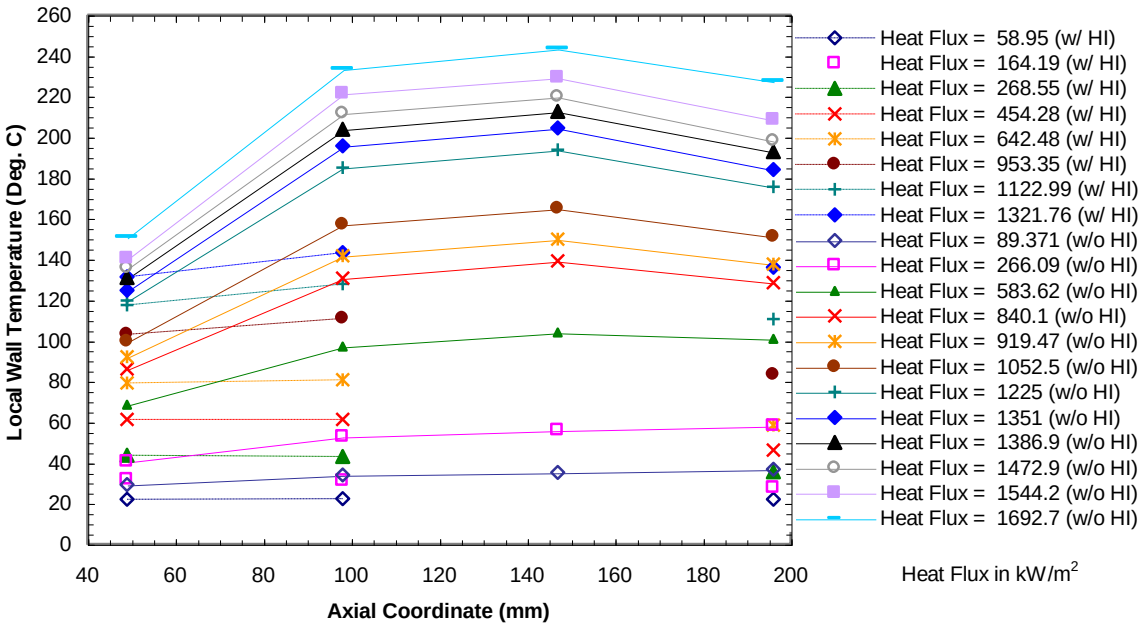

Figure 204: Monoblock w/ HI Comparison to Monoblock w/o HI for Axial Wall Temperature at φ = 0 Degree, Close to the Outside Boundary as a Function of the Average Net Incident Heat Flux (G = 3.2 Mg/m^{2}s, P_{exit} = 0.572 MPa, and T_{sat} = 157 ^{o}C).

location helical flow trends of Figure 195 appear to be inconsistent with this hypothesis, they are not. Before the INT (3rd data point from the left) temperature reading of this figure, this hypothesis is true. However, beyond this INT point, the slope of the HWI-data exceeds that w/o the HWI. The reason being: (1) at this small value of Z under any conditions, the TS wall temperature tends to be low and near the inlet fluid temperature; but (2) as the radius increases, the wall temperature increases more as the heated boundary is approached; and hence (3) the slope of the wall temperature profile increases. As Z increases, the effect of the heated boundary diminishes compared to the HWI. With this in mind, the radial trends at Z_1 become consistent with the radial trends for the remaining Z locations. The helical flow also resulted in steeper circumferential wall temperature gradients away from the plane of symmetry as shown in Figures 199 through 201.

All 3-D measurements (Figures 195 through 204) of $T_w(r, \phi, z)$ were used to produce the 2-D boiling curves for all cases. As expected, the helical flow TS inside wall heat fluxes at φ = 0 deg appear to be higher than their respective incident heat fluxes (Figures 205 through 208), in most cases. For ϕ = 0 degrees, examples of these curves are presented in Figures 205 through 208 for the four axial stations (Z_1, Z_2, Z_3, and Z_4). For $Z \leq Z_2$ (Figure 205), there is no enhancement with the HWI; and at Z_1, the monoblock without the HI performs better. However,

for values of Z near Z_3 and Z_4, Figures 207 and 208 *show significant enhancement--greater than a factor of four (4)*.

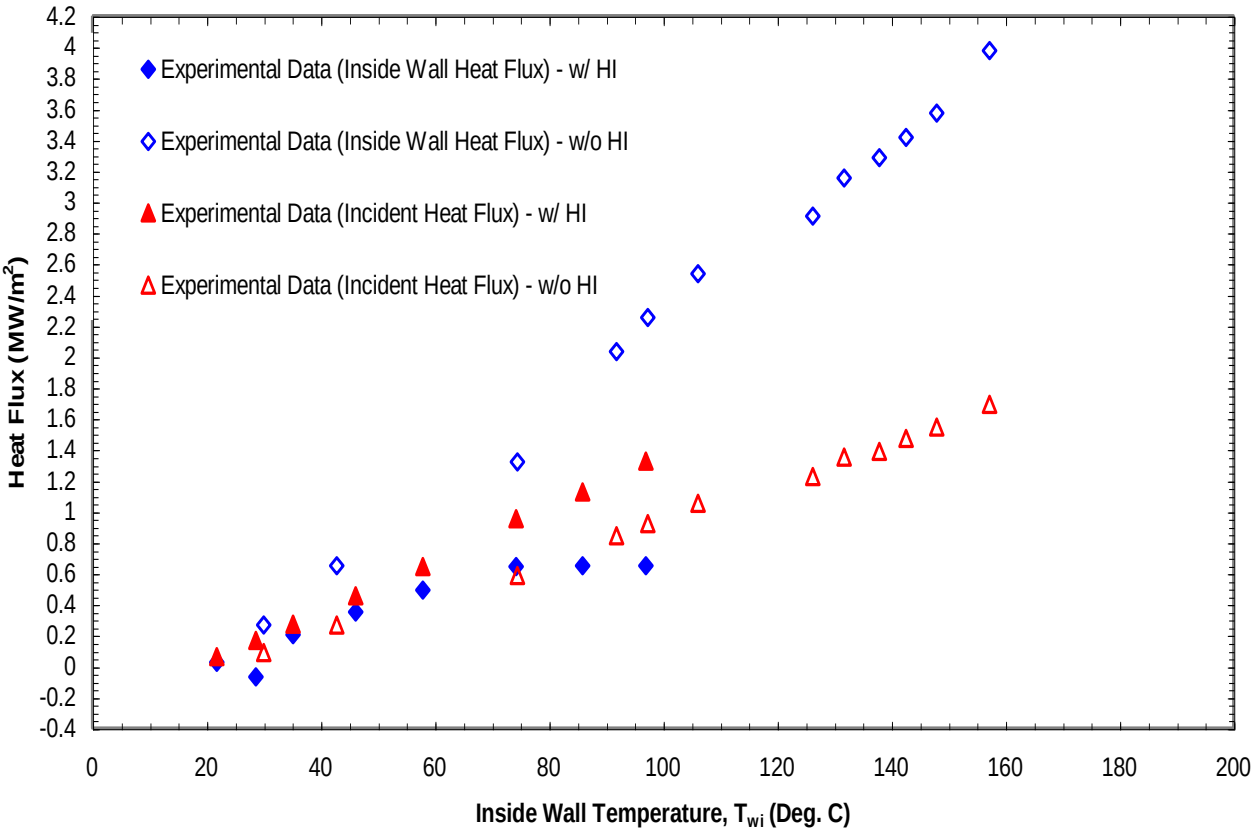

Figure 205: Monoblock w/ HWI Comparison to Monoblock w/o HWI for Inside (2-D Boiling Curve) and Net Average Incident Wall Heat Flux vs the Inside Wall Temperature at φ = 0 Degree and Z = Z1 = 49.022 mm (G = 3.2 Mg/m^2s, P_{exit} = 0.572 MPa, and T_{sat} = 157 ^oC).

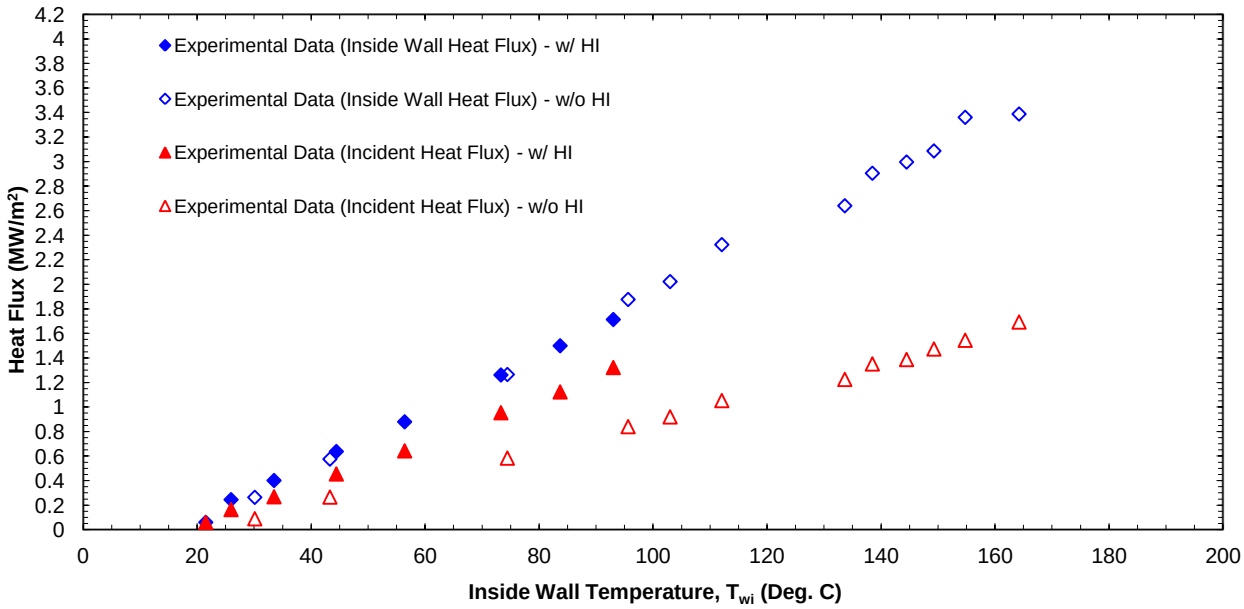

Figure 206: Monoblock w/ HWI Comparison to Monoblock w/o HWI for Inside (2-D Boiling Curve) and Net Average Incident Wall Heat Flux vs the Inside Wall Temperature at φ = 0 Degree and Z = Z2 = 98.044 mm (G = 3.2 Mg/m^{2}s, P_{exit} = 0.572 MPa, and T_{sat} = 157 ^{o}C).

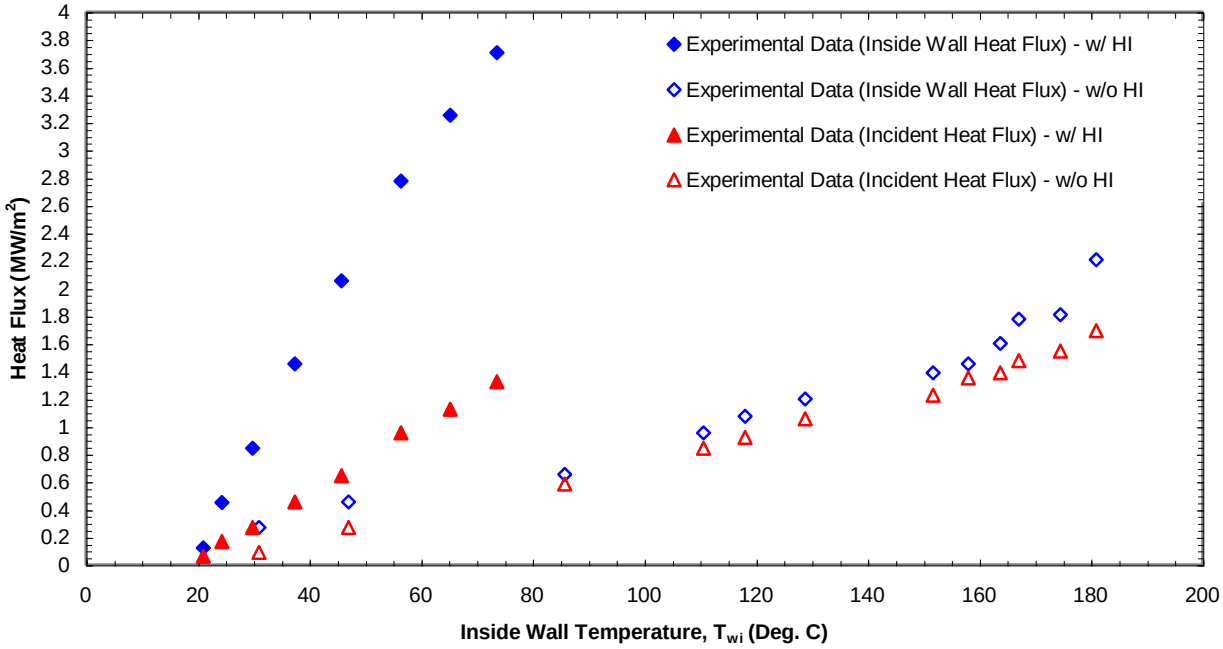

Figure 207: Monoblock w/ HWI Comparison to Monoblock w/o HWI for Inside (2-D Boiling Curve) and Net Average Incident Wall Heat Flux vs the Inside Wall Temperature at φ = 0 Degree and Z = Z3 = 147.066 mm (G = 0.59 Mg/m^{2}s, P_{exit} = 0.207 MPa, and T_{sat} = 121.3 ^{o}C)

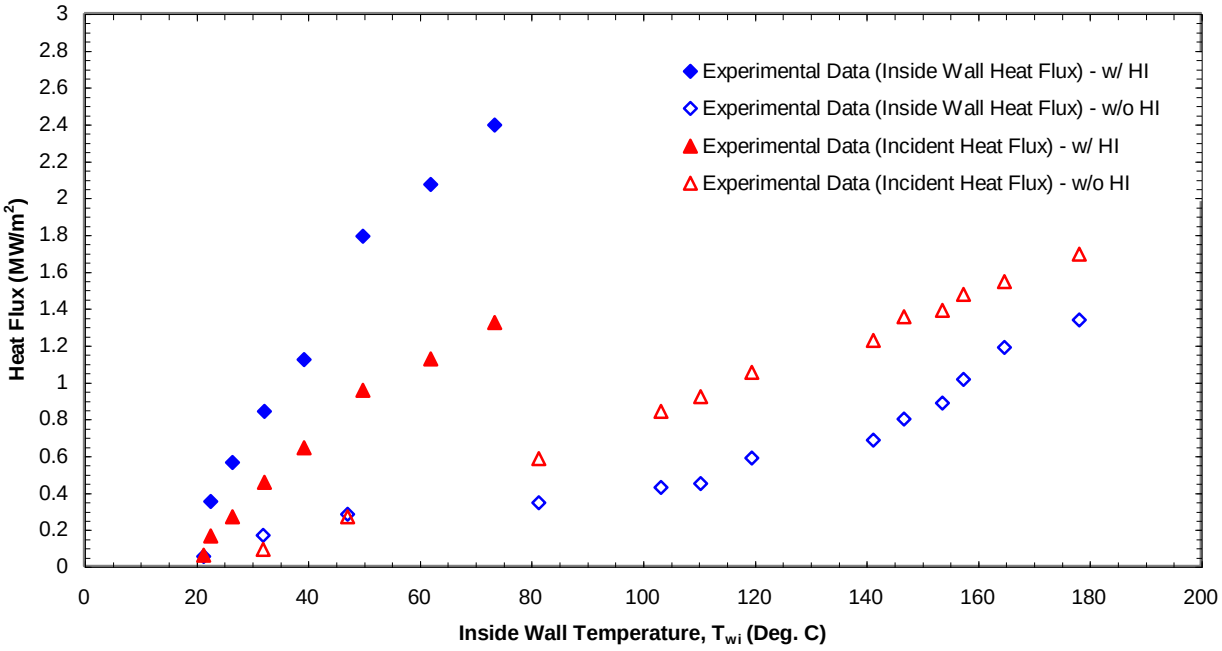

Figure 208: Monoblock w/ HWI Comparison to Monoblock w/o HWI for Inside (2-D Boiling Curve) and Net Average Incident Wall Heat Flux vs the Inside Wall Temperature Profiles at φ = 0 Degree and Z = Z4 = 196.088 mm (G = 0.59 Mg/m^{2}s, P_{exit} = 0.207 MPa, and T_{sat} = 121.3 ^{o}C).

20.0 CONJUGATE HEAT TRANSFER HIGH HEAT FLUX FLOW CHANNEL SIMULATION

20.1 BACKGROUND

High heat flux removal (HHFR) limits can be formidable technological barriers which prevent or limit the normal implementation or optimization of new and novel devices or processes. A conjugate heat transfer HHFR simulation methodology has been developed with excellent resulting accuracy (> 98.0% accurate) for predicting peak heat fluxes and peaking factors. The methodology can be used directly or expanded to a correlation form. Although the simulation utilized fully-developed turbulent subcooled flow boiling and single-phase water axial and swirl flows in a single-side heated circular inside flow channel, the methodology appears to be fluid-independent so that other fluids and flow regimes can be employed possibly for HHFR applications requiring specialized fluids and/or flow conditions. For the prototypic cases considered, the circumferential inside flow channel heat transfer coefficient distribution ($h(\varphi)$) was not known a prior; so, $h(\varphi)$ was determined from iterative finite element conjugate heat transfer analyses for flow regimes ranging from fully developed turbulent subcooled flow boiling (at the top of the flow channel) to single-phase turbulent (at the bottom of the flow channel).

20.2. INTRODUCTION

In an effort to develop new economical and ecological energy sources, an international team is preparing to build ITER which is projected to be operational in the year 2023. It will be the first plasma fusion reactor its size and will be operating at over 100 million degrees C, producing 500 MW of fusion power. Inside the reactor, a divertor has been designed to exhaust the flow of energy from charged particles produced by the fusion reactions and to remove helium ash and other impurities from the plasma. The divertor is categorized as a plasma-facing component (PFC) given that it will be "facing" the plasma and bombarded by high energy particles. The plasma will impose high heat flux (HHF) loads of up to 20 MW/m^2 on the divertor's vertical targets. Monoblock-type HHF coolant channels [e.g., see Figs. 209 through 211] will be integrated into the walls of the divertor to accommodate such high thermal and particle loadings. This application involves single-side heating (SSH) of the cooling channels.

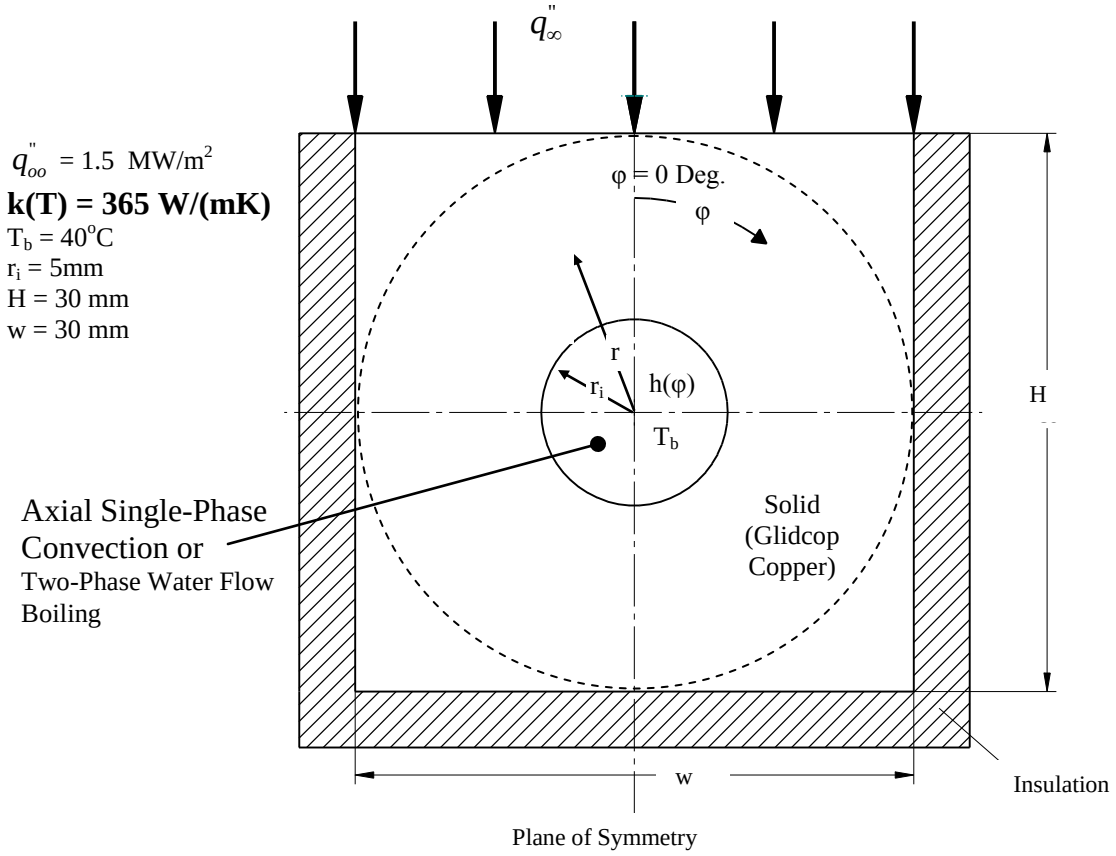

Figure 209: Idealized IHHFR Monoblock Flow Channel Used to Initially Explore a Peaking Factor Relationship. The Values of the Selected Parameters Only Serve to Make the Quantitative Comparisons to Verify the Finite Element Analysis (FEA) Accuracy Under Extreme Conditions.

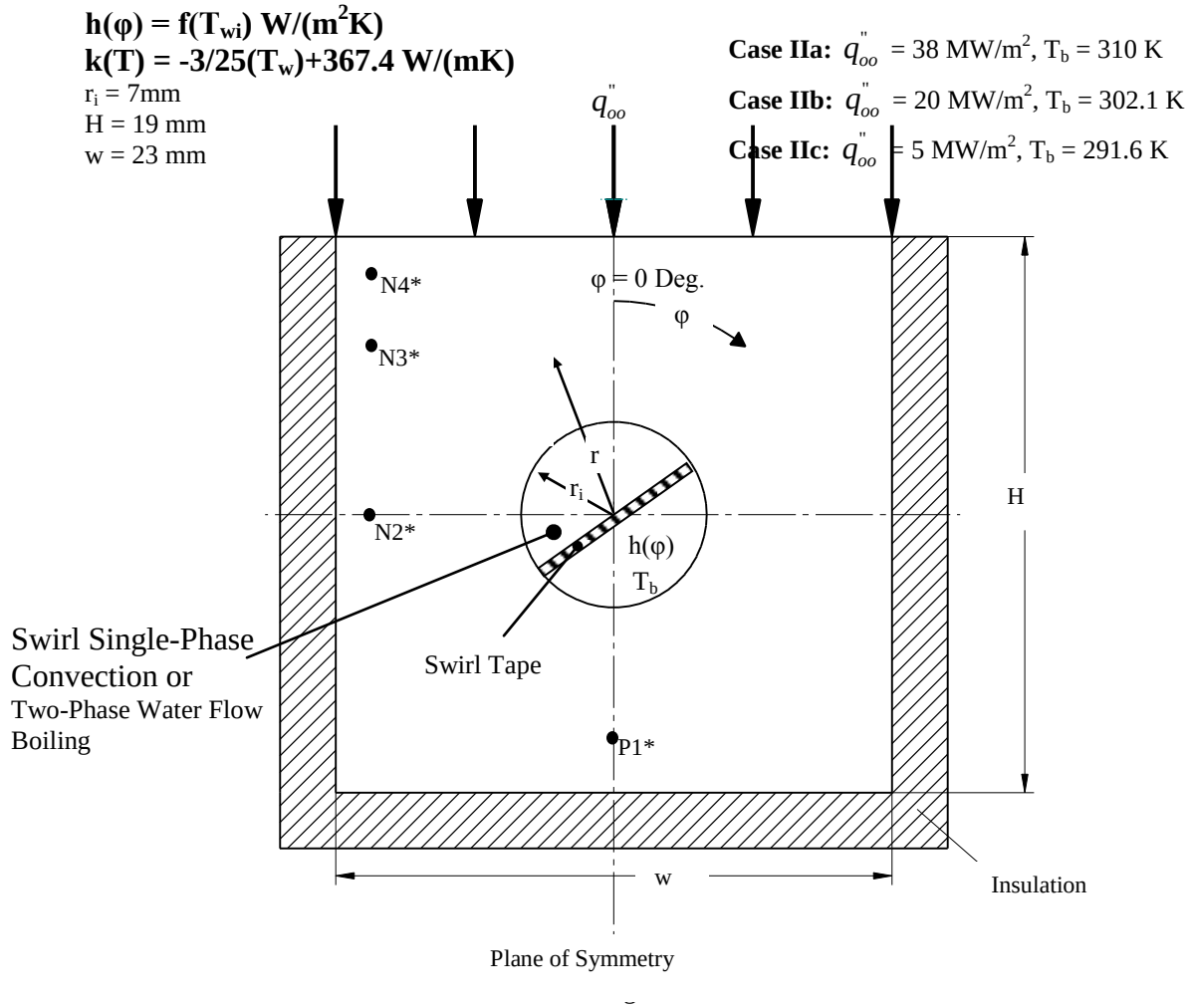

Figure 210: The Cadarache CEA Monoblock With a Twisted Tape and Subjected to a Single-Side Heat Flux at Prototypic Levels. Note that the Function, $f(Tw_i)$ is Not Known Apriori and was Determined From an Iterative Conjugate FEA Heat Transfer Analysis; e.g., See Fig. 215 for Typical Results. The Results Show Flow Regimes Varying From Single-Phase (near bottom) to Fully-Developed Nucleate Boiling.

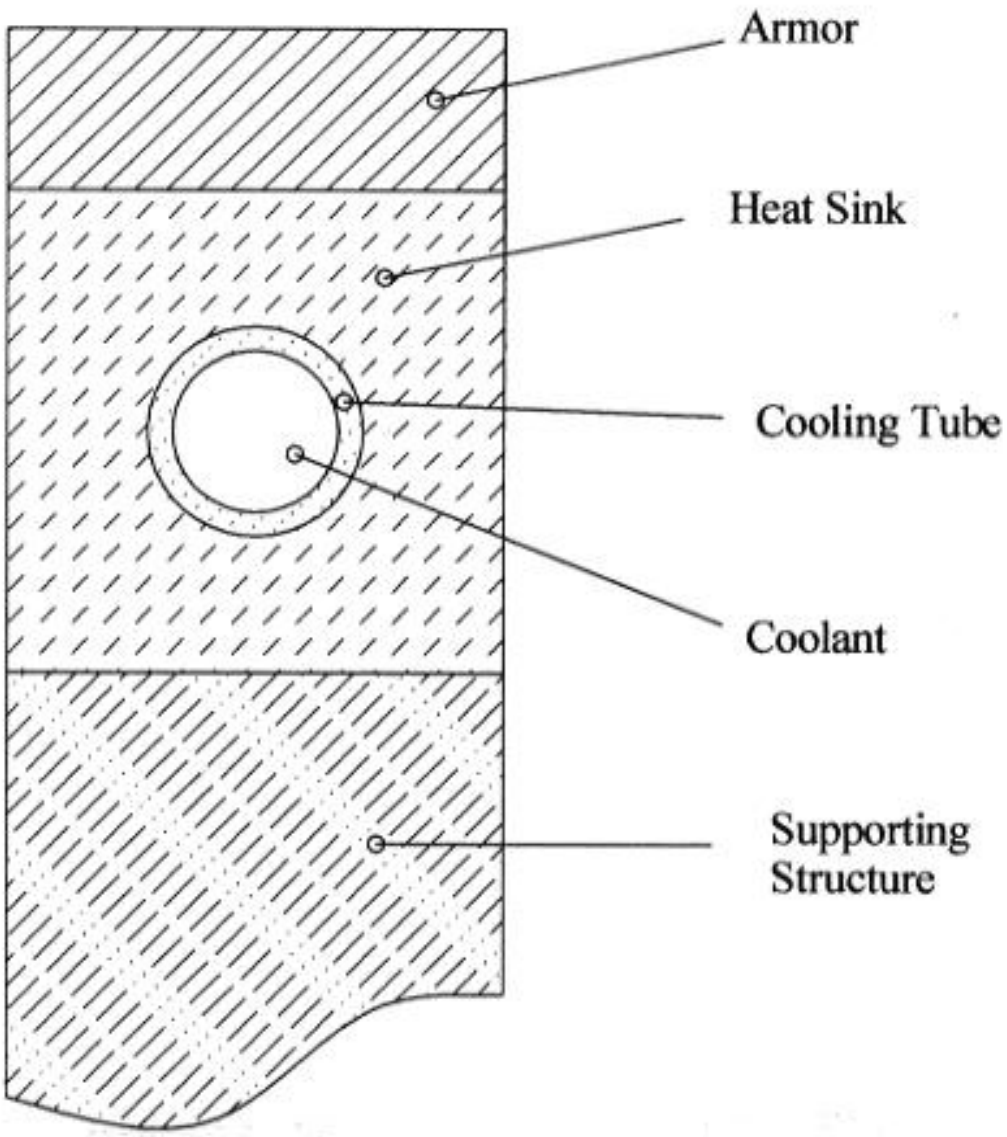

Figure 211: Typical Structure of a PFC ITER Monoblock.

Although this simulation utilizes examples from fusion reactor technology development, it may be applicable equally (e.g., other compatible fluids, and flow configurations may be needed) to many other high heat flux removal (HHFR) applications such as hypersonic vehicles, high power avionics, high-density electronic cooling and packaging, gas turbine and turbine blade cooling, aerospace vehicles, laser and optical power systems, etc. All these applications required robust, and optimized HHFR components (HHFRC). "The success of ITER [and these other HHFR technologies] depend not only on good physics, but [on] reliable operation of the PFCs [and HHFRCs]….[119, 120]." This statement emphasizes the importance of three factors of the PFC and HHFRC development, design, improvement and definition of workable acceptance criteria: reliability, robustness, and optimization. For example, ITER represents the next significant step in the development of fusion reactors. Among the numerous components in ITER, PFCs play a major role in both accommodating the plasma high heat flux, as well as insuring the effective performance of the reactor.

International attention on HHFR phenomena is increasing. With an inclusion of contact resistance effects, at incident heat fluxes (q''_{oo}) < 4.0 MW/m^2, Song et al. [121] presented finite element analyses (FEAs) for three PFC configurations for the Experimental Advanced Superconducting Tokamak. Salavy et al. [122] performed HHFR testing and thermal analyses on different composite mock-ups with swirl water flow; and they, among other parameters, computed the maximum temperatures for 5.0 MW/m $\leq q''_{oo} \leq$ 18.0 MW/m^2. An international (involving five international facilities) Round-Robin Test (see Rödig et al. [123]) and supporting FEA thermal analyses were conducted on a carbon fiber reinforced carbon (CFC) monoblock and was used to establish a criteria for assessment. D'Agata and Tivey [124], and later Fouquet et al. [125], described the ITER CFC monoblock and armour and divertor acceptance criteria (also see Bissio et al. [126]). Finally, Jahangeer et al. [127] performed benchmarking and grid sensitivity testing for a conjugate analysis of a vertical plate with internal energy generation. The present work extends this literature in that the HHF conjugate heat transfer simulation of the flow channel heat flux peaking factor and peak inside wall temperature are examined over a

similar prototypic range of q''_{oo} (between 1.5 and 33.0 MW/m^2); and the benchmarking is examined over a slightly broader range of q''_{oo} (1.5 to 38.0 MW/m^2).

As it relates to PFC HHFR with water, a substantial single-side heated flow channel data base exists to characterize the parametric variation of the critical heat flux (CHF) with selected flow and substrate parameters (e.g., [128-132]). This data base and other work (e.g., [133, 134]) have made it possible to consistently specify some coolant channel and flow characteristics which will allow the safe operation of the PFC below the CHF. Hence, an acceptable and tested PFC design has been adopted for initial deployment in ITER [128]. Since there will be opportunities for PFC upgrading after this initial deployment, one of the next steps is to develop a fundamental conjugate heat transfer simulation to support future efforts aimed at accurately optimizing the criteria for improvement and development for robust and reliable PFC (and HHFRC) operation. This will result when, among other factors, the local PFC internal flow channel temperature and heat flux distributions, peak inside temperature, and heat flux peaking factors can be predicted readily, reliably, and verified.

Since a complete engineering optimization analysis of a HHFRC could involved complex, coupled thermal-stress/strain-ablation-interfacial (etc.) effects, the existence of a HHFR monoblock thermal simulation correlation would reduce the complexity of the initial phase of the optimization improvement and coupled analyses by producing functional relations between the incident heat flux (q''_{oo}) and the flow channel inside peak wall temperature ($T_{wi)_{\max}}$), heat flux ($q''_{wi)_{\max}}$), conjugate flow conditions, and monoblock geometry. To the authors' knowledge, this capability does not exist presently in the technical literature; and, it could reduce the time required for this complex optimization analysis.

In the present context, the peaking factor (PF) is defined as the ratio of the peak inside heat flux of the flow channel to the peak incident heat flux. The simulation methodology is described and displayed in the form of comparisons; and, these comparisons show excellent simulation for the reliable prediction of high heat flux PF and the peak inside channel wall temperature. In many cases, it will be shown that qualitative simulation predictions result for both the inside heat flux and wall temperature distributions. The simulation involves using the geometry in Fig. 212, which is more amenable to analytical PF correlation development, to simulate the high heat flux geometries of Figs. 209 and 210 (and later that geometry in Fig. 211).

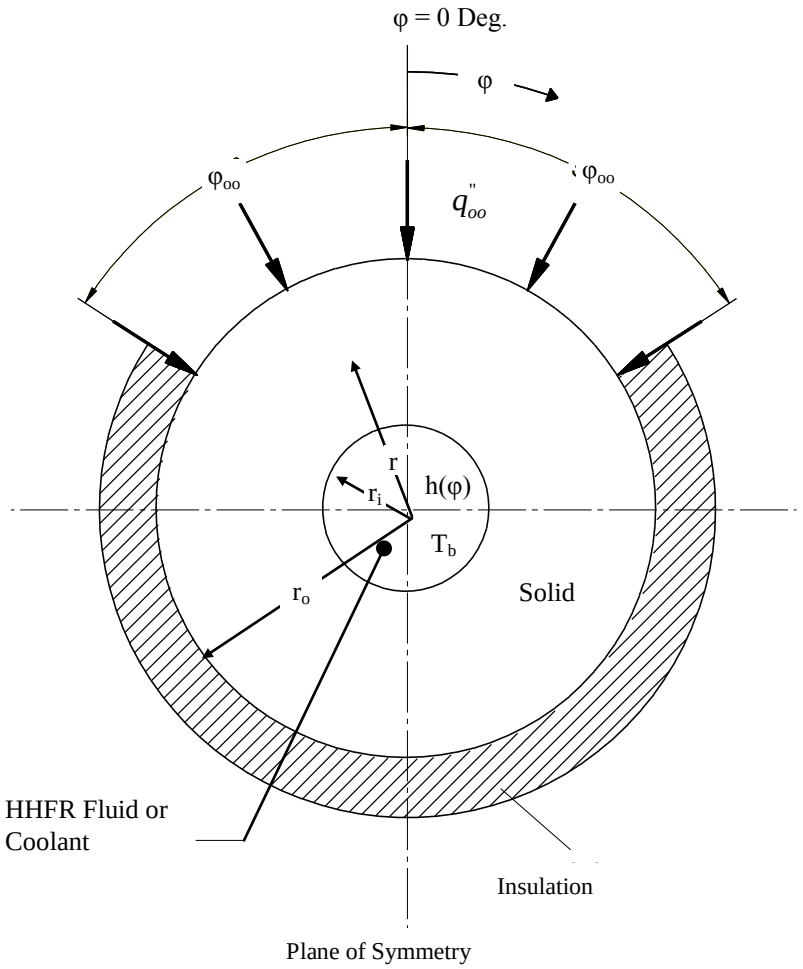

Figure 212: Partially-Heated Circular Flow Channel Used as a Basis for Comparison With IHHFR and CEA Monoblocks and Simulation Correlation Development [the simulation may be fluid-independent]. For the CEA Monoblock Simulation, h(ϕ) is Not Known Apriori and was Determined From an Iterative Conjugate FEA Heat Transfer Analysis; e.g., See Fig. 218 for Typical Results. The Results Show Flow Regimes Varying From Single-Phase (near bottom) to Fully-Developed Nucleate Boiling.

In order to examine the feasibility of two-dimensional (2-D) thermal finite-element analysis (FEA) for the comparative simulation procedure, the FEA was benched-marked for three different physical cases. Before the FEA benchmarking was performed, an indepth FEA grid refinement study was completed so that the following extreme HHFR conditions could be resolved: (1) peak heat flux, (2) large thermal gradients, and (3) large variations of flow regime, between single-phase and fully developed nucleate boiling. Flow channel axial variations were not considered; and hence, the fluid flow was assumed to be fully-developed turbulent (axial or swirl) single-phase and/or subcooled flow boiling with water for a given circumferential (ϕ) location.

20.3 GRID REFINEMENT AND BENCHMARKING

Before either simulation case was considered, the conjugate heat transfer FEAs of the flow channels were bench-marked by making comparisons using the: (1) SSH circular geometry in Fig. 212 for idealization involving three values of R_o (= r_o/r_i; 1.04, 1.34, and 3.0), ϕ_{oo} = 90.0 degrees [135], and for two values of Bi differing by three orders of magnitude (from 0.5 to 10^3) which corresponds to flow channel wall variations (high or low k or low or high h_m) or heat flux gradient levels ranging from low to very high; (2) French Commissariat á l Énergic Atomique (CEA) Cadarache monoblock geometry in Fig. 210 [136] for low to high incident heat flux levels between 5.0 and 33.0 MW/m^2, and at four different cross-section locations (P_1, N_2, N_3, and N_4 in Fig. 210); and (3) CEA monoblock shown in Fig. 210 but with a change in geometry (i.e., H = w = 19 mm) and at a high heat flux of 38.0 MW/m^2. The first case is strictly an idealization (hypothetical) and is used to examine the FEA accuracy under extreme effects of very high and low local thermal gradients, k, and h_m. The latter two cases are prototypic and have axial swirl fully-developed turbulent single-phase and subcooled flow boiling water flow. For all cases presented below, the conjugate heat transfer FEA predictions are referred to as TSRC-FEA or TSRC and the bench-marks are referred to as either "Exact" (Solution), Schlosser et al. FEA, Schlosser et al. – Measured, or Schlosser et al.

For this idealized or hypothetical SSH circular geometry case, comparisons were made with the exact solution [135] (see Fig. 213); and for the prototypic monoblock case, comparisons were made with CEA experimentally measured data and FEA results [136] (see Figs. 214 and

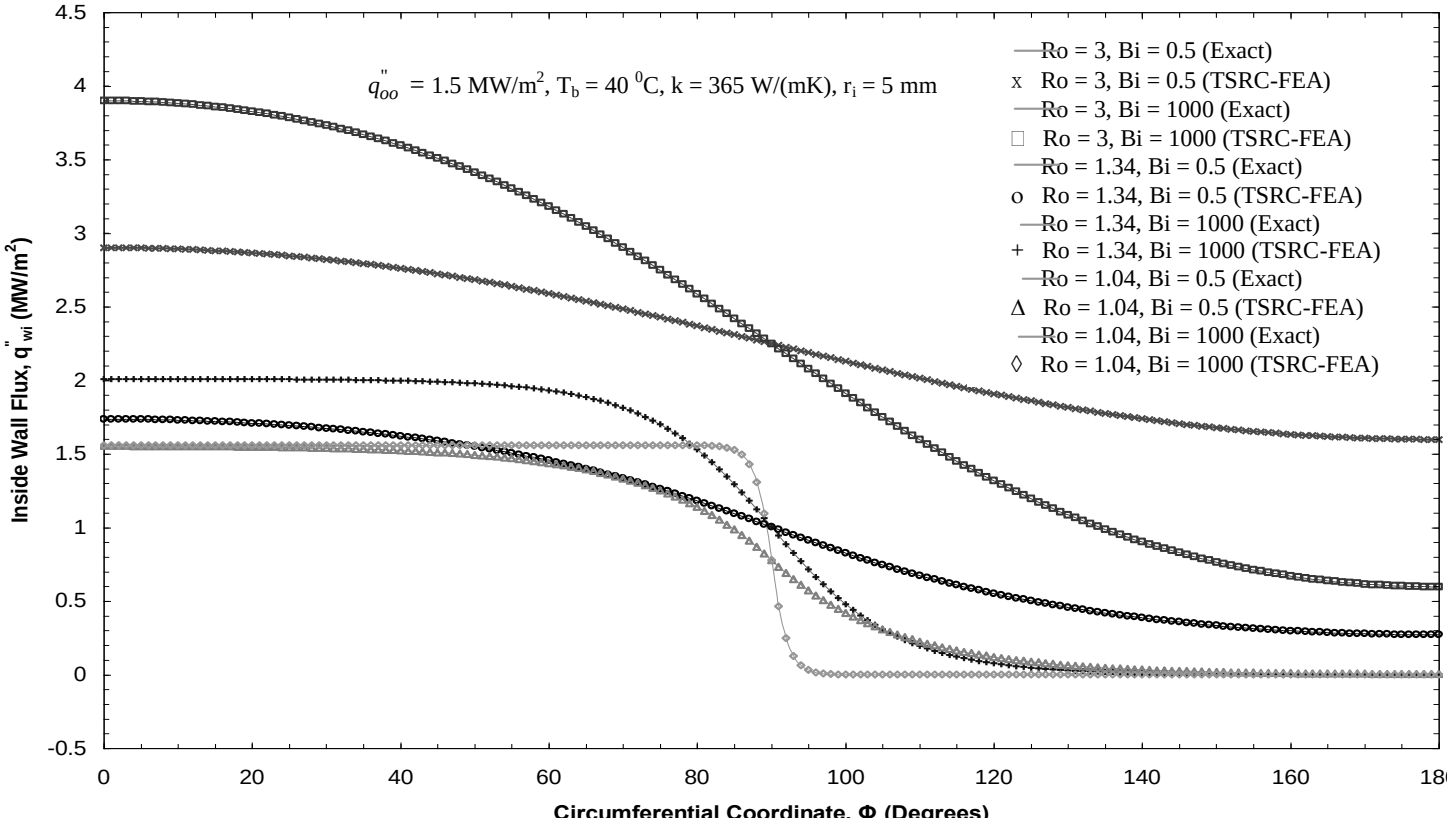

Figure 213: Bench-Marking Comparisons of FEA and the Exact Solutions for the Circumferential Distribution of the Inside Wall Radial Heat Flux for a SSH Circular Flow Channel (ϕ_{oo} = 90 degrees).

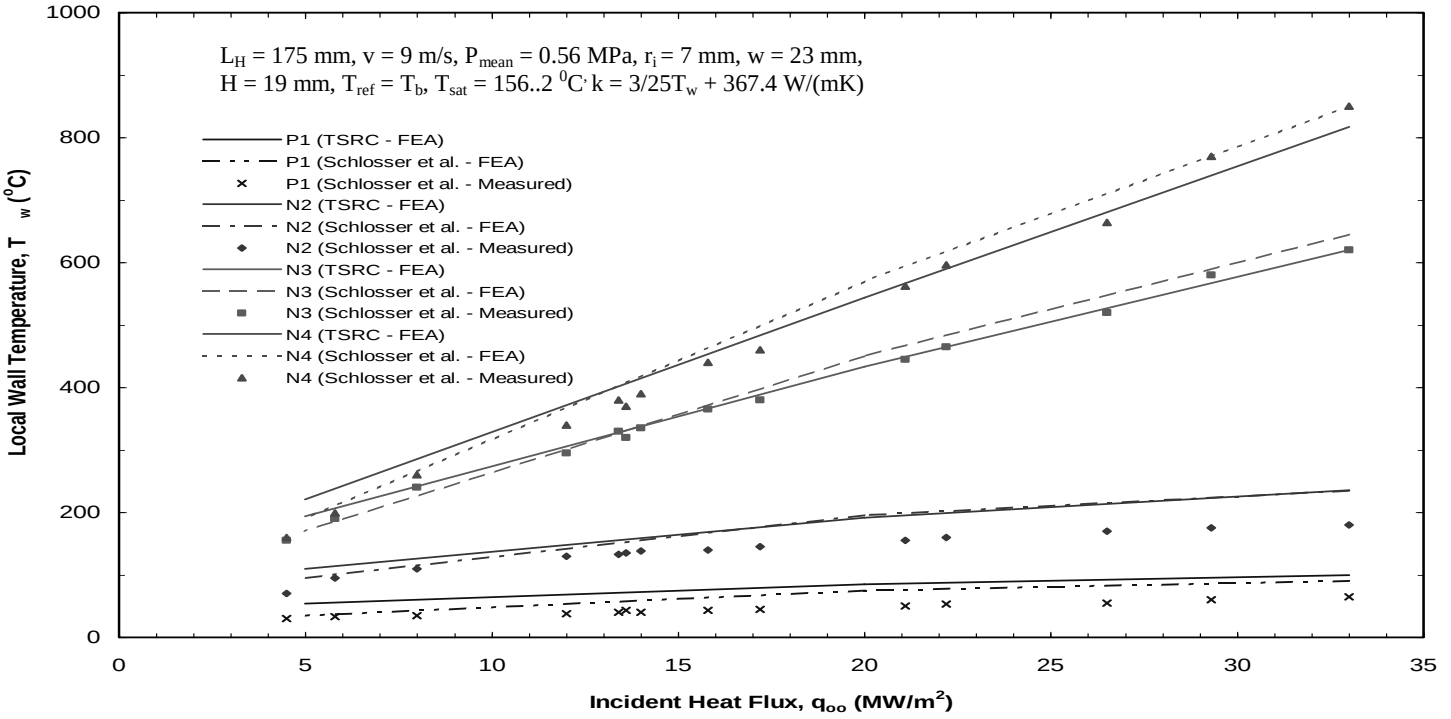

Figure 214: TSRC FEA Bench-Marking Predictions of Local Wall Temperature vs Incident Heat Flux Solutions Which Are Compared With Schlosser's et al. CEA FEA and Data.

215). The hypothetical case is an idealization in which the flow channel properties and the inside heat transfer coefficient (= 20 kWm^2) were assumed constant. These conditions will allow a critical assessment of the FEA results using an exact solution for the above noted extreme conditions. However, the prototypic cases contain all the physical complexity of the prototype conditions which includes: (1) all thermo-physical properties were temperature-dependent and, (2) the local heat transfer coefficient circumferential variation (h(ϕ) ranging from turbulent single-phase to flow boiling) was **not known or specified a priori** but was determined in an iterative conjugate heat transfer analysis. In all cases, the bench-marking agreement was good to excellent. Hence, good confidence could be placed in the high heat flux PF FEA simulation comparisons which will be presented next. Although the comparisons were good in all cases, the larger deviations for the prototypic CEA monoblock case were possibly due to the assumed [137] thermal conductivity temperature-dependence (k(T)). An assumption was necessary because no documentation for k(T) was given in reference [136].

20.4 SIMULATION COMPARISONS

As the first part of the simulation verification process, FEA computations were used to evaluate the new simulation methodology for predicting monoblock flow channel peaking factors and inside wall thermal profiles around: (1) Case I - an Institute for High Heat Flux Removal (IHHFR) monoblock [137] (with axial water flow; see Fig. 209), and (2) Case II - a CEA Cadarache monoblock [136] (with swirl water flow; see Fig. 210).

20.4.1. Case I: IHHFR Monoblock Hypothetical Simulation

Case I involved using the single-side partially heated circular geometry (see Fig. 212) to simulate the inside flow channel radial heat flux and temperature of the IHHFR monoblock in Fig. 209. This case has the least complexity and the second case (Case II) has many of the complexities found in the prototypic application. As such, this first case was exploratory and utilized constant fluid/solid properties and boundary conditions. These restrictions were relaxed in Case II. In order to obtain an initial indication of the viability of obtaining a peaking-factor simulation (and later a correlation), quantitative comparisons were made between two geometries (in Figs. 209 and 212 for Case I and Figs. 210 and 212 for Case II) which are subjected to a single-side incident high heat flux (q''_{oo}). A favorable comparison would mean that the simulation is successful and a correlation model is possible for this case.

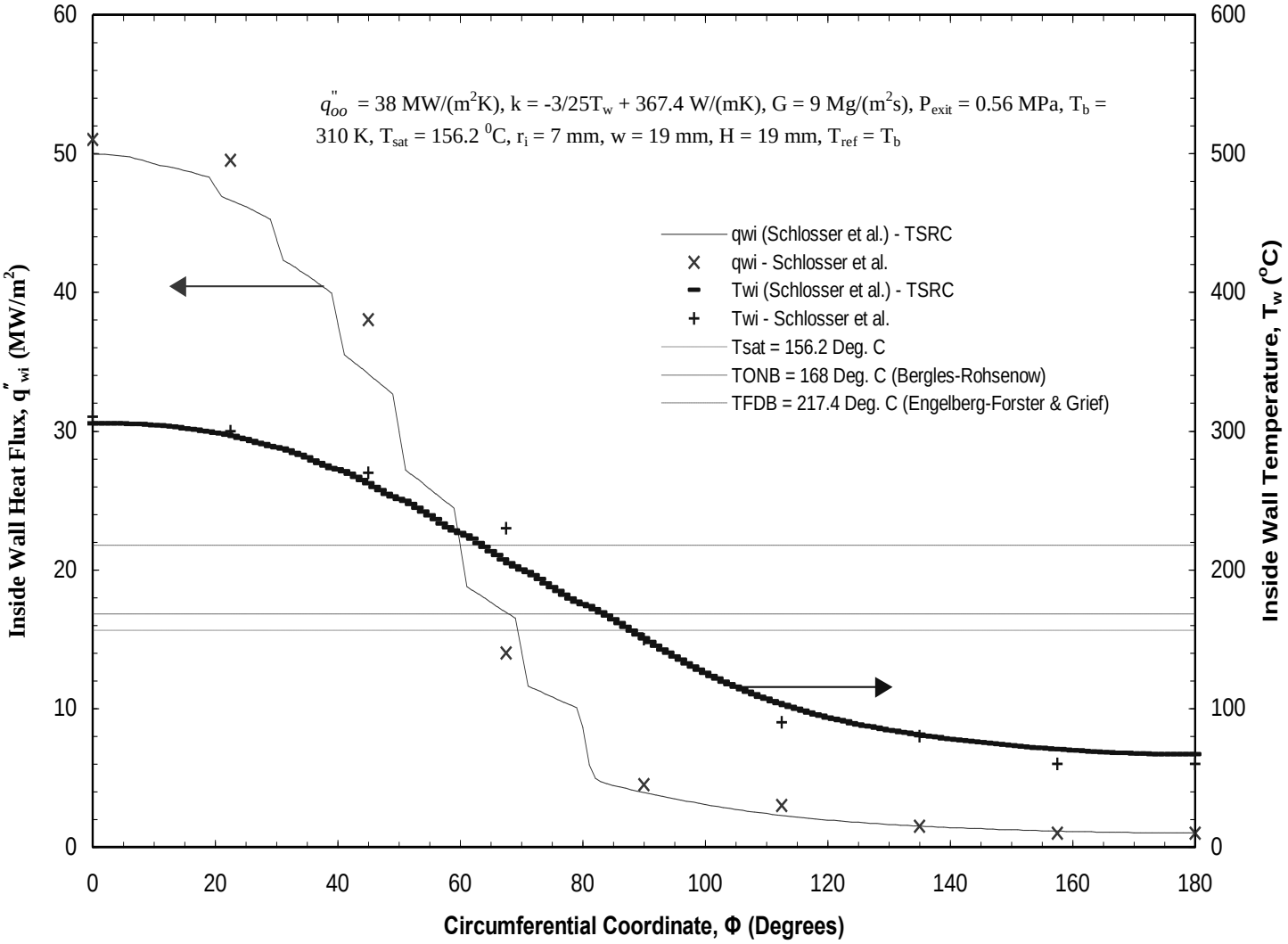

Figure 215: Comparison of Schlosser et al. FEA with TSRC FEA Solutions for CEA Monoblock (see Fig. 221 but with H = w = 19 mm) Inside Wall Temperature and the Radial Heat Flux.

The first geometry simulated was the idealized IHHFR monoblock shown in Fig. 209. The simulating geometry is shown in Fig. 212 and is a partially-heated circular flow channel used as a basis for the model formulation and quantitative PF comparisons with results for the two geometries in Figs. 209 and 210. Using a similarity criteria of equal thermal hydraulic diameters, the partial heated half-angle, ϕ_∞, in Fig. 212 was computed to be 57.3 degrees for the conditions shown in Fig. 209. The comparisons simply require that for the same incident heat flux and inside flow channel diameters, the heated perimeters for both geometries be identical.

The simulation FEA flow channel wall heat flux and temperature comparative results for Case I are presented in Figs. 216 and 217 and show comparisons of the local flow channel wall radial heat flux for both configurations in Figs. 209 ("monoblock") and 212 ("circular" simulation geometry) at various radii. Here, the PF is defined as the ratio of the peak inside (occurs at $\phi = 0$ and $r = r_i = 5$ mm for this case) heat flux to the peak incident heat flux, q''_∞. As the comparison shows, the inside heat flux at $\phi = 0$ for the two different geometries compare very well at $r = r_i$. The radial heat flux results at this location are 1.837 MW/m^2 and 1.803 MW/m^2 for the single-side and partially-heated circular (Fig. 212) and IHHFR monoblock (Fig. 209) cases, respectively. The corresponding peaking factors are 1.225 and 1.202, respectively. As can be seen in Fig. 217, the radial heat flux and channel wall temperature at the inside boundary ($r = r_i$) for both cases agree very well for all circumferential locations--an added bonus! The simulation (in Fig. 212) over-predicts the actual IHHFR monoblock inside wall heat flux by 1.9% at $\phi = 0$ degrees and under-predicts it by 2.4% at 180 degrees. Similar trends (see Fig. 217) resulted in the simulated inside wall temperature (0.4% over-predicted at $\phi = 0$ degrees, and 0.3% under-predicted [--each based on a relative temperature scale shown in the figure] at $\phi =$ 180 degrees)--an excellent simulation for $q_{wi)_{max}}$ and $T_{wi)_{max}}$. Finally, the simulation predictions of $q_{wi}(\phi)$ and $T_{wi}(\phi)$ were generally quantitative; however for $r > r_i$, $q_w(r, \phi)$ and $Tw(r, \phi)$ were qualitative.

20.4.2 Case II: CEA Monoblock Prototypic Simulation

Under prototypic conditions, the Case II simulation was evaluated at an incident heat flux level of 20.0 MW/m^2 (Case IIb in Fig. 210). Using a similar criterion as was used in Case I, the simulation half-angle in Fig. 212 is 69.4 degrees. As noted earlier, $h(\phi)$ was characterized using

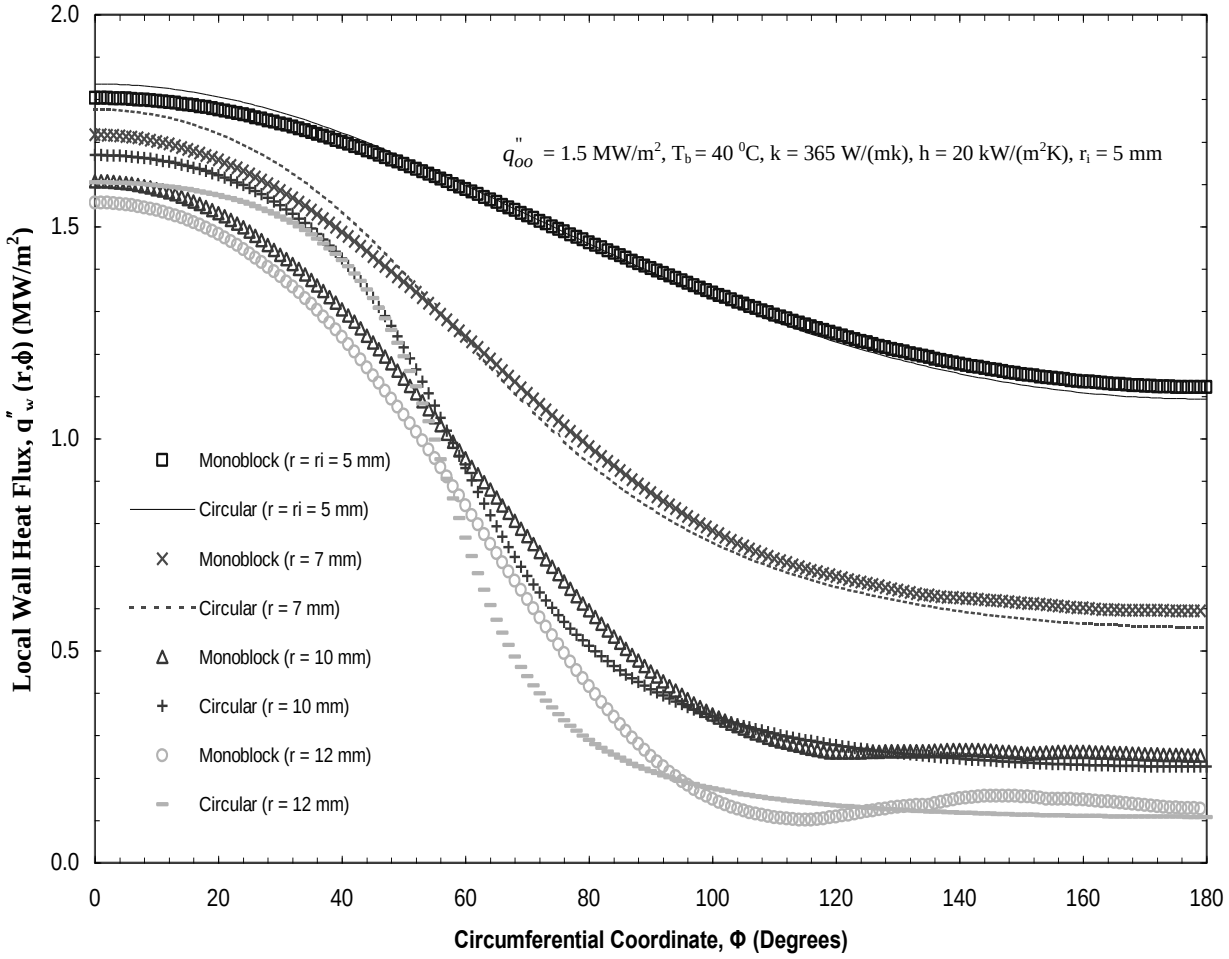

Figure 216: FEA Simulation Comparisons of the Flow Channel Wall Local Radial Heat Flux for the IHHFR Monoblock (Fig. 209) and the Partially Heated Circular Flow Channel (simulation geometry, Fig. 212). Quantitative Simulation PF Comparisons Should Be Made Only at r = r_1 = 5.0 mm and ϕ = 0 degrees (ϕ_{oo} = 57.3 degrees).

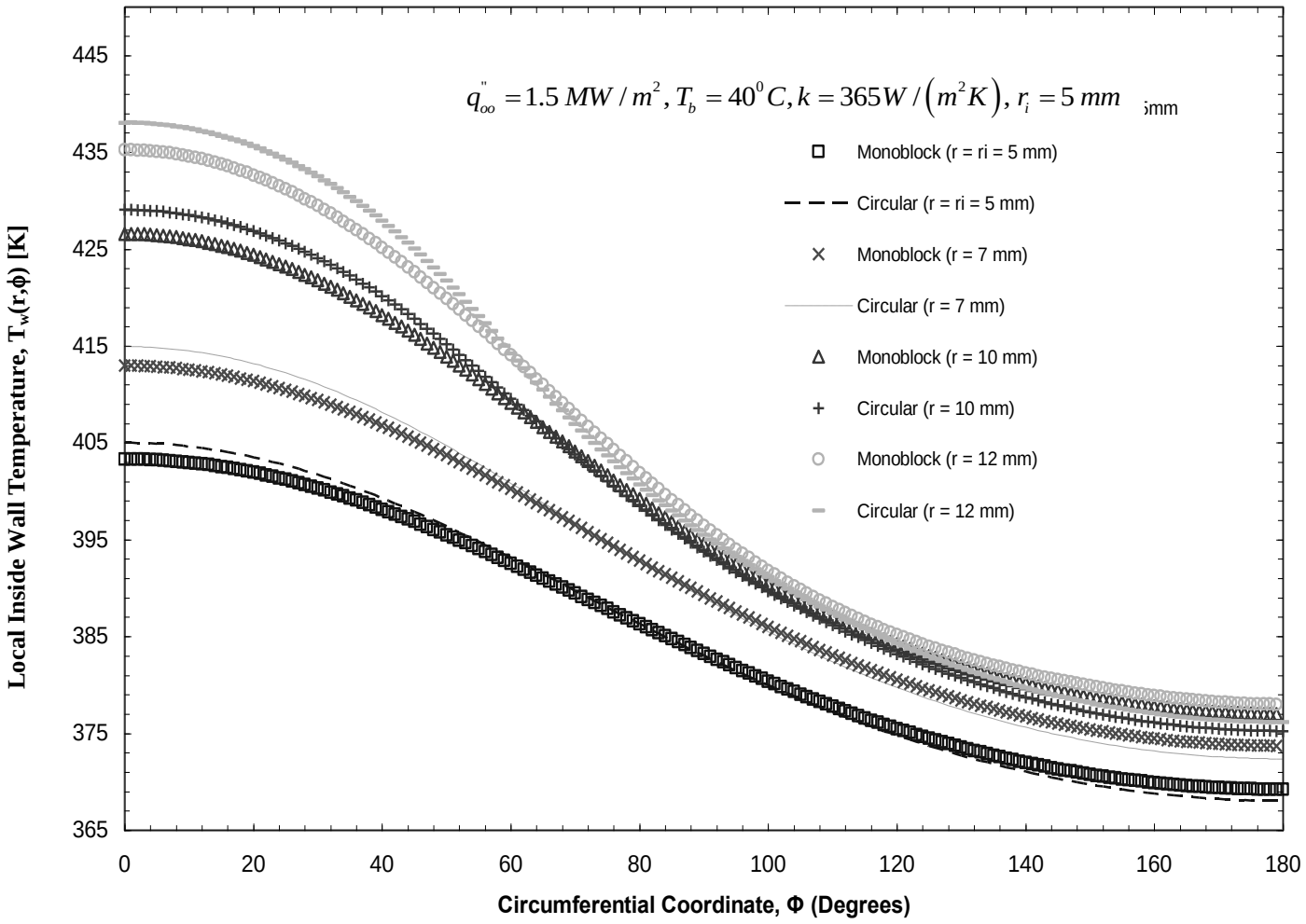

Figure 217: Flow Channel Local Circumferential Wall Temperature Simulation Comparison for the IHHFR Monoblock (Fig. 209) and Paritally Heated Circular (simulating geometry Fig. 212) Cases. Quantitative Simulation PF Comparisons Should Be Made Only at r = r_1 = 5.0 mm and ϕ = 0 degrees (ϕ_{oo} = 57.3 degrees).

the correlation supplied by Schlosser et al. [136]; and, k(T) was characterized by the relation developed by Boyd and Zhang [137]. This HHFR case involves turbulent swirl water flow with circumferentially varying flow: from subcooled flow boiling at $\phi = 0.0$ degrees to single-phase at $\phi = 180.0$ degrees.

The simulation results (referred to as "circular") for Case II are presented in Figs. 218 and 219. In both figures, the case being simulated is referred to as "monoblock." Noting that the simulation was intended to strictly apply to $r = r_i$ and $\phi = 0.0$ degree, the simulation is excellent. Specifically at this location, the radial heat flux and wall temperature for the actual and "circular" geometries were 26.44 MW/m^2 & 263.8 ^{0}C and 26.46 MW/m^2 & 263.76 ^{0}C, respectively. This corresponds to a 0.08% and 0.02% (on relative scale) difference for the $q_{wi)_{\max}}$ and $T_{wi)_{\max}}$ simulation predictions. The corresponding PFs for the actual and simulated geometries were 1.322 and 1.323--again, an excellent simulation! Therefore, both Cases I and II indicate that additional future work should be devoted to developing the flow channel wall PF and temperature correlations for quantitative characterization at $r = r_i$ and $\phi = 0$ degrees. The resulting correlation would be useful in future optimization studies to improve the robustness of HHFR from PFCs, HHFRCs, and other high-technology devices (e.g., thermal management devices for aviation and electronic cooling applications).

Further inspection of Figs. 218 and 219 indicates that the simulation gives good qualitative results for: (1) $r = r_i$ and at all other circumferential locations, and (2) $\phi = 0$ degree and most radii. These qualitative results for $\phi > 0$ degrees and $r > r_i$ are not surprising because the methodology was developed to emphasize accurate determination of PF under complex HHFR thermal and flow conditions at $r = r_i$ and $\phi = 0$. Finally, HHFR flow-regime indications are shown in Fig. 219 ($r = r_i$) to display circumferential ϕ-intervals corresponding to single-phase ($T_w < T_{ONB}$), partial nucleate boiling ($T_{FDB} > T_w > T_{ONB}$) and fully-developed nucleate boiling ($T_w > T_{FDB}$) flow variations in the circumferential direction.

20.5 DISCUSSION

With the success of this monoblock HHFR simulation, the methodology can be used for future development of the simulation correlations for quantitative PF and $T_{wi)_{\max}}$ predictions and qualitative (the inaccuracy appears to be reduced for higher levels of q_{oo}) $q_{wi}(\phi)$ and $T_{wi}(\phi)$ predictions. The utility of the simulation can be expanded if any or all of the following are added

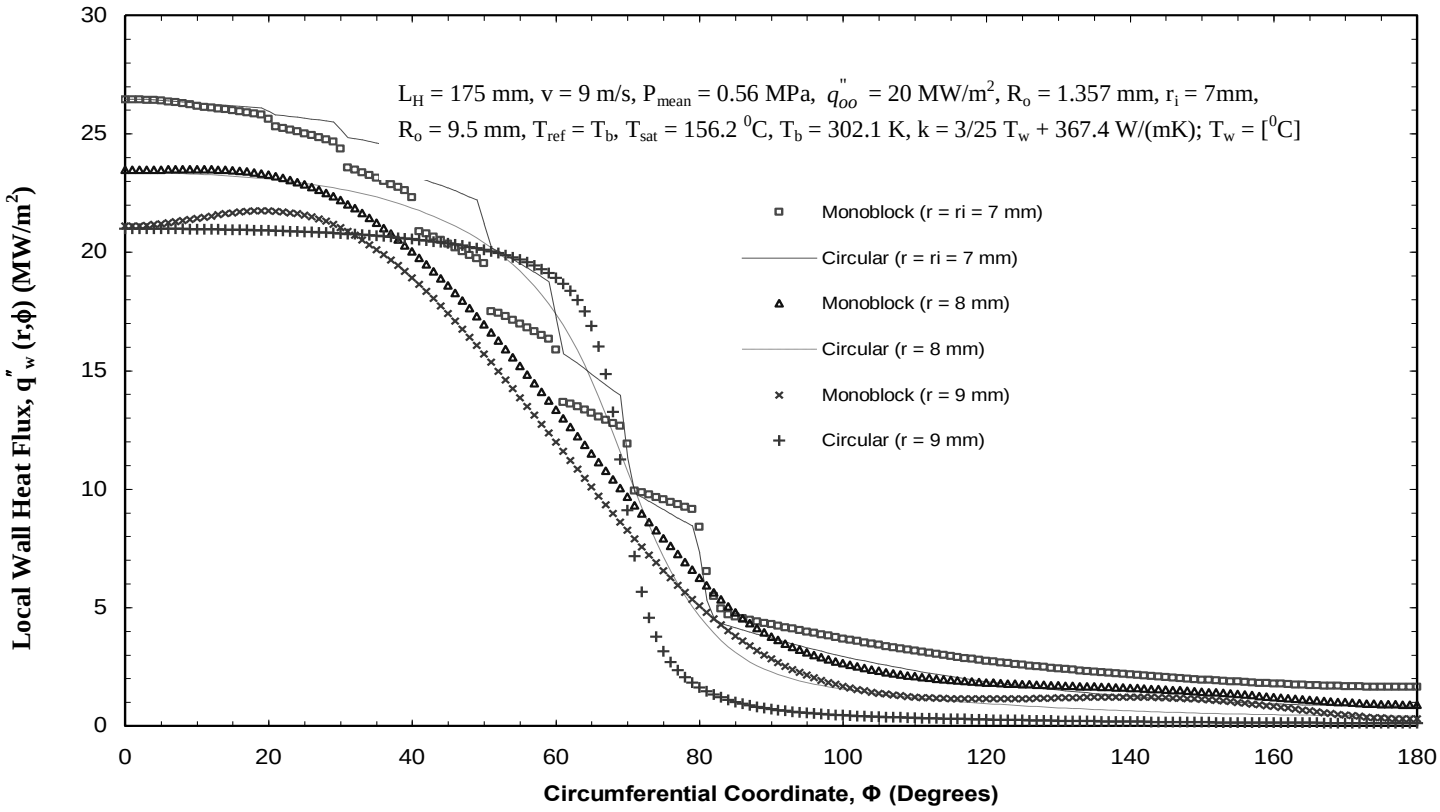

Figure 218: FEA Simulation Comparisons of the Flow Channel Wall Local Radial Heat Flux for the CEA Monoblock (Fig. 210) and the Partially Heated Circular Flow Channel (simulation geometry, Fig. 212); Quantitative Simulation PF Comparisons Should Be Made Only at r = r_i = 7.0 mm and ϕ = 0 degrees (ϕ_{oo} = 69.4 degrees).

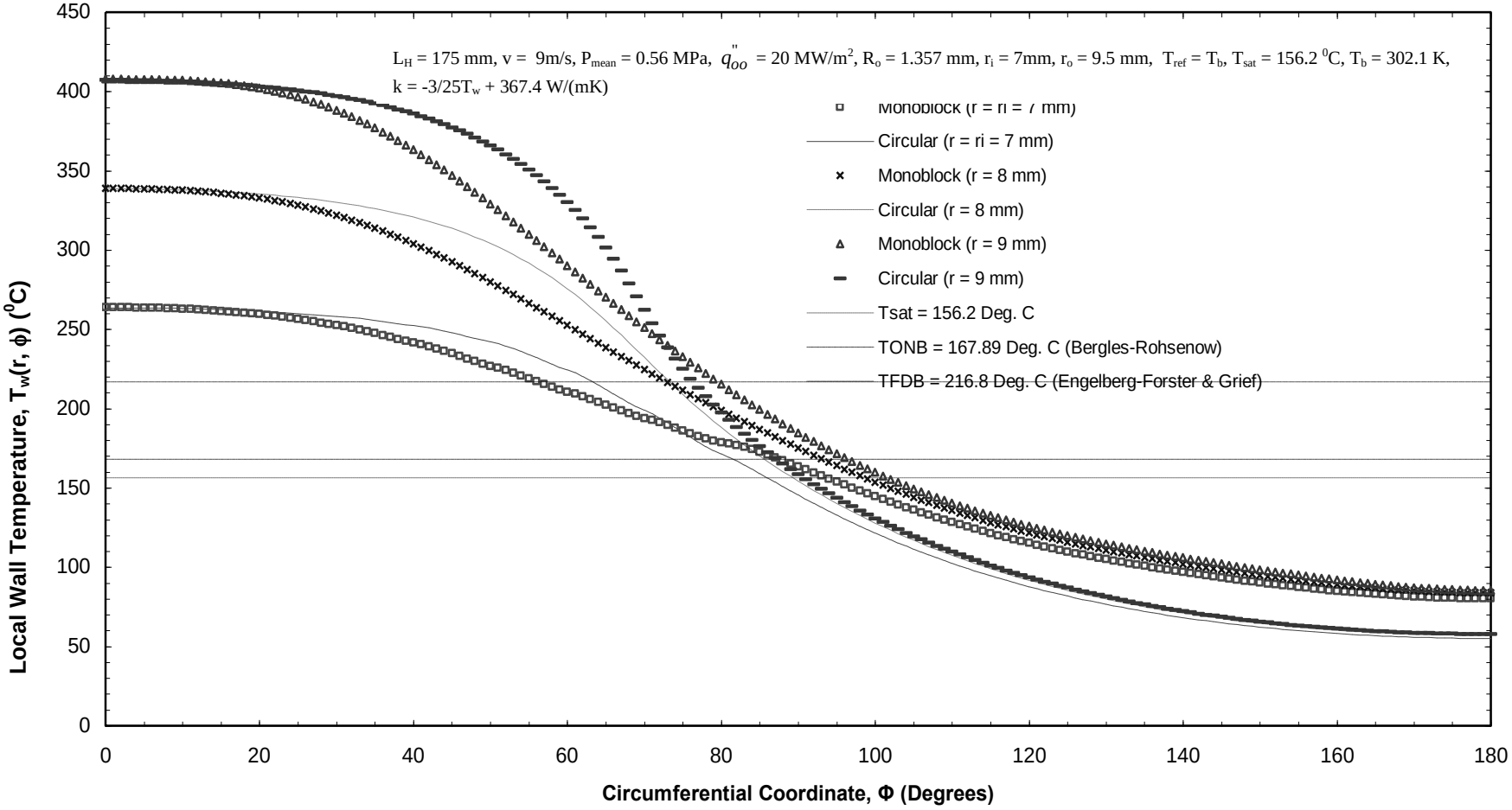

Figure 219: Flow Channel Local Circumferential Wall Temperature Simulation Comparison for the CEA Monoblock (Fi. 221) and Partially Heated Circular (simulating geometry, Fig. 223) Cases. Quantitative Simulation PF Comparisons Should Be Made Only at r = r_i = 7.0 mm and ϕ = 0 degrees (ϕ_{oo} = 69.4 degrees).

to the monoblock: (1) multiple material layers, (2) joints and/or finite thickness interfaces, and (3) verification of and/or an examination of under what conditions the simulation methodology is fluid-independent.

Although ϕ_{oo} and $h(\phi)$ will be fundamental parameters [along with the previously-mentioned parameters] in the final correlation, the correlations for T_{wi} and q_{wi} for ϕ_{oo} = 90 degrees and a constant value of $h(\phi)$ (=h_m) are [135]

$$\frac{T_{wi}-T_b}{\left(q''_{oo}\ r_o/k\right)}=\left(2\,Bi\right)^{-1}+\sum_{n=1}^{oo}\frac{2\sin\left[n\left(\frac{\pi}{2}-\phi\right)\right]\left[1-Bi_n\right]}{\pi\ n^2\ R_o^n\left[1+Bi_n\ R_o^{-2n}\right]} \tag{20-1}$$

where,

$$Bi_n=\frac{\left(Bi-n\right)}{\left(Bi+n\right)}; \tag{20-2}$$

and,

$$\frac{q''_{wi}}{q''_{oo}\ R_o}=\frac{1}{2}+\sum_{n=1}^{oo}\frac{4\sin\left[n\left(\frac{\pi}{2}-\phi\right)\right]}{\pi\ n\ R_o^n}\frac{Bi}{\left[\left(Bi+n\right)+\left(Bi-n\right)R_o^{-2n}\right]} \tag{20-3}$$

where n = 1, 3, 5, 7,….

As progress is made in the initial deployment of the approved ITER PFC or any HHFRC and in the scheduled component evaluations and upgrades, definitive allowances will no doubt be made if clear improvements are needed. Since implementation time will be critical, an approach and technical tools for improvements and further optimization, with an emphasis on robustness and reliability, will be needed. A correlation based on the present methodology may be a useful tool in obtaining timely optimization results for immediate improvements.

Briefly, the complete analysis and evaluation of a HHFRC under prototypic conditions require a complex coupled analysis involving: (1) HHFR PF and peak temperature constraint determination, (2) local and whole field stress-strain distribution and corresponding peak constraint determination, (3) corresponding effects on joints and interfaces [125], (4) the effects of the ablation (e.g., plasma-material or atmosphere-material) iteration on the above, (5) the effect of clearly identified changes due to physics or operational requirements, etc. In order to minimize the time and expense associated with mandatory component modifications (e.g.

materials, dimensions, system operation parameters), the simulation correlation will be useful as a quantitative PF, $T_{wi)max}$, and $q_{w)max}$ functional tool that could be used initially (along with the qualitative simulation results for $q_{wi}(\phi)$, $T_{wi}(\phi)$) with for example a stress analysis FEA (or similar) computer code to quickly include the extreme thermal parameters in preserving the critical thresholds for the updated modification(s). The procedure may reduce the modification optimization effort so that fewer completely-coupled analyses would be needed for the required change(s).

21.0 HIGH EHAT FLUX REMOVAL USING A HYPERVAPOTRON

21.1 SOME CONTROLLING PARAMETERS

21.1.1 OVERVIEW

A hypervapotron is an excellent candidate for single-side high heat flux removal (HHFR). In order to effectively characterize additional optimal operating characteristics using computational fluid dynamics (CFD) and/or experimental approaches (EA, and/or design approaches (DA)), knowledge of the controlling hypervapotron parameters would be essential for timely HHFR enhancement configuration identification. To that end, four controlling parameters have been identified: (1) $Bi = h_{eq}\, t/k_1$, (2) w_c/t, (3) $(w/2 - w_c)/L^*$, and (4) $q''_\infty\, w_c/k_1 T^*$. These parameters include effects of conjugate heat transfer, two-dimensional channel wall dimensionless aspect ratios and characteristic temperature. By relating some of these (and future) parameters to previous results, coolant channel configuration modifications were suggested which may improve HHFR in high heat flux applications. Finally, these parameters may be useful in CFD (and EA and/or DA) studies for optimizing HHFR and thermal protection in fusion and aerospace systems.

21.1.2 INTRODUCTION

High heat flux removal (HHFR) entails aspects of thermal management (TM), stability, and control. Among the numerous applications where HHFR is critical, high-performance nuclear fusion and aerodynamic-aerospace systems offer some of the greatest challenges. In the present work, HHFR is the focus. Whether the application involves HHFR from fusion reactor plasma facing components (PFC) or a propulsion power system or a thin leading edge or directed energy systems or a high-density electronic array, improved capability is possible only if the fundamental HHFR peaking factor (i.e. heat flux amplification/reduction), maximum coolant flow channel inside wall temperature ($T_{wi_{max}}$), maximum coolant flow channel wall temperature($T_{w_{max}}$), and normal temperature gradient $\left(\frac{\partial T}{n_i} max\right)$ can be related to heat transfer mechanisms, fluids, flow regimes, and/or geometries while being conducive to increasingly higher demands. The peaking factor (PF) is defined as the ratio of the maximum flow channel inside wall heat flux to the absorbed incident heat flux. In many applications, HHFR is

accomplished by a large array of monoblocks (e.g., see Fig 220 [138] for a PFC and Fig. 221 [139] for a rocket engine). These applications involve single-side heating (SSH) of the coolant flow channels; and, each application will have different PFs, depending on: (1) the flow channel internal high heat flux enhancement configuration, (2) coolant flow regimes, (3) channel geometry, and (4) fluid/channel thermo-physical properties. In this work, the term monoblock refers to a SSH flow channel which is cooled by a fluid flowing internally (e.g., see Figs. 220 through 222).

A conjugate heat transfer HHFR finite element analysis (FEA) simulation methodology [140] was developed with excellent resulting accuracy for predicting the heat transfer amplification (peaking factors, PF), the peak flow channel inside wall temperature $\left(T_{wi_{max}}\right)$, and inside wall maximum temperature gradient in a prototype single-side heated monoblock flow channel (see Fig. 220) with an inside circular flow channel up to about 30 MW/m^2 absorbed incident heat flux. Recently, that simulation was expanded and used as a basis to develop the first phase of PF, $\left.\frac{\partial T}{\partial n_i}\right)_{max}$, and $T_{wi_{max}}$ correlations [142] for a single-side heated monoblock with the same geometry. Those developed correlations [142] were exploratory in nature; and thus, the simplified condition of a constant inside heat transfer coefficient (HTC) was used. However, the earlier simulation methodology [140] included locally varying circumferential-dependent heat transfer coefficients (h(ϕ)) for the full range of single-side absorbed heat flux up to 38 MW/m^2. Future phases of these correlations [142] will include h(ϕ). The first–phase correlations depend on three parameters: (1) ϕ_∞, (2) $R_o = {}^{r_o}/_{r_i}$, and (3) $Bi_m = \frac{r_i\, h_m}{k_{solid}}$.

Although not alluded or referred to widely in the aerospace/aerodynamic TM technical literature, Boyd [142] recently noted that hypervapotrons [141-149] (see Fig. 222) have a possibility of significantly enhancing HHFR in aerospace/aerodynamic TM systems.

The recent literature contains many examples which address a variety of HHFR/TM issues, improvements, and recent results. Weaver and Alexeenko [150] noted a need for improved characterization of thermal protection systems to lessen “large factors of safety.” Pizzarelli, Nasuti, and Onofri [139], using computational fluid dynamics (CFD) for turbulent hydrogen flow in double-curvature high aspect ratio rectangular flow channels, found on the thrust-chamber of a

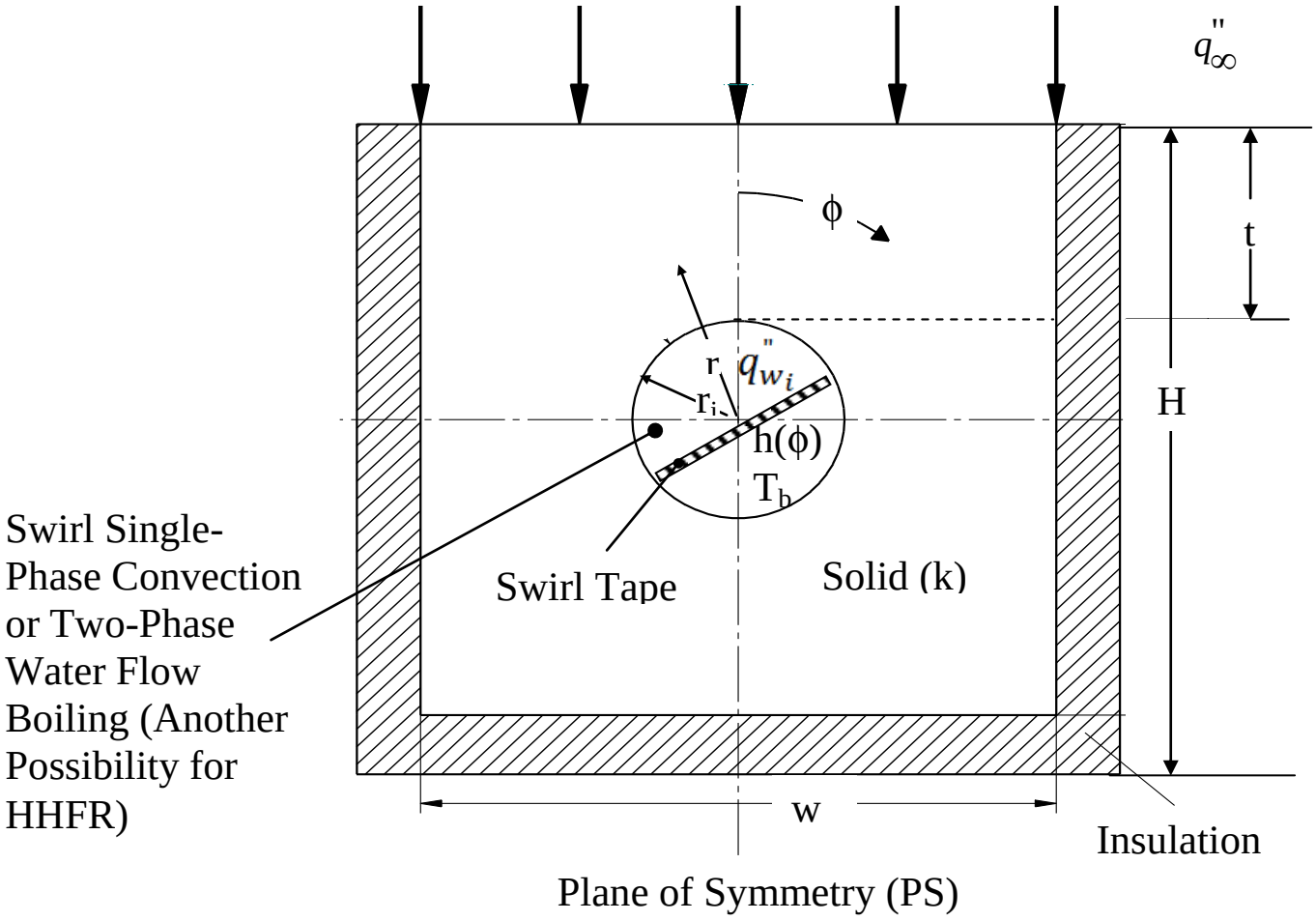

Figure 220: Monblock Prototype [138] For a Fusion Reactor Plasma-Facing Component (PFC).

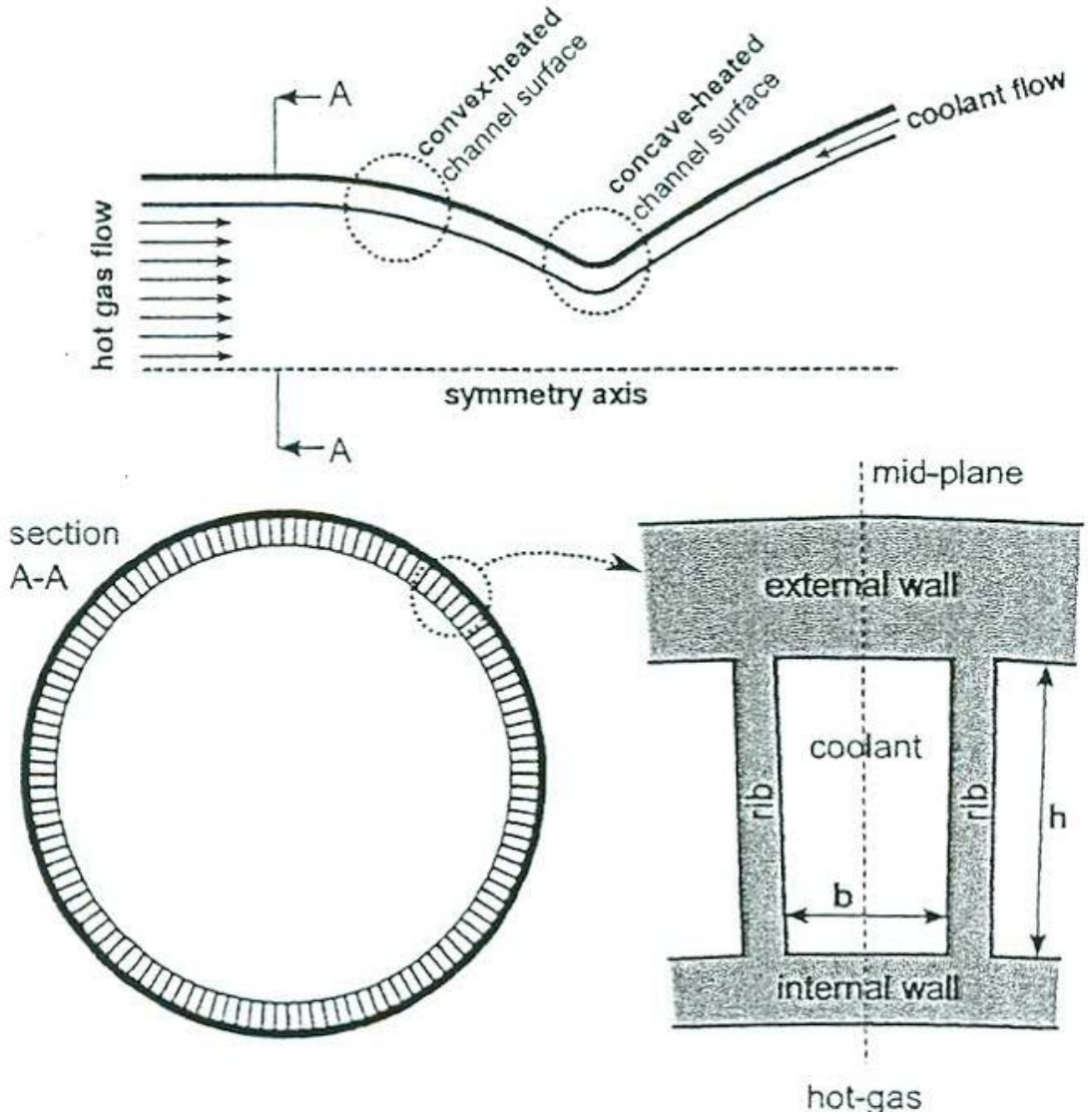

Figure 221: Sketch of Combustion Chamber and Cooling-Channel Geometry [139].

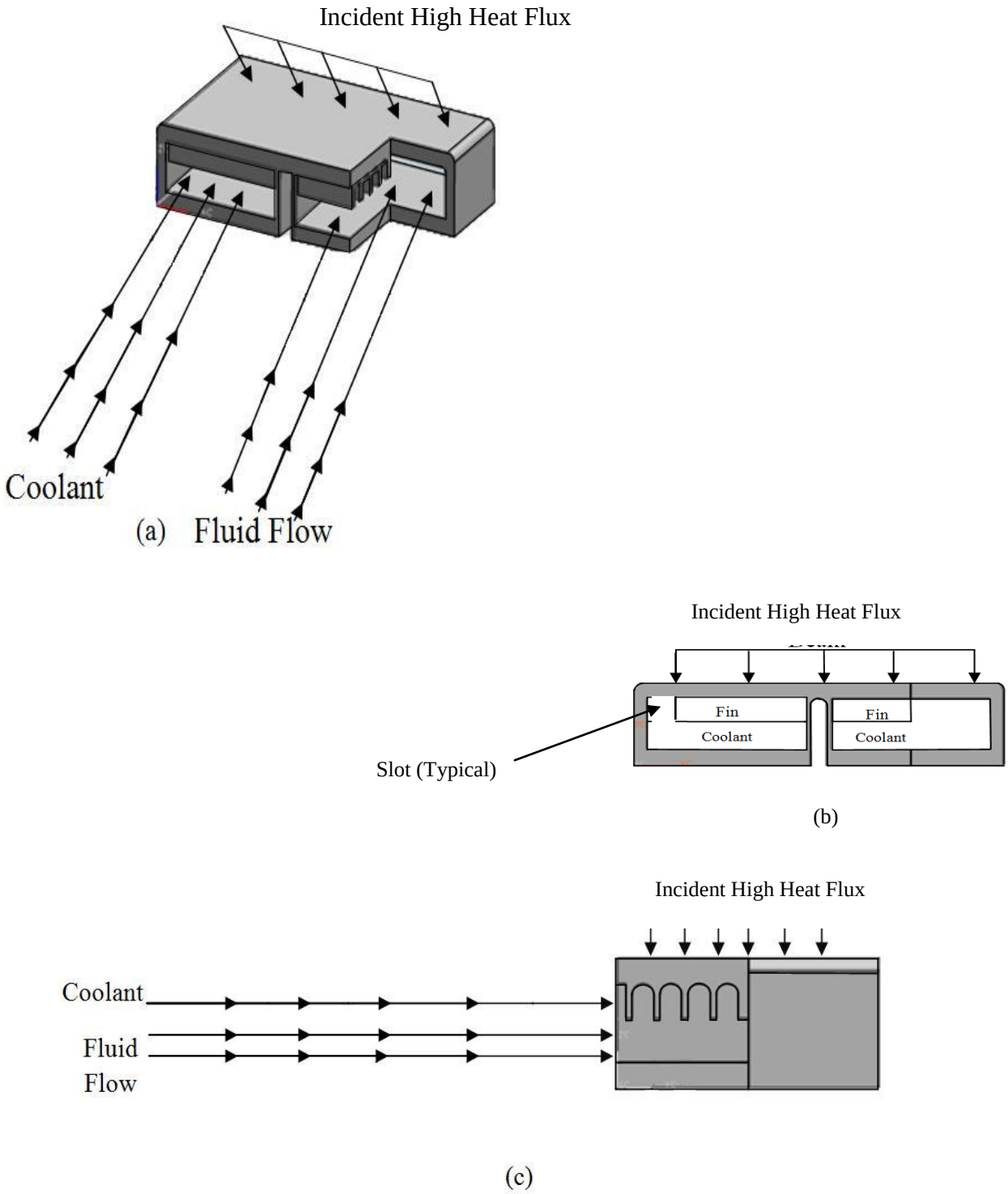

Figure 222: Another Possibility for TM is a Hypervapotron Monoblock Which is Here Subjected to a Single-Side Incident (absorbed) Heat Flux with an Internally Flowing Channel [141].

rocket engine (q''_∞ of the order of 160 MW/m^2) that a reduction in the heat rate occurred downstream of the convexed section and a counter flow configuration resulted in more efficient thermal management. Youchison, Ulrickson, and Bullock [148] using CFD for turbulent two-phase water flow in a hypervapotron flow channel, attempted to compute the critical heat flux and reported encouraging heat flux comparisons up to 10 MW/m^2. Ulas and Boysan [151] made comparative steady-state CFD studies of monoblock flow channels with rectangular cross sections and selected aspect of ratios (AR), for heat fluxes ranging from 27.0 to less than 30.0 MW/m^2. Their geometries were similar to the hypervapotron geometry but without the fins. Although their emphasis was not on heat flux amplification (HFA) or PF, they did emphasize the parameter-dependence of the maximum wall temperature $\left(T_{w_{max}}\right)$ on the gas side of the prototype case involving rocket combustion chamber cooling. For example, $T_{w_{max}}$ decreased with increased AR (~15% absolute temperature reduction for AR increasing from 2.0 to 8.0). In addition, there was an optimum number of channels in a given prototype for a minimum value of $T_{w_{max}}$. Clearly, their study would be improved by an inclusion of HFA and possibly a hypervapotron. Visca et al. [145] summarized the following accomplished testing conditions in preparation for the production of the inner vertical target for the International Thermonuclear Experimental Reactor: (1) 20 MW/m^2 (worst operating conditions), (2) heat flux fatigue testing (20 MW/m^2 for 2000 cycles for the carbon/carbon fiber composite (CFC) part and 15 MW/m^2 for 2000 cycles for the tungsten part) and with an achieved CHF of 35 MW/m^2—a "margin of 1.75 with regard to…normal thermal loading," and (3) a 400 mm long divertor prototype unit (20 MW/m^2 for 3000 cycles for the CFC part, and 15 MW/m^2 for 3000 cycles for the tungsten part). In another CFD study, Youchison, Ulrickson, and Bullock [148] examined two geometric parameters which included fin length and back-channel depth (see Fig. 223) for a 52 mm wide hypervaporton with a 6 mm pitch, 3 mm side slots, 100 mm heated length for 70 ^{0}C inlet water coolant at 2.7 MPa. In their work, the back-channel depth is the distance between fin tip and opposite surface (= $2H_c - L_f$ in Fig. 223). For example, the 4 mm/5 mm case in their work represents a 4 mm long fin and 5 mm high back-channel depth. In their parameter study, the short fin/deep back-channel (2 mm/5 mm) performed better ("surprisingly") than the short fin/shallow back channel (2 mm/3 mm) under off-normal conditions (5.0 MW/m^2). For normal conditions (0.5 MW/m^2), all cases had equivalent [wall] temperatures. Under single-phase flow conditions, other observations include: (1) the 2 mm/3 mm case ("more optimal") required a

factor of two less flow rate than the 4 mm/5 mm case, had the highest local heat transfer coefficients (h), but required a 15% higher pressure drop; and (2) the 4 mm/3 mm case had the highest averaged h and thus the lower surface temperatures. The authors concluded that "a big advantage of the short teeth/shallow back-channel design is the performance it provides at half the mass flow rate." Further, they noted that "hypervapotron channel widths less than 50 mm allow efficient removal of water vapor from the grooves for the same teeth [fin], side slot and back channel dimensions, and therefore, perform better." Escourbiac et al. [147] made fifty-four (54) CHF (up to 25-30 MW/m^2) measurements on similar SSH hypervapotrons (for PFCs) with different widths with water as the working fluid; and, they found that at low velocities (2-6 m/s), the CHF decreased as the outer width (27.0, 40.0, and 50.0 mm) increased. Further, they found that the surface temperature increased when q''_∞ > 20 MW/m^2 and noted that 20 MW/m^2 maybe the upper limit for q''_∞. Finally, Ruan and Meng [152] found that shallow SSH cooling rectangular channels (for engine cooling in aerospace systems) perform well as for as HHFR but suffers severe pressure loss.

21.1.3 MODEL DEVELOPMENT

Thus far, the HHFR enhancement literature for single-side heated (SSH) monoblocks with a rectangular flow channel identifies the following parameters: (1) AR (= H_c/w_c) for cases without fins, (2) the ratio ($L_f/(2H_c - L_f) = 1/[2H_c/L_f - 1]$) of the fin length to the back flow channel depth for a hypervapotron, and (3) the width ($2w_c$) for a hypervapotron. Are these parameters solely responsible for controlling the optimal HHFR performance of SSH hypervapotrons? Although AR was not specifically identified as a hypervapotron controlling parameter (HCP), it was identified as a rectangular flow channel controlling parameter and will be probably in later extensions of the present work. Is it an HCP? The answer to the latter question is probably "yes" based on the fact that both H_c/L_f and w_c appear to be related to HCPs. More importantly, what other HCPs are there? Although the hypervapotron is a 3-D geometry, the controlling parameters identified thus far in the literature are related to the flow channel 2-D cross-section normal to the flow direction. As such, the present work addressed this 2-D geometry with the aim of identifying more fundamental controlling parameters. Once the 2-D model is completed and verified, it will be extended in the future to include 3-D effects.

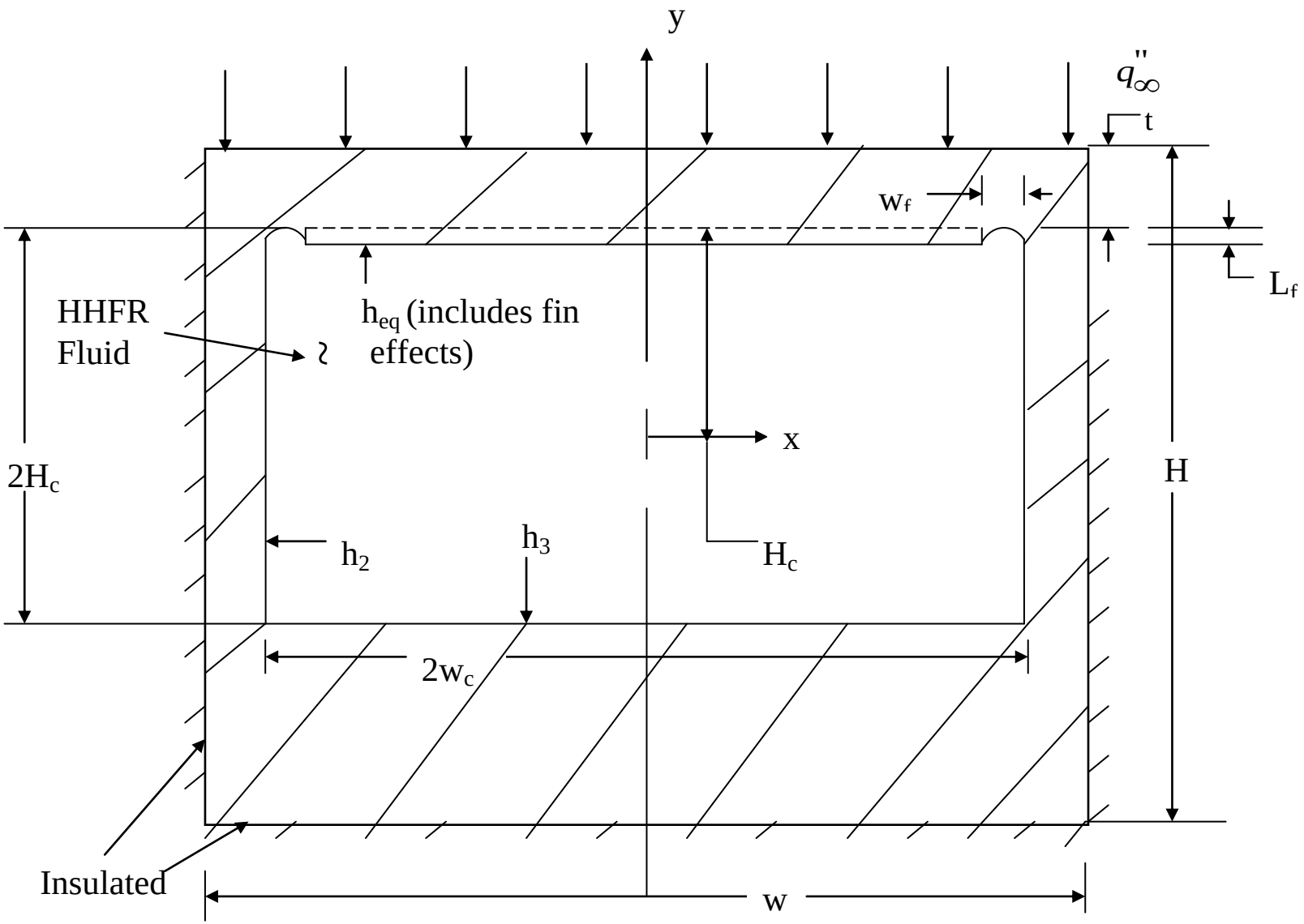

Figure 223: Simplified 2-D Hypervapotron Unit Cell.

The HHFR model used for the SSH hypervapotron is shown in Fig. 224. In addition to the charactering dimensions and single-side incident/absorbed heat flux, there are three characterizing uniform heat transfer coefficients used on the inside of the flow channel. For the flow channel vertical side wall and upward-facing surface, h_2 and h_3 were assumed to exist, respectively. Further, h_{eq} is given by

$$h_{eq} = h_f \, \eta_o \left(\frac{A_T}{A_b} \right) \tag{21-1}$$

where h_f is the mean heat transfer coefficient for the hypervapotron finned and bare areas between the fins, η_o is the overall finned surface efficiency, A_T/A_b is the ratio of the total surface area of the finned surface to that of the downward facing flow channel surface if it did not have fins.

Because the boundary conditions are discontinuous at some coordinate locations, the model in Fig. 224 has been subdivided into five domains as shown in Fig. 225. From Fig. 224, the monoblock temperature distribution is characterized for the case of a constant thermal conductivity by the following governing equation and boundary conditions:

$$\frac{\partial^2 T}{\partial x^2} + \frac{\partial^2 T}{\partial y^2} = 0 \tag{21-2}$$

with the following boundary conditions:

$$@ \; x \le w_c, \text{ and } y = H_c,$$
$$-k \frac{\partial T}{\partial y} = h_{eq} \left(T_b - T \right); \tag{21-3a}$$

$$@ \; y = H_c + \text{t} = \text{y}_2,$$
$$-k \frac{\partial T}{\partial y} = -q''_{oo}; \tag{21-3b}$$

$$@ \; x \le w_c \text{ and } y = -H_c,$$
$$-k \frac{\partial T}{\partial y} = h_3 \left(T - T_b \right); \tag{21-3c}$$

$$@ \; y = -y_3 = -\left(H - t - H_c \right),$$
$$\frac{\partial T}{\partial y} = 0. \tag{21-3d}$$

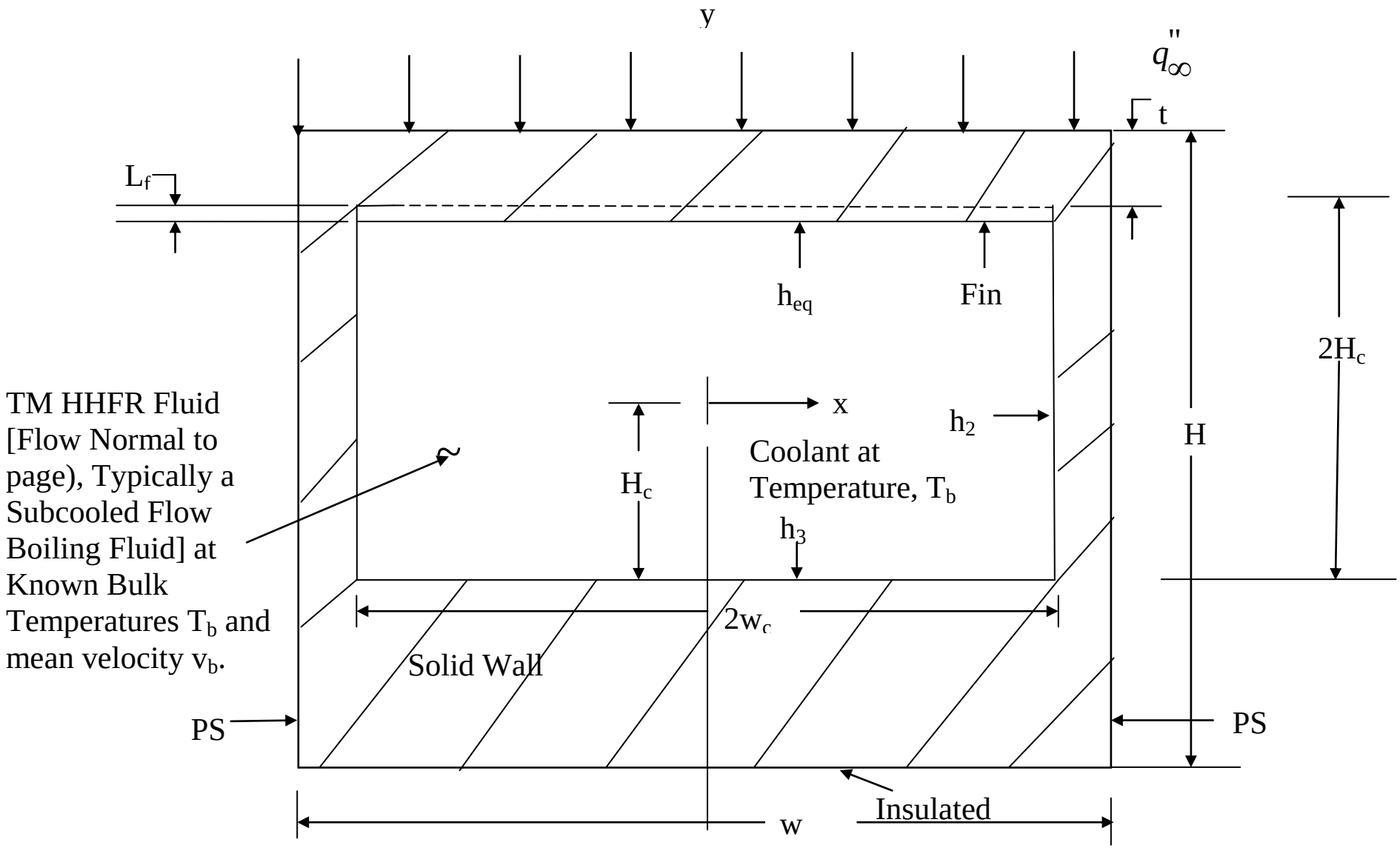

Figure 224: 2-D Monoblock Unit Cell Used for Modeling.

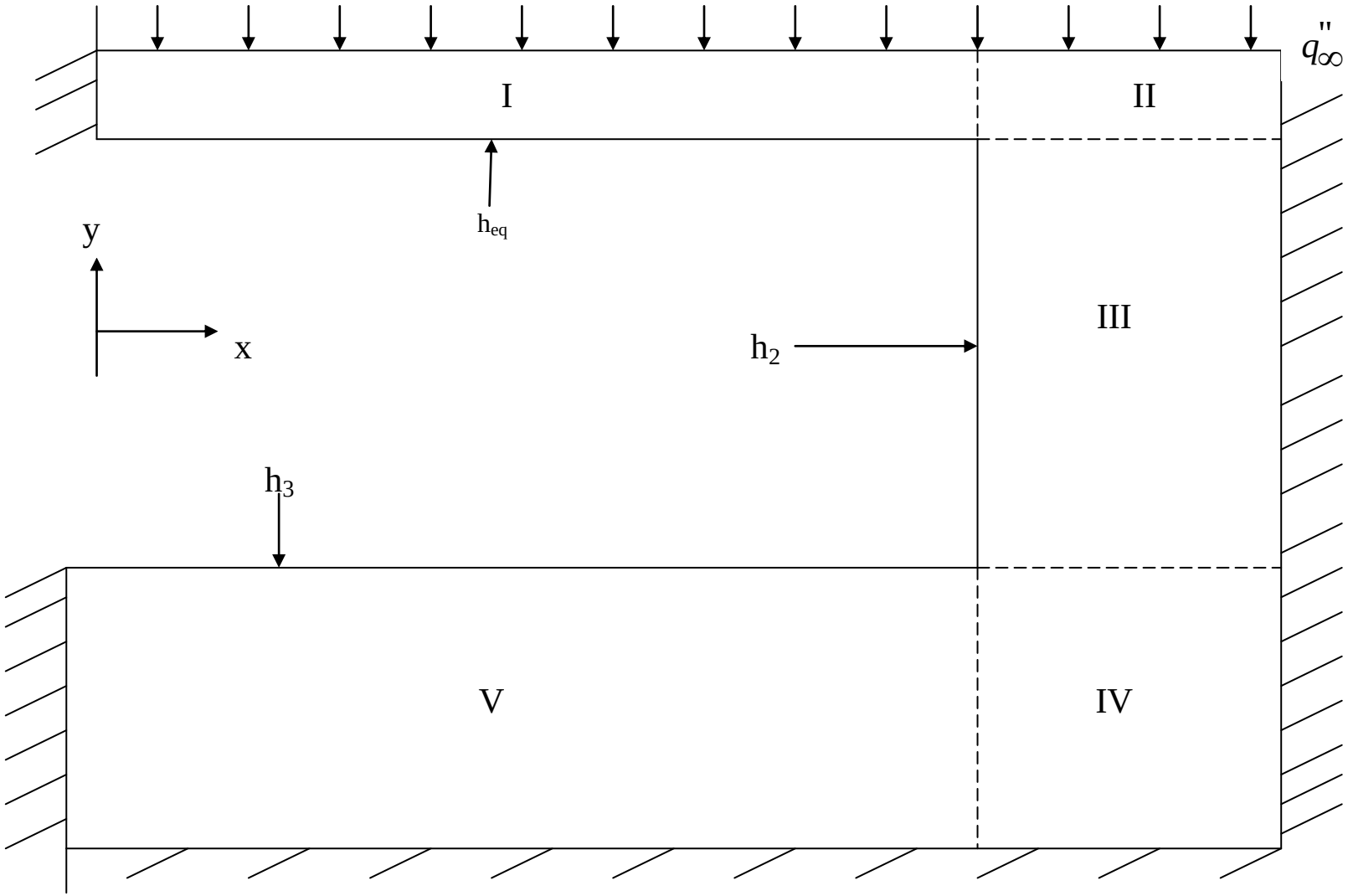

Figure 225: 2-D Monoblock (rectangular flow channel) Unit Cell Model Domains.

$$@\ x = w_c \text{ and } H_c \geq y \geq -H_c,$$
$$-k\frac{\partial T}{\partial x} = h_2\left(T_b - T\right); \tag{21-3e}$$

$$@\ x = 0,\ \frac{\partial T}{\partial x} = 0; \text{ and} \tag{21-3f}$$

$$@\ x = \frac{w}{2}, \frac{\partial T}{\partial x} = 0. \tag{21-3g}$$

As usual, let

$$\theta = T - T_b. \tag{21-4}$$

Using superposition, each of the five domains' governing equations and boundary conditions are obtained. For Domain I, the above equations become

$$\frac{\partial^2 \theta_I}{\partial x^2} + \frac{\partial^2 \theta_I}{\partial y^2} = 0; \tag{21-5}$$

$$@\ x = 0, \frac{\partial \theta_I}{\partial x} = 0; \tag{21-6a}$$

$$@\ x = w_c, \theta_I = \theta_{II}; \tag{21-6b}$$

$$@\ y = y_2, k_I \frac{\partial \theta_I}{\partial y} = q''_\infty; \text{ and} \tag{21-6c}$$

$$@\ y = H_c, k_I \frac{\partial \theta_I}{\partial y} = h_{eq}\,\theta_I. \tag{21-6d}$$

Similarly for Domain II,

$$\frac{\partial^2 \theta_{II}}{\partial x^2} + \frac{\partial^2 \theta_{II}}{\partial y^2} = 0; \tag{21-7}$$

$$@\ x = w_c, \mathrm{k_I} \frac{\partial \theta_I}{\partial x} = k_{II} \frac{\partial \theta_{II}}{\partial x}; \tag{21-8a}$$

$$@\ x = \frac{w}{2},\ \frac{\partial \theta_{II}}{\partial x} = 0; \tag{21-8b}$$

$$@\ y = y_2,\ k_{II} \frac{\partial \theta_{II}}{\partial y} = q''_{\infty};\ \text{and} \tag{21-8c}$$

$$@\ y = H_c,\ \theta_{II} = \theta_{III}. \tag{21-8d}$$

For Domain III,

$$\frac{\partial^2 \theta_{III}}{\partial x^2} + \frac{\partial^2 \theta_{III}}{\partial y^2} = 0; \tag{21-9}$$

$$@\ x = w_c,\ \mathrm{k_{III}} \frac{\partial \theta_{III}}{\partial x} = h_2 \theta_{\mathrm{III}}; \tag{21-10a}$$

$$@\ x = \frac{w}{2},\ \frac{\partial \theta_{III}}{\partial x} = 0; \tag{21-10b}$$

$$@\ y = H_c,\ \mathrm{k_{II}} \frac{\partial \theta_{II}}{\partial y} = k_{III} \frac{\partial \theta_{III}}{\partial y};\ \text{and} \tag{21-10c}$$

$$@\ y = H_c,\ \theta_{III} = \theta_{IV}. \tag{21-10d}$$

For Domain IV,

$$\frac{\partial^2 \theta_{IV}}{\partial x^2} + \frac{\partial^2 \theta_{IV}}{\partial y^2} = 0; \tag{21-11}$$

$$@\ x = w_c,\ \theta_{IV} = \theta_V; \tag{21-12a}$$

$$@\ x = \frac{w}{2},\ \frac{\partial \theta_{IV}}{\partial x} = 0; \tag{21-12b}$$

$$@\ y = -H_c, k_{IV} \frac{\partial \theta_{IV}}{\partial y} = k_{III} \frac{\partial \theta_{III}}{\partial y};\ \text{and} \tag{21-12c}$$

$$@\ y=-y_3,\ \frac{\partial \theta_{\mathrm{IV}}}{\partial \mathrm{y}}=0. \tag{21-12d}$$

Finally for Domain V,

$$\frac{\partial^2 \theta_V}{\partial x^2}+\frac{\partial^2 \theta_V}{\partial y^2}=0; \tag{21-13}$$

$$@\ x=0,\ \frac{\partial \theta_{\mathrm{V}}}{\partial \mathrm{x}}=0; \tag{21-14a}$$

$$@\ x=w_c,\ \mathrm{k_V}\frac{\partial \theta_{\mathrm{V}}}{\partial \mathrm{x}}=k_{IV}\frac{\partial \theta_{IV}}{\partial x}; \tag{21-14b}$$

$$@\ y=-y_3,\ \frac{\partial \theta_{\mathrm{V}}}{\partial \mathrm{y}}=0;\ \text{and} \tag{21-14c}$$

$$@\ y=-H_c,\ -k_V\frac{\partial \theta_V}{\partial y}=h_3\theta_V. \tag{21-14d}$$

Because of the nonhomegeneities (see Fig. 226) in the θ_I formulation, let

$$\theta_I(x,y)=\theta_{I_1}(x,y)+\theta_{I_2}(x,y); \tag{21-15}$$

so that,

$$\frac{\partial^2 \theta_{I_1}}{\partial x^2}+\frac{\partial^2 \theta_{I_1}}{\partial y^2}=0; \tag{21-16}$$

$$@\ x=0,\ \frac{\partial \theta_{\mathrm{I}_1}}{\partial \mathrm{x}}=0; \tag{21-17a}$$

$$@\ x=w_c,\ \theta_{I_1}=\theta_{II}; \tag{21-17b}$$

$$@\ y=y_2,\ \frac{\partial \theta_{\mathrm{I}_1}}{\partial y}=0; \tag{21-17c}$$

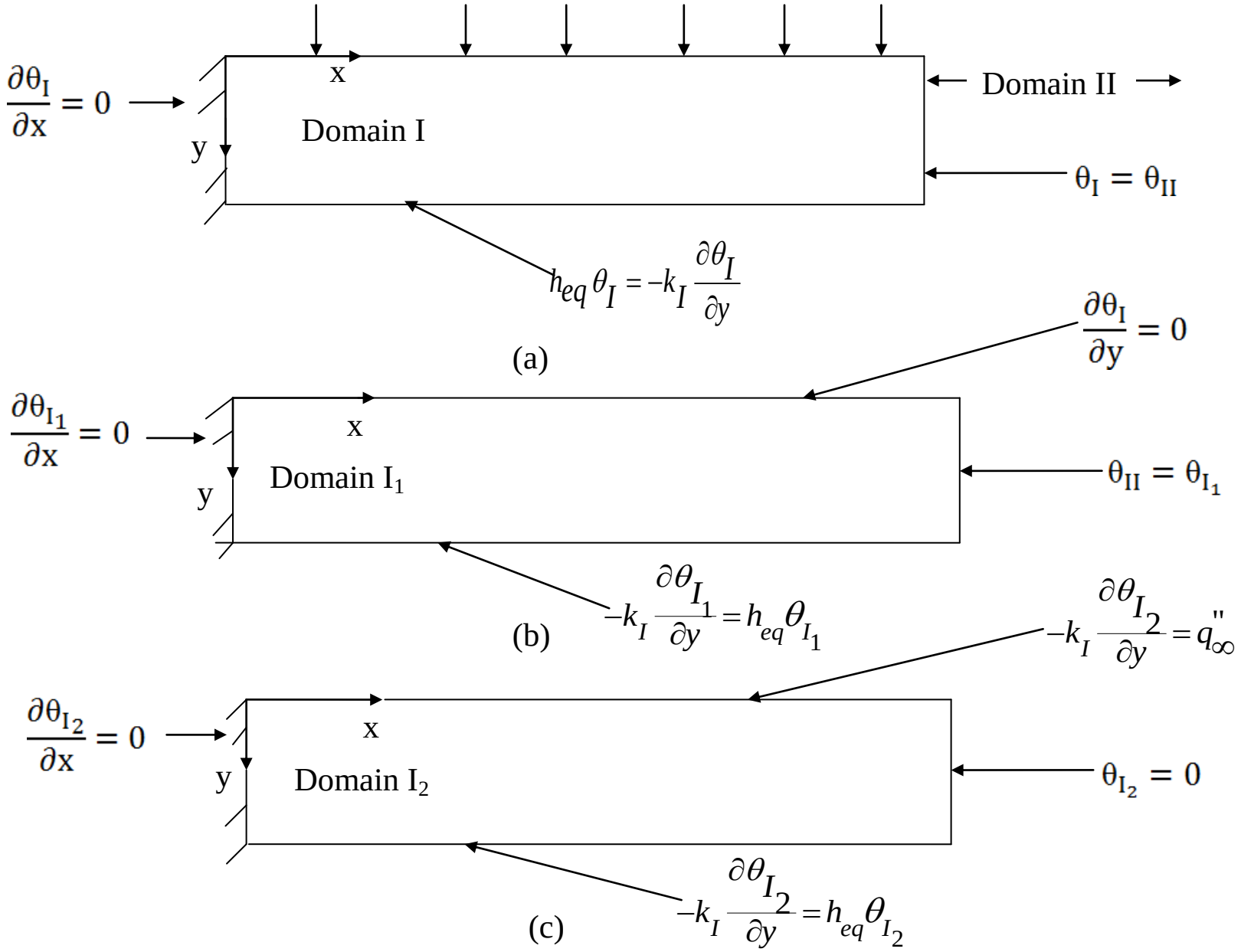

Figure 226: Domain I (a), and It's Two Superposition Sub-Domains I_1 (b) and I_2 (c).

$$@\ y = H_c,\ k_I \frac{\partial \theta_{I_1}}{\partial y} = h_{eq}\, \theta_{I_1}; \tag{21-17d}$$

$$\frac{\partial^2 \theta_{I_2}}{\partial x^2} + \frac{\partial^2 \theta_{I_2}}{\partial y^2} = 0; \tag{21-18}$$

$$@\ x = 0,\ \frac{\partial \theta_{I_2}}{\partial x} = 0; \tag{21-19a}$$

$$@\ x = w_c,\ \theta_{I_2} = 0; \tag{21-19b}$$

$$@\ y = y_2,\ k_I \frac{\partial \theta_{I_2}}{\partial y} = q''_{\infty}; \text{ and} \tag{21-19c}$$

$$@\ y = H_c,\ k_I \frac{\partial \theta_{I_2}}{\partial y} = h_{eq}\, \theta_{I_2}. \tag{21-19d}$$

Unnecessary complexities will result unless the y-coordinate axis is changed to the location shown in Fig. 227. As such, the remainder of the formulation uses this axis location for the rectangular flow channel (RFC) monoblock unit cell.

21.1.4 RESULTS

Some controlling thermal management parameters have been identified; and these parameters can be related to the coolant flow channel wall heat flux peaking/reduction factors. The present results include parameters associated with the analyses for Domains I_1 and I_2 which are directly associated with both the heat flux and convective boundaries.

For Domain I_1, θ_{I_1} (x,y) is given by

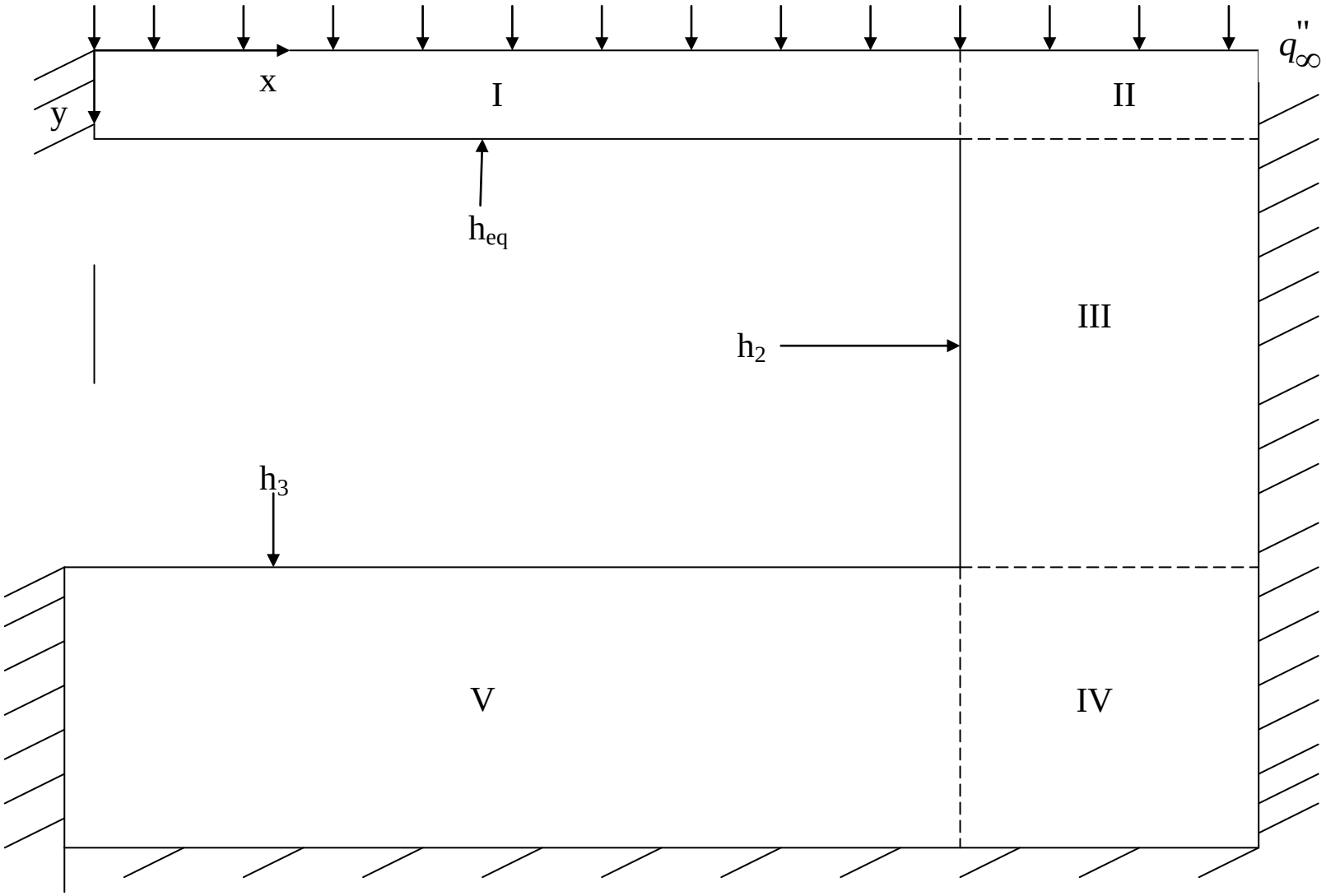

Figure 227: 2-D RFC Unit Cell Model Domains With the Origin for the y-axis Changed So That Simpler Conditions Result.

$$\theta_{I_1}(x,y) = T_{I_1}(x,y) - T_b =$$

$$\Sigma_{n=0}^{\infty} a_{I_{1_n}} \left(e^{\lambda_{I_{1_n}} x} + e^{-\lambda_{I_{1_n}} x} \right) \cos\left(\lambda_{I_{1_n}} y \right), \tag{21-20a}$$

where n = 1, 2, 3, 4, … and $\lambda_{I_{1_n}}$ is characterized by

$$\cot\left(\lambda_{I_{1_n}} t \right) = \frac{\lambda_{I_{1_n}} t}{Bi} \tag{21-20b}$$

and where

$$Bi = \frac{h_{eq} t}{k_I}. \tag{21-20c}$$

The eignvalues, $\lambda_{I_{1_n}}$ are the intersection of the $cot\left(\lambda_{I_{1_n}} t \right)$ function plotted as a function of $\left(\lambda_{I_{1_n}} t \right)$ and a straight line $\left(\lambda_{I_{1_n}} t \right)$ with a slope of

$$\frac{1}{Bi} = \frac{\cot\left(\lambda_{I_{1_n}} t \right)}{\left(\lambda_{I_{1_n}} t \right)}. \tag{21-20d}$$

In addition, $a_{I_{1_n}}$ is characterized by

$$\left(e^{\lambda_{I_{1_n}} w_C} + e^{-\lambda_{I_{1_n}} w_C} \right) a_{I_{1_n}} =$$

$$\frac{\int_o^t \theta_{II}(w_C, y) \cos\left(\lambda_{I_{1_n}} y \right) dy}{\int_o^t \cos^2\left(\lambda_{I_{1_n}} y \right) dy} \tag{21-20e}$$

Finally,

$$\theta_{I_2} = T_{1_2}(x,y) = \sum_{n=1}^{\infty} E_{I_{2_n}} \cos\left(\lambda_{I_{2_n}} \right)$$

$$\left\{ e^{\lambda_{I_{2_n}} y} + e^{\lambda_{I_{2_n}} (2t-y)} \left[\frac{1 + Bi\left(\frac{w_C}{t} \right)\left(\frac{2}{n\pi} \right)}{1 - Bi\left(\frac{w_C}{t} \right)\left(\frac{2}{n\pi} \right)} \right] \right\}, \tag{21-21a}$$

where, n = 1, 3, 5… and $E_{I_{2n}}$ is the next n-dependent coefficient to be determined. This latter coefficient is found using the last boundary condition for θ_{I_2} but now using this condition for y = 0 to account for the relocation of the y-axis origin. Using this condition,

$$\lambda_{I_{2n}}\left\{1-e^{2\lambda_{I_{2n}}t}\,Bi_{w_{c_n}}\right\}E_{I_{2n}} = \frac{\int_o^{w_c}\left(-\frac{q''_\infty}{k_I}\cos\left(\lambda_{I_{2n}}x\right)\right)dx}{\int_o^{w_c}\cos^2\left(\lambda_{I_{2n}}x\right)dx}, \qquad \text{(21-21b)}$$

where

$$Bi_{w_{c_n}} = \frac{\left[1+Bi\left(\frac{w_c}{t}\right)\left(\frac{2}{n\pi}\right)\right]}{1-Bi\left(\frac{w_c}{t}\right)\left(\frac{2}{n\pi}\right)} \qquad \text{(21-21c)}$$

and the eigenvalues, $\lambda_{I_{2n}}$, are given by

$$\lambda_{I_{2n}} = \frac{n\pi}{2w_c}, \qquad \text{where } 1, 3, 5\ldots . \qquad \text{(21-21d)}$$

The Domain I analyses provide an initial glimpse of the array of HHFR controlling parameters. These parameters will not only be useful control parameters for future CFD/experimental studies, but will be also useful in improving designs to enhance HHFR. Examples of the latter advantages will be given after some of the parameters have been identified. Thus far, the following controlling parameters have been found:

(a) $$Bi = h_{eq}\,t/k_I, \qquad \text{(21-22a)}$$

(b) $$\left(w_c/t\right)Bi = \frac{h_{eq}w_c}{k_I} \text{ or } w_c/t \qquad \text{(21-22b)}$$

(c) $$\frac{q''_\infty\, w_c}{k_I T^*} \qquad \text{(21-22c)}$$

(d) $$\left(w/2-w_c\right)/L^*, \qquad \text{(21-22d)}$$

where h_{eq} is defined in equation (21-1) and where T^* and L^* are characteristic temperature and length, respectively; and, these are yet to be determined. One could arbitrarily let the parameter in eq. (21-22c) be equal one (i.e., 1.0) which reduces the number of controlling parameters--an obvious advantage. However, there may be a later "natural" choice for T^*; and therefore, the above noted arbitrary selection of 1.0 for that parameter will be used when there appears to be no other "natural" choice for T^*. The parameter in eq. (21-22d) arises from θ_{II} and an arbitrary selection for L^* could be, for example, $L^* = t$ or $L^* = w_c$; but again, future work will reveal the "natural" choice for L^*.

The future compilation of the analyses for the five primary domains will result in HHFR correlations for both local flow channel/wall heat flux and temperature for a hypervapotron; and, these can be used for: (1) validation and verification purposes; (2) CFD and/or experimental studies using the control parameters to enhance HHFR; (3) parameter map creation for possible HHFR design improvements; and, (4) parameter regions distinction and identification (demonstrated below).

Two examples are now given of some important additional consequences and advantages of HHFR control parameter identification and use. Consider a SSH circular coolant channel with inside and outside radii r_i and r_o, respectively. The absorbed incident heat flux (q_o) and inside HTC (h_m) are constant. The steady state solution for the local 2-D flow channel wall heat flux (and temperature) distribution(s) results in the parameter map shown in Fig. 228 [135], where q_i is the local inside flow channel heat flux. The obvious advantages of the map are the identification of parameter ranges where: (1) no local heat flux amplification (HFA) will occur (Region I), (2) minimal HFA will occur (Region II), and (3) significant HFA will occur (Region III). In addition, classical correlations with minimum correction can be used in Regions I and II. Further, the map was used to suggest basic flow channel design modifications which resulted in enhanced HHFR and reduced PF and HFA. Two suggested ideal modifications will be summarized. First, the ideal modification of including a lower thermal conductivity inner half shell below the heated region is implied by the map (Fig. 228). In addition to the justification given in reference [135], the added shell thermal resistance reduces the total, effective inner overall heat transfer coefficient and hence the corresponding value of Bi_m. The result is a

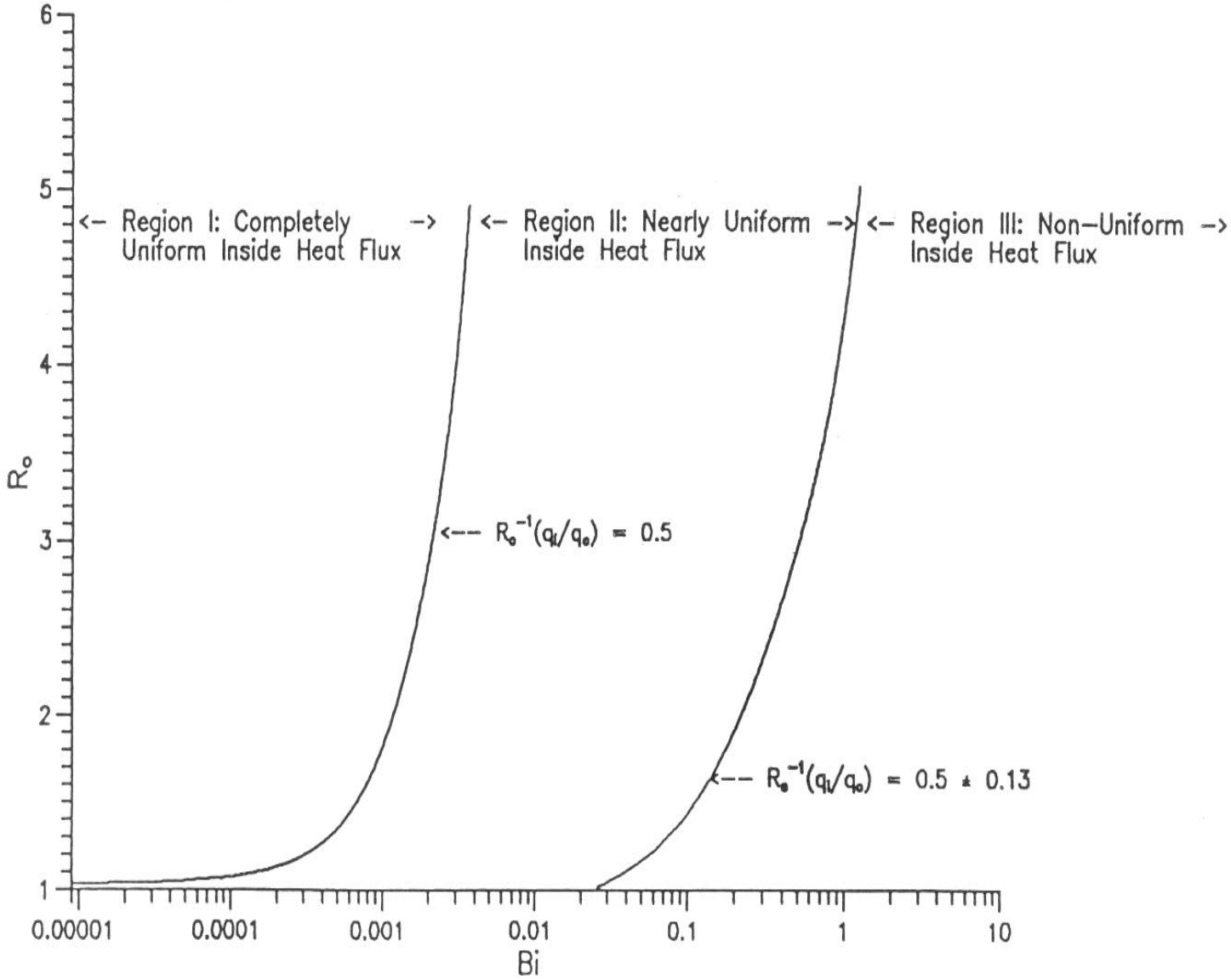

Figure 228: Inside Flow Channel Surface Heat Flux Map [135].

redistribution of the incident single-side heat flux to a more uniform distribution on the inside flow channel surface. The addition of the shell was originally predicted in reference [135]. The practical extension of this modification is to extend the inner shell so that it becomes an inner lower thermal conductivity tube. Federici and Raffray [153] found that a stainless steel tube insert inside a copper monoblock reduced peaking factors up to about 30%. They and Raffray et al. [154] also investigated a carbon fiber composite monoblock with a inner copper tube. This same concept can be extended to both the designs in Figs. 220 and 221 (future aerodynamic and hypervapotron applications). In concert with this extension, the fins on the conventional (e.g., [146]) hypervapotron could be added to the inside surfaces of Domains III and/or V depending their ability to enhance HHFR; and, these possibilities could be examined via further CFD and/or experimental design studies and analogous parameters as shown in this study. Next, reconsider the lower thermal conductivity inner half shell but now with variable thickness decreasing as the unheated region is a approached. This inner layer could be part of a design modification or it could be a flaw which resulted from possible assembly errors or material defect (for example) of a multi-layered cooling channel. Originally predicted in reference [135], the surprising result of (for example) the flaw at ϕ = 0.0 degrees is to reduce the HFA [155]. These two examples are implications of the importance of the controlling parameters for both HHFR design improvements and CFD and experimental optimization.

Finally, the flow channel wall heat flux peaking/reduction factors (PF) can be determine from

$$T_I(x, y) = T_b + \theta_{I_1} + \theta_{I_2}, \tag{21-23}$$

where θ_{I_1} and θ_{I_2} are given in eqs. (21-20a) and (21-21a). The PF is defined as the ratio of the local maximum inside heat flux (at y = t) to the incident (absorbed) heat flux, q''_∞. Thus,

$$PF = \left[-k_I \left(\frac{\partial \theta_{I_1}}{\partial y} + \frac{\partial \theta_{I_2}}{\partial y} \right) \Bigg|_{y=t} \right]_{\max} / q''_\infty. \tag{21-24}$$

The controlling HHFR parameters for $T_I(x , y)$ and PF are given in eqs. (21-22a) through (21-22d). PF can be defined similarly later for Domains III and V. However, eq. (21-24) will probably characterize the largest PF. The maximum flow channel wall temperature is related to both θ_I and θ_{II} and will be determined in the future.

By developing an isotherm-heat flow line map of the flow channel wall, it can be demonstrated that the maximum wall temperature $\left(T_{w_{max}}\right)$ will occur in Domain II at y = 0 and x

= w/2. This has been observed by many other investigators (e.g., see [149]). Although the actual expression for $T_{w_{max}}$ will be determined in future parts of this work, it will be dependent on, among other parameters, the parameters given in eqs. (21-22a) through (21-2d). Hence, four HHFR controlling parameters have been identified thus far that influence both PF and $T_{w_{max}}$ for a single-side heated hypervapotron flow channel. Additional parameters will result in future parts of this work. Finally, $\frac{\partial T}{\partial n_i}\Big)_{max}$ can be found directly from equation (21-24); and, it is also controlled by the above noted parameters.

21.2 ADDITIONAL CONTROLLING PARAMETERS

21.2.1 OVERVIEW

The hypervapotron (HV) has been demonstrated to be a superior thermal management (TM) and high heat flux removal (HHFR) technique for fusion reactor plasma-facing component applications involving a single-side absorbed heat flux (up to between 20 and 30 MW/m^2). However, the conjugate heat transfer HV flow channel (HVFC) performance only can be optimized completely when the related HHFR controlling parameters have been identified. Part 21.1 of the present effort identified three HV controlling TM and HHFR dimensionless parameters and a dimensionless temperature. In the present work, four additional dimensionless primary controlling parameters and five secondary controlling parameters have been identified. The controlling parameters include effects of: (1) most geometric specifications of the array of fins; (2) variations in the HV wall thermal conductivity and heat transfer coefficient; (3) effective Biot numbers charactering two-dimensional effects which include the fin array, a typical fin, and the vertical side wall; (4) HVFC unobstructive portion flow aspect ratio, and (5) the HVFC wall aspect ratio. Future work should assess the sensitivity of these parameters.

21.2.2 INTRODUCTION

As advancements are made in alternative energy options, thermal management (TM) and high heat flux removal (HHFR) will become increasingly important. For example, ITER is being constructed in France and will be the world's largest tokamak fusion reactor [157]. There are regions in the reactor where the incident absorbed steady-state heat flux $\left(q''_{\infty}\right)$ can be and sometimes exceed the range between 0.5 and 15 MW/m^2 [158, 159]. Some devices which will experience heat fluxes in this range are the blank modular wall and the divertor and both require active water cooling." In the case of water cooling, strict TM design criteria must be established so that the critical heat flux (CHF) is not exceeded. The CHF is the maximum heat flux at the water-solid coolant channel interface, beyond which the heated area could be irreversibly damaged, compromised, or even destroyed [156].

Among the many alternative TM and HHFR schemes and devices investigated to accommodate the above high heat flux demands, the hypervapotron (see Figure 222) has been used over the past thirty (30) years to demonstrate HHFR capability up to heat fluxes between

20.0 and 30.0 MW/m^2 [156] with lower pumping power than some other alternatives [158]. Clearly, the hypervapotron (HV) should be a prime TM and HHFR approach for ITER and many other future demanding HHFR applications. In the past, design improvements to the HV have "been traditionally sought experimentally which is both inefficient and costly" [156]--especially when improvements are sought without knowledge of the TM and HHFR controlling parameters.

Therefore, the HV is an excellent candidate for TM in cases where single-side HHFR is of prime importance. In order to effectively characterize additional optimal operating characteristics using computational fluid dynamics (CFD) and/or experimental approaches (EA, and/or design approaches (DA)), knowledge of the controlling TM hypervapotron parameters would be essential for timely HHFR enhancement configuration identification. The HHFR in a HV involves conjugate heat transfer which is characterized by both flow parameters (e.g., the Reynolds and Prandtl numbers) as well flow channel parameters (e.g., the Biot number). Further, there will be also unique geometric and heat transfer parameters associated with the hypervapotron fins. A combination of all these parameters must establish a basis for defining optimal [159, 141] operating conditions. From the HV flow channel (HFC) model (see Figure 229) used in Part 21.1 of this work [161], three controlling parameters and a characteristic temperature were identified: (1) $Bi = h_{eq}\, t/k_1$, (2) w_c/t, (3) $(w/2 - w_c)/L^*$, and (4) $q''_\infty\, w_c/k\, T^*$. Although most of these quantities are illustrated in Figures 229 and 227, Bi is the Biot number which includes the HV wall and fin heat transfer and geometric parameters, L^* is a yet unidentified characteristic length, and T^* is a characteristic HV temperature (in degrees Kelvin).

Once HHFR HV controlling parameters have been identified, a suitable [162] computational fluid dynamic (CFD) code must be used for HV design and optimization. Milnes, Burns, and Drikakis [156] recommended a RANS-based multiphase CFD code.

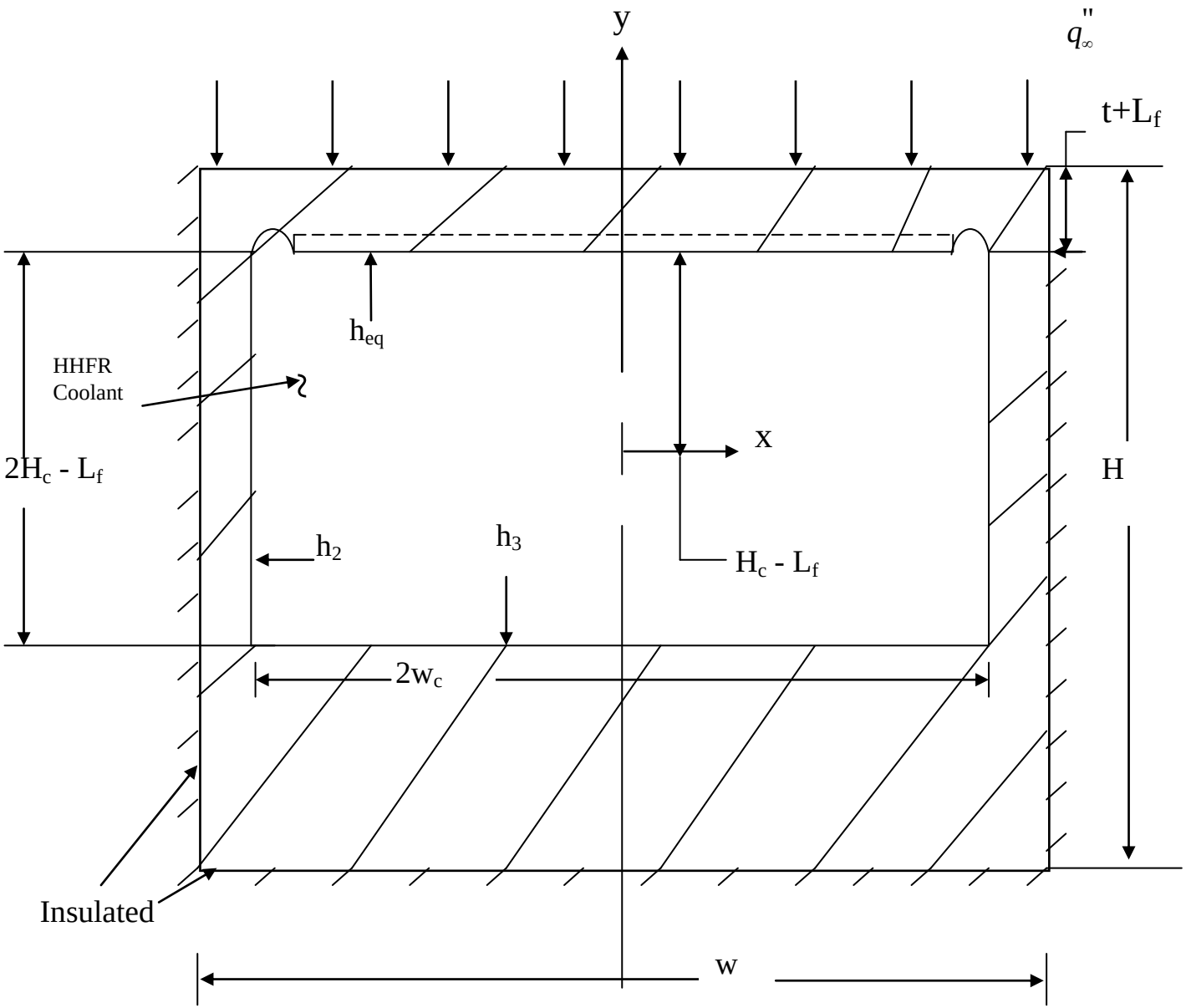

Figure 229: Simplified 2-D HFC Unit Cell Used for Modeling.

Pascal-Ribot et al. [163] recommended the coupled computer codes Neptune CFD and Syrthes. Ovchinniko, et al. [164] investigated a HHFR enhancing modification to the HV which included for example "chevron" fins or fins which are at a different angle relative to the coolant flow as compared to the HV fin-coolant normal flow angle. Lee et al. [165] used the ANSYS CFX-II CFD code for HV simulation comparisons with experimental data and obtained large differences. For a 2nd qualification of the ITER first wall, Lee et al [166] had better agreement. Wang, Song, and Huang [158, 167] studied six (6) HV fin configurations and concluded that the triangle fin "against the flow direction" was most effective. Mazul et al. [168] upgraded the ITER first wall design to improve resistance to electromagnetic loads while using a HV coolant channel with CuCrZr – SS bimetallic walls. Cattadori et al. [169] presented boiling curves and other data for a modified HV for high heat fluxes (above 10 MW/m^2) and as a function of the fin geometric dimensions. Escourbiac et al. [170], based on HV tests up to 25 MW/m^2 with up to 1000 cycles and up to 15 MW/m^2 with up to 3000 cycles (and a critical heat flux higher than 30 MW/m^2), concluded that CuCrZr HV armoured with flat tiles of carbon fibre composite Sepcarb NS31 is a mature industrial solution for ITER.

The focus of this work is to investigate some fundamental aspects of HHFR that will increase the possibility of determining additional HHFR controlling parameters for a HV which is subjected to a heat flux from a single-side.

21.2.3. MODEL

Although the incident heat flux $\left(q''_{\infty}\right)$ is a significant function of the flow channel axial coordinate, it will be assumed constant for the initial modeling effort. This limitation will be relaxed and included in future work after the 2-D characterization is completed. The HFC shown in Figure 229 is a unit cell of an array of such units which make up the basic aspects of the HHFR system. This figure will be used to develop the model for the 2-D HFC unit cell. The model was subdivided into the domains shown in Figure 227. The two-dimensional steady-state thermal diffusion equation was used to obtain the local wall temperature distributions for Domains I [161], II, and III.

21.2.4 MODEL DEVELOPMENT DOMAIN RESULTS

The results for Domain I (with k now being replaced by k_I) was completed by Boyd [161] in Section 21.1 [161] of this work. As Boyd noted, complexities can be avoided if the y-coordinate is relocated to the location shown in Figure 227. The remaining analysis employs this

coordinate relocation. An illustration of how all domains were examined is given below for Domain II and in reference [161] for Domain I.

Because of the three nonhomogeneities in the θ_{II} formulation, let

$$\theta_{II}(x,y) = \theta_{II_1}(x,y) + \theta_{II_2}(x,y) + \theta_{II_3}(x,y); \tag{21.2-1}$$

where the boundary conditions are summarized in Figure 230.

Therefore,

$$\theta_{II_1}(x,y) = \sum_{n=1}^{\infty} E_{II_{1_n}} \left[e^{\lambda_{II_{1_n}} x} + e^{\lambda_{II_{1_n}}(w-x)} \right] \cos\left(\lambda_{II_{1_n}} y\right), \tag{21.2-2a}$$

where,

$$\lambda_{II_{1_n}} = \frac{n\pi}{2t}, \text{ with n = 1, 3, 5, ...;} \tag{21.2-2b}$$

and the coefficient $E_{II_{1_n}}$ is given by

$$E_{II_{1_n}} = \frac{\int_o^t \theta_I(x,y)\big|_{x=w_c} \cos\left(\lambda_{II_{1_n}} y\right) dy}{\left[e^{\lambda_{II_{1_n}} w_c} + e^{\lambda_{II_{1_n}}(w-w_c)} \right] \int_o^t \cos^2\left(\lambda_{II_{1_n}} y\right) dy}, \tag{21.2-2c}$$

where θ_I (x,y) is given by Boyd [161]. Another coordinate transformation (see Figure 230) was used to obtain a simplified form for θ_{II_2}; so that,

$$\theta_{II_2} = \sum_{n=1}^{\infty} E_{II_{2_{1_n}}} \cos\left(\lambda_{II_{2_{1_n}}} x_1\right) \left[e^{\lambda_{II_{2_{1_n}}} y} - e^{\lambda_{II_{2_{1_n}}}(2t-y)} \right] \tag{21.2-3a}$$

where,

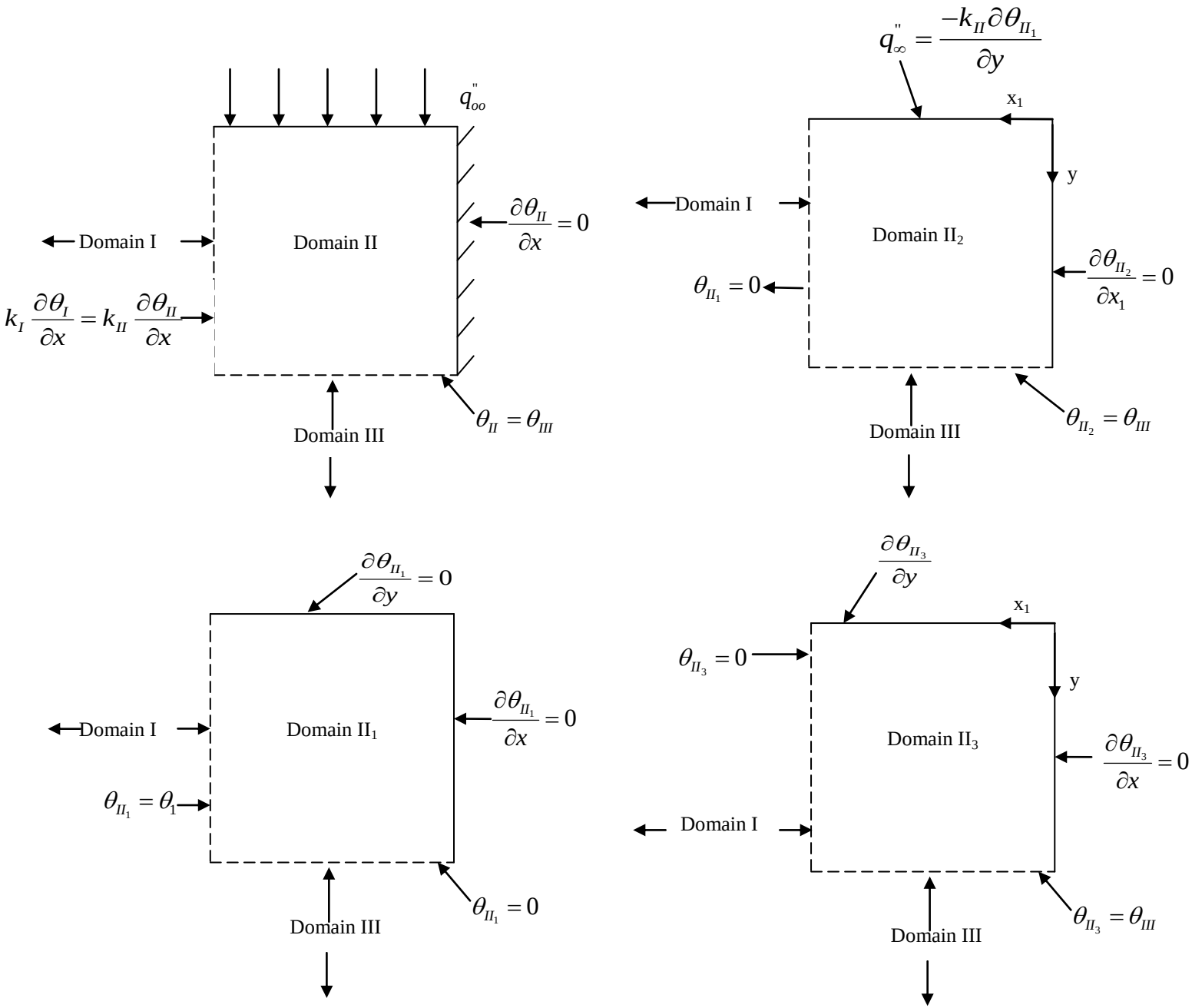

Figure 230: Domain II (a), and Its Sub-Domains II_1, II_2, and II_3 (Figures b, c, d, respectively.

$$E_{II_{2_{1_n}}} = \frac{\int_o^{\frac{w}{2}-w_c}\left[\frac{-q''_{oo}}{\lambda_{II_{2_{1_n}}} k_{II}\left(1+e^{2t\lambda_{II_{2_{1_n}}}}\right)}\right]\cos\left(\lambda_{II_{2_{1_n}}} x_1\right)dx_1}{\int_o^{\frac{w}{2}-w_c}\cos^2\left(\lambda_{II_{2_{1_n}}} x_1\right)dx_1}. \quad (21.2\text{-}3b)$$

n = 1, 3, 5, and (21.2-3c)

$$\lambda_{II_{2_{1_n}}} = \frac{n}{\left(\frac{w}{2}-w_c\right)}\frac{\pi}{2} = \frac{n\pi}{\left(w-2w_c\right)}\ldots, \quad (21.2\text{-}3d)$$

The final sub-domain temperature distribution for Domain II is given by

$$\theta_{II_3} = \sum_{n=1}^{\infty} E_{II_{3_n}} \cos\left(\lambda_{II_{2_{1_n}}} x_1\right)\left[e^{\lambda_{II_{3_n}}} + e^{-\lambda_{II_{3_n}} y}\right],\ \text{n = 1, 3, 5, 7, … },\ \lambda_{II_{3_n}} = \frac{n\pi}{\left(w-2w_c\right)},\ \text{and} \quad (21.2\text{-}4a)$$

$$E_{II_{3_n}} = \frac{\int_o^{\frac{w}{2}-w_c}\left[\frac{\theta_{III}\big|_{y=t}}{\left(e^{\lambda_{II_{3_n}} t} + e^{-\lambda_{II_{3_n}} t}\right)}\right]\cos\left(\lambda_{II_{3_n}} x_1\right)dx_1}{\int_o^{\frac{w}{2}-w_c}\cos^2\left(\lambda_{II_{3_n}} x_1\right)dx_1} \quad (21.2\text{-}4b)$$

For Domain III, let

$$\theta_{III}\left(x,y\right) = \theta_{III_1} + \theta_{III_2}, \quad (21.2\text{-}5)$$

where

$$\theta_{III_1} = \sum_n D_{III_{1_n}} \cos\left(\lambda_{III_{1_n}} x_1\right)\left[e^{\lambda_{III_{1_n}} y} - e^{\left[\lambda_{III_{1_n}}\left(2\left[t+H_c\right]-y\right)\right]}\right], \quad (21.2\text{-}6a)$$

$$D_{III_{1_n}} = \frac{\int_o^{\frac{w}{2}-w_c}\left[\frac{\theta_{II}\big|_{y=t}}{\left(e^{\lambda_{III_{1_n}} t} - e^{\left[\lambda_{III_{1_n}}\left(2H_c+t\right)\right]}\right)}\right]\cos\left(\lambda_{III_{1_n}} x_1\right)dx_1}{\int_o^{\frac{w}{2}-w_c}\cos\left(\lambda_{III_{1_n}} x_1\right)dx_1}, \quad (21.2\text{-}6b)$$

$$\frac{1}{Bi_2} = \frac{\cot\left[\lambda_{III_{1_n}}\left(\frac{w}{2} - w_c\right)\right]}{\left[\lambda_{III_{1_n}}\left(\frac{w}{2} - w_c\right)\right]}, \text{ and} \tag{21.2-6c}$$

$$Bi_2 = \frac{h_2\left(\frac{w}{2} - w_c\right)}{k_{III}}, \tag{21.2-6d}$$

where n and λ_{III_1} will be determined by eq (21.2-6c). Because of the similarity between the convective-conductive boundary condition of Domains III_1 and III_2, $\lambda_{III_2} = \lambda_{III_1}$. Further,

$$\theta_{III_2} = \sum_n D_{III_{2_n}} \cos\left(\lambda_{III_{2_n}} x_1\right)\left[e^{\lambda_{III_{1_n}} y} - e^{\left[\lambda_{III_{1_n}}(2t-y)\right]}\right], \tag{21.2-7a}$$

where

$$D_{III_{2_n}} = \frac{\int_o^{\frac{w}{2}-w_c}\left[\frac{\theta_{IV}\big|_{y=t+2H_c}}{\left(e^{\lambda_{III_{1_n}}(t+2H_c)} - e^{\left[\lambda_{III_{1_n}}(t-2H_c)\right]}\right)}\right]\cos\left(\lambda_{III_{1_n}} x_1\right)dx_1}{\int_o^{\frac{w}{2}-w_c} \cos^2\left(\lambda_{III_{1_n}} x_1\right)dx_1}. \tag{21.2-7b}$$

The last effect that will be included in this Part is the hypervapotron fins. In this model, the effect of the fins is completely included in h_{eq}, which is given by [171]

$$h_{eq} = h_1 \eta_o \left(\frac{A_T}{A_b}\right) \tag{21.2-8}$$

where a 1-D fin analysis was used and h_1 is the mean heat transfer coefficient for the hypervapotron fin sides (h_e will later be used as the fin tip heat transfer coefficient) and bare areas between the fins, η_o is the overall finned surface efficiency, A_T/A_b is the ratio of the total surface area of the finned surface to that of the downward facing flow channel surface if it did not have fins. In addition, the classical literature (e.g. [171]) defines η_o as

$$\eta_o = 1 - \frac{NA_f}{A_T}\left(1-\eta_f\right) \tag{21.2-9}$$

where a 1-D fin analysis is assumed, N is the number of fins used in a monoblock unit cell, A_f is the exposed surface area of a single fin, and η_f is the fin efficiency. For the straight, rectangular cross-section fins of the typical hypervapotron, η_f is given by

$$\eta_f = \frac{1}{\left(Bi_{f_1}/\delta^*\right)^{\frac{1}{2}}\left(1+\delta^*\right)}\left[\frac{\sinh\left(mL_f\right)+Bi_{f_2}\cosh\left(mL_f\right)}{\cosh\left(mL_f\right)+Bi_{f_2}\sinh\left(mL_f\right)}\right] \tag{21.2-10}$$

and where δ is the fin thickness, L_f is the fin length,

$$w_1 = 2w_c - 2w_f, \delta^* = \left[\frac{\delta/L_F}{2\left(1+\frac{\delta}{w_1}\right)}\right], Bi_{f_1} = \frac{h_1 L_f}{k_I}, Bi_{f_2} = \frac{h_1}{mk_I}, \text{ and}$$

$$m = \left[2h_1\left(\delta/w_1+1\right)/k_I\delta\right]^{\frac{1}{2}}. \tag{21.2-11}$$

For some HHFR flow conditions, the simplier approximation [171] for η_f cannot be used. Further, other contributions to the above are the following area ratios,

$$\frac{A_T}{A_b} = \frac{2\frac{L_f}{\delta}\left(1+\frac{\delta}{w_1}\right)+1}{\left(\frac{S}{\delta}\right)-1} = \frac{\delta^{*^{-1}}+1}{\frac{S}{\delta}-1}, \text{ and } \frac{NA_f}{A_T} = \left[1+\frac{\left(\frac{S}{\delta}-1\right)}{\left(\delta^{*^{-1}}+1\right)}\right]^{-1}. \tag{21.2-12}$$

21.2.5. ADDITIONAL HV CONTROLLING PARAMETERS

The characteristic reference temperature (T^*) was included in Part 21.1 [161] but was not specified. From Domain II, T^* could be defined using eqs (21.2-3b) and (21.2-3d) as

$$\frac{q''_\infty\left(\frac{w}{2}-w_c\right)}{k_{II}} \tag{21.2-13}$$

or using Domain I, it could be defined as

$$T^* = \frac{q''_\infty w_c}{k_I}. \tag{21.2-14}$$

Since eq (2.1.2-14) will result in the highest reference temperature, this will be used for T^*, with T^* being in units of degrees Kelvin. Further, the unspecified characteristic length (L^*) in Part I can now be determined by referring to eqs (21.2-4a) and (21.2-4b), and it is given by

$$L^* = t. \tag{21.2-15}$$

When T^* is used in eq. (21.2-3), the following additional parameter results:

$$\frac{\left(\frac{w}{2} - w_c\right)k_I}{w_c\, k_{II}} \text{ or } \frac{k_I}{k_{II}}\left(\frac{w}{2w_c} - 1\right). \tag{21.2-16}$$

From eqs (21.2-6a), (21.2-6b), and (21.2-7b) three additional parameters appear:

$$\mathrm{Bi}_2 = \frac{h_2\left(\frac{w}{2} - w_c\right)}{k_{III}}, \quad \frac{2\mathrm{H_c} + t}{\frac{w}{2} - w_c}, \text{ and } \quad \frac{2\mathrm{H_c} - t}{\frac{w}{2} - w_c}, \tag{21.2-17}$$

where the latter two parameters appear to be similar. For the fins, the parameters are η_o, and $\frac{\mathrm{A_T}}{\mathrm{A_b}}$ where m is given in eq (21.2-11). It should be noted that η_o, η_f, $\frac{\mathrm{A_T}}{\mathrm{A_b}}$, $\frac{\mathrm{NA_f}}{\mathrm{A_T}}$ are controlled by the following parameters: (1) $\mathrm{mL_f}$, (2) δ^*, (3) S/δ, (4) Bi_{f_1}, and (5) Bi_{f_2}.

The conjugate heat transfer parameters can be defined as internal and external. Internal or fluid flow parameters such as the Reynolds and Prandtl numbers will have a direct influence on the heat transfer coefficients which appeared in specified boundary conditions. The effect of these internal parameters is included in resulting HV parameters summarized below. Another internal parameter which will greatly influence the convective HHFR capability is $(\mathrm{H_c} - \mathrm{L_f}/2)/\mathrm{w_c}$,

which represents the un-obstructed flow aspect ratio (AR). The AR will clearly affect [147, 151] HHFR enhancement.

21.3 SUMMARY OF CONTROLLING PARAMETERS

21.3.1 OVERVIEW

A hypervapotron is an excellent candidate for high heat flux removal (HHFR) in cases where single-side heat flux removal is of prime importance. In order to effectively characterize additional optimal operating characteristics using computational fluid dynamics (CFD) and/or experimental approaches (EA, and/or design approaches (DA)), knowledge of the controlling HHFR hypervapotron parameters would be essential for timely enhancement configuration identification. To that end, three controlling parameters have been identified in this third part of a three-part study. Sections 21.1 and 21.2 of this study resulted in HHFR control parameters for other conjugate heat transfer and geometric aspects. Local temperature distribution closure relations have been identified. Finally, these parameters could be useful in CFD (and EA and/or DA) studies for optimizing HHFR and thermal protection. These results can be considered as enabling HHFR technology for aerospace and nuclear systems.

21.3.2 INTRODUCTION

Efficient high heat flux removal (HHFR) in single-side heated engineering components is essential for long-term, robust, and safe operation. Recently, Milnes, Burns, and Drikakis [156] and Boyd [161] noted that “fusion power (Divertor)” and aerospace/aerodynamic components are among engineering components requiring the highest HHFR demands. Among the many approaches [156] to accommodate these demands, hypervapotron cooling [141, 146, 147, 156, 159, 161, and 172-175] is a foremost possibility (see Fig. 222).

This section is the third part of a three-part study (see Sections 21.1 and 21.2) focusing on identifying some physical HHFR controlling parameters of the hypervapotron (HV). Depending on the absorbed heat flux level for a given application, the conjugate heat transfer and fluid flow in Fig. 222 could be turbulent, developing, and/or two-phase (with local subcooled boiling) flow. The controlling parameters can be classified into three physical group types: (1) thermophysical flow parameters, (2) geometric parameters, and (3) conjugate parameters. Further, the geometric parameters can be classified as: (1) internal flow channel parameters, (2) internal flow fin parameters, (3) combined flow channel/fin parameters, and (4) flow channel wall parameters. Any attempts in using design, experimentation, or computational fluid dynamics (CFD) to optimize (e.g., [147, 156, and 159]) the HHFR of a hypervapotron must employ critical

controlling parameters from the above classification types. Examples of internal thermophysical flow parameters which may be inclusive in conjugate parameters are the: (1) Reynolds numbers, (2) Prandtl number, (3) Boiling number, (4) Weber number, (5) Peclet number, (6) Marangoni number, and (7) relative fluid subcooling.

What are the geometric and conjugate controlling parameters? This three-part study has focused on identifying parameters in these two groups. The simplified model shown in Fig. 229 was used as a 2-D cross-sectional representation of the HV; and, this representation is further illustrated in Fig. 227 with the HV walls sub-divided into five subsections (Domains I, II, III, IV, and V) and with different characteristic channel wall thermal conductivities and heat transfer coefficients (HTC) on the three inside flow channel walls. The HTC on the top wall includes the effects of the HV fins [175]. Sections 21.1 and 21.2 of this study have produced functional forms for the: (1) local peaking factor associated with Domain I; (2) local wall temperature (and heat flux) distributions for Domains I, II, and III; and (3) seven geometric and conjugate controlling parameters.

21.3.3 MODEL DEVELOPMENT

The model development will focus on Domains IV and V. Fig. 231 will be used in examining Domain IV. Let

$$T_{IV} = T_{IV_1} + T_{IV_2}. \qquad (21.3\text{-}1)$$

Following the previous results (e.g., for Domains II_2 and II_3 [175]),

$$T_{IV_1}(x_1\, y_1) = \sum_{n=1}^{\infty} E_{IV_1} \cos\left(\lambda_{IV_1} x_1\right) \cosh\left(\lambda_{IV_1} y_1\right), \qquad (21.3\text{-}2)$$

where

$$\lambda_{IV_1} = \frac{n\pi}{2} \frac{1}{\left(\frac{w}{2} - w_c\right)},\ \text{n = 1, 3, 5, 7, ...,} \qquad (21.3\text{-}3)$$

and the x_1 & y_1 coordinates are shown in Figure 231. Further E_{IV_1} is obtained from the condition at $y_1 = H - 2H_c - t = H_1$ or

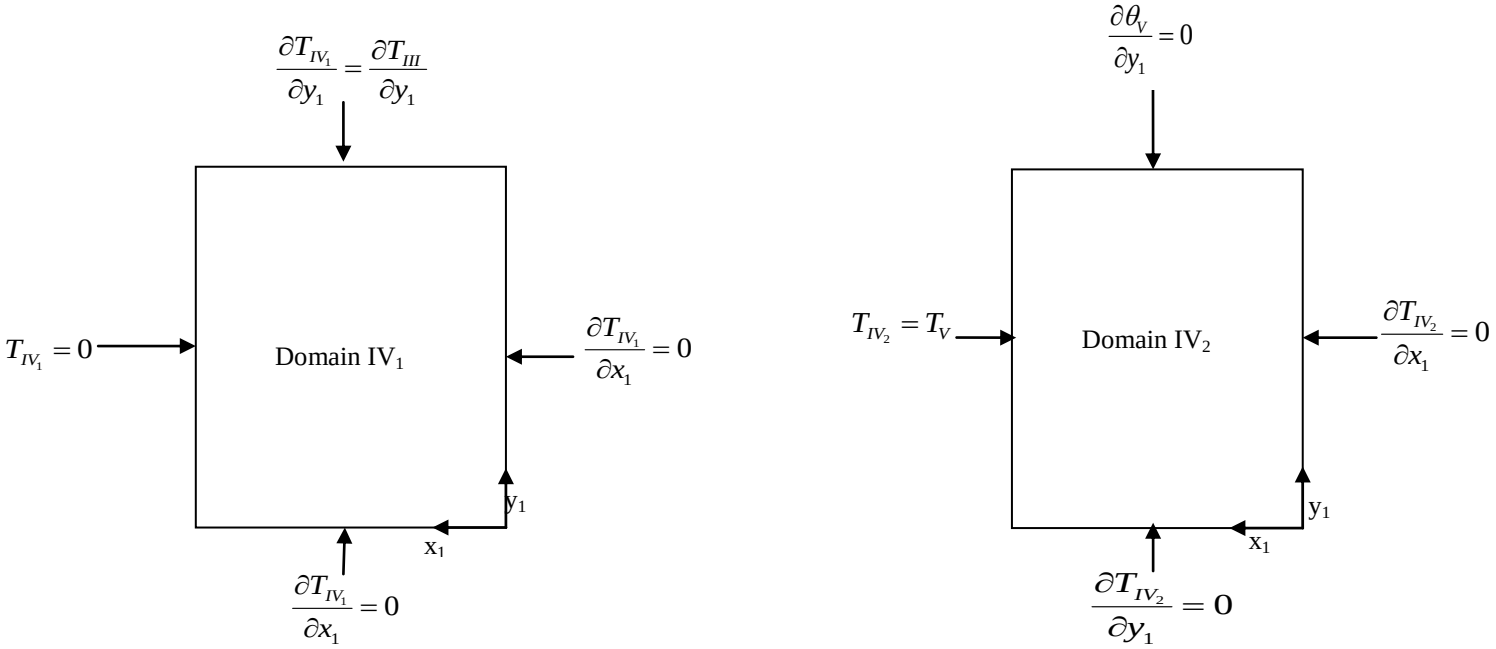

Figure 231: Boundary Conditions for Domain IV Using New Coordinates.

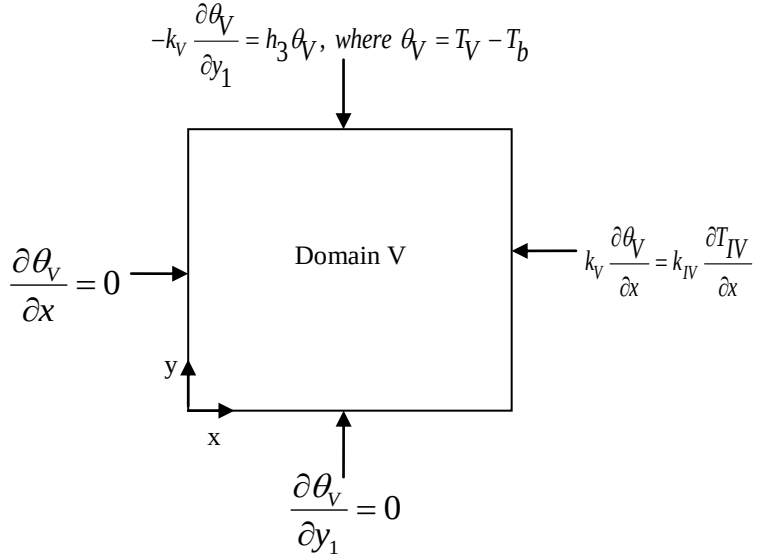

Figure 232: Domain V.

where

$$\left.\frac{\partial T_{III}}{\partial y_1}\right|_{y_1=H_1} = \sum_{n=1}^{\infty} E_{IV_1} \cos\left(\lambda_{IV_1} x_1\right) \cosh\left(\lambda_{IV_1} H_1\right), \tag{21.3-4}$$

$$E_{IV_1} = \frac{\int_o^{\frac{w}{2}-w_c} \left.\frac{\partial T_{III}}{\partial y_1}\right|_{y_1=H_1} \cos\left(\lambda_{IV_1} x_1\right) dx_1}{\cosh\left(\lambda_{IV_1} H_1\right) \int_o^{\frac{w}{2}-w_c} \cos^2\left(\lambda_{IV_1} x_1\right) dx_1}, \tag{21.3-5a}$$

and

$$H_1 = H - 2H_c - t. \tag{21.3-5b}$$

Further,

$$T_{IV_2} = \sum_{n_{IV_2}=1}^{\infty} E_{IV_2} \cos\left(\lambda_{IV_2} y_1\right) \cosh\left(\lambda_{IV_2} x_1\right), \tag{21.3-6}$$

where

$$\lambda_{IV_2} = \frac{n_{IV_2}\pi}{H_1},\ n_{IV_2} = 1, 2, 3, \ldots . \tag{21.3-7}$$

The last boundary condition requires

$$T_{IV_2}\Big|_{x_1=\frac{w}{2}-w_c} = T_V\Big|_{x_1=\frac{w}{2}-w_c},\ \text{or} \tag{21.3-8}$$

$$T_V\Big|_{x_1=\frac{w}{2}-w_c} = \sum_{n_{IV_2}=1}^{\infty} E_{IV_2} \cos\left(\lambda_{IV_2} y_1\right) \cosh\left(\lambda_{IV_2}\left[\frac{w}{2} - w_c\right]\right) \tag{21.3-9}$$

which results in

$$E_{IV_2} = \frac{\int_o^{H_1} T_V\Big|_{x_1=\frac{w}{2}-w_c} \cos\left(\lambda_{IV_2} y_1\right) dy_1}{\cosh\left[\lambda_{IV_2}\left(\frac{w}{2} - w_c\right)\right] \int_o^{H_1} \cos^2\left(\lambda_{IV_2} y_1\right) dy_1}, \tag{21.3-10}$$

where the following geometric HV wall parameter results: a parameter associated with the product of

$$\lambda_{IV_2}\left(\frac{w}{2}-w_c\right), \text{ or} \tag{21.3-11}$$

(1) $$\frac{1}{H_1}\left(\frac{w}{2}-w_c\right). \tag{21.3-12}$$

Using the x_1–x $\left(x_1=\frac{w}{2}-x\right)$ transformation, eq. (21.3-6) shows that another geometric parameter results:

(2) $$\frac{w}{2}\lambda_{IV_2} \text{ or } \frac{w/2}{H_1}. \tag{21.3-13}$$

The boundary conditions of the last domain, Domain V, are illustrated in Fig. 243. Domain V is similar to Domain I; or,

$$\theta_V\left(x,y_1\right)=\sum_{n=V}^{\infty}a_V\cosh\left(\lambda_V\,x\right)\cos\left(\lambda_V\,y_1\right), \tag{21.3 -14}$$

where

$$Bi_3=\frac{\cot\left(\lambda_V\,H_1\right)}{\left(\lambda_V\,H_1\right)}, Bi_3=\frac{h_3\,H_1}{k_V}, \tag{21.3-15}$$

$$k_{IV}\left.\frac{\partial T_{IV}}{\partial x}\right|_{x=w_c}=\sum_{n_V=}^{\infty}k_{IV}\,\lambda_V\,a_V \sinh\left(\lambda_V w_c\right)\cos\left(\lambda_V y_1\right), \tag{21.3-16}$$

$$a_V=\frac{k_{IV}}{\lambda_V k_V\sinh\left(\lambda_V w_c\right)} \frac{\int_o^{H_1}\left.\frac{\partial T_{IV}}{\partial x}\right|_{x=w_c}\cos\left(\lambda_V y_1\right)dy_1}{\int_o^{H_1}\cos^2\left(\lambda_V y_1\right)dy_1}. \tag{21.3-17}$$

From the last relations, the following conjugate and geometric parameters result:

(3) $$Bi_3=\frac{h_3\,H_1}{k_V} \tag{21.3-18}$$

(4) $$\lambda_V\,w_c\sim\frac{w_c}{H_1} \tag{21.3-19}$$

with Bi_3 being a nested parameter for λ_V;

$$\lambda_{IV_2}\left(\frac{w}{2}-w_c\right)\sim\frac{w/2-w_c}{H_1},\ \text{and} \tag{21.3-20}$$

$$\frac{k_{IV}}{k_V}, \tag{21.3-21}$$

where the former parameter has already appeared and the impact of the latter parameter may be minimal. Further, the combination of parameters **#(1)** and **#(2)** above may diminish the need for parameter **#(4)**. Thus, parameters **#(1)**, **(2)**, and **(3)** are unique HV HHFR control parameters from the analysis of Domains IV and V. Finally, equations (21.3-6) through (21.3-10) and (21.3-14) through (21.3-17) represent closure relations for the model's local temperature and heat flux distributions.

21.3.4 SECTIONS 21.1 AND 21.2 CONTROL PARAMETERS

From Section 21.1 [161], the identified parameters were:

(5) $Bi=\dfrac{h_{eq}t}{k_I}$,

(6) w_c/t, and (21.3-22)

(7) $\left(w/2-w_c\right)/t$.

From Section 21.2 [175], the parameters found were:

(8) $\dfrac{\mathrm{k_I}}{k_{II}}\left(\dfrac{w}{2w_C}-1\right)$, (21.3-23)

(9) $\mathrm{Bi_2}=\dfrac{\mathrm{h_2}\left(\dfrac{w}{2}-w_C\right)}{k_{\mathrm{III}}}$, (21.3-24)

(10) $\dfrac{2\mathrm{H_C}+t}{\dfrac{w}{2}-w_C}$, and (21.3-25)

(11) $\left(\mathrm{H_C}-L_f/2\right)\Big/w_C$ (21.3-26)

where the characteristic reference temperature in degrees Kelvin is

$$T^*=q_\infty^{''}\,{}^{w_C}\!\!\diagup\!\!{}_{k_I}. \tag{21.3-27}$$

Additional HV rectangular/straight fin configuration-dependence and relate control parameters are also covered in Section 21.2 [175]. However, the definition of h_{eq} applies to any fin cross-section or orientation.

22.0 PEAKING FACTOR CORRELATION AND POWER DISTRIBUTION SYSTEM

22.1 PEAKING FACTOR CORRELATION

22.1.1 OVERVIEW

Unanticipated high heat flux amplification in thermal management schemes can compromise or limit the optimization in new and emerging engineering systems. A conjugate thermal management and heat flux removal finite element analysis simulation was developed with excellent resulting accuracy for predicting heat flux amplification and the peak inside wall temperature $\left(T_{wi_{\max}}\right)$ in single-side heated flow channels. The simulation was expanded in this section by developing a conceptual model which identifies some of the parameters controlling the amplification. Although the model appears to be fluid- and flow regime-independent, more work is required to validate this. The model was used to develop amplification and $T_{wi_{\max}}$ correlation comparisons for a single-side heated monoblock with a circular flow channel. At a 1.5 MW/m^2 incident absorbed heat flux, the model predictions had excellent agreement with the simulation and prototype predictions. At this heat flux for example, the model amplification prediction was 1.20 – i.e., the inside flow channel maximum heat flux was 20% higher than the incident heat flux. The corresponding amplification predictions for the simulation and prototype were 1.22 and 1.20, respectively. Finally, the model was developed to be applicable in the r_i - ϕ_o region and had very good inside wall radial heat flux and temperature circumferential distribution predictions.

22.1.2 INTRODUCTION

An evolving myriad of thermal management-dependent technologies require the accommodation of higher and higher heat flux levels. With increasing technological demands involving high heat flux removal and advanced thermal management, the capability of many future engineering systems may be either seriously limited or unknowingly compromised. In other cases, "a large safety factor is typically assumed for the thermal protection system…" [150]. By properly incorporating thermal management advances, applicable future engineering systems will be more efficient and robust, and safer. This engineering development must be based on proven fundamentals of high heat flux removal and thermal management. For example, some typical applications require steady-state heat flux levels between: (1) 0.5 and 25.0 MW/m^2 in hypersonic and supersonic vehicles [177, 178], (2) 0.01 and 25.0 MW/m^2 in energy [140,

149], and (3) 0.01 and 4.0 MW/m^2 in electronic systems. To accommodate these heat flux levels, both basic and applied thermal management and high heat flux removal techniques may include, an applicable fluid flow with, for example: (1) transpiration cooling [177], (2) swirl twisted tape or helical wire inside a circular flow passage [138, 179], (3) hypervapotron [143, 144], (4) fibrous porous structure [177], (5) honeycomb porous media, (6) micro-pin and pin-fin heat sinks [180], (7) spray cooling [181] and jet impingement, (8) venturi flow [182], or (9) combined cooling techniques [183].

Depending on the specific geometrical configuration of the high heat flux removal technique, the incident heat flux could be amplified as much as 40% [83, 153, and 154]. In designs which are based on incident heat flux levels, such un-noted amplifications could compromise robustness, component survivability, or even human safety. Therefore, fundamental heat flux peaking factor studies must be incorporated into the matrix of thermal management concerns in future system development and design.

Recently, a numerical conjugate heat transfer heat flux peaking factor simulation [140] was developed for the single-side heated (SSH) monoblock (e.g., for a rocket engine combustion chamber, see [139]; and for nuclear fusion components, see [138]) flow channel shown in Fig. 233. The dashed line in Fig. 233 represents the outer boundary for the simulation geometry. The term "monoblock" in the context of this section refers to a SSH device with an internal coolant channel. The monoblock was subjected to a single-side heat flux and was cooled internally (e.g., with flow boiling, jet impingement or spray cooling). The resulting accuracy of the finite element analysis simulation (see Fig. 234) was excellent for incident heat fluxes between 1.5 and 20.0 MW/m^2 [140]. For example, a thermal management or high heat flux removal system might include a compilation of tens, hundreds, or thousands of monoblock unit cells (see Fig. 233). System and development design efforts, with effective thermal management and high heat flux removal, could be enhanced by the existence of a heat flux peaking factor correlation. To the PI's knowledge, the peaking factor correlation by Boscary et al. [83] appears to be the only one in the technical literature. Further, their correlation was applied only to Glidcop A1-25 and had no dimensionless direct thermophysical or thermal-hydraulic parameter dependence for a heat flux < the critical heat flux (CHF) but was dependent on: (1) w/r_i ($2.66 < w/r_i < 3.4$), and (2) t/r_i ($0.16 < t/r_i < 0.6$), where t is the distance the flow channel is located below the surface with the incident heat flux q''_{oo}. However, their correlation was developed for a range of inlet water

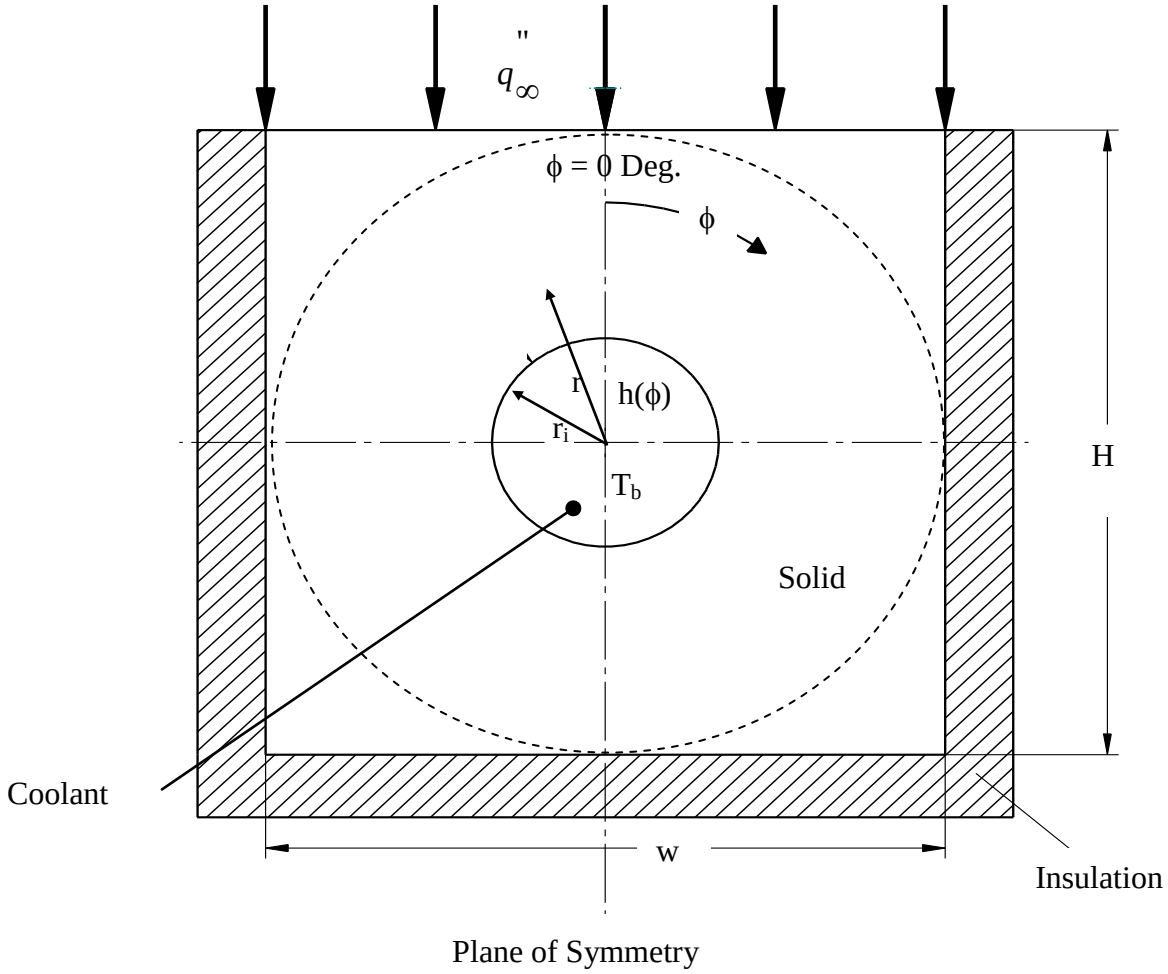

Figure 233: Typical Prototype Monoblock Flow Channel Used For High Heat Flux Removal and Thermal Management.

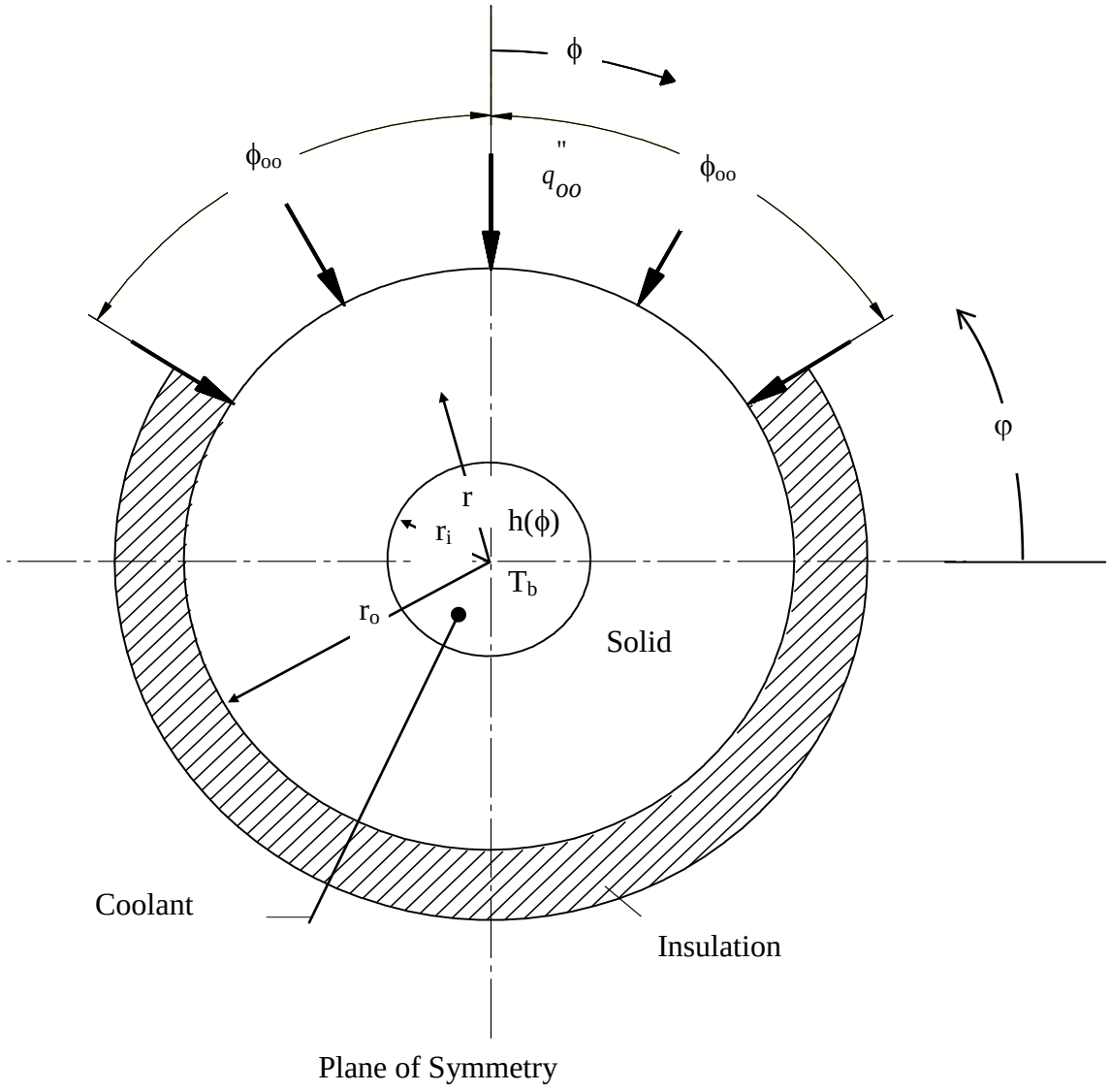

Figure 234: Thermal Management High Heat Flux Peaking Factor Conceptual Model Geometry.

temperature (50-170 0C), outlet pressure (1.3-3.5 MPa) and mass flow rate (5.0-15.0 Mg/m^2s). Federici and Raffray [153] evaluated peaking factors in a number monoblock/tube insert combinations (e.g., carbon fibre composites or CFC monoblock with and without a copper alloy insert or a copper alloy monoblock with and without 316 stainless steel insert). In addition, Raffray et al. [154] noted that "the heat flux peaking factor needs also to be better assessed for the prototypical geometries." This is no doubt tied to a need they noted previously of performing additional high heat flux testing for different geometries to "better [assess] the CHF performance" and provide "a reasonable CHF margin." That work was presented as functions of t and w for a carbon fibre composite monoblick with a CuCrZr tube insert. Further, Boscary et al. [82] performed a dimensional analysis of subcooled flow CHF for SSH monoblock geometries. They also characterized the inside flow channel wall heat flux and temperature distributions by two dimensionless numbers: (1) "a peaking factor," and (2) "a full width angle at half maximum of wall heat flux at the inner wall…." Both they [82] and Boyd [30] (also see Boyd and Meng [24]) addressed the differences between SSH and uniformly heated coolant channels. Recently, Boyd [161] reemphasized how these differences can be used to enhance (see Boyd [30]) and increase heat flux removal limits and reduce heat flux peaking factor in SSH coolant channels.

Based on the success of the previously noted simulation [140], the present work involves the development of a thermal management high heat flux peaking factor conceptual model. If the model has similar success as the simulation, it will provide a conceptual advantage of identifying dimensionless physical groups and parameter combinations which affect both the local radial heat flux peaking factor and the peak inside wall temperature of the flow channel. Because this initial model development is exploratory, it retained only the basic elements of the simulation. Because reasonable success was achieved, additional prototype complexities will be added in the future. However, the present model provides functional relationships which may be useful in future design and development studies.

22.1.3 HEAT FLUX PEAKING FACTOR CONCEPTUAL MODEL

The motivation for the present model (see Fig. 234), and the possibility of excellent accuracy near $r = r_i$ and $\phi = 0$ (referred to below as the r_i - ϕ_o region), came from observations from many previous studies found in the technical literature (e.g., see [83, 139, 153, and 154]). Fundamentally, the location of highest heat flux and the eventual critical heat flux $\left(q''_{CHF}\right)$ and

"burnout" is in the r_i - ϕ_o region. As such, the r_i - ϕ_o region is the location where the most efficient high heat flux removal initially (i.e., at moderate heat flux levels compared to q''_{CHF}) occurs for heat fluxes < q''_{CHF}. This is also the region where the prototype monoblock and simulation geometries and boundary conditions influence have the best matching. Decreasing heat flux removal initially occurs with increasing $\phi > 0$ and $r > r_i$. These observed characteristics are all well suited to the results from the present model of: (1) excellent simulation in the r_i - ϕ_o region, where r is near r_i, (2) very good simulation for $\phi = 0$, and (3) qualitative simulation for other locations when $r < r_o$. Not surprising, the worst simulation (as high as 50% inaccuracy) occurred [140] at the largest value of r (= r_o) for $\phi > 0$. These latter locations denote a region where the monoblock and the simulation geometries are drastically different, and far, far away from the region of high heat flux simulation. This is the region where the monoblock and simulation have the greatest mismatch.

The heat flux peaking factor and $T_{wi_{\max}}$ models will be developed initially to predict these quantities for Fig. 233; and, Fig. 234 will be used as a basis for the model development. From Fig. 234, the two dimensional (radial and circumferential) steady-state thermal energy equation and boundary conditions for the solid flow channel with constant thermal properties and heat transfer coefficient are:

$$\frac{1}{r^2}\frac{\partial^2 T}{\partial \phi^2}+\frac{1}{r}\frac{\partial}{\partial r}\left(r\frac{\partial T}{\partial r}\right)=0 \qquad (22.1\text{-}1)$$

or

$$\frac{1}{r^2}\frac{\partial^2 \Theta}{\partial \phi^2}+\frac{1}{r}\frac{\partial}{\partial r}\left(r\frac{\partial \Theta}{\partial r}\right)=0, \qquad (22.1\text{-}2)$$

where,

$$\Theta=\left(T-T_b\right); \qquad (22.1\text{-}3)$$

and the boundary conditions (BC) are as follows:

$$\text{(i) } @\ r=r_i,\ k\frac{\partial \Theta}{\partial r}-h\Theta\Big|_{r=r_i}=0; \qquad (22.1\text{-}4)$$

$$\text{(ii) } @\ r=r_o \quad -k\frac{\partial \Theta}{\partial r}\bigg|_{r=r_o}=\begin{cases}-q''_\infty, & 0\le\phi\le\phi_\infty\\ 0, & \phi>\phi_\infty;\end{cases} \qquad (22.1\text{-}5)$$

$$\text{(iii) } \Theta\left(r,\phi\right)=\Theta\left(r,\phi+2\pi\right);\ \text{and} \qquad (22.1\text{-}6)$$

$$\text{(iv)}\ \left.\frac{\partial \Theta}{\partial \phi}\right|_{\phi=0} = 0. \tag{22.1-7}$$

From the above discussion, the heat flux peaking factor ratio is defined as

$$PF = q''_{w_{i_{\max}}} \Big/ q''_{\infty}, \tag{22.1-8}$$

where $q''_{wi_{\max}}$ is the maximum flow channel wall radial heat flux at r = r_i.

22.1.4 RESULTS

From the exploratory formulation, the dimensionless 2-D temperature conceptual model distribution is given by

$$\Theta^* = \frac{\Theta(r,\varphi)}{\left(\frac{q''_{oo}\, r_o}{k}\right)} = \frac{\phi_{oo}}{180}\left[Bi_m^{-1} + \ln(R)\right]$$

$$+\sum_{n=1}^{oo} \frac{2R_o^{2n}\sin\left(\frac{n\pi}{2}\right)\sin\left(n\phi_{oo}\right)}{\pi n^2 \left(R_o R\right)^n \left[1+\frac{R_o^{2n}}{Bi_n}\right]}\left[\frac{R^{2n}}{Bi_n} - 1\right]\sin\left(n\varphi\right), \tag{22.1-9}$$

where,

$$Bi_n = \frac{Bi_m - n}{Bi_m + n}, Bi_m = \frac{h\, r_i}{k}, R = \frac{r}{r_i}, R_o = \frac{r_o}{r_i}, \tag{22.1-10}$$

and

$$n = 1, 3, 5\ldots .$$

Further, the dimensionless local radial heat flux is given by,

$$q''_*\left(R,\varphi\right) \equiv \frac{-q''\left(r,\varphi\right)}{R_o\, q''_{\infty}} = \frac{\phi_{\infty}}{180} R^{-1} + \frac{2}{\pi}\sum_{n=1}^{\infty} \frac{n\sin\left(n\frac{\pi}{2}\right)\sin\left(n\phi_{\infty}\right)\left(R_o/\ R\right)^n}{n^2\, R\left[1 + Bi_n^{-1}\, R_o^{-2n}\right]}\Big[1$$

$$+\ R^{2n}\, Bi_n^{-1}\Big]\sin\left(n\varphi\right). \tag{22.1-11}$$

Based on Fig. 234, the radial heat flux peaking factor is defined using

$q''\left(R=1,\ \varphi=\ 90 \text{ degrees}\right)$ or,

$$PF \equiv \frac{-q''\left(R=1, \varphi=\ 90 \text{ degrees}\right)}{q''_{\infty}}. \tag{22.1-12}$$

As such, PF is given by

$$PF = R_o \left\{ \frac{\phi_\infty}{180} + \frac{2}{\pi} \sum_{n=1}^{\infty} \frac{n \sin\left(n\frac{\pi}{2}\right) \sin\left(n\phi_\infty\right) R_o^n}{n^2 \left[1 + Bi_n^{-1} R_o^{-2n}\right]} \left[1 + Bi_n^{-1}\right] \sin\left(\frac{n\pi}{2}\right) \right\}. \qquad (22.1\text{-}13)$$

The criterion used to compute ϕ_∞ from Figs. 233 and 234 was determined by requiring the overall incident heat rates be identical for both the model and prototype; and, ϕ_∞ is in circumferential angular units of degrees in Eqs (22.1-11) through (22.1-13).

The results from the temperature model (referred to in all figures as temperature correlation) were compared with finite element analyses for the prototype monoblock (referred to below as monoblock FEA) shown in Fig. 233 and the methodology simulation (referred to below as monoblock simulation FEA) shown in Fig. 234. Each of these cases involved a single-side heated geometry. All results are presented for different radii and for the following conditions: q''_{oo} = 1.5 MW/m^2, T_b = 40°C, k = 365 W/mK, r_i = 5 mm, h = 20.0 $\frac{kW}{m^2 K}$ and a 30 mm by 30 mm cross-section monoblock.

The best anticipated predictions are expected at r = r_i (inside flow channel radius) and ϕ = 0 degrees. As shown in Fig. 235a, the temperature correlation agrees very well with both finite element analysis predictions. However, there is a slightly better agreement with the prototype. Similar, but progressively less accurate temperature correlation, predictions occurred at larger radii of 7.0 (Fig. 235b), 10.0 (Fig. 235c), and 12.0 mm (Fig. 235d). In addition, the temperature correlation predictions for r = r_i are surprisingly good for all circumferential locations. The heat flux model (referred to in all figures as radial heat flux correlation) results are presented in Figs. 236a and 236b for r = r_i (5.0 mm) and r = 7.0 mm, respectively. Because all conceptual model correlations were developed to have the best accuracy at r = r_i and ϕ = 0 degrees, both the temperature (Fig. 235) and radial heat flux (Fig. 236) correlations have very good predictions at this location. As was the case for the temperature correlation, the heat flux predictions for r = r_i are surprisingly good at all circumferential locations. For the above noted conditions and with r = r_i, the best anticipated heat flux peaking factor prediction did occur at r = r_i and ϕ = 0 degrees. More specifically, the model prediction for the peaking factor was 1.20; i.e., the inside maximum radial heat flux was 20% higher than the incident heat flux. The corresponding peaking factor for the finite element analyses for the simulation and prototype

were 1.22 and 1.20, respectively. In all cases, the temperature correlation was slightly better than the heat flux correlation.

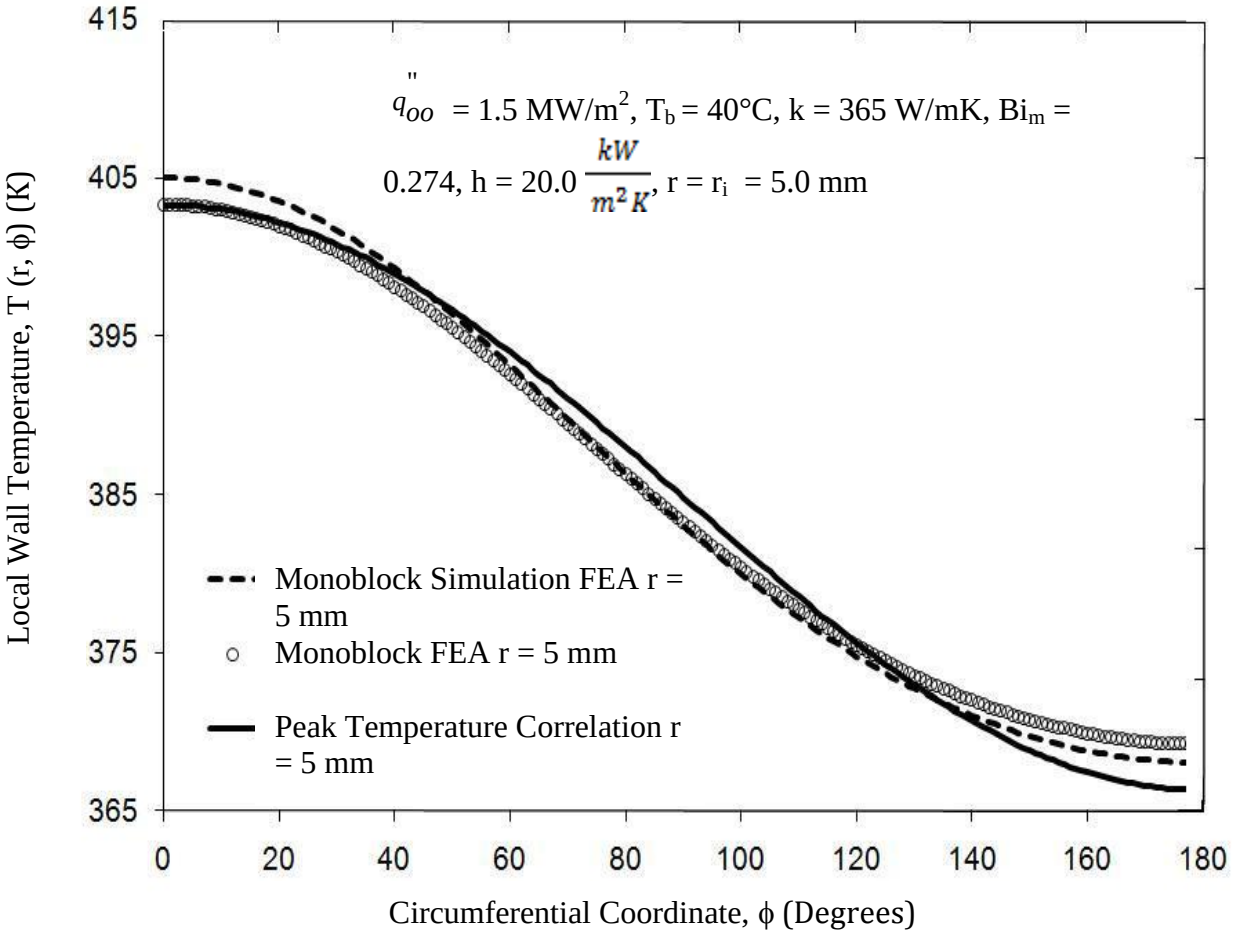

a) r = r_i = 5 mm

Figure 235a: Comparison of the Model's Temperature (Correlation) Circumferential Distribution Predictions with the Prototype Finite Element Analysis (Monoblock FEA) and the Simulation Finite Element Analysis (Monoblock-Simulation FEA) Predictions.

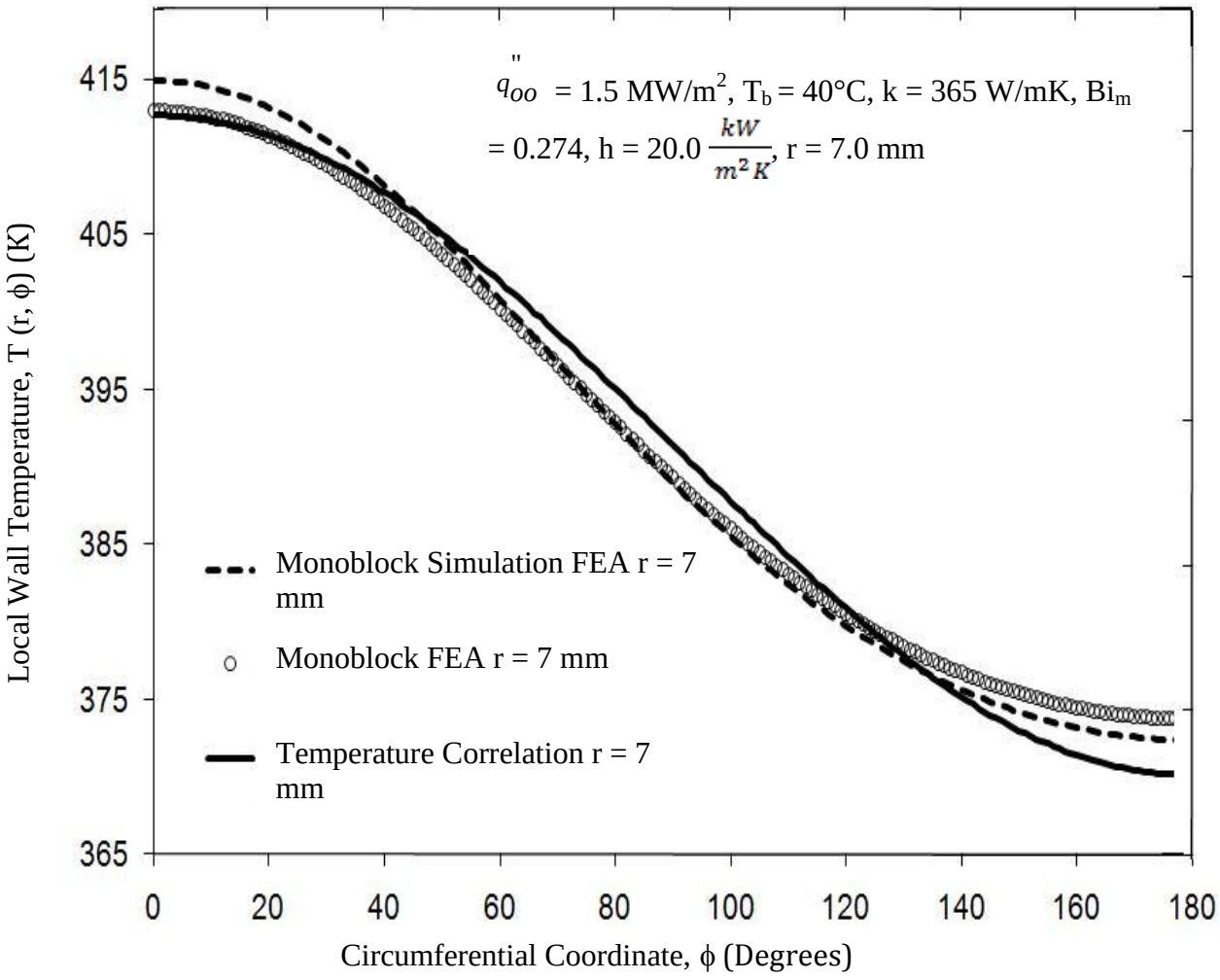

b) r = 7 mm

Figure 235b: Comparison of the Model's Temperature (Correlation) Circumferential Temperature Predictions with the Prototype Finite Element Analysis (Monoblock FEA) and the Simulation Finite Element Analysis (Monoblock-Simulation FEA) Predictions.

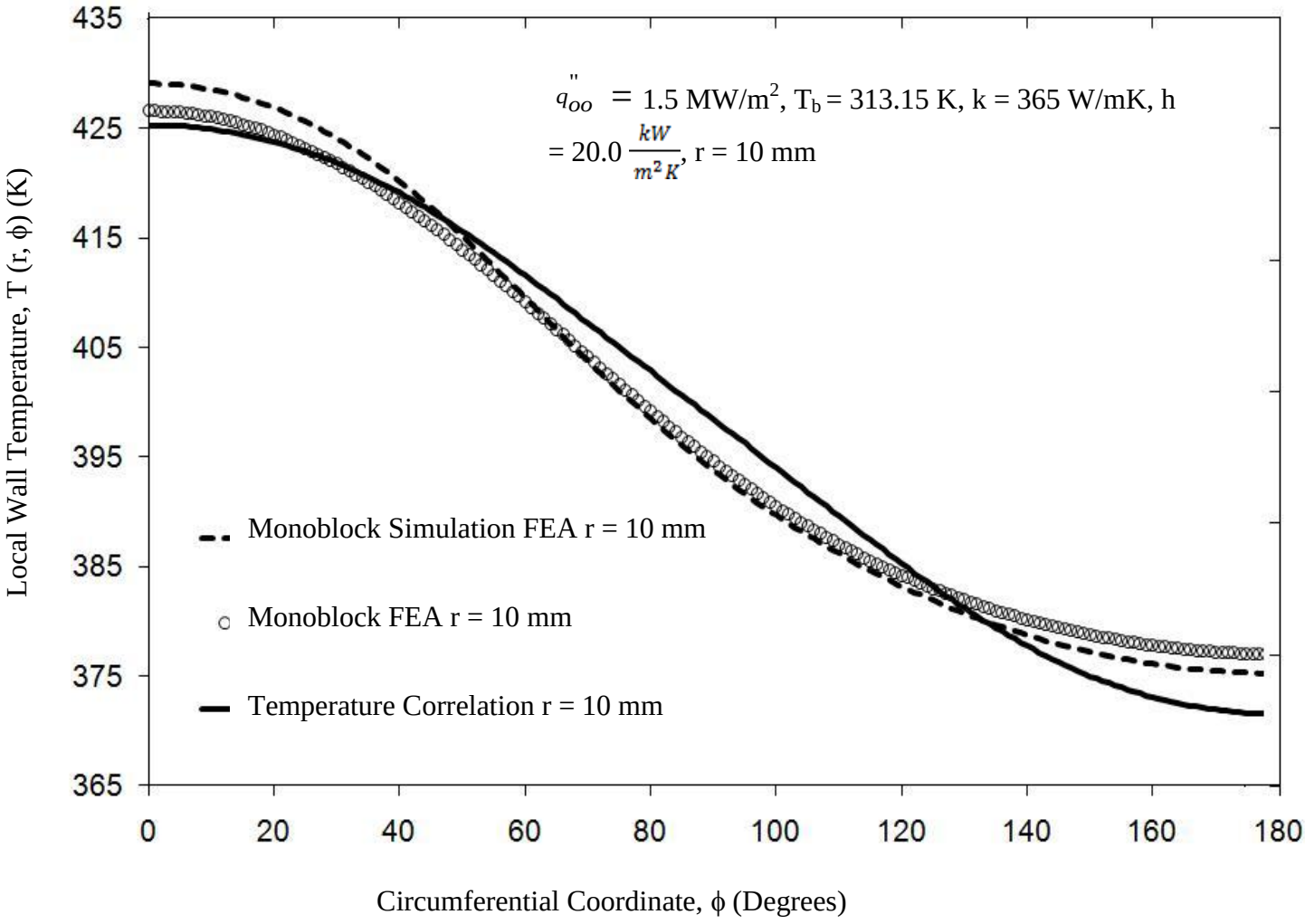

c) r = 10 mm

Figure 235c: Comparison of the Model's Temperature (Correlation) Circumferential Temperature Predictions with the Prototype Finite Element Analysis (Monoblock FEA) and the Simulation Finite Element Analysis (Monoblock-Simulation FEA) Predictions.

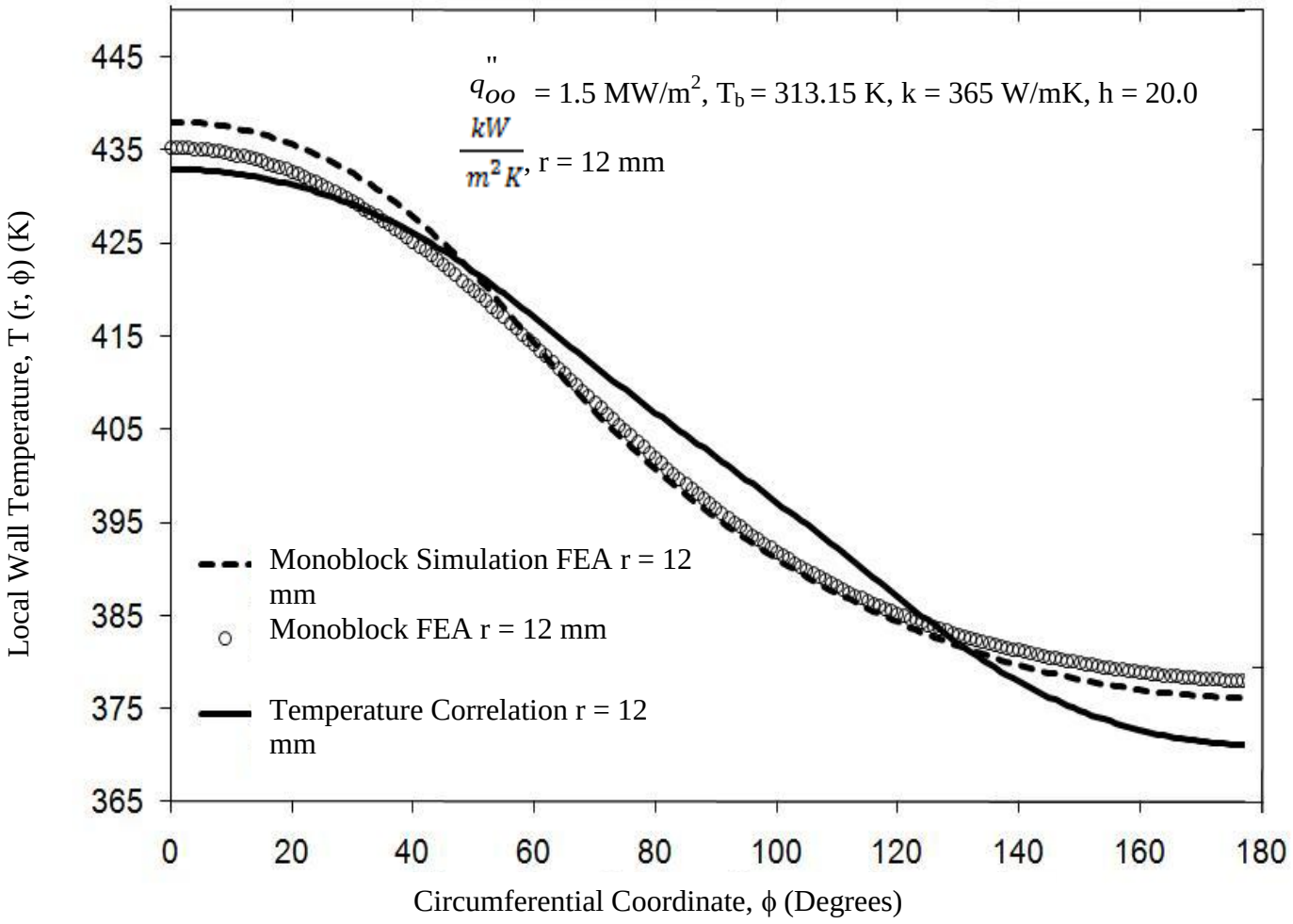

d) r = 12 mm

Figure 235d: Comparison of the Model's Temperature (Correlation) Circumferential Temperature Predictions with the Prototype Finite Element Analysis (Monoblock FEA) and the Simulation Finite Element Analysis (Monoblock-Simulation FEA) Predictions.

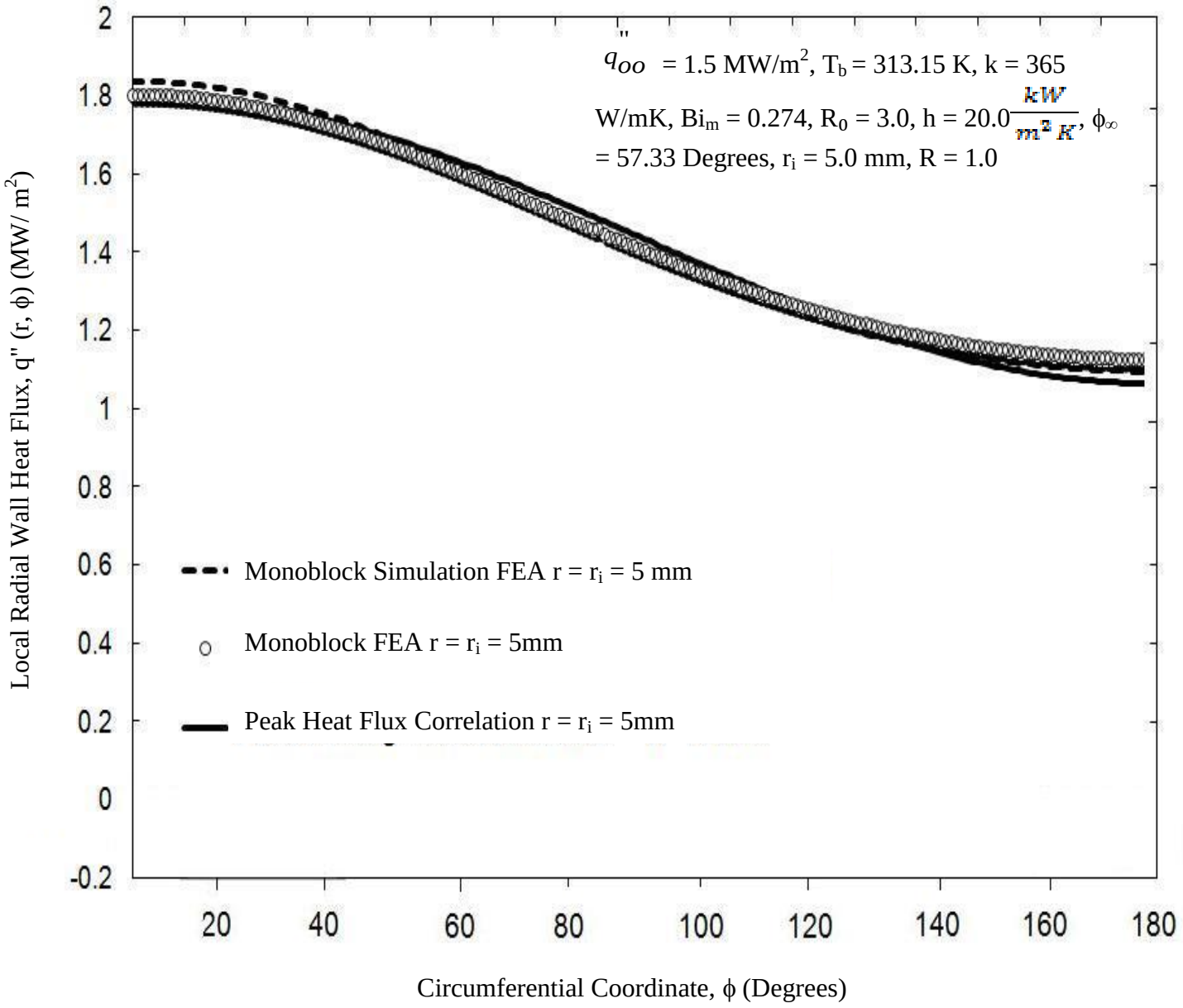

a) r = r_i = 5 mm

Figure 236a: Comparison of the Circumferential Distribution Predictions of the Model's Radial Heat Flux Correlation with the Prototype Finite Element Analysis (Monoblock FEA) and the Simulation Finite Element Analysis (Monoblock-Simulation FEA) Predictions.

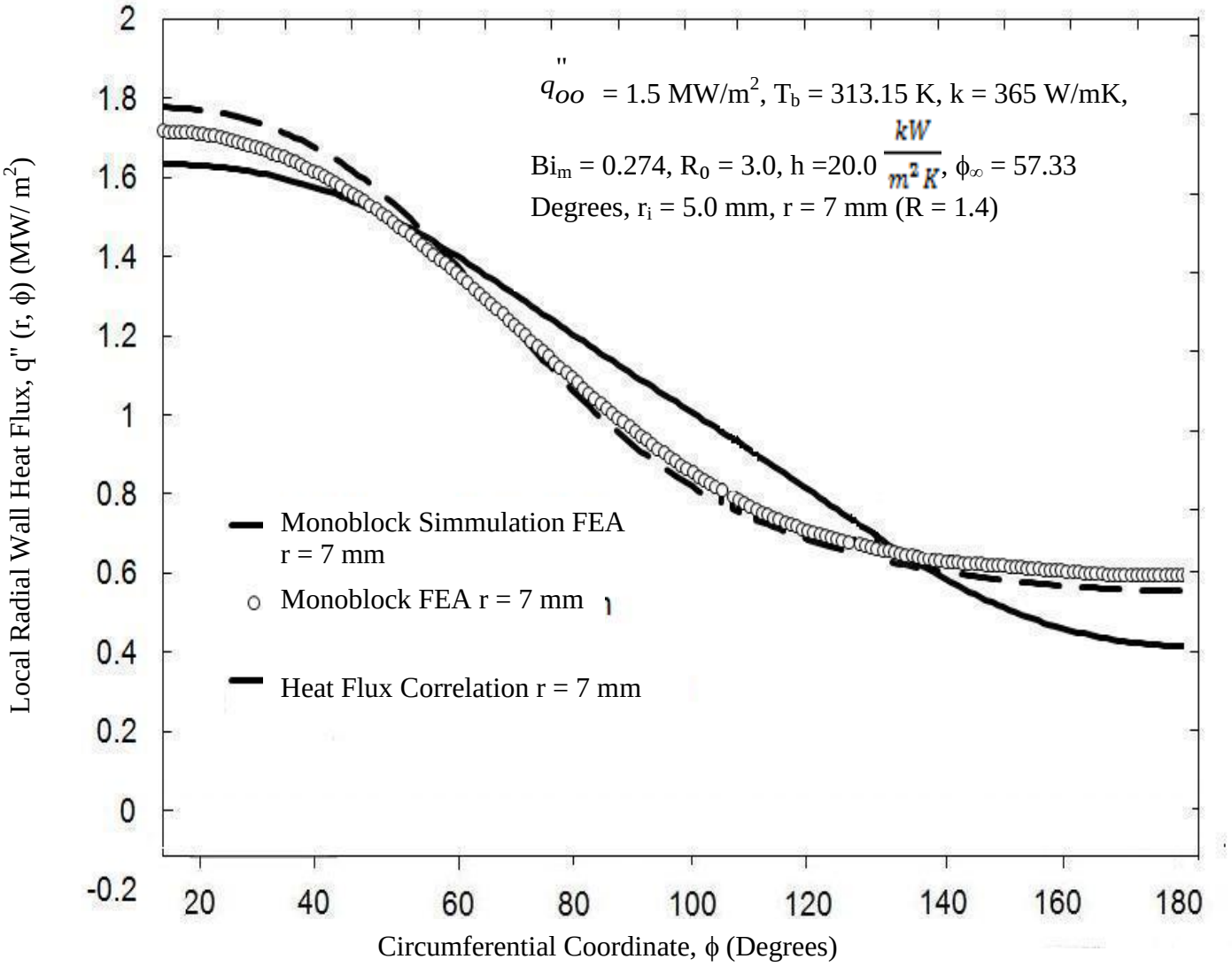

b) r = 7 mm

Figure 236b: Comparison of the Circumferential Distribution Predictions of the Model's Radial Heat Flux Correlation with the Prototype Finite Element Analysis (Monoblock FEA) and the Simulation Finite Element Analysis (Monoblock-Simulation FEA) Predictions.

22.2 POWER DISTRIBUTION MEASUREMENT SYSTEM

22.2.1 OVERVIEW

A 2-D translation device was developed, designed, and built in the IHHFR and was used to determine the axial power distribution profile of the HHF heater/power generation unit for a typical monoblock. Voltage measurements on an energized graphite heater used in High Heat Flux experiments showed that the power along the heater length was fairly constant.

22.2.2 TEST SECTION HEATER POWER DISTRIBUTION (PD) MEASUREMENT

Experimental investigations have been carried out to determine the power distribution along the axial length of a monoblock graphite heater. This section presents the results of: (1) the development, design, fabrication, and operation of the new power distribution (PD) measurements translation stage; (2) experimental procedures; and, (3) PD data analysis. Three different approaches for analyzing the data were compared and typical results are shown below. These results will serve as a gauge to correct previous measurement procedures and observe the trend of future investigative data. The overall results will shed light on the heat flux distribution for high heat flux removal tests [101, 90]. In all these experiments, electrically excited graphite heaters were utilized to generate a one side incident heat flux on the prototype test sections. However, the power distribution along this graphite heater and thus the incident heat flux distribution on the prototype test sections have not been experimentally ascertained. In fact, it has been theoretically assumed that these distributions are uniform and therefore much of the analytical computations, relating to the HHF experimental results, were based on this uniform heat flux distribution assumption.

This part of the present work deals with efforts to experimentally determine the actual distribution of power along the graphite heater as its energizing voltage and current are varied. Due to the low resistivity of the graphite material and its short length, it is necessary to have the experimental data captured with high accuracy and over a wide range of temperatures so as to characterize the distribution in the regime of temperatures where the heat flux experiments have been conducted. As noted, three different techniques were employed in the experimental data reduction and their results are compared for accuracy. The PD apparatus (DPA) was tested, developed, designed, and built in the TSRC.

22.2.2-1 Description of the HHF and the PDA

Figure 7 shows a schematic diagram of the TSRC HHF Facility [90]. The top section of the diagram illustrates a closed water flow loop with a test section that forms an integral part. The bottom portion shows the system computer, signal conditioners and other data acquisition hardware. The test section with numerous thermocouples inserted in it, receives heat from a graphite block which is electrically energized from a 300 kW, 30V DC power supply. The system data such as temperatures, pressures, coolant mass flow rates, etc. are captured and stored by the system data acquisition system. The detailed description of this facility is presented in [90].

Most of the work presented in this section of the report is centered on the heater section of the facility, indicated in Figure 168. In this illustration, the graphite heater sits above the test section with a thermally conducting and electrically insulating aluminum nitrite strip sandwiched between the two components. Two electrically insulated copper bus bars connect the heater to the 300 kW, 30V DC power supply. In its original set-up, the heater- test- section assembly hardly provided any room to access the heater in order to make any measurements. Therefore it became necessary to design and construct the DPA (see Fig. 237) as a retrofit to the assembly so the power distribution measurements could easily be accomplished. Fig. 237 shows the DPA, heater and its accompanying hardware, retrofitted with the major components of the designed power distribution measurement system. This measurement system provides axial and translational movements of a set of measurement probes that can be software controlled via micro drive motors. Here, the measurement parameter of interest is the voltage drop at predetermined intervals of 1.27 cm or 0.5 inch along the heater length that generates the heat flux. The probe leads are brought out of the assembly environment and can be terminated in a Keithley 2182 nanovoltmeter instrument or a National Instrument precision virtual voltmeter. The probes system can be programmed to travel from one end of the heater along its length to the other end, stopping at regular intervals (noted above). At each interval, the probes can be moved axially back and forth to contact the heater for a measurement. A thermocouple mounted on the probe measures the temperature of the heater surface and can also measure the temperature of the environment when the probe is retracted.

22.2.2-2 DC Power Supply Settings and Heater Voltage Measurement

The 300 kW DC power supply that feeds the heater is a rectifier that has a 2.0% ripple at full load. It is set at an initial voltage of zero and a current supply of zero. The voltage is then

incremented in steps of 0.5V. Currently the maximum voltage that has been attained is 3.5V. At this setting, the temperature in the heater environment reaches 80 ^{0}C, which is close to the recommended operating temperature of the probe DPA drive motors.

Accuracy in the heater voltage measurement is critical to the power distribution investigation. Prior experiments were conducted to determine the voltage error contribution of the connecting leads to the measurement. This is important since the heater probe measurements can be in the order of microvolts, and therefore the error contribution from the connecting leads cannot be ignored. Also the zero error readings of the precision instruments used in recording the measurements was checked before any data was recorded for each DC power supply voltage setting. This ensured that there was no extraneous contribution of error to the recorded data aside from that due to manufacturer's error specification.

22.2.3 ELEMENTAL HEATER RESISTANCE AND POWER

From the graphite manufacturer's material specifications data sheet, grade G-20 Graphite has a resistivity, ρ, of 1.174 milli-Ohms – cm at a temperature range of 28 to 100 ^{0}C. Using the cross-sectional area, A, and the length, l, of an element, the resistance $R = \rho\, l / A$ was then evaluated**.** The heater cross-sectional area is 6 cm^2 (3 cm X 2 cm). The elemental length is 1.27 cm (0.5 in). These values translate into the elemental heater resistance, **R** = (1.174 *1.27)/ (6*1000) = 0.0002485 Ohms.

From the probe measurement values of the heater elemental voltages (V) the DC power supply current (I) and the derived resistance value (R), three power calculations, [Power1 (P1), Power2 (P2), and Power3 (P3)] were made using the formulae P1 = VI, P2 = V^2 / R, and P3 = I^2 R. These three values were then tabulated and compared based on an error analysis.

22.2.3-1 Error Analysis

From the measured values of heater elemental voltage (V) and heater current (I), the Power1 (P1) error [184] is

$$\delta P1 = (\partial P1 / \partial V) * \delta V + (\partial P1 / \partial I) * \delta I$$

$$= I * \delta V + V*\delta I.$$

Therefore, the per unit error in Power1 is

$$\delta P1/P1 = (\delta V/ V) + (\delta I / I). \qquad (22.2\text{-}1)$$

Based on Equation 36, two distinct error sources in the power computation are apparent. The first one comes from the voltage measurement; and, the second error contribution is from the heater current measurement. The percentage $\delta V/ V = \pm 0.0001\%$, and was obtained from the

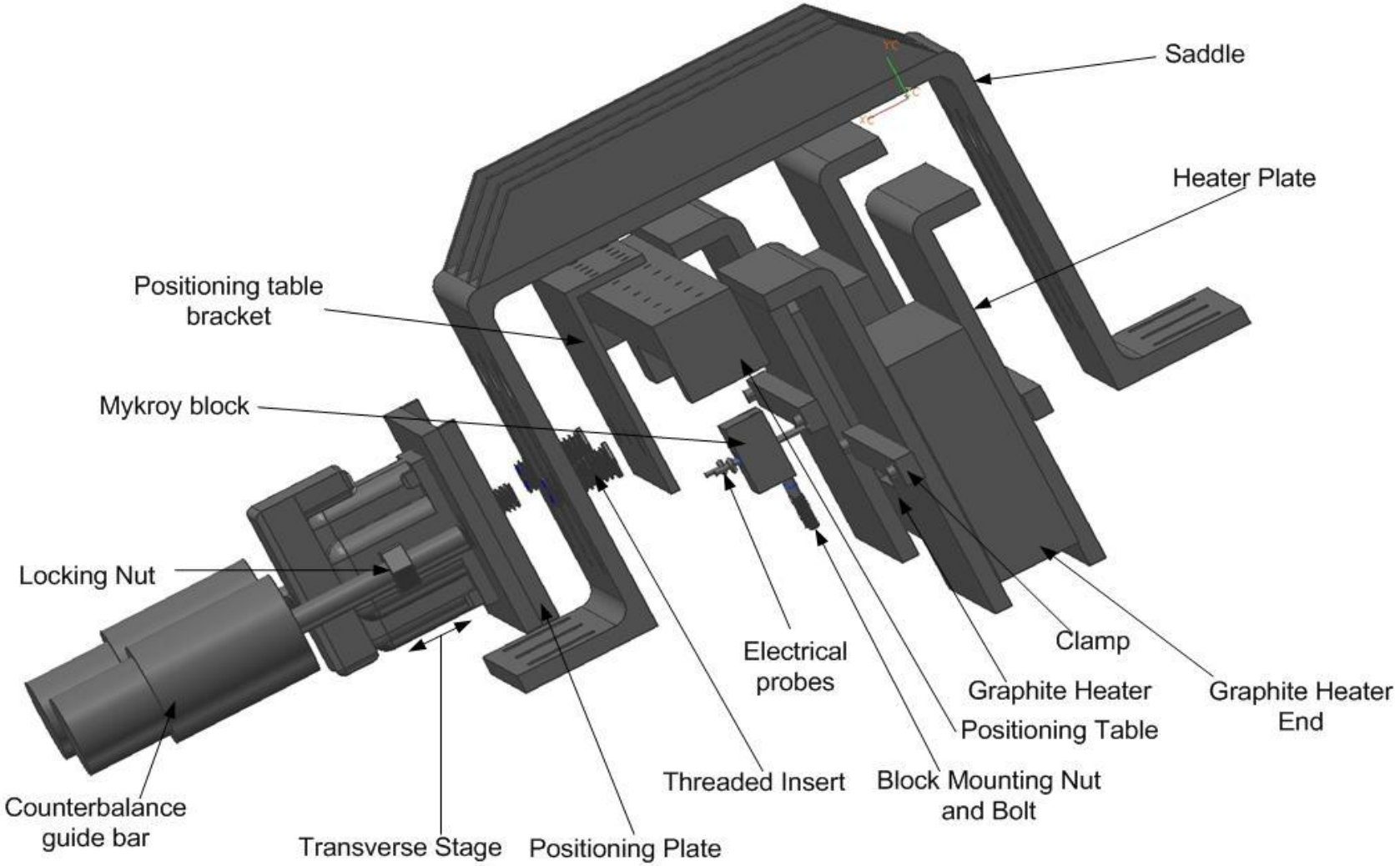

Figure 237: This is the DPA Which was Developed, Designed, and Built in the TSRC. The Graphite Heater and Related Bus Bars (clamp, heater plate, and saddle) are Also Shown.

specifications of the Keithely instrument used in recording the probe voltage data. Similarly, the percentage $\delta I / I = \pm 2\%$, and was acquired from the DC power supply manufacturer's specification. This yields a percent error in Power1 of 4.0002%. From the measured values of V and the computed value of the heater incremental resistance (R), the Power2 (P2) error is

$$\delta P2 / P2 = 2^* (\delta V / V) + (\delta R / R). \quad (22.2\text{-}2)$$

The uncertainty of evaluating R is approximately ± 0.1%, and that for V is ± 0.0001%. Therefore, the percentage error in Power2 is 0.2004% (or 2* .0002 + 0.2). Finally, the relative error in Power3 (P3) is

$$\delta P3 / P3 = 2^* (\delta I / I) + (\delta R / R). \quad (22.2\text{-}3)$$

The resulting percentage error for P3 is 8.2 %.

22.2.3-2 Measured Power Distributions

A typical table of experimental data obtained for power supply voltage of 3.5 V and a corresponding heater current of 653 A is shown in Table XIV. This table also compares the P1, P2, and P3 power data. Fig. 238 shows the plot of the power values with incremental heater length. In general, the estimated % errors in the three power data P1, P2, and P3 are 4.0%, 0.2% and 8.2%. Similar plots for voltages of 3.0V (and 533A) and 2.5V (and 424A) are shown in Fig. 239 and 240, respectively. These figures demonstrate some level of linearity in the heater power**.** P1 and P2 appear to exhibit a pronounced variation in the power level because of the variations that accompany the measured elemental heater voltages**;** whereas P3 shows a constant uniform value**.** The latter result is expected since the computed elemental heater resistance employed in generating the power data is assumed constant and the current is also constant**.** However, the values of the elemental resistances may differ depending on possible defects in the graphite material such as hairline cracks or existence of internal air pockets along its length**.** From the analysis, Power2 (P2) gives the least error in the results.

Thus far, voltage measurements on an energized graphite heater used in High Heat Flux experiments show that the variation of power along the heater length is fairly constant**.**

Table XIV: Examples of Recorded and Computed Data at the Heater Power Supply Level, V=3.5V, where I = 653A. P1, P2, and P3 Represent Power1, Power2, and Power3 (T = 29.0 ^{0}C).

ΔL(in)	V(V)	P1=V.I(W)	P2=V^2/ R(W)	P3=I^2 R(W)	R(Ohms)
1.0-1.5	0.2101	137.1953	180.5399	104.2570	0.0002445
1.5-2.0	0.2083	136.0199	177.4597	104.2570	0.0002445
2.0-2.5	0.2120	138.4360	183.8200	104.2570	0.0002445
2.5-3.0	0.2113	137.9789	182.6081	104.2570	0.0002445
3.0 3.5	0.2116	138.1748	183.1270	104.2570	0.0002445
3.5-4.0	0.2108	137.6524	181.7449	104.2570	0.0002445
4.0-4.5	0.2110	137.7830	182.0899	104.2570	0.0002445
4.5-5.0	0.2109	137.7177	181.9174	104.2570	0.0002445
5.0-5.5	0.2111	137.8483	182.2626	104.2570	0.0002445

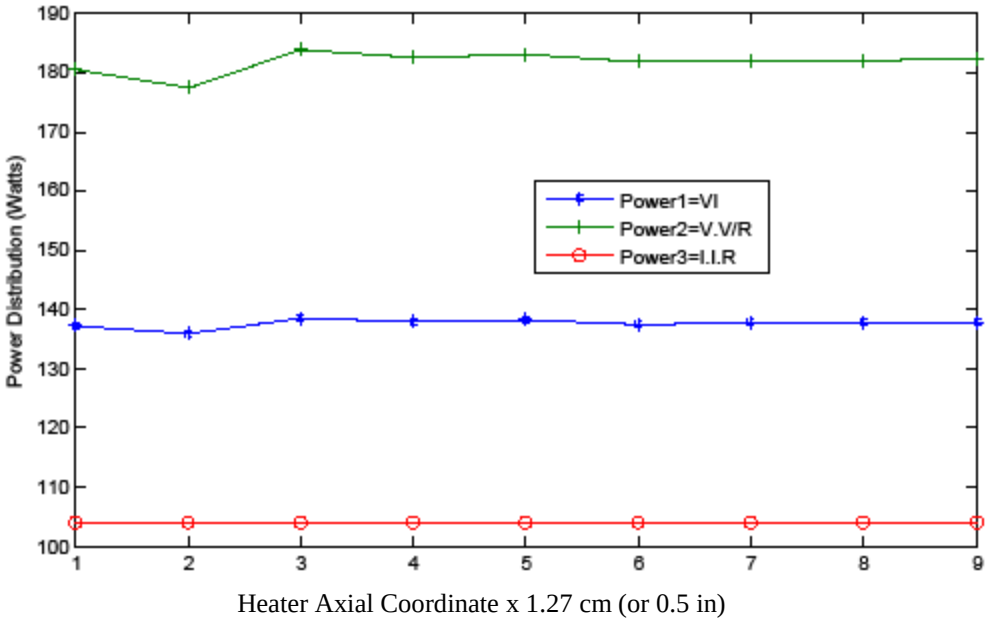

Figure 238: Power Distribution Along Heater Axial Coordinates – Power Supply Voltage = 3.5V, and Current = 653A.

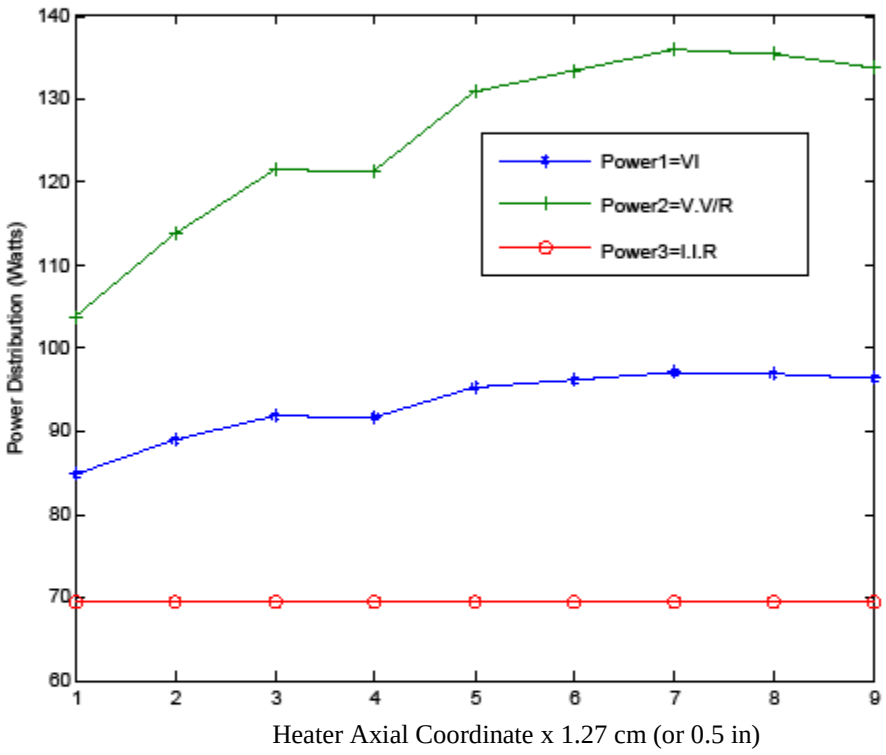

Figure 239: Power Distribution Along Heater Axial Coordinates – Power Supply Voltage = 3.0V, and Current = 533A.

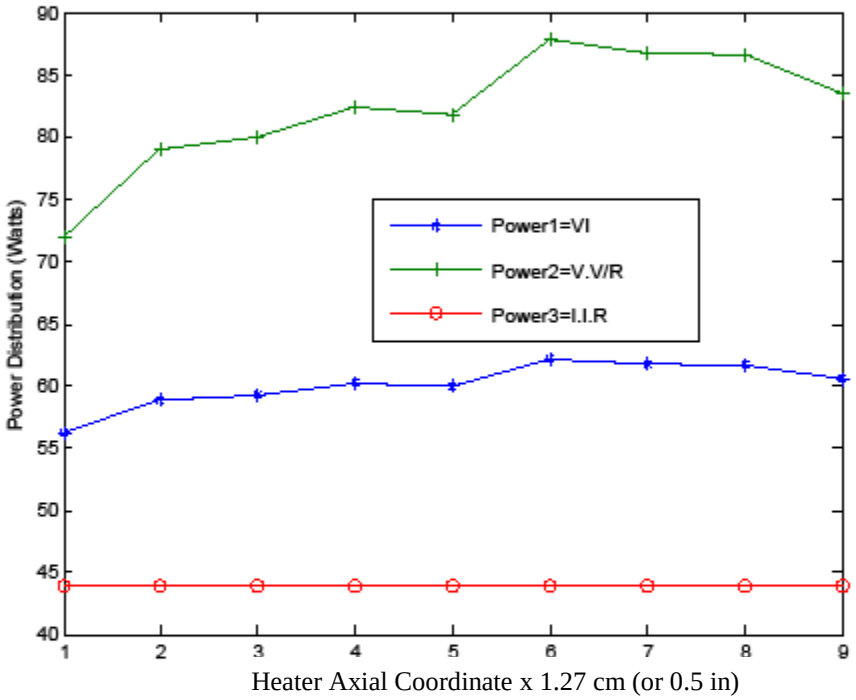

Figure 240: Power Distribution Along Heater Axial Coordinates – Power Supply Voltage = 2.5V, and Current = 424A.

23.0 SUMMARY AND CONCLUSIONS

The Thermal Science Research Center (TSRC) Personnel (Faculty, Students, and Staff) has developed a new high heat flux testing facility which is part of the Institute for High Heat Flux Removal (IHHFR) at Prairie View A&M University. The facility is operational and several speciality bus bars, test sections, and heater designs have been completed, constructed, and tested. Although degassed and deionized water is the working fluid, the facility can be expanded to accommodate other working fluids. The facility consists of:

1. A 4.0 MPa closed water flow loop;
2. A 300 kW, 30.0 V D-C power supply for test section heating;
3. Utilities for the power supply;
4. A copper bus bar grid between the test section and the power supply;
5. Monoblock and circular test sections (TS) and bus bar-TS interface;
6. An array of graphite heater elements;
7. Instrumentation and data acquisition; and
8. A 250.0 kW, 30.0 V D-C power supply for the pre-heater.

Three-dimensional local test section wall temperatures were monitored and related to the two-dimensional convective and flow boiling wall heat flux as a function of subcooling, mass velocity, exit pressure, test section (TS) geometry, and internal fluid flow inserts. The resulting thermal data applies to internal convective flow which is thermally-developing, single- and two-phase, laminar and turbulent with an externally applied single-side incident (absorbed) heat flux boundary condition. The resulting two-dimensional (2-D) boiling curves may be the first 2-D boiling curves appearing in the technical literature. This work should be expanded to produce boiling curves from the entire data base. The boiling curves are essential for accurate computational fluid dynamics and heat transfer code validation, verification, and prediction.

The TSRC has been involved in designing various test sections with graphite electric heaters. Each design meets the above noted constraints. The heaters have been designed with particular shapes to fit each of the four test sections. Bus bars interface each heater with a direct current electric supply. To avoid direct contact with test section, the heaters are electrically insulated with A1N, which is an excellent thermal conductor.

The mechanism to interface of the test section heater to the electric power supply bus-bar has been designed, and the details of this design are shown in Figs. 33 and 43. The unique

features of these designs are: (1) thermal expansion will not change the pressure between different components, (2) the heater is easy to install, and (3) no bolt will be needed to connect the bus-bar to the heater.

High heat flux removal (HHFR) form plasma-facing and aerodynamic components and electronic heat sinks involve conjugate heat transfer analysis of the applicable substrate and flowing fluid. Three-dimensional thermal measurements for a one-side heated circular-like cross section show: (1) the three-dimensional variation of the wall temperature close to both the heated and fluid-solid surface boundaries, (2) the resultant effects of local subcooled flow boiling on the 3-D wall temperature/outside heat flux relationship--one of which is the 3-D wall temperature profile is almost unchanged in the vicinity for incident heat flux levels between the onset to fully developed boiling and local dry-out, (3) well-defined 2-D flow boiling curves, and (4) the effects of the varying local flow regimes from single-phase to two-phase thermally developed flow.
These results are very encouraging in that they:

1. are among the first full set of truly 3-D test section wall temperature measurements for one-side heated circular-like cross section flow channels which contain the effect of conjugate heat transfer from laminar and turbulent single- and two-phase thermally developing flows;
2. contain, for the first time, 2-D boiling curves for the above noted conjugate heat transfer conditions;
3. provide a unique two-phase, turbulent, flow boiling data base for one-sided heated flow channels which can be used for base-line comparisons with future computational fluid dynamic and heat transfer predictions; and,
4. in some cases, contain 2-D distributions of $q_i(\phi, z)$ and $T_i((\phi, z)$ along with $T_b(z)$--all of which can be used to obtain $h_i(\phi, z)$.

For the present case, the radial aspect ratio (R_o = outside radius to inside radius) was 3.0. For an incident heat flux of 728.3 kW/m^2 and a Reynolds number of 6,900, the inside channel heat flux and heat transfer coefficient at the heated part of the plane of symmetry were 1,350.0 kW/m^2 and 22.5 kW/m^{2}K, respectively. At the cooler part of the plane of symmetry for the same incident heat flux, these thermal quantities were 896.0 kW/m^2 and 19.9 kW/m^{2}K, respectively. For applications requiring $R_o < 3.0$, these differences will increase. Tabulated two-dimensional (2-D) results for q_i (ϕ, z) and T_i (ϕ, z) are presented.

The optimized design of single-side heated plasma-facing components (PFCs) and other high heat flux heat sinks is dependent on knowing the local distribution of inside wall heat flux and temperature in the flow channels. This knowledge will result in a reliable description of the different heat transfer regimes at the wall of cooling channels. The wall heat flux can be obtain from selectively chosen local wall temperatures close to the inside boundary of the flow channel. To this end, three-dimensional thermal measurements for a single-side heated square cross-section monoblock test section (with an inside circular flow channel) were made and show: (1) the three-dimensional variation of the wall temperatue close to both the heated and fluid-solid surface boundaries, (2) two-dimensional boiling curves, (3) up to a factor four increase in the HHFR inside heat flux when a helical wire insert is used [176], and (4) good agreement with the Petukhov [93] correlation in the single-phase region when the thermal hydraulic diameter was used. From additional comparisons with selected correlations, good agreement was obtained only on the heated side of the plane of symmetry: (1) for the entire boiling curve at the highest mass velocity (G = 3.2 Mg/m^2s) using Boyd-Meng correlation with $D_T = 1.4\ D_i$; and, (2) for the $q_o^{"}$ vs T_{wi} relationship in the single-phase region only at the lower levels of the mass velocity (G < 1.2 Mg/m^2s), and using either the Sieder-Tate correlation and the Petukhov correlation with $D_T = 1.2\ D_i$ (slightly better). Clearly, additional correlation development and adaptation are needed. However, the developed 2-D boiling curve monoblock data base provides a basis for future correlational development so that single-side heating and conjugate heat transfer effects with both circumferential and axial dependence can be correlated. **These results (1) are among the first full set of three-dimensional wall temperature and 2-D boiling curve measurements for single-side heated monoblock flow channels which contain the effect of conjugate heat transfer from laminar and turbulent single-phase and flow boiling, and (2) provide a unique two-phase, laminar and turbulent, flow boiling data base for single-sided heated monoblock flow channels which can be used for comparisons with future computational fluid dynamic and heat transfer predictions and existing correlations.**

Conjugate heat transfer modeling has proved useful in forming baselines and identifying important parameters affecting peaking factors (PFs) and data reduction for the spectrum of high heat fluxes found in a wide variety of applications. For various applications requiring different fluids, the results show the following:

1. the coexistence of three flow boiling regimes inside a single-side heated circular geometry (for water only),
2. the correlational dependence of the inside wall heat flux and temperature (fluid independent), and
3. inaccuracies that could arise in some data reduction procedures (fluid independent).

However for PFC applications, work to expand conjugate heat transfer analyses from simple circular and complex geometries to PFC geometries is still needed for consistently predicting PFs for single-side heated channels. Consistent and accurate PF predictions would result if the 2-D boiling curves are known.

A conjugate heat transfer, high heat flux simulation methodology has been developed which accurately predicts the flow channel radial heat flux amplification or peaking factors (PF), and inside peak wall temperature under axial and swirl turbulent single-phase and flow boiling conditions with water. The methodology was demonstrated using finite-element analysis (FEA) comparisons; and, the FEA predictions were benchmarked for the following extreme high heat flux conditions: (1) very large and small local temperature gradients, (2) low to high heat flux levels with axial, turbulent single- and two-phase flow, and (3) moderate to high prototypic heat flux levels with turbulent swirl single-phase and subcooled flow boiling flow and geometry variations. **In all cases, the simulation resulted in excellent predictions of: (1) the PF to within 0.1 to 1.9% inaccuracy, and (2) $T_{wi)_{max}}$ to within 0.4 to 0.02%.** The simulation predicted qualitatively the local circumferential inside flow channel wall temperature and radial heat flux distributions for $\phi > 0$. Since the primary objective of this simulation was to accurately predict HHF amplification and $T_{wi)_{max}}$, these results indicate that the simulation methodology can be used presently for monoblock simulation in the future development of useful HHFR amplification and peak $T_{wi)_{max}}$ correlations. Finally and although water was used as the coolant in the present simulation, the methodology may be fluid-independent; and hence, the simulation and correlation may be applicable to other fluids (i.e. other liquids, gases, and liquid metals) for other specialized HHFR applications. More work is needed to validate the applicability of this methodology (and the correlation) to other fluids, channel wall materials, and flow regime experimental data.

Although the hypervapotron (HV) is an excellent candidate for HHFR, past design improvements have "been traditionally sought experimentally which is both inefficient and costly" [156]--especially when improvements are sought without knowledge of the HHFR controlling parameters. In order to effectively characterize additional optimal operating characteristics using CFD and/or experimental approaches, knowledge of the controlling TM hypervapotron parameters would be essential for timely HHFR enhancement and configuration identification. To that end, four controlling parameters were identified in Section 21.1: (1) $Bi = h_{eq}\, t/k_I$, (2) w_c/t, (3) $(w/2 - w_c)/L^*$, and (4) $q''_\infty\, w_c/k_I T^*$. These parameters result from an analyses of Domain I of the five-domain model used for the hypervapotron. Further, these and additional parameters were determined and may be useful in the future characterization of optimal flow channel wall local heat flux and temperature distribution correlations. The form of these correlations for Domain I has been determined and hence that for the heat flux peaking/reduction factors for that domain. From predictions in reference [135], it has been suggested via previous examples that the optimized addition of an inner lower thermal conductivity shell along with additional fins on the HV bottom and/or side inside surfaces may improve HHFR and reduce HFA. Similar future improvements may be possible from the identified and future control parameters produced from this work.

In addition to the three controlling parameters identified in Section 21.1, four additional primary hypervapotron controlling parameters were identified in Section 21.2:

(1) $\frac{k_I}{k_{II}}\left(\frac{w}{2w_c} - 1\right)$, (2) $Bi_2 = \frac{h_2\left(\frac{w}{2} - w_c\right)}{k_{III}}$, (3) $\frac{2H_C + t}{\frac{w}{2} - w_c}$, and (4) $\left(H_c - L_f/2\right)/w_c$. In addition, the reference temperature (in degrees Kelvin) and length are $T^* = q''_\infty\, w_c/k_I$ and $L^* = t$, respectively. Further, the hypervapotron HHFR is also related to η_o, η_f, $\frac{A_T}{A_b}$, $\frac{NA_f}{A_T}$ along with the fin effectiveness [171] which are functions of the following secondary parameters: (1) mL_f, (2) δ^*, (3) Bi_{f_2}, (4) S/δ, and (5) Bi_{f_1}. The above primary and secondary controlling parameters along with those identified in Section 21.1 [161] are directly related to the high heat flux removal

in a hypervapotron; and they may be useful for optimizing operating configurations and conditions. More parameters resulted from analyses of Domains IV and V, which were presented in Section 21.3 (Summary of HV Parameters) of this work.

The final part of this three-part study was presented in Section 21.3 and has resulted in three additional HV HHFR control parameters: **(1)** $Bi_3 = \frac{h_3 H_1}{k_V}$, **(2)** $(w/2)/H_1$, and **(3)** $\left(w/2 - w_c\right)/H_1$. In addition, closure relations have been generated for the HV local temperature and heat flux distributions. Further, Section 21.2 contains example control parameters for a HV with rectangular/straight fins. However, the above with h_{eq} can be used for any HV fin cross-section or orientation. Finally, future work should address the sensitivity of these identified hypervapotron control parameters.

Unanticipated high heat flux amplification in thermal management schemes can compromise or limit the optimization of new and emerging engineering systems. A conjugate heat transfer high heat flux removal simulation methodology has been developed with excellent resulting accuracy (> 98.0% accurate) for predicting heat flux amplification and the peak flow channel inside wall temperature $\left(T_{wi_{\max}}\right)$ [140]. The methodology was used to develop a conceptual model to produce heat flux amplification and $T_{wi_{\max}}$ correlations for single-side heated monoblocks with an inside circular flow channels. At a 1.5 MW/m^2 incident heat flux, the correlations' predictions had excellent agreement with the finite element analyses for both the monoblock simulation and prototype monoblock. Based on the present success, the conceptual model should be refined in the future to include some of the following effects: (1) circumferentially varying convective heat transfer coefficient, (2) multiple materials and thermal contact resistance, (3) verify the fluid- and flow regime-independence, and (4) extend to include other flow channel geometries and boundary conditions. Thus far, the high heat flux amplification and the dimensionless form for $T_{wi_{\max}}$ have been shown to be dependent on three parameters: ϕ_{oo}, R_o, and Bi_m. As such, the present model provides functional relationships which may be useful in future high heat flux removal and thermal management design and development studies.

A 2-D translation device was developed and designed in the IHHFR and was used to determine the axial power distribution profile of the HHF heater/power generation unit in a

monoblock heater. Voltage measurements on an energized graphite heater used in High Heat Flux experiments showed that the variation of power along the heater length is fairly constant.

In summary, the Institute for High Heat Flux Removal (IHHFR) at Prairie View A&M University (PVAMU) has made a number "State-of-the-Art" contributions to fusion science, design, and technology as well as other applications where high heat flux removal (IHHFR) and thermal management (TM) are enabling technologies. Further advances in HHFR and TM applications will in part be possible only if the convective fluid/solid boundary conditions can be clearly defined for all fluid flow regimes (turbulent, laminar, thermally developing and/or boiling where fluid phase-change is likely). Existing computer codes have some computer fluid dynamics (CFD) models which may approximate to various degrees some of the applicable flow regimes--*but not all! However, the IHHFR has produced convective data which contains all the physical characteristics of laminar, turbulent, thermally developed and two-phase flow boiling at the fluid/solid boundary as well as related conjugate heat transfer data. In fact the IHHFR has produced some of the first measured two-dimensional boiling curves for single-side heated (SSH) monoblocks and one other flow channel test section (TS) configuration.* In addition and among the first data produced in the technical literature, 3-D conjugate heat transfer TS wall data was also produced in most experiments. This data was produced using the unique IHHFR Facility which was developed, designed, built in part and construction-managed, and tested by PVAMU Faculty, Students, and Staff. Another HHFR enabling technology need is to have the capability to determine the peaking factor (PF) for a given SSH monoblock. In the IHHFR, monoblock simulation was developed which produced high accuracy PF and maximum monoblock wall temperature predicitions for up to a SSH monoblock incident heat flux of 38.0 MW/m^2. Exploratory work was begun to extend this simulation to a correlation. As another HHFR alternative to the SSH monoblock, a SSH hypervapotron (HV) was analyzed from the point-of-view of physically defining HHFR and TM Control Parameters which may aid in optimization. Although the HV is an excellent candidate for HHFR, past design improvements have "been traditionally sought experimentally which is both ineffective and costly" [156]—especially when improvements are sought without knowledge of the HHFR controlling parameters. The present work in the IHHFR has identified three high heat flux-side and six wall conjugate heat transfer HV controlling parameters. The extension of the above may assist in the fulfillment of one ("Fusion Predictive Modelling") of four DOE *"Vision 2025"* Recommendations.

24.0 PUBLISHED PAPERS, PRESENTATIONS, AND STUDENT PROJECTS

24.1 REFEREED JOURNAL PAPERS

1. Boyd, R.D., "Thermal Management High Heat Flux Amplification Conceptual Model," Journal of Propulsion and Power, Vol. 29 (No. 1), pp. 16-20, 2013.
2. Boyd, R.D. and May, A.M., "Conjugate Heat Transfer High-Heat-Flux Amplification Simulation, Fusion Science and Technology, Vol. 57, pp. 129-141, 2010.
3. Boyd, R.D. and Zhang, H., "Conjugate Heat Transfer Measurements with Single-Phase and Water Flow Boiling in a Single-Side Heated Monoblock Flow Channel," International J. of Heat and Mass Transfer, Vol. 49, pp. 1320-1328, 2006.
4. Boyd, R.D., Cofie, P., Zhang, H., and Ekhlassi., A., "Single-Side Heated Monoblock, High Heat Flux Removal Using Water Subcooled Turbulent Flow Boiling," J. of Heat Transfer, Vol. 126, pp. 17-21, 2004.
5. Boyd, R.D., Ekhlassi, A., Cofie, P., and Zhang, H., "High Heat Flux Removal From a Single-Side Heated Monoblock Using Flow Boiling," International J. of Heat and Mass Transfer, Vol. 47, pp. 2183-2189, 2004.
6. Boyd, R.D., Strahan, M. Cofie, P., Ekhlassi, A., and Martin, R., "High Heat Flux Removal Using Subcooled Flow Boiling in a Single-Side Heated Circular Channel," International J. of Heat and Mass Transfer, Vol. 46, pp. 4105-4117, 2003.
7. Boyd, R.D., Cofie, P., and Ekhlassi, A., "Conjugate Heat Transfer Measurements in Non-Uniformly Heated Circular Flow Channel Under Flow Boiling Conditions," International J. of Heat and Mass Transfer, Vol. 45, pp. 1605-1613, 2002.
8. Boyd, R.D., Cofie, P., Li, Q.-Y., and Ekhlassi, A., "A New Facility for Measurements of Three-Dimensional, Local Subcooled Flow Boiling Heat Flux and Related Critical Heat Flux for PFC's," Fusion Technology, Vol. 41, pp. 1-12, 2002.
9. Boyd, R.D., Cofie, P., and Ekhlassi, A., "Measurements of Three-Dimensional, Local Subcooled Flow Boiling Heat Flux and Related Critical Heat Flux for PFCs," 14th Topical American Nuclear Society Meeting on the Technology of Fusion Energy," October, 2000; also published by Fusion Technology, Vol. 39 (#2, part 2), pp. 856-862, March, 2001,.
10. Peatiwala, Q., and Boyd, R.D., "Subcooled Flow Boiling in Circumferential Nonuniform and Uniform Heated Vertical Channels with Downward Flow," ASME Journal of Heat Transfer, Vol. 122, pp. 620-626, 2000.
11. Boyd, R.D., "Single-Side Conduction Modelling for High Heat Flux Coolant Channels, J. Of Fusion Technology, January, 1999.

24.2 CONFERENCE PUBLICATIONS AND PRESENTATIONS

1. Boyd, R.D., Cofie, P., May, A.M., and Martin, R., "High Heat Flux Removal Measurements in a Single-Side Heated Monoblock Flow Channel With a Helical Wire Insert," The 41st IEEE International Conference on Plasma Science and the 20th International Conference on High-Power Particle Beams, Washington, DC, 2014.
2. Boyd, R.D., "Thermal Management Using a Hypervapotron; Part II: Additional Controlling Parameters," 34th Annual Conference of the Canadian Nuclear Society, Toronto (ON), Canada, June 9-12, 2013.

3. Boyd, R.D., “Peaking Factor (PF) Correlation Development & Helical Wire Insert Enhancement for Thermal Management,” AFRL, March 22, 2012.
4. Boyd, R.D. and Clark Jr., Kenneth, “Thermal Management,” Minority Leaders Program Review for Sensors and Materials & Manufacturing Directorates, Baton Rouge, LA, November 14-17, 2011.
5. Boyd, R.D., “High Heat Flux Peaking Factors and Enhancement,” Annual Plasma-Facing Component Workshop, Massachusetts Institute of Technology (MIT), Cambridge, MA, July 8-10, 2009.
6. Boyd, R.D., “Upgrade Results, Institute for High Heat Flux Removal (IHHFR),” Plasma Facing Components (PFC) Annual Meeting, Albuquerque, NM, July 21-23, 2008.
7. Boyd, R.D., “Institute for High Heat Flux Removal (IHHFR)--Phase II, Upgrade,” Plasma Facing Components (PFC) e-Meeting, February 13, 2008.
8. Boyd, R.D., “Institute for High Heat Flux Removal (IHHFR)--Phase II,” Plasma Facing Components (PFC) Meeting, Argonne National Laboratory, Argonne, IL, June 4-6, 2007.
9. Boyd, R.D., “Institute for High Heat Flux Removal (IHHFR)--Phase I,” Annual Fusion Plasma Component (PFC) Meeting, University of California, San Diego (California), February 28-March 2, 2006.
10. Boyd, R.D., Ekhlassi A., Cofie, P., and Zhang, H., “High Heat Flux Removal Using Water Subcooled Flow Boiling in a Single-Side Heated Monoblock Channel,” ASME International Mechanical Engineering Congress and R&D Exp, Washington, DC, 2003.
11. Boyd, R.D., Ekhlassi A., Cofie, P., Martin, R., and Zhang, H., “Single-Side Heated Monoblock, High Heat Flux Removal Using Water Subcooled Flow Boiling,” National Heat Transfer Conference, Las Vegas, Nevada, 2003.
12. Boyd, R.D., Ekhlassi, A., Cofie, Penrose, and Zhang, H., “ High Heat flux Removal From A Single-Side Heated Monoblock Using Flow Boiling,” 5th International Conference on Boiling Heat Transfer, Montego Bay, Jamaica, 2003.
13. Boyd, R.D., Cofie, P., Ekhlassi., A., and Strahan, M., “Conjugate Heat Transfer Measurements in a Single-Side Heated Circular Flow Channel Under Turbulent, Subcooled Flow Boiling Conditions,” 12th International Heat Transfer Conference, Elsevier Publishing, Grenoble (France), pp. 713-718, 2002.
14. Boyd, R., Cofie, P., and Ekhlassi, A., “3-D Conjugate Heat Transfer Measurements in a Non-Uniform Heated Circular Flow Channel Under Flow Boiling Conditions,” 5th World Conference on Experimental Heat Transfer, Fluid Mechanics and Thermodynamics (ExHFT-5), Thessaloniki (Greece), September, 2001.
15. Boyd, R.D., Cofie, P., Li, Q.Y., and Ekhlassi, A., “A New Facility for Measurements of Three-Dimensional, Local Subcooled Flow Boiling Heat Flux and Related Critical Heat Flux,” 2000 International Mechanical Engineering Congress and Exposition (IMECE-2000), November, 2000.
16. Boyd, R.D., Cofie, P., and Ekhlassi, A., “Measurements of Three-Dimensional, Local Subcooled Flow Boiling Heat Flux and Related Critical Heat Flux for PFCs,” 14th Topical American Nuclear Society Meeting on the Technology of Fusion Energy,” October, 2000; also published by *Fusion Technology*, Vol. 39 (#2, part 2), March, 2001, pp. 856-862.
17. “Boyd, R.D., “Single-Side Conduction Modelling for High Heat Flux Coolant Channels,” 7th AIAA/ASME Joint Thermophysics and Heat Transfer Proceedings, Vol. 3, (HTD-Vol. 357-3), Albuquerque, NM, July, 1998.

24.3 SYMPOSIUM PUBLICATIONS

1. Boyd, R.D., "Thermal Management Using a Hypervapotron; Part III: Summary of Controlling Parameters," 25th Symposium on Fusion Engineering (SOFE), Paper 1086, San Francisco, CA, June 10-14, 2013.
2. Boyd, R.D., "Thermal Management Using a Hypervapotron; Part I: Some Controlling Parameters," Nuclear and Emerging Technologies for Space (NETS-2013), Paper 6903, Albuquerque, NM, February 25-28, 2013.
3. Boyd, R., Cofie, P., and Ekhlassi, A., "Conjugate Heat Transfer Measurements in a Non-Uniformly Heated Circular Flow Channel Under Flow Boiling Conditions," Third International Symposium on Measurements Techniques for Multiphase Flows, Fukui University, Fukui (Japan), August, 2001.
4. Peatiwala, Q. and Boyd, R.D., "The Effect of Orientation on Flow Boiling in Single-Side Heated Channels," Proceedings for the Thermal and Fluid Analyses Workshop (TFAWS 2000), Cleveland, OH, August 21-25, 2000.
5. Boyd, R.D., "Flow Boiling Heat Transfer and CHF for Uniformly and One-Side Heated Channels, E&A Symposium, Prairie View A&M University, Februayr, 1997.

24.4 GRADUATE THESES

1. Aaron May, "Conjugate Heat Transfer Measurements and Finite Element Analysis of One-Side Heated Flow Channels with Forced Convective Single-Phase and Flow Boiling, Department of Mechanical Engineering, Prairie View A&M University, Prairie View, TX, 2006.
2. Hongtao Zhang, "Steady-State Single-Phase, Flow Boiling, and Conjugate Heat Transfer Measurements in One-Side Heated Circular Cylindrical and Monoblock Flow Channels," Department of Mechanical Engineering, Prairie View A&M University, Prairie View, TX, 2004.
3. Jerry Turknett, "Forced Convection and Flow Boiling With and Without Enhancement Devices for Top-Side-Heated Horizontal Channels," Department of Mechanical Engineering, Prairie View A&M University, Prairie View, TX, 1989.
4. D.C. Ogbuaku, "A Theoretical Study of Laser Beam Induced Mixed Convection," Department of Mechanical Engineering, Prairie View A&M University, Prairie View, TX, 1989.

24.5 UNDERGRADUATE REPORTS

1. Xavier Bennett, "Inventory Progress," Thermal Science Research Center, Prairie View A&M University, 2003.
2. Corlisa Delesbore, "Temperature Distribution and Heat Flux Distribution," Inventory Progress," Thermal Science Research Center, Prairie View A&M University, 2003.
3. Kenesha Hyatt, "Specifications on the Data Acquistion System," Thermal Science Research Center, Prairie View A&M University, 2003.
4. Anthony Mack, "Results of Geometric Characterization," Thermal Science Research Center, Prairie View A&M University, 2003.

5. Avione Northcutt, "Geometric Characterization of a Monoblock Test Section and Transformer Test Bed," Thermal Science Research Center, Prairie View A&M University, 2002.
6. Edward Cramer, "Biot Numbers Analyzed," Inventory Progress," Thermal Science Research Center, Prairie View A&M University, 2002.
7. Jervale Phillips, "IHHFR Test Section Characterization," Thermal Science Research Center, Prairie View A&M University, 2002.

24.6 PROJECTS AND POSTER PRESENTATIONS (Including Posters Developed by Faculty, Graduate and Undergraduate Students)

1. Ronald D. Boyd, "Thermal Management Using a Hypervapotron, Part III. Sumamry of Controlling Parameters," Presented at the 25th Symposium on Fusion Engineering (SOFE), June 10-14, 2013, San Francisco, CA.
2. Ronhoward McNeil, Ronald D. Boyd, and Penrose Cofie, "Electromechanical Remote Controlled Power Measurements System (EMRPS), Thermal Science Reseearch Center, Prairie View A&M University.
3. Aaron May and Ronald D. Boyd, "Benchmarking Analysis of Single-Side Heated (SSH) Flow Channels with Forced Convective Single-Phase and Flow Boiling, Thermal Science Reseearch Center, Prairie View A&M University.
4. Marcella Strahan, Ronald D. Boyd, and Penrose Cofie, "Incident Heat Flux Data Reduction for a High Heat Flux Experiment, Thermal Science Research Center, Prairie View A&M University.
5. Rashad Martin, Ronald D. Boyd, and Ali Ekhlassi, "Design and Fabrication of Monoblock Test Section, Thermal Science Research Center, Prairie View A&M University.
6. Richard Ellis, Ronald D. Boyd, Penrose Cofie, Ali Ekhlassi, and Rashad Martin, "Experimenting With One Side Heated Plasma Facing Components, Thermal Science Research Center, Prairie View A&M University.
7. Avione Northcutt and Ronald D. Boyd, "Geometrical and Thermal Characterizations of a Cylindrical Test Section, Thermal Science Research Center, Thermal Science Research Center, Prairie View A&M University.

24.7 GRADUATE PROJECTS

1. Cordell Booker, "Peaking Factors of a Hypervapotron," Prairie View A&M University, Thermal Science Research Center, Prairie View A&M University.
2. Yasir Abbasi, "Experimental and Numerical Analyses of Single-Side Heated Heat Sinks," Prairie View A&M University, Thermal Science Research Center, Prairie View A&M University.
3. Brodny Carmichael, "Finite Difference Solutions and Heat Transfer Measurements for a Single-Side Heated Flow Channel," Thermal Science Reseearch Center, Prairie View A&M University.
4. Lori Davenport, "Inverse Heat Conduction Engineering Problem," Prairie View A&M University, Thermal Science Research Center, Prairie View A&M University.

5. Alicia Garrett, "Preliminary Comparison of Swirl Flow Surface Enhancements for Subcooled Flow Boiling (Water), High Velocity Helium Convection, and Liquid Metal Heat Transfer," Prairie View A&M University, Thermal Science Research Center, Prairie View A&M University.

24.8 STUDENT INTERNSHIPS (GRADUATE AND UNDERGRADUATE)

1. Cordell Booker, Graduate Student, "Peaking Factors of a Hypervapotron," Thermal Science Research Center, Prairie View A&M University.
2. Christian Guzman, Undergraduate Student, "Temperature, Heat Flux, and Amplification Computations, Thermal Science Research Center, Prairie View A&M University.
3. Kenneth Clark, Jr., Undergraduate Student, "Preliminary Desigh Computations," Thermal Science Research Center, Prairie View A&M University.
4. Richard Martin, Undergraduate Student, "Design and Fabrication of a Helical Wire Insert for a Monoblock Test Section," Prairie View A&M University.
5. Avione Northcutt, Undergraduate Student, "IHHFR Test Section Characterization and Verification," Thermal Science Research Center, Prairie View A&M University.

24.9 OTHER UNDERGRADUATE AND GRADUATE PROJECTS

Mr. Christian Guzman and Professor Boyd are working on: (1) monoblock flow channel peaking factor correlations comparison and characterization; and, (2) hypervapotron local temperature and heat flux distributions characterization, validation and verification. In the Summer of 2014, Christian completed an internship at Los Alamos National Laboratory.

Mr. Jermaine Chambers has been very helpful to the Thermal Science Research Center (TSRC). Mr. Chambers and Professor Ronald D. Boyd are working on analyzing thermal parameter effects on classical hypervapotron fins. In the Summer of 2014, Jermaine completed an internship at Los Alamos National Laboratory.

In addition to making great contributions to the Thermal Science Research Center (TSRC), Mr. David Cheri, Jr. has been a "role model" for younger students. He is responsible for making a presentation to the Texas A&M University System (TAMUS) Federal Relations Team.

Mr. Cordell Booker and Professor Boyd are investigating ways to correlate high heat flux amplification.

Further, Mr. Abimbola Daramola successfully completed a formalization involving an illustration for fluid flow through a hypervapotron.

Mr. Francois Martin not only completed validation and verification computations--he also was responsible for conducting an extensive high heat flux peaking factor literature search.

Finally, Mr. Emad Alzoebi was responsible for assisting Professor Penrose Cofie with the wiring for the data acquisition for the circular and monoblock test sections.

24.10 OTHER IHHFR REPORTS

1. Kevin Lee, "Reducing Contact Thermal Resistance on High Heat Flux Flow Loop," Project Progress Report, Thermal Science Research Center, Prairie View A&M University, 2003.
2. Kevin Lee, "High Heat Flux Flow," Project Progress Report, Thermal Science Research Center, Prairie View A&M University, 2003.

ACKNOWLEDGMENTS

Foremost, the PI is appreciative to the U.S. Department of Energy (DOE) and DOE Personnel for their support of this work under contracts #DE-FG02-97ER54452 and #DE-FG03-97ER54452. In addition, the PI is appreciative to all the Thermal Science Research Center (TSRC) personnel (See contributors' list on page viii) and to Mrs. Vivian J. Glover-Simmons for their work. Mrs. Glover-Simmons has worked with Professor Boyd (PI) to establish an unmistakable atmosphere of mentorship and excellence in the TSRC and the Roy G. Perry College of Egnineering at Prairie View A&M University. As faculty members, Professor Penrose Cofie and Mr. Ali Ekhlassi have consistently contributed significantly to many aspects. Further, Aaron May and Hongtao Zhang (Graduate Students), Rashad Martin, Avione Northcutt, Semaj Northcutt, Marcella Strahan, and Ronhoward McNeil (all Undergraduate Students) have exemplified excellence and professionalism in all TSRC Activities. In addition, Mr. Kevin Lee made early contributions to the IHHFR Facility and test procedures. Finally, the PI has valued the excellent support, interaction and feedback from the following: Dr. Sam Barish, Dr. Michael Crisp, Mr. John Sauter, Dr. Donald Priester, and Dr. G. Nardella. Without the honest and sincere support of all the above noted individuals, many of the successes made would not have been possible.

REFERENCES

1. Youchison, Dennis L., et al., 1997, "Critical Heat Flux Performance of Hypervapotrons Proposed for Use in the ITER Divertor Vertical Target," SPIE, Vol. 3151 (0277-786X), pp. 27-44.
2. Celata, G.P., and Cumo, M., 1991, "A Review of Recent Experiments and Predicition Aspects of Burnout at Very High Heat Fluxes," *Energia Nucleare*, Vol. 8(#3), pp. 47-65.
3. Gaspari, G.P., and Cattadori, G., 1994, "Subcooled Flow Boiling Burnout in Tubes With and Without Turbulence Promoters," *Experimental Thermal and Fluid Science*, Vol. 8, pp. 28-34.
4. Marshall, T., 1998, "Experimental Examination of the Post-Critical Heat Flux and Loss of Flow Accident Phenomena for Prototypical ITER Divertor Channels," Ph.D. Thesis, Nuclear Engineering Department, Rensselaer Polytechnic Institute.
5. Schlosser, J., et al., 1998, "Design Fabrication, and Testing of an Improved High Heat Flux Element, Experience Feedback on Steady State Plasma Facing Components in Tore Supra," Fusion Engineering and Design, Vol. 39-40 (pt A), pp. 235-240.
6. Marshall, T.D., Watson, R.D., McDonald, J.M., and Youchison, D.L., 1995, "Experimental Investigation of Post-CHF Enhancement Factor for a Prototypical ITER Divertor Plate with Water Coolant," Symposium on Fusion Engineering, IEEE, pp. 206-209.
7. Tolubinskiy, V.I., and Matorin, A.S., 1973, "Forced Convection Boiling Heat Transfer Crisis with Binary Mixtures," *Heat Transfer-Sov. Res.*, **5**, 2, 98.
8. Bergles, A.E., 1963, "Subcooled Burnout in Tubes of Small Diameter," WAM 63-WA-182, American Society of Mechanical Engineering.
9. Groeneveld, D.C., 1981, "Heat Transfer Phenomena Related to the Boiling Crisis," AECL-7239, Chalk River Nuclear Laboratory, Atomic Energy of Canada, Ltd.
10. Maulbetsch, J.S., and Griffith, P., 1966, "System Induced Flow Instabilities in Forced-Convection Flows with Subcooled Boiling," *Proc. 3rd Int. Heat Transfer Conference*, Vol. 4, p. 247, Hemisphere Publishing Corporation.
11. Boyd, R.D., 1990, "Subcooled Water Flow Boiling Transition and the L/D Effect on CHF for a Horizontal Uniformly Heated Tube," *Fusion Technology*, **18**, 317-324.

12. Boyd, R.D. and Meng, X., 1996, "Local Subcooled Flow Boiling Model Development," *Fusion Technology*, **29**, 459-467.
13. Hall, D.D. and Mudawar, I., 2000a, "Critical Heat Flux (CHF) for Water Flow in Tubes--I: Compilation and Assessment of World CHF Data," *Int. J. Heat and Mass Transfer*, Vol. 43 (No. 14), pp. 2573-2604.
14. Hall, D.D. and Mudawar, I., 2000a, "Critical Heat Flux (CHF) for Water Flow in Tubes--II: Subcooled CHF Correlations," *Int. J. Heat and Mass Transfer*, Vol. 43 (No. 14), pp. 2605-2640.
15. Celata, G.P., Cumo, M., and Mariani, A., 1994, "Assessment of Correlations and Models for the Prediction of CHF in Subcooled Flow Boiling," *Int. J. Heat and Mass Transfer*, Vol. 37 (No. 2), pp. 237-255.
16. Katto, Y., 1994, "Critical Heat Flux," *Int. J. Multiphase Flow*, **20** (suppl.), 53.
17. Akiba, M., et al., 1994, "Experiments on Heat Transfer of the Smooth and the Swirl Tubes Under One-Sided Heating Conditions," presented at the U.S./Japan Workshop, Q182, on Helium-Cooled High Heat Flux Components Design, San Diego, General Atomics Corporation.
18. Araki, M., et al., 1996, "Critical-Heat-Flux Experiment on the Screw Tube Under One-Sided-Heating Conditions," *Fusion Technology*, **29**. 519-528.
19. Araki, M., et al., 1995, "Heat Transfer Experiments on the Cooling Tubes for Divertor Plates Under One-Sided Heating Conditions," JAERI-Tech 95-022, Japan Atomic Energy Research Institute.
20. Baxi, C., 1992, "A Model for Analytical Performance Prediction of Hypervapotron," JET-P (92) 56, JET Team.
21. Boscary, J., Araki, M., and Akiba, M., 1997a, "Critical Heat Flux Database of JAERI for High Heat Flux Components for Fusion Application," JAERI-Data/Code 97-037, Japan Atomic Energy Research Institute.
22. Boscary, J., Araki, M., and Akiba, M., 1997b "Analysis of the JAERI Critical Heat Flux Data Base for Fusion Application," JAERI-Data/Code 97-037, Japan Atomic Energy Research Institute.

23. Boyd, R.D., Meng, X., and Maughan, H., 1995, "Heat Transfer for Plasma Facing Components," *Proceedings National Heat Transfer Conference*, Portland, Oregon, ASME HTD-Vol. 316, F.B. Cheung, Y.A. Hassan, and A. Singh, Eds.
24. Boyd, R.D. and Meng, X., 1995, "Similarities and Differences Between Single-Side and Uniform Heating for Fusion Applications—II: Sine Heat Flux," *Fusion Technology*, **27**, 401-407.
25. Escourbiac F., and Schlosser, J., 1996, "Critical Heat Flux Tests Results on Various Tube Concepts for the ITER Divertor," *Proceedings ITER Thermal-Hydraulic Technical Meeting; Focus: High Heat Flux Cooling*, Abingdon, United Kingdom, p. 2.1-2.38.
26. Falter, H.D. and Thompson, E., 1996, "Performance of Hypervapotron Beam Stopping Elements at JET," *Fusion Technology*, **29**, 584-595.
27. Marshall, T., et al., 1996, "Experimental Time to Burnout of a Prototypical ITER Divertor Plate During a Simulated Loss of Flow Accident," SAND96-2611, Sandia National Laboratories.
28. Inasaka, R. and Nariari, H., 1996, "Critical Heat Flux of Subcooled Flow Boiling in Swirl Tubes Relevant to High-Heat-Flux Components," *Fusion Technology*, **29**, p. 487.
29. TORE SUPRA TEAM, 1996 "Toward Long-Pulse, High-Performance Discharges in Tore Supra: Experimental Knowledge and Technological Developments for Heat Exhaust," *Fusion Technology*, **29**, 417.
30. Boyd, R.D., 1994, "Similarities and Differences Between Single-Side and Uniform Heating for Fusion Applications--I: Uniform Heat Flux," *Fusion Technology*, **25**, 411-418.
31. Boyd, R.D., et al., 1984, "Preliminary Design Analysis of the ALT-II Limiter for TEXTOR," *Journal of Nuclear Material*, **121**, 309-315.
32. Huque, Z., Boyd, R. D., and Harrison, R., 1994, "Two-Dimensional Data Reduction for Single-Phase Convection and Flow Boiling: A Benchmarking Analysis," Engineering and Architecture Proceedings, Prairie View A&M University.
33. Boyd, R.D., Ekhlassi, A., and Shade, L., 1995, "Conceptual Design of a High Heat Flux Experiment," Prairie View A&M University, College of Engineering & Architecture Symposium, Vol. I, p. 73-77.

34. Mohan, N., Undeland, T.M., and Robbins W.P., 1995, "Power Electronics," 2nd Edition, John Wiley & Sons, Inc.
35. Clinton Power Company Product Guide, 1995.
36. National Instrument Data Acquisition Product Guide, 1995.
37. National Instruments Instrumentation Reference and Catalogue, 1995.
38. "An Instrument That Isn't Really," IEEE Spectrum, August, 1990, pp. 36-39.
39. Boyd, R.D., 1994, "High Heat Flux Research in the Thermal Science Research Center," Mechanical Engineering Symposium (Invited), Prairie View A&M University, Prairie View, TX, pp. 1-24.
40. Boyd, R.D., 1996, "High Heat Flux Facility Development for ITER," E&A '96 Symposium, Prairie View A&M University, Prairie View, TX, pp. 217-222.
41. Cofie, P., et al., 1996, "Design and Adaptation of a Power Supply for A High Heat Flux Experiment," Prairie View A&M College of Engineering and Architecture Symposium, pp. 197-202.
42. Gibson, H.B., 1986, "Recent Developments in Terminating Aluminum Conductors," IEEE PCIC Conference Record, paper PCI-71-13.
43. General Electric Buylog Catalog, Low and Medium Voltage Component and Equipment.
44. Ekhlassi, A., Maughan, H. Davenport, L., Boyd, R.D., and Chenevert, Lisa, 1996, "Design of An Experiment Flow Loop for High Heat Flux Measurements," E&A '96 Symposium, Prairie View A&M University, Prairie View, TX, pp. 106-108.
45. Masterton, W. and Slowinski, E., 1977, Chemical Principles, W. B. Saunders Co., Philadelphia, p. 292.
46. Camp, T.R., and Meserve, R.L., 1974, Water and Its Impurities, Second Edition, Dowden, Hutchingson & Ross, Inc. Stoudsburg (PA).
47. Biney, P.O., 1993, "Development of a Chemical Kinetic Measurement Apparatus and the Determination of the Reaction Rate Constants for Lithium-Lead/Water Interaction," Prepared for DOE, Mechanical Engineering Department, Prairie View A&M University.
48. Boyd, R.D., 1985, "Subcooled Flow Boiling Critical Heat Flux and Its Application to Fusion Energy Components; Part I: Review of Fundamentals of CHF and Related Data Base," *Fusion Technology*, Vol. 7 pp. 7-30.

49. Halliday, D., and Resnick, R., 1993, Fundamentals of Engineering Physics, 4th Edition, New York, John Wiley & Sons, Inc.
50. Gere, J.M., and Timoshenko, S.P., 1990, Mechanics of Materials, 3rd Edition, PWS-KENT Publishing Company.
51. Boyd, R.D., Cofie, P., Li, Q.Y., and Ekhlassi, A., 2000, "A New Facility for Measurements of Three-Dimensional, Local Subcooled Flow Boiling Heat Flux and Related Critical Heat Flux," International Mechanical Engineering Congress and Exposition (IMECE); American Society of Mechanical Engineering **HTD-866-4**, Orlando, FL, pp. 199-208.
52. Youchison, D.L., Schlosser, J., Escourbiac, F., Ezato, K., Akiba, M., and Baxi, C.B., 1999, "Round Robin CHF Testing of an ITER Vertical Target Swirl Tube," 18th IEEE/NPSS Symposium on Fusion Engineering, Albuquerque, NM, pp. 385-387.
53. Akiba, M., Ezato, K., Sato, K. Suzuki, S., and Hatano, T., 1999, "Development of High Heat Flux Components in JAERI," 18th IEEE/NPSS Symposium on Fusion Engineering, Albuquerque, NM, pp. 381-384.
54. Youchison, D.L., Nygren, R.E., Griegoriev, S., and Driemeyer, D.E., 1999, "CHF Comparison of an Attached-Fin Hypervapotron and Porous-Coated Channels," 18th IEEE/NPSS Symposium on Fusion Engineering Albuquerque, NM, pp. 388-391.
55. Youchison, D.L., Cadden, C.H., Driemeyer, D.E., and Wille, G.W., 1999, "Evaluation of Helical Wire Inserts for CHF Enhancement," 18th IEEE/NPSS Symposium on Fusion Engineering, Albuquerque, NM, pp. 119-122.
56. Celata, G.P., Cumo, M., and Mariani, A., 1996, "A Mechanistic Model for the Prediction of Water-Subcooled-Flow-Boiling Critical Heat Flux at High Liquid Velocity and Subcooling," *Fusion Technology*, **29** (4), p. 499.
57. Araki, M., et al., 1994, "Experiment on Heat Transfer of the Smooth and the Swirl Tubes Under One-Side Heating Conditions," Department of Fusion Engineering Research, Japan Atomic Energy Research Institute (JAERI) Report.
58. Becker, K.M., et al., 1988, "Heat Transfer in an Evaporator Tube with Circumferentially Non-Uniform Heating," *Int. J. Multiphase Flow*, **14** (5), pp. 575-586.

59. Gärtner, D., et al., 1974, "Turbulent Heat Transfer in a Circular Tube With Circumferentially Varying Thermal Boundary Conditions," *Int. J. Heat Mass Transfer*, **17**, pp. 1003-1018.
60. Boyd, R.D., 1999, "Single-Side Conduction Modeling for High Heat Flux Coolant Channel," Fusion Technology, Vol. 35, pp. 8-17.
61. Youchison, D.L., et al., 1996, "Thermal Fatique Testing at a Diffusion-Bonded Beryllium Divertor Mock-up Under ITER-Relevant Conditions," Fusion Technology, Vol. 29, pp. 599-614.
62. Marshall, T.D., Youchison, D.L., and Cadwallader, L.C., 2001, "Modeling the Nukiyama Curve for Water-Cooled Fusion Divertor Channels," Fusion Technology, **35**, pp. 8-16.
63. Snowmass 2002 Fusion Energy Sciences Summer Study, 2002.
64. Tivey, R. et al., 1999, "ITER Divertor, Design Issues and Research and Development," Fusion Engineering and Design, **46** (2-4) pp. 207-220.
65. Tivey, R., et al., 2001, "ITER R&D: Vacuum Vessel and In-Vessel Components: Divertor Cassette," Fusion Engineering and Design, **55** (2-3) pp. 219-229.
66. Raffray, A.R., et al., 1999, "Critical Heat Flux Analysis and R&D for the Design of the ITER Divertor," Fusion Engineering and Design, **45** (4) pp. 377-407.
67. Merola, M., et al., 2001, "European Achievements for ITER High Heat Flux Components," Fusion Engineering and Design, **56-57,** pp. 173-178.
68. Vieider, G., et al., 1999, "European Development of the ITER Divertor Target," Fusion Engineering and Design, **46** (2-4) pp. 221-228.
69. Vieider, G., et al., 2000, "European Development of Prototypes for ITER High Heat Flux Components," Fusion Engineering and Design, **49-50**, pp. 135-143.
70. Hino, T. and Akiba, M., 2000, "Japanese Developments of Fusion Reactor Plasma Facing Components, Fusion Engineering and Design, **49-50**, pp. 97-105.
71. Akiba, M. and Suzuki, S., 1998, "Overview of the Japanese Mock-Up Tests for ITER High Heat Flux Components," Fusion Engineering and Design, **39-40**, pp. 219-225.
72. Nygren, R.E., 2002, "Actively Cooled Plasma Facing Components for Long Pulse High Power Operation," Fusion Engineering and Design, **60**, pp. 547-564.
73. Baxi, C.B. and Wong, C.P.C., 2000, "Review of Helium Cooling for Fusion Reactor Applications," Fusion Engineering and Design, **51-52**, pp. 319-324.

74. Merola, M., et al., 2000, "Manufacturing and Testing of a Prototypical Divertor Vertical Target for ITER," Journal of Nuclear Materials, **283-287**, pp. 1068-1072.
75. Wille, G.W., et al., 1998, "Development of 316L(N)-IG Stainless Steel Fabrication Approaches for ITER Divertor and Limiter Applications," Fusion Engineering and Design, **39-40**, pp. 499-504.
76. Hatano, T., et al., 1998, "High Heat Flux Testing of a HIP Bonded First Wall Panel with Built-In Circular Cooling Tubes," Fusion Engineering and Design, **39-40**, pp. 363-370.
77. Ulrickson, M.A., et al., 2001, "Physics Basis for the Fusion Ignition Research Experiment Plasma Facing Components," Fusion Engineering and Design, **58-59**, pp. 907-912.
78. Baxi, C.B., 2001, "Thermal Hydraulics of Water Cooled Divertors," Fusion Engineering and Design, **56-57**, pp. 195-198.
79. Nygren, R.E., 1995, "High Quality Actively Cooled Plasma-Facing Components for Fusion," Fusion Engineering and Design, **28**, pp. 3-12.
80. Chappius, Ph., et al., 1997, "Possible Divertor Solutions for a Fusion Reactor. Part 2. Technical Aspects of a Possible Divertor," Fusion Engineering and Design, **36** (1), pp. 109-117.
81. Rödig, M., et al., 2000, "Comparison of Electron Beam Test Facilities for Testing of High Heat Flux Components," Fusion Engineering and Design, **51-52**, pp. 715-722.
82. Boscary, J., et al., 1998, "Dimensional Analysis of Critical Heat Flux in Subcooled Water Flow Under One-Side Heating Conditions for Fusion Application," Fusion Engineering and Design, **43** (2), pp. 147-171.
83. Boscary, J., Fabre, J., and Schlosser, J., 1999, "Critical Heat Flux of Water Subcooled Flow in One-Side Heated Swirl Tubes," International Journal of Heat and Mass Transfer, **42** (2), pp. 287-301.
84. Inasaka, Fujio and Nariai, Hideki, 1998, "Enhancement of Subcooled Flow Boiling Critical Heat Flux for Water in Tubes with Internal Twisted Tapes Under One-Sided-Heating Conditions," Fusion Engineering and Design, **39-40**, pp. 347-354.
85. Celata, G.P., et al., 1999, "Prediction of the Critical Heat Flux in Water Subcooled Flow Boiling Using A New Mechanistic Approach," International Journal of Heat and Mass Transfer, **42** (8), pp. 1457-1466.

86. Celata, G.P., et al., 1995, "The Prediction of the Critical Heat Flux in Water-Subcooled Flow Boiling," International Journal of Heat and Mass Transfer, **38** (6), pp. 1111-1119.
87. Liu, W., Nariai, H., and Inasaka F., 2000, "Prediction of Critical Heat Flux for Subcooled Flow Boiling, International Journal of Heat and Mass Transfer, **43** (18), pp. 3371-3390.
88. Celata, Gian Piero, et al., 1998, "Physical Insight in the Burnout Region of Water-Subcooled Flow Boiling," Revue Générale de Thermique, **37** (6), pp. 450-458.
89. Celata, Gian Piero, et al., 2000, "Burnout in Subcooled Flow Boiling of Water. A Visual Experimental Study," International Journal of Thermal Sciences, **39** (9-11), pp. 896-908.
90. Boyd, Ronald D., et al., 2002, "A New Facility for Measurements of Three-Dimensional, Local Subcooled Flow Boiling Heat Flux and Related Critical Heat Flux for PFCs," Fusion Science and Technology, **41**, pp. 1-12.
91. Boyd, Ronald D., et al., 2002, "Conjugate Heat Transfer Measurements in as Single-Side Heated Circular Flow Channel Under Turbulent, Subcooled Flow Boiling Conditions," Twelfth International Heat Transfer Conference, Grenoble (France), pp.173-718.
92. Bergles, A.E., and Rohsenow, W., 1964, "The Determination of Forced-Convection Surface-Boiling Heat Transfer," J. of Heat Transfer, p. 365-372.
93. Petukhov, B.S., 1970, "Heat Transfer and Friction in Turbulent Pipe Flow with Variable Physical Properties," Advances in Heat Transfer, Vol. 6, pp. 503-564.
94. Collier, J. G., 1981, "Convective Boiling and Condensation," 2nd Edition, McGraw-Hill Inc.
95. Boyd, R.D. and Meng, X., 1992, "Local Heat Transfer for Subcooled Flow Boiling with Water," Fusion Technology, Vol. 22, pp. 501-510.
96. Araki, M., Akiba, M., Watson, R.D., Baxi, C.D., Youchison, D.L., 1995, "Data Bases for Thermo-Hydrodynamic Coupling with Coolants," Atomic Plasma-Material Interaction Processes in Controlled Thermonuclear Fusion, Journal of Nuclear Fusion Science, Vol. 5, pp. 245-265.
97. Thom, J.R.S., Walker, W.M., Fallon, T.A., Reising, G.F.S., 1965, "Boiling in Subcooled Water During Flow Up Heated Tubes or Annuli," Proc. Inst. Mech. Eng., Machester, UK.
98. Shah, M., 1996, "Part I: A General Correlation for Heat Transfer During Subcooled Boiling in Pipes and Annuli," ASHRAE Transaction, **83**, pp. 205-215.

99. Chen, J.C., 1996, "Correlation for Boiling Heat Transfer to Saturated Fluids in Convective Flow," I & EC Process Design and Development **5** (3), pp. 322-329.
100. Kandlikar, S.G., 1998, "Heat Transfer Characteristics in Partial Boiling, Fully Developed Boiling, and Significant Void Flow Regions of Subcooled Flow Boiling," Journal of Heat Transfer, Vol. 120, pp. 395-401.
101. Boyd, R.D., Cofie, P., Zhang, H., and Ekhlassi, A., 2004, "Single-Side Heated Monoblock, High Heat Flux Removal Using Water Subcooled Turbulent Flow Boiling," Journal of Heat Transfer, Vol. 126, pp. 17-21.
102. Araki, M., Ogawa, M., Kunugi, T., Ikeda, S., Satoh, K., and Suzuki, S., 1996, "Experiment on Heat Transfer of Smooth and Swirl Tubes Under One-Sided Heating Conditions," International Journal of Heat and Mass Transfer, **39** (14), pp. 3045-3055.
103. Izumi, Masaaki and Shimada, Ryohachi, 2003, "Heat Transfer Mechanism Based on Temperature Profiles and Bubble Motion in Microbubble Emission Boiling," 6th ASME-JSME Thermal Engineering Joint Conference, Hawaii, USA, pp. 16-20.
104. Koizumi, Yasuo, Matsishita, Naohiro, and Ohtake, Hiroyasu, 2003, "Experimental Examination of Triggering Mechanism of CHF of Sub-Cooled Flow Boiling," 6th ASME-JSME Thermal Engineering Joint Conference, Hawaii, USA, pp. 16-20.
105. www. Cheresources.com/convection.shtml
106. Kandlikar, S.G., 1989, "Development of a Flow Boiling Map for Subcooled and Saturated Flow Boiling of Different Fluids Inside Circular Tubes," Heat Transfer with Phase change, HTD-Vol. 114.
107. Jens, W.H. and Lottes, P.A., 1951, "An Analysis of Heat Transfer, Burnout, Pressure Drop and Density Data for High Pressure Water," Argonne Natl. Lab Report No. ANL-4627.
108. Schlosser, J. and Boscary, J., 1993, "Thermal Hydraulic Tests at NET/ITER Relevant Conditions on Divertor Targets Using Swirl Tubes," 3rd Specialists' Workshop on High-Heat-Flux Component Cooling, Cadarache, France.
109. Araki, M., Ogawa, M., Ikeda, S., Kunugi, T., Satoh, K., and Akiba, M., 1994, "Heat Transfer Experiment Under Highly Subcooled One-Side Heating Conditions," Proceedings of 1994 Fall Meeting of the Atomic Energy Society of Japan, **2**, p. 141.

110. Sider E.N. and Tate, G.E., 1936, "Heat Transfer and Pressure Drop of Liquids in Tubes," Industrial and Engineering Chemistry, **28** (12), pp. 1429-1435.
111. Northcutt, Avione, 2001, "Test Section II: Local Temperature and Heat Flux Measurements," Thermal Science Research Center.
112. SCM Metal Products, Inc., Research Triangle Park, NC 27709.
113. Araki, M. Akiba, M., Watson, R.D., Baxi, C.B., and Youchison, D.L., 1995, "Data Base for Thermohydrodynamic Coupling with Coolants, Atomic Plasma-Material Interaction Processes in Controlled Thermonuclear Fusion," J. of Nuclear Fusion Science, **5**, pp. 245-265.
114. Shim, S.Y., Soliman, H.M., and Sims, G.E., 2000, "Turbulent Fluid Flow, Heat Transfer and Onset of Nucleate Boiling in Annular Finned Passages," Int. J. of Thermal Science, **39**, pp. 709-720.
115. Raffray, A.R., Chiocchio, S., Ioki, K., Krassovski, D., Kubik, D., and Tivey, R., 1998, "High Heat Flux Thermal-Hydraulics Analysis of ITER Divertor and Blanket Systems," Fusion Engineering and Design, **39-40**, pp. 323-331.
116. Baxi, C.B., Reis, E.E., Ulrickson, M.A., Heizenroeder, P., and Driemeyer, D., 2003, "Thermal Stress Analysis of FIRE Divertor," Fusion Engineering and Design, **66-68**, pp. 23-327.
117. Razmerov, A.V. and Molochnikov, Y.S., 2000, "Port-Limiter and Divertor Cooling Hydraulic Stability Analysis," Plasma Devices and Operations, **8**, pp. 215-224.
118. Peatiwala, Q. and Boyd, R.D., 2000, "Subcooled Flow Boiling in Circumferentially Nonuniform and Uniform Heated Verical Channels with Downward Flow," Journal of Heat Transfer, **122**, pp. 620-626.
119. www.iter.org/index.htm
120. United States Department of Energy (DOE), Scientific Challenges, Opportunities, and Priorities for the U.S., Fusion Energy Sciences Program--Report to the Fusion Energy Sciences Advisory Committee, 2005.
121. Song, Y.T., Yao, D.M., Wu, S.T., and Weng, P.D., 2005, "Thermal and Mechanical Analysis of the EAST Plasma Facing Components," *Fusion Engineering and Design* **75-79**, pp. 499-503.

122. Salavy, J.F., Giancarli, L., Merola, M., Picard, F., and Rödig, M., 2003, Analysis of High Heat Flux Testing of Mock-Ups, *Fusion Engineering and Design* **66-68**, pp. 277-281.

123. Rödig M., Bobin-Vastra, I., Cox, S., Escourbiac, F., Gervash, A., Kapoustina, A., Kuchnleim, W., Kuznetsov, V., Merola, M., Nygren, R., and Youchison, D. L., 2005 "Testing of Actively Cooled Mock-Ups in Several High Heat Flux Facilites--An International Round Robin Test," *Fusion Engineering and Design* **75-79**, pp. 303-306.

124. D'Agatta, E. and Tivey, R., 2005, "Towards the Development of Workable Acceptance Criteria for the Divertor CFC Monoblock Armour," *Fusion Engineering and Design* **75-79**, pp. 441-445.

125. Fouquet, S., Schlosser, J., Merola, M., Durocher, A., Escourbiac, F., Grosman, A., Missirlian, M., and Portafaix, C., 2006, "Acceptance Criteria for the ITER Divertor Vertical Target," *Fusion Engineering and Design* **81**, pp. 265-268.

126. Bissio, M., Branca, V., Di Marco, M., Federici, A., Grattarola, M., Gualco, G., Guarnone, P., Luconi, U., Merola, M., Ozzano, C., Pasquale, G., Poggi, P., Rizzo, S., and Varone, F., 2005, "Manufacturing and Testing in Reactor Relevant Conditions of Brazed Plasma Facing Components of the ITER Divertor," *Fusion Engineering and Design* **75-79**, pp. 277-283.

127. Jahangeer, S., Ramis, M.K., and Jilani, G., 2007 "Conjugate Heat Transfer Analysis of a Heat Generating Vertical Plate," *Int. J. of Heat and Mass Transfer* **50**, pp. 85-93.

128. Merola, M., "Engineering of Plasma-Facing Components," ITER International Team, Joint Work Site of Cadarche, France, IDM Ref.: ITER_D_Z4UA53, **v. 1.0**, October 7, 2006 [Private Communication].

129. Bobin-Vastra, I. Escourbiac, F., Merola, M., and Lorenzetto, P., 2005 "Activity of the European High Heat Flux Test Facility: FE200, *Fusion Engineering Design* **75-79**, pp. 357-363.

130. Schlosser, J., Escourbiac, F., Merola, M., Fouquet, S., Bayetti, O., Cordier, J.J., Grosman, A., Missirlian, M., Tivey, R., and Rödig, M., 2005, "Technologies for ITER Divertor Vertical Target Plasma Facing Components," *Nuclear Fusion* **45,** 512-518.

131. Ezato, K., Dairaku, M., Taniguchi, M., Sato, K., Suzuki, S., and Akiba, M., 2004, "Development of ITER Divertor Vertical Target With Annular Flow Concept-I Thermal-

Hydraulic Characteristics of Annular Swirl Tube," *Fusion Science and Technology*, **Vol. 46**, pp. 521-529.

132. Boscary, J. Araki, M., and Akiba, M., 1997, "Critical Heat Flux Database of JAERI for High Heat Flux Components for Fusion Applications, JAERI-Data/Code 97-037, Japan Atomic Energy Research Institute.

133. Merola, M. and Palmer, J., 2006, "EU Activities in Preparation of the Procurement of the ITER Divertor, *Fusion Engineering and Design* **81**, pp. 105-112.

134. Missirlian M., Escourbiac, F., Merola, M., Bobin-Vastra, I., Schlosser, J., and Durocher, A., 2005 "Results and Analysis of High Heat Flux Tests On a Full Scale Vertical Target Prototype of ITER Divertor," *Fusion Engineering and Design* **75-79**, pp. 435-440.

135. Boyd, R.D., 1994, "Similarities and Differences Between Single-Side and Uniform Heating For Fusion Applications-I: Uniform Heat Flux," *Fusion Technology,* **Vol. 25,** pp. 411-418.

136. Schlosser, J., Cardella, A., Massmann, P., Chappuis, P., Falter, H.D., Deshamps, P., and Deshamps, G.H., 1991, "Thermal-Hydraulic Tests on Net Divertor Targets Using Swirl Tubes," CEA CEN Cadarache, France, pp. 26-31.

137. Boyd, R.D. and Zhang, H., 2006, "Conjugate Heat Transfer Measurements With Single-Phase and Water Flow Boiling in a Single-Side Heated Monoblock Flow Channel," *Int. J. of Heat and Mass Transfer* **49**, pp. 1320-1328.

138. Schlosser, J., Cardella, A., Massmann, P., and et al., 1991, "Thermal-Hydraulic Tests on Net Divertor Targets Using Swirl Tubes," Seventh Proceedings of Nuclear Thermal Hydraulics, **26**.

139. Pizzarelli, M., Nasuti, F., and Onofri, M., 2011, Analysis of Curved-Cooling-Channel Flow and Heat Transfer in Rocket Engines," *Journal of Propulsion and Power*, **27,** pp. 1045-1053.

140. Boyd, R.D. and May, A.M., 2010, "Conjugate Heat Transfer High-Heat-Flux Amplification Simulation," *Fusion Science and Technology*, **57**, pp. 129-141.

141. Milnes J. and Drikakis D., 2009, "Qualitative Assessment of RANS Models for Hypervapotron Flow and Heat Transfer," *Fusion Engigneering and Design,* **84**, pp. 1305-1312.

142. Boyd, R.D. 2013, "Thermal Management High Heat Flux Amplification Conceptual Model," *Journal of Propulsion and Power*, **29**, pp. 16-20.
143. Altmann H., Falter, H.D., Hemsworth, R.S., and et al., 1990, "A Comparison Between Hypervapotron and Multitude High Heat Flux Beam Stopping Elements," IEEE Thirteenth Symposium on Fusion Engineering, **931**.
144. Ciric, D., Akiba, M., Falter, H-D., and et al., 1999, "Design Issues and Fatigue Lifetime of Hypervapotron Elements of the JET neutral Beam Injectors," 18th IEEE/NPSS Symposium on Fusion Engineering, **407**.
145. Visca, E., Pizzuto, A., Riccardi, B., and et al., 2012, "A Reliable Technology to Manufacture the ITER Inner Vertical Target," Fusion Science and Technology, **61**, pp. 118-123.
146. Youchison, D.L, Ulrickson, M.A., and Bullock, J.H., 2012, "Effects of Hypervapotron Geometry on Thermalhydraulic Performance," IEEE Transaction on Plasma Science, **40**, pp. 653-658.
147. Escourbiac, F., Schlosser, J., Merola, M., and et al., 2003, "Experimental Optimisation of a Hypervapotron Concept for ITER Plasma Facing Components," *Fusion Engineering and Design*, **66-68**, pp. 301-304.
148. Youchison, D.L., Ulrickson M.A., and Bullock J.H., 2011, "Prediction of Critical Heat Flux in Water-Cooled Plasma Facing Components Using Computational Fluid Dynamics," *Fusion Science and Technology*, **60**, pp. 177-184.
149. Schlosser, J., Escourbiac, F., Merola, M., and et al., 2004 "Flat Tile Armour Cooled by a Hypervapotron Tube: A Possible Technology for ITER," Phys. Scr. T111 pp. 199-202.
150. Weaver, A. B., Alexeenko, A. A., Greendyke, R. B., and et al., 2011 "Flowfluid Uncertainty Analysis for Hypersonic Computational Fluid Dynamics Simulations," *Journal of Thermophysics and Heat Transfer*, **25** pp. 10-20.
151. Ulas, A., and Boysan, E., 2013 "Numerical Analysis of Regenerative Cooling in Liquid Propellant Rocket Engines," *Aerospace Science and Technology*, **24**, pp. 187-197.
152. Ruan, B. and Meng, H., 2012 "Supercritical Heat Transfer to Cryogenic-Propellant Methane in Rectangular Engine Cooling Channels," *Journal of Thermophysics and Heat Transfer*, **26**, pp. 313-321.

153. Federici, G. and Raffray, A.R., 1997, "RACLETTE: A Model for Evaluating the Thermal Response of Plasma Facing Components to Slow High Power Plasma Transients. Part II: Analysis of ITER Plasma Facing Components," *Journal of Nuclear Mater*, **244,** pp. 101-130.
154. Raffray, A.R., Schlosser, J., Akiba, M., and et al., 1999 "Critical Heat Flux Analysis and R&D for the Design of the ITER Divertor," *Fusion Engineering and Design*, **45**, pp. 377-407.
155. Escourbiac, F., Guigon, R., Richou, M., and et al., "Acceptance Criteria for the ITER Divertor," 12th International Workshop on Plasma-Facing Materials and Components (PFMC-12) for Fusion Applications, Forschungszentrum, Jülich, Germany, May 2009.
156. Milnes, J., Burns, A., and Drikakis, D., 2012 "Computational Modeling of Hypervapotron Cooling Technique," *Fusion Engineering and Design*, **87**, pp. 1647-1661.
157. www.iter.org/mach.
158. Wang, Z., Song, Y., and Huang, S., 2012 "Design of the Hypervapotron Module for the EAST Device," *Fusion Engigneering and Design*, **87**, pp. 868-871.
159. Youchison, D.L., Ulrickson, M.A. and Bullock, J.H., 2011, "Thermalhydraulic Optimization of Hypervapotron geometries for First Wall Applications," 24th IEEE/NPSS Symposium on Fusion Engineering, pp. 1-6.
160. Tao, L., Xie, Y., Hu, C., and et al., 2010, "Numerical Analysis of a Cooling System for High Heat Flux Components in the Neutral Beam Injection System," *Fusion Engineering and Dessign*, **85**, pp. 2095-2099.
161. Boyd, R.D., 2013 "Thermal Management Using a Hypervapotron; Part I: Some Controlling Parameters," Nuclear and Emerging Technologies for Space (NETS-2013) Paper 6903.
162. Youchison, D.L., Ulrickson, M.A., and Bullock, J.H., 2010, "A Comparison of Two-Phase Computational Fluid Dynamic Codes Applied to the ITER First Wall Hypervapotron," IEEE Transactions on Plasma Science, **38**, **Iss. 7**, pp. 1704-1708.
163. Pascal-Ribot, S., Saroli, A.F., Grandotto, M., and et al., 2007, "3D Numerical Simulations of Hypervapotron Cooling Concept," *Fusion Engineering and Design*, **82**, pp. 1781-1785.

164. Ovchinnikov, I.B., Bondarchuk, D.E., Gervash, A.A., and et al., 2011, "ITER FW Cooling By a Flat Channel, Adapted to Low Flow Rate and High Pressure Drop," *Fusion Engineering and Design*, **86**, pp. 2971-2982.

165. Lee, D.W., Bae, Y.D., Kim, S.K., and et al., 2010, "Design Evaluation of the Semi-Prototype for the ITER Blanket First Wall Qualification," *Journal of Thin Solid Films*, **518**, pp. 6676-6681.

166. Lee, D.W., Bae, Y.D., Kim S.K., and et al., 2010, "Experimental and Analysis of Hypervapotron Mock-Ups for Preparing the 2nd Qualification of the ITER Blanket First Wall, *Fusion Engineering and Design*, **85**, pp. 2155-2159.

167. Wang, Z.W., Song, Y.T., and Huang, S.H., 2011, "Analysis and Experiment of the Hypervapotron Mock-Up for the EAST Upgrade," 24th IEEE/NPSS Symposium on Fusion Engineering SP2-10, pp. 1-4.

168. Mazul, I., Alekseev, A., Belyakov, V. and et al., 2012, "Russian Development of Enhanced Heat Flux Technologies for ITER First Wall," *Fusion Engineering and Design*, **87**, pp. 437-442.

169. Cattadori, G., Gaspari, G.P., Celata, G.P., and et al., 1993, "Hypervapotron Technique in Subcooled Flow Boiling CHF," *Experimental Thermal and Fluid Science*, **7**, pp. 230-240.

170. Escourbiac, F., Vastra, I.B., Kuzentsov, V., and et al., 2005, "A Mature Industrial Solution for ITER Divertor Plasma Facing Components: Hypervapotron Cooling Concept Adapted to Tore Supra Flat Tile Technology, *Fusion Engigneering and Design*, **75-79**, pp. 387-390.

171. Incropera, F.P., Dewitt, D.P., Bergman, T.L., and et al., 2007, "Fundamentals of Heat and Mass Transfer, Sixth Ed., John Wiley & Sons, pp. 144-154.

172. Domalapally, P., Rizzo, E., Richard, L.S., and et al., 2012, "CFD Analysis of Flow Boiling in the ITER First Wall, *Fusion Engineering and Design*, **87**, pp. 556-560.

173. Ying, A., Waku, T., Youchison, D.E., and et al., 2011, "A Subcooled Boiling Heat Transfer Predictive Model for ITER EHF FW Designs, *Fusion Engineering and Design*, **86**, pp. 667-670.

174. ShengHong, H., WeiRong, W., ZongWei, W., and et al., 2013, "Eperimental Study of Hypervapotron Under Conditions of High Heat Flux," Science China: Technological Sciences, **56**, pp.222-227.

175. Boyd, R.D., "High Heat Flux removal Using a Hypervapotron; Part II: Additional Controlling Parameters," 34th Annual Conference of the Canandian Nuclear Society, Toronto (ON) Canada, June 9-12, 2013.
176. Boyd, R.D., May, A.M., Cofie, P., and Martin, R., "High Heat Flux Removal Measurements in a Single-Side Heated Monoblock Flow Channel with a Helical Wire Insert," The 41th IEEE International Conference on Plasma Science and the 20th International Conference on High-Power Particle Beams, Washington, D.C., 2014.
177. Song, K.D., Choi, S.H., and Scotti, S.J., 2006 "Transpiration Cooling Experiment for Scramjet Engine Combustion Chamber by High Heat Fluxes," *Journal of Propulsion and Power*, **22**, pp. 96-102.
178. deRidder, M.A. and Anderson, W.E., 2010, "Heat Flux and Pressure Profiles in an Oxygen/Hydrogen Multielement Rocket Combustor," *Journal of Propulsion and Power*, **26,** pp. 696-705.
179. Garcia, A., Vicente, P.G., and Viedma, A., 2005, "Experimental Study of Heat Transfer Enhancement with Wire Coil Inserts in Laminar-Transition-Turbulent Regimes at Different Prandtl Numbers," *International Journal of Heat and Mass Transfer*, **48**, pp. 4640-4651.
180. Feng, S.S., Kim, T., and Lu, T.J., 2011 "Thermal Resistance Analysis of Pin-Fin Heat Sinks Under Nonuniform Impingement Heating," *Jorunal of Thermophysics and Heat Transfer*, **25**, pp. 119-129.
181. Michalak T.E., et al., 2010 "Accerleration Effects on the Cooling Performance of a Partially Confined FC-72 Spray," *Jorunal of Thermophysics and Heat Transfer*, **24**, pp. 463-479.
182. Ponnappan, R., et al., 1996 "Active Cooling of Metal Oxide Semiconductor Controlled Thyristor Using Venturi Flow," *Journal of Propulsion and Power*, **12**, pp. 398-404.
183. Arnold, R., Suslov, D., and Haidn, O.J., 2009, "Film Cooling of Accelerated Flow in a Subscale Combustion Chamber," *Journal of Propulsion and Power*, **25**, pp. 443-451.
184. Wheeler, A.J. and Ganji, A.R., 1996 "Introduction to Engineering Experimentation," Prentice Hall, Englewood Cliffs.

APPENDIX A: IHHFR LABORATORY PHOTO GALLERY

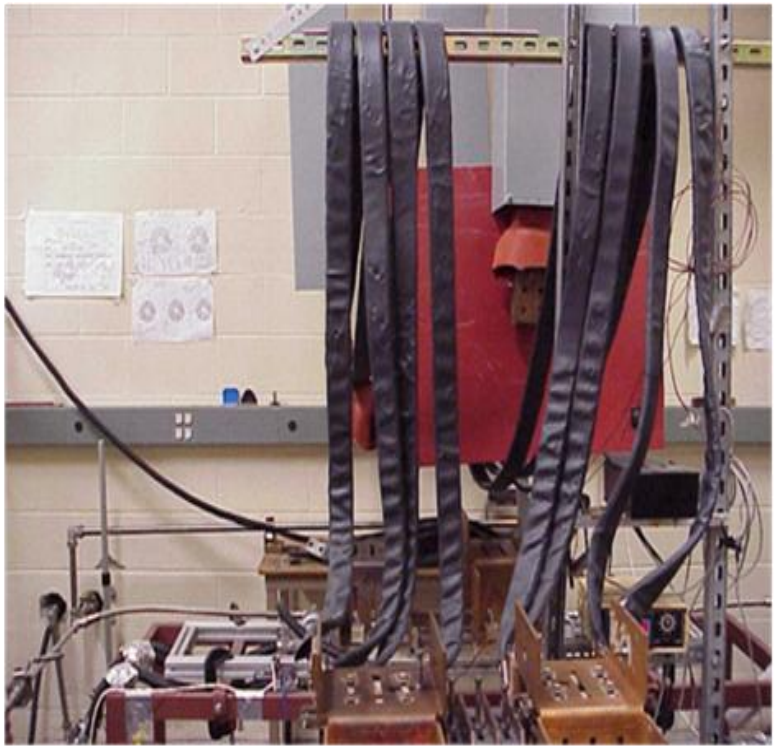

TEST CENTER CLOSE CENTER VIEW

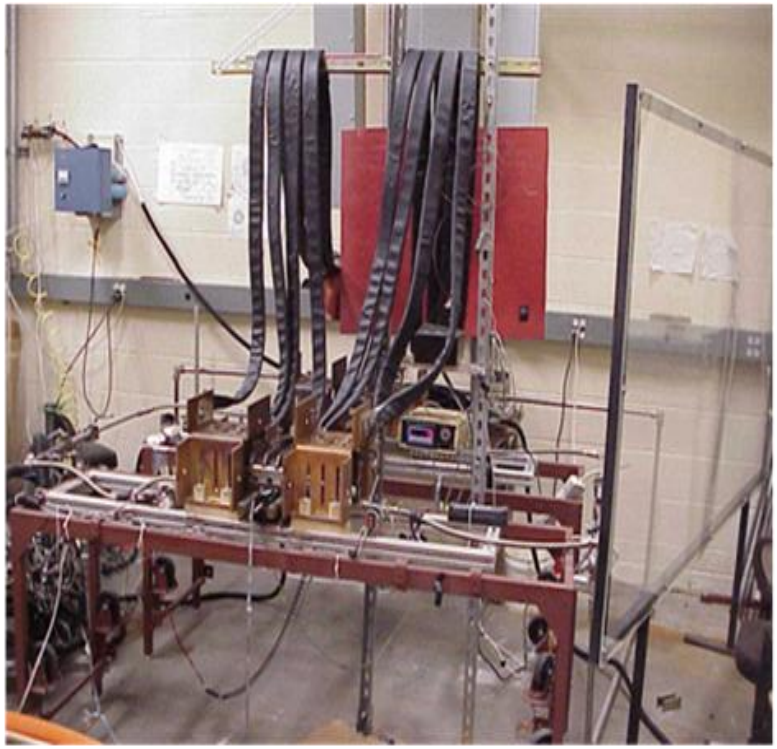

TEST CENTER CLOSE RIGHT VIEW

FRONT VIEW OF RIGHT DELL COMPUTER MONITOR

FRONT VIEW OF TYPICAL COMPUTER WIRE CONNECTIONS

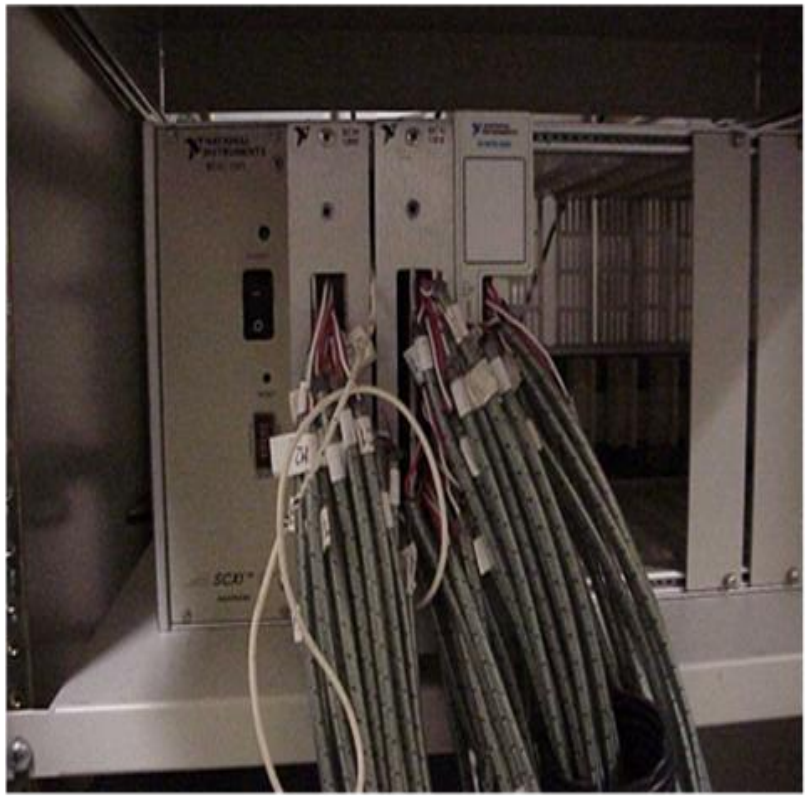

FRONT CLOSE UP OF TYPICAL COMPUTER WIRE CONNECTIONS

RIGHT SIDE CLOSE UP OF TYPICAL COMPUTER WIRE CONNECTIONS

A-5

LEFT SIDE VIEW OF TYPICAL COMPUTER CONNECTIONS

LEFT CLOSE VIEW OF RIGHT COMPUTER WIRE CONNECTIONS

LEFT VIEW OF CONNECTION WIRES FROM THE COMPUTER TO TESTING BLOCK

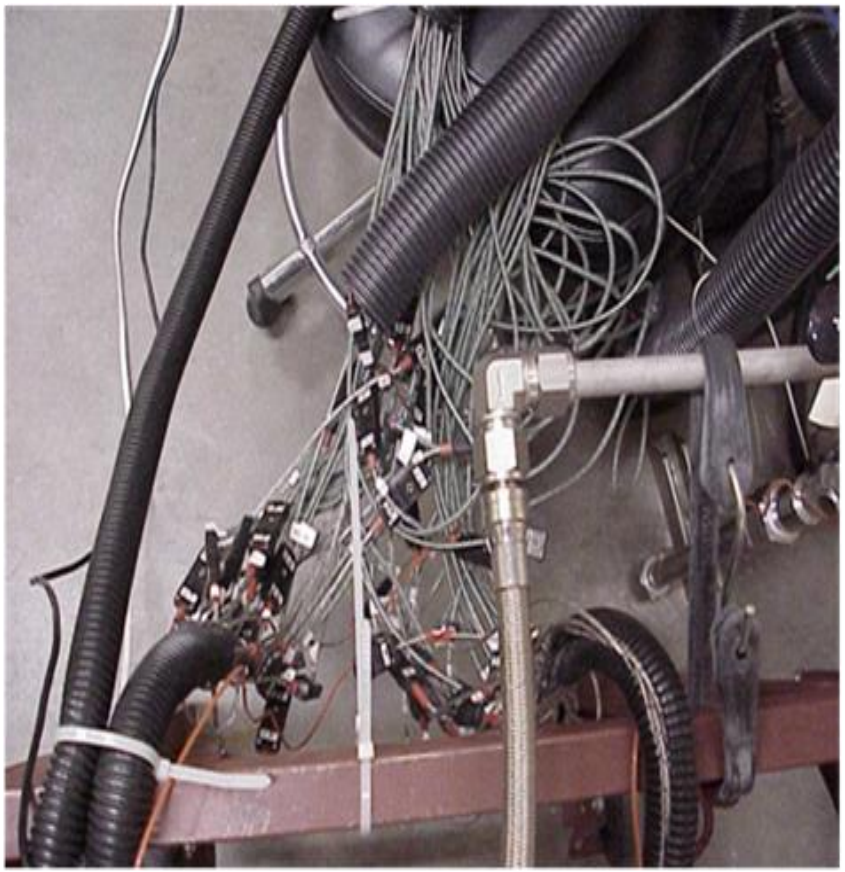

RIGHT VIEW OF CONNECTION WIRES FROM THE COMPUTER TO TESTING BLOCK

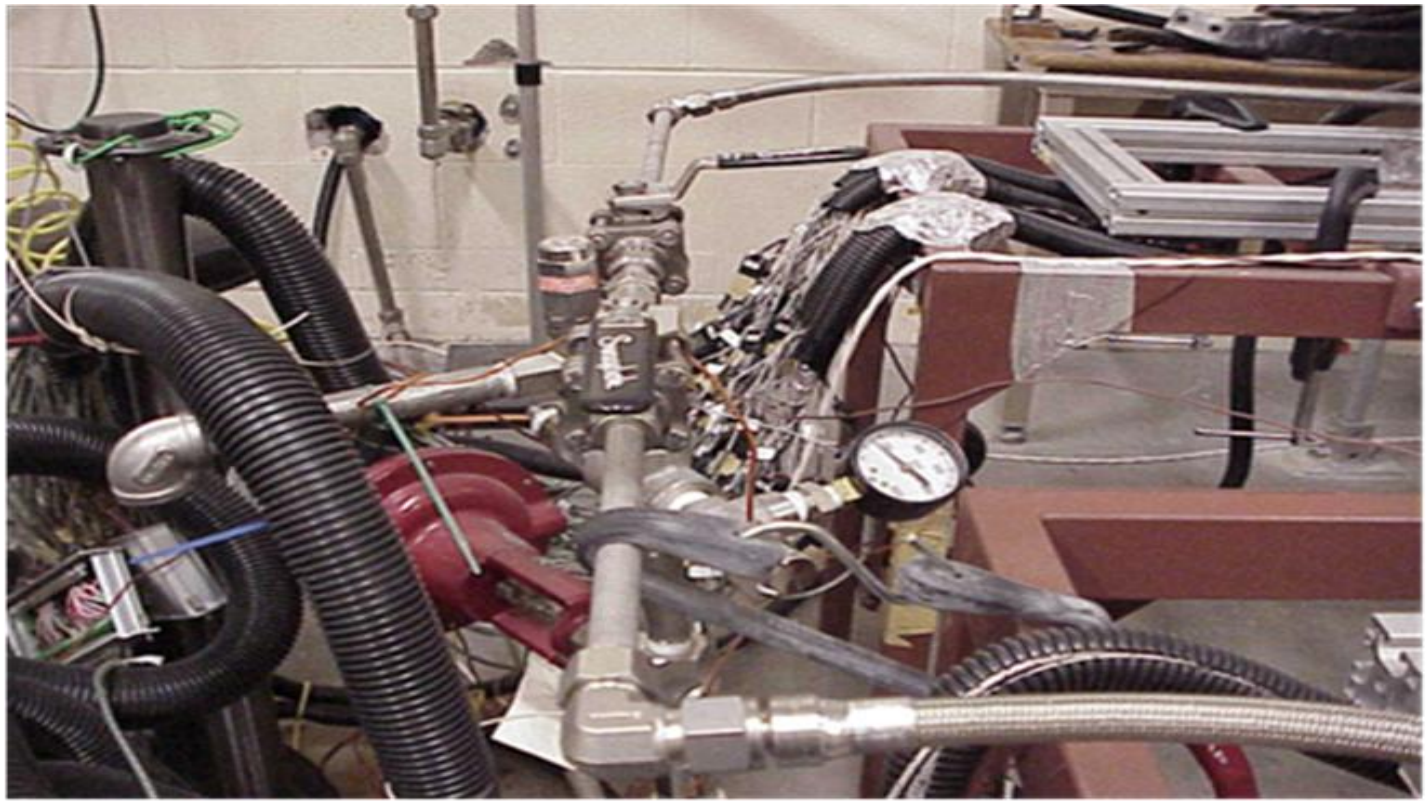

FRONT VIEW OF LEAD TEST CENTER WATER PIPE, WATER QUALITY METER AND FLOW METER

TOP VIEW OF LEAD TEST
CENTER WATER PIPE

BACK VIEW OF LEAD TEST
CENTER WATER PIPE

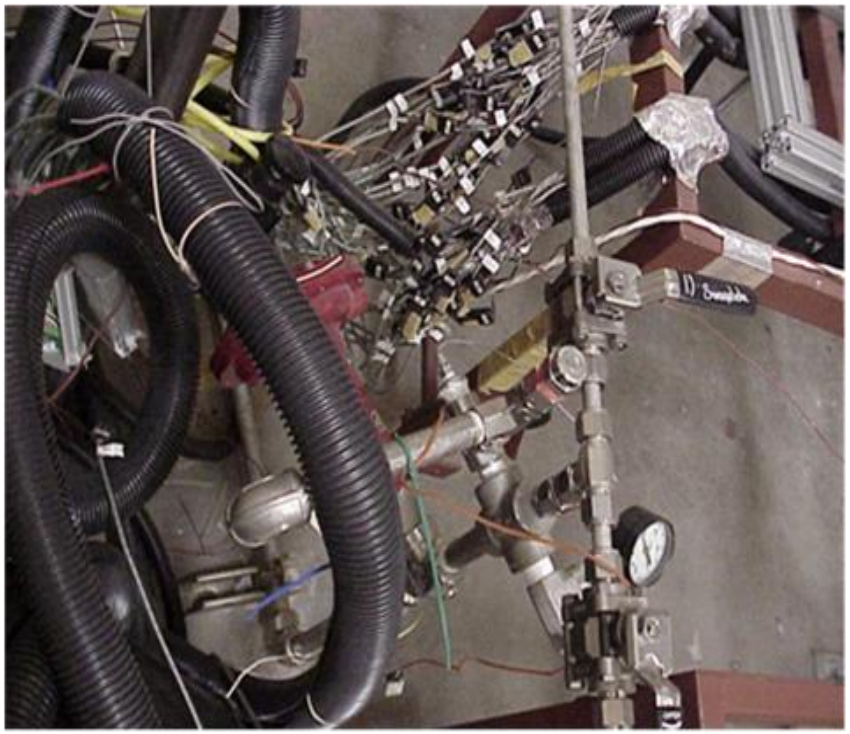

LEFT VIEW OF LEAD TEST CENTER WATER PIPE

SIDE VIEW OF TEST CENTER WITH BUS CABLES, TEST SECTION, ALUMINUM NITRIDE, FLUID FLOW, HEATER & MYKROY

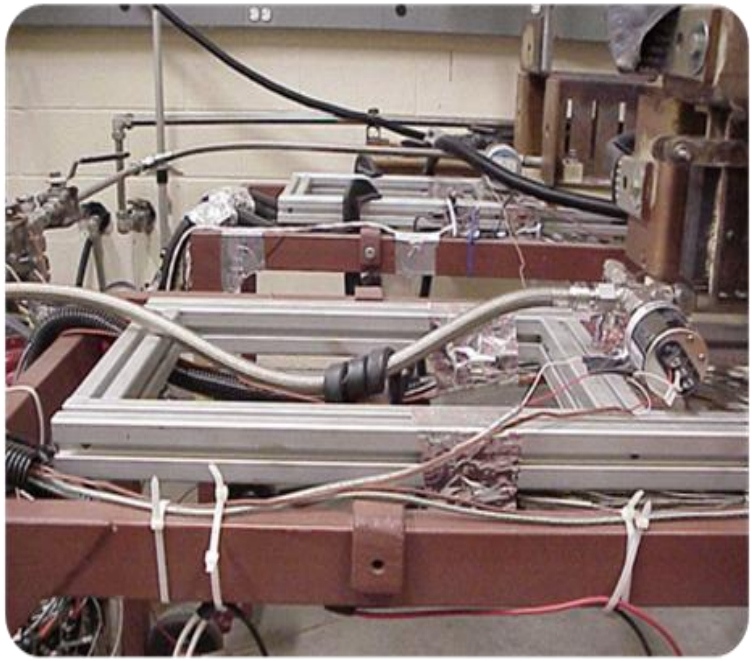

FRONT VIEW OF TEST BEDS
FOR MONOBLOCKS WITH
AND WITHOUT HWI

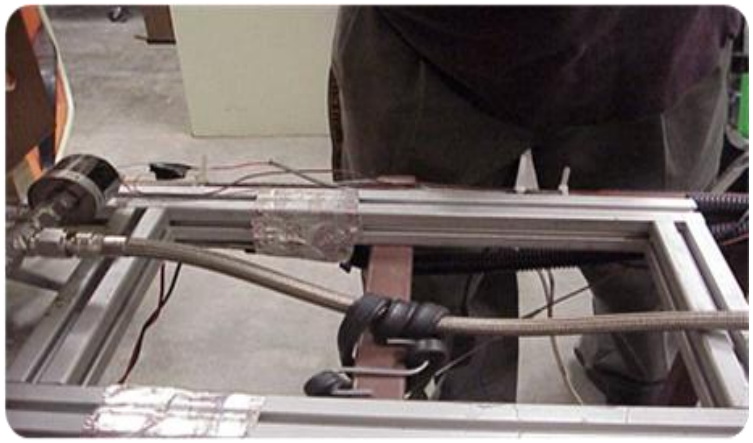

BACK VIEW OF TEST
FRAMES AND FLEXIBLE PIPE

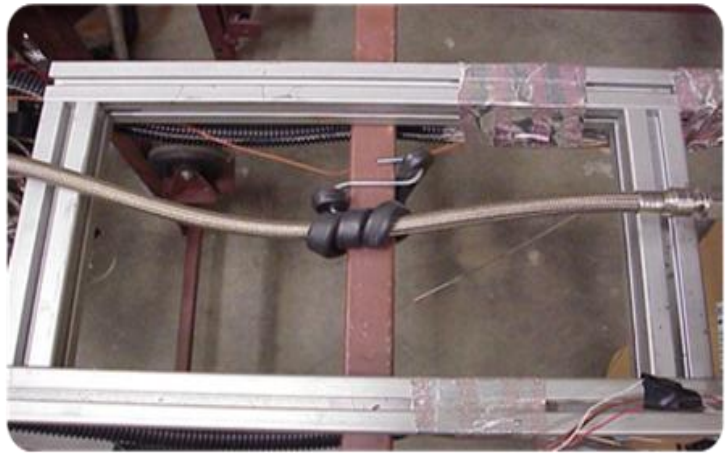

TOP VIEW OF TEST FRAMES
AND FLEXIBLE PIPE

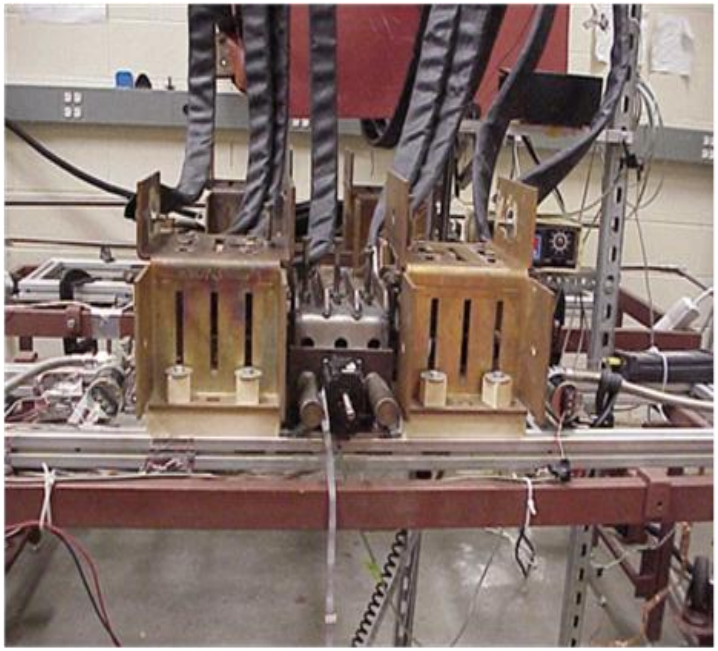

FRONT VIEW OF MONOBLOCK* SADDLE, COUNTERBALANCE GUIDE BAR, POSITIONING TABLE BRACKET, HEATER* PRESSURE APPLICATOR, BUS BAR SUPPORT, & STEEL BAR

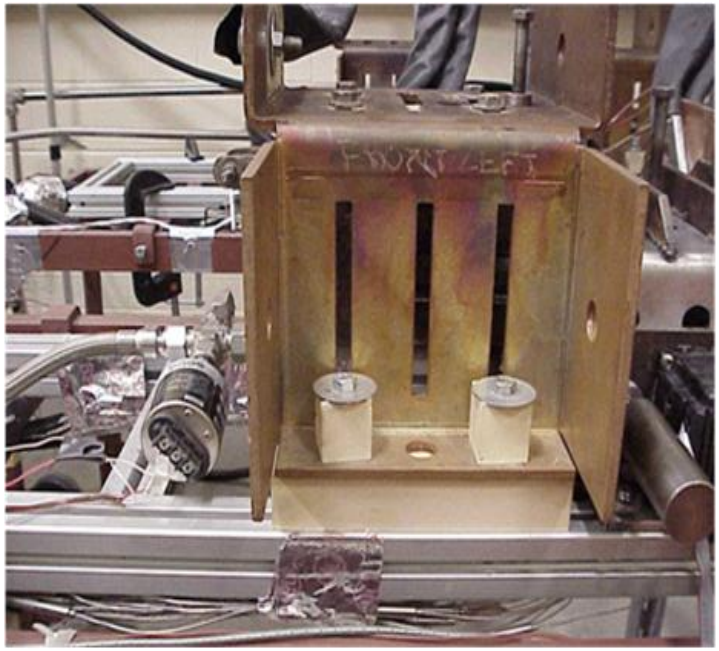

FRONT VIEW OF LEFT MONOBLOCK SADDLE BUS BAR SUPPORT

*LOCATED INSIDE SADDLE

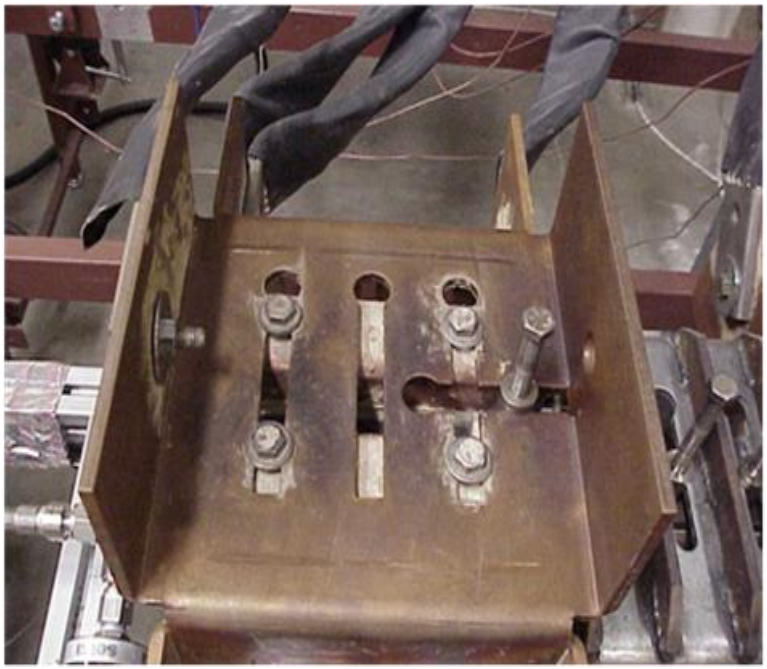

LEFT TOP VIEW OF MONOBLOCK SADDLE, BUS BAR SUPPORT, BUS BAR SUPPORT, HEATER PRESSURE APPLICATOR

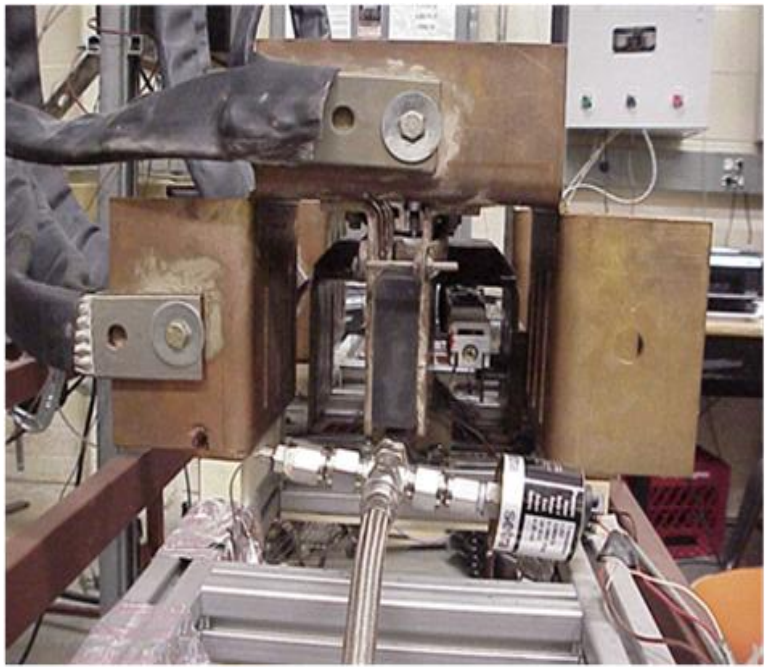

AXIAL VIEW OF MONOBLOCK SADDLE, BUS BAR SUPPORT, GRAPHITE HEATER, HEATER TRANSITION PLATE, MYKROY BLOCK, TEST BED, TEST SECTION, FLUID FLOW FLEXIBLE PIPING, STEEL BAR, POSITIONING TABLE BRACKET, ELECTRICAL PROBES, BLOCK MOUNTING NUT & BOLT AND CLAMP.

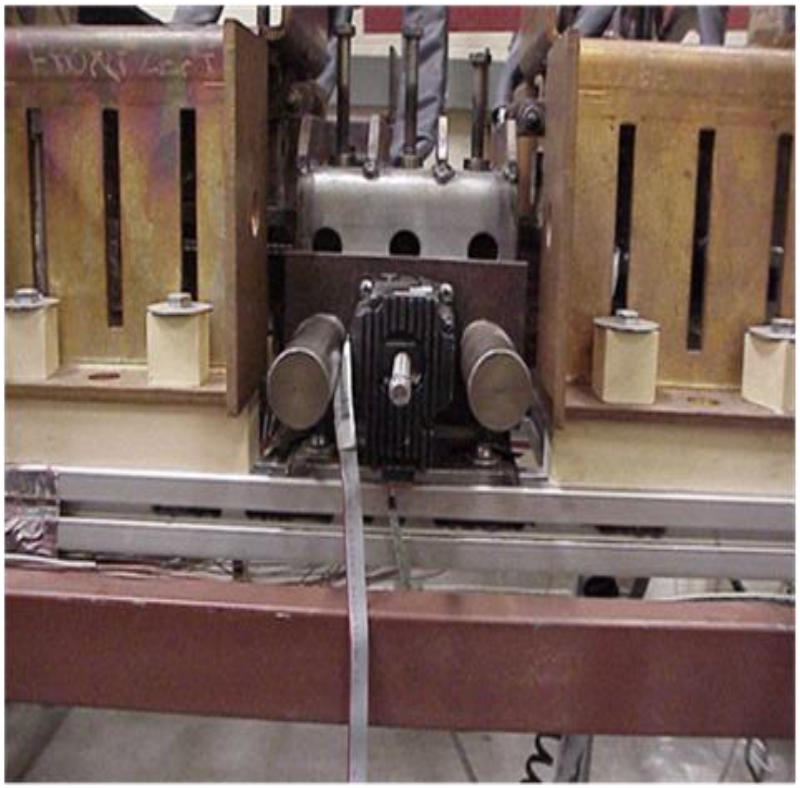

FRONT CLOSE VIEW OF MONOBLOCK SADDLE, HEATER POWER DISTRIBUTION COUNTERBALANCE GUIDE BAR, AND LOCKING NUT

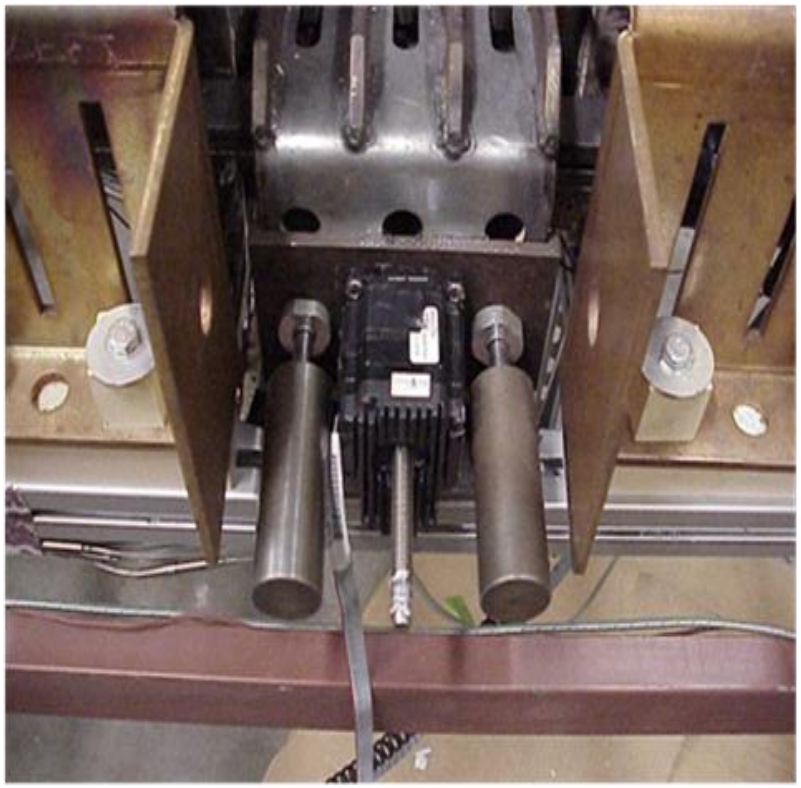

TOP VIEW OF MONOBLOCK SADDLE, COUNTERBALANCE GUIDE BAR, & LOCKING NUT

LEFT SIDE VIEW OF COUNTERBALANCE GUIDE BAR, LOCKING NUT AND SADDLE

RIGHT VIEW OF COUNTERBALANCE GUIDE, LOCKING NUT AND SADDLE

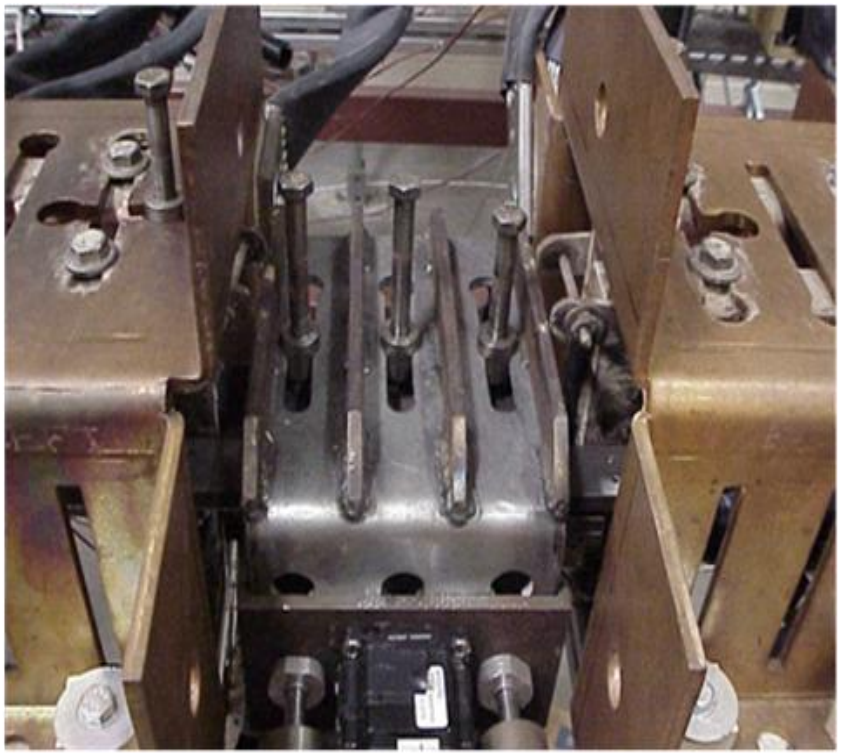

FRONT VIEW OF SADDLE & HEATER PRESSURE APPLICATOR AND BUS BAR SUPPORTS

TOP VIEW OF SADDLE & HEATER PRESSURE APPLICATOR

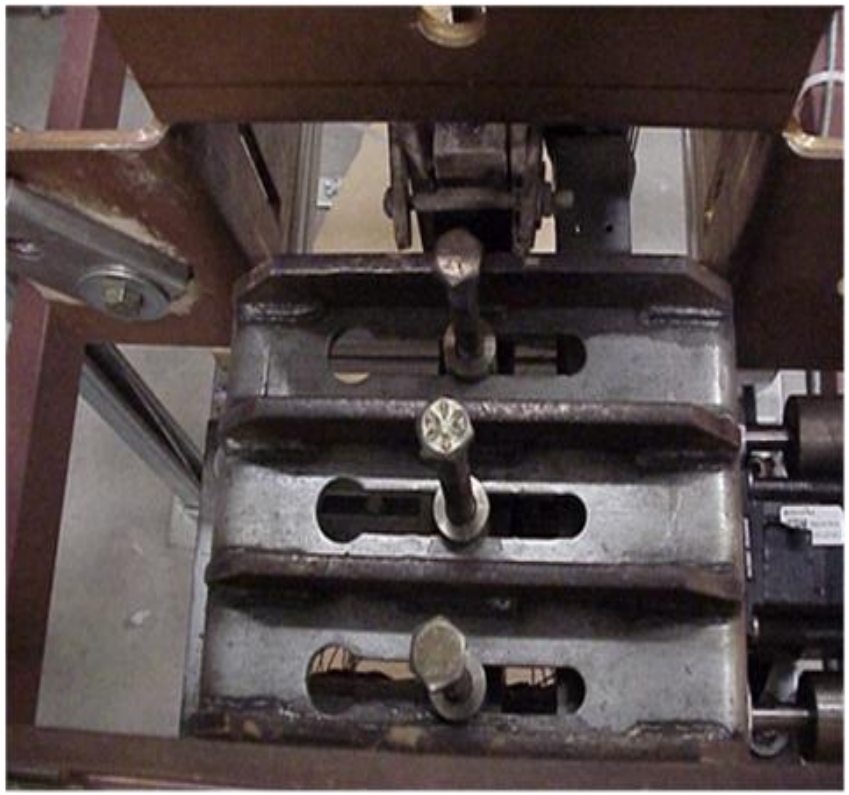

TOP VIEW OF HEATER
PRESSURE APPLICATOR

BACK TOP VIEW OF HEATER
PRESSURE APPLICATOR

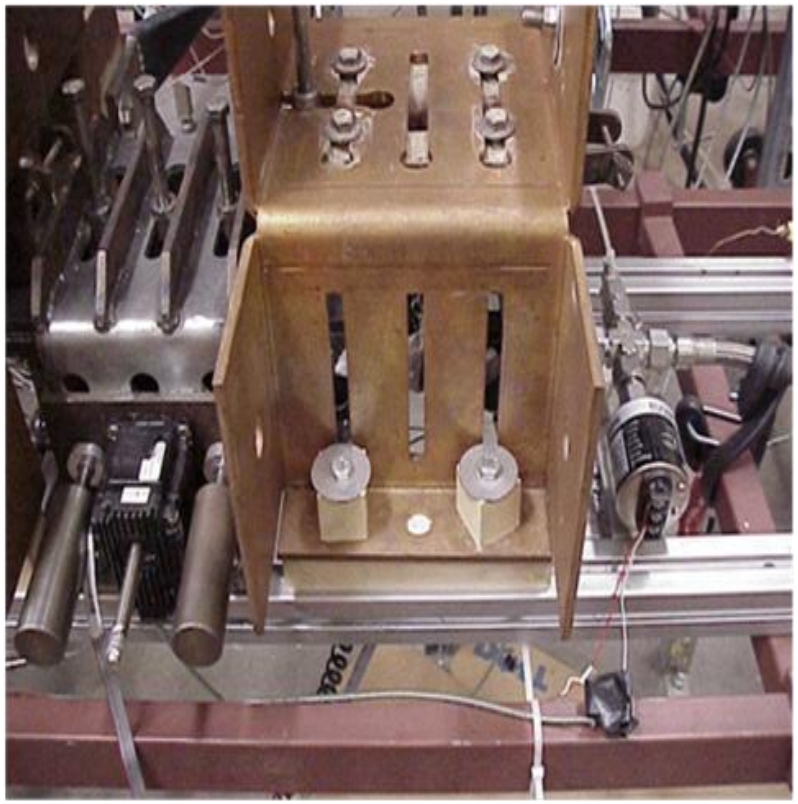

FRONT VIEW OF RIGHT BUS BAR SUPPORT, FLOW METER, MASS FLOW RATE AND FLEXIBLE PIPE

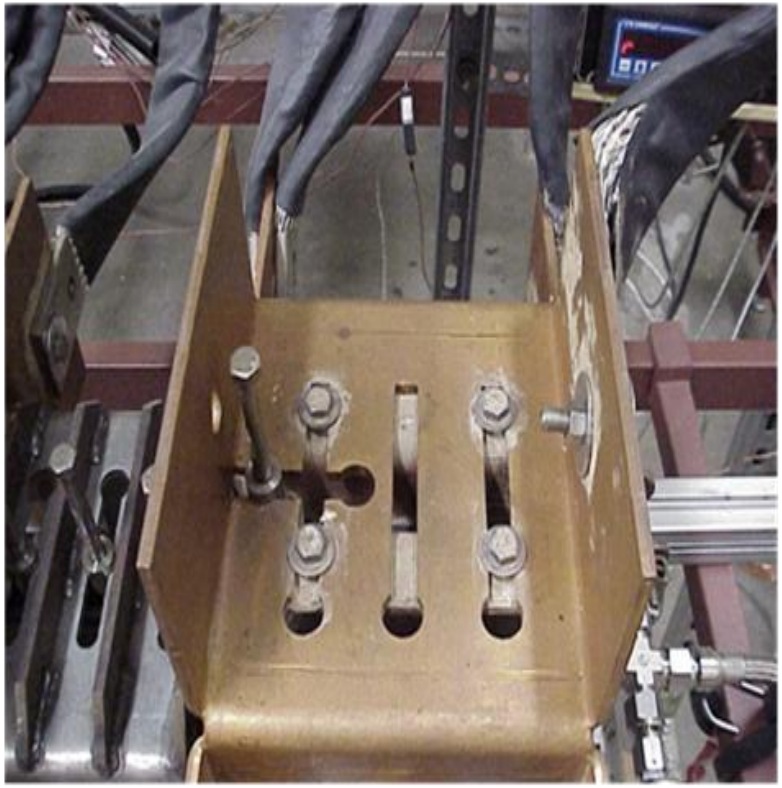

TOP VIEW OF RIGHT BUS BAR SUPPORT FLOW METER, MASS FLOW RATE AND FLEXIBLE PIPE

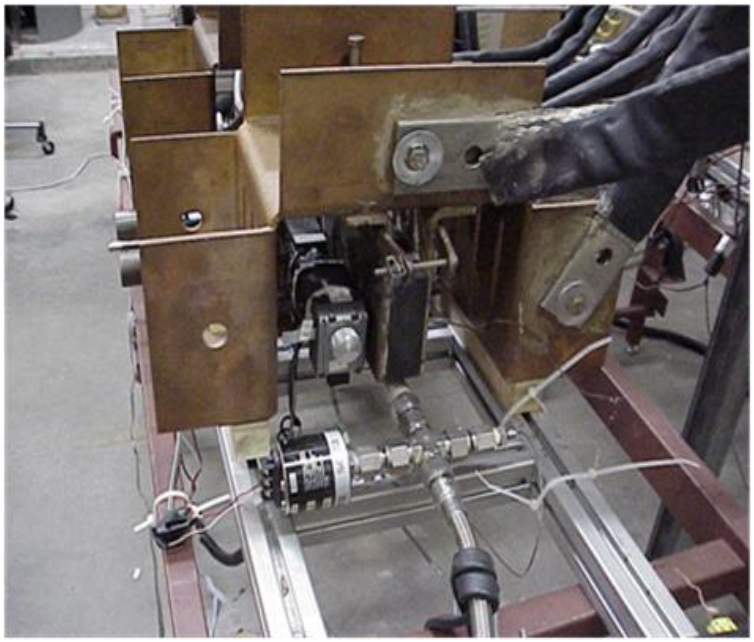

RIGHT SIDE OF MONOBLOCK SADDLE, BUS BAR SUPPORT, GRAPHITE HEATER, HEATER TRANSITION PLATE, MYKROY BLOCK, TEST BED, TEST SECTION*, FLEXIBLE FLOW DUCTING, POSITIONING TABLE BRACKET, ELECTRICAL PROBES, BLOCK MOUNTING NUT & BOLT, AND CLAMP

*LOCATED UNDER THE HEATER

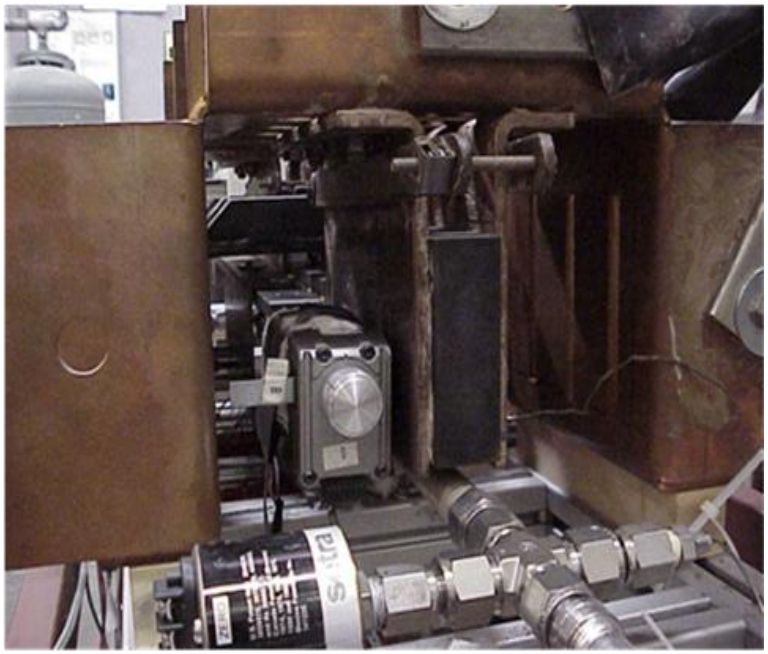

RIGHT CLOSE VIEW OF MONOBLOCK SADDLE, BUS BAR SUPPORT, GRAPHITE HEATER, HETAER TRANSITION PLATE, MYKROY BLOCK, TEST BED, TEST SECTION, FLEXIBLE FLOW DUCTING, ALUMINUM NITRIDE*, STEEL BAR, POSITIONING TABLE BRACKET, ELECTRICAL PROBES, BLOCK MOUNTING NUT & BOLT, AND CLAMPS

*LOCATED ABOVE THE TEST SECTION

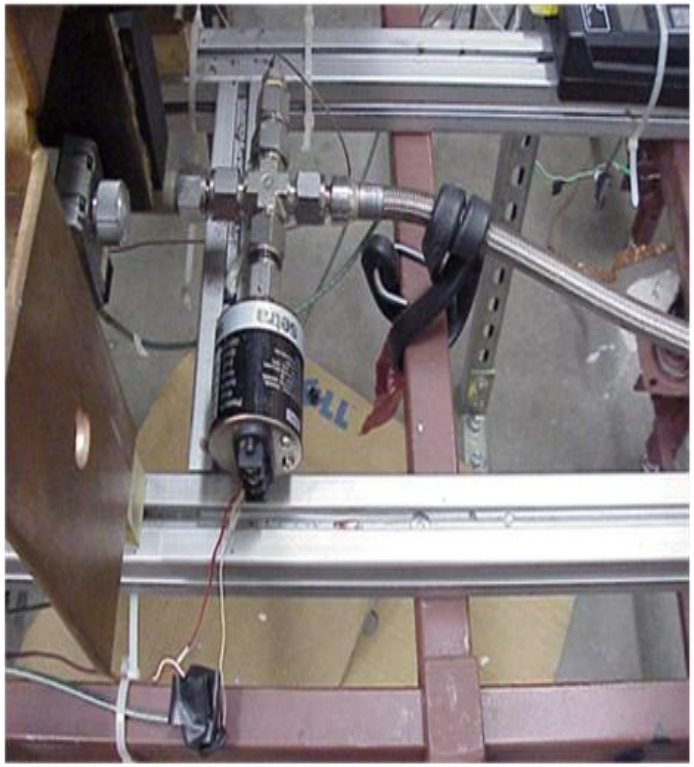

TOP VIEW OF FLOW METER, FLEXIBLE PIPE, AND TEST BED FRAMES

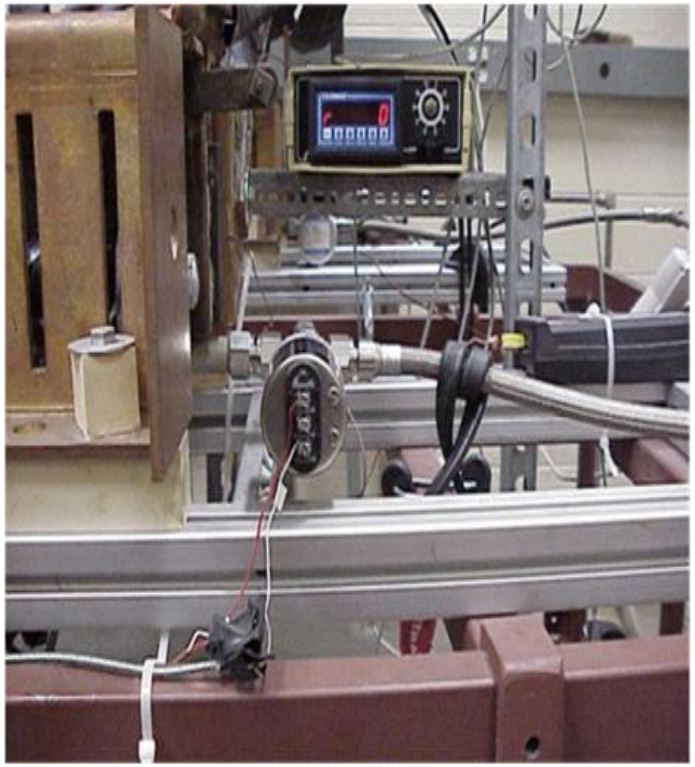

FRONT VIEW OF FLOW METER, FLEXIBLE PIPE, AND TEST BED FRAMES

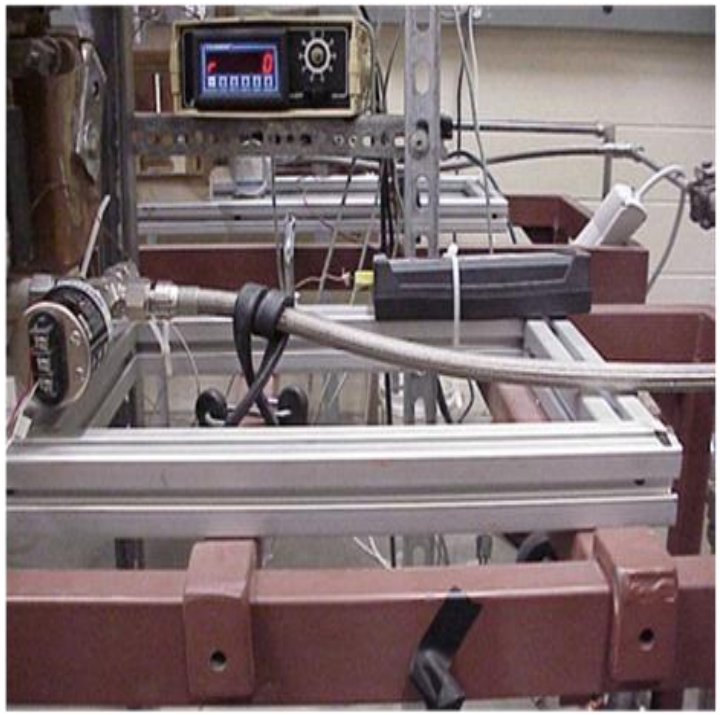

RIGHT VIEW OF FLOW METER, FLEXIBLE PIPE, AND TEST BED FRAMES

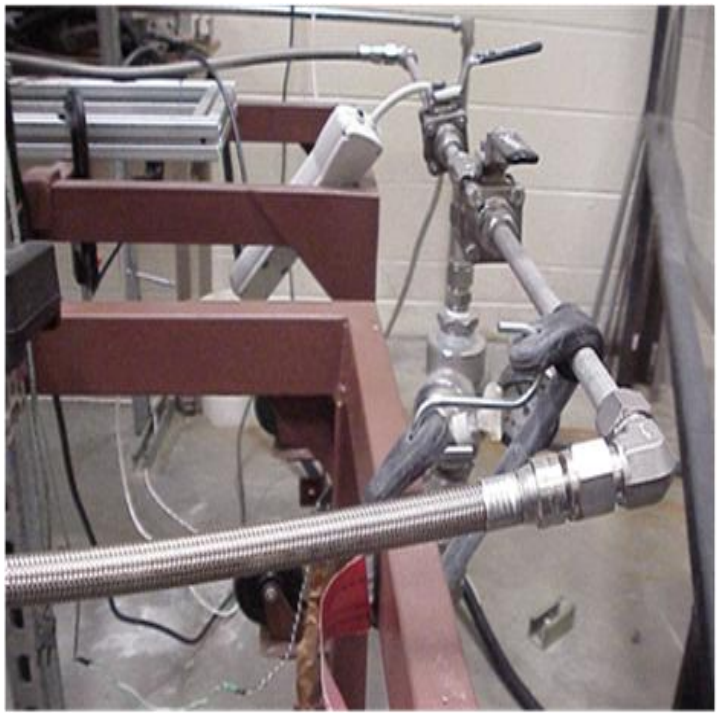

FRONT VIEW OF WATER VALVES, FLEXIBLE PIPE, FINE FILTER, AND FLOW METER

TOP VIEW OF WATER VALVES

BOTTOM VIEW OF TEST CENTER WIRES

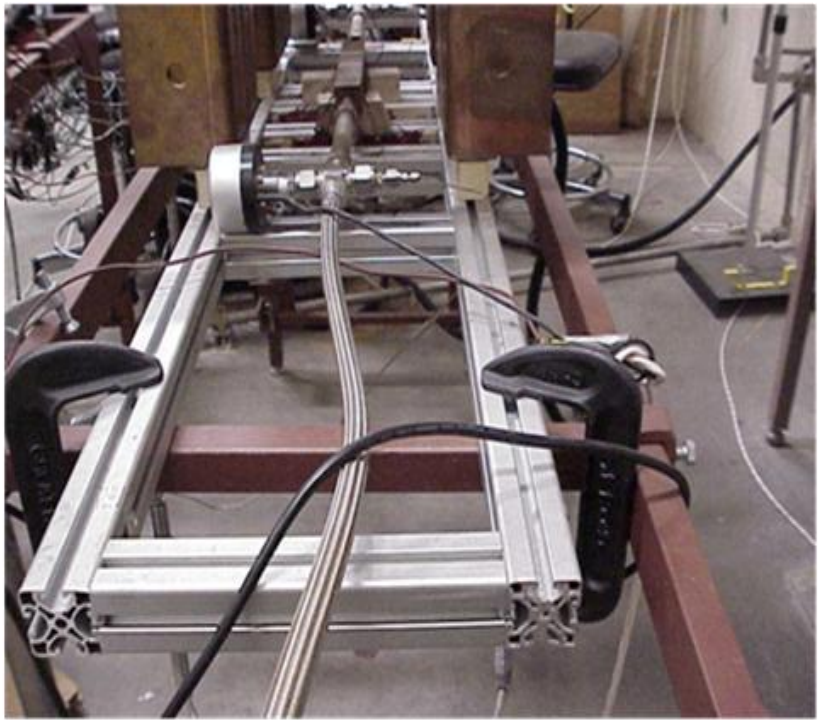

RIGHT, BACK VIEW OF MONOBLOCK TEST CENTER, FLEXIBLE PIPE, THERMOCOUPLES, PRESSURE TRANSDUCER, BYPASS VALVE, AND FLOW METER

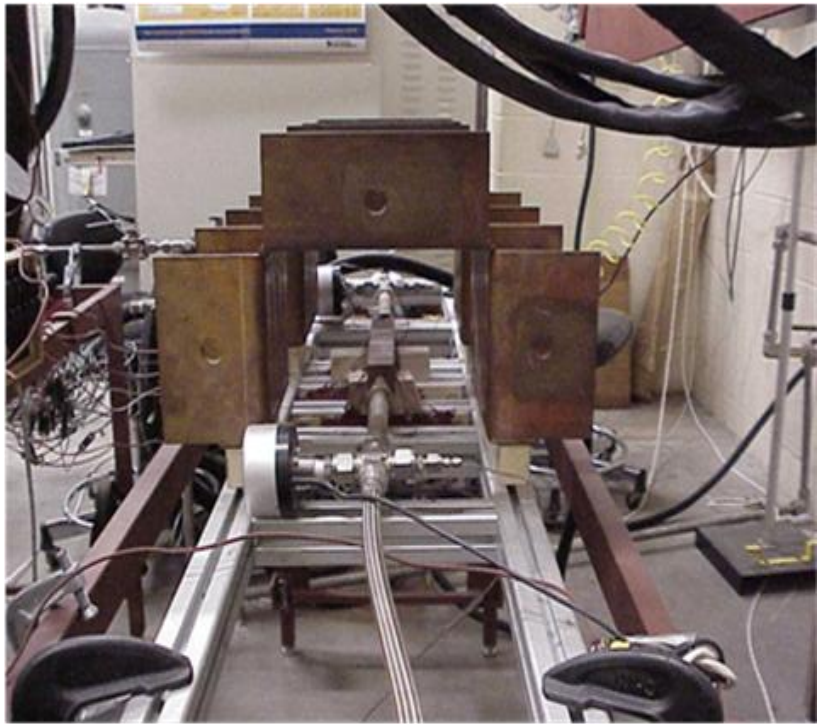

RIGHT, BACK VIEW OF MONOBLOCK TEST CENTER, FLEXIBLE PIPE, THERMOCOUPLES, PRESSURE TRANSDUCER, BYPASS VALVE, AND FLOW METER

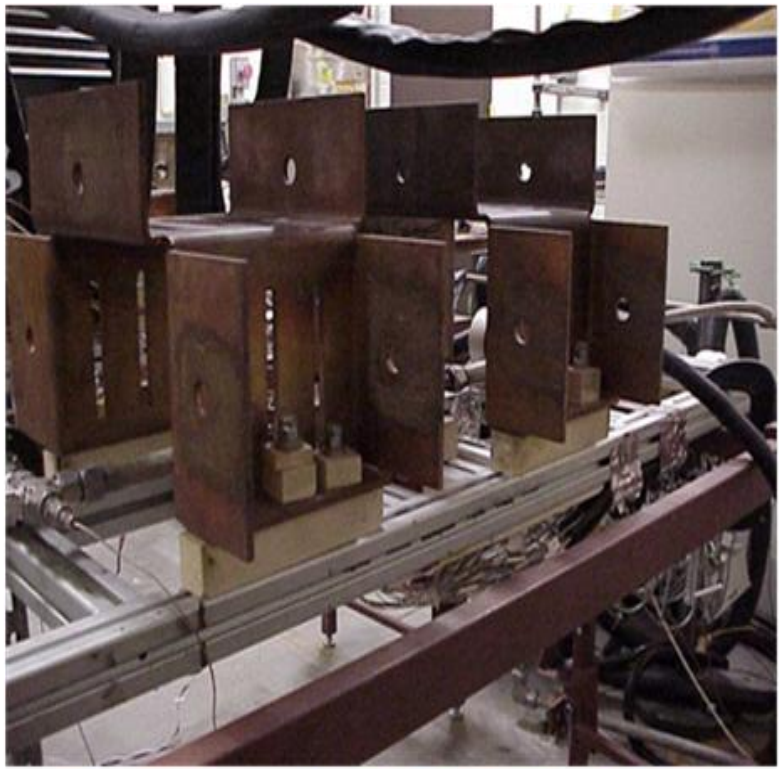

BACK VIEW OF MONOBLOCK TEST BED, FLEXIBLE PIPE, THERMOCOUPLE LEADS, AND PRESSURE TRANSDUCER

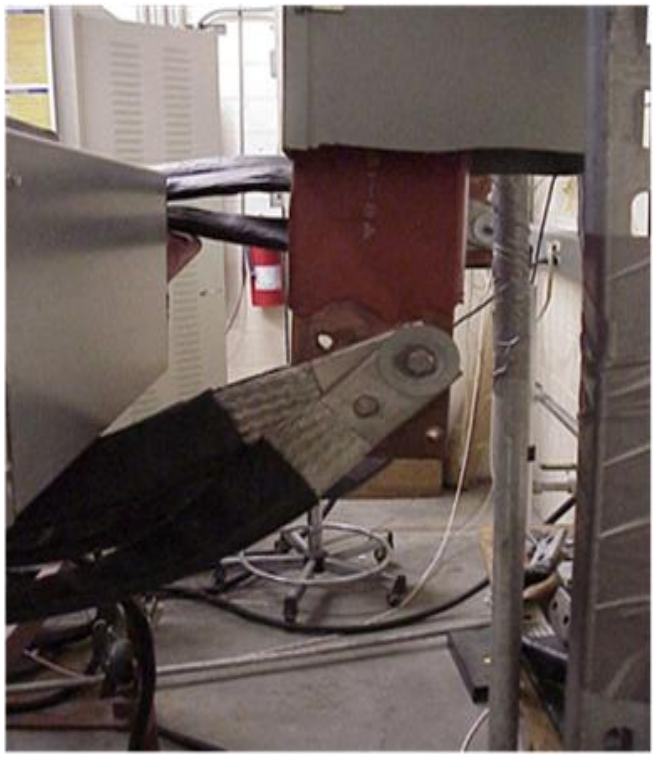

FLEXIBLE POWER CONNECTION TO POWER SUPPLY SOLID BUS BARS

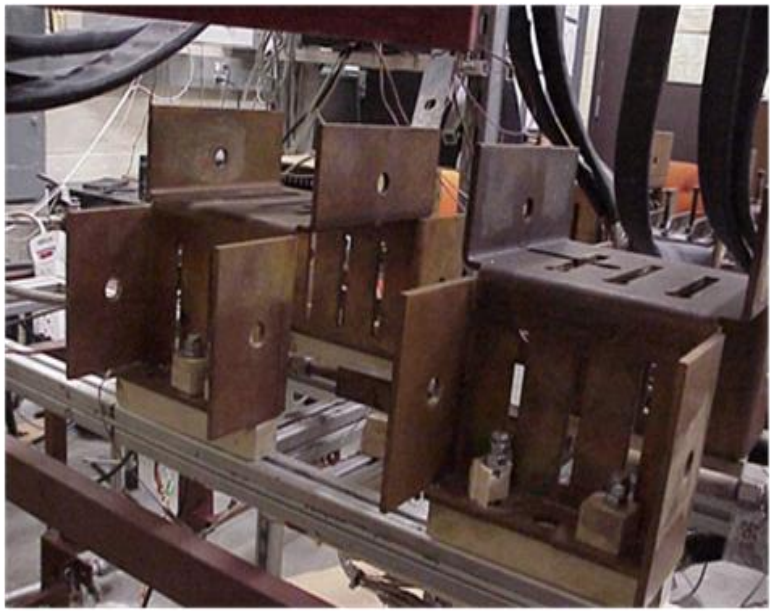

BACK VIEW OF MONOBLOCK BUS BAR SUPPORT, FINE FILTER, AND TEST BED

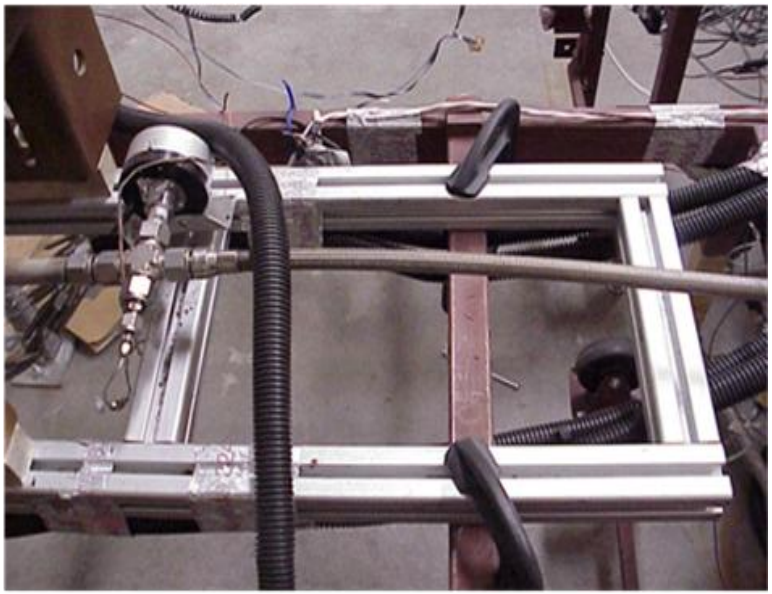

BACK VIEW OF ONE END OF A TEST BED

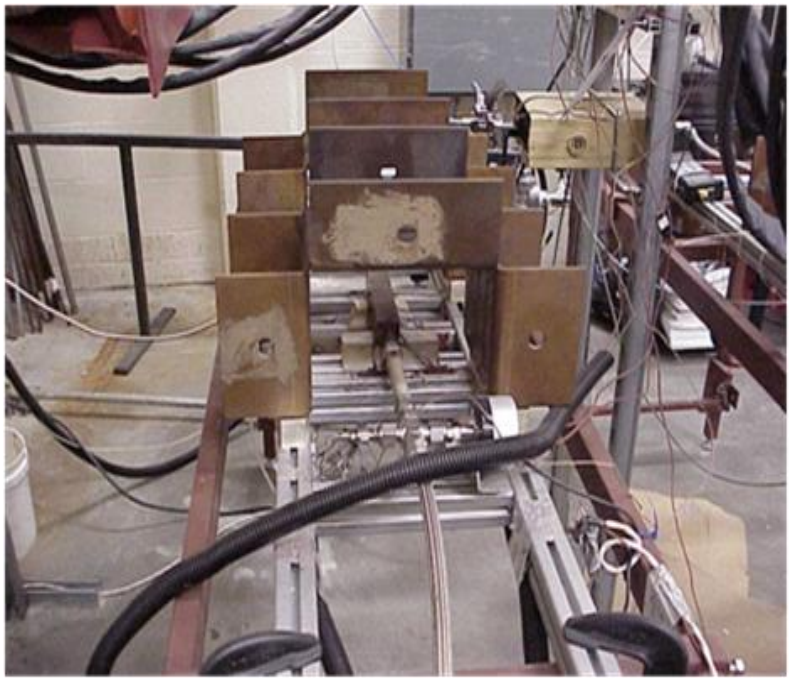

BACK RIGHT VIEW OF MONOBLOCK SADDLE, TEST BED, TEST SECTION, FLUID FLOW DUCTING, MYKROY BLOCK , FINE FILTER, BYPASS VALVE, AND MULTIPLE THERMOCOUPLES

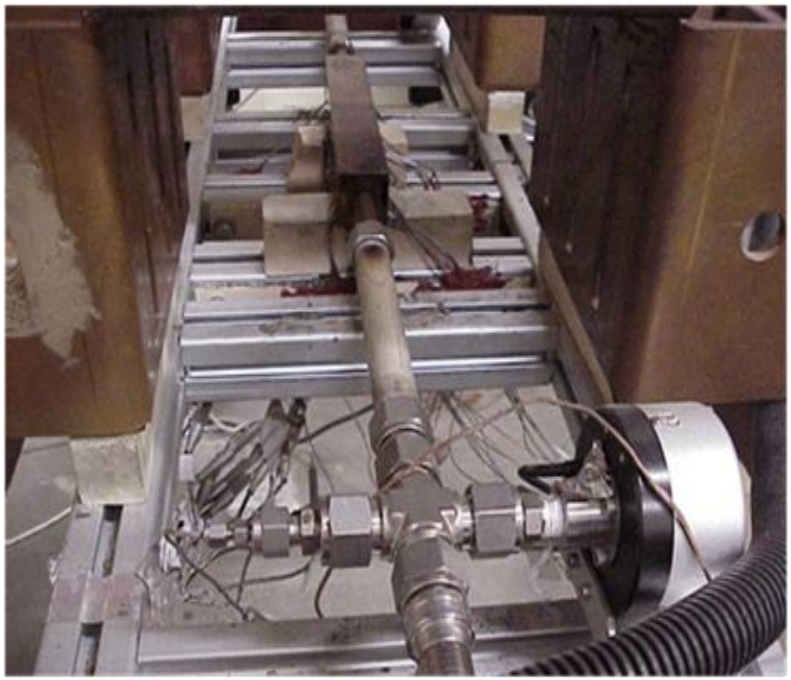

BACK RIGHT CLOSE VIEW OF MONOBLOCK SADDLE, TEST BED, TEST SECTION, FLUID FLOW DUCTING, MYKROY BLOCK, FINE FILTER, BYPASS VALVE, AND MULTIPLE THERMOCOUPLES

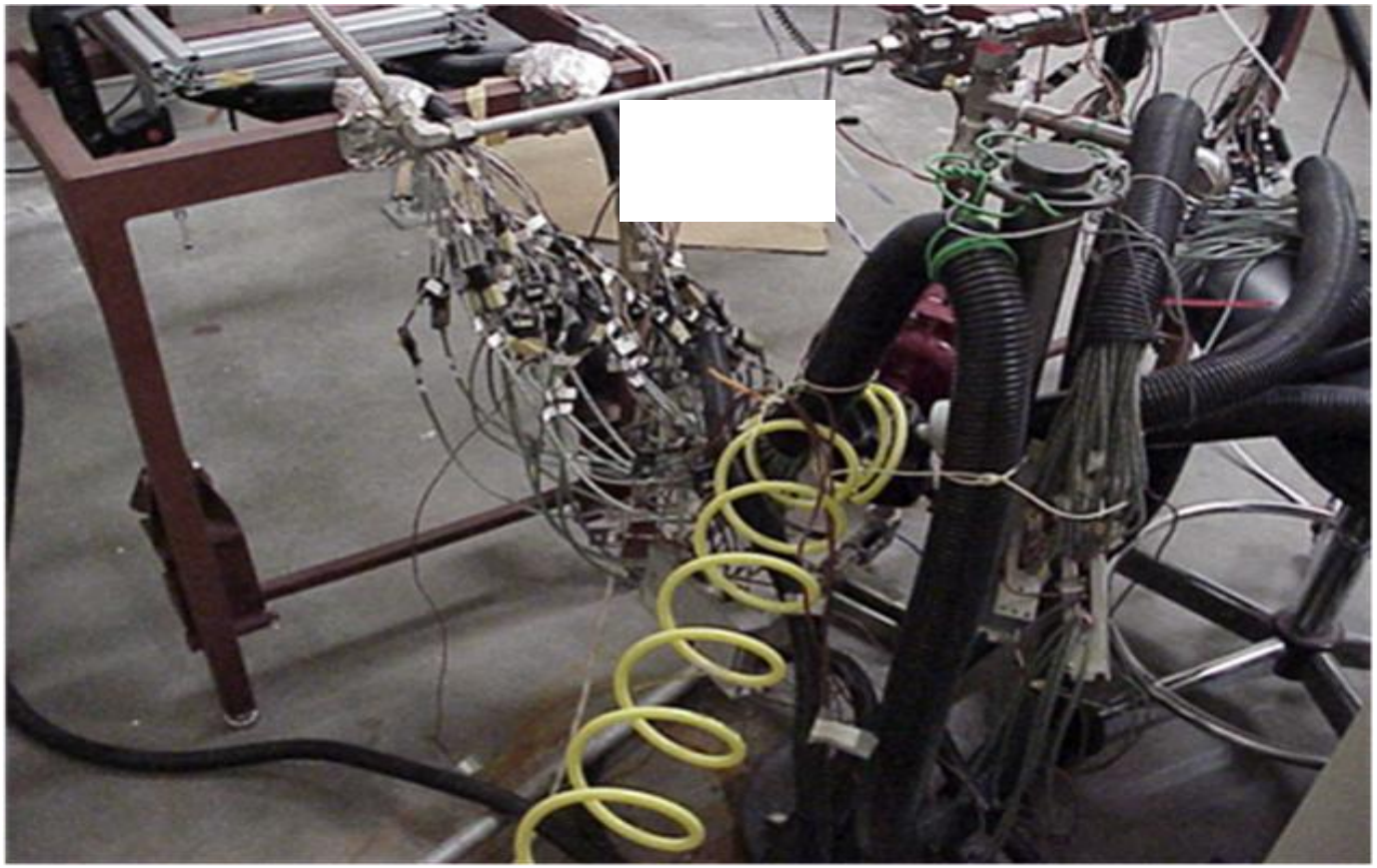

BACK FAR VIEW OF CONNECTION WIRES FROM COMPUTERS TO TEST BED

BACK/TOP WIRE CONNECTIONS CLOSE UP

BACK CLOSE BOTTOM WIRE CONNECTIONS CLOSE UP

FRONT VIEW OF BACK WALL
SECONDARY POWER SUPPLY
MANUAL CONTROL PANEL

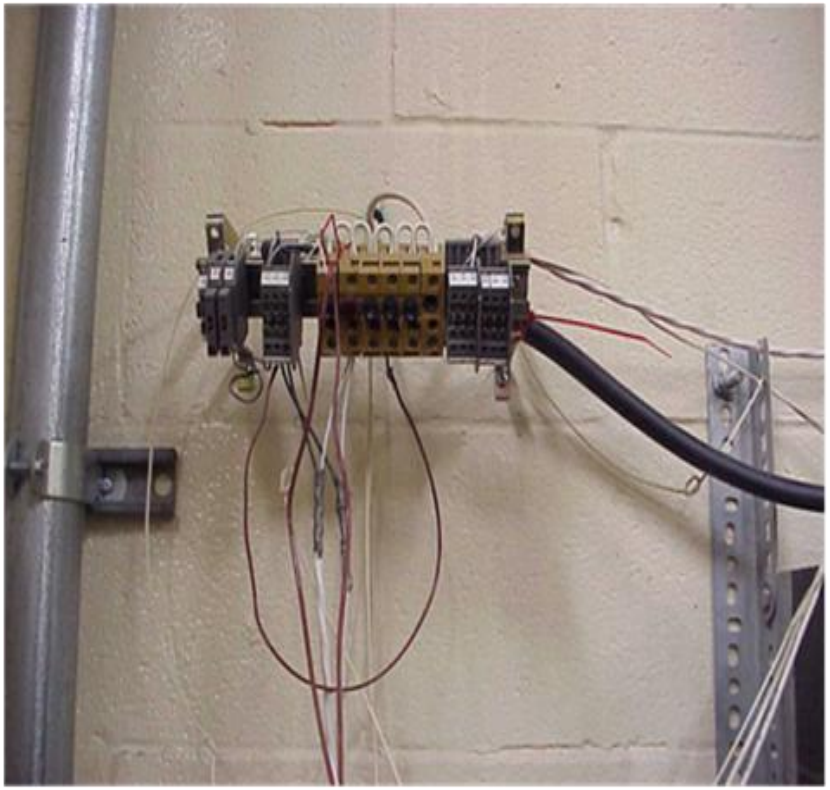

LEFT BACK WALL
SECONDARY POWER SUPPLY
TO PUMP WATER

RIGHT SIDE VIEW OF BACK WALL SECONDARY POWER SUPPLY

FRONT BACK WALL SECONDARY POWER SUPPLY LEFT/BOTTOM VIEW

FRONT VIEW OUTSIDE GATE TO TSRC LAB

LEFT VIEW OF OUTSIDE POWER SUPPLYS

LEFT SIDE VIEW OF OUTSIDE POWER SUPPLYS

FRONT FAR VIEW OF OUTSIDE POWER SUPPLYS

RIGHT CLOSE UP VIEW OF OUTSIDE POWER SUPPLY BUS BAR DUCTS

CENTER TOP CLOSE UP OF OUTSIDE POWER SUPPLY BUS BAR DUCTS

RIGHT CLOSE-UP OF OUTSIDE POWER SUPPLY BOX

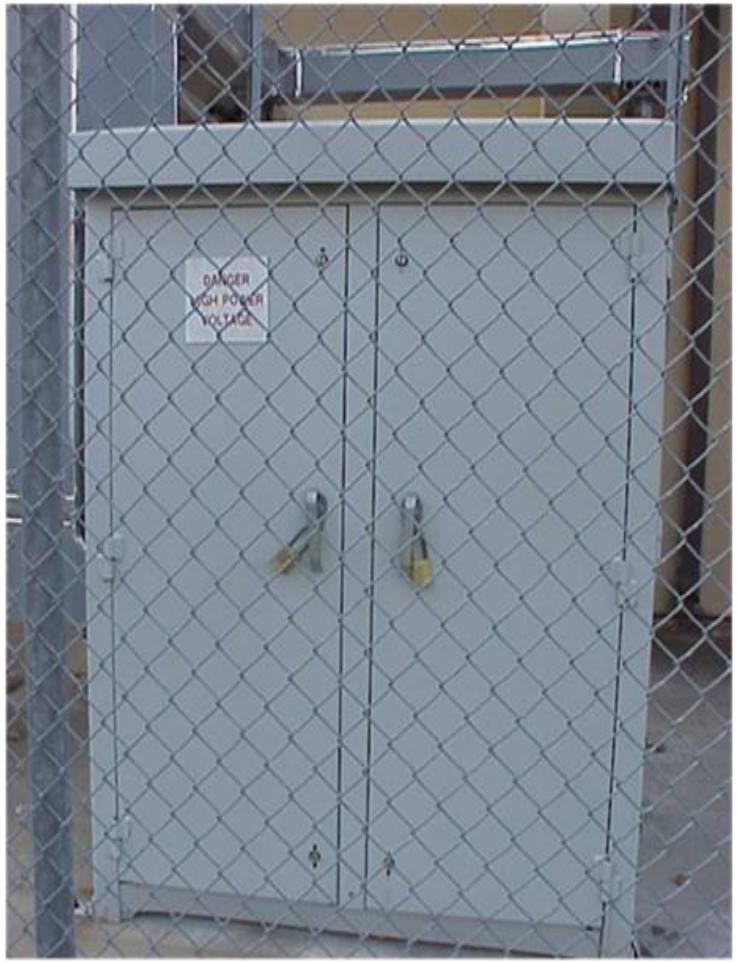

FRONT CLOSE-UP OF OUTSIDE POWER SUPPLY BOX

DATA WIRE FROM WATER PUMP ROOM TO CONTROLS LAB

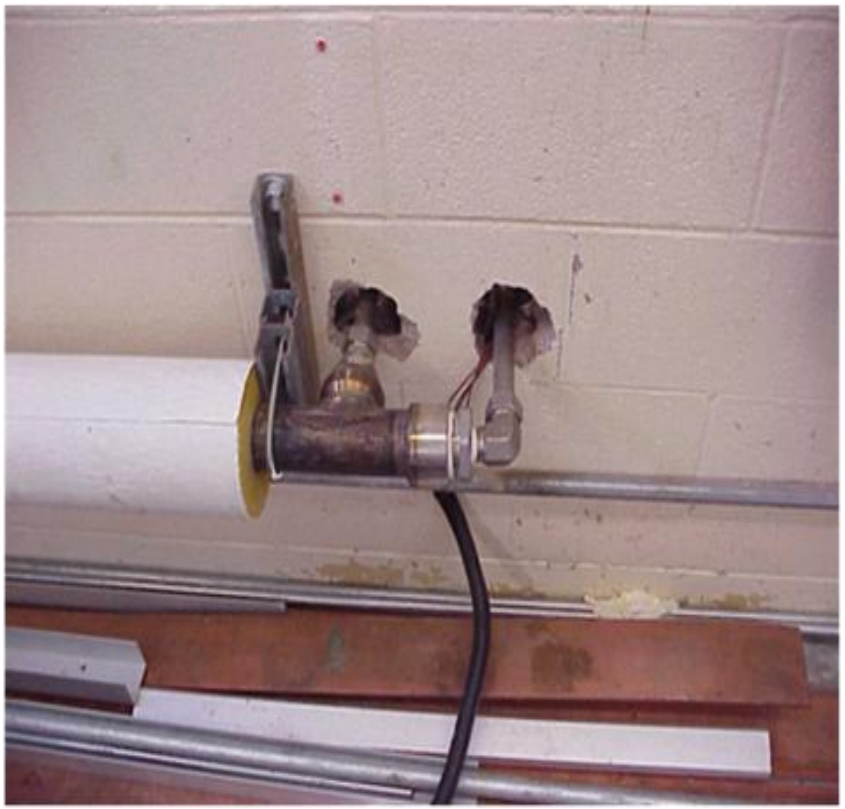

INSERT OF PIPE FROM HEAT EXCHANGER WITH COOLING WATER IN AND OUT TO DRAINAGE

SIDE VIEW OF INSULATED HEAT EXCHANGER WITH COOLING WATER IN AND OUT TO DRAINAGE

TOP VIEW OF INSULATED HEAT EXCHANGER WITH COOLING WATER IN AND OUT TO DRAINAGE

TOP FAR VIEW OF INSULATED HEAT EXCHANGER, FRONT VIEW OF CONTORL VALVE, AIR PACK FILTER REGULATOR, COOLING WATER IN AND OUT TO DRAINAGE AND CHILLED WATER SUPPLY

FRONT VIEW OF HEAT EXCHANGER, PUMP CONTROL, CONTROL VALVE, AIR PACK FILTER REGULATOR, COOLING WATER IN AND OUT TO DRAINAGE AND CHILLED WATER SUPPLY

FRONT VIEW OF CONTROL VALVE, AIR PACK FILTER REGULATOR, AND PRESSURE REGULATOR

TOP VIEW OF CONTROL VALVE, AIR PACK FILTER REGULATOR, AND PRESSURE REGULATOR

LEFT VIEW OF CONTROL VALVE, AIR PACK FILTER REGULATOR, AND PRESSURE REGULATOR

BACK VIEW OF CONTROL VALVE, AIR PACK FILTER REGULATOR, AND PRESSURE REGULATOR

TOP VIEW OF HEAT EXCHANGER

OPEN & CLOSE VALVE FOR CHILLED WATER SUPPLY

FRONT FAR VIEW OF CHILLED WATER SUPPLY & CHILLED WATER RETURN

FRONT CLOSE VIEW OF CHILLED WATER SUPPLY & CHILLED WATER RETURN

RIGHT SIDE VIEW OF CHILLED WATER SUPPLY & CHILLED WATER RETURN

SIDE VIEW OF PRESSURE TRANSDUCER WITH THERMOCOUPLE (PTC)

SIDE VIEW OF PRESSURE TRANSDUCER WITH THERMOCOUPLE (PTC) WITH PUMPS AND PRESSURE RELIEF VALVE

FRONT VIEW OF PRESSURE TRANSDUCER WITH THERMOCOUPLE (PTC), DEIONIZER SYSTENM, FINE FILTER AND PUMPS

FRONT VIEW OF PRESSURE STABILIZER (DAMPER)

RIGHT SIDE VIEW OF NITROGEN TANK AND DEIONIZATION BEDS

BACK SIDE VIEW OF NITROGEN TANK, DEIONIZATION BED, AND RESERVOIR

FRONT SIDE VIEW OF NITROGEN TANK, DEIONIZATION BED, AND RESERVOIR

SIDE VIEW OF DEIONIZED WATER RESERVOIR

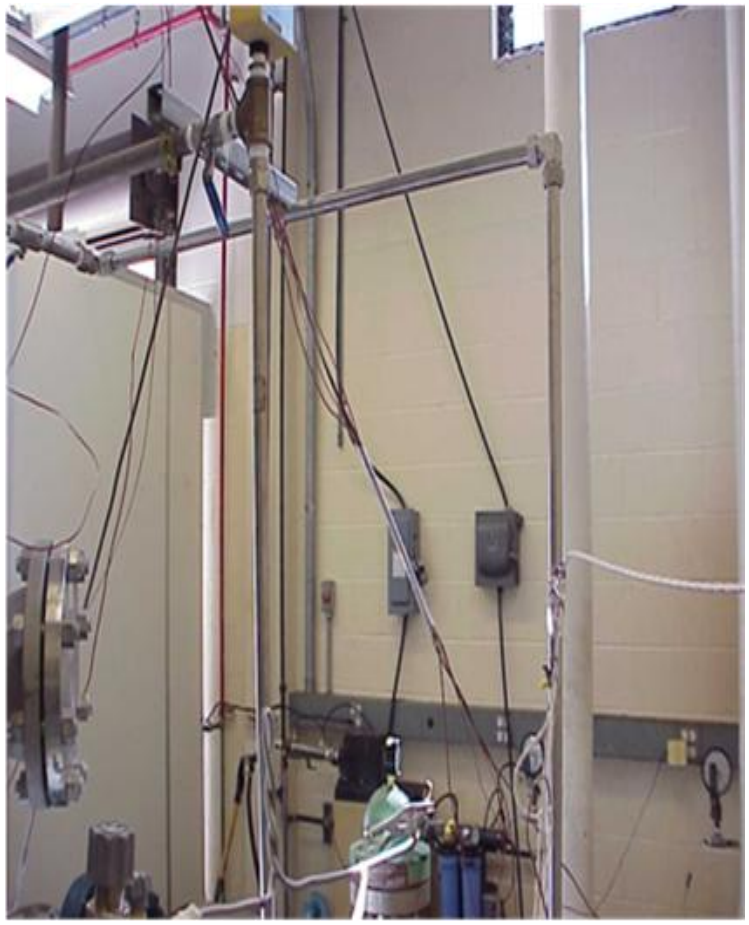

CONNECTION WIRES TO PUMPS AND SYSTEM

FRONT VIEW OF PRESSURE TRANSDUCER WITH THERMOCOUPLE, FLOW LOOP PUMPS, AND PRESSURE STABILIZER

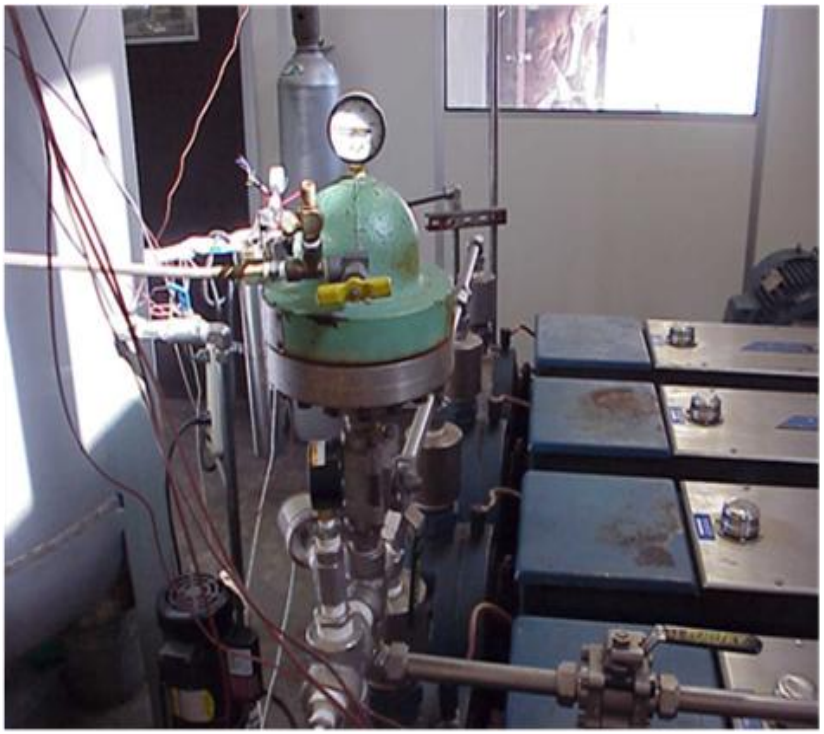

RIGHT SIDE VIEW OF PRESSURE TRANSDUCER WITH THERMOCOUPLE, DAMPER, FLOW LOOP PUMPS, AND PRESSURE STABILIZER

BACK VIEW OF PRESSURE TRANSDUCER WITH THERMOCOUPLE, RESERVOIR AND PRESSURE STABILIZER

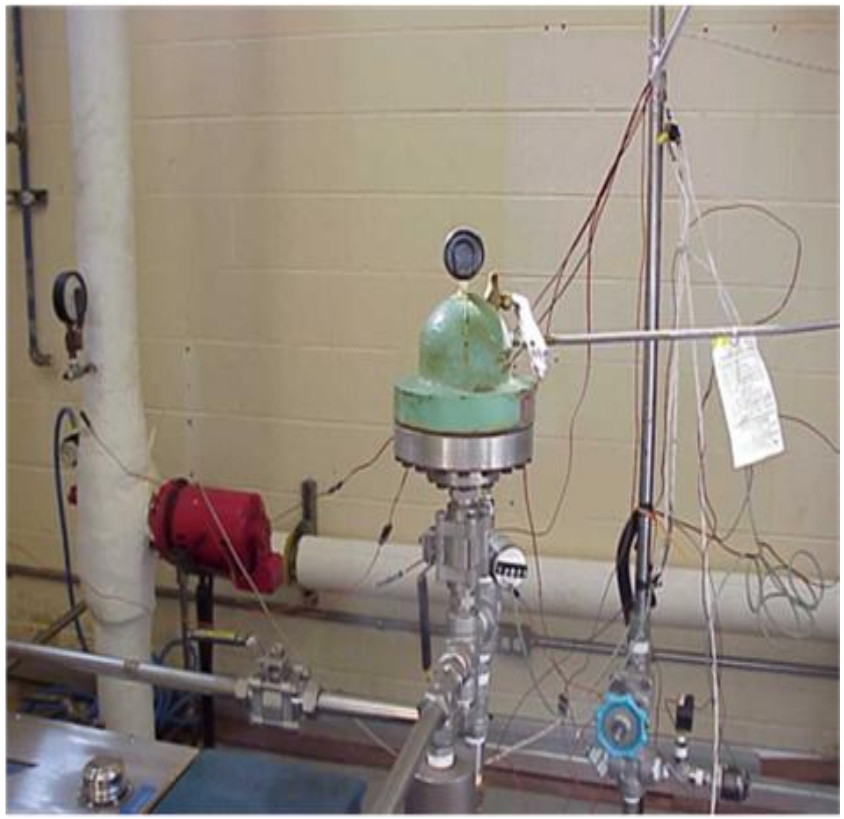

CLOSE VIEW OF PRESSURE TRANSDUCER WITH THERMOCOUPLE AND PRESSURE STABILIZER

LEFT VIEW OF PRESSURE TRANSDUCER WITH THERMOCOUPLE AND PRESSURE STABILIZER AND DEIONIZED WATER RESERVOIR

BACK LEFT VIEW OF PRESSURE TRANSDECUER WITH THERMOCOUPLE AND PRESSURE STABILIZER AND DEIONIZED WATER RESERVOIR

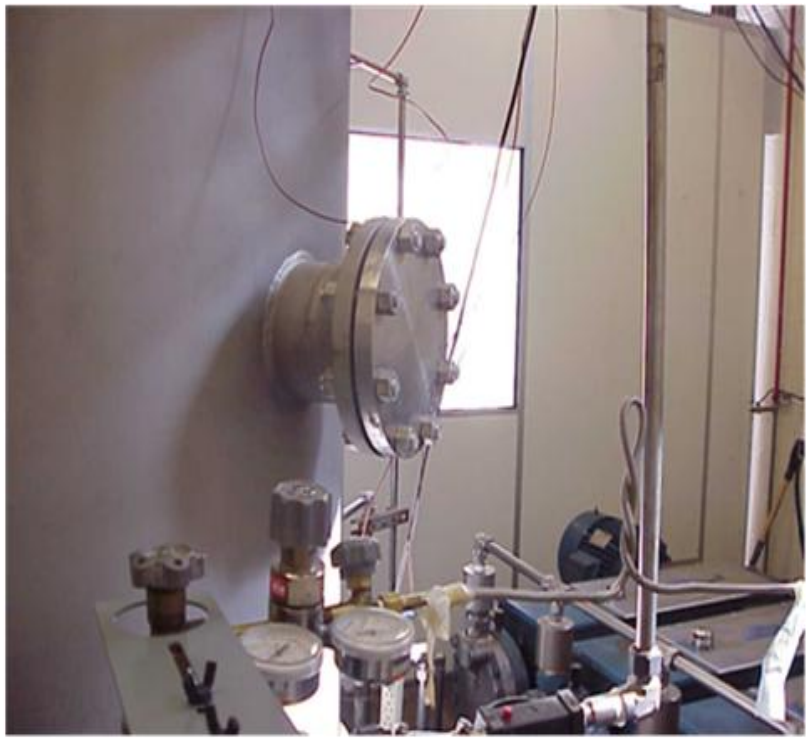

SIDE VIEW OF DEIONIZED WATER RESERVOIR AND CONTROL VALVES

FRONT VIEW OF RESERVOIR VACUMM PUMP, DEIONIZATION BED, AND FLOW LOOP PUMPS

BACK VIEW OF RESERVOIR PUMP

RIGHT VIEW OF RESERVOIR PUMP

TOP VIEW OF WATER QUALITY METER

FRONT VIEW OF WATER QUALITY METER

BACK VIEW OF WATER FINE FILTER (FLOW LOOP PUMPS IN BACKGROUND)

SIDE VIEW OF WATER RESERVOIR

SIDE VIEW OF DEIONIZED WATER RESERVOIR CONNECTIONS

FRONT FAR VIEW OF DEIONIZED WATER RESERVOIR

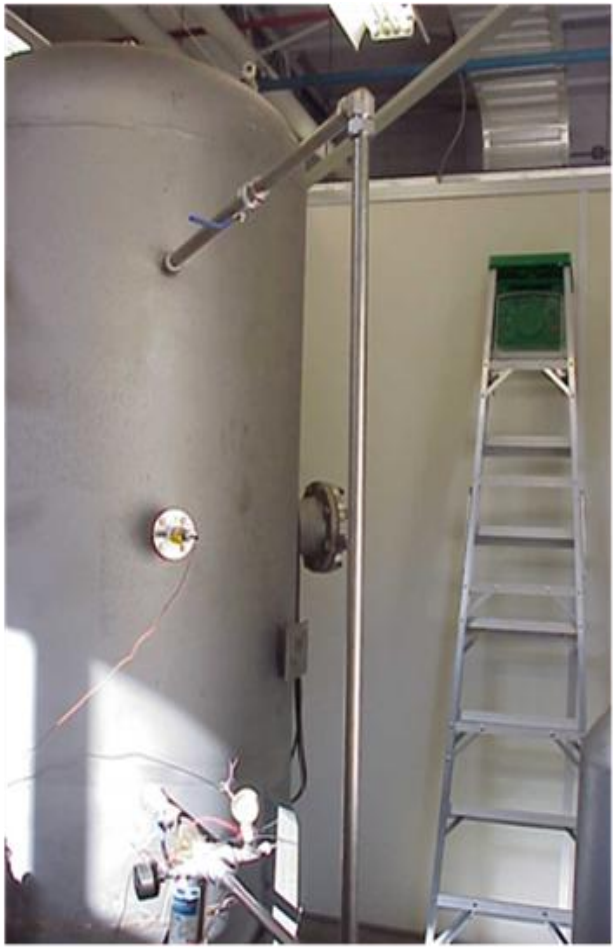

SIDE VIEW OF DEIONIZED WATER RESERVOIR CONNECTIONS

TOP FRONT VIEW OF FINE FILTER AND BYPASS VALVE

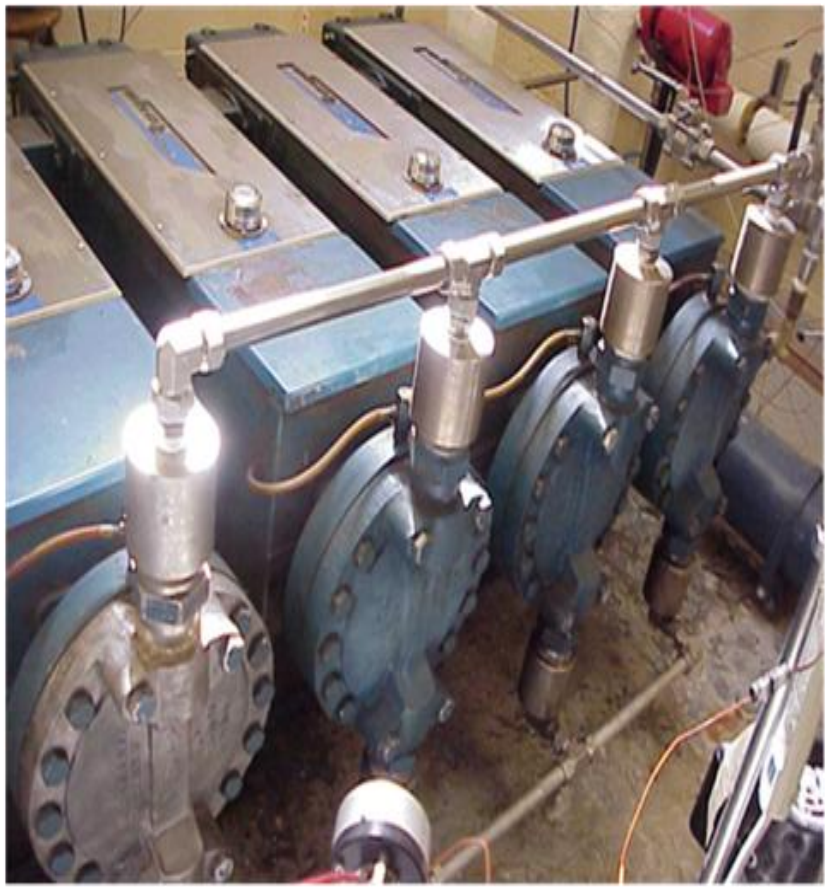

FRONT VIEW OF PIPE CONNECTIONS TO PUMPS

RIGHT SIDE VIEW OF PIPE CONNECTIONS TO PUMPS

LEFT SIDE VIEW OF PIPE CONNECTIONS TO PUMPS

LEFT VIEW OF POSITIVE-DISPLACEMENT FLOW LOOP PUMPS

RIGHT VIEW OF POSITIVE-DISPLACEMENT PUMPS

FRONT VIEW OF MOTOR TO CONTROL FLOW LOOP PUMPS

RIGHT SIDE VIEW OF BACK OF FLOW LOOP PUMPS AND FLOW CONTROL VALVES

LEFT SIDE VIEW OF BACK OF FLOW LOOP PUMPS AND FLOW CONTROL VALVES

RIGHT SIDE VIEW OF PH CONTROLSYSTEM

TOP VIEW OF PH CONTROL SYSTEM

FRONT VIEW OF PH CONTROL SYSTEM

LEFT SIDE VIEW OF PH CONTROLSYSTEM

FAR VIEW OF PH CONTROL SYSTEM

SIDE VIEW OF WATER PUMPS, CHILLED WATER RETURN, CHILLED WATER SUPPLY & PRESSURE TRANSDUCER WITH THERMOCOUPLE (PTC)

TOP LEFT AERIAL VIEW OF WATER PUMPS, PH CONTROL SYSTEM, PRESSURE RELIEF VALVE, FINE FILTER FLOW CONTROL VALVE, CHILLED WATER RETURN, AND CHILLED WATER SUPPLY

TOP RIGHT AERIAL VIEW OF WATER PUMPS, PH CONTROL SYSTEM, PRESSURE RELIEF VALVE, FINE FILTER, FLOW CONTROL VALVE, CHILLED WATER RETURN, CHILLED WATER SUPPLY, DEIONIZED WATER RESERVOIR, HEAT EXCHANGER, VALVE, PRESSURE STABILIZER (DAMPER), AND WATER QUALITY METER

TOP AERIAL VIEW OF NITROGEN TANK, DEIONIZATION BEDS, NITROGEN TANK, VACUUM PUMP, FLOW LOOP (WATER) PUMPS, AND HEAT EXCHANGER

FRONT TOP AERIAL VIEW OF HEAT EXCHANGER, VALVES, CHILLED WATER RETURN, CHILLED WATER SUPPLY, WATER PUMPS, PRESSURE TRANSDUCER WITH THERMOCOUPLE, AND PH CONTROL SYSTEM, AND FLOW CONTROL VALVES

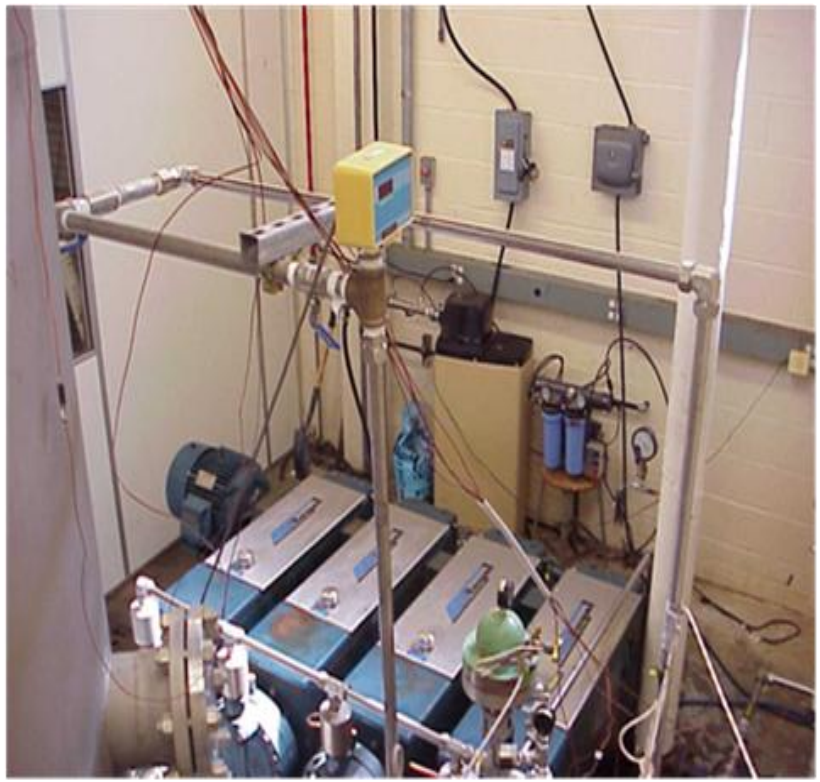

TOP AERIAL RIGHT VIEW OF WATER QUALITY METER, WATER PUMPS & CONNECTIONS, PTC, PRESSURE STABILIZER, CHILLED WATER RETURN, PH CONTROL SYSTEM, FLOW CONTROL VALVE, & PUMP MOTOR

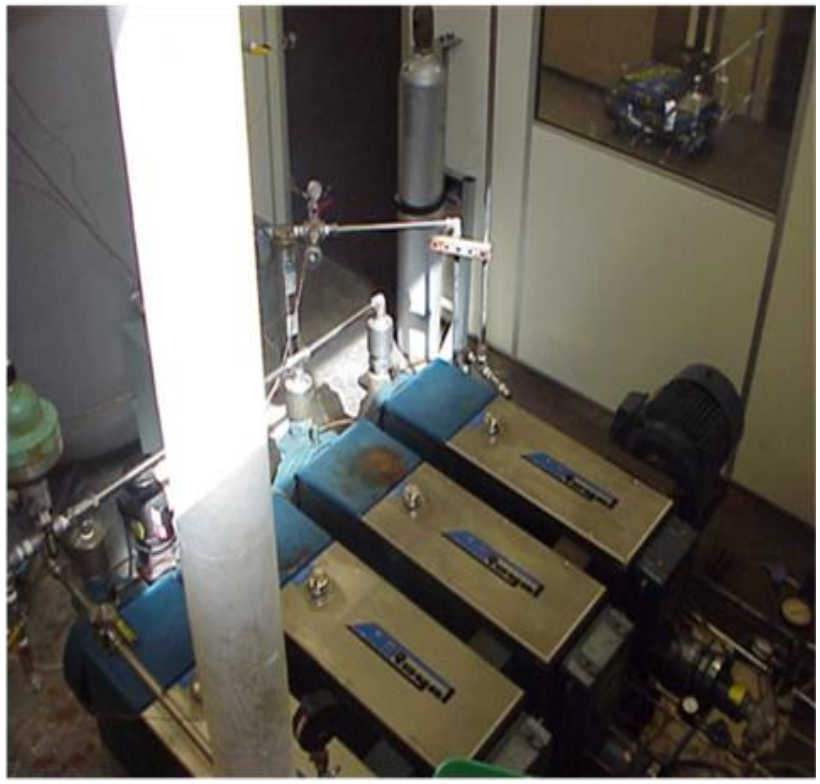

TOP AERIAL LEFT VIEW OF WATER QUALITY METER, WATER PUMPS & CONNECTIONS, PTC, PRESSURE STABILIZER, CHILLED WATER RETURN, PH CONTROL SYSTEM, FLOW CONTROL VALVE, & PUMP MOTOR

AERIAL SIDE OF DEIONIZED WATER RESERVOIR, WATER QUALITY METER, DEIONIZED BED FLOW LOOP, THERMOCOUPLES, PRESSURE STABILIZER, PTC

TOP AERIAL VIEW OF CHILLED WATER SUPPLY

TOP AERIAL VIEW OF WATER PUMPS AND PRESSURE RELIEF VALVE, FLOW CONTROL VALVE AND PH CONTROL SYSTEM

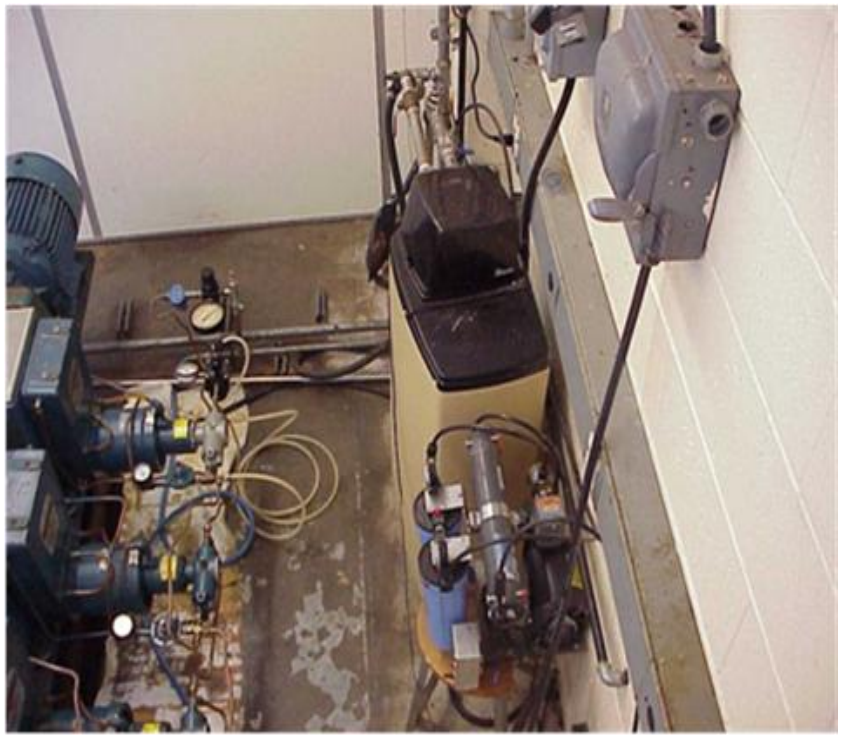

TOP AERIAL VIEW OF WATER PUMPS AND PRESSURE RELIEF VALVE, FLOW CONTROL VALVE AND PH CONTROL SYSTEM

APPENDIX B: ELECTROMECHANICAL REMOTE CONTROLLED POWER MEASUREMENT SYSTEM (EMRPS)

INTRODUCTION

In an effort to develop new economical energy sources, an international team is preparing to build an International Thermonuclear Experimental Reactor, ITER by the year 2023. It will be the first plasma fusion reactor its size and will be operating at over 100 million degrees C, producing 500 MW of fusion power. Inside of the reactor, a divertor is being designed, to exhaust the flow of energy from charged particles produced by the fusion reactions and to remove helium ash and other impurities from the plasma. The divertor is categorized as a plasma-facing component (PFC) given that it will be "facing" the plasma and bombarded by high energy particles. The plasma will impose high heat flux (HHF) loads of up to 20 MW/m² on the diverter's vertical targets. Monoblock-type coolant channels may be integrated into the vertical target walls of the divertor to accommodate such high thermal loadings.

INTRODUCTION
(continued)

This application involves single-side heating (SSH) of cooling channels. When evaluating single-side heating applications, past investigators and designers have simply approximated SSH channel conditions with conditions corresponding to the heat flux being distributed equally on all surfaces, or uniform heating (UH). As a part of the Institute for High Heat Flux Removal (IHHFR), the Thermal Science Research Center (TSRC) at Prairie View A&M University has been studying the effects of SSH on water cooled circular and monoblock channels. A High Heat Flux facility was constructed to measure High Heat Flux removal from flow channels to develop a database.

DESCRIPTION OF IHHFR FACILITY

The Thermal Science Research Center's IHHFR Facility is composed of a closed stainless steel water flow loop with two integrated test sections (TS) of monoblock geometry--one with a helical wire insert (HWI) and another without a HWI. The flow loop condition capabilities include a mass velocity range from 0.3 to 10 Mg/m²s, an exit pressure range from 0.2 to 4. MPa and an inlet temperature range from 16ºC to 130ºC. A dionizing unit, degassing tank, filter, and accumulator are included in the loop for purification and degassing purposes. Each test section is heated from a single side by a grade G-20 graphite flat heater that is electrically, but not thermally, isolated from the test section.

DESCRIPTION OF IHHFR FACILITY
(continued)

The heater is powered by a 5% ripple at full load 300 kW DC, at 30V, 10000A power supply. Each of the test sections have 48 stainless steel sheathed Type-J thermocouples (calibrated to ±0.1ºC with a precision calibrator) embedded in the monoblock walls. These thermocouples were terminated to a data acquisition (DAQ) system, which reads the data output from thermocouples, and pressure transducers (inserted into the flow loop at locations near the inlet and exit of the test section).

HEATER ASSEMBLY

The basic heater assembly is shown below. On top of the test section sits a 1mm thick aluminum nitride strip that serves to electrically isolate the test section from the heater (which conducts electricity) while conducting thermal energy from the heater to the test section due to its high thermal conductivity. The electricity is conducted to the copper heater transition plates (from the DC Power Supply), which are in good contact with the bus bar supports (turkeys) during an experiment. The bus bars (not shown in the figure) are copper bus/duct cables running from the power supply to the turkey. The purpose of the saddle is to support the three center heater pressure applicators that are torques to over 100 in-lb (11.3 N-m) to maximize contact of the graphite heater and aluminum nitride that sit on the test section.

HEATER ASSEMBLY
(continued)

Thus, thermal conduction from the heater to the test section was maximized. Two additional pressure applicators were also applied through the turkey slots (indicated by dotted lines) with minimal torquing so that a uniform heat flux was achieved. However, these latter pressure applicators were torqued between 25 in-lb (2.82 N-m) and 60 in-lb (6.78 N-m). Used to support and evenly distribute the load of the pressure applicators, the steel bar protected the brittle mykroy block from cracking. The mykroy served as both a thermal and electrical insulator between the heater and the steel bar. Since the mykroy itself is a good electrical insulator, the aluminum nitride strips "sandwiching" the mykroy are not necessarily needed.

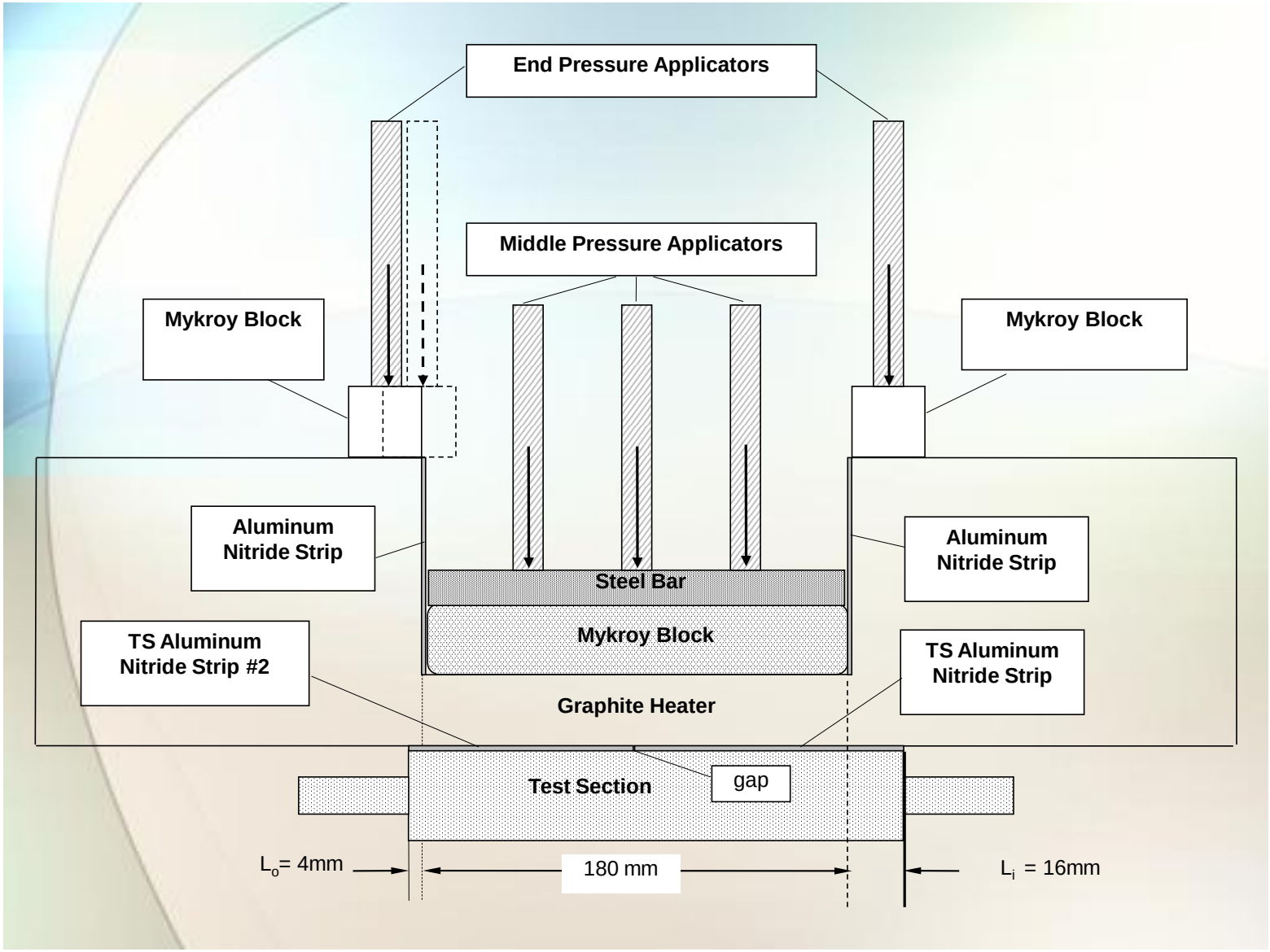
End Pressure Applicators
Middle Pressure Applicators
Mykroy Block
Mykroy Block
Aluminum Nitride Strip
Aluminum Nitride Strip
Steel Bar
Mykroy Block
TS Aluminum Nitride Strip #2
TS Aluminum Nitride Strip
Graphite Heater
Test Section
gap
L_o= 4mm
180 mm
L_i = 16mm

GRAPHITE HEATERS

There are three graphite heater types used for experiment: identified as type 008, 009, and 011 with thicknesses of 10, 30 and 20 mm, respectively (see the figure below). The heater type most often used for experiments was type 011 (20 mm thickness). The portion with the "A" dimensions represents the main heater portion with a distance of 180 mm. The two corners of the heater portion are subject to cracking during test preparation if excessive torque is applied to unsupported areas of the heater transition portion. This disqualifies the 10 mm thickness heater (type 008) in that it is most subject to cracking. The type 011 heater was chosen over the 009 based on its consistently good performance capability during experiments.

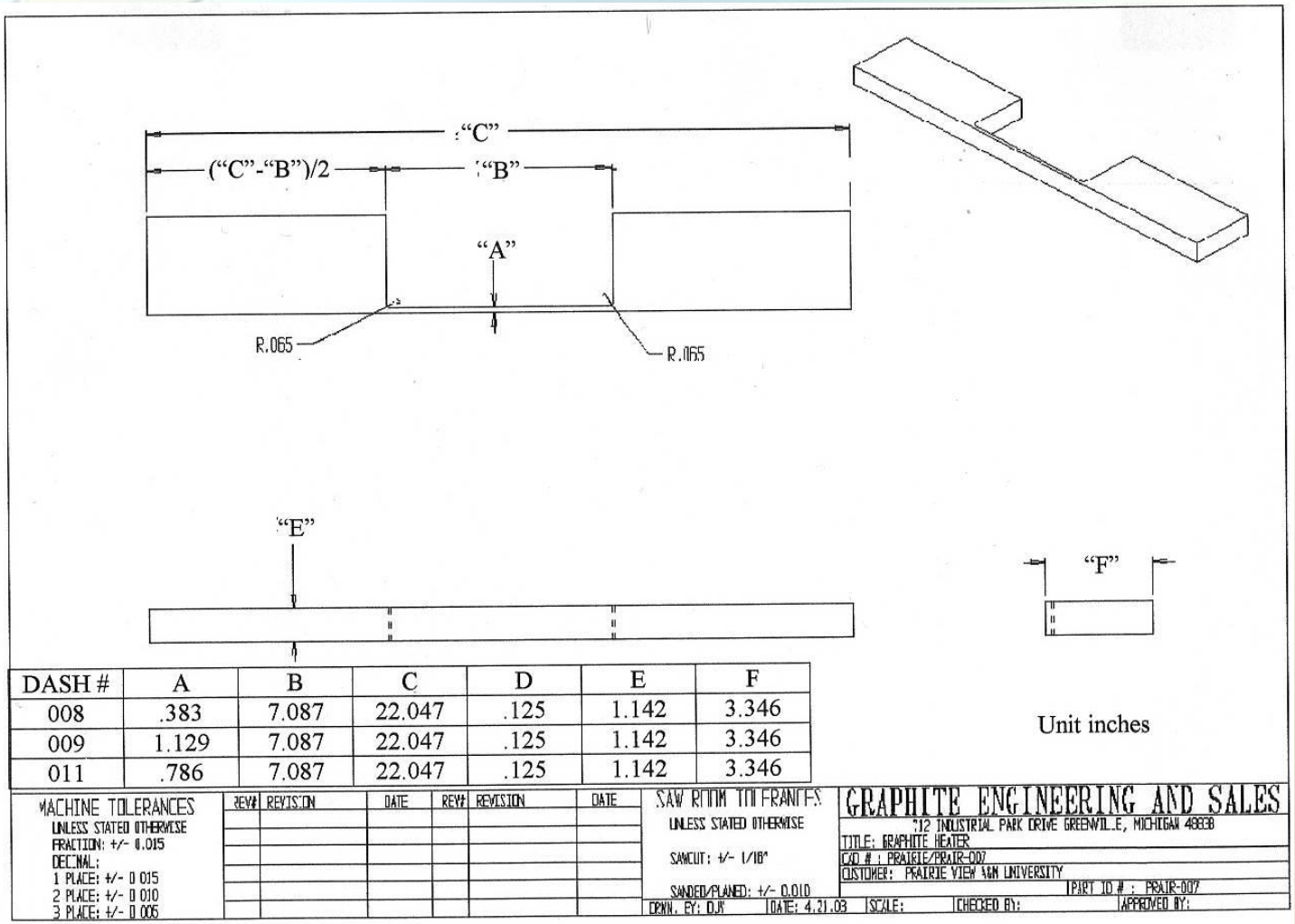

DASH #	A	B	C	D	E	F
008	.383	7.087	22.047	.125	1.142	3.346
009	1.129	7.087	22.047	.125	1.142	3.346
011	.786	7.087	22.047	.125	1.142	3.346

MACHINE TOLERANCES
UNLESS STATED OTHERWISE
FRACTION: +/- 0.015
DECIMAL:
1 PLACE: +/- 0.015
2 PLACE: +/- 0.010
3 PLACE: +/- 0.005

REV#	REVISION	DATE	REV#	REVISION	DATE

SAW RTDM TOLERANCES
UNLESS STATED OTHERWISE
SAWCUT: +/- 1/16"
SANDED/PLANED: +/- 0.010
DRWN. BY: DJF | DATE: 4.21.03 | SCALE: | CHECKED BY: | APPROVED BY:

GRAPHITE ENGINEERING AND SALES
712 INDUSTRIAL PARK DRIVE GREENVILLE, MICHIGAN 48838
TITLE: GRAPHITE HEATER
CAD # : PRAIRIE/PRAIR-007
CUSTOMER: PRAIRIE VIEW A&M UNIVERSITY
PART ID # : PRAIR-007

Figure 3.6. Manufacturer Specified Dimensions for Monoblock Heating Assembly Type Heaters

ELECTROMECHANICAL VOLTMETER SYSTEM

As part of the experimental verification efforts, the power distribution of the IHHFR monoblock heater was to be examined. The figure shows the cross-section and associated inner test section assembly components. A new two-dimensional translational measuring stage was developed. The automated stage was needed to measure the potential distribution along the graphite heater at ½ “(12.7 mm) intervals. These measurements could then be used to determine the power distribution along the heater.

ELECTROMECHANICAL VOLTMETER SYSTEM
(continued)

Based on the limited space available between the heater and the saddle, a small yet sturdy design had to be developed that could safely measure the voltage potential in increments along the thin section of the heater with relatively high accuracy and automation. A very simple design was chosen that allowed the existing saddle to be used as a support for the entire system whilst allowing for easy assembly and disassembly. This design provided translational and axial movement and thus enabled movement for the probes used to measure local differential heater voltage.

HARDWARE

For the hardware, a series of plates, screws, bolts and nuts were used to assemble the entire system together; and, two motion controller motors were used to provide movement of a stage on which the voltage probes were mounted. Shown below is each component --complete with dimensions.

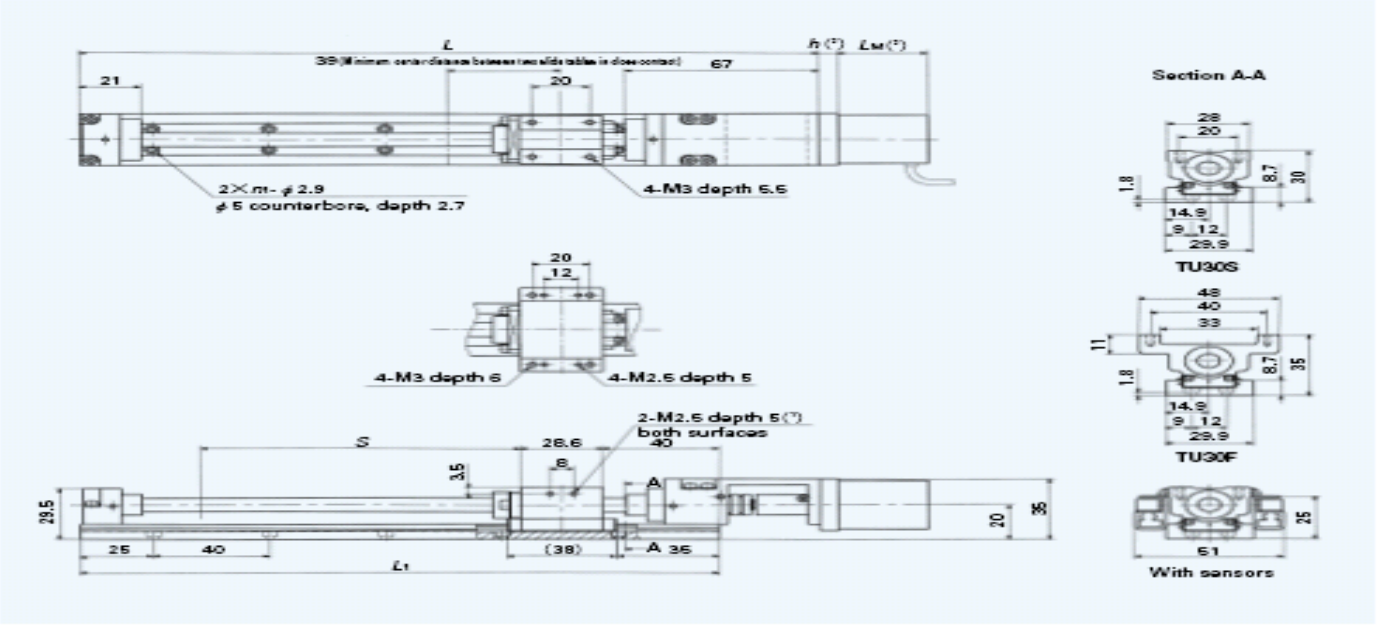

Note (*1) : These threaded holes are not provided on TU30F.
(*2) : See the dimension table for the motor unit on page 12.

Dimensions

unit : mm

Model number	Track rail length L_1	Total length L	Stroke length S(*1)	n_1	Mass of slide table kg		Mass(*2) kg	
					TU30S	TU30F	TU30S	TU30F
TU30S TU30F	140	175	30(—)	3	0.09	0.12	0.49	0.52
	180	215	70(45)	4			0.56	0.59
	220	255	110(85)	5			0.63	0.66
	260	295	150(125)	6			0.70	0.73
	300	335	190(165)	7			0.77	0.80
	340	375	230(205)	8			0.84	0.87

Note (*1) : This indicates the limit stroke length when limit sensors are attached. The values in ( ) are for two slide tables in close contact.
(*2) : The values indicate the whole table mass when one slide table is attached. The mass of the motor is not included.
Remark : The track rail and the casing are made of stainless steel.

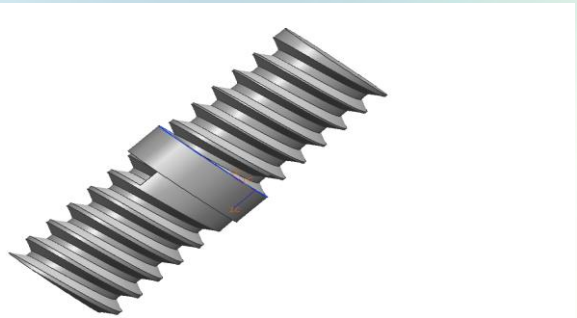

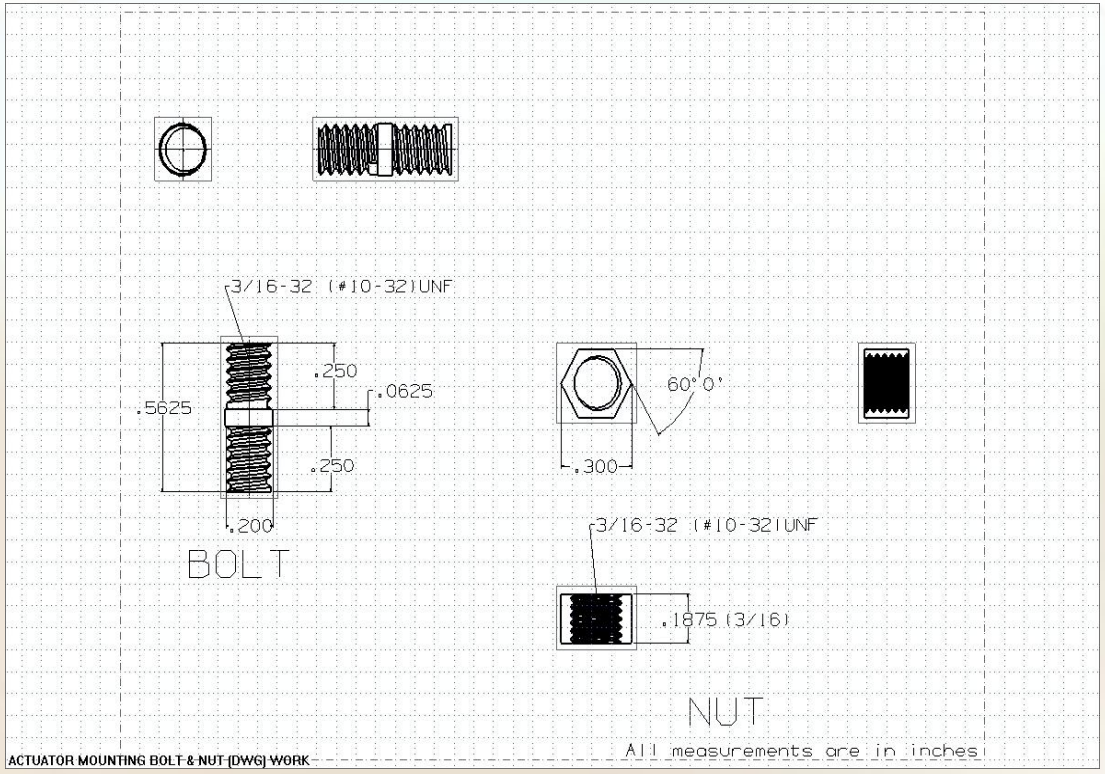
3/16-32 (#10-32)UNF
.250
.0625
.5625
.250
.200
BOLT
60° 0'
.300
3/16-32 (#10-32)UNF
.1875 (3/16)
NUT
All measurements are in inches
ACTUATOR MOUNTING BOLT & NUT (DWG) WORK

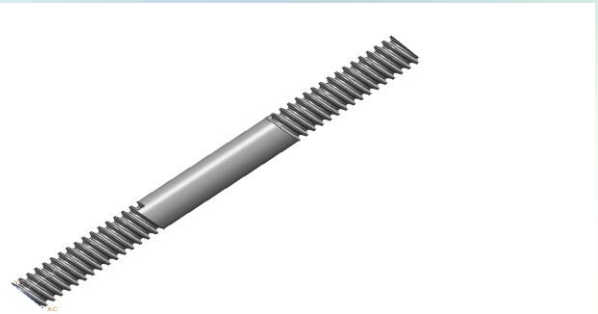

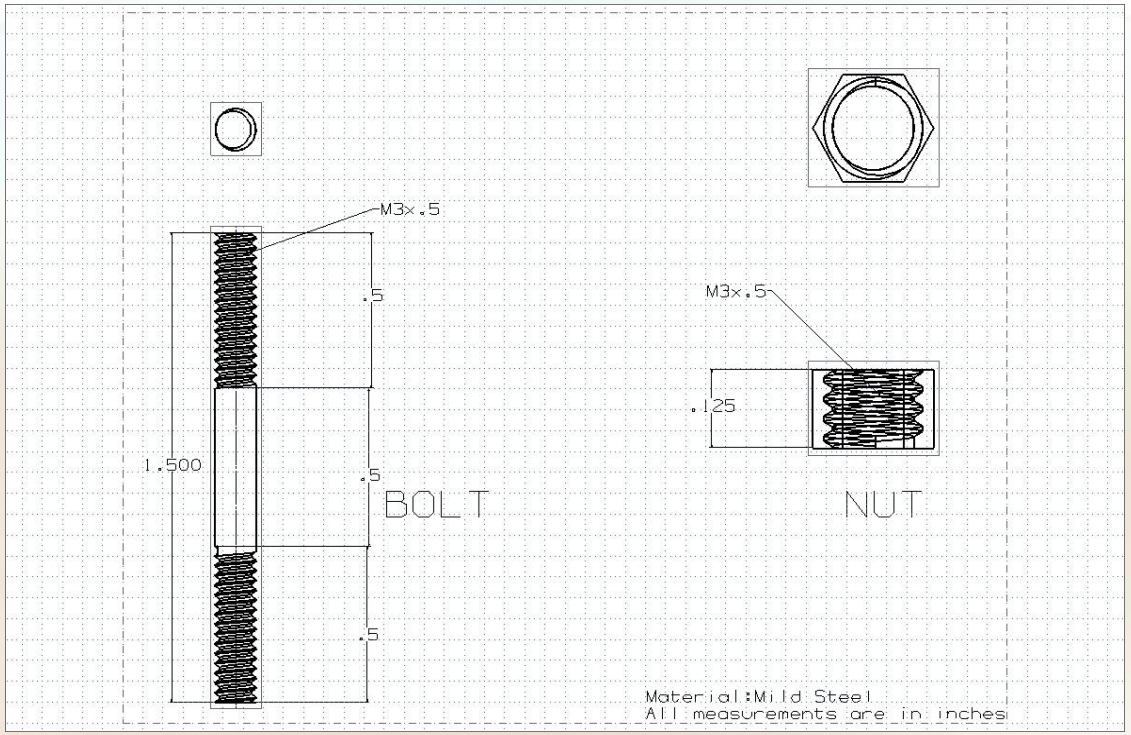
M3x.5
.5
1.500
.5
.5
BOLT
M3x.5
.125
NUT
Material:Mild Steel
All measurements are in inches

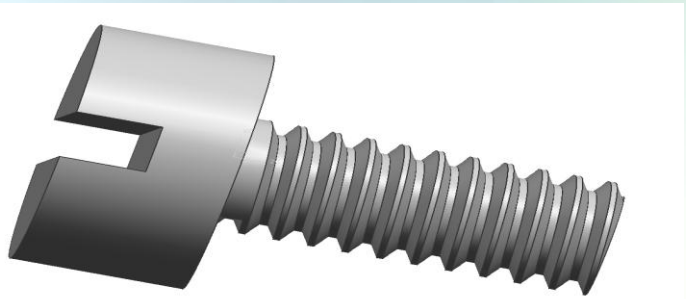

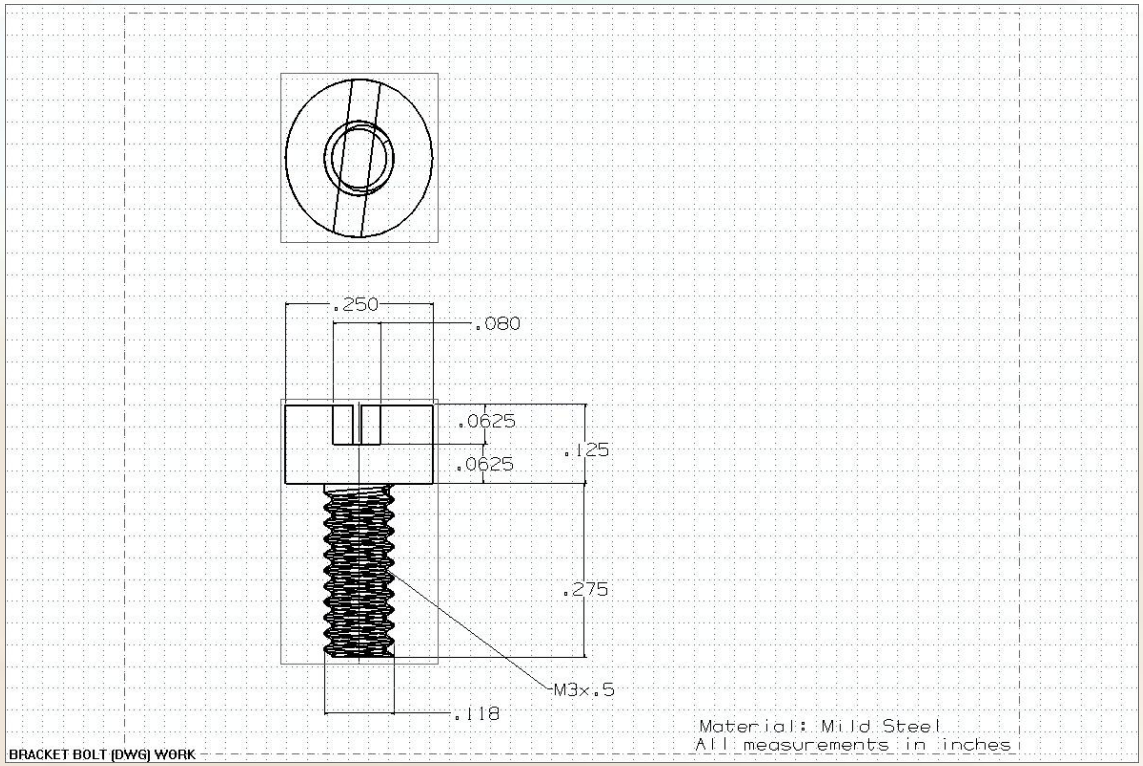
.250
.080
.0625
.0625
.125
.275
M3x.5
.118
Material: Mild Steel
All measurements in inches
BRACKET BOLT (DWG) WORK

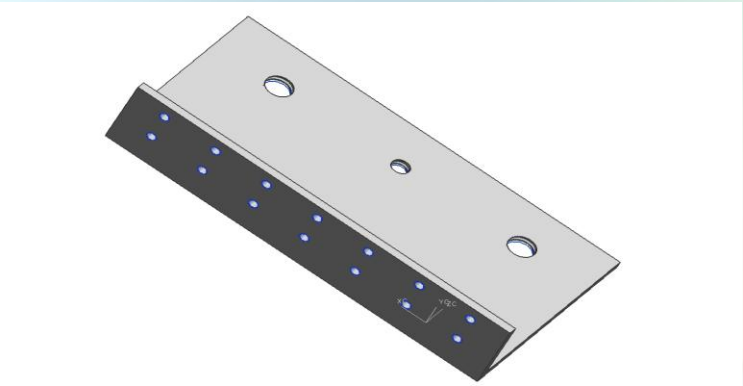

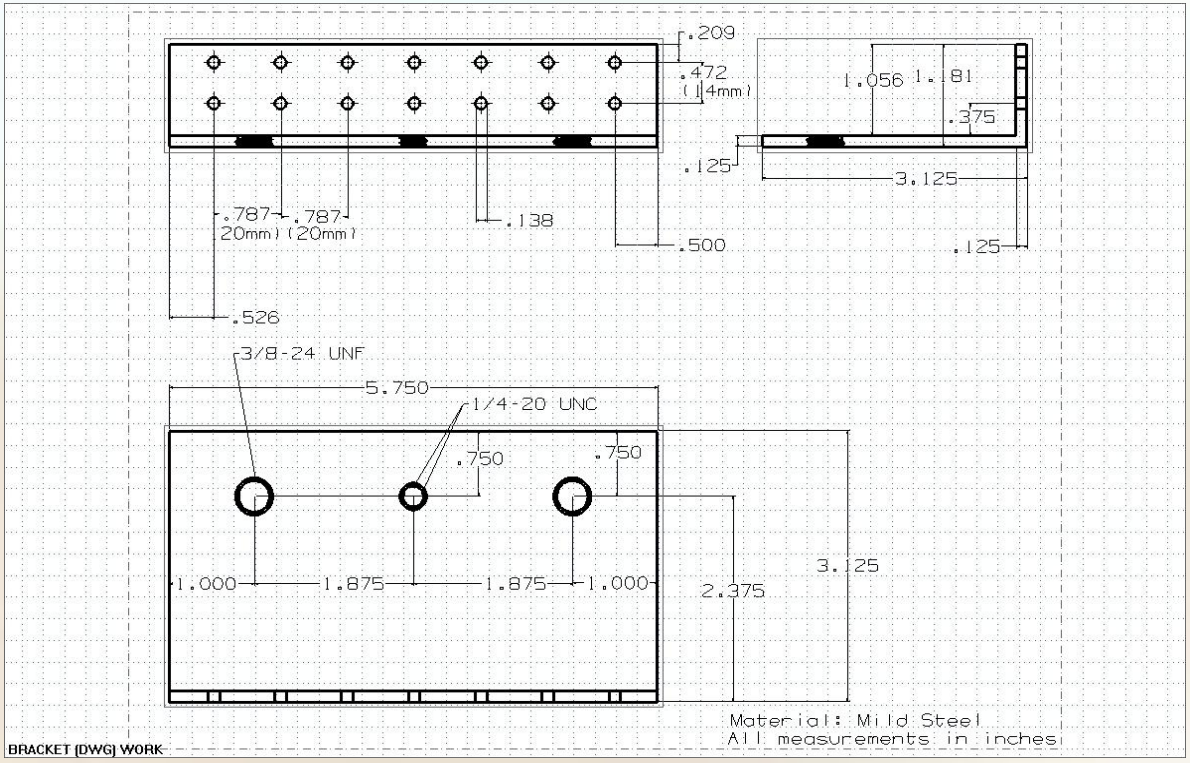
.209
.472
(14mm)
1.056
1.181
.375
.125
3.125
.125
.787
(20mm)
.787
(20mm)
.138
.500
.526
3/8-24 UNF
5.750
1/4-20 UNC
.750
.750
1.000
1.875
1.875
1.000
3.125
2.375
Material: Mild Steel
All measurements in inches
BRACKET (DWG) WORK

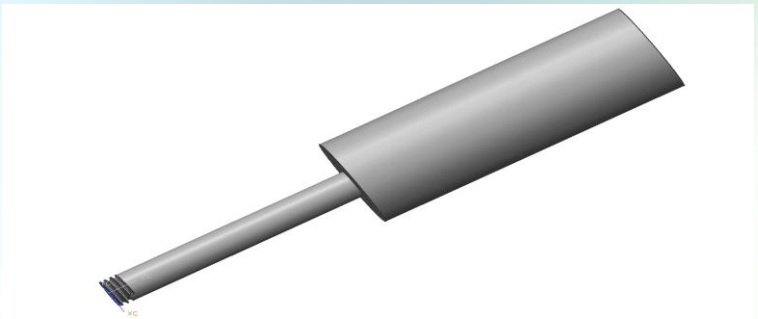

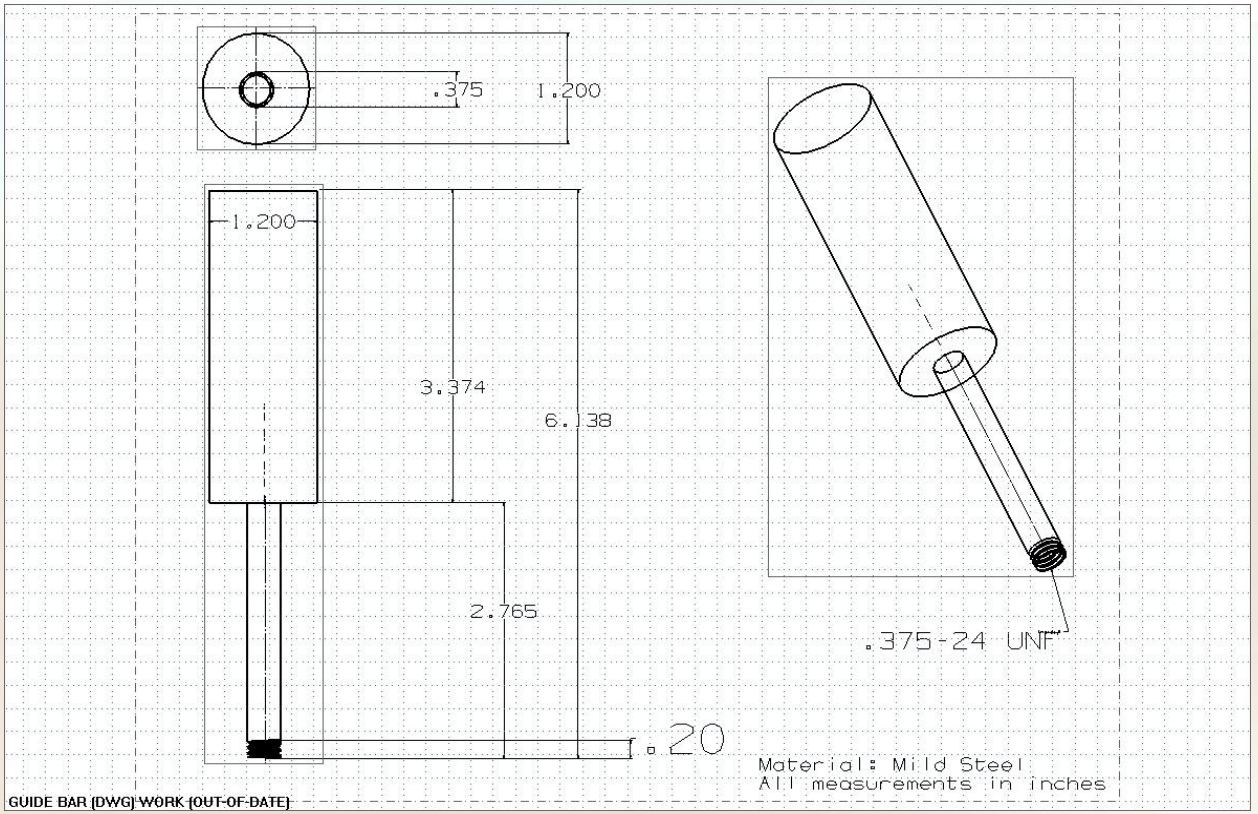
.375
1.200
1.200
3.374
6.138
2.765
.20
.375-24 UNF
Material: Mild Steel
All measurements in inches
GUIDE BAR (DWG) WORK (OUT-OF-DATE)

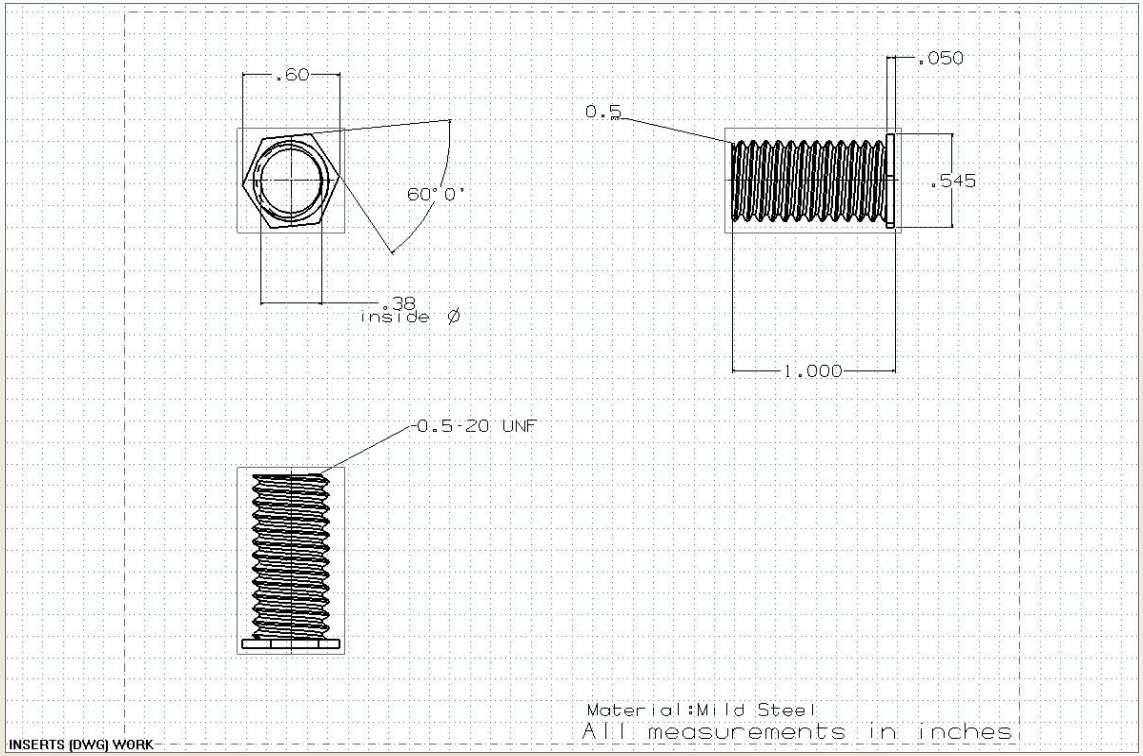
.60
60° 0'
.38
inside Ø
.050
0.5
.545
1.000
0.5-20 UNF
Material:Mild Steel
All measurements in inches
INSERTS (DWG) WORK

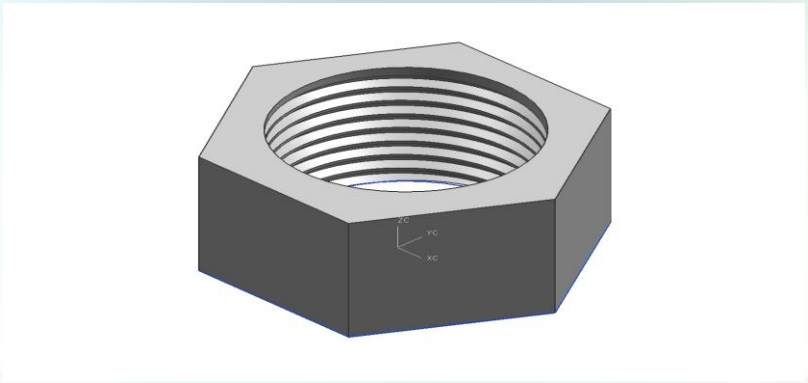

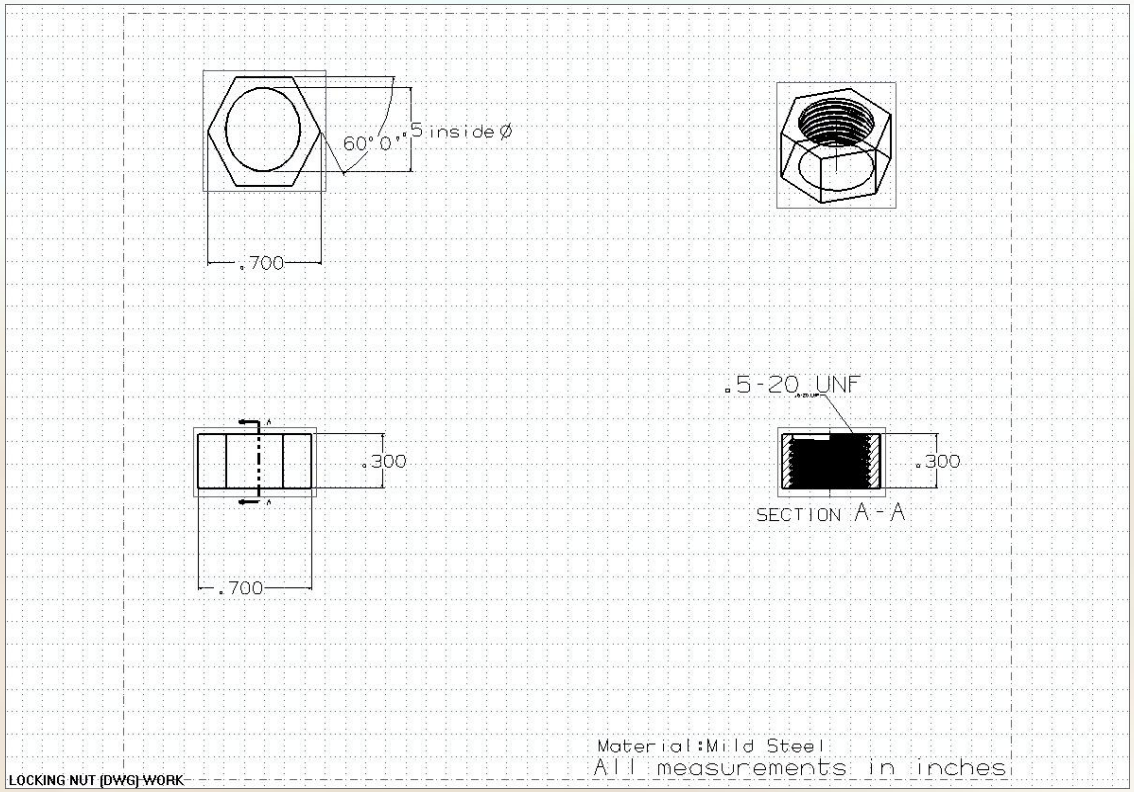
60° 0'
.5 inside Ø
.700
.5-20 UNF
.300
.300
.700
SECTION A-A
Material:Mild Steel
All measurements in inches
LOCKING NUT (DWG) WORK

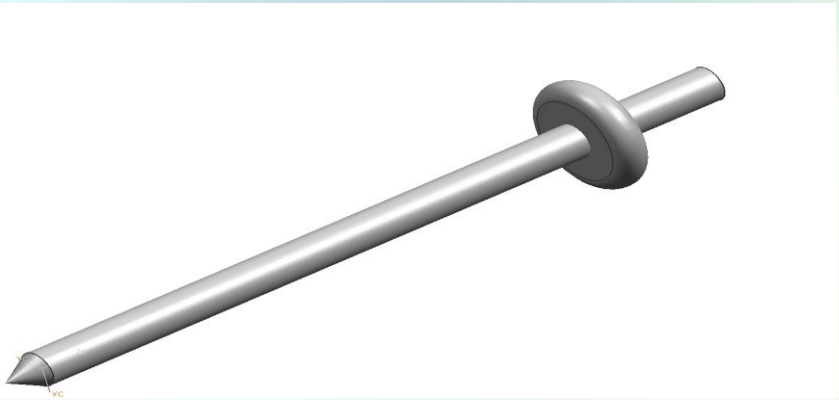

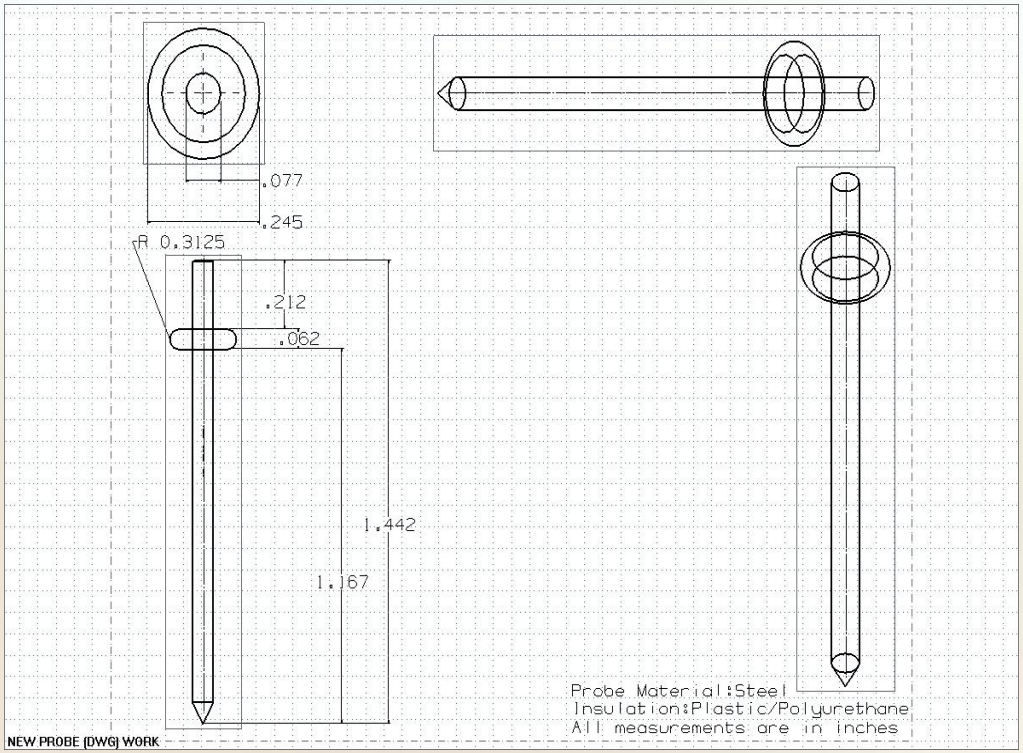
.077
.245
R 0.3125
.212
.062
1.442
1.167
Probe Material:Steel
Insulation:Plastic/Polyurethane
All measurements are in inches
NEW PROBE (DWG) WORK

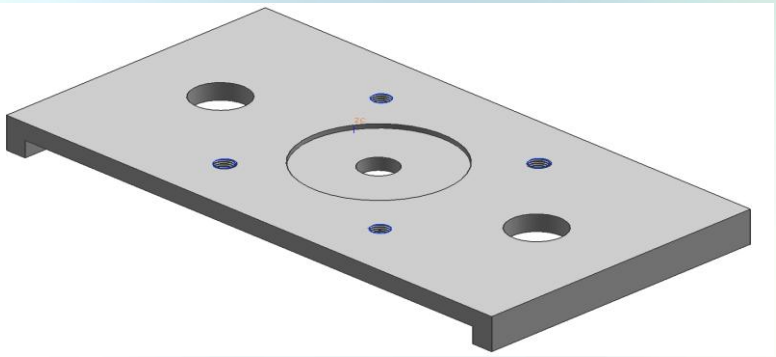

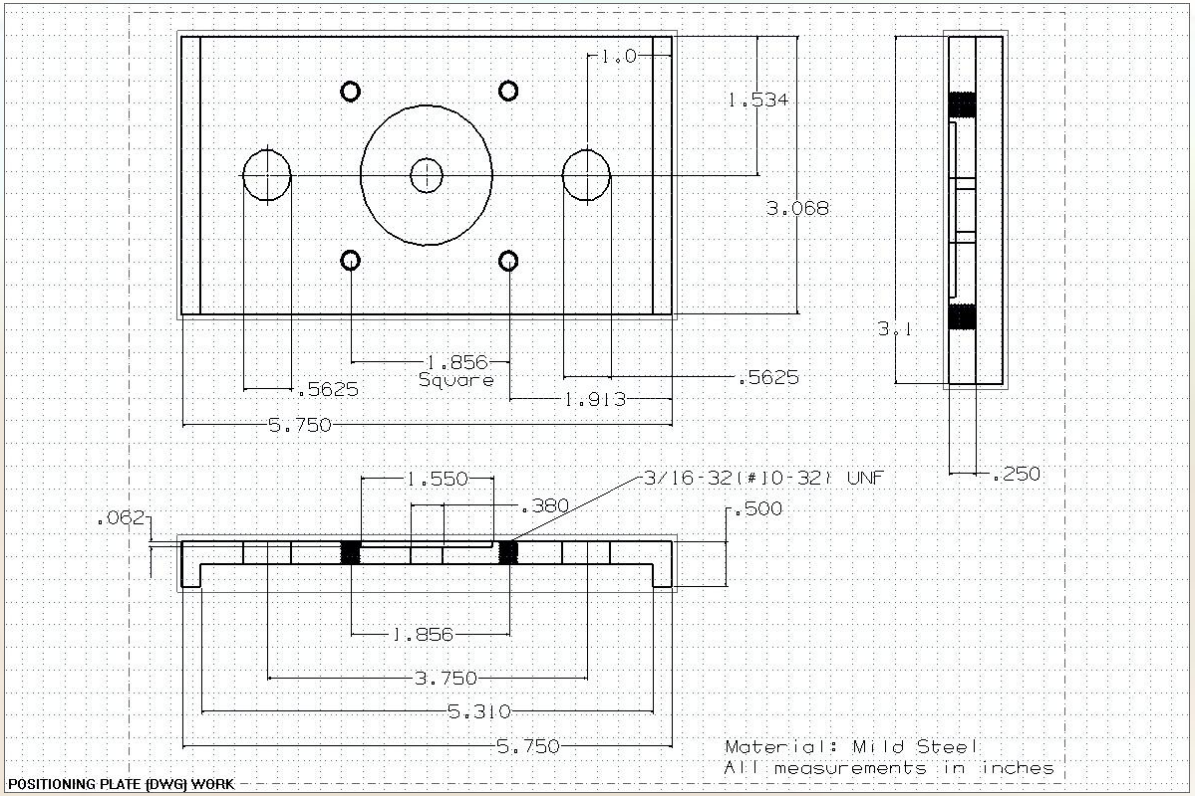
1.0
1.534
3.068
3.1
.250
1.856
Square
.5625
.5625
1.913
5.750
1.550
.380
3/16-32(#10-32) UNF
.062
.500
1.856
3.750
5.310
5.750
Material: Mild Steel
All measurements in inches
POSITIONING PLATE (DWG) WORK

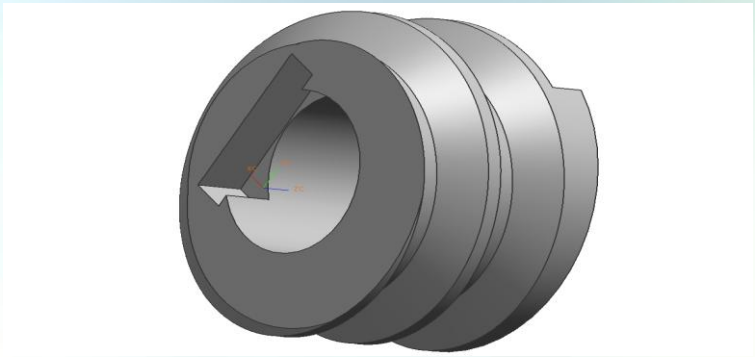

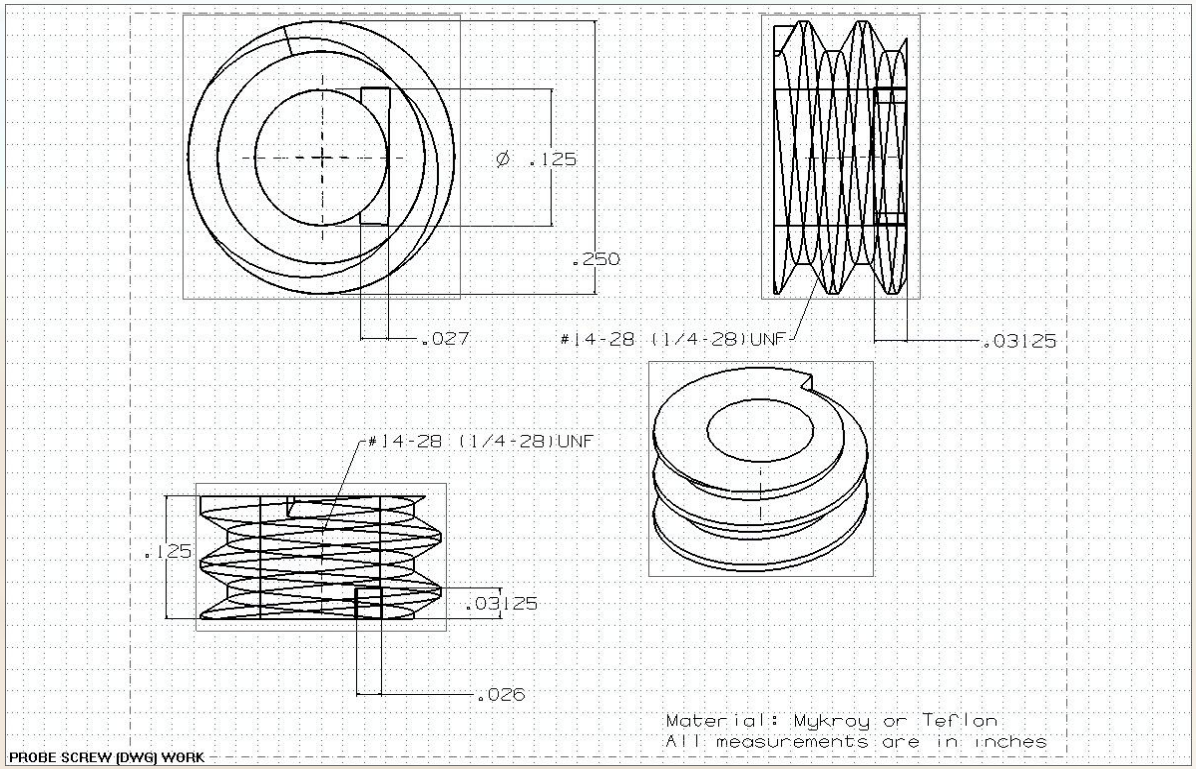
Ø .125
.250
.027
#14-28 (1/4-28)UNF
.03125
#14-28 (1/4-28)UNF
.125
.03125
.026
Material: Mykroy or Teflon
All measurements are in inches
PROBE SCREW (DWG) WORK

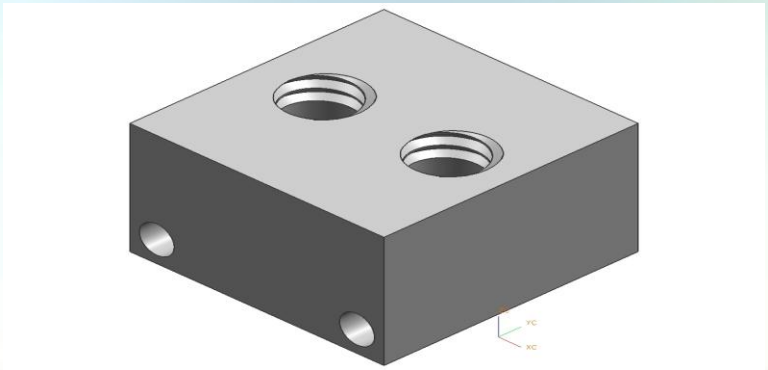

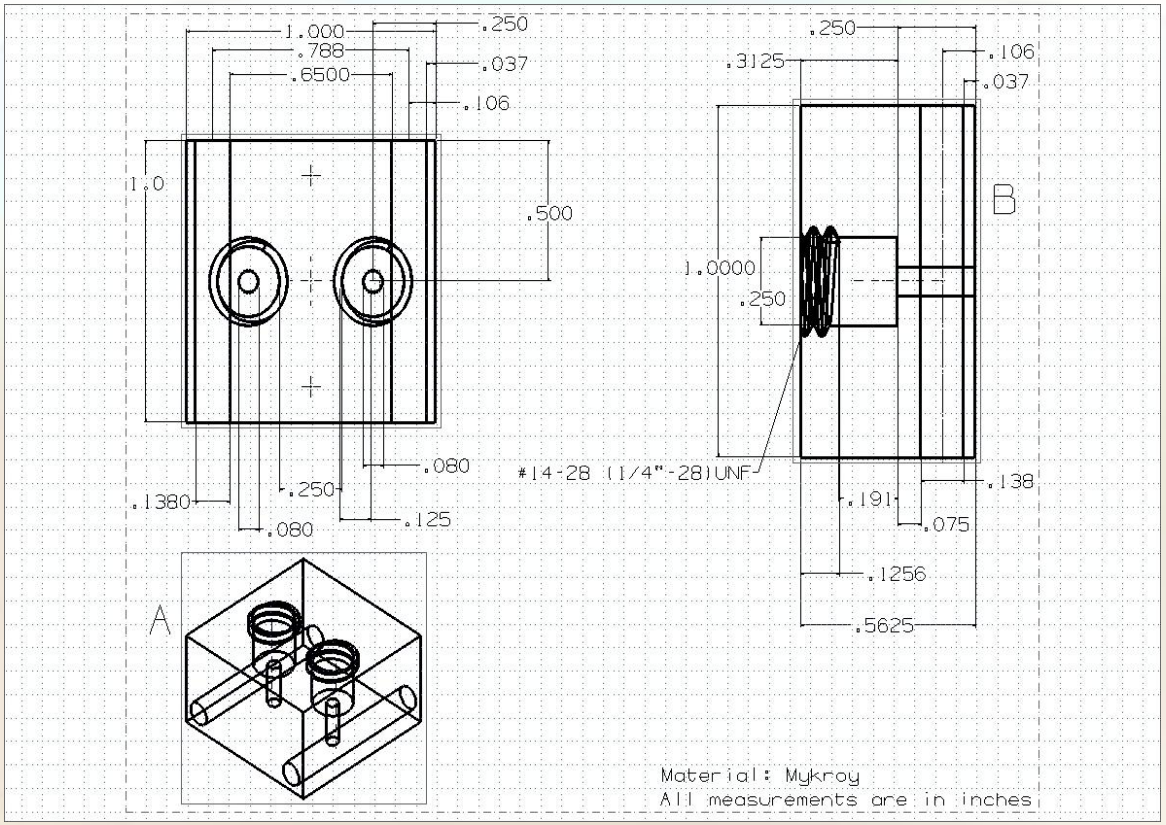
1.000
.788
.6500
.250
.037
.106
1.0
.500
.080
.1380
.250
.080
.125
A
.250
.3125
.106
.037
B
1.0000
.250
#14-28 (1/4"-28)UNF
.138
.191
.075
.1256
.5625
Material: Mykroy
All measurements are in inches

Linear Motor Specifications

Mechanical Specifications - Dimensions in Inches (mm)

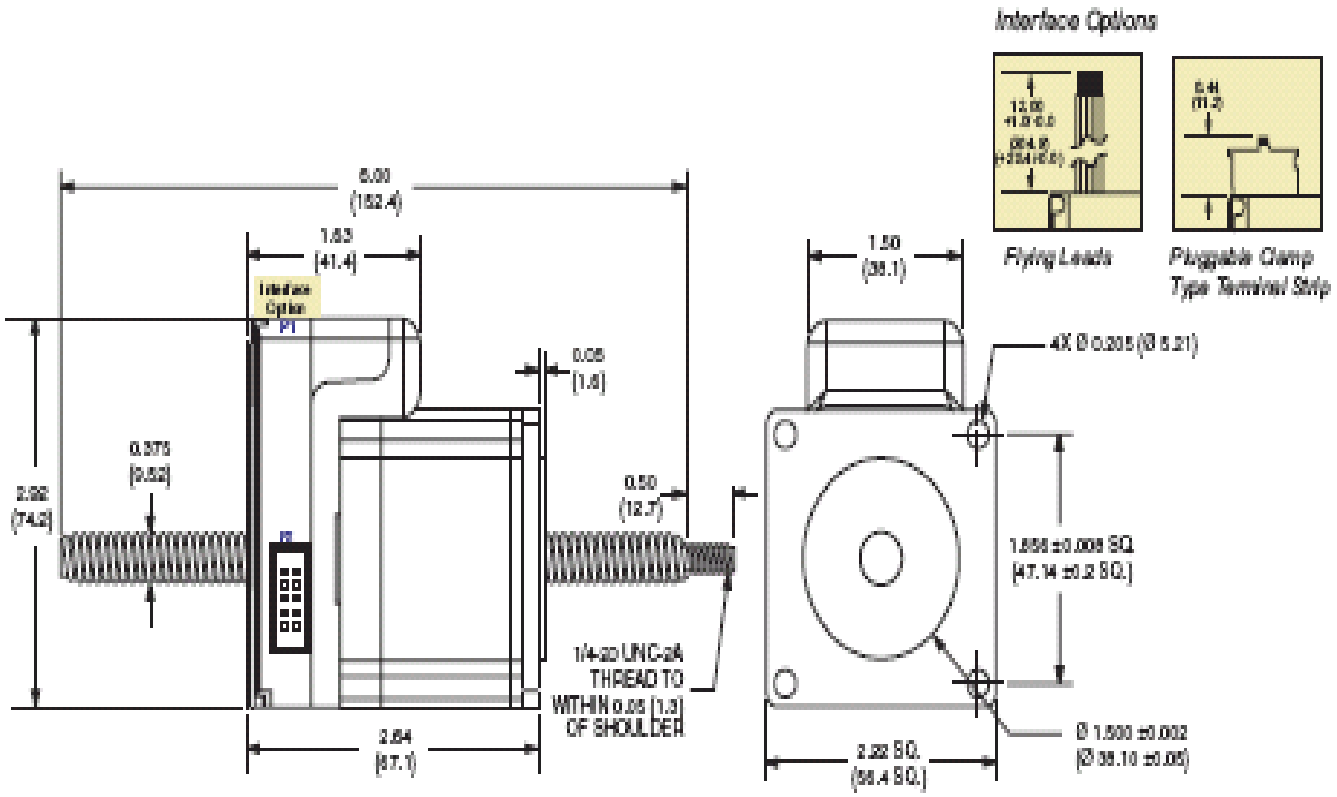

Figure 1.10: Linear Actuator MDrive23 Motion Control Mechanical Specifications

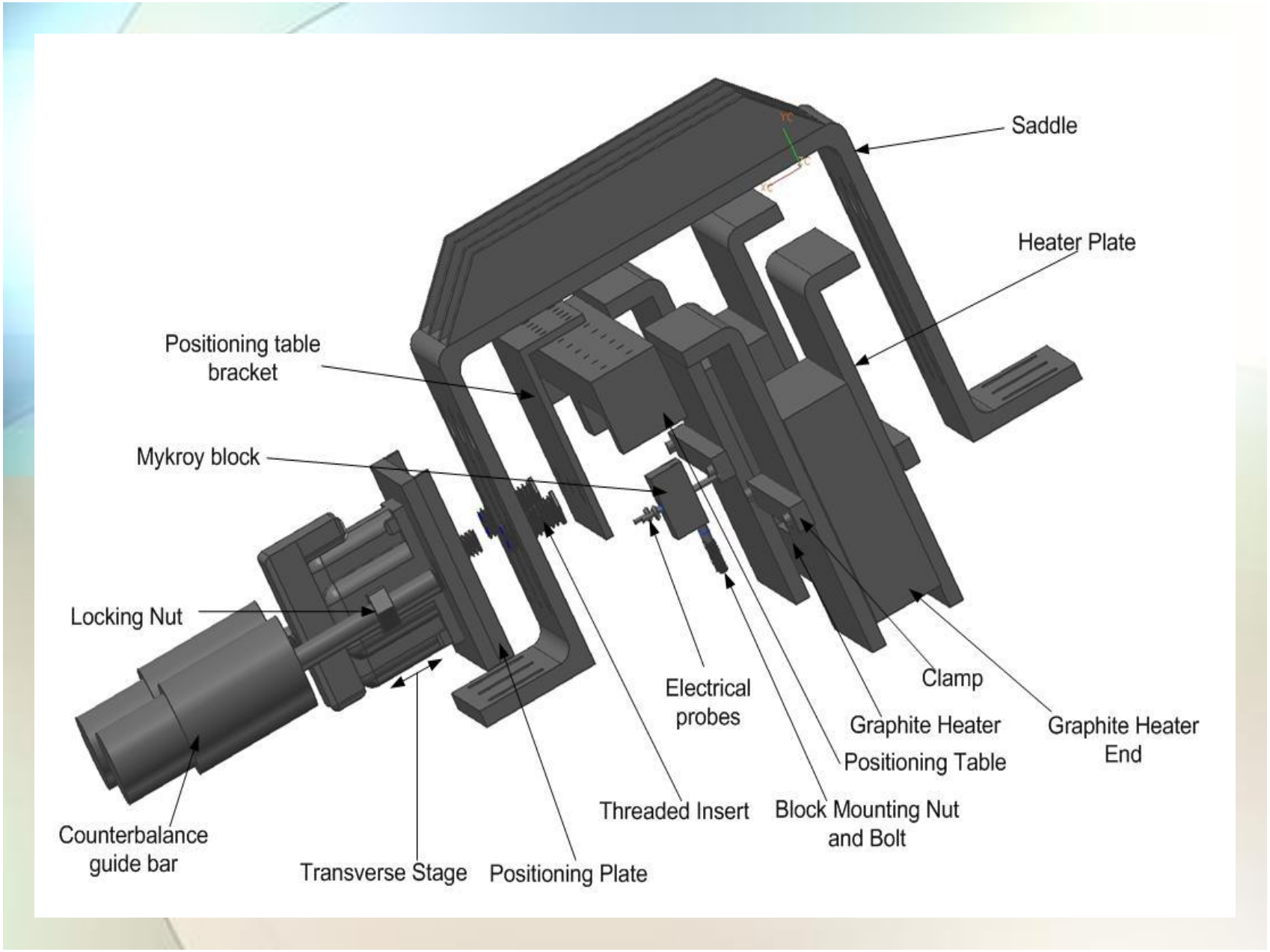
Saddle
Heater Plate
Positioning table bracket
Mykroy block
Locking Nut
Electrical probes
Clamp
Graphite Heater
Graphite Heater End
Positioning Table
Threaded Insert
Block Mounting Nut and Bolt
Counterbalance guide bar
Transverse Stage
Positioning Plate

FABRICATION

HARDWARE

Although this system has quite a few parts, most components were either ready-made or were sent to a machine shop to be fabricated. There were only a few that were made in-house which included: the inserts, linear actuator mounting bolts and the probe screw.

SOFTWARE

The digital multimeter (DMM) software was self-installing software (meaning that once the CD was placed in the CD drive, it proceeded to install with little or no entries from the computer user). The control software for the motors, however, took a lot more time and required installation as well as configuration in order to work correctly. The next page is a sample installation and configuration process introduction for the IMS motion control software.

SECTION 2.2

MDrive Motion Control Software Introduction

Section Overview

This section will acquaint the user with basics of MDrive Motion Control Programming

- Installing IMS Terminal Software
- Upgrading the MDrive Firmware
- The MDrive Program

Installing and Using IMS Terminal Software

System Requirements

- IBM Compatible PC.
- Windows 9x (95/98) or Windows NT (Windows NT4.0 SP6, Windows 2000 SP1, Windows XP)
- 10 MB hard drive space.
- A free serial communications port.

Installation

The IMS Terminal Software is a programming/communications interface. This program was created by IMS to simplify programming and upgrading the MDrive Motion Control. The IMS Terminal Software is also necessary to upgrade the firmware in your MDrive Motion Control. These updates will be posted to the IMS web site at www.imshome.com as they are made available.

To install the IMS Terminal Software onto your hard drive, insert the IMS Product CD into your CD-ROM Drive. The CD should autostart to the IMS Main Index Page. If the CD does not autostart, click "Start > Run" and type "x:\IMS.exe" in the "Open" box and click OK.

NOTE: "x" is your CD ROM drive letter.

Figure 2.16: IMS CD Main Index Page

1) The IMS Main Index Page will be displayed.
2) Place your mouse pointer over the MDrive Icon. The text message "MDrive Integrated Motor & Electronics" will be displayed. This verifies you have selected the correct software.
3) Click the MDrive Motor Icon. This opens the MDrive Index Page.

APPENDIX C: DESIGN AND FABRICATION OF A HELICAL WIRE INSERT FOR A MONOBLOCK TEST SECTION

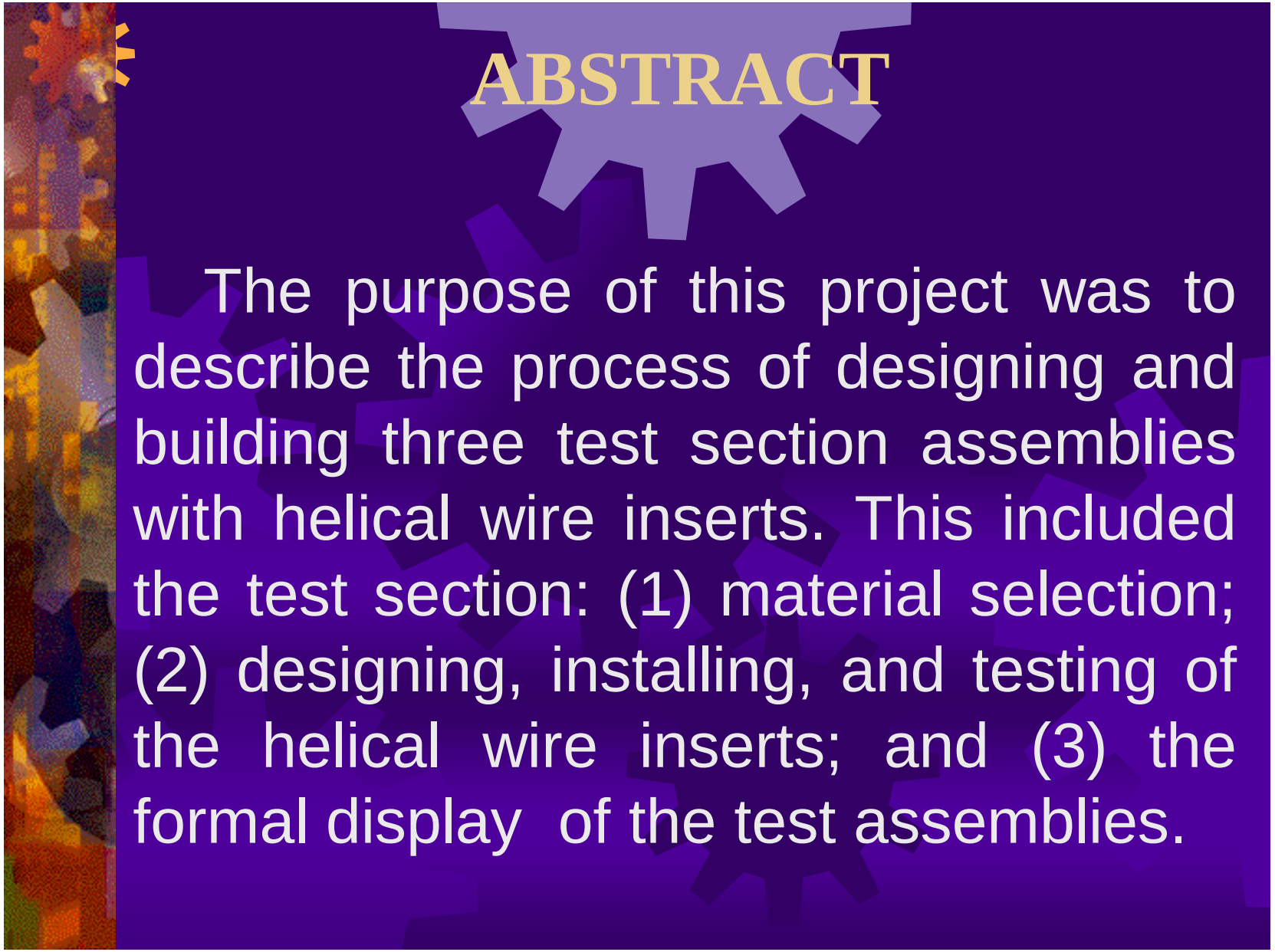
ABSTRACT
The purpose of this project was to describe the process of designing and building three test section assemblies with helical wire inserts. This included the test section: (1) material selection; (2) designing, installing, and testing of the helical wire inserts; and (3) the formal display of the test assemblies.

INTRODUCTION

Critical heat flux (CHF) refers to the heat transfer limit causing a sudden decrease in the transfer coefficient and possible catastrophic failure of a device in which evaporation or boiling is occurring, forming an insulating layer of vapor between a surface and coolant. The test section being studied in the Thermal Science Research Center is a cylindrical-like copper tube with a gun-drilled channel, through which flows a two-phase water mixture (coolant). The purpose of the test section is to remove heat from a high heat flux (HHF) surface to the coolant. Heat transfer-enhancing devices, like turbulence promoters (e.g., helical wire inserts (HWI), and swirl tape inserts (STI)), are being used in some heat exchanger equipment in the nuclear and process industries. They are used with the purpose of increasing the heat removal ratios from a HHF surface. HWI or STI can enhance CHF and is attractive because of increased high heat flux removal at low cost, a minimum of additional machining, and the inserts can be integrated into test sections that are already fabricated.

GOALS/OBJECTIVES

This project involves:

1. Designing and building HWIs for existing test sections and making production drawings of the designs;
2. Researching methodologies of HWI fabrication and installation so that mechanical properties of test sections remain intact;
3. Researching and soliciting bids from companies; and,
4. Monitoring the production of the HWI- test section (TS) to assure the integrity of the HWI-TS.

HWI MONOBLOCK TEST SECTION FABRICATION

- Background

Fabrication of the monoblock TS includes placing helical wire inserts into the TS cooling channel. To determine the preferred size helical wire insert and pitch, two bare copper mockups were fabricated with 1.0 mm and 1.5 mm diameter (dia.) wire. Each diameter wire insert had two pitches extending half of the length of the channel, 5 mm and 10 mm for the 1 mm dia. and 10 mm and 20 mm for the 1.5 dia. wire. Inconel was selected as the material for the wire so that the future HWI experiments could be used to expand HHF data found in the technical literature.

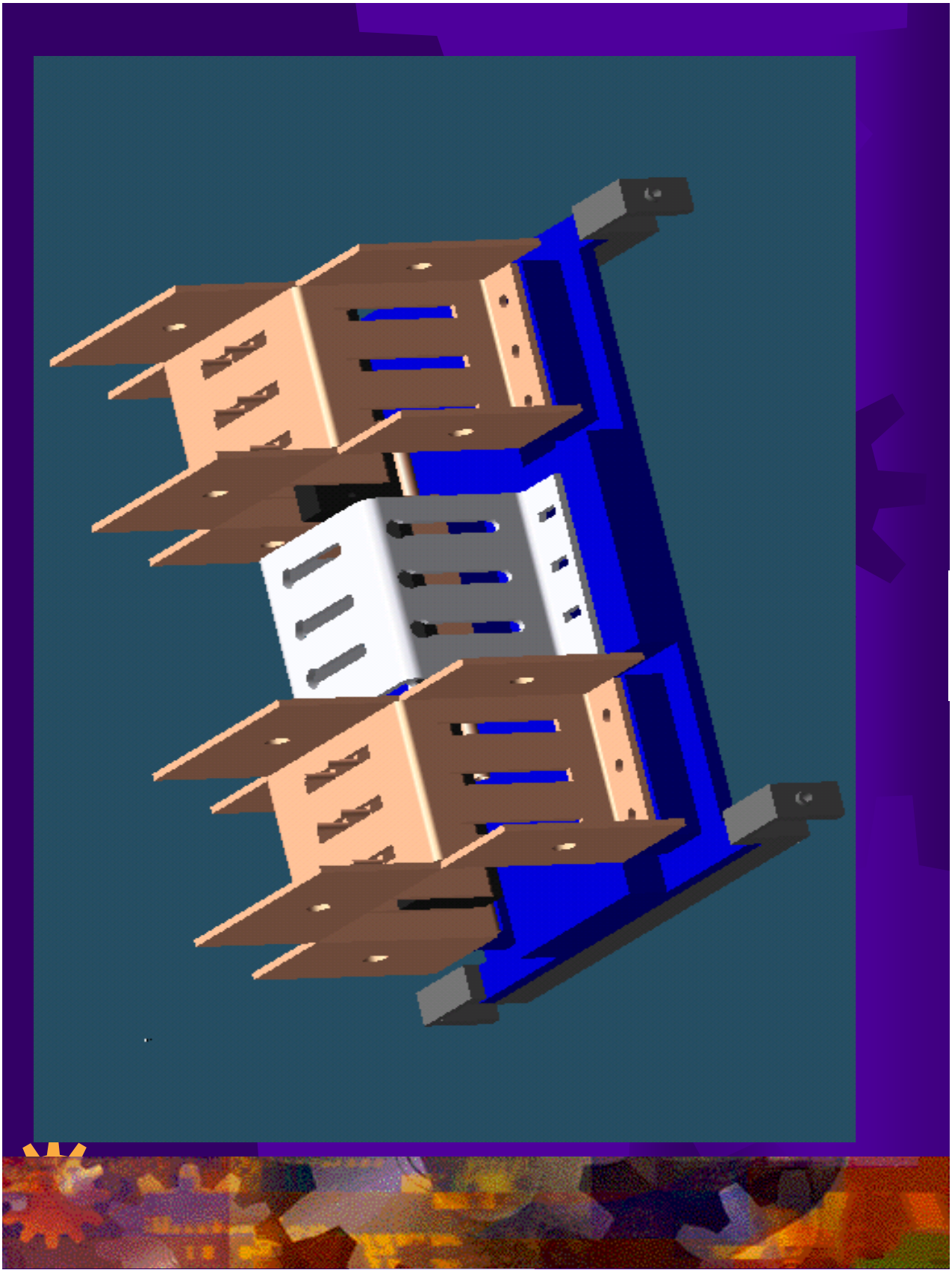

Braze Selection

The Cu-Mn-Ni brazing alloy (67.5Cu-23.5Mn-9Ni) was used by other investigators for its resistance to chemical corrosion and oxidation and corrosion caused by water. The Cu-Mn-Ni alloy could not be found for the present work. However, a more common brass alloy (65Cu-35Zn) that contained the same properties was available in most welding supply shops in the form of .01x3x10 (0.254 mm x 76.2 mm x 254 mm) inch sheets.

Melting Point Measurement

The vendor reported the melting temperature of this brass alloy to be 649.0 °C. To insure precision, a 1/4x12x.015 (6.35 mm x 304.8 mm x 0.381 mm) inch piece was purchased. From this piece, three small samples were cut. These samples were placed on a heating plate in three separate tests to verify the melting temperature. The resulting averaged measurement was 647.0 °C.

TO POWER SUPPLY
0 - 250 DC
DRAWN OUT OF SCALE
THERMAL SCIENCE RESEARCH CENTER
PRAIRIE VIEW A&M
AUTHOR: R.J. MARTIN
DIRECTOR: Dr. RONALD BOYD
TEST SECTION

➢ Monoblock Material Properties

The monoblock is made of Glidcop Al-15, an aluminum dispersion-strengthened copper. The melting point of Glidcop and copper are the same (1083° C). However, unlike copper, Glidcop shows no permanent deformation until it nears the melting point. Glidcop has a yield stress of 45000 psi .

➢ Brazing Process

The brass alloy shims were rolled into tubes of the same diameter as the cooling tube. They were coated with brazing flux and inserted into the cooling tube. The inconel HWI was then placed into the brass tubes. The entire setup was placed into a vacuum furnace and heated to the melting temperature of the brass alloy for a duration of five minutes. This process successfully brazed the interior of the cooling tube.

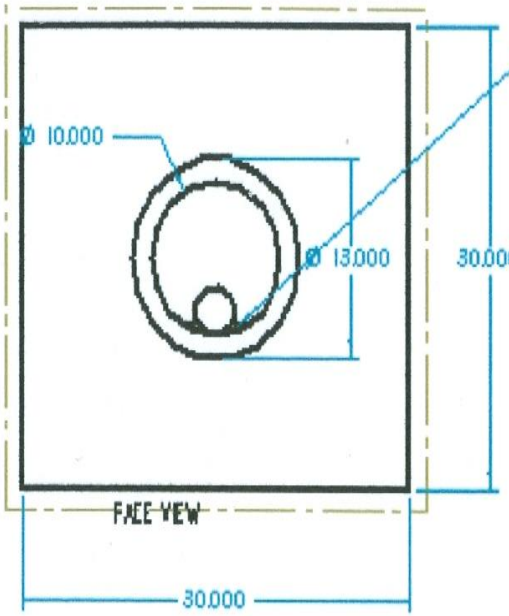

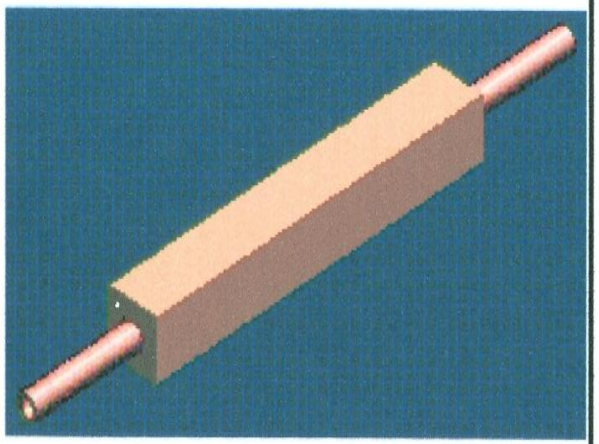

HWI: Inconel – 600
Braze Material : 65 Cu – 35 Zn

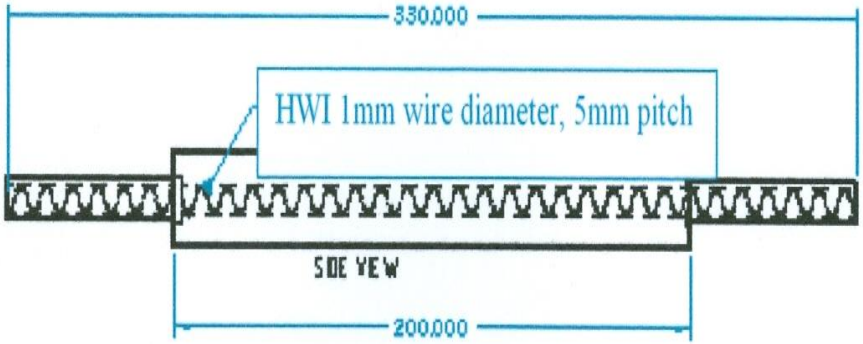

CONCLUSIONS

- Unique and new test beds were redesigned and produced for the monoblock test section.
- Detailed and assembly test section and test set-up illustrations have been completed.
- The procedure and final preparation for HWI installation in a second monoblock test section was successfully tested both non-destructively and destructively.